

**NIST Special Publication 1018-2**  
**Sixth Edition**

**Fire Dynamics Simulator  
Technical Reference Guide  
Volume 2: Verification**

Kevin McGrattan  
Simo Hostikka  
Jason Floyd  
Randall McDermott  
Marcos Vanella  
Eric Mueller

<http://dx.doi.org/10.6028/NIST.SP.1018>



**Fire Safety Research Institute**  
A UL Research Institute

**NIST**  
**National Institute of  
Standards and Technology**  
U.S. Department of Commerce



**NIST Special Publication 1018-2**  
**Sixth Edition**

**Fire Dynamics Simulator  
Technical Reference Guide  
Volume 2: Verification**

Kevin McGrattan  
Randall McDermott  
Marcos Vanella  
Eric Mueller

*Fire Research Division, Engineering Laboratory, Gaithersburg, Maryland*

Simo Hostikka  
*Aalto University, Espoo, Finland*

Jason Floyd  
*Fire Safety Research Institute, UL Research Institutes, Columbia, Maryland*

<http://dx.doi.org/10.6028/NIST.SP.1018>

April 8, 2024  
Revision: FDS-6.9.1-0-g889da6a



U.S. Department of Commerce  
*Gina M. Raimondo, Secretary*

National Institute of Standards and Technology  
*Laurie E. Locascio, NIST Director and Undersecretary of Commerce for Standards and Technology*

Certain commercial entities, equipment, or materials may be identified in this document in order to describe an experimental procedure or concept adequately. Such identification is not intended to imply recommendation or endorsement by the National Institute of Standards and Technology, nor is it intended to imply that the entities, materials, or equipment are necessarily the best available for the purpose.

**National Institute of Standards and Technology Special Publication 1018-2**  
**Natl. Inst. Stand. Technol. Spec. Publ. 1018-2, 316 pages (October 2013)**  
**CODEN: NSPUE2**

# FDS Developers

The Fire Dynamics Simulator and Smokeview are the products of an international collaborative effort led by the National Institute of Standards and Technology (NIST) and Fire Safety Research Institute, UL Research Institutes. Its developers and contributors are listed below.

## Principal Developers of FDS

Kevin McGrattan, NIST, Gaithersburg, Maryland

Simo Hostikka, Aalto University, Espoo, Finland

Jason Floyd, Fire Safety Research Institute, UL Research Institutes, Columbia, Maryland

Randall McDermott, NIST, Gaithersburg, Maryland

Marcos Vanella, NIST, Gaithersburg, Maryland

Eric Mueller, NIST, Gaithersburg, Maryland

## Principal Developer of Smokeview

Glenn Forney, NIST, Gaithersburg, Maryland

## Collaborators and Contributors

Anthony Hamins, NIST, Gaithersburg, Maryland

Jonathan Hodges, Jensen Hughes, Blacksburg, Virginia

Emanuele Gissi, Corpo Nazionale dei Vigili del Fuoco, Italy

William Mell, U.S. Forest Service, Seattle, Washington

Julio Cesar Silva, Rio on Fire, Orlando, Florida

Craig Weinschenk, Fire Safety Research Institute, UL Research Institutes, Columbia, Maryland



# About the Developers

**Kevin McGrattan** is a mathematician in the Fire Research Division of NIST. He received a bachelor of science degree from the School of Engineering and Applied Science of Columbia University in 1987 and a doctorate at the Courant Institute of New York University in 1991. He joined the NIST staff in 1992 and has since worked on the development of fire models, most notably the Fire Dynamics Simulator.

**Simo Hostikka** is an associate professor of fire safety engineering at Aalto University School of Engineering, since January 2014. Before joining Aalto, he worked as a Principal Scientist and Team Leader at VTT Technical Research Centre of Finland. He received a master of science (technology) degree in 1997 and a doctorate in 2008 from the Department of Engineering Physics and Mathematics of the Helsinki University of Technology. He is the principal developer of the radiation and solid phase sub-models within FDS.

**Jason Floyd** is a Lead Research Engineer at the Underwriters Laboratories Fire Safety Research Institute in Columbia, Maryland. He received a B.S. (1993), M.S. (1995), and a Ph.D. (2000) from the Nuclear Engineering Program of the University of Maryland. After graduating, he was awarded a National Research Council Post-Doctoral Fellowship at the Building and Fire Research Laboratory of NIST. He is a principal developer of the combustion, control logic, aerosol, droplet evaporation, and HVAC sub-models within FDS.

**Randall McDermott** joined the Fire Research Division at NIST in 2008. He received a B.S. from the University of Tulsa in Chemical Engineering in 1994 and a Ph.D. from the University of Utah in 2005. His research interests include subgrid-scale models and numerical methods for large-eddy simulation, turbulent combustion, immersed boundary methods, and Lagrangian particle methods.

**Marcos Vanella** joined the Fire Research Division at NIST in 2019. He received diplomas in Mechanical and Aeronautical Engineering from the National University of Cordoba, Argentina, and M.S. and Ph.D. degrees in Mechanical Engineering from the University of Maryland, College Park. His research interests include computer simulation and scientific software development applied to engineering systems, mainly in the areas of fluid flow and multiphysics interaction problems.

**Glenn Forney** is a computer scientist in the Fire Research Division of NIST. He received a bachelor of science degree in mathematics from Salisbury State College and a master of science and a doctorate in mathematics from Clemson University. He joined NIST in 1986 (then the National Bureau of Standards) and has since worked on developing tools that provide a better understanding of fire phenomena, most notably Smokeview, an advanced scientific software tool for visualizing Fire Dynamics Simulation data.

**Eric Mueller** joined the Fire Research Division at NIST in 2021. He received a B.S. in Engineering Physics from Tufts University (2010), an M.S. from Worcester Polytechnic Institute (2012), and a Ph.D. from the University of Edinburgh (2017), both in fire safety engineering. His research interests include the

development of sub-models relevant to heat and mass transfer in wildland and wildland-urban interface fires.

**Emanuele Gissi** is a professional fire chief of the Italian Fire and Rescue Service (CNVVF) since 2002. He received a Ph.D. in Engineering Physics from the University of Ancona, Italy, in 2000. In addition to managing fire brigades, his main interest is bridging the gap between fire research and fire safety engineering practice. He develops open source tools for FDS.

**Anthony Hamins** joined the Fire Research Division at NIST in 1989. He received his B.S. from the University of California, Berkeley, in Physics and is Ph.D. from U.C. San Diego in Engineering Physics in 1985. His research interests include fire model validation, fire dynamics, heat and mass transfer processes in fires of multiple scales, fire suppression, flame structure, wildland-urban interface fires, and micro-gravity combustion.

**Jonathan Hodes** is a Lead Engineer in the Research, Development, Testing, and Evaluation Division at Jensen Hughes in Blacksburg, Virginia. He received a B.S. (2012) and M.S. (2014) from Clemson University and Ph.D. (2018) from Virginia Tech in Mechanical Engineering. His research interests include compartment fire dynamics, heat transfer from fires to surfaces, predicting fire growth, wildland-urban interface fires, and the intersection of physics modeling and artificial intelligence.

**William (Ruddy) Mell** is an applied mathematician currently at the U.S. Forest Service in Seattle, Washington. He holds a B.S. degree from the University of Minnesota (1981) and doctorate from the University of Washington (1994). His research interests include the development of large-eddy simulation methods and sub-models applicable to the physics of large fires in buildings, vegetation, and the wildland-urban interface.

**Julio Cesar Silva** is a Lead Researcher at Rio on Fire. He worked in the Fire Research Division of NIST as a Guest Researcher from National Council for Scientific and Technological Development, Brazil. He received a M.Sc. in 2010 and a doctorate in 2014 from Federal University of Rio de Janeiro in Civil Engineering. His research interests include fire-structure interaction and he develops coupling strategies between FDS and finite-element codes.

**Craig Weinschenk** is a Lead Research Engineer at the Underwriters Laboratories Fire Safety Research Institute, in Columbia, Maryland. He worked in the Fire Research Division at NIST as a National Research Council Postdoctoral Research Associate in 2011. He received a B.S. from Rowan University in 2006 in Mechanical Engineering. He received an M.S. in 2007 and a doctorate in 2011 from The University of Texas at Austin in Mechanical Engineering. His research interests include numerical combustion, fire-structure interaction, and human factors research of fire-fighting tactics.

# Preface

This is Volume 2 of the FDS Technical Reference Guide [1]. Volume 1 describes the mathematical model and numerical method. Volume 3 documents past and present experimental validation work. Instructions for using FDS are contained in a separate User’s Guide [2].

The three volumes of the FDS Technical Reference Guide are based in part on the “Standard Guide for Evaluating the Predictive Capability of Deterministic Fire Models,” ASTM E 1355 [3]. ASTM E 1355 defines *model evaluation* as “the process of quantifying the accuracy of chosen results from a model when applied for a specific use.” The model evaluation process consists of two main components: verification and validation. *Verification* is a process to check the correctness of the solution of the governing equations. Verification does not imply that the governing equations are appropriate; only that the equations are being solved correctly. *Validation* is a process to determine the appropriateness of the governing equations as a mathematical model of the physical phenomena of interest. Typically, validation involves comparing model results with experimental measurement. Differences that cannot be explained in terms of numerical errors in the model or uncertainty in the measurements are attributed to the assumptions and simplifications of the physical model.

Evaluation is critical to establishing both the acceptable uses and limitations of a model. Throughout its development, FDS has undergone various forms of evaluation. This volume provides a survey of verification work conducted to date to evaluate FDS.



# **Disclaimer**

The US Department of Commerce makes no warranty, expressed or implied, to users of the Fire Dynamics Simulator (FDS), and accepts no responsibility for its use. Users of FDS assume sole responsibility under Federal law for determining the appropriateness of its use in any particular application; for any conclusions drawn from the results of its use; and for any actions taken or not taken as a result of analysis performed using these tools.

Users are warned that FDS is intended for use only by those competent in the fields of fluid dynamics, thermodynamics, heat transfer, combustion, and fire science, and is intended only to supplement the informed judgment of the qualified user. The software package is a computer model that may or may not have predictive capability when applied to a specific set of factual circumstances. Lack of accurate predictions by the model could lead to erroneous conclusions with regard to fire safety. All results should be evaluated by an informed user.

Throughout this document, the mention of computer hardware or commercial software does not constitute endorsement by NIST, nor does it indicate that the products are necessarily those best suited for the intended purpose.



# Acknowledgments

The following individuals contributed to the verification process of FDS.

- Chris Lautenberger and Carlos Fernandez-Pello contributed the “two-reaction” test case.
- Matthias Münch of the Freie Universität Berlin provided useful test cases for the basic flow solver.
- Clara Cruz, a student at the University of Puerto Rico and Summer Undergraduate Research Fellow at NIST, helped develop useful Matlab scripts to automate the process of compiling this guide.
- Bryan Klein, now at Thunderhead Engineering, developed the source code version control system that is an essential part of the verification process.
- Joonas Ryyränen of VTT, Finland, designed and documented the FED/FIC test cases.
- Max Gould, Summer Undergraduate Research Fellow, helped develop and produce the “2D Vortex” test case.
- Howard Baum, NIST Fellow Emeritus, contributed the analytical solution “Collapse of a Hot Layer in a Micro-gravity Environment”.
- Tony Saad and James Sutherland of the University of Utah developed an analysis for temporal order of accuracy for variable-density projection schemes.
- Chao Zhang of Tongji University provided the finite-element analysis for the HT3D I-beam test case.
- Salah Benkorichi of Ulster University, Belfast, developed the HT3D sphere test case.
- Kiyoung Moon and Jung-il Choi of Yonsei University, Seoul, South Korea, provided the Heat Channel Flow case.
- Jesus Alberto Mejias Tuni of Politecnico di Torino provided the 1-D tunnel cases with heat release.
- Morteza Gholami Haghghi Fard of Aalto University, Finland, contributed to the development of 3-D pyrolysis.
- Jonathan Hodges of Jensen Hughes developed the FED for a moving particle test case.



# Contents

<b>FDS Developers</b>	i
<b>About the Developers</b>	iii
<b>Preface</b>	v
<b>Disclaimer</b>	vii
<b>Acknowledgments</b>	ix
<b>Contents</b>	xi
<b>List of Figures</b>	xix
<b>List of Tables</b>	xxvii
<b>1 What is Verification?</b>	1
<b>2 Survey of Past Verification Work</b>	3
2.1 Analytical Tests . . . . .	3
2.2 Numerical Tests . . . . .	4
2.3 Sensitivity Analysis . . . . .	5
2.3.1 Grid Sensitivity . . . . .	5
2.3.2 Sensitivity of Large Eddy Simulation Parameters . . . . .	7
2.3.3 Sensitivity of Radiation Parameters . . . . .	7
2.3.4 Sensitivity of Thermophysical Properties of Solid Fuels . . . . .	8
2.4 Code Checking . . . . .	9
<b>3 The Basic Flow Solver</b>	11
3.1 Analytical Solution to the Navier-Stokes Equation ( <code>ns2d</code> ) . . . . .	11
3.2 Analytical Solution to the Continuity Equation . . . . .	14
3.2.1 Pulsating 1-D solution . . . . .	14
3.2.2 Pulsating 2-D solution ( <code>pulsating</code> ) . . . . .	15
3.2.3 Stationary compression wave in 1-D . . . . .	16
3.2.4 Stationary compression wave in 2-D ( <code>compression_wave</code> ) . . . . .	16
3.3 Scalar Transport . . . . .	18
3.3.1 Uniform Velocity Field ( <code>move_slug</code> ) . . . . .	18
3.3.2 Solid Body Rotation Velocity Field ( <code>soborot</code> ) . . . . .	20
3.4 Temporal Error Analysis for a Variable-Density Projection ( <code>saad</code> ) . . . . .	23
3.5 Variable-Density Manufactured Solution ( <code>shunn3</code> ) . . . . .	24

3.6	Collapse of a Hot Layer in a Micro-gravity Environment ( <code>hot_layer_360</code> ) . . . . .	28
3.7	2-D Vortex Simulation ( <code>vort2d</code> ) . . . . .	30
3.8	Boundedness Tests . . . . .	33
3.8.1	Species Bounds ( <code>bound_test_*</code> ) . . . . .	33
3.8.2	Isothermal Helium Wave ( <code>helium_1d_isothermal</code> ) . . . . .	34
3.8.3	Temperature Bounds for Isothermal Helium Jet ( <code>helium_air_jet_floor</code> ) . . . . .	34
3.8.4	Temperature Bounds for Large Differences in Molecular Weight ( <code>mwtest_cfl</code> ) . . . . .	35
3.8.5	Temperature Lower Bound in a Fire Simulation ( <code>tmp_lower_limit</code> ) . . . . .	36
3.9	Constant Specific Heat Ratio . . . . .	37
3.9.1	Helium Wave using Constant Specific Heat Ratio ( <code>helium_1d_const_gamma</code> ) . . . . .	37
3.9.2	Fire Plume using Constant Specific Heat Ratio ( <code>fire_const_gamma</code> ) . . . . .	38
3.9.3	Evaporation with Constant Specific Heat Ratio ( <code>water_evap_1_const_gamma</code> )	39
3.10	Tunnel Flow . . . . .	40
3.10.1	1-D Flow in a Tunnel ( <code>tunnel_const_gamma</code> ) . . . . .	40
3.10.2	1-D Flow in a Tunnel ( <code>tunnel_linear_cp</code> ) . . . . .	42
<b>4</b>	<b>Turbulence</b>	<b>45</b>
4.1	Decaying Isotropic Turbulence . . . . .	45
4.1.1	Constant Smagorinsky ( <code>csmag</code> ) . . . . .	45
4.1.2	Dynamic Smagorinsky ( <code>dsmag</code> ) . . . . .	47
4.1.3	Deardorff ( <code>deardorff</code> ) . . . . .	48
4.1.4	Vreman ( <code>vreman</code> ) . . . . .	49
4.1.5	WALE ( <code>wale</code> ) . . . . .	49
4.2	Jet Centerline Velocity Decay ( <code>jet</code> ) . . . . .	53
<b>5</b>	<b>Boundary Effects</b>	<b>55</b>
5.1	The FDS Moody Chart ( <code>poiseuille,moody,z0</code> ) . . . . .	55
5.1.1	Laminar Results . . . . .	55
5.1.2	Turbulent Results . . . . .	56
5.2	Blasius boundary layer ( <code>blasius</code> ) . . . . .	58
5.3	Pohlhausen thermal boundary layer ( <code>Pohlhausen</code> ) . . . . .	60
5.4	Near-Wall Grid Resolution ( <code>yplus</code> ) . . . . .	61
5.5	Heated Channel Flow ( <code>heated_channel</code> ) . . . . .	61
5.6	Forced Convection Flat Plate Boundary Layer ( <code>forced_conv_flat_plate</code> ) . . . . .	63
5.7	Natural Convection . . . . .	66
5.7.1	Horizontal Plate ( <code>nat_conv_hot_plate</code> ) . . . . .	66
5.7.2	Horizontal Enclosure ( <code>natconh</code> ) . . . . .	67
5.7.3	Vertical Enclosure ( <code>natconv</code> ) . . . . .	68
5.7.4	Sphere ( <code>free_conv_sphere</code> ) . . . . .	69
5.8	Impinging Jet ( <code>impinging_jet</code> ) . . . . .	70
5.9	Ribbed Square Duct Flow ( <code>ribbed_channel</code> ) . . . . .	72
5.9.1	Cartesian Geometry . . . . .	72
5.9.2	Complex Geometry . . . . .	74
<b>6</b>	<b>Atmospheric Flows</b>	<b>77</b>
6.1	Monin-Obukhov Similarity Profiles ( <code>MO_velocity_profile</code> ) . . . . .	77
6.2	Ekman Layers ( <code>ekman_</code> ) . . . . .	77

<b>7 Mass and Energy Conservation</b>	<b>81</b>
7.1 Mass Conservation . . . . .	81
7.1.1 Flow of a Gas through a Simple Duct ( <code>simple_duct</code> ) . . . . .	81
7.1.2 Species Mass Flux ( <code>species_conservation</code> ) . . . . .	81
7.1.3 Mass Flux through Domain Boundaries ( <code>mass_flux_wall</code> ) . . . . .	82
7.1.4 Mass Balance on a Gas Control Volume ( <code>mass_balance_gas_volume</code> ) . . . . .	84
7.1.5 Mass Balance for Species in a Reacting Flow ( <code>mass_balance_reac</code> ) . . . . .	84
7.1.6 Checking the Equation of State ( <code>particle_offgas</code> ) . . . . .	85
7.1.7 Realizability of Species Mass Fractions ( <code>realizable_mass_fractions</code> ) . . . . .	85
7.1.8 Integral Mass Test for Complex Geometry ( <code>geom_mass_file_test</code> ) . . . . .	85
7.2 Energy Conservation . . . . .	89
7.2.1 The Heat from a Fire ( <code>energy_budget</code> ) . . . . .	89
7.2.2 Gas Injection via an Isentropic Process ( <code>isentropic</code> ) . . . . .	89
7.2.3 Gas Injection via a Non-Isentropic Process ( <code>isentropic2</code> ) . . . . .	90
7.2.4 Mixing Gases ( <code>energy_budget_dns</code> ) . . . . .	92
7.2.5 Mixing with Variable Specific Heats ( <code>energy_budget_tmix</code> ) . . . . .	93
7.2.6 Combustion Chamber ( <code>energy_budget_combustion</code> ) . . . . .	93
7.2.7 Solid phase energy conservation ( <code>energy_budget_solid</code> ) . . . . .	94
7.2.8 Energy Conservation at Walls ( <code>mass_heat_wall_device_test</code> ) . . . . .	95
7.2.9 Energy Conservation for Solid Particles ( <code>energy_budget_particles</code> ) . . . . .	95
<b>8 Checking for Coding Errors</b>	<b>97</b>
8.1 Symmetry Tests . . . . .	97
8.1.1 Counter-Flowing Jets ( <code>symmetry_test</code> ) . . . . .	97
8.1.2 Fire in a Thin-Walled Pan ( <code>symmetry_test_2</code> ) . . . . .	97
8.1.3 Axial symmetry ( <code>cyl_test</code> ) . . . . .	97
8.2 Velocity boundary condition implementation ( <code>velocity_bc_test</code> ) . . . . .	100
8.3 Checking the divergence constraint . . . . .	101
8.3.1 Isothermal flow ( <code>divergence_test_1</code> ) . . . . .	101
8.3.2 Sealed compartment ( <code>divergence_test_2</code> ) . . . . .	101
8.3.3 Creating/Removing Obstructions ( <code>divergence_test_3</code> ) . . . . .	101
8.4 Multi-mesh Pressure and Temperature Lapse ( <code>lapse_rate</code> ) . . . . .	102
8.5 Randomly Overlapping Meshes ( <code>random_meshes</code> ) . . . . .	103
8.6 Overlapping INIT Regions ( <code>init_overlap</code> ) . . . . .	103
8.7 Spurious Obstruction Effects ( <code>hole</code> ) . . . . .	107
8.8 OpenMP Thread Checking ( <code>race_test</code> ) . . . . .	108
8.9 Multi-Mesh Layer Height Calculation ( <code>layer</code> ) . . . . .	109
8.10 The Restart Feature . . . . .	110
<b>9 Thermal Radiation</b>	<b>111</b>
9.1 Radiation View Factors . . . . .	111
9.1.1 Hot Plate ( <code>plate_view_factor</code> ) . . . . .	111
9.1.2 Plates at a Right Angle ( <code>geom_rad</code> ) . . . . .	111
9.1.3 Plates at a Right Angle, Part 2 ( <code>geom_rad_2</code> ) . . . . .	112
9.2 Radiation inside a Box ( <code>radiation_box</code> ) . . . . .	113
9.3 Radiation from a Polygonal Plate ( <code>radiating_polygon</code> ) . . . . .	114
9.4 Radiation from a Layer of Hot Gas ( <code>radiation_plane_layer</code> ) . . . . .	115
9.5 Wall Internal Radiation ( <code>wall_internal_radiation</code> ) . . . . .	115

9.6	Radiation Emitted by Hot Spheres ( <code>hot_spheres</code> ) . . . . .	116
9.7	Radiation Absorbed by Liquid Droplets ( <code>droplet_absorption</code> ) . . . . .	117
9.8	Consistency of Particle Absorbed Energy and the Radiative Loss Term . . . . .	118
9.9	Radiation Attenuation by Scattering Particles ( <code>part_attenuation</code> ) . . . . .	118
9.10	Radiation Attenuation by Non-Scattering Particles ( <code>radiation_gas-veg_consistency</code> ) . . . . .	119
9.11	Transient Thermocouple Response ( <code>TC_heating</code> ) . . . . .	120
9.12	Radiation and Thermocouples ( <code>TC_view_factor</code> ) . . . . .	121
9.13	Radiation Targets ( <code>target_test</code> ) . . . . .	122
9.14	Radiation Shield ( <code>radiation_shield</code> ) . . . . .	122
9.15	Radiation from a gas-fired panel ( <code>radiation_gas_panel</code> ) . . . . .	123
9.16	Radiation in Angled Geometry ( <code>net_rad_1000</code> ) . . . . .	124
<b>10</b>	<b>Species and Combustion</b>	<b>125</b>
10.1	Gas Properties ( <code>species_props</code> ) . . . . .	125
10.2	Humidity ( <code>humidity</code> ) . . . . .	126
10.3	Product Yields ( <code>methane_flame</code> ) . . . . .	127
10.4	Reaction Rates ( <code>reactionrate</code> ) . . . . .	127
10.4.1	Mixing-Controlled Reactions ( <code>reactionrate_EDC</code> ) . . . . .	128
10.4.2	Finite Rate Reactions ( <code>reactionrate_arrhenius</code> ) . . . . .	133
10.4.3	Fast-Slow Reaction Scheme ( <code>reactionrate_fast_slow</code> ) . . . . .	137
10.5	Heat Release Rates from Reaction Mechanisms ( <code>hrrpuv_reac</code> ) . . . . .	138
10.6	Mixture Fraction ( <code>burke_schumann</code> ) . . . . .	141
10.7	Ideal and Non-Ideal Heat of Combustion ( <code>HoC</code> ) . . . . .	142
10.8	Single Step and Two Step Chemistry Heat of Combustion . . . . .	143
10.9	Fractional Effective Dose (FED) and Fractional Irritant Concentration (FIC) ) . . . . .	143
10.9.1	FED and FIC of gas mixtures ( <code>FED_FIC</code> ) . . . . .	145
10.9.2	FED from post-combustion yield of CO and HCN ( <code>FED_CO_HCN</code> ) . . . . .	145
10.9.3	FED for a moving particle ( <code>FED_moving</code> ) . . . . .	145
10.10	Smoke Detector Model ( <code>smoke_detector</code> ) . . . . .	149
10.11	Aerosol Behavior . . . . .	150
10.11.1	Gravitational Settling and Deposition of Aerosols ( <code>aerosol_gravitational_deposition</code> ) . . . . .	150
10.11.2	Thermophoretic Settling and Deposition of Aerosols ( <code>aerosol_thermophoretic_deposition</code> ) . . . . .	151
10.11.3	Turbulent Deposition of Aerosols ( <code>aerosol_turbulent_deposition</code> ) . . . . .	152
10.11.4	Mass Conservation of Depositing Aerosols ( <code>propane_flame_deposition</code> ) . . . . .	152
10.11.5	Agglomeration of Aerosols ( <code>aerosol_agglomeration</code> ) . . . . .	153
10.11.6	Scrubbing of Aerosols ( <code>aerosol_scrubbing</code> ) . . . . .	155
10.11.7	Oxidation of Soot on Surfaces ( <code>soot_oxidation_wall</code> ) . . . . .	155
10.12	Condensation . . . . .	156
10.12.1	Condensation and Evaporation in the Gas Phase ( <code>condensation_1</code> and <code>condensation_2</code> ) . . . . .	156
10.12.2	Condensation and Evaporation in the Solid Phase ( <code>wall_cond</code> ) . . . . .	156
10.12.3	Radiation for Condensed Phase ( <code>condensation_3</code> ) . . . . .	157
<b>11</b>	<b>Heat Conduction</b>	<b>159</b>

11.1	Heat Conduction Through a Solid Slab ( <code>heat_conduction</code> ) . . . . .	159
11.2	Temperature-Dependent Thermal Properties ( <code>heat_conduction_kc</code> ) . . . . .	160
11.3	Convective Cooling ( <code>convective_cooling</code> ) . . . . .	161
11.4	Simple Thermocouple Model ( <code>thermocouples</code> ) . . . . .	162
11.5	Heat Conduction through Insulated Steel ( <code>insulated_steel_x</code> ) . . . . .	163
11.6	Heat Conduction across Mesh Boundaries ( <code>back_wall_test</code> ) . . . . .	164
11.7	Heat Conduction through Immersed Boundaries ( <code>back_wall_test_2</code> ) . . . . .	165
11.8	Specified Heat Flux Boundary Conditions ( <code>adiabatic_xxx_flux</code> ) . . . . .	165
11.9	Solid Heat Transfer 3-D (Beta) . . . . .	167
11.9.1	Energy Conservation in a 3-D Solid ( <code>ht3d_energy_conservation</code> ) . . . . .	167
11.9.2	Heat Transfer to an I-Beam ( <code>ht3d_beam_heating</code> ) . . . . .	169
11.9.3	Mass Conservation in a 3-D Solid ( <code>ht3d_mass_conservation</code> ) . . . . .	170
11.9.4	Continuous Heat Flux Boundary ( <code>ht3d_slab</code> ) . . . . .	171
11.9.5	3-D Heat Diffusion in a Steel I-Beam ( <code>ht3d_ibeam</code> ) . . . . .	171
11.9.6	3-D Heat Diffusion in Thin Steel Plates ( <code>ht3d_network</code> ) . . . . .	172
11.9.7	3-D Heat Diffusion in a Sphere ( <code>ht3d_sphere</code> ) . . . . .	173
11.9.8	3-D Heat Conduction in a Layered Solid ( <code>ht3d_pile</code> ) . . . . .	174
<b>12 Pyrolysis</b>		<b>175</b>
12.1	Conservation of Pyrolyzed Mass ( <code>surf_mass_conservation</code> ) . . . . .	175
12.1.1	Pyrolysis at a Solid Surface . . . . .	175
12.1.2	Pyrolysis of Discrete Particles . . . . .	176
12.1.3	Rate of Solid Particle Decomposition ( <code>part_baking_soda</code> ) . . . . .	181
12.2	Conservation of Pyrolyzed Energy ( <code>mat1_e_cons</code> ) . . . . .	183
12.3	Burning Rate of a Small Object ( <code>cell_burn_away</code> ) . . . . .	187
12.4	Evaporation of a Liquid Surface . . . . .	187
12.4.1	Mass Conservation ( <code>surf_mass_vent_liquid</code> ) . . . . .	187
12.4.2	Evaporation Rate ( <code>water_pool</code> ) . . . . .	188
12.5	Change in Surface Emissivity ( <code>emissivity</code> ) . . . . .	189
12.6	Shrinking and swelling materials ( <code>shrink_swell</code> ) . . . . .	190
12.7	Enthalpy of Solid Materials ( <code>enthalpy</code> ) . . . . .	191
12.8	A Simple Two-Step Pyrolysis Example ( <code>two_step_solid_reaction</code> ) . . . . .	192
12.9	Interpreting Bench-Scale Measurements . . . . .	193
12.9.1	General Theory . . . . .	193
12.9.2	Interpreting TGA Data ( <code>tga_sample</code> ) . . . . .	194
12.9.3	Effect of the TGA Heating Rate ( <code>birch_tga</code> ) . . . . .	196
12.9.4	TGA for a Charring Sample ( <code>Needle_TGA</code> ) . . . . .	196
12.9.5	TGA of various Mediterranean vegetation ( <code>Morvan_TGA</code> ) . . . . .	202
12.9.6	Interpreting MCC Data ( <code>cable_XX_mcc</code> ) . . . . .	203
12.10	Scaling Pyrolysis (SPyro) Model ( <code>spyro_cone_demo_2</code> and <code>spyro_cone_demo_3</code> ) . . . . .	206
12.11	Melting Ice Cube ( <code>ice_cube</code> ) . . . . .	207
<b>13 Lagrangian Particles</b>		<b>209</b>
13.1	Particle and Droplet Drag . . . . .	209
13.1.1	Dragless Particle ( <code>cannon_ball</code> ) . . . . .	209
13.1.2	Particles Swept Up in a Free Stream ( <code>fluid_part_mom</code> ) . . . . .	209
13.1.3	Particles Slowing Down a Gas Flow ( <code>particle_drag</code> ) . . . . .	210

13.1.4	Stationary Spherical Particles in a Duct ( <i>sphere_drag</i> ) . . . . .	210
13.1.5	Drag Caused by Vegetation ( <i>vegetation_drag</i> ) . . . . .	213
13.1.6	Mesh Screen in a Duct ( <i>screen_drag</i> ) . . . . .	215
13.1.7	Flow through Porous Media ( <i>porous_media</i> ) . . . . .	216
13.1.8	Particle Terminal Velocity ( <i>terminal_velocity</i> ) . . . . .	216
13.1.9	Particle Trajectory ( <i>flat_fire</i> ) . . . . .	217
13.2	Solid Particle Mass and Energy Transfer . . . . .	219
13.2.1	Radiation Absorption by Vegetation . . . . .	219
13.2.2	Heating a Metal Sphere via Radiation and Convection . . . . .	219
13.3	Water Droplet Evaporation ( <i>water_evaporation</i> ) . . . . .	221
13.3.1	Case 1 . . . . .	221
13.3.2	Case 2 . . . . .	223
13.3.3	Case 3 . . . . .	225
13.3.4	Case 4 . . . . .	227
13.3.5	Case 5 . . . . .	227
13.3.6	Case 6 . . . . .	228
13.3.7	Case 7 . . . . .	229
13.3.8	Case 8 . . . . .	230
13.4	Water Droplets on Solid Surfaces . . . . .	230
13.4.1	Basic Flow and Mass Conservation ( <i>geom_sprk_mass</i> ) . . . . .	230
13.4.2	Obstructions of Different Orientations ( <i>geom_particle_cascade_2</i> ) . . . . .	231
13.4.3	Adiabatic Surface Temperature ( <i>adiabatic_surf_temp_spray</i> ) . . . . .	231
13.4.4	Droplet Movement on Solid Surfaces with MPI ( <i>cascademp</i> ) . . . . .	232
13.5	Flow Rate and Pipe Networks ( <i>flow_rate_2</i> ) . . . . .	233
13.6	Turbulent Dispersion ( <i>random_walk</i> ) . . . . .	233
<b>14</b>	<b>Heating, Ventilating, and Air Conditioning (HVAC)</b> . . . . .	<b>235</b>
14.1	Duct Flow Losses ( <i>HVAC_flow_loss</i> ) . . . . .	235
14.2	Node Flow Losses ( <i>HVAC_tee_loss_1</i> , <i>HVAC_tee_loss_2</i> ) . . . . .	235
14.3	HVAC Mass Conservation ( <i>HVAC_mass_conservation</i> ) . . . . .	236
14.4	HVAC Energy Conservation and Pressure ( <i>HVAC_energy_pressure</i> ) . . . . .	237
14.5	HVAC Dampers ( <i>HVAC_damper</i> ) . . . . .	238
14.6	HVAC Filters ( <i>HVAC_filter</i> ) . . . . .	239
14.7	HVAC Fans ( <i>fan_test</i> ) . . . . .	240
14.8	HVAC Operation Point Single Fan ( <i>qfan_test</i> ) . . . . .	241
14.9	HVAC Operation Point Multiple Fans ( <i>qfan_multi</i> ) . . . . .	242
14.10	Leakage . . . . .	243
14.10.1	Single Zone Leakage ( <i>leak_test</i> ) . . . . .	243
14.10.2	Multiple Zone Leakage ( <i>leak_test_2</i> ) . . . . .	244
14.10.3	Leakage through Immersed Boundary Wall ( <i>leak_test_3</i> ) . . . . .	244
14.10.4	Leakage through Immersed Boundary Compartment ( <i>leak_test_4</i> ) . . . . .	245
14.10.5	Localized Leakage ( <i>leak_enthalpy</i> ) . . . . .	245
14.10.6	Multiple Zone, Multiple Mesh Leakage ( <i>zone_shape_2</i> ) . . . . .	246
14.10.7	Leak Pressure Exponent ( <i>HVAC_leak_exponent</i> ) . . . . .	247
14.11	ASHRAE Sample Problem 7 ( <i>ashrae_7_fixed_flow</i> , <i>ashrae_7_quadratic</i> , <i>ashrae_7_table</i> ) . . . . .	248
14.12	HVAC transient mass transport . . . . .	249
14.12.1	Convergence study for HVAC mass transport ( <i>HVAC_convergence_study_x</i> ) . . . . .	249

14.12.2	Transport time (HVAC_mass_transport) . . . . .	250
14.12.3	Duct definition sensitivity analysis (HVAC_mass_transport_x) . . . . .	251
14.12.4	Mass conservation 1 (HVAC_mass_transport_conservation_1) . . . . .	251
14.12.5	Mass conservation 2 (HVAC_mass_transport_conservation_2) . . . . .	252
14.12.6	Mass conservation 3 (HVAC_mass_transport_conservation_3) . . . . .	252
14.12.7	Transient transport branching ducts (HVAC_mass_transport_branch) . . . . .	253
14.12.8	Transient transport combining ducts (HVAC_mass_transport_combine) . . . . .	254
14.12.9	Energy conservation and pressure (HVAC_mass_transport_energy) . . . . .	255
<b>15</b>	<b>Wildland Fire Spread</b>	<b>257</b>
15.1	Level Set Model . . . . .	257
15.1.1	Elliptical Fire Spread . . . . .	257
15.1.2	Ember Generation (LS4_ember_yield) . . . . .	259
15.1.3	Ember ignition (LS4_ember_ignition) . . . . .	259
<b>16</b>	<b>Unstructured Geometry (Beta)</b>	<b>261</b>
16.1	Verification of setup checks on broken geometries . . . . .	261
16.2	Simple geometry and properties definitions . . . . .	262
16.2.1	Simple Geometry . . . . .	262
16.2.2	Cuboid Obstacle . . . . .	262
16.2.3	Self-generated Sphere Geometry . . . . .	263
16.2.4	Terrain from Digital Elevation Map . . . . .	266
16.2.5	Adding Texture Map . . . . .	266
16.2.6	Adding Multiple Texture Maps . . . . .	267
16.2.7	Adding Texture Maps with Different Methods . . . . .	268
16.3	Computational Geometry . . . . .	269
16.3.1	Cut-cell Definition Around Immersed Cone: Split Cells, Piercing and Alignment	269
16.4	Cut-cell Method for Scalar Transport - Stress Method . . . . .	271
16.4.1	Temporal Error Analysis for Variable Density Projection . . . . .	271
16.4.2	Variable-Density Manufactured Solution . . . . .	271
16.4.3	Stress Method on Manufactured Solution Around Rotated Cube . . . . .	272
16.4.4	Poiseuille Flow in Channel Created by Two GEOMs . . . . .	276
16.5	Geometry Tests Involving Heat and Mass Transfer . . . . .	277
16.5.1	Radiating Sphere . . . . .	277
16.5.2	Leaking Sphere . . . . .	278
16.6	Restart Function . . . . .	278
<b>17</b>	<b>Outputs</b>	<b>281</b>
17.1	Statistical Quantities . . . . .	281
17.1.1	RMS, Co-Variance, and Cross-Correlation (rms_cov_corr) . . . . .	281
17.1.2	RMS as a Running Average (rms_example) . . . . .	283
17.1.3	Favre Average (shunn3_FavreZ) . . . . .	283
17.2	Interpolation . . . . .	284
<b>Bibliography</b>		<b>285</b>
<b>A Summary of Verification Results</b>		<b>293</b>
<b>B Installation Testing</b>		<b>313</b>



# List of Figures

3.1	Initial and final states of Navier-Stokes solution . . . . .	12
3.2	Velocity time history, qualitative convergence . . . . .	13
3.3	Navier-Stokes convergence study . . . . .	13
3.4	Pulsating wave convergence . . . . .	16
3.5	Stationary compression wave convergence . . . . .	18
3.6	Multi-mesh square wave transport . . . . .	19
3.7	Solid body rotation scalar transport . . . . .	20
3.8	Solid body rotation square wave convergence . . . . .	21
3.9	Solid body rotation cosine wave convergence . . . . .	22
3.10	The <code>saad</code> temporal order test case . . . . .	24
3.11	Evolution of the variable-density manufactured solution . . . . .	27
3.12	Convergence of the manufactured solution . . . . .	28
3.13	The <code>hot_layer-collapse</code> test case . . . . .	30
3.14	Vector field of a two-dimensional vortex . . . . .	31
3.15	Velocity in the <code>vort2d</code> test case . . . . .	32
3.16	Convergence study for the <code>vort2d</code> test case . . . . .	32
3.17	Time history of velocity at a point showing qualitative convergence . . . . .	33
3.18	Results of the <code>bound_test_1</code> case . . . . .	33
3.19	Results of the <code>bound_test_2</code> case . . . . .	34
3.20	Results of the <code>helium_1d_isothermal</code> cases . . . . .	35
3.21	Results of the <code>helium_air_jet_floor</code> case . . . . .	35
3.22	Results of the <code>mwtest_cfl</code> case . . . . .	36
3.23	Results of the <code>tmp_lower_limit</code> cases . . . . .	37
3.24	Results of the <code>helium_1d_const_gamma</code> cases . . . . .	38
3.25	Results of the <code>fire_const_gamma</code> case . . . . .	39
3.26	Sample case <code>water_evap_1_const_gamma</code> . . . . .	40
3.27	Sample case <code>tunnel_const_gamma</code> . . . . .	42
3.28	Sample case <code>tunnel_linear_cp</code> . . . . .	44
4.1	Initial and final states for isotropic turbulence . . . . .	46
4.2	Integrated and spectral energy decay for CBC experiment using constant Smagorinsky . . . . .	47
4.3	Dynamic Smagorinsky coefficient . . . . .	48
4.4	Integrated and spectral energy decay for CBC experiment using dynamic Smagorinsky . . . . .	49
4.5	Integrated and spectral energy decay for CBC experiment using Deardorff's model . . . . .	50
4.6	Integrated and spectral energy decay for CBC experiment using Vreman's model . . . . .	51
4.7	Integrated and spectral energy decay for CBC experiment using the WALE model . . . . .	52
4.8	Jet centerline velocity decay . . . . .	53
5.1	Convergence for laminar (Poiseuille) flow in a 2-D channel . . . . .	56

5.2	LES of square duct flow . . . . .	57
5.3	FDS Moody chart . . . . .	58
5.4	Blasius profile and convergence . . . . .	59
5.5	Pohlhausen similarity solution and vertical profile . . . . .	60
5.6	Near-wall grid resolution . . . . .	61
5.7	Mean velocity and temperature profiles for heated channel flow . . . . .	62
5.8	Forced convection flat plate boundary layer . . . . .	63
5.9	Nusselt correlation local turbulent flat plate . . . . .	65
5.10	Nusselt correlation natural convection from a hot, horizontal plate . . . . .	67
5.11	Nusselt correlation Rayleigh-Bénard convection . . . . .	68
5.12	Nusselt correlation natural convection vertical enclosure . . . . .	69
5.13	Nusselt correlation free convection from a sphere . . . . .	69
5.14	Impinging jet Nusselt correlation . . . . .	70
5.15	Impinging jet Nusselt profile . . . . .	71
5.16	Bulk velocity ribbed_channel test case . . . . .	72
5.17	The ribbed_channel test case . . . . .	73
5.18	Mean and RMS velocity profiles for ribbed square duct flow . . . . .	73
5.19	Bulk velocity ribbed_channel_geom test case . . . . .	74
5.20	Mean and RMS velocity profiles for ribbed channel geom . . . . .	75
6.1	Monin-Obukhov velocity profiles . . . . .	77
6.2	Schoenberg Ekman Layers . . . . .	79
7.1	The simple_duct test case . . . . .	81
7.2	The species_conservation test cases . . . . .	83
7.3	The mass_flux_wall test cases . . . . .	84
7.4	The mass_balance_gas_volume test case . . . . .	84
7.5	The mass_balance_reac test case . . . . .	86
7.6	The particle_offgas test cases . . . . .	87
7.7	The realizable_mass_fractions test case . . . . .	87
7.8	The geom_mass_file_test test case . . . . .	88
7.9	The energy_budget_adiabatic_walls test case . . . . .	90
7.10	The energy_budget_cold_walls test case . . . . .	90
7.11	The isentropic test case . . . . .	91
7.12	The isentropic2 test case . . . . .	92
7.13	The energy_budget_dns test case . . . . .	93
7.14	The energy_budget_tmix test case . . . . .	93
7.15	The energy_budget_combustion test case . . . . .	94
7.16	The energy_budget_solid test case . . . . .	94
7.17	The mass_heat_wall_device_test results . . . . .	95
7.18	The energy_budget_particles test case . . . . .	96
8.1	The symmetry_test cases . . . . .	98
8.2	The symmetry_test_2 case . . . . .	98
8.3	The cyl_test test cases . . . . .	99
8.4	Images of the velocity_bc_test test case . . . . .	100
8.5	The velocity_bc_test test case . . . . .	101
8.6	The divergence_test cases 1 and 2 . . . . .	102

8.7	The divergence_test case 3 . . . . .	102
8.8	The lapse_rate test case . . . . .	103
8.9	The random_meshes test case . . . . .	103
8.10	The overlapping init_overlap test case . . . . .	105
8.11	The overlapping init_overlap test case . . . . .	106
8.12	Results of the hole/no hole test case . . . . .	107
8.13	Result of the race_test . . . . .	108
8.14	Result of the layer test cases . . . . .	109
8.15	Result of the device_restart test case . . . . .	110
9.1	The plate_view_factor test case . . . . .	112
9.2	Results of the geom_rad test case . . . . .	112
9.3	Results of the geom_rad_2 test case . . . . .	113
9.4	Radiation inside a box geometry. . . . .	113
9.5	Incident heat flux. . . . .	114
9.6	The radiating_polygon test case . . . . .	115
9.7	Radiation from hot spheres . . . . .	117
9.8	Radiation absorption by liquid droplets . . . . .	118
9.9	The particle_isotropic_radi and particle_anisotropic_radi test cases . . . . .	118
9.10	Radiation attenuation by Lagrangian particles . . . . .	119
9.11	The radiation_gas-veg_consistency test cases . . . . .	120
9.12	Transient thermocouple heating . . . . .	121
9.13	Radiation/thermocouple test case . . . . .	121
9.14	The target_test case . . . . .	122
9.15	The radiation_shield test case . . . . .	123
9.16	The radiation_gas_panel case . . . . .	123
9.17	The net_rad_1000 case . . . . .	124
9.18	The net_rad_1000 case . . . . .	124
10.1	Results of the species_props cases . . . . .	126
10.2	Test of 30 % relative humidity at 70 °C . . . . .	127
10.3	Yield of combustion products for alternative reactions . . . . .	127
10.4	Species evolution in a 1-step methane EDC reaction . . . . .	128
10.5	Temperature and pressure evolution in a 1-step methane EDC reaction . . . . .	129
10.6	Species evolution in a 1-step propane EDC reaction . . . . .	129
10.7	Temperature and pressure evolution in a 1-step propane EDC reaction . . . . .	129
10.8	Species evolution in 1-Step methane EDC reaction . . . . .	130
10.9	Temperature and pressure evolution in a 1-step Methane EDC reaction . . . . .	130
10.10	Species evolution in 2-step methane EDC reaction . . . . .	131
10.11	Results of the reactionrate_series_reaction case . . . . .	131
10.12	Species evolution in two parallel EDC reactions . . . . .	132
10.13	Results of the reactionrate_lumped_two_species case . . . . .	132
10.14	Species evolution in a 0-order 1-step finite rate reaction . . . . .	133
10.15	Species evolution in a 2-order 1-step finite rate reaction . . . . .	134
10.16	Species evolution in a 1.75-order 2-step finite rate reaction . . . . .	135
10.17	Species evolution in a 1.75-order 2-step reversible finite rate reaction . . . . .	135
10.18	Species evolution in an equilibrium case . . . . .	136
10.19	Temperature and pressure evolution for equilibrium case . . . . .	137

10.20	Species evolution in a fast-slow reaction scheme . . . . .	138
10.21	Results of the <code>hrrpuv_reac</code> test cases . . . . .	140
10.22	Mixture fraction state relations for species ( <code>burke_schumann</code> ) . . . . .	142
10.23	Mixture fraction state relations for temperature ( <code>burke_schumann</code> ) . . . . .	142
10.24	<code>HoC_Ideal</code> and <code>HoC_NonIdeal</code> test cases . . . . .	143
10.25	Result of the <code>1_step_2_step_compare</code> test case . . . . .	143
10.26	The FED and FIC values in <code>FED_FIC</code> test cases . . . . .	146
10.27	The FED and FIC values in <code>FED_FIC_SMIX</code> test cases . . . . .	147
10.28	The FED value in <code>FED_CO_HCN</code> case . . . . .	148
10.29	The FED value in <code>FED_CO_HCN</code> case . . . . .	148
10.30	Smoke detector chamber obscuration for <code>smoke_detector</code> case . . . . .	149
10.31	Gas phase soot mass fractions and wall surface densities for gravitational deposition . . . . .	150
10.32	Gas phase soot densities and wall surface densities for thermophoretic deposition . . . . .	151
10.33	Wall surface densities for the <code>aerosol_turbulent_deposition</code> case . . . . .	152
10.34	Soot mass conservation for <code>propane_flame_deposition</code> case . . . . .	153
10.35	Gas phase soot mass fractions the <code>aerosol_agglomeration</code> cases . . . . .	154
10.36	Gas phase soot mass fractions the <code>aerosol_agglomeration_2</code> cases . . . . .	154
10.37	Gas phase soot mass fractions the <code>aerosol_scrubbing</code> cases . . . . .	155
10.38	Results of the <code>soot_oxidation_wall</code> case . . . . .	156
10.39	Results of the <code>condensation_1</code> (top) and <code>condensation_2</code> (bottom) cases . . . . .	157
10.40	Results of the <code>wall_cond</code> case . . . . .	158
10.41	Radiative heat flux for the <code>condensation_3</code> case . . . . .	158
11.1	The <code>heat_conduction</code> test cases . . . . .	160
11.2	The <code>heat_conduction_kc</code> test case . . . . .	161
11.3	The <code>convective_cooling</code> test case . . . . .	162
11.4	Convergence study for the <code>convective_cooling</code> test case . . . . .	162
11.5	The <code>thermocouples</code> test case . . . . .	163
11.6	The <code>insulated_steeel</code> test cases . . . . .	164
11.7	The <code>back_wall_test</code> test case . . . . .	164
11.8	The <code>back_wall_test_2</code> test cases . . . . .	165
11.9	The <code>adiabatic_con_flux</code> and <code>adiabatic_net_flux</code> test cases . . . . .	166
11.10	The <code>ht3d_energy_conservation</code> test case . . . . .	167
11.11	Additional <code>ht3d_energy_conservation</code> test cases . . . . .	168
11.12	Additional <code>ht3d_energy_conservation</code> test cases, 4, 5, 6, and 7 . . . . .	168
11.13	Additional <code>ht3d_energy_conservation</code> test cases 8 and 9 . . . . .	169
11.14	The <code>ht3d_beam_heating</code> test cases . . . . .	170
11.15	The <code>ht3d_mass_conservation</code> test case . . . . .	170
11.16	The <code>ht3d_slab</code> test cases . . . . .	171
11.17	The <code>ibeam-ht3d</code> test case: contours . . . . .	172
11.18	The <code>ibeam-ht3d</code> test case: time history . . . . .	172
11.19	The <code>ht3d_network</code> test case . . . . .	173
11.20	The <code>ht3d_sphere</code> temperature profiles and convergence rate . . . . .	174
11.21	The <code>ht1d_pile</code> and <code>ht3d_pile</code> test cases . . . . .	174
12.1	The <code>surf_mass_vent_char</code> test cases . . . . .	176
12.2	The <code>surf_mass_vent_nonchar</code> test cases . . . . .	177
12.3	The <code>surf_mass_part_char</code> test cases . . . . .	178

12.4	The <code>surf_mass_part_nonchar</code> test cases . . . . .	179
12.5	The <code>surf_mass_two_species</code> test cases . . . . .	180
12.6	The <code>part_baking_soda</code> test cases . . . . .	183
12.7	The <code>matl_e_cons</code> test cases 1-6 . . . . .	185
12.8	The <code>matl_e_cons</code> test cases 7-9 . . . . .	186
12.9	The <code>cell_burn_away</code> test case . . . . .	187
12.10	The <code>surf_mass_vent_liquid_fuel</code> test cases . . . . .	188
12.11	The <code>water_pool</code> test case . . . . .	189
12.12	The <code>emissivity</code> test case . . . . .	189
12.13	The <code>shrink_swell</code> test case . . . . .	191
12.14	The <code>enthalpy</code> test case . . . . .	192
12.15	The <code>two_step_solid_reaction</code> test case . . . . .	193
12.16	Results of a TGA analysis . . . . .	195
12.17	An example of TGA data . . . . .	196
12.18	Needle_TGA calibration curves . . . . .	197
12.19	Results of pine Needle_TGA calibration exercise, Cases A and B . . . . .	198
12.20	Results of pine Needle_TGA calibration exercise, Cases C and D . . . . .	199
12.21	Results of pine Needle_TGA calibration exercise, Cases E and F . . . . .	200
12.22	Results of pine Needle_TGA calibration exercise, Cases G and H . . . . .	201
12.23	Results of Morvan_TGA analysis . . . . .	202
12.24	Results of a micro-calorimetry analysis of cable materials . . . . .	204
12.25	Check of the Scaling Pyrolysis (SPryo) model (the <code>spyro_cone_demo_2</code> case) . . . . .	206
12.26	Check of the Scaling Pyrolysis (SPryo) model (the <code>spyro_cone_demo_3</code> case) . . . . .	206
12.27	Check of the particle production by surface reaction feature (the <code>ice_cube</code> case) . . . . .	207
13.1	The <code>cannon_ball</code> case . . . . .	210
13.2	Test of fluid-particle momentum transfer for nonstationary particles . . . . .	211
13.3	Sample cases <code>particle_drag</code> . . . . .	212
13.4	Sample case of <code>particle_drag sum</code> . . . . .	213
13.5	The <code>sphere_drag</code> cases . . . . .	213
13.6	The <code>vegetation_drag</code> test cases . . . . .	215
13.7	Sample cases <code>screen_drag</code> . . . . .	215
13.8	Results of the <code>porous_media</code> test case . . . . .	216
13.9	Convergence analysis of the <code>terminal_velocity</code> case . . . . .	217
13.10	Results of the <code>flat_fire</code> test case . . . . .	218
13.11	Results of the <code>vegetation_absorb</code> test case . . . . .	219
13.12	The <code>particle_heating</code> test cases . . . . .	220
13.13	Sample case <code>water_evaporation_1</code> . . . . .	222
13.14	Sample case <code>water_evaporation_2</code> . . . . .	224
13.15	Sample case <code>water_evaporation_3</code> . . . . .	226
13.16	Sample case <code>water_evaporation_4</code> . . . . .	227
13.17	Sample case <code>water_evaporation_5</code> . . . . .	228
13.18	Sample case <code>water_evaporation_6</code> . . . . .	229
13.19	Sample case <code>water_evaporation_6a</code> . . . . .	229
13.20	Sample case <code>water_evaporation_7</code> . . . . .	230
13.21	Sample case <code>water_evaporation_8</code> . . . . .	230
13.22	The <code>geom_sprk_mass</code> test case . . . . .	231
13.23	The <code>geom_particle_cascade_2</code> test case . . . . .	231

13.24	The adiabatic_surface_temperature_spray test case . . . . .	232
13.25	Results of the cascadempi test case . . . . .	232
13.26	The flow_rate_2 case . . . . .	233
13.27	Turbulent dispersion of tracer particles . . . . .	234
14.1	The HVAC_flow_loss test case . . . . .	235
14.2	The HVAC_tee_loss test cases . . . . .	236
14.3	The HVAC_mass_conservation case . . . . .	237
14.4	The HVAC_energy_pressure case . . . . .	238
14.5	Example case HVAC_damper . . . . .	239
14.6	Results for the HVAC_filter sample case . . . . .	240
14.7	Results of the fan_test case . . . . .	241
14.8	Results of the qfan_test case . . . . .	242
14.9	Results of the qfan_multi case . . . . .	243
14.10	The leak_test case . . . . .	244
14.11	The leak_test_2 test case . . . . .	244
14.12	The leak_test_3 test case . . . . .	245
14.13	The leak_test_4 test case . . . . .	246
14.14	The leak_enthalpy test case . . . . .	246
14.15	The zone_shape_2 test case . . . . .	247
14.16	The HVAC_leak_exponent cases . . . . .	248
14.17	Results of ashrae7 test cases . . . . .	249
14.18	HVAC_mass_transport_conv_x test case result . . . . .	250
14.19	HVAC_mass_transport_conv_x L1 and L2 error results . . . . .	250
14.20	HVAC_mass_transport test case . . . . .	251
14.21	HVAC_mass_transport_x test case . . . . .	251
14.22	HVAC_mass_transport_conservation_1 test case . . . . .	252
14.23	HVAC_mass_transport_conservation_1 test case . . . . .	252
14.24	HVAC_mass_transport_conservation_2 test case . . . . .	253
14.25	HVAC_mass_transport_conservation_3 test case . . . . .	253
14.26	HVAC_mass_transport_branch test case . . . . .	254
14.27	HVAC_mass_transport_branch test case . . . . .	254
14.28	HVAC_mass_transport_energy Δ p and enthalpy results . . . . .	255
15.1	Level set fire front ellipse shape . . . . .	258
15.2	Level set fire front ellipse error . . . . .	258
15.3	Level set ember generation . . . . .	259
15.4	Level set ember ignition . . . . .	260
16.1	Simple triangulated geometry . . . . .	262
16.2	Block geometry using XB . . . . .	263
16.3	Recursive sphere discretization . . . . .	264
16.4	Latitude/longitude sphere discretization . . . . .	265
16.5	Defining digital elevation maps using ZVALS . . . . .	266
16.6	Applying a texture map to a GEOM surface . . . . .	267
16.7	Applying multiple texture maps to a GEOM surface . . . . .	268
16.8	Applying texture maps to a GEOM surface, different methods . . . . .	269
16.9	Generating polyhedral cutcells around an immersed cone . . . . .	270

16.10	The <code>saad</code> CC temporal order test case . . . . .	272
16.11	The <code>Shunn</code> CC accuracy order test case . . . . .	273
16.12	Reference frame for a rotated immersed body . . . . .	274
16.13	The <code>Rotated Cube</code> CC accuracy order test case . . . . .	275
16.14	The <code>Rotated Cube</code> CC accuracy order test case . . . . .	275
16.15	The <code>Rotated Cube</code> CC accuracy order test case . . . . .	276
16.16	Poiseuille flow between two unstructured geometries . . . . .	277
16.17	Poiseuille flow convergence with unstructured geometry . . . . .	277
16.18	The <code>sphere_radiate</code> test case . . . . .	278
16.19	The <code>sphere_leak</code> test case . . . . .	278
16.20	The <code>geom_restart</code> test case . . . . .	279
17.1	Sample case <code>rms_cov_corr</code> . . . . .	282
17.2	Sample case <code>rms_example</code> . . . . .	283
17.3	Favre average test <code>shunn3_FavreZ</code> . . . . .	284
17.4	Test of <code>devc_interpolation</code> . . . . .	284



# List of Tables

3.1	Parameters for manufactured solution . . . . .	25
3.2	Shunn temporal error norms . . . . .	28
3.3	Helium constant specific heat ratio . . . . .	38
5.1	Case matrix for Moody chart . . . . .	57
5.2	Forced convection boundary layer resolution . . . . .	63
5.3	Natural convection correlation parameters for horizontal plates . . . . .	66
5.4	Natural convection correlation parameters for a horizontal enclosure . . . . .	67
5.5	Free convection correlation parameters for a vertical enclosure . . . . .	68
6.1	Schoenberg Ekman Layer parameters . . . . .	78
10.1	Arrhenius values for a single step CO reaction . . . . .	133
10.2	Arrhenius values for a single step C <sub>3</sub> H <sub>8</sub> reaction . . . . .	133
10.3	Arrhenius values for a two-step C <sub>3</sub> H <sub>8</sub> reaction . . . . .	134
10.4	Arrhenius values for a two-step reversible C <sub>3</sub> H <sub>8</sub> reaction . . . . .	134
10.5	Arrhenius values for a two-step reversible C <sub>3</sub> H <sub>8</sub> reaction . . . . .	136
12.1	Parameters for shrinking and swelling of materials . . . . .	190
12.2	Parameters for pine needle TGA experiments . . . . .	197
12.3	Parameters for kinetic constants for cable materials . . . . .	205
16.1	Conservation tests for polyhedra . . . . .	271
A.1	Summary of verification cases . . . . .	294
B.1	FDS Installation Test Suite . . . . .	314



# Chapter 1

## What is Verification?

The terms *verification* and *validation* are often used interchangeably to mean the process of checking the accuracy of a numerical model. For many, this entails comparing model predictions with experimental measurements. However, there is now a fairly broad-based consensus that comparing model and experiment is largely what is considered *validation*. So what is *verification*? ASTM E 1355 [3], “Standard Guide for Evaluating the Predictive Capability of Deterministic Fire Models,” defines verification as

The process of determining that the implementation of a calculation method accurately represents the developer’s conceptual description of the calculation method and the solution to the calculation method.

and it defines validation as

The process of determining the degree to which a calculation method is an accurate representation of the real world from the perspective of the intended uses of the calculation method.

Simply put, verification is a check of the math; validation is a check of the physics. If the model predictions closely match the results of experiments, using whatever metric is appropriate, it is assumed by most that the model suitably describes, via its mathematical equations, what is happening. It is also assumed that the solution of these equations must be correct. So why do we need to perform model verification? Why not just skip to validation and be done with it? The reason is that rarely do model and measurement agree so well in all applications that anyone would unquestionably just accept the results. Because there is inevitably differences between model and experiment, we need to know if these differences are due to limitations or errors in the numerical solution, or physical sub-models, or both.

Whereas model validation consists mainly of comparing predictions with measurements, as documented for FDS in Volume 3 of the Technical Reference Guide, model verification consists of a much broader range of activities, from checking the computer program itself to comparing calculations to analytical (exact) solutions to considering the sensitivity of the dozens of numerical parameters. The next chapter discusses these various activities, and the rest of the Guide is devoted mainly to comparisons of various sub-model calculations with analytical solutions.



# Chapter 2

## Survey of Past Verification Work

This chapter documents work of the past few decades at NIST, VTT and elsewhere to verify the algorithms within FDS.

### 2.1 Analytical Tests

Most realistic combustion processes, including fire, are turbulent and time-dependent. There are no closed-form mathematical solutions for the fully-turbulent, time-dependent Navier-Stokes equations. CFD provides an approximate solution for the non-linear partial differential equations that describe fluid flow by replacing them with discretized algebraic equations that can be solved using a powerful computer. While there is no general analytical solution for fully-turbulent flows, certain sub-models address phenomena that do have analytical solutions, for example, one-dimensional heat conduction through a solid. These analytical solutions can be used to test sub-models within a complex code such as FDS. The developers of FDS routinely use such practices to verify the correctness of the coding of the model [4, 5]. Such verification efforts are relatively simple and routine and the results may not always be published nor included in the documentation. Examples of routine analytical testing include:

- The radiation solver has been verified for scenarios in which simple objects, like cubes or flat plates, are positioned in simple, sealed compartments. All convective motion is turned off, the object is given a fixed surface temperature and emissivity of one (making it a black body radiator). The heat flux to the cold surrounding walls is recorded and compared to analytical solutions. These studies help determine the appropriate number of solid angles to be set as the default.
- Solid objects are heated with a fixed heat flux, and the interior and surface temperatures as a function of time are compared to analytical solutions of the one-dimensional heat transfer equation. These studies help determine the number of nodes to use in the solid phase heat transfer model. Similar studies are performed to check the pyrolysis models for thermoplastic and charring solids.
- Early in its development, the hydrodynamic solver that evolved to form the core of FDS was checked against analytical solutions of simplified fluid flow phenomena. These studies were conducted at the National Bureau of Standards (NBS)<sup>1</sup> by Rehm, Baum and co-workers [6, 7, 8, 9]. The emphasis of this early work was to test the stability and consistency of the basic hydrodynamic solver, especially the velocity-pressure coupling that is vitally important in low Mach number applications. Many numerical algorithms developed to that point in time were intended for use in high-speed flow applications, like

---

<sup>1</sup>The National Institute of Standards and Technology (NIST) was formerly known as the National Bureau of Standards.

aerospace. Many of the techniques adopted by FDS were originally developed for meteorological models, and as such needed to be tested to assess whether they would be appropriate to describe relatively low-speed flow within enclosures.

- A fundamental decision made by Rehm and Baum early in the FDS development was to use a direct (rather than iterative) solver for the pressure. In the low Mach number formulation of the Navier-Stokes equations, an elliptic partial differential equation for the pressure emerges, often referred to as the Poisson equation. Most CFD methods use iterative techniques to solve the governing conservation equations to avoid the necessity of directly solving the Poisson equation. The reason for this is that the equation is time-consuming to solve numerically on anything but a rectilinear grid. Because FDS is designed specifically for rectilinear grids, it can exploit fast, direct solvers of the Poisson equation, obtaining the pressure field with one pass through the solver to machine accuracy. FDS employs double-precision (8 byte) arithmetic, meaning that the relative difference between the computed and the exact solution of the discretized Poisson equation is on the order of  $10^{-12}$ . The fidelity of the numerical solution of the entire system of equations is tied to the pressure/velocity coupling because often simulations can involve hundreds of thousands of time steps, with each time step consisting of two solutions of the Poisson equation to preserve second-order accuracy. Without the use of the direct Poisson solver, build-up of numerical error over the course of a simulation could produce spurious results. Indeed, an attempt to use single-precision (4 byte) arithmetic to conserve machine memory led to spurious results simply because the error per time step built up to an intolerable level.

## 2.2 Numerical Tests

Numerical techniques used to solve the governing equations within a model can be a source of error in the predicted results. The hydrodynamic model within FDS is second-order accurate in space and time. This means that the error terms associated with the approximation of the spatial partial derivatives by finite differences is of the order of the square of the grid cell size, and likewise the error in the approximation of the temporal derivatives is of the order of the square of the time step. As the numerical grid is refined, the “discretization error” decreases, and a more faithful rendering of the flow field emerges. The issue of grid sensitivity is extremely important to the proper use of the model and will be taken up in the next chapter.

A common technique of testing flow solvers is to systematically refine the numerical grid until the computed solution does not change, at which point the calculation is referred to as a Direct Numerical Solution (DNS) of the governing equations. For most practical fire scenarios, DNS is not possible on conventional computers. However, FDS does have the option of running in DNS mode, where the Navier-Stokes equations are solved without the use of sub-grid scale turbulence models of any kind. Because the basic numerical method is the same for LES and DNS, DNS calculations are a very effective way to test the basic solver, especially in cases where the solution is steady-state. Throughout its development, FDS has been used in DNS mode for special applications. For example, FDS (or its core algorithms) have been used at a grid resolution of roughly 1 mm to look at flames spreading over paper in a microgravity environment [10, 11, 12, 13, 14, 15], as well as “g-jitter” effects aboard spacecraft [16]. Simulations have been compared to experiments performed aboard the US Space Shuttle. The flames are laminar and relatively simple in structure, and the comparisons are a qualitative assessment of the model solution. Similar studies have been performed comparing DNS simulations of a simple burner flame to laboratory experiments [17]. Another study compared FDS simulations of a counterflow diffusion flames to experimental measurements and the results of a one-dimensional multi-step kinetics model [18].

Early work with the hydrodynamic solver compared two-dimensional simulations of gravity currents with salt-water experiments [19]. In these tests, the numerical grid was systematically refined until almost

perfect agreement with experiment was obtained. Such convergence would not be possible if there were a fundamental flaw in the hydrodynamic solver.

## 2.3 Sensitivity Analysis

A sensitivity analysis considers the extent to which uncertainty in model inputs influences model output. Model parameters can be the physical properties of solids and gases, boundary conditions, initial conditions, etc. The parameters can also be purely numerical, like the size of the numerical grid. FDS typically requires the user to provide several dozen different types of input parameters that describe the geometry, materials, combustion phenomena, etc. By design, the user is not expected to provide numerical parameters besides the grid size, although the optional numerical parameters are described in both the Technical Reference Guide and the User's Guide.

FDS does not limit the range of most of the input parameters because applications often push beyond the range for which the model has been validated. FDS is used for research at NIST, VTT, and elsewhere, and the developers do not presume to know in all cases what the acceptable range is of any parameter. Plus, FDS solves the fundamental conservation equations and is much less susceptible to errors resulting from input parameters that stray beyond the limits of simpler empirical models. However, the user is warned that he/she is responsible for the prescription of all parameters. The FDS manuals can only provide guidance.

The grid size is the most important numerical parameter in the model, as it dictates the spatial and temporal accuracy of the discretized partial differential equations. The heat release rate is the most important physical parameter, as it is the source term in the energy equation. Property data, like the thermal conductivity, density, heat of vaporization, heat capacity, etc., ought to be assessed in terms of their influence on the heat release rate. Validation studies [20] have shown that FDS predicts well the transport of heat and smoke when the HRR is prescribed. In such cases, minor changes in the properties of bounding surfaces do not have a significant impact on the results. However, when the HRR is not prescribed, but rather predicted by the model using the thermophysical properties of the fuels, the model output is sensitive to even minor changes in these properties.

The sensitivity analyses described in this chapter are all performed in basically the same way. For a given scenario, best estimates of all the relevant physical and numerical parameters are made, and a “baseline” simulation is performed. Then, one by one, parameters are varied by a given percentage, and the changes in predicted results are recorded. This is the simplest form of sensitivity analysis. More sophisticated techniques that involve the simultaneous variation of several parameters are impractical with a CFD model because the computation time is too long and the number of parameters too large to perform the necessary number of calculations to generate decent statistics.

### 2.3.1 Grid Sensitivity

The most important decision made by a model user is the size of the numerical grid. In general, the finer the numerical grid, the better the numerical solution of the equations. FDS is second-order accurate in space and time, meaning that halving the grid cell size will decrease the discretization error in the governing equations by a factor of 4. Because of the non-linearity of the equations, the decrease in discretization error does not necessarily translate into a comparable decrease in the error of a given FDS output quantity. To find out what effect a finer grid has on the solution, model users usually perform some form of grid sensitivity study in which the numerical grid is systematically refined until the output quantities do not change appreciably with each refinement. Of course, with each halving of the grid cell size, the time required for the simulation increases by a factor of  $2^4 = 16$  (a factor of two for each spatial coordinate, plus time). In the end, a compromise is struck between model accuracy and computer capacity.

Some grid sensitivity studies have been documented and published. Since FDS was first publicly released in 2000, significant changes in the combustion and radiation routines have been incorporated into the model. However, the basic transport algorithm is the same, as is the critical importance of grid sensitivity. In compiling sensitivity studies, only those that examined the sensitivity of routines no longer used have been excluded.

As part of a project to evaluate the use of FDS version 1 for large scale mechanically ventilated enclosures, Friday and Mowrer [21] performed a sensitivity analysis to find the approximate calculation time based on varying grid sizes. A propylene fire with a nominal heat release rate was modeled in FDS. There was no mechanical ventilation and the fire was assumed to grow as a function of the time from ignition squared. The compartment was a 3 m by 3 m by 6.1 m space. Temperatures were sampled 12 cm below the ceiling. Four grid sizes were chosen for the analysis: 30 cm, 15 cm, 10 cm, 7.5 cm. Temperature estimates were not found to change dramatically with different grid dimensions.

Using FDS version 1, Bounagui et al. [22] studied the effect of grid size on simulation results to determine the nominal grid size for future work. A propane burner 0.1 m by 0.1 m was modeled with a heat release rate of 1,500 kW. A similar analysis was performed using Alpert's ceiling jet correlation [23] that also showed better predictions with smaller grid sizes. In a related study, Bounagui et al. [24] used FDS to evaluate the emergency ventilation strategies in the Louis-Hippolyte-La Fontaine Tunnel in Montreal, Canada.

Xin [25] used FDS to model a methane fueled square burner (1 m by 1 m) in the open. Engineering correlations for plume centerline temperature and velocity profiles were compared with model predictions to assess the influence of the numerical grid and the size of the computational domain. The results showed that FDS is sensitive to grid size effects, especially in the region near the fuel surface, and domain size effects when the domain width is less than twice the plume width. FDS uses a constant pressure assumption at open boundaries. This assumption will affect the plume behavior if the boundary of the computational domain is too close to the plume.

Ierardi and Barnett [26] used FDS version 3 to model a 0.3 m square methane diffusion burner with heat release rate values in the range of 14.4 kW to 57.5 kW. The physical domain used was 0.6 m by 0.6 m with uniform grid spacings of 15 cm, 10 cm, 7.5 cm, 5 cm, 3 cm, 1.5 cm for all three coordinate directions. For both fire sizes, a grid spacing of 1.5 cm was found to provide the best agreement when compared to McCaffrey's centerline plume temperature and velocity correlations [27]. Two similar scenarios that form the basis for Alpert's ceiling jet correlation were also modeled with FDS. The first scenario was a 1 m by 1 m, 670 kW ethanol fire under a 7 m high unconfined ceiling. The planar dimensions of the computational domain were 14 m by 14 m. Four uniform grid spacings of 50 cm, 33.3 cm, 25 cm, and 20 cm were used in the modeling. The best agreement for maximum ceiling jet temperature was with the 33.3 cm grid spacing. The best agreement for maximum ceiling jet velocity was for the 50 cm grid spacing. The second scenario was a 0.6 m by 0.6 m 1,000 kW ethanol fire under a 7.2 m high unconfined ceiling. The planar dimensions of the computational domain were 14.4 m by 14.4 m. Three uniform grid spacings of 60 cm, 30 cm, and 20 cm were used in the modeling. The results show that the 60 cm grid spacing exhibits the best agreement with the correlations for both maximum ceiling jet temperature and velocity on a qualitative basis.

Petterson [28] also completed work assessing the optimal grid size for FDS version 2. The FDS model predictions of varying grid sizes were compared to two separate fire experiments: The University of Canterbury McLeans Island Tests and the US Navy Hangar Tests in Hawaii. The first set of tests utilized a room with approximate dimensions of 2.4 m by 3.6 m by 2.4 m and fire sizes of 55 kW and 110 kW. The Navy Hangar tests were performed in a hangar measuring 98 m by 74 m by 15 m in height and had fires in the range of 5.5 MW to 6.6 MW. The results of this study indicate that FDS simulations with grids of 0.15 m had temperature predictions as accurate as models with grids as small as 0.10 m. Each of these grid sizes produced results within 15 % of the University of Canterbury temperature measurements. The 0.30 m grid produced less accurate results. For the comparison of the Navy Hangar tests, grid sizes ranging from 0.60 m

to 1.80 m yielded results of comparable accuracy.

Musser et al. [29] investigated the use of FDS for course grid modeling of non-fire and fire scenarios. Determining the appropriate grid size was found to be especially important with respect to heat transfer at heated surfaces. The convective heat transfer from the heated surfaces was most accurate when the near surface grid cells were smaller than the depth of the thermal boundary layer. However, a finer grid size produced better results at the expense of computational time. Accurate contaminant dispersal modeling required a significantly finer grid. The results of her study indicate that non-fire simulations can be completed more quickly than fire simulations because the time step is not limited by the large flow speeds in a fire plume.

### 2.3.2 Sensitivity of Large Eddy Simulation Parameters

FDS uses Deardorff's isotropic eddy viscosity along with the gradient diffusion hypothesis to close the subgrid stress in the LES equations. The turbulent viscosity has the form

$$\mu_{\text{LES}} = \rho C_V \Delta \sqrt{k_{\text{sgs}}} \quad (2.1)$$

where  $C_V$  is an empirical constant,  $\Delta$  is a length on the order of the size of a grid cell, and  $k_{\text{sgs}}$  is the unresolved (subgrid scale) kinetic energy. Related to the "turbulent viscosity" are comparable expressions for the thermal conductivity and material diffusivity:

$$k_{\text{LES}} = \frac{\mu_{\text{LES}} c_p}{\text{Pr}_t} ; \quad (\rho D)_{\text{LES}} = \frac{\mu_{\text{LES}}}{\text{Sc}_t} \quad (2.2)$$

where  $\text{Pr}_t$  and  $\text{Sc}_t$  are the turbulent Prandtl and Schmidt numbers, respectively. Thus,  $C_V$ ,  $\text{Pr}_t$  and  $\text{Sc}_t$  are a set of empirical constants. Most FDS users simply use the default values of (0.1,0.5,0.5), but some have explored their effect on the solution of the equations. The value of  $C_V = 0.1$  is a theoretical value developed from Lilly's analysis. The value is confirmed for a canonical flow, decaying isotropic turbulence, within this volume.

Previous versions of FDS used the constant coefficient Smagorinsky model for the eddy viscosity. In an effort to validate FDS with some simple room temperature data, Zhang et al. [30] tried different combinations of the Smagorinsky parameters, and suggested the current default values. Of the three parameters, the viscosity coefficient is the most sensitive. Smagorinsky [31] originally proposed a value of 0.23, but researchers over the past three decades have used values ranging from 0.1 to 0.23. There are also refinements of the original Smagorinsky model [32, 33, 34] that do not require the user to prescribe the constants, but rather generate them automatically as part of the numerical scheme.

### 2.3.3 Sensitivity of Radiation Parameters

Radiative heat transfer is included in FDS via the solution of the radiation transport equation for a non-scattering gray gas, and in some limited cases using a wide band model. The equation is solved using a technique similar to finite volume methods for convective transport, thus the name given to it is the Finite Volume Method (FVM). There are several limitations of the model. First, the absorption coefficient for the smoke-laden gas is a complex function of its composition, wavelength, and temperature. Because of the simplified combustion model, the chemical composition of the smoky gases, especially the soot content, can affect both the absorption and emission of thermal radiation. Second, the radiation transport is discretized via approximately 100 solid angles. For targets far away from a localized source of radiation, like a growing fire, the discretization can lead to a non-uniform distribution of the radiant energy. This can be seen in the visualization of surface temperatures, where "hot spots" show the effect of the finite number of solid angles. The problem can be lessened by the inclusion of more solid angles, but at a price of longer computing

times. In most cases, the radiative flux to far-field targets is not as important as those in the near-field, where coverage by the default number of angles is much better.

Hostikka [35] examined the sensitivity of the radiation solver to changes in the assumed soot production, number of spectral bands, number of control angles, and flame temperature. Some of the more interesting findings were:

- Changing the soot yield from 1 % to 2 % increased the radiative flux from a simulated methane burner about 15 %
- Lowering the soot yield to zero decreased the radiative flux about 20 %.
- Increasing the number of control angles by a factor of 3 was necessary to ensure the accuracy of the model at the discrete measurement locations.
- Changing the number of spectral bands from 6 to 10 did not have a strong effect on the results.
- Errors of 100 % in heat flux were caused by errors of 20 % in absolute temperature.

The sensitivity to flame temperature and soot composition are consistent with combustion theory, which states that the source term of the radiative transport equation is a function of the absorption coefficient multiplied by the absolute temperature raised to the fourth power. The number of control angles and spectral bands are user-controlled numerical parameters whose sensitivities ought to be checked for each new scenario. The default values in FDS are appropriate for most large scale fire scenarios, but may need to be refined for more detailed simulations such as a low-sooting methane burner.

### 2.3.4 Sensitivity of Thermophysical Properties of Solid Fuels

An extensive amount of verification and validation work with FDS version 4 has been performed by Hietaniemi et al. [36] at VTT, Finland. The case studies are comprised of fire experiments ranging in scale from the cone calorimeter (ISO 5660-1) to full-scale fire tests such as the room corner test (ISO 9705). Comparisons are also made between FDS results and data obtained in the SBI (Single Burning Item) Euro-classification test apparatus (EN 13823) as well as data obtained in two *ad hoc* experimental configurations: one is similar to the room corner test but has only partial linings and the other is a space to study fires in building cavities.

All of the case studies involve real materials whose properties must be prescribed so as to conform to the assumption in FDS that solids are of uniform composition backed by a material that is either cold or totally insulating. Sensitivity of the various physical properties and the boundary conditions were tested. Some of the findings were:

- The measured burning rates of various materials often fell between two FDS predictions in which cold or insulated backings were assumed for the solid surfaces. FDS lacks a multi-layer solid model.
- The ignition time of upholstery is sensitive to the thermal properties of the fabric covering, but the steady burning rate is sensitive to the properties of the underlying foam.
- Moisture content of wooden fuels is very important and difficult to measure.
- Flame spread over complicated objects, like cables laid out in trays, can be modeled if the surface area of the simplified object is comparable to that of the real object. This suggests sensitivity not only to physical properties, but also geometry. It is difficult to quantify the extent of the geometrical sensitivity.

There is little quantification of the observed sensitivities in the study. Fire growth curves can be linear to exponential in form, and small changes in fuel properties can lead to order of magnitude changes in heat release rate for unconfined fires. The subject is discussed in the FDS Validation Guide [20] where it is noted in many of the studies that predicting fire growth is difficult.

Recently, Lautenberger et al. [37] developed a method to automate the process of estimating material properties to input into FDS. The methodology involves simulating a bench-scale test with the model and iterating via a “genetic” algorithm to obtain an optimal set of material properties for that particular item. Such techniques are necessary because most bench-scale apparatus do not provide a complete set of thermal properties.

## 2.4 Code Checking

An examination of the structure of the computer program can be used to detect potential errors in the numerical solution of the governing equations. The coding can be verified by a third party either manually or automatically with profiling programs to detect irregularities and inconsistencies [3].

At NIST, VTT, and elsewhere, FDS has been compiled and run on computers manufactured by IBM, Hewlett-Packard, Sun Microsystems, Digital Equipment Corporation, Apple, Silicon Graphics, Dell, Compaq, and various other personal computer vendors. The operating systems on these platforms include Unix, Linux, Microsoft Windows, and Mac OS X. Compilers used include Lahey Fortran, Digital Visual Fortran, Intel Fortran, IBM XL Fortran, HPUX Fortran, Forte Fortran for SunOS, the Portland Group Fortran, and several others. Each combination of hardware, operating system and compiler involves a slightly different set of compiler and run-time options and a rigorous evaluation of the source code to test its compliance with the Fortran 90 ISO/ANSI standard [38]. FDS is now compliant with the Fortran 2003 standard. Through this process, out-dated and potentially harmful code is updated or eliminated, and often the code is streamlined to improve its optimization on the various machines. However, simply because the FDS source code can be compiled and run on a wide variety of platforms does not guarantee that the numerics are correct. It is only the starting point in the process because it at least rules out the possibility that erratic or spurious results are due to the platform on which the code is running.

Beyond hardware issues, there are several useful techniques for checking the FDS source code that have been developed over the years. One of the best ways is to exploit symmetry. FDS is filled with thousands of lines of code in which the partial derivatives in the conservation equations are approximated as finite differences. It is very easy in this process to make a mistake. Consider, for example, the finite difference approximation of the thermal diffusion term in the  $ijk$ th cell of the three-dimensional grid:

$$\begin{aligned} (\nabla \cdot k \nabla T)_{ijk} &\approx \frac{1}{\delta x} \left[ k_{i+\frac{1}{2},jk} \frac{T_{i+1,jk} - T_{ijk}}{\delta x} - k_{i-\frac{1}{2},jk} \frac{T_{ijk} - T_{i-1,jk}}{\delta x} \right] + \\ &\quad \frac{1}{\delta y} \left[ k_{i,j+\frac{1}{2},k} \frac{T_{i,j+1,k} - T_{ijk}}{\delta y} - k_{i,j-\frac{1}{2},k} \frac{T_{ijk} - T_{i,j-1,k}}{\delta y} \right] + \\ &\quad \frac{1}{\delta z} \left[ k_{ij,k+\frac{1}{2}} \frac{T_{ij,k+1} - T_{ijk}}{\delta z} - k_{ij,k-\frac{1}{2}} \frac{T_{ijk} - T_{ij,k-1}}{\delta z} \right] \end{aligned}$$

which is written as follows in the Fortran source code:

```
DTDX = (TMP(I+1,J,K)-TMP(I,J,K))*RDXN(I)
KDTDX(I,J,K) = .5*(KP(I+1,J,K)+KP(I,J,K))*DTDX
DTDY = (TMP(I,J+1,K)-TMP(I,J,K))*RDYN(J)
KDTDY(I,J,K) = .5*(KP(I,J+1,K)+KP(I,J,K))*DTDY
DTDZ = (TMP(I,J,K+1)-TMP(I,J,K))*RDZN(K)
KDTDZ(I,J,K) = .5*(KP(I,J,K+1)+KP(I,J,K))*DTDZ
```

```

DELKDELT = (KDTDX(I,J,K)-KDTDX(I-1,J,K))*RDX(I) +
(KDTDY(I,J,K)-KDTDY(I,J-1,K))*RDY(J) +
(KDTDZ(I,J,K)-KDTDZ(I,J,K-1))*RDZ(K)

```

This is one of the simpler constructs because the pattern that emerges within the lines of code make it fairly easy to check. However, a mis-typing of an *I* or a *J*, a plus or a minus sign, or any of a hundred different mistakes can cause the code to fail, or worse produce the wrong answer. A simple way to eliminate many of these mistakes is to run simple scenarios that have perfectly symmetric initial and boundary conditions. For example, put a hot cube in the exact center of a larger cold compartment, turn off gravity, and watch the heat diffuse from the hot cube into the cold gas. Any simple error in the coding of the energy equation will show up almost immediately. Then, turn on gravity, and in the absence of any coding error, a perfectly symmetric plume will rise from the hot cube. This checks both the coding of the energy and the momentum equations. Similar checks can be made for all of the three dimensional finite difference routines. So extensive are these types of checks that the release version of FDS has a routine that generates a tiny amount of random noise in the initial flow field so as to eliminate any false symmetries that might arise in the numerical solution.

The process of adding new routines to FDS is as follows: typically the routine is written by one person who takes the latest version of the source code, adds the new routine, and writes a theoretical and numerical description for the FDS Technical Reference Guide, plus a description of the input parameters for the FDS User's Guide. The new version of FDS is then tested with a number of benchmark scenarios that exercise the range of the new parameters. Provisional acceptance of the new routine is based on several factors: (1) it produces more accurate results when compared to experimental measurement, (2) the theoretical description is sound, and (3) any empirical parameters are obtainable from the open literature or standard bench-scale apparatus. If the new routine is accepted, it is added to the working version of the software and evaluated by running the standard verification and validation test cases. Assuming that there are no intractable issues that arise during the testing period, the new routine eventually becomes part of the release version of FDS.

Even with all the code checking, it is still possible for errors to go unnoticed. One remedy is the fact that the source code for FDS is publicly released. Although it consists of on the order of 100,000 lines of Fortran statements, various independent researchers have been able to work with it, add enhancements needed for very specific applications or for research purposes, and report back to the developers bugs that have been detected. The source code is organized into 27 separate files, each containing subroutines related to a particular feature of the model, like the mass, momentum, and energy conservation equations, sprinkler activation and sprays, the pressure solver, etc. The lengthiest routines are devoted to input, output and initialization. Most of those working with the source code do not concern themselves with these lengthy routines but rather focus on the finite-difference algorithm contained in a few of the more important files. Most serious errors are found in these files, for they contain the core of the algorithm. The external researchers provide feedback on the organization of the code and its internal documentation, that is, comments within the source code itself. Plus, they must compile the code on their own computers, adding to its portability.

# Chapter 3

## The Basic Flow Solver

In this chapter we present test cases aimed at exercising the advective, pressure, and viscous terms, as well as the time integration for non-reacting flows.

### 3.1 Analytical Solution to the Navier-Stokes Equation (`ns2d`)

In this section we present an analytical solution that is useful for confirming the convergence rates of the truncation errors in the discretization of the terms in the governing equations. Consider the 2-D incompressible Navier-Stokes equations

$$\frac{\partial \mathbf{u}}{\partial t} + \mathbf{u} \cdot \nabla \mathbf{u} = -\nabla p + \nu \nabla^2 \mathbf{u}, \quad (3.1)$$

where the velocity is given by  $\mathbf{u} = [u, w]^T$ , and the kinematic viscosity and pressure are denoted  $\nu$  and  $p$ , respectively. An analytical solution of these equations is given by [39]

$$u(x, z, t) = 1 - A \cos(x-t) \sin(z-t) e^{-2\nu t}, \quad (3.2)$$

$$w(x, z, t) = 1 + A \sin(x-t) \cos(z-t) e^{-2\nu t}, \quad (3.3)$$

$$p(x, z, t) = -\frac{A^2}{4} [\cos(2(x-t)) + \cos(2(z-t))] e^{-4\nu t}. \quad (3.4)$$

Here,  $A$  represents an arbitrary amplitude and is assumed to take a value of 2 in this example. Note that this solution satisfies continuity for all time,

$$\nabla \cdot \mathbf{u} = 0, \quad (3.5)$$

is spatially periodic on an interval  $2\pi$  in each direction, and is temporally periodic on  $2\pi$  if  $\nu = 0$ ; otherwise, the solution decays exponentially. Below we present two series of tests which demonstrate the second-order accuracy of the FDS numerical scheme and thus provide a strong form of code verification for the advective and viscous terms which are exercised.

The physical domain of the problem is a square of side  $L = 2\pi$ . The grid spacing is uniform  $\delta x = \delta z = L/N$  in each direction with  $N = \{8, 16, 32, 64\}$  for each test series. The staggered grid locations are denoted  $x_i = i \delta x$  and  $z_k = k \delta z$ , and the cell centers are marked by an overbar,  $\bar{x}_i = x_i - \delta x/2$  and  $\bar{z}_k = z_k - \delta z/2$ .

First, we present qualitative results for the case in which  $\nu = 0$ . Thus, only the advective discretization and the time integration are being tested. Figure 3.1 shows the initial and final ( $t = 2\pi$ ) numerical solution for the case  $N = 64$ . As mentioned, with  $\nu = 0$  the solution is periodic in time and this figure demonstrates that, as should be the case, the FDS numerical solution is unaltered after one flow-through time.

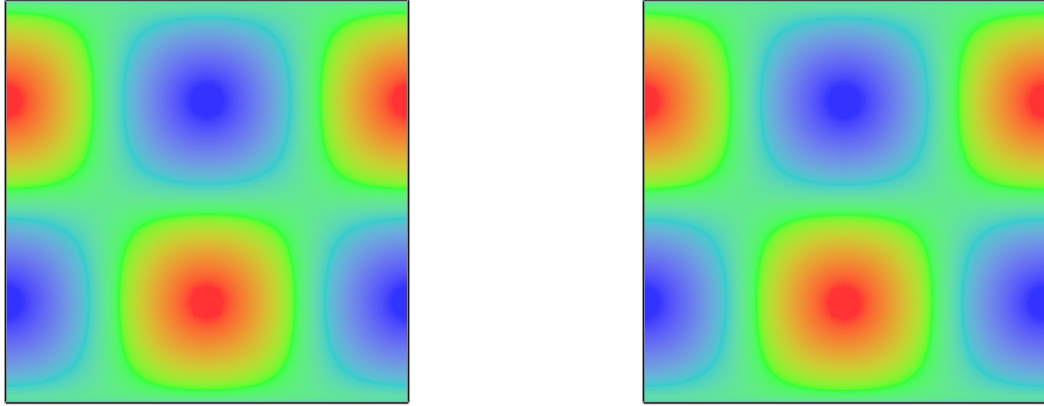


Figure 3.1: Initial and final states of the  $u$ -component of velocity.

Next, in Fig. 3.2, we show time histories of the  $u$ -component of velocity at the center of the domain for the case in which  $v = 0.1$ . It is clearly seen that the FDS solution (dashed line) converges to the analytical solution (solid line). Note that the analytical solution is evaluated at the same location as the FDS staggered grid location for the  $u$ -component of velocity,  $(x_{N/2}, \bar{z}_{N/2})$ , which is different in each case,  $N = \{8, 16, 32, 64\}$ .

Figure 3.3 is the key quantitative result of this verification test. In this figure we plot the rms error,  $\epsilon_{\text{rms}}$ , in the  $u$ -component of velocity against the grid spacing. The error is defined by

$$\epsilon_{\text{rms}} \equiv \sqrt{\frac{1}{M} \sum_{m=1}^M \left[ U_{ij}^m - u(x_i, \bar{z}_k, t_m) \right]^2}, \quad (3.6)$$

where  $M$  is the number of time steps and  $k$  is the time step index. The spatial indices are ( $i = N/2, k = N/2$ ) and  $U_{ij}^k$  represents the FDS value for the  $u$ -component of velocity at the staggered storage location for cell  $(i, j)$  at time step  $m$ ;  $u(x_i, \bar{z}_k, t_m)$  is the analytical solution for the  $u$ -component at the corresponding location in space and time. The figure confirms that the advective terms, the viscous terms, and the time integration in the FDS code are convergent and second-order accurate.

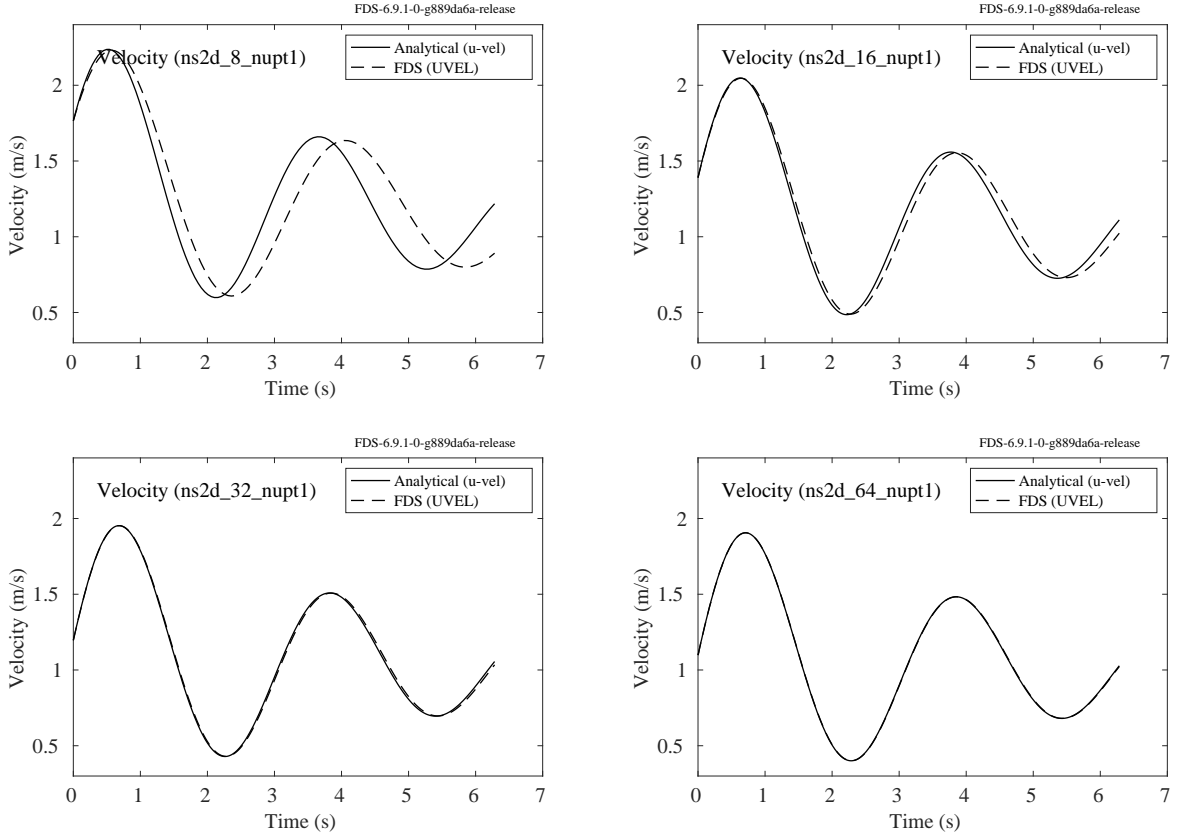


Figure 3.2: Time history of the  $u$ -component of velocity half a grid cell below the center of the domain for a range of grid resolutions. The domain is a square of side  $L = 2\pi$  m. The  $N \times N$  grid is uniform. Progressing from left to right and top to bottom we have resolutions  $N = \{8, 16, 32, 64\}$  clearly showing convergence of the FDS numerical solution (dashed line) to the analytical solution (solid line). The case is run with constant properties,  $\rho = 1$  kg/m<sup>3</sup> and  $\mu = 0.1$  kg/m/s, and a Courant-Friedrichs-Lowy (CFL) of 0.25.

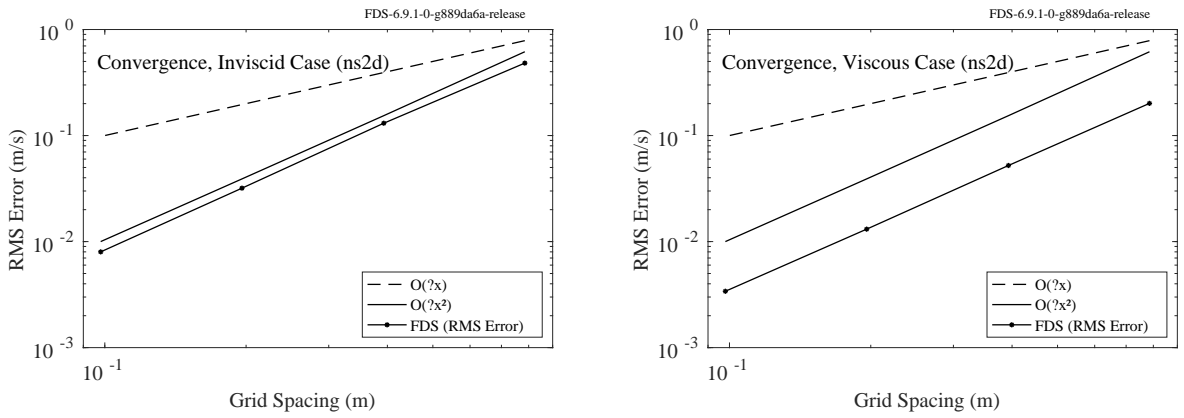


Figure 3.3: (Left) Convergence rate for the  $u$ -component of velocity with  $v = 0$  showing that the advective terms in the FDS code are second-order accurate. The asterisks represent the RMS error in the  $u$ -component for grid spacings of  $\delta x = L/N$  where  $L = 2\pi$  m and  $N = \{8, 16, 32, 64\}$ . The solid line represents first-order accuracy and the dashed line represents second-order accuracy. The simulation is run to a time of  $t = 2\pi$  s with a CFL of 0.25. The  $u$ -component at the center of the domain is compared with the analytical solution at the same location. (Right) Same case, except  $v = 0.1$ , showing that the viscous terms in the FDS code are second-order accurate.

## 3.2 Analytical Solution to the Continuity Equation

Analytical solutions for primitive flow variables (density, velocity, pressure, etc.) are useful in the development and testing of numerical schemes for CFD. For example, an analytical solution to the 2-D incompressible Navier-Stokes (NS) equations is presented in Section 3.1 and is used to verify the spatial and temporal accuracy of momentum equation.

The aim of the present work is to develop analytical solutions for the compressible NS equations that can be used for verification of both compressible and variable-density low-Mach flow solvers. The main idea is that, given a specified velocity field, the continuity equation can be rearranged into a linear hyperbolic PDE for the logarithm of the density. Let  $\rho$  denote the density and let  $\mathbf{u} = [u, v]^T$  denote the velocity. The continuity equation (conservation of mass) can then be written as

$$\frac{\partial \ln \rho}{\partial t} + \mathbf{u} \cdot \nabla \ln \rho + \nabla \cdot \mathbf{u} = 0. \quad (3.7)$$

Further, for certain simple specifications of the velocity this PDE can be solved using the method of characteristics.

In what follows we present 1-D and 2-D solutions to (3.7) for two basic irrotational flow fields. All the solutions are periodic in space. The first configuration is a pulsating flow that cycles between compressing the fluid toward the center and then the corners of the domain. In the second configuration, time periodicity is achieved by using a constant and uniform advection velocity in combination with the compression waves. This results in a solution with a qualitatively different character than the first.

### 3.2.1 Pulsating 1-D solution

We specify the velocity as

$$u(x, t) = B \sin(x) \cos(\omega t), \quad (3.8)$$

where  $B$  is a constant amplitude and  $\omega$  is the frequency of the compression cycle. The velocity divergence in 1-D is then

$$\frac{\partial u}{\partial x} = B \cos(x) \cos(\omega t). \quad (3.9)$$

Let  $q \equiv \ln \rho$  (this notation is used throughout this work). The 1-D continuity equation can then be written as the following linear hyperbolic PDE:

$$\frac{\partial q}{\partial t} + B \sin(x) \cos(\omega t) \frac{\partial q}{\partial x} + B \cos(x) \cos(\omega t) = 0, \quad (3.10)$$

which can be solved using the method of characteristics to obtain the solution

$$q(x, t) = q(x_0[x, t], 0) + \ln \left\{ \frac{1 + \tan^2 \left( \frac{x_0[x, t]}{2} \right) \exp \left( \frac{2B}{\omega} \sin[\omega t] \right)}{1 + \tan^2 \left( \frac{x_0[x, t]}{2} \right)} \right\} - \frac{B}{\omega} \sin(\omega t), \quad (3.11)$$

where the initial position is given by

$$x_0(x, t) = 2 \arctan \left( \tan \left[ \frac{x}{2} \right] \exp \left[ -\frac{B}{\omega} \sin(\omega t) \right] \right). \quad (3.12)$$

Note that we have taken the initial time to be zero, as is done throughout this work.

### 3.2.2 Pulsating 2-D solution (pulsating)

There is a simple extension of the 1-D stationary wave solution to 2-D. In this section we consider the velocity field  $\mathbf{u} = [u, v]^T$  with components and velocity divergence given by

$$u(x, t) = B \sin(x) \cos(\omega t), \quad (3.13)$$

$$v(y, t) = B \sin(y) \cos(\omega t), \quad (3.14)$$

$$\nabla \cdot \mathbf{u} = B(\cos[x] + \cos[y]) \cos(\omega t), \quad (3.15)$$

where, again,  $B$  is a constant amplitude and  $\omega$  is the compression frequency. The 2-D continuity equation may then be written as

$$\frac{\partial q}{\partial t} + B \sin(x) \cos(\omega t) \frac{\partial q}{\partial x} + B \sin(y) \cos(\omega t) \frac{\partial q}{\partial y} + B(\cos[x] + \cos[y]) \cos(\omega t) = 0, \quad (3.16)$$

where, again,  $q \equiv \ln \rho(\mathbf{x}, t)$ .

The solution to (3.16) can be obtained by adding the solutions of the following two PDEs:

$$\frac{\partial q_1}{\partial t} + B \sin(x) \cos(\omega t) \frac{\partial q_1}{\partial x} + B \cos(x) \cos(\omega t) = 0, \quad (3.17)$$

$$\frac{\partial q_2}{\partial t} + B \sin(y) \cos(\omega t) \frac{\partial q_2}{\partial y} + B \cos(y) \cos(\omega t) = 0. \quad (3.18)$$

Thus, utilizing (3.11) and (3.12), and replacing  $q_1(x_0[x, t], 0) + q_2(y_0[y, t], 0)$  with  $q_0(x, y, t)$ , we find that the solution to (3.16) is

$$\begin{aligned} q(x, y, t) &= q_0(x, y, t) \\ &+ \ln \left\{ \frac{1 + a(x_0[x, t]) \exp\left(\frac{2B}{\omega} \sin[\omega t]\right)}{1 + a(x_0[x, t])} \right\} \\ &+ \ln \left\{ \frac{1 + a(y_0[y, t]) \exp\left(\frac{2B}{\omega} \sin[\omega t]\right)}{1 + a(y_0[y, t])} \right\} \\ &- \frac{2B}{\omega} \sin(\omega t), \end{aligned} \quad (3.19)$$

where

$$a(z) \equiv \tan^2\left(\frac{z}{2}\right), \quad (3.20)$$

and the initial positions are given by

$$x_0(x, t) = 2 \arctan \left( \tan \left[ \frac{x}{2} \right] \exp \left[ -\frac{B}{\omega} \sin(\omega t) \right] \right), \quad (3.21)$$

$$y_0(y, t) = 2 \arctan \left( \tan \left[ \frac{y}{2} \right] \exp \left[ -\frac{B}{\omega} \sin(\omega t) \right] \right). \quad (3.22)$$

Note that the initial condition  $q_0(x, y, t)$  is restricted to cases where  $\frac{\partial q_0}{\partial x}$  is independent of  $y$  and  $\frac{\partial q_0}{\partial y}$  is independent of  $x$ . That is, the function  $q_0$  must be *additively separable*.

An example of the solution to (3.19) is shown in Fig. 3.4. The initial condition for the density is specified as  $\rho(\mathbf{x}, 0) = 1$  and the amplitude and frequency are set to unity,  $B = 1$  and  $\omega = 1$ . FDS is run with three scalar transport schemes: central differencing, Superbee, and the CHARM flux limiter. The solution at  $(x, y) = (3\pi/2, 3\pi/2)$  for successively finer grid resolutions is plotted as a time series on the left and may be compared with the analytical solution (black line). On the right, we confirm second-order convergence for the FDS implementation. Central differencing and the CHARM limiter outperform Superbee for this problem because the solution is relatively smooth.

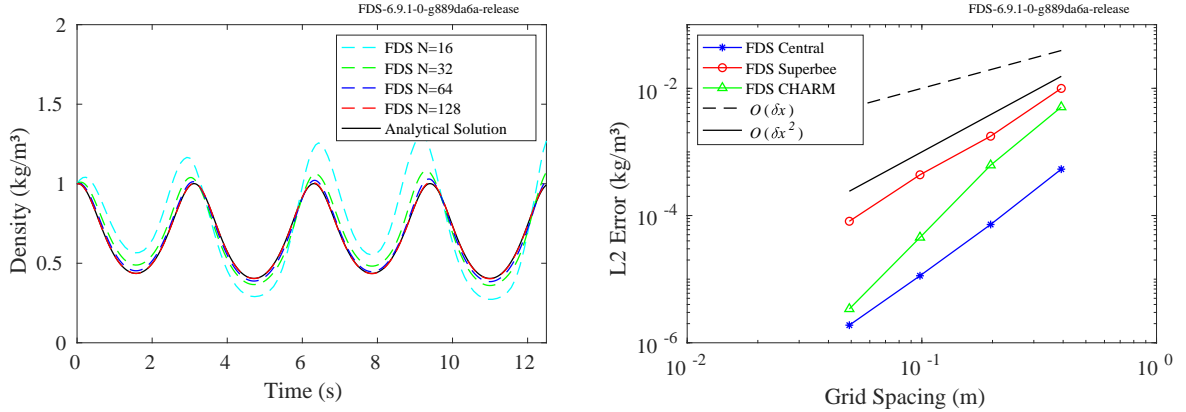


Figure 3.4: (Left) Time series of  $\rho$  at the position  $(x, y) = (3\pi/2, 3\pi/2)$  for several grid resolutions using the Superbee limiter. (Right) Convergence plot for central differencing, Superbee, and CHARM. All schemes are second-order accurate.

### 3.2.3 Stationary compression wave in 1-D

Another problem which can be solved analytically is that of a stationary compression wave. In this section we consider a stationary compression wave combined with a constant and uniform advection velocity in 1-D. The velocity is specified to be

$$u(x) = c + \sin(x), \quad (3.23)$$

where  $|c| > 1$  is a constant. The 1-D continuity equation becomes

$$\frac{\partial q}{\partial t} + [c + \sin(x)] \frac{\partial q}{\partial x} + \cos(x) = 0. \quad (3.24)$$

A solution to (3.24) is

$$\begin{aligned} q(x, t) &= q(x_0[x, t], 0) \\ &+ \ln \left\{ -c^2 - \cos(bt + 2 \arctan[\gamma(x, t)]) + b \sin(bt + 2 \arctan[\gamma(x, t)]) \right\} \\ &- \ln \left\{ -c^2 - \cos(2 \arctan[\gamma(x, t)]) + b \sin(2 \arctan[\gamma(x, t)]) \right\}, \end{aligned} \quad (3.25)$$

where

$$b \equiv \sqrt{-1 + c^2} > 0, \quad (3.26)$$

$$\gamma(x, t) = \frac{1 + c \tan\left(\frac{x_0[x, t]}{2}\right)}{b}, \quad (3.27)$$

and

$$x_0(x, t) = 2 \arctan\left(\frac{b}{c} \tan\left[\arctan\left\{\frac{1 + c \tan[x/2]}{b}\right\} - \frac{bt}{2}\right] - \frac{1}{c}\right). \quad (3.28)$$

### 3.2.4 Stationary compression wave in 2-D (`compression_wave`)

As with the pulsating flow, there is a simple extension of the 1-D stationary wave solution to 2-D. In this section we consider the velocity field with components

$$u(x) = c_1 + \sin(x), \quad (3.29)$$

$$v(y) = c_2 + \sin(y). \quad (3.30)$$

The continuity equation can be written as

$$\frac{\partial q}{\partial t} + [c_1 + \sin(x)] \frac{\partial q}{\partial x} + [c_2 + \sin(y)] \frac{\partial q}{\partial y} + \cos(x) + \cos(y) = 0. \quad (3.31)$$

A solution to (3.31) is

$$\begin{aligned} q(x, y, t) &= q_0(x, y, t) \\ &+ \mathcal{I}_1(x, t) - \mathcal{I}_1^0(x, t) \\ &+ \mathcal{I}_2(y, t) - \mathcal{I}_2^0(y, t), \end{aligned} \quad (3.32)$$

where

$$\mathcal{I}_i(z, t) = \ln \left\{ -c_i^2 - \cos(b_i t + 2 \arctan[\gamma_i(z, t)]) + b_i \sin(b_i t + 2 \arctan[\gamma_i(z, t)]) \right\}, \quad (3.33)$$

$$\mathcal{I}_i^0(z, t) = \ln \left\{ -c_i^2 - \cos(2 \arctan[\gamma_i(z, t)]) + b_i \sin(2 \arctan[\gamma_i(z, t)]) \right\}, \quad (3.34)$$

and

$$b_i \equiv \sqrt{-1 + c_i^2} > 0, \quad (3.35)$$

$$\gamma_i(z, t) = \frac{1 + c_i \tan\left(\frac{z_0[z, t]}{2}\right)}{b_i}, \quad (3.36)$$

$$z_0(z, t) = 2 \arctan\left(\frac{b_i}{c_i} \tan\left[\arctan\left\{\frac{1 + c_i \tan[z/2]}{b_i}\right\} - \frac{b_i t}{2}\right] - \frac{1}{c_i}\right). \quad (3.37)$$

Note that  $z_0 \Rightarrow x_0$  for  $i = 1$  and  $z_0 \Rightarrow y_0$  for  $i = 2$ . To be clear, no summation is implied over repeated indices. Also, note that the same restrictions apply to the initial condition as did in Section 3.2.2. Namely, that  $\frac{\partial q_0}{\partial x}$  is independent of  $y$  and  $\frac{\partial q_0}{\partial y}$  is independent of  $x$ .

An example of the solution to (3.32) is shown in Fig. 3.5. In this case we set  $c_1 = 2$  and  $c_2 = 3$  to create an asymmetry in the flow. The periodicity in time depends on the choices of  $c_1$  and  $c_2$ ; it is possible that no periodicity exists. We have not found a case that generates a singularity. The analytical time series of the density at the position  $(x, y) = (3\pi/2, 3\pi/2)$  is shown as the solid black line. FDS is run with the CHARM flux limiter scheme (as this is a DNS flow field). The solution at successively finer grid resolutions is plotted and compared with the analytical solution, demonstrating convergence of the scheme. On the right side of the figure we demonstrate second-order convergence of the central, Superbee, and CHARM limiter schemes in FDS.

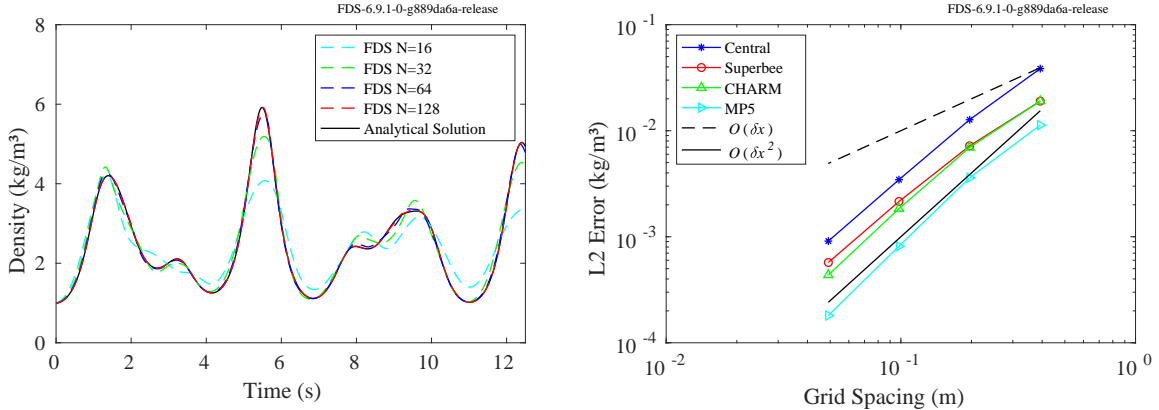


Figure 3.5: (Left) Time series of  $\rho$  at the position  $(x, y) = (3\pi/2, 3\pi/2)$  for several grid resolutions using the CHARM flux limiter. (Right) Convergence plot for three different scalar transport schemes in FDS: central, Superbee, and CHARM. All schemes are second-order accurate. In addition, notice that Superbee gives the lowest error at the coarsest resolution while CHARM gives the lowest error at higher resolution. This is one reason why Superbee is recommended for VLES and CHARM is the default for LES and DNS.

### 3.3 Scalar Transport

#### 3.3.1 Uniform Velocity Field (`move_slug`)

In this section we demonstrate the qualitative behavior of the Superbee flux limiter scheme for transport of a square wave. The diffusivity is set to zero and the advecting velocity is constant and uniform  $\mathbf{u} = [1.0 \ 1.0]$ . The domain is the unit square with a passive scalar marker initialized to zero everywhere, except for two ‘slugs’ of mass. The first slug is set to unity over the region  $x \times z = [0.125, 0.375] \times [0.125, 0.375]$ . The second slug is set to 1/2 over the region  $x \times z = [0.500, 0.750] \times [0.500, 0.750]$ . With the scalar bounds set to [0,1], these slugs demonstrate both the boundedness and TVD (total variation diminishing) behavior of the transport scheme.

This case also tests two different types of boundary conditions applied in FDS. First, the domain is periodic and the simulation runs for one flow through time. The scalar slugs therefore ideally arrive back to their original locations with as little diffusion as possible. Also, the domain is broken into four equally sized meshes, each with  $40 \times 40$  uniform cells. To increase temporal accuracy and focus on the potential spacial error, we run the case with a CFL of 0.25. In FDS, we refer to the mesh interface as an ‘interpolated boundary’.

The results of the test are shown visually in Fig. 3.6. The upper-left image shows the initial condition. The black lines indicate the mesh interfaces. To the right of the initial condition we show the first slug crossing the mesh interfaces without incurring spurious noise. The lower left image shows the final result for the Superbee limiter. By comparison with a first-order scheme (lower right), this test case confirms that relatively low levels of diffusion are incurred at both periodic and interpolated boundaries in FDS.

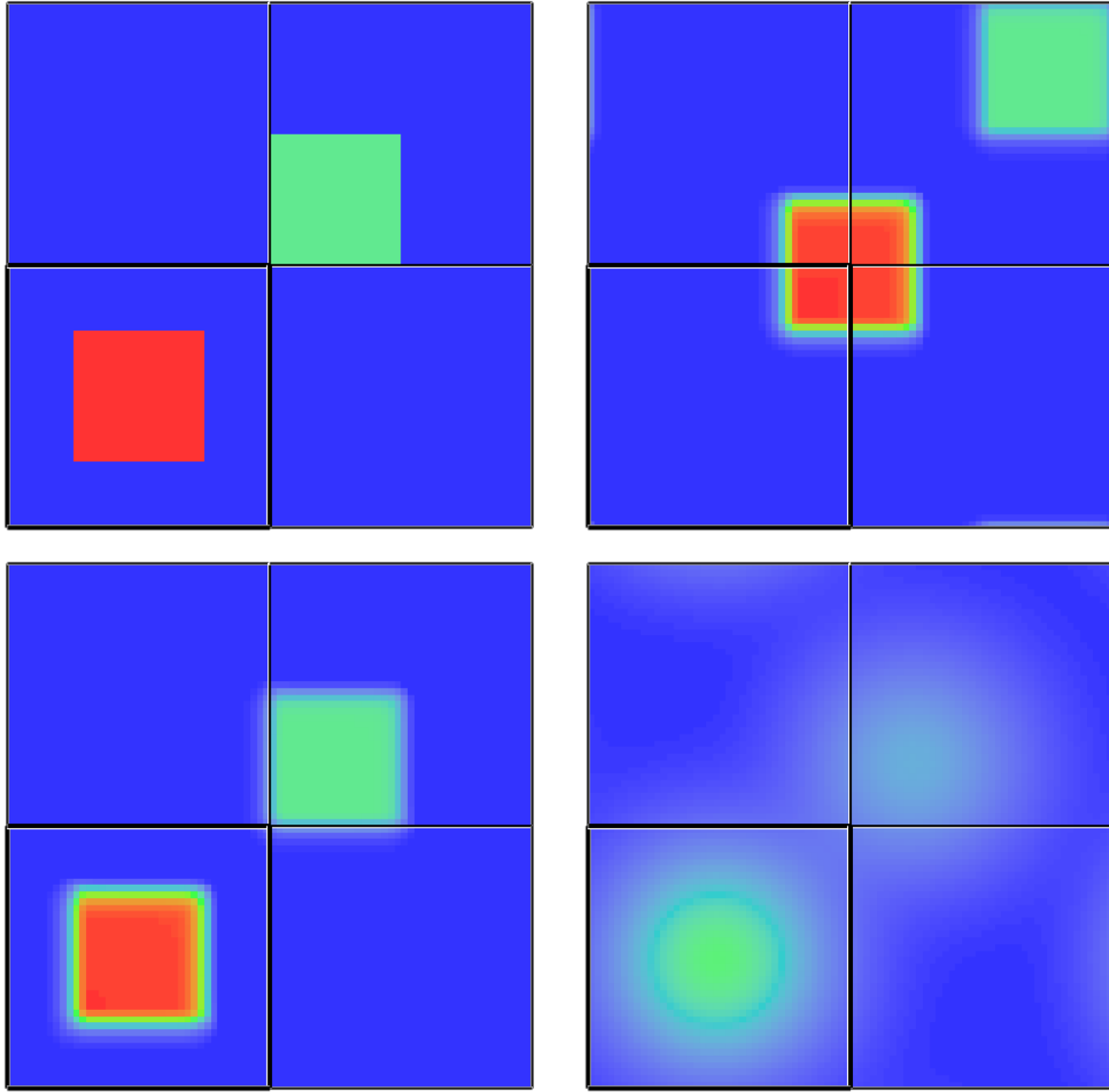


Figure 3.6: (Upper left) Initial condition. (Upper right) Superbee solution after 0.175 seconds showing the scalar slug cleanly passing through the mesh interface. (Lower left) Final result for Superbee after one flow through time. (Lower right) Result for first-order upwinding after one flow through time, illustrating the relatively low dissipation of the Superbee scheme. Note that, though the first-order scheme is available as an option in FDS, it is presented here for comparison purposes only. In practice, the higher order Superbee scheme is preferred for VLES (FDS default).

### 3.3.2 Solid Body Rotation Velocity Field (`soborot`)

In this series of tests, the velocity field is a simple solid-body rotation about the origin. The field is given by

$$u = z \quad (3.38)$$

$$w = -x \quad (3.39)$$

The domain is a unit square with the origin at the lower-right. Two wave forms are examined. The first is a simple square wave with a passive scalar introduced at the  $z = 0$  boundary plane with a mass fraction value of 1 for  $0.25 \leq r \leq 0.75$ , where  $r$  is the radial position from the origin. The second is a section of a compressed cosine wave with the phase shifted so that the minimum aligns with the start and end of the square wave. The initial condition is given by  $\frac{1}{2}(1 + \cos(4\pi r))$  for  $0.25 \leq r \leq 0.75$ . The velocity field is held fixed. The scalar fields are evolved for  $\pi/2$  s (1/4 rotation). The scalar concentration is measured along the upper-left diagonal as shown in Fig. 3.7. The constant velocity field is shown on the left and the solution of the square wave for the CHARM scheme at  $\delta x = 1/64$  m is shown on the right.

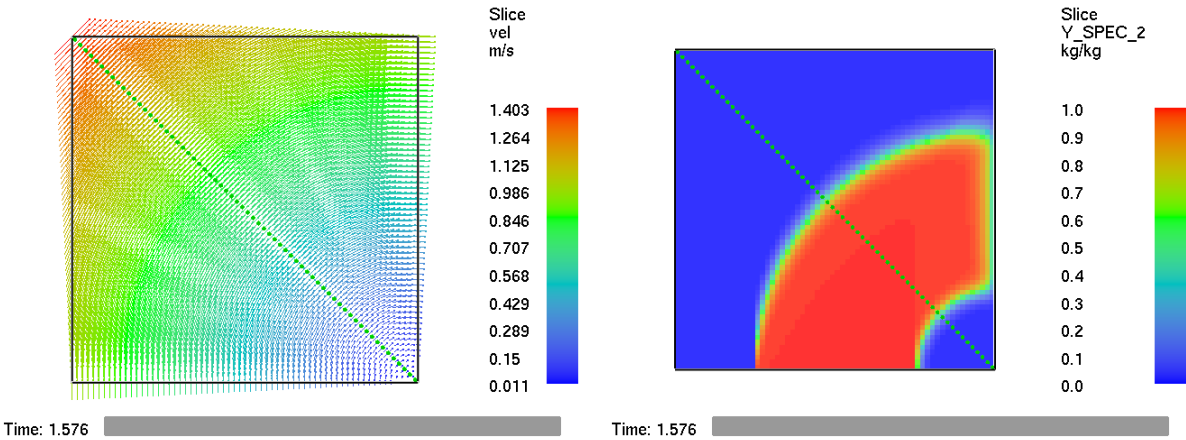


Figure 3.7: (Left) Solid body rotation velocity field. (Right) Tracer concentration at time  $\pi/2$  (1/4 rotation).

The steady state analytical solution to this problem is that the scalar field remains constant as a function of radius from the origin. In Fig. 3.8 we plot the L2 Error for Godunov, CHARM, and Superbee flux limiter schemes for the square wave initial condition. As shown in [40], the Godunov scheme shows  $\mathcal{O}(\delta x^{1/2})$  convergence for this discontinuous solution. Other schemes have smaller initial errors, but also ultimately converge at the same rate for this problem.

For the cosine wave initial condition the derivatives of the scalar field are continuous. Therefore, we see  $\mathcal{O}(\delta x^2)$  convergence of the CHARM and MP5 schemes, as shown in Fig. 3.9. Superbee shows smaller error at coarse resolution, but the gradient steepening degrades its accuracy at higher resolutions—hence CHARM is selected for LES and DNS.

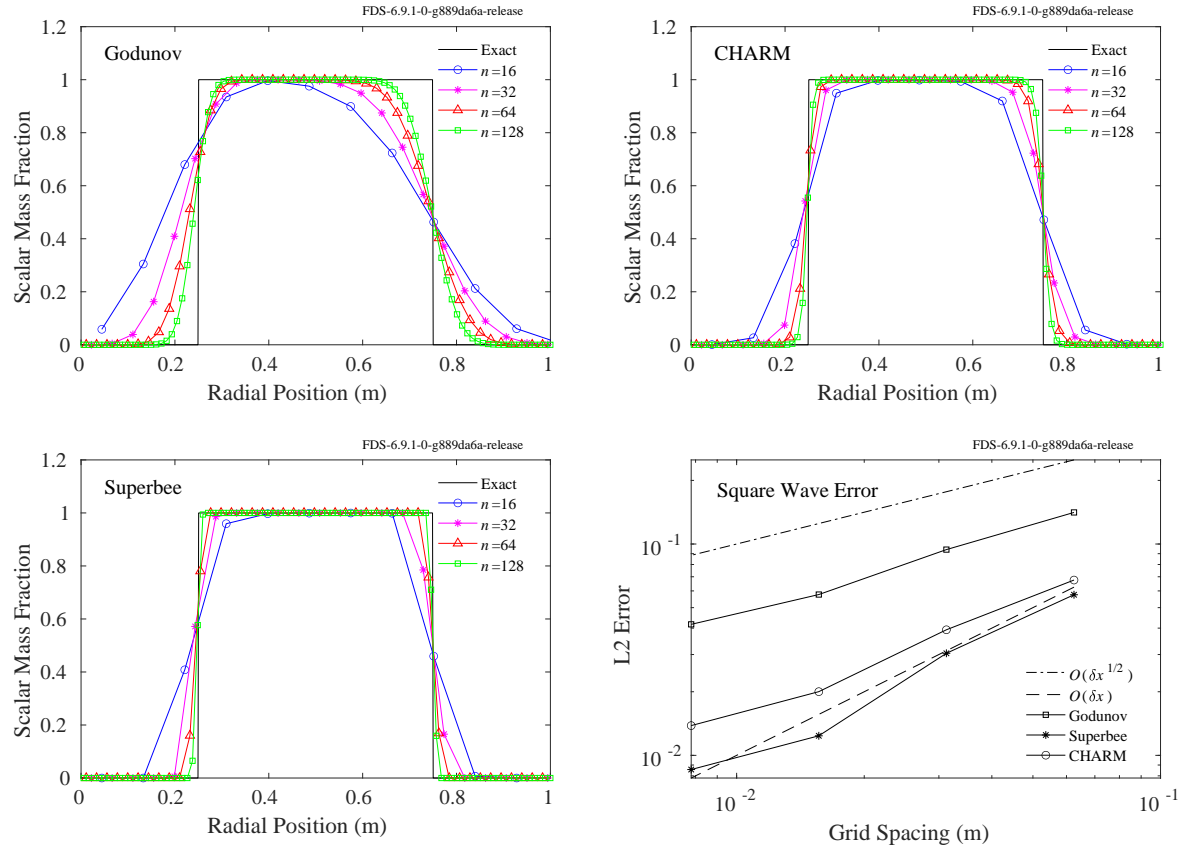


Figure 3.8: Solid body rotation square wave solution convergence. Scalar fields along upper-left diagonal for Godunov (upper-left), CHARM (upper-right), and Superbee (lower-left). (Lower-right) L2 Error.

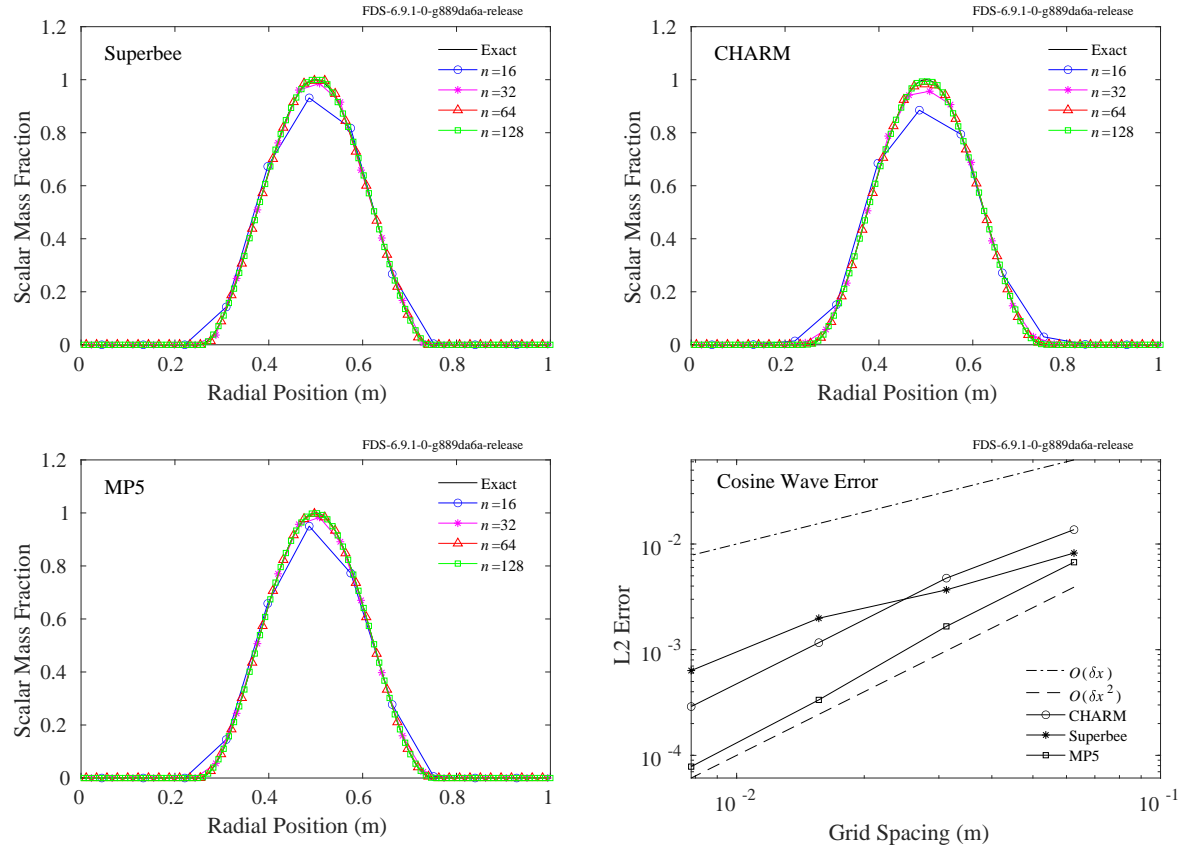


Figure 3.9: Solid body rotation cosine wave solution convergence. Scalar fields along upper-left diagonal for Superbee (upper-left), CHARM (upper-right), and MP5 (lower-left). (Lower-right) L2 Error.

## 3.4 Temporal Error Analysis for a Variable-Density Projection (`saad`)

Tony Saad and James Sutherland, The University of Utah

This is a 1-D variable-density benchmark solution for an inviscid, non-reacting mixture of two fluids with different densities (10:1 ratio) in a plug-flow system [41]. The diffusivity is set to zero. The governing equations for the mixture fraction,  $Z$ , and the  $x$  component of momentum,  $u$ , are

$$\frac{\partial Z}{\partial t} = -u \frac{\partial Z}{\partial x}, \quad (3.40)$$

$$\frac{\partial u}{\partial t} = -u \frac{\partial u}{\partial x} - \frac{1}{\rho} \frac{\partial \tilde{p}}{\partial x}. \quad (3.41)$$

The equation of state gives the following relationship between the mixture fraction and the density:

$$\frac{1}{\rho} = \frac{(1-Z)}{\rho_0} + \frac{Z}{\rho_1}. \quad (3.42)$$

The FDS input files may be found in

`/Verification/Scalar_Analytical_Solution/saad_512_cfl*.fds.`

The densities are set to  $\rho_0 = 0.5 \text{ kg/m}^3$  and  $\rho_1 = 5 \text{ kg/m}^3$ , respectively. The initial field for  $Z$  is specified as a sine wave on a 1-D domain of length  $L = 2 \text{ m}$  (see Fig. 3.10 below).

$$Z(x, 0) = \frac{1}{2} (1 + \sin(2\pi x/L)) \quad (3.43)$$

All cases are run with  $N_x = 512$  grid points. The effect of the spatial error is discussed below. The velocity field is initialized to  $u(x, 0) = U_0 = 1 \text{ m/s}$ , which is the analytical solution for the velocity for all time,  $u(x, t) = U_0$ . Note, however, that the velocity field is not “frozen” in the calculations, it is subject to variation by the projection scheme (if we are doing things correctly, then the velocity will not change). The analytical solution for the mixture fraction is given by a characteristic solution:

$$Z(x, t) = Z_0(x - U_0 t). \quad (3.44)$$

**Computing Temporal Order without an Analytical Solution** Despite having an analytical solution for this case, it is difficult to use this solution to assess the temporal error in the time integration scheme alone. This is because the spatial errors will typically dominate for an explicit scheme. To overcome this, we use a method based on Richardson extrapolation (see, e.g., Moin [42]). The idea is to expand a quantity  $f$  in a Taylor series with different time increments with a constant ratio  $r = \frac{\Delta t_{\text{fine}}}{\Delta t_{\text{coarse}}} < 1$ .

$$f_1 = f_0 + a_0 \Delta t^p + \mathcal{O}(\Delta t^{p+1}) \quad (3.45)$$

$$f_2 = f_0 + a_0(r \Delta t)^p + \mathcal{O}(r^{p+1} \Delta t^{p+1}) \quad (3.46)$$

$$f_3 = f_0 + a_0(r^2 \Delta t)^p + \mathcal{O}(r^{2p+2} \Delta t^{p+1}) \quad (3.47)$$

The temporal order of accuracy is given by  $p$ , which may be written as

$$p = \frac{\ln \left( \frac{f_3 - f_2}{f_2 - f_1} \right)}{\ln r} \quad (3.48)$$

This procedure effectively filters out the spatial error. It is, in fact, possible to run this case with a first-order spatial scheme (e.g., Godunov) and still see second-order temporal convergence.

**Temporal Order Results** The `saad*.fds` cases are run with three different time steps, each refined by a factor of 2, and integrated to a total time  $T = 0.390625$  s. This time represents 100 time steps for a case with  $\text{CFL} = 1$ . To assess the asymptotic temporal order from Eq. (3.48), we use the three finest time steps corresponding to  $\text{CFL} = [0.25, 0.125, 0.0625]$  for the solutions  $[f_1, f_2, f_3]$ , respectively.

The results are shown in Fig. 3.10. At the top of the figure you can see the initial and final fields for the mixture fraction and density for the finest time step. Both fields have been advected to the right. In the lower-left we plot the numerator and denominator in Eq. (3.48) for the density solution. On the bottom-right we show the order  $p$  computed pointwise on the 1-D domain. The deviations from second-order behavior correspond to degenerate in the formula for  $p$  (as shown in the lower-left plot) where either the denominator is near zero ( $p$  spikes up) or the numerator and denominator cross (thus  $p = 0$ ). The  $l_2$  norm of  $p$  computed pointwise is 2.0053. Note that the  $l_\infty$  norm (computed pointwise) is degenerate for the reasons just discussed. A method to overcome this issue is discussed in Sec. 3.5.

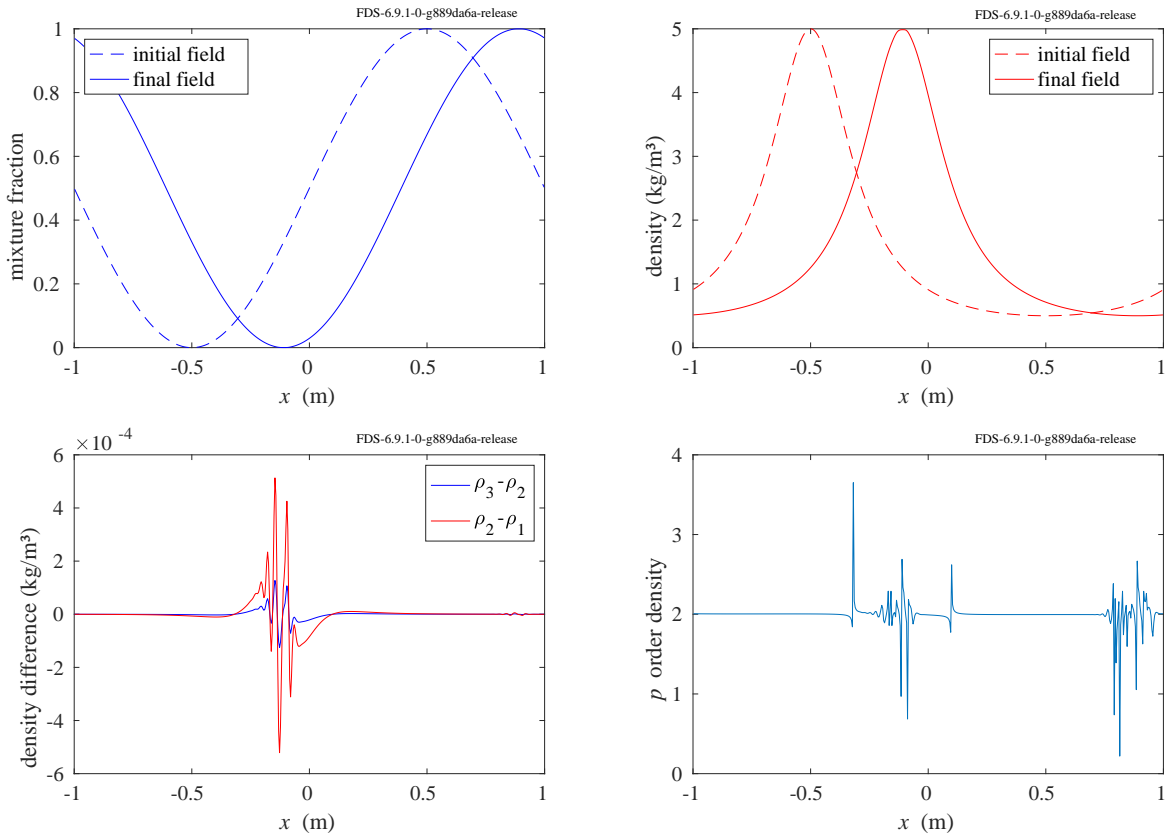


Figure 3.10: Temporal order for a variable-density projection. (Upper-left) Initial and final field for mixture fraction. (Upper-right) Initial and final field for density. (Lower-left) Plot of numerator and denominator in Eq. (3.48) for density at final time. (Lower-right) Plot of  $p$  computed pointwise from Eq. (3.48). Fluctuations are due to degenerate points in the formula for  $p$ . The temporal order is  $p = 2.0053$ .

### 3.5 Variable-Density Manufactured Solution (`shunn3`)

To demonstrate second-order accuracy of the FDS time-marching algorithm, here we present numerical results for the manufactured solution proposed by Shunn et al. [43] (with a modified pressure solution).

The parameters for this problem are given in Table 3.1. In the 2-D sinusoidal solution given below,  $Z$  is the mixture fraction,  $\rho$  is the density,  $u$  and  $v$  are velocity components, and  $H$  is the Bernoulli integral ( $H \equiv \tilde{p}/\rho + \frac{1}{2}|\mathbf{u}|^2$  where  $\tilde{p}$  is the hydrodynamic pressure). The solution translates diagonally across the domain with velocity  $[u_f, v_f]$ . The translated positions are defined by  $\hat{x} \equiv x - u_f t$  and  $\hat{y} \equiv y - v_f t$ . The solution is spatially periodic on a square domain extending from  $-1$  m to  $1$  m ( $L = 2$  m) on each side and has a time period of  $1$  s.

Table 3.1: Parameters for Shunn et al. [43] manufactured solution.

Parameter	Value	Units
$\rho_0$	5	$\text{kg}/\text{m}^3$
$\rho_1$	1	$\text{kg}/\text{m}^3$
$k = \omega$	2	$1/\text{m}, 1/\text{s}$
$u_f = v_f$	0.5	$\text{m}/\text{s}$
$\rho D = \mu$	0.001	$\text{kg}/(\text{ms})$

$$Z(x, y, t) = \frac{1 + \sin(\pi k \hat{x}) \sin(\pi k \hat{y}) \cos(\pi \omega t)}{(1 + \frac{\rho_0}{\rho_1}) + (1 - \frac{\rho_0}{\rho_1}) \sin(\pi k \hat{x}) \sin(\pi k \hat{y}) \cos(\pi \omega t)} \quad (3.49)$$

$$\rho(x, y, t) = \left( \frac{Z(x, y, t)}{\rho_1} + \frac{1 - Z(x, y, t)}{\rho_0} \right)^{-1} \quad (3.50)$$

$$u(x, y, t) = u_f + \frac{\rho_1 - \rho_0}{\rho(x, y, t)} \left( \frac{-\omega}{4k} \right) \cos(\pi k \hat{x}) \sin(\pi k \hat{y}) \sin(\pi \omega t) \quad (3.51)$$

$$v(x, y, t) = v_f + \frac{\rho_1 - \rho_0}{\rho(x, y, t)} \left( \frac{-\omega}{4k} \right) \sin(\pi k \hat{x}) \cos(\pi k \hat{y}) \sin(\pi \omega t) \quad (3.52)$$

$$H(x, y, t) = \frac{1}{2}(u(x, y, t) - u_f)(v(x, y, t) - v_f) \quad (3.53)$$

The source terms for the manufactured solution,  $\dot{Q}_\rho$ , etc., are defined as the residuals of the transport equations:

$$\frac{\partial \rho}{\partial t} + \nabla \cdot (\rho \mathbf{u}) = \dot{Q}_\rho, \quad (3.54)$$

$$\frac{\partial(\rho Z)}{\partial t} + \nabla \cdot (\rho Z \mathbf{u}) - \nabla \cdot (\rho D \nabla Z) = \dot{Q}_Z, \quad (3.55)$$

$$\frac{\partial \mathbf{u}}{\partial t} - \mathbf{u} \times (\nabla \times \mathbf{u}) + \nabla H - \tilde{p} \nabla (1/\rho) - \frac{1}{\rho} \nabla \cdot \mathbf{T} = \dot{Q}_{\mathbf{u}}, \quad (3.56)$$

where the components of the deviatoric stress tensor,  $\mathbf{T}$ , are given by

$$T_{ij} = 2\mu \left( S_{ij} - \frac{1}{3} S_{kk} \delta_{ij} \right) ; \quad S_{ij} \equiv \frac{1}{2} \left( \frac{\partial u_i}{\partial x_j} + \frac{\partial u_j}{\partial x_i} \right). \quad (3.57)$$

The mass source terms (which are complex sinusoidal functions) may be obtained from [43], by looking at the source code in the FDS repository [44] (see module `MANUFACTURED_SOLUTIONS` in `turb.f90`), or by running the `sympy` (Symbolic Python) script provided under

`/Utilities/Python/shunn3_stokes_mms_sym.py`. A feature of this particular solution is that the

mass source is zero,  $\dot{Q}_\rho = 0$ , which provides a more realistic test case and simplifies the MMS implementation. Note that the pressure solution has been modified from Shunn et al. [43] so that the  $H$  solution is compatible with periodic boundary conditions. A new momentum source term is derived  $\dot{Q}_{\mathbf{u}}$  that differs from Shunn et al.

### Manufactured Solution Procedure

Two species transport equations are solved. The mixture fraction in the manufactured solution is set as component 2 while the background species is set to component 1:

$$\frac{\partial(\rho Z_1)}{\partial t} + \nabla \cdot (\rho Z_1 \mathbf{u}) - \nabla \cdot (\rho D \nabla Z_1) = -\dot{Q}_Z, \quad (3.58)$$

$$\frac{\partial(\rho Z_2)}{\partial t} + \nabla \cdot (\rho Z_2 \mathbf{u}) - \nabla \cdot (\rho D \nabla Z_2) = +\dot{Q}_Z. \quad (3.59)$$

The density is obtained via  $\rho = (\rho Z)_1 + (\rho Z)_2$ .

The RHS of the momentum equation is augmented as follows:

$$\frac{\partial \mathbf{u}}{\partial t} = -(\mathbf{F} + \nabla H) + \dot{Q}_{\mathbf{u}}. \quad (3.60)$$

The Poisson equation for  $H$  becomes

$$\nabla^2 H = - \left[ \nabla \cdot (\mathbf{F} - \dot{Q}_{\mathbf{u}}) + \frac{\partial}{\partial t} (\nabla \cdot \mathbf{u}) \right]. \quad (3.61)$$

Simulations were performed for  $N = \{32, 64, 128, 256, 512\}$ , where  $N$  is the number of cells in each direction, using an adaptive time step satisfying both convective and diffusive CFL numbers of 0.5. The time step criterion and the simulation parameters in Table 3.1 were chosen to match Shunn et al. [43]. The species mass density equations, (3.58) and (3.59), are solved using the CHARM flux limiter. Qualitative results for the  $256^2$  case are shown in Fig. 3.11. These images may be compared to the images presented in [43]. In Fig. 3.12, we plot the  $L_2$  error at time  $t = 0.9$  s<sup>1</sup> as a function of grid spacing,  $\Delta x = L/N$ , confirming second-order accuracy of the solutions for density, mixture fraction, and velocity. As shown in Fig. 3.12, schemes such as ours, where the pressure is set to zero at the beginning of each stage of the integration (in other words, no pressure gradient term shows up in the force on the RHS of the Poisson equation), are known to be first-order accurate for pressure [45]. This is not a severe limitation of the algorithm since the hydrodynamic pressure does not factor into the equation of state for low-Mach flows.

### Temporal Error Analysis

The convergence plot in Fig. 3.12 is based on a constant CFL with increasing spatial resolution. From this plot, the temporal accuracy is hard to discern. Further, the temporal accuracy for the Saad problem in Sec. 3.4 may be a special case since most of the terms in the divergence are zero for that problem. For the Shunn case, the right-hand-side of the Poisson equation is non-trivial and so it is useful to re-examine the temporal order for this case. As with the Saad case, here we run a series of tests at constant grid resolution  $256 \times 256$  while decreasing the time step. The three finest time steps correspond to  $\text{CFL} = [0.25, 0.125, 0.0625]$  for the solutions  $[f_1, f_2, f_3]$  in Eq. (3.48). The simulations are run to a total time equivalent to 2 time steps for a  $\text{CFL}=1$  calculation.

---

<sup>1</sup>At  $t = 1$  s the  $H$  manufactured solution is trivially zero everywhere and fortuitous error cancellation occurs.

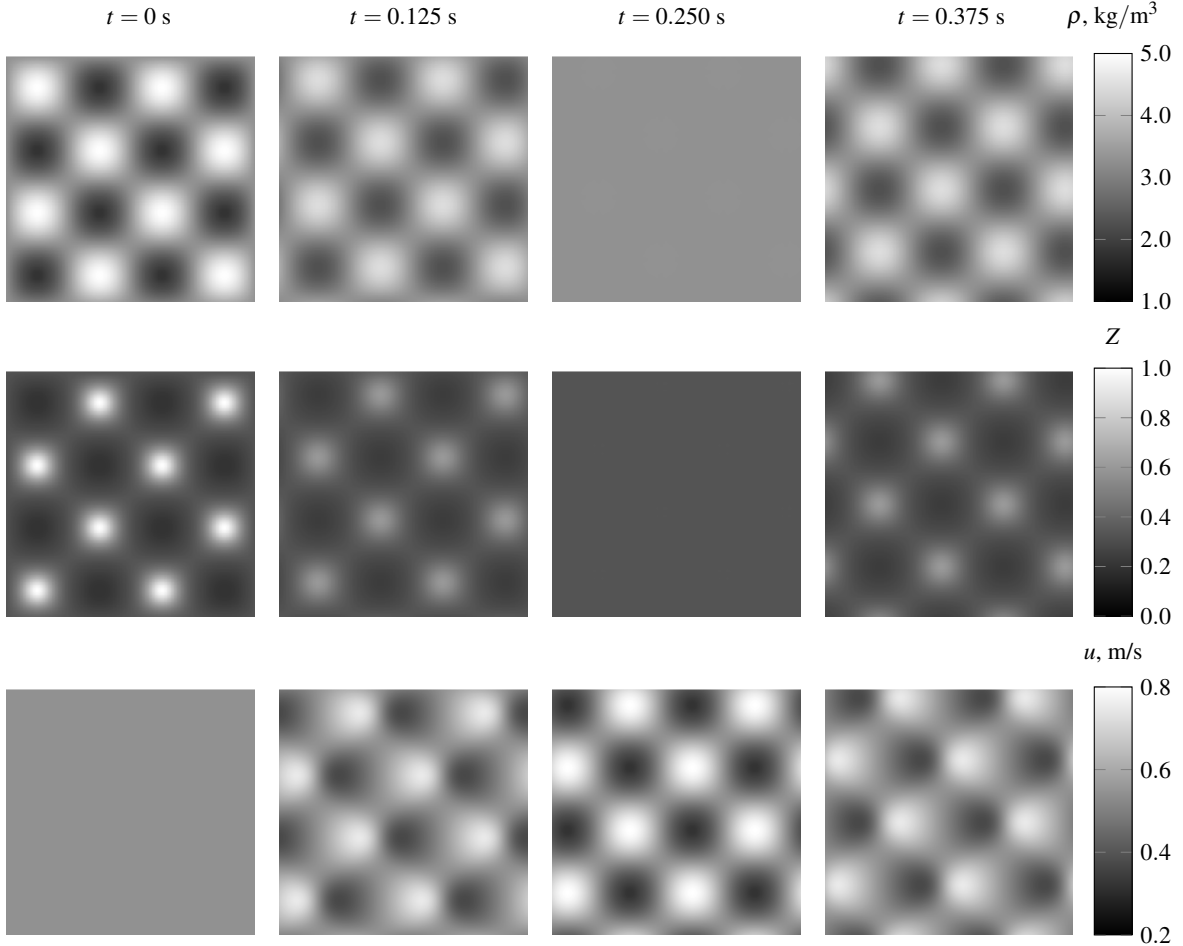


Figure 3.11: Evolution of the variable-density manufactured solution. From top to bottom, the images show density,  $\rho$ , mixture fraction,  $Z$ , and the  $u$ -velocity component from the  $256^2$  simulation at the times shown at the top of the columns. These results may be compared to [43] to confirm the validity of the numerical solution.

Several different norms are considered and the results are listed in Table 3.2. In the left column of the table, the  $L_1$  and  $L_2$  norms are taken from the vector  $p$  computed pointwise on the domain. Note that, as discussed in Sec. 3.4, the infinity norm for this approach is degenerate. The “Saad” norms are formed by taking the norms of the differences in the numerator and denominator of Eq. (3.48),

$$\|p\|_{\text{Saad}} = \frac{\ln \left( \frac{\|f_3 - f_2\|}{\|f_2 - f_1\|} \right)}{\ln r} \quad (3.62)$$

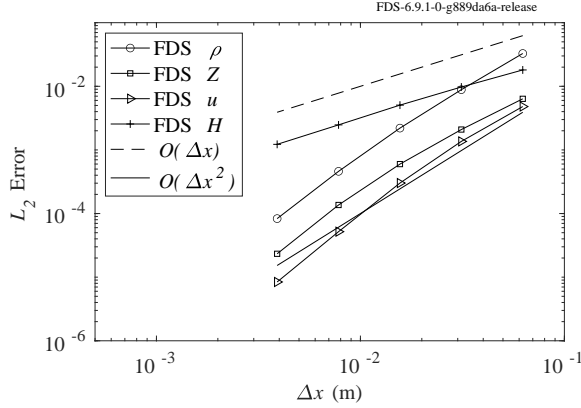


Figure 3.12: Convergence for the manufactured solution. The  $L_2$  error at time  $t = 0.9$  s is plotted as a function of grid spacing for  $N = \{32, 64, 128, 256, 512\}$  points in each direction. The grid spacing is  $\Delta x = L/N$ , where  $L = 2$  m. Calculations were performed with an adaptive time step satisfying both convective and diffusive CFL (Von Neumann) limits of 0.5. These results confirm second-order accuracy of the flow solver for density, mixture fraction, and velocity. As is known for projection schemes like ours, the pressure solution (represented by  $H$ ) is first-order accurate [45].

Table 3.2: Shunn temporal error norms for the order  $p$ .

Norm	$\rho$	$Z$	$u$	$H$
$L_1$	2.0266	2.0274	2.0309	1.0067
$L_2$	2.0528	2.0518	2.0792	1.0274
$L_1$ Saad	2.0229	2.038	2.0408	0.99928
$L_2$ Saad	2.0608	2.1103	2.1235	0.99894
$L_\infty$ Saad	2.1745	2.2374	2.188	0.99125

## 3.6 Collapse of a Hot Layer in a Micro-gravity Environment (`hot_layer_360`)

**Howard R. Baum, NIST Fellow Emeritus**

This problem describes the collapse of a hot layer of depth  $d$  adjacent to a wall at plane  $y = 0$  in zero gravity. The wall is presumed to remain cool at the ambient temperature  $T_0$  while the hot layer is initially  $T_h$ . The initial velocity field is quiescent. Starting at time  $t = 0$  the hot layer begins to diffuse into the upper cool ambient atmosphere and to expand due to dilatation. There is also heat transfer to the wall. The problem is 1-D in the spatial coordinate  $y$  and time dependent. We are interested in the evolution of the temperature  $T(y, t)$  and the velocity  $v(y, t)$ .

For the present problem the governing equations are

$$\frac{\partial \rho}{\partial t} + \frac{\partial}{\partial y}(\rho v) = 0 \quad (3.63)$$

$$\rho C_p \left( \frac{\partial T}{\partial t} + v \frac{\partial T}{\partial y} \right) = \frac{\partial}{\partial y} \left( k \frac{\partial T}{\partial y} \right) \quad (3.64)$$

$$\rho T = \rho_0 T_0 \quad (3.65)$$

Here,  $\rho(y, t)$  is the mass density,  $C_p$  is the heat capacity (assumed constant), and  $k$  is the thermal conductivity of the gas, which we assume obeys  $\rho k = \rho_0 k_0$ . The initial conditions are

$$v(y, 0) = 0 \quad (3.66)$$

$$T(y, 0) = \begin{cases} T_h & \text{for } 0 < y \leq d \\ T_0 & \text{for } y > d \end{cases} \quad (3.67)$$

The boundary conditions are

$$v(0, t) = 0 \quad (3.68)$$

$$T(0, t) = T_0 \quad (3.69)$$

$$T(y, t) \rightarrow T_0 \text{ as } y \rightarrow \infty \quad (3.70)$$

Note that no boundary condition can be imposed on  $v$  far from the boundary. In FDS, an OPEN boundary is applied.

Introducing the dimensionless coordinate  $\lambda$  and dimensionless time  $\tau$ , the dimensionless physical coordinate  $Y(\lambda, \tau)$ , velocity  $V(\lambda, \tau)$ , and temperature  $\theta(\lambda, \tau)$  are related to dimensional quantities as follows:

$$t = \rho_0 C_p d^2 / k_0 \tau \quad (3.71)$$

$$y = d Y(\lambda, \tau) \quad (3.72)$$

$$v = k_0 / (\rho_0 C_p d) V(\lambda, \tau) \quad (3.73)$$

$$T = T_0 \theta(\lambda, \tau) \quad (3.74)$$

The solution is then given by the following (for coding details see `hot_layer_collapse.m`):

$$f(\lambda, \tau, a) = -2\sqrt{\tau/\pi} \exp(-(a - \lambda)^2/(4\tau)) + (a + \lambda) \operatorname{erfc}((a + \lambda)/(2\sqrt{\tau})) \quad (3.75)$$

$$F(\lambda, \tau, a) = f(\lambda, \tau, a) - f(0, \tau, a) \quad (3.76)$$

$$Y(\lambda, \tau, T_h, T_0) = \lambda + (T_h - T_0)/T_0 (-F(\lambda, \tau, 0) + \frac{1}{2}(F(\lambda, \tau, T_0/T_h) + F(\lambda, \tau, -T_0/T_h))) \quad (3.77)$$

$$U(\lambda, \tau, T_h, T_0) = -\operatorname{erfc}(\lambda/(2\sqrt{\tau})) + \frac{1}{2}(\operatorname{erfc}((\lambda - T_0/T_h)/(2\sqrt{\tau})) + \operatorname{erfc}((\lambda + T_0/T_h)/(2\sqrt{\tau}))) \quad (3.78)$$

$$\theta(\lambda, \tau, T_h, T_0) = 1 + ((T_h - T_0)/T_0) U(\lambda, \tau, T_h, T_0) \quad (3.79)$$

$$G(\lambda, \tau, a) = 1/\sqrt{\pi\tau} (-\exp(-(a + \lambda)^2/(4\tau)) + \exp(-a^2/(4\tau))) \quad (3.80)$$

$$V(\lambda, \tau, T_h, T_0) = (T_h - T_0)/T_0 (-G(\lambda, \tau, 0) + \frac{1}{2}(G(\lambda, \tau, T_0/T_h) + G(\lambda, \tau, -T_0/T_h))) \quad (3.81)$$

Figure 3.13 shows the analytical solution (solid lines) plotted together with the FDS (DNS) numerical results (open symbols). The plots on the left are of temperature profiles at several times (different colors demarcate different nondimensional times  $\tau$ ). The plots on the right are velocity. As can be seen, the agreement is excellent.

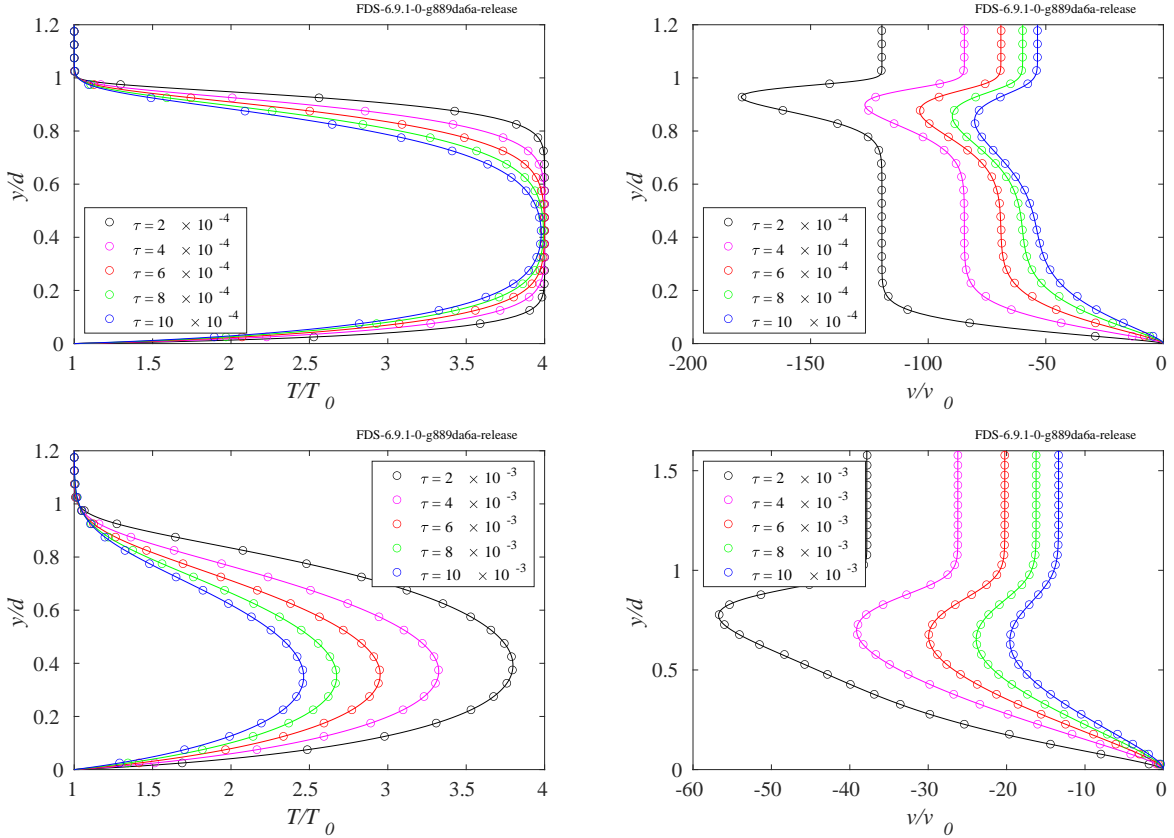


Figure 3.13: Hot layer solution. Lines are the analytical solution. Symbols are the FDS results.

### 3.7 2-D Vortex Simulation (`vort2d`)

**Max Gould, NIST SURF student**  
**Ragini Acharya, United Technologies Research Center**

In this section we present another case that demonstrates the second-order accuracy of the FDS transport algorithm. We consider the analytically stable flow field consisting of a single vortex advected by a uniform flow, a test case developed by CERFACS<sup>2</sup> [46]. Maintaining the geometry of the vortex over time provides a good measure of the order of accuracy of the transport scheme.

The vortex is initially defined as the gradient of the potential field,

$$\Psi_0(x, z) = \Gamma \exp \left[ -\frac{x^2 + z^2}{2 R_c^2} \right], \quad (3.82)$$

where  $\Gamma$  determines its intensity and  $R_c$  its characteristic size. The velocity components are determined by taking the gradient of the potential field superimposed on the constant flow field of velocity  $U_0$  in the positive  $x$  direction,

$$u(x, z) \equiv U_0 + \frac{\partial}{\partial z} \Psi_0 = U_0 - \frac{\Gamma z}{R_c^2} \exp \left[ -\frac{x^2 + z^2}{2 R_c^2} \right], \quad (3.83)$$

<sup>2</sup>Centre Européen de Recherche et de Formation Avancée en Calcul Scientifique

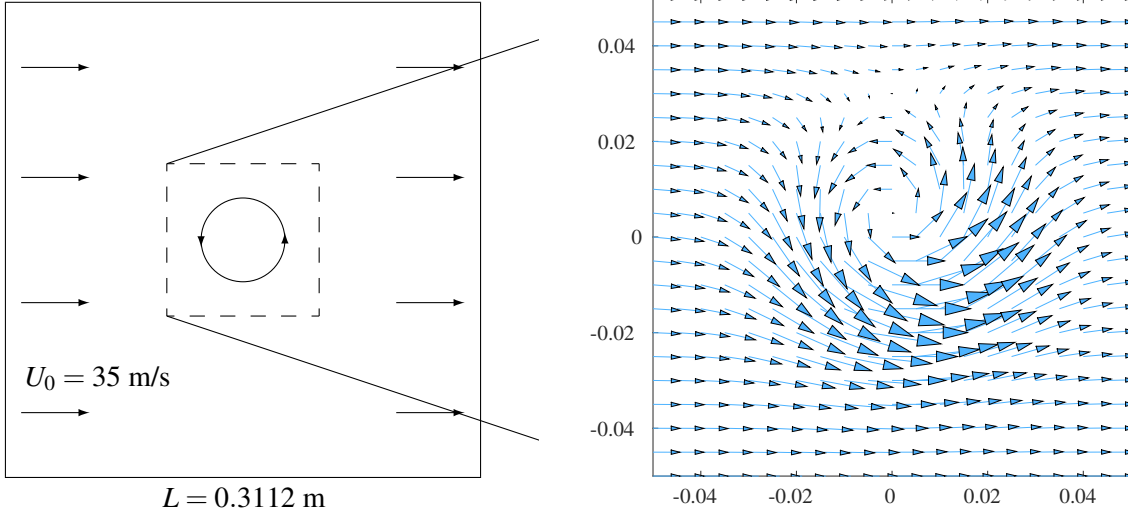


Figure 3.14: Vector field of a two-dimensional vortex in a constant flow field.

$$w(x, z) \equiv -\frac{\partial}{\partial x} \Psi_0 = \frac{\Gamma x}{R_c^2} \exp \left[ -\frac{x^2 + z^2}{2 R_c^2} \right], \quad (3.84)$$

where  $u$  and  $w$  refer to velocity in the  $x$  and  $z$ -directions, respectively. For our purposes we need only analyze one component of the velocity field. We will focus our attention on the  $u$ -component of velocity.

We define the computational domain as a two-dimensional square region,  $L = 0.3112$  m on a side, with periodic boundary conditions. The domain is discretized for a range of square, two-dimensional meshes of  $40^2$ ,  $80^2$ ,  $160^2$ , and  $320^2$  grid cells. For the purposes of this test, we set the flow parameters as

$$\begin{aligned} U_0 &= 35 \text{ m/s} \\ R_c &= L/20 = 0.01556 \text{ m} \\ \Gamma &= 0.04 U_0 R_c \sqrt{e} = 0.0359157 \end{aligned}$$

The constant flow field and periodic boundary conditions cause the vortex to repeatedly pass through the computational domain. The “pass-through” time,  $t_f$ , is defined as the time period required for the stable vortex to return to its original position,

$$t_f = L/U_0 \simeq 8.8914 \times 10^{-3} \text{ s.}$$

To ensure that the numerical solution converges to the analytical solution, we set the time step,  $\delta t$ , so that the Courant-Friedrichs-Lowy (CFL) number is 0.5.

A plot of  $u$ -velocity values just along the  $z$ -axis provides a simple characterization of the vortex geometry. The extent to which this geometry changes over time provides a qualitative measure of the accuracy of the transport algorithm. Figure 3.15 displays these plots for two different grid resolutions. Each line represents a plot taken for a different number of flow-through times such that the red lines represent the vortex after it has undergone the most passes through the computational domain while the green lines represent the vortex in the initial phase. The broken black line represents the analytical solution. As the vortex undergoes more passes through the computational domain, its velocity profile diverges further and further from the analytical profile. While divergence still occurs on the finer mesh, the extent to which it diverges after the same number of flow-through times is significantly smaller.

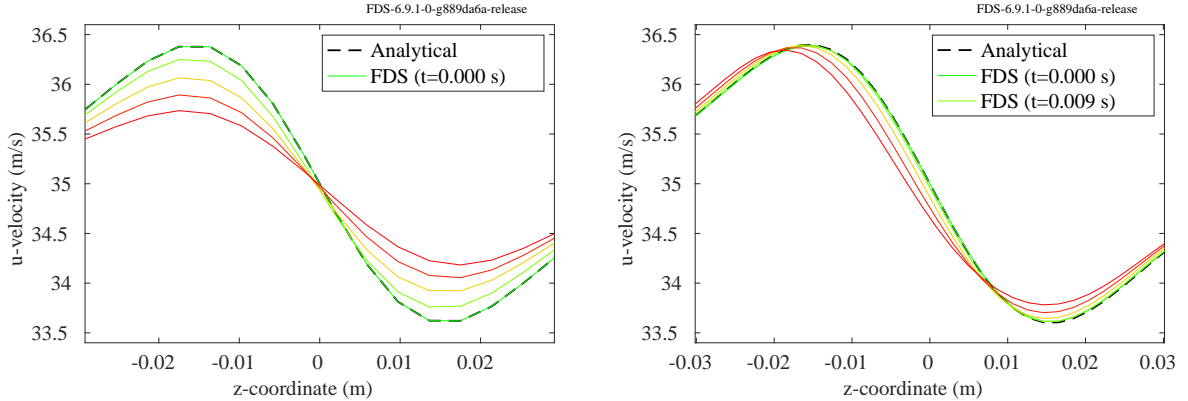


Figure 3.15:  $u$ -velocity along the  $z$ -axis at  $x = 0$  plotted for each of the vortex's first four loops through the computational domain. (Left)  $80^2$  grid cell model. (Right)  $160^2$  grid cell model.

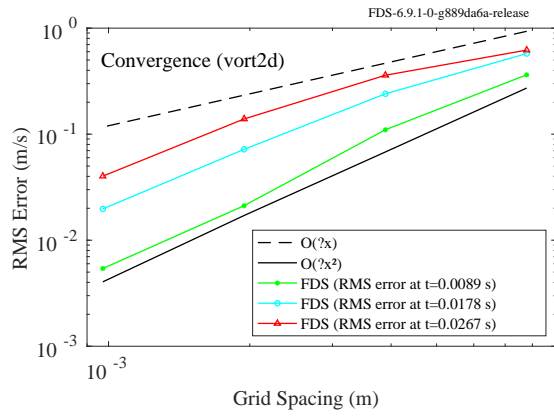


Figure 3.16: RMS error between simulated and analytical  $u$ -velocity values along the  $z$ -axis plotted for each grid resolution at each of three subsequent passes of the vortex through the computational domain.

The rate with which the simulated profiles converge to the analytical one defines the order of accuracy of the numerical scheme. In Fig. 3.16 we plot the rms error of the numerical solution as a function of the grid resolution. The three colored curves represent the rms error at three different pass-through times. The broken and solid black lines represent the plot gradient corresponding to first and second order error respectively. While the error increases with each flow-through time, the gradients of the lines are roughly parallel to the solid black line, indicating second-order accuracy of the numerical scheme.

To analyze the stability of the vortex at times other than discrete multiples of the pass-through time, consider the time-dependent potential field and its corresponding  $u$ -velocity component:

$$\Psi(x, z, t) = \Psi_0 \exp \left[ \frac{2 U_0 x t - U_0^2 t^2}{2 R_c^2} \right], \quad (3.85)$$

$$u(x, z, t) = U_0 - \Psi_0 \frac{z}{R_c^2} \exp \left[ \frac{2 U_0 x t - U_0^2 t^2}{2 R_c^2} \right]. \quad (3.86)$$

In Fig. 3.17, we show the  $u$ -velocity at a single point, on the lower left fringe of the vortex, for two different mesh resolutions,  $80^2$  and  $160^2$ . A mesh resolution of  $320^2$  grid cells produces a plot (not shown) that is, to the eye, a perfect match out to four pass-through times.

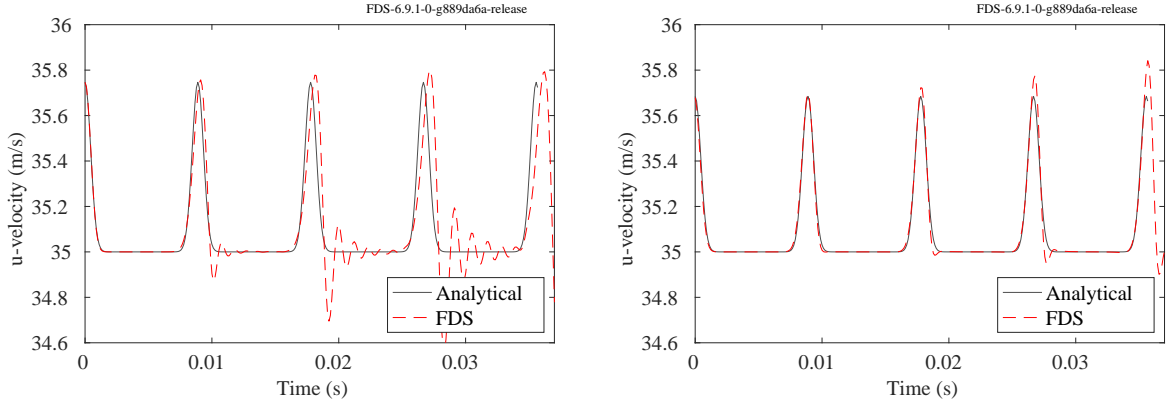


Figure 3.17: Simulated and analytical values of  $u$ -velocity at a point plotted as a function of time over a time period equal to four times the flow-through time. (Left)  $80^2$  grid cell model. (Right)  $160^2$  grid cell model.

## 3.8 Boundedness Tests

### 3.8.1 Species Bounds (`bound_test_*`)

When multiple infinitely fast reactions are present it is not trivial to correctly partition the limiting reactant and maintain species bounds. FDS uses a special subcycling algorithm by Kahane [47] to maintain boundedness for species when time integrating the ODEs for the chemical reaction step (the method is further discussed in the FDS Tech Guide [48]). In this section, we examine two test cases designed to verify the time integration method.

The first case, `bound_test_1`, consists of two independent reactions, one with air as the limiting reactant, one with fuel as the limiting reactant. The stoichiometry of each reaction is the same:  $F + A \rightarrow 2P$ . The initial volume fractions of determine which species are limiting. The results are shown in Fig. 3.18. For the first reaction,  $X_{F1}$  is initially 0.3 and  $X_{A1}$  is initially 0.2. Therefore, all the  $A1$  is converted to  $P1$ , which has a final volume fraction of  $X_{P1} = 0.4$ . In the second reaction, the initial fuel volume fraction is  $X_{F2} = 0.1$  (limiting) and the initial air volume fraction is  $X_{A2} = 0.4$ . As can be see in Fig. 3.18, the resulting final values give a product volume fraction of twice the limiting reactant,  $X_{P2} = 0.2$ .

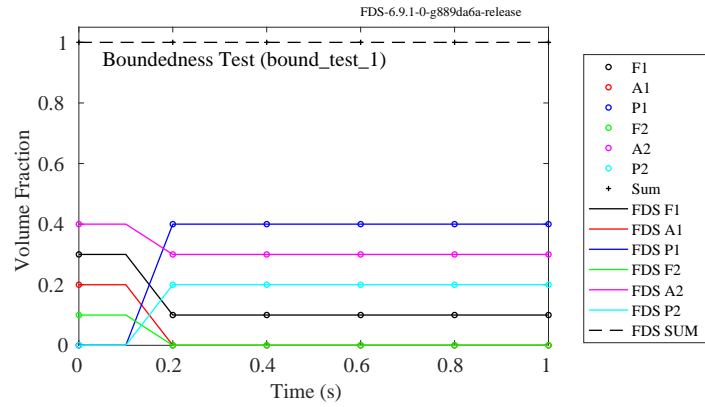


Figure 3.18: Results of the `bound_test_1` case.

The second test case, `bound_test_2`, is more challenging—we add a third reaction that uses the same

fuel species as the first and the same air species as the second. The reaction scheme is as follows:



The initial conditions and final results are shown in Fig. 3.19. As discussed in the FDS Tech Guide [48], the right-hand-side of the chemistry ODE is set up assuming a large Arrhenius constant and no activation energy and (in this case) second-order concentration dependence for each reaction. It can be shown through numerical experiments that this assumption is equivalent to applying Curl's mixing model (Coalescence-Dispersion) [49] in a batch reactor with infinitely fast chemistry.

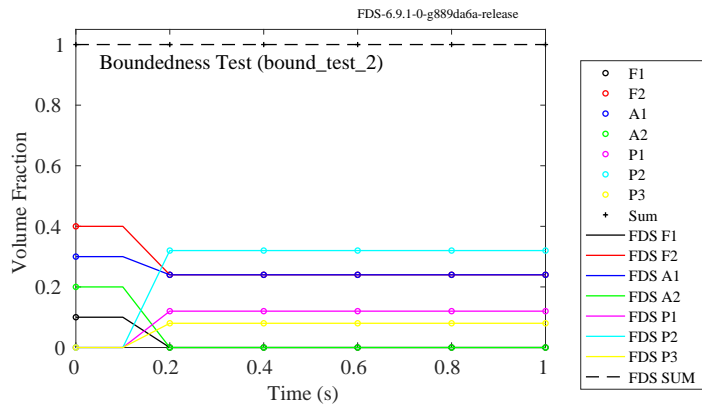


Figure 3.19: Results of the bound\_test\_2 case.

### 3.8.2 Isothermal Helium Wave (`helium_1d_isothermal`)

This is a test of isothermal advection and mixing of gases with different molecular weights using the default algorithm. A companion case using a simplified algorithm for `CONSTANT_SPECIFIC_HEAT_RATIO` is given below in Sec. 3.9.1. In the present case, a wave of helium propagates in one dimension down the length of a square duct with frictionless walls. The initial and inlet temperatures are 25 °C and should remain so throughout the course of the simulation. In Fig. 3.20 we plot the simulation results for temperature, sensible enthalpy, and velocity. The temperature should remain constant at 25 °C. The sensible enthalpy, which is referenced to 25 °C, should remain at 0 kJ/m³. And the velocity should level off at 1 m/s and hold steady. This output is checked to make sure that no boundary effects manage to pollute the simulation.

### 3.8.3 Temperature Bounds for Isothermal Helium Jet (`helium_air_jet_floor`)

In this test, a jet of helium is generated from a floor vent. The mass flux is ramped up from 0 m/s to 1 m/s in 1 s. The flow field should remain isothermal at 20 °C. The results are shown in Fig. 3.21.

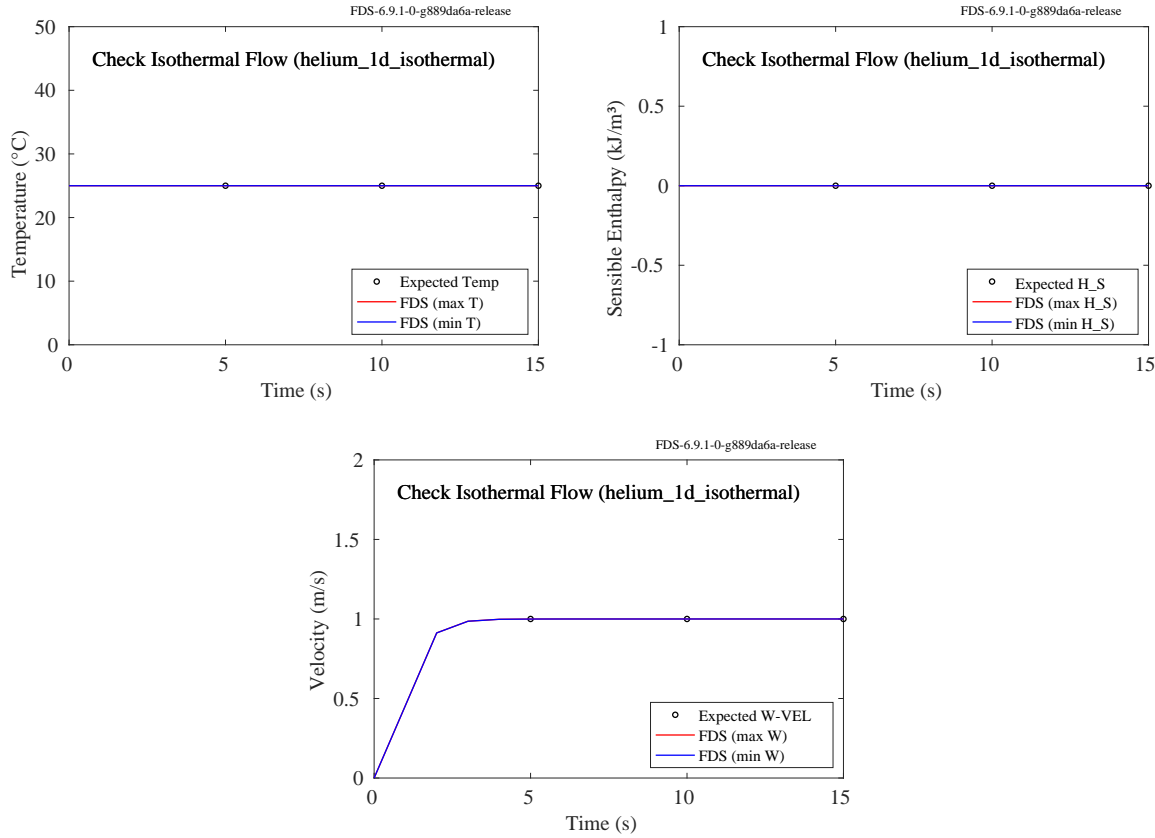


Figure 3.20: Results of the `helium_1d_isothermal` cases.

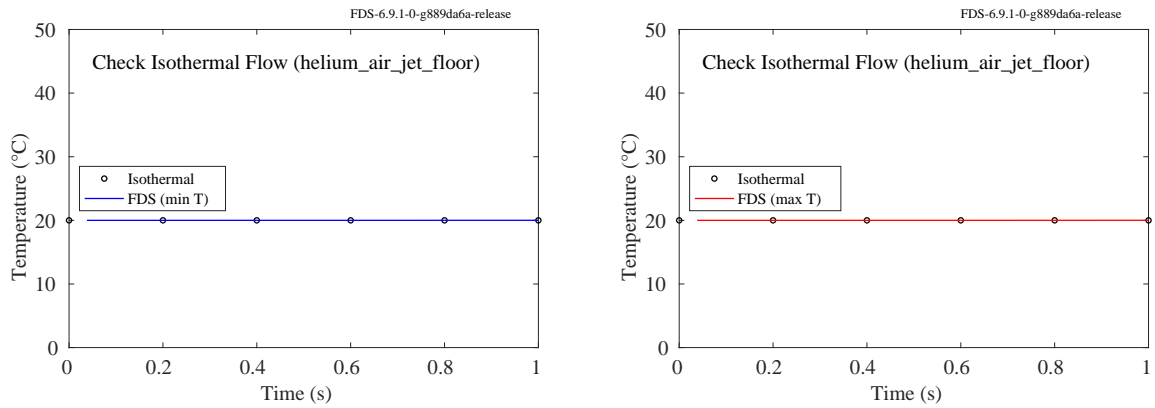


Figure 3.21: Results of the `helium_air_jet_floor` case.

### 3.8.4 Temperature Bounds for Large Differences in Molecular Weight (`mwttest_cf1`)

Hydrogen gas (2 g/mol) is injected into a small compartment filled with sulfur hexafluoride (146 g/mol). There should be no change in temperature, as shown in Fig. 3.22.

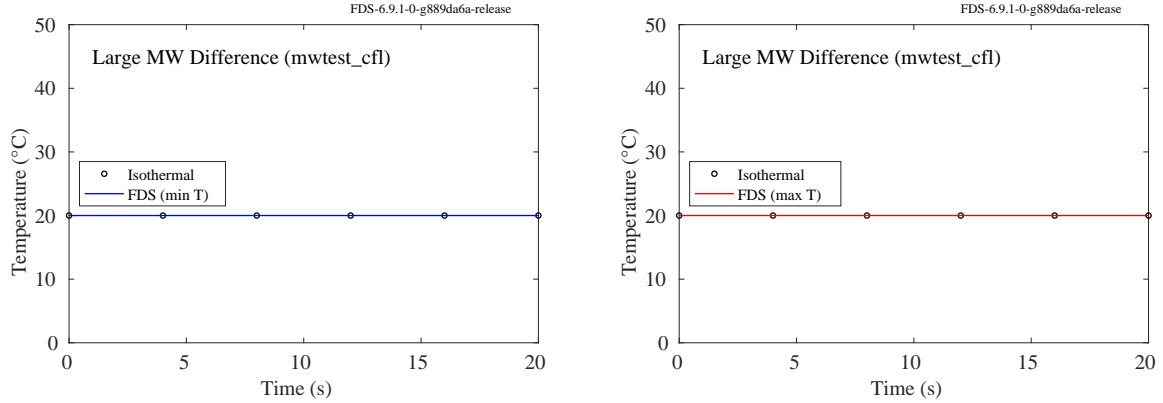


Figure 3.22: Results of the `mwtest_cfl` case.

### 3.8.5 Temperature Lower Bound in a Fire Simulation (`tmp_lower_limit`)

A 2-D methane-air diffusion flame calculation is run three different ways to check that the temperature does not fall below the ambient ( $20^{\circ}\text{C}$ ). The results are shown in Fig. 3.23. The upper left plot shows the global minimum temperature for the case where the reaction stoichiometry is specified explicitly. The upper right plot is for the case where the initial time step is lowered to 0.001 s. The lower plot is for the case where the simple chemistry model is used.

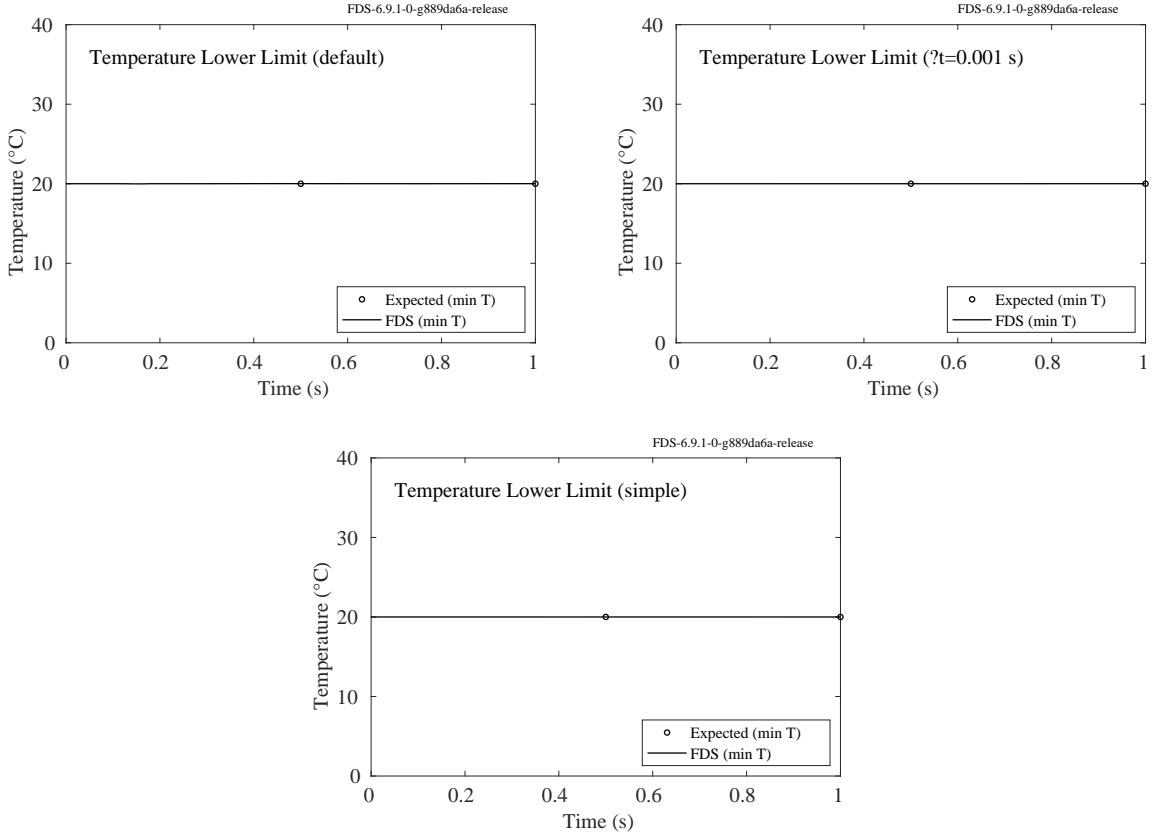


Figure 3.23: Results of the `tmp_lower_limit` cases.

## 3.9 Constant Specific Heat Ratio

The ratio  $\gamma = c_p/c_v$  is called the “ratio of specific heats”. For many simple gases,  $\gamma = \text{constant}$  is a good approximation. The specific heat of species  $\alpha$  in the gas phase is then given by

$$c_{p,\alpha} = \frac{R}{W_\alpha} \frac{\gamma_\alpha}{\gamma_\alpha - 1} \quad (3.90)$$

where  $R$  is the ideal gas constant. When this assumption is viable, many terms in the energy equation drop out, greatly simplifying the divergence expression and thus speeding up the code. These simplifications require that the sensible enthalpy of the gas is referenced to 0 K (see the FDS Tech Guide [48]). In this section, we examine three cases using the assumption of constant specific heat ratio: one tests mixing of two gases with different molecular weights (`helium_1d_const_gamma`), one tests fire conditions (`fire_const_gamma`), and one tests evaporation of water droplets (`water_evap_1_const_gamma`). Each of these cases is a clone of cases we develop later in this guide for the default version of the code.

### 3.9.1 Helium Wave using Constant Specific Heat Ratio (`helium_1d_const_gamma`)

In this problem, a wave of helium propagates in one dimension down the length of a square duct with frictionless walls. The initial and inlet temperatures are 25 °C and should remain so throughout the course of the simulation. The ratio of specific heats is kept at the default value of  $\gamma = 1.4$ . The molar weights, heat

Table 3.3: Helium constant specific heat ratio parameters.

Species	$W_\alpha$ (kg/kmol)	$\rho_\alpha$ (kg/m <sup>3</sup> )	$c_{p,\alpha}$ (kJ/kg/K)	$h_{s,\alpha}$ (kJ/m <sup>3</sup> )
Air	28.73167	1.174	1.0128	355
Helium	4.00260	0.164	7.2705	355

capacities, and enthalpies for both air and helium are given in Table 3.3. Notice that the sensible enthalpies,  $h_{s,\alpha} = \rho_\alpha c_{p,\alpha} T$ , are the same for both species.

In Fig. 3.24 we plot the simulation results for temperature, sensible enthalpy, and velocity. The temperature should remain constant at 25 °C. The sensible enthalpy should remain constant at 355 kJ/m<sup>3</sup>. And the velocity should level off at 1 m/s and hold steady. This output is checked to make sure that no boundary effects manage to pollute the simulation.

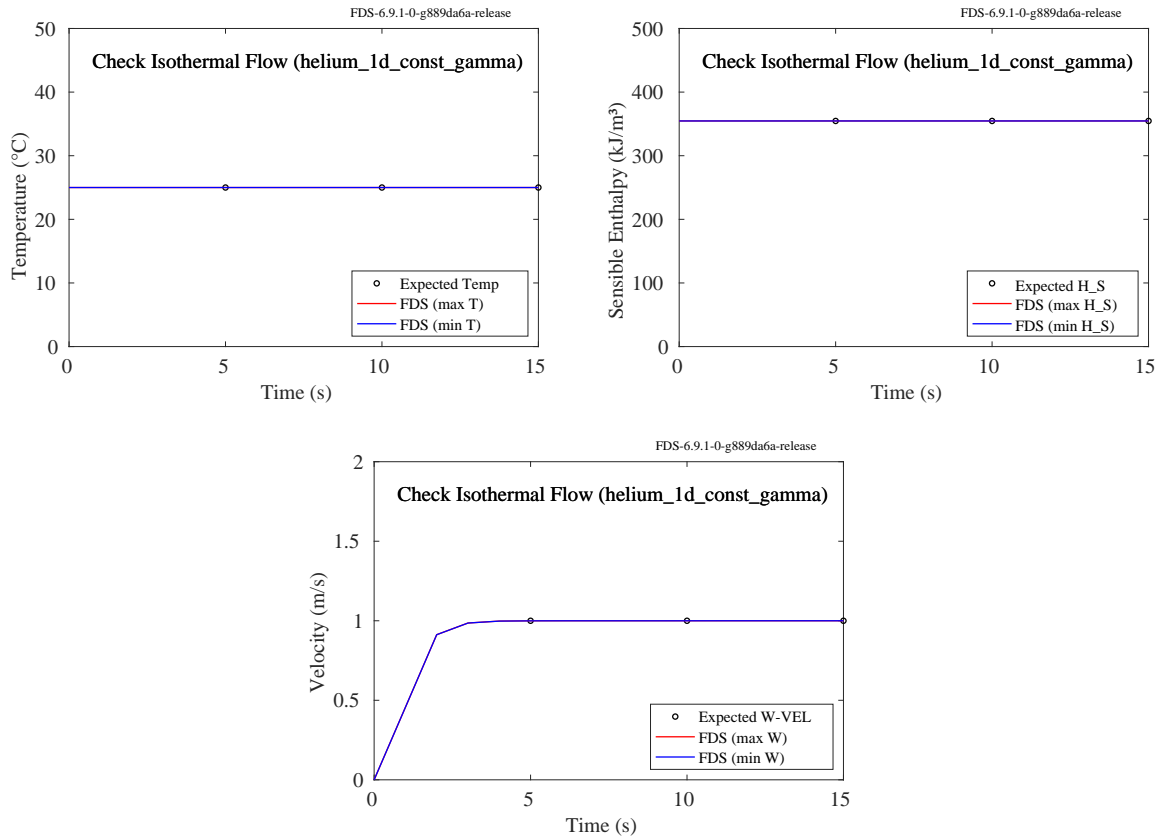


Figure 3.24: Results of the `helium_1d_const_gamma` cases.

### 3.9.2 Fire Plume using Constant Specific Heat Ratio (`fire_const_gamma`)

In this case a 128 m<sup>3</sup> box is initially filled with air at 20 °C. A 1000 MW propane fire with a 5 % soot yield is placed at the bottom of the box for 20 s. All the compartment surfaces are adiabatic. The net change in enthalpy and pressure can be computed using the specific heat ratio based constant specific heat values for the air and product species along with the pressure work required to inject the fuel. The FDS predicted

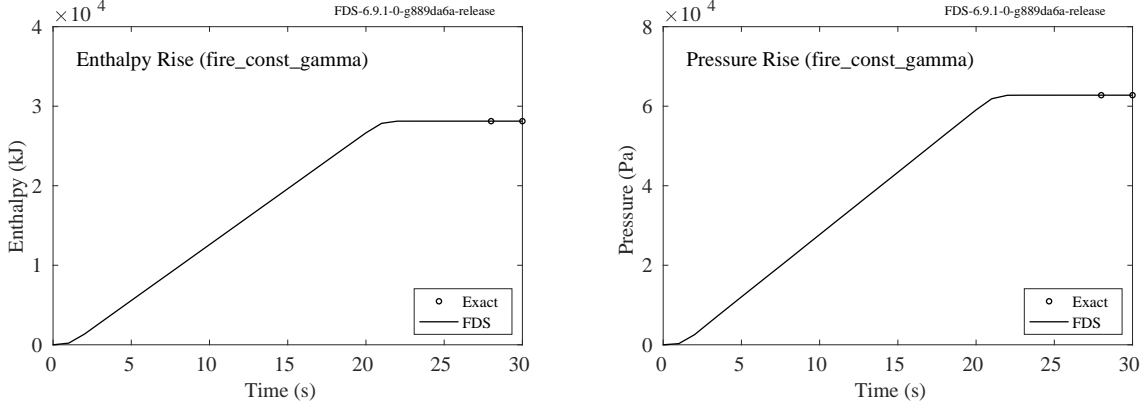


Figure 3.25: Results of the `fire_const_gamma` case.

enthalpy and pressure change are shown in Fig 3.25 compared with the predicted values.

### 3.9.3 Evaporation with Constant Specific Heat Ratio (`water_evap_1_const_gamma`)

This test case is a replica of `water_evaporation_1` in Sec. 13.3.1 using constant specific heat ratio. A 1 m<sup>3</sup> box is initially filled with dry air at 200 °C and monodisperse water droplets totaling 0.01 kg in mass initially at 20 °C. In this case, all the water evaporates. The final gas temperature may be computed from energy conservation. Pressure change may be computed from the ideal gas law. Results are shown in Fig. 3.26. Details of the expected results may be found in `water_evap_1_const_gamma.m` in the Utilities/Matlab/scripts/ directory in the FDS repository [44].

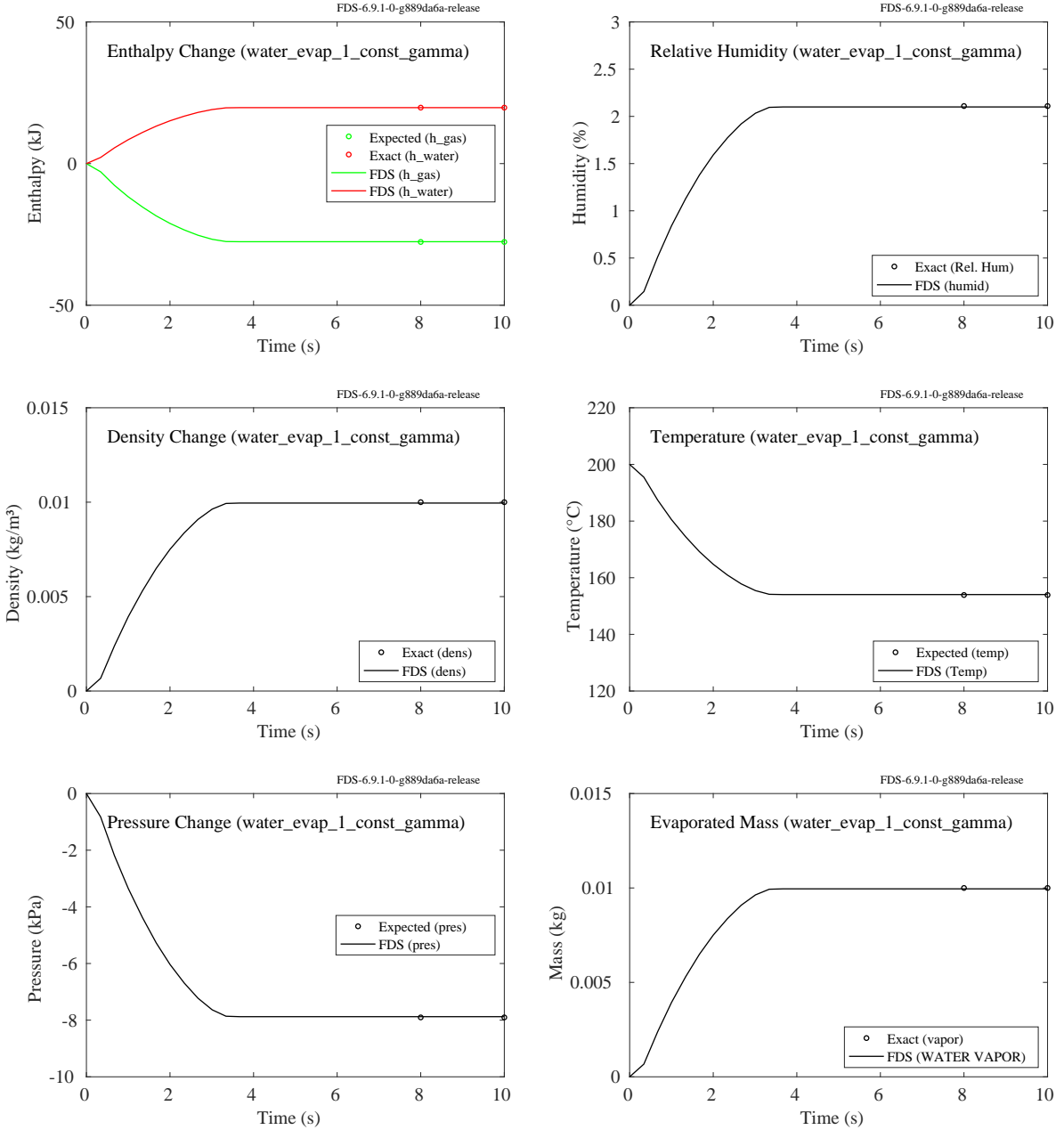


Figure 3.26: Output of the `water_evap_1_const_gamma` test case.

## 3.10 Tunnel Flow

Jesus Alberto Mejias Tuni, Politecnico di Torino

### 3.10.1 1-D Flow in a Tunnel (`tunnel_const_gamma`)

Consider a long tube with rectangular cross section. Air with density  $\rho_\infty = 1.200 \text{ kg/m}^3$ , temperature  $T_\infty = 293.15 \text{ K}$ , and pressure  $p_\infty = 101325 \text{ Pa}$ , is blown at a constant rate,  $u_\infty = 1 \text{ m/s}$ , through the tube. A steady volumetric heat source is located in the middle of the tube. Ignoring wall friction, gravity, radiation transport,

thermal conductivity, viscosity, and assuming that the heat source uniformly spans the cross section of the tube, a set of 1-D equations can be derived for the steady-state velocity,  $u(x)$ , density,  $\rho(x)$ , perturbation pressure,  $\tilde{p}(x)$ , and temperature,  $T(x)$ :

$$\rho u = \rho_\infty u_\infty \quad ; \quad \frac{d}{dx} \left( \frac{u^2}{2} \right) + \frac{1}{\rho} \frac{d\tilde{p}}{dx} = 0 \quad (3.91)$$

$$p_\infty = R\rho T/W \quad ; \quad \frac{du}{dx} = \frac{1}{\rho c_p T} \left( \dot{q}''' - u \frac{d}{dx}(\rho h_s) - (c_p T - h_s) u \frac{dp}{dx} \right) \quad (3.92)$$

Note that  $R = 8314.5 \text{ J/kmol/K}$  and the sensible enthalpy,  $h_s = \int_{T_\infty}^T c_p(T') dT'$ . The tube is 10 cm long, 1 mm wide and 4 mm tall, and discretized with 1 mm grid cells. A vertical column of cells contains a volumetric heat source that introduces heat at a rate of  $\dot{q}''' = 2.5133 \times 10^8 \text{ W/m}^3$  within each 1 mm cell. The velocity, density, pressure and temperature are constant starting at the inlet, and at the heat source, the velocity and temperature jump up, and the density and pressure drop down over the span of a single cell and remain steady until the outlet is reached, where the perturbation pressure is set to zero.

For the case where the ratio of specific heats are constant with  $\gamma = 1.4$  and  $W = 28.85 \text{ kg/kmol}$  for air,  $c_p = \gamma(R/W)/(\gamma - 1) = 1008.7 \text{ J/kg/K}$  and  $\rho c_p T = \gamma p_\infty / (\gamma - 1)$ . In the second equation of (3.92), the second two terms on the right hand side are identically zero; thus, the jump in velocity can be computed

$$\Delta u = \frac{\gamma - 1}{\gamma p_\infty} \dot{q}''' \Delta x \approx 0.7087 \text{ m/s} \quad (3.93)$$

Using the first equations of (3.91) and (3.92), the density and temperature downstream of the heat source are computed to be  $0.7023 \text{ kg/m}^3$  and  $500.61 \text{ K}$ , respectively. To determine the drop in pressure, Eq. (3.91) must be written in discretized form. Assume that the subscript 0 refers to the cell containing the heat source, 1 to the first cell downstream, and -1 to the first cell upstream. The velocity in cell 0 is the average of the velocity upstream and downstream,  $u_0 = 1.3544 \text{ m/s}$ .

$$\tilde{p}_1 - \tilde{p}_0 = -\frac{u_1^2 - u_0^2}{2} \rho_1 \approx -0.3811 \text{ Pa} \quad (3.94)$$

$$\tilde{p}_0 - \tilde{p}_{-1} = -\frac{u_0^2 - u_{-1}^2}{2} \rho_0 \approx -0.3968 \text{ Pa} \quad (3.95)$$

Summing the two equations yields  $\Delta\tilde{p} \equiv \tilde{p}_1 - \tilde{p}_{-1} \approx -0.7779 \text{ Pa}$ . The jump in energy across the heat source is

$$\frac{d}{dx}(u \rho c_p T) \approx 2.5113 \times 10^8 \text{ W/m}^3 \quad (3.96)$$

Plots of  $u(x)$ ,  $\rho(x)$ ,  $\tilde{p}(x)$ , and  $T(x)$  are shown in Fig. 3.27.

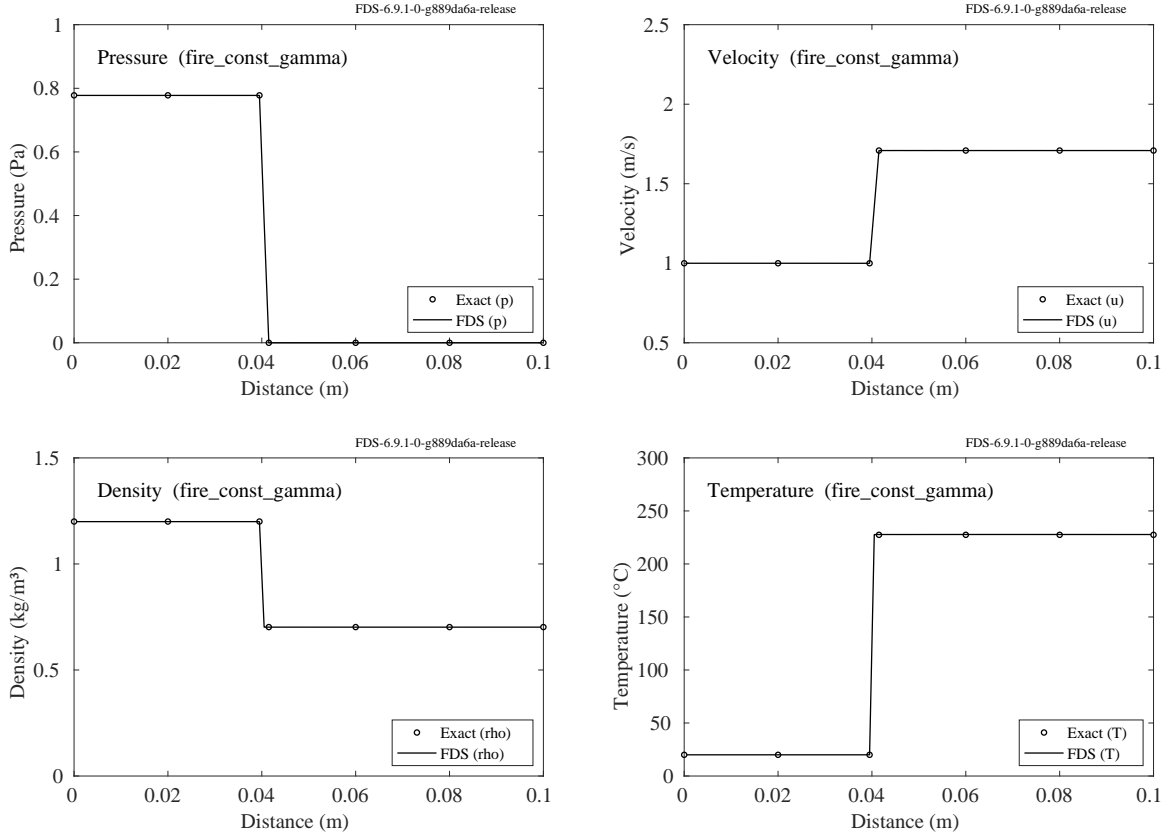


Figure 3.27: Output of the `tunnel_const_gamma` test case.

### 3.10.2 1-D Flow in a Tunnel (`tunnel_linear_cp`)

Considering the same layout and the same environmental conditions of the previous case. Air is blown at a constant rate,  $u_\infty = 1 \text{ m/s}$ , through a 10 cm long, 1 mm wide and 4 mm tall tube. A steady heat source is located in the middle of the tube, composed of a vertical column of cells containing a volumetric heat source that introduces heat at a rate of  $\dot{q}''' = 2.5133 \times 10^8 \text{ W/m}^3$  within each 1 mm cell. Ignoring wall friction, gravity, radiation transport, thermal conductivity, viscosity, and assuming that the heat source uniformly spans the cross section of the tube, a set of 1-D equations can be derived for the steady-state velocity,  $u(x)$ , density,  $\rho(x)$ , perturbation pressure,  $\tilde{p}(x)$ , and temperature,  $T(x)$ . This equations are the same used in the previous example in (3.91) and (3.92).

Remembering that  $R = 8314.5 \text{ J/kmol/K}$  and the sensible enthalpy,  $h_s = \int_{T_\infty}^T c_p(T') dT'$ . The velocity, density, pressure and temperature are constant starting at the inlet, until the heat source, where the velocity and temperature jump up, and the density and pressure drop down over the span of a single cell and remain steady until the outlet is reached, where the perturbation pressure is set to zero.

For the case where the specific heat varies as a function of the temperature. In the second equation of (3.92), using the first equation of (3.91) and (3.92), and some relationships among the variables is possible to arrive to a simpler expression.

$$\rho c_p T \frac{du}{dx} = \dot{q}''' - u\rho \frac{d}{dx}(h_s) - uh_s \frac{d}{dx}(\rho) - c_p Tu \frac{dp}{dx} + h_s u \frac{dp}{dx} \quad (3.97)$$

$$c_p \rho_\infty u_\infty \frac{dT}{dx} = \dot{q}''' - u\rho \frac{d}{dx}(h_s) + c_p u \rho \frac{dT}{dx} \quad (3.98)$$

$$\dot{q}''' = u\rho \frac{d}{dx}(h_s) \quad (3.99)$$

$$\frac{\dot{q}'''}{\rho_\infty u_\infty} = \frac{d}{dx}(h_s) \quad (3.100)$$

Through the steps, the continuity, in (3.91), and state equation, in (3.92), are used to make the temperature the only variable and simplifying equivalent terms until the equation (3.100) is obtained. Equation (3.100) corresponds to a 1-D form of the first law of thermodynamics, proving the divergence equation as a consistent energy balance. Then, for the case where the  $c_p$  is a linear function of the temperature,  $c_p = aT + b$ , we have

$$\frac{\dot{q}'''}{\rho_\infty u_\infty} \Delta x = T^2 \frac{a}{2} + bT - (T_\infty^2 \frac{a}{2} + bT_\infty) \quad (3.101)$$

Substituting in Eq. (3.101) for  $a = 0.1584 \text{ J/kg/K}^2$  and  $b = 953.5650 \text{ J/kg/K}$  (these coefficients give  $c_p(T_\infty) = 1000 \text{ J/kg/K}$ ) the temperature downstream of the heat source is computed to be 499.2 K. Correspondingly, the density and velocity are,  $\rho_1 = 0.7046 \text{ kg/m}^3$  and  $u_1 = 1.7030 \text{ m/s}$ . To determine the drop in pressure, Eq. (3.91) is written in discretized form as in the previous verification. Then assuming that the subscript 0 refers to the cell containing the heat source, 1 to the first cell downstream, and -1 to the first cell upstream. The velocity in cell 0 is the approximated as the average of the velocity upstream and downstream,  $u_0 = 1.3515 \text{ m/s}$ .

$$\tilde{p}_1 - \tilde{p}_0 = -\frac{u_1^2 - u_0^2}{2} \rho_1 \approx -0.3783 \text{ Pa} \quad (3.102)$$

$$\tilde{p}_0 - \tilde{p}_{-1} = -\frac{u_0^2 - u_{-1}^2}{2} \rho_0 \approx -0.3936 \text{ Pa} \quad (3.103)$$

Summing both of the equations yields  $\Delta\tilde{p} \equiv \tilde{p}_1 - \tilde{p}_{-1} \approx -0.7718 \text{ Pa}$ . The jump in energy across the heat source is

$$\frac{d}{dx}(u\rho c_p T) \approx 2.6685 \times 10^8 \text{ W/m}^3 \quad (3.104)$$

Plots of  $u(x)$ ,  $\rho(x)$ ,  $\tilde{p}(x)$ , and  $T(x)$  are shown in Fig. 3.28.

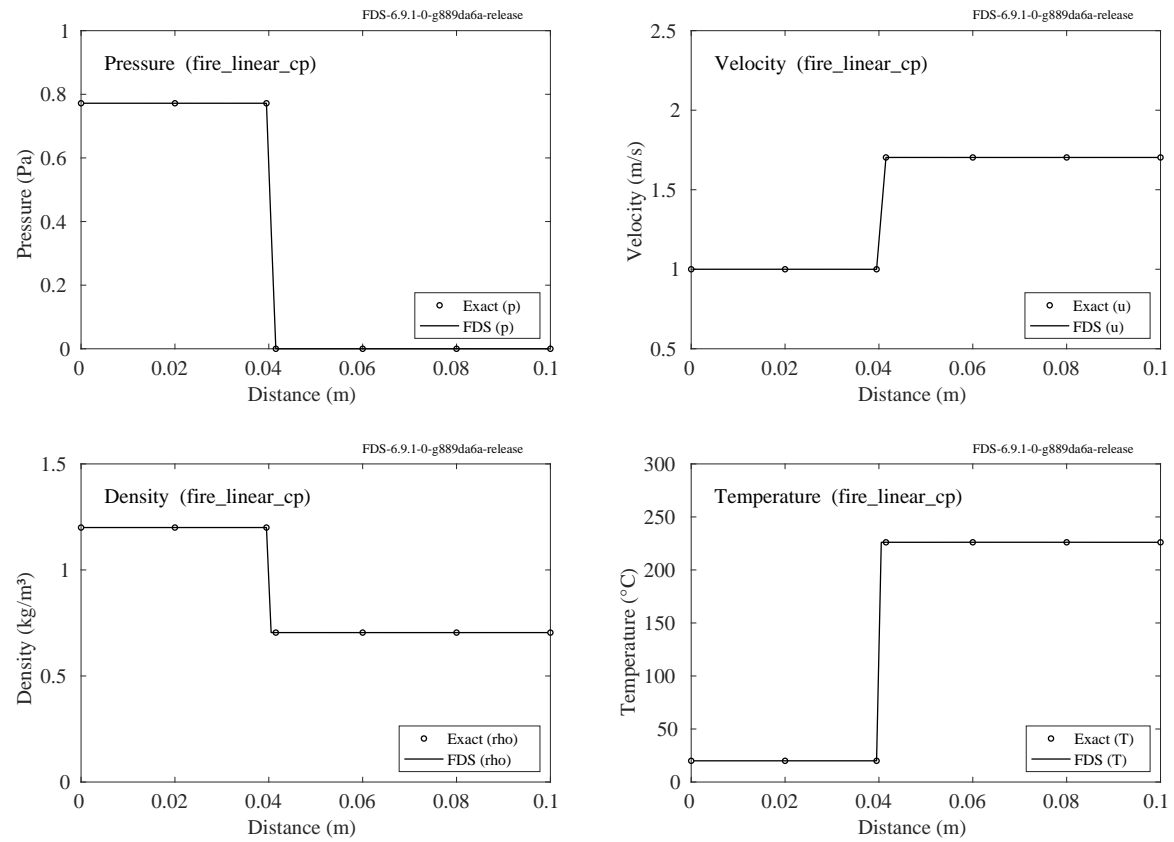


Figure 3.28: Output of the `tunnel_linear_cp` test case.

# Chapter 4

## Turbulence

### 4.1 Decaying Isotropic Turbulence

In this section we present a canonical flow for LES which tests whether the subgrid stress model has been coded properly. In some cases the difference between verification and validation is not so clear. Once a model is well-established and validated it may actually be used as a form of verification. Granted, such a test is not as strong a verification as the convergence study shown in Section 3.1. Nevertheless, these tests are often quite useful in discovering problems within the code. The case we examine in this section, decaying isotropic turbulence, is highly sensitive to errors in the advective and diffusive terms because the underlying physics is inherently three-dimensional and getting the problem right depends strongly on a delicate balance between vorticity dynamics and dissipation. An even more subtle yet extremely powerful verification test is also presented in this section when we set both the molecular and turbulent viscosities to zero and confirm that the integrated kinetic energy within the domain remains constant. In the absence of any form of viscosity, experience has shown that the slightest error in the advective terms or the pressure projection will cause the code to go unstable. This verification is therefore stronger than one might initially expect.

In this section we test the FDS model against the low Reynolds number ( $\text{Re}$ ) data of Comte-Bellot and Corrsin (CBC) [50]. Viscous effects are important in this data set for a well-resolved LES, testing the model's  $\text{Re}$  dependence. Following [51], we use a periodic box of side  $L = 9 \times 2\pi \text{ cm} (\approx 0.566 \text{ m})$  and  $\nu = 1.5 \times 10^{-5} \text{ m}^2/\text{s}$  for the kinematic viscosity. The non-dimensional times for this data set are:  $x/M = 42$  (initial condition), 98, and 171, where  $M$  is the characteristic mesh spacing of the CBC wind tunnel and  $x$  is the downstream location of the data station. Considering the mean velocity in the CBC wind tunnel experiment, these correspond to dimensional times of  $t = 0.00 \text{ s}$ ,  $0.28 \text{ s}$ , and  $0.66 \text{ s}$  in our simulations.

The initial condition for the FDS simulation is generated by superimposing Fourier modes with random phases such that the spectrum matches that of the initial CBC data. An iterative procedure is employed where the field is allowed to decay for small time increments subject to Navier-Stokes physics, each wavenumber is then injected with energy to again match the initial filtered CBC spectrum. The specific filter used here is discussed in [52].

To provide the reader with a qualitative sense of the flow, Fig. 4.1 shows the initial and final states of the velocity field in the 3-D periodic domain. The flow is unforced and so if viscosity is present the total energy decays with time due to viscous dissipation.

#### 4.1.1 Constant Smagorinsky (`csmag`)

Because the viscous scales are unresolved, a subgrid stress model is required. Here the stress is closed using the gradient diffusion hypothesis and the eddy viscosity is modeled by the constant coefficient Smagorinsky

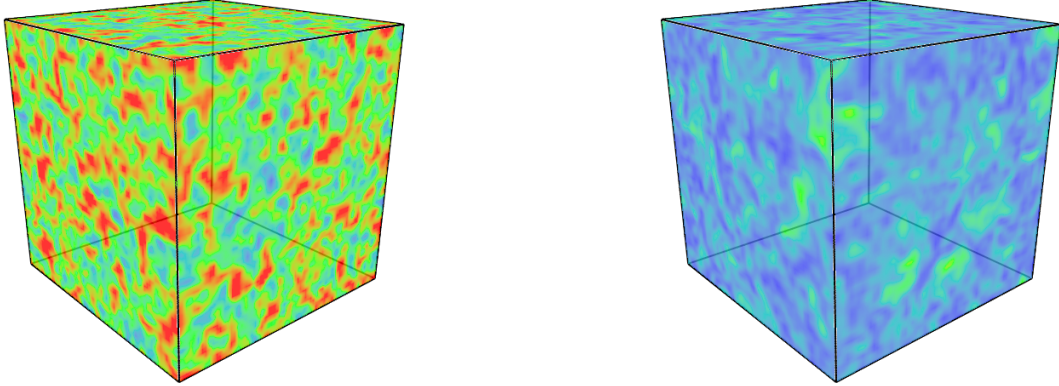


Figure 4.1: Initial and final states of velocity magnitude for the isotropic turbulence field.

model with the coefficient taken to be  $C_s = 0.2$  (see the Technical Reference Guide for further details).

The decay curves for two grid resolutions are shown on the left in Fig. 4.2. For an LES code such as FDS which uses a physically-based subgrid model, an important verification test is to run this periodic isotropic turbulence simulation in the absence of both molecular and turbulent viscosity. For so-called “energy-conserving” explicit numerics the integrated energy will remain nearly constant in time. This is demonstrated by the dash-dot line in the top-left plot in Fig. 4.2. The deviations from identical energy conservation (to machine precision) are due solely to the time discretization (the spatial terms are conservative as discussed in [53]) and converge to zero as the time step goes to the zero. Note that strict energy conservation requires implicit time integration [54, 55] and, as shown by the dashed curve on the same plot where only molecular viscosity is present in the simulation, this cost is unwarranted given that the molecular dissipation rate clearly overshadows the relatively insignificant amount of numerical dissipation caused by the explicit method. The FDS result using the Smagorinsky eddy viscosity (the black solid line) matches the CBC data (red open circles) well for the  $32^3$  case (top-left). However, the FDS results are slightly too dissipative in the  $64^3$  case (bottom-left). This is due to a well-known limitation of the constant coefficient Smagorinsky model: namely, that the eddy viscosity does not converge to zero at the appropriate rate as the filter width (here equivalent to the grid spacing) is decreased.

To the right of each decay curve plotted in Fig. 4.2 is the corresponding spectral data comparison. The three black solid lines are the CBC spectral data for the points in time corresponding to dimensional times of  $t = 0.00$  s,  $0.28$  s, and  $0.66$  s in our simulations. As described above, the initial FDS velocity field (represented by the black dots) is specified to match the CBC data up to the grid Nyquist limit. From there the spectral energy decays rapidly as discussed in [52]. For each of the spectral plots on the right, the results of interest are the values of the red and blue dots and how well these match up with the corresponding CBC data. For the  $32^3$  case (top-right) the results are remarkably good. Interestingly, the results for the more highly resolved  $64^3$  case are not as good. This is because the viscous scales are rather well-resolved at the later times in the experiment and, as mentioned, the constant coefficient Smagorinsky model is too dissipative under such conditions. (The choice of the model constant also affects these results—better agreement with the  $64^3$  case could be achieved with a lower value of  $C_s$ , but the agreement in the  $32^3$  case would then be worse.)

Overall, the agreement between the FDS simulations and the CBC data is satisfactory and any discrepancies can be explained by limitations of the model. Therefore, as a verification the results here are positive in that nothing points to coding errors.

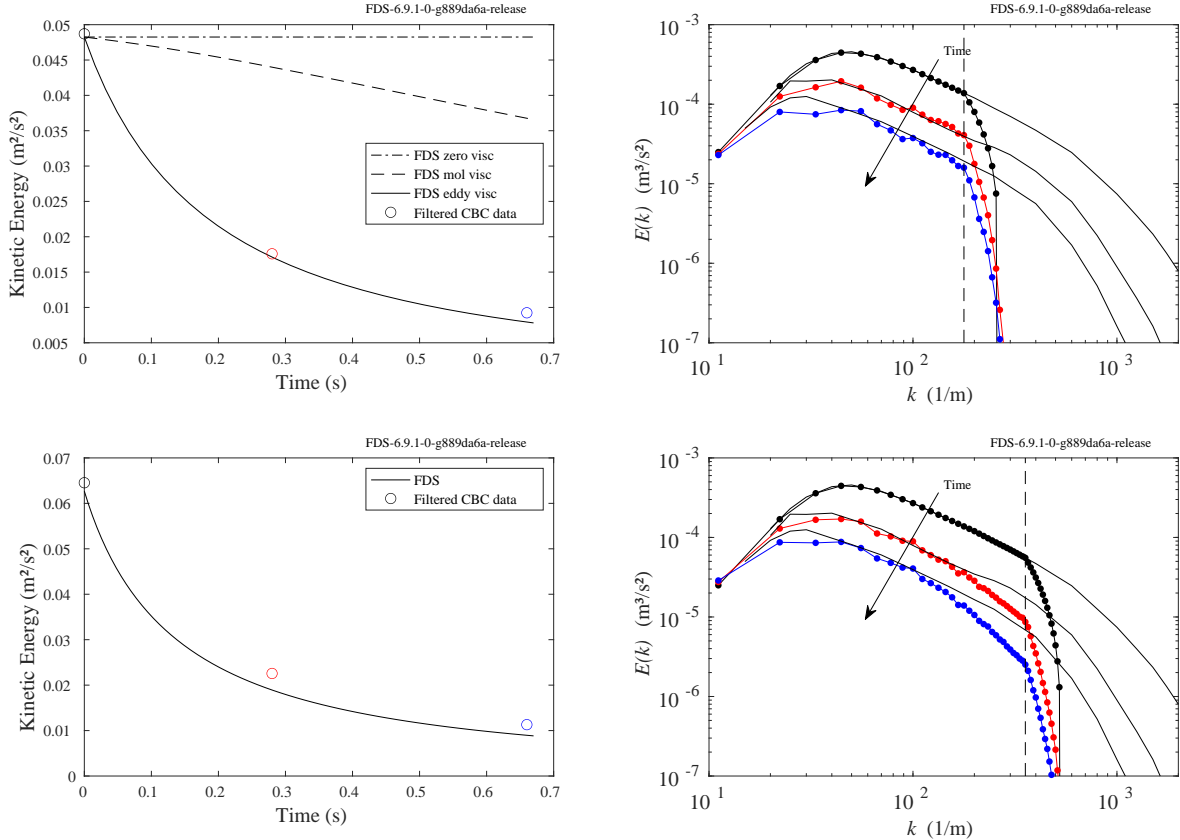


Figure 4.2: (Left) Time histories of integrated kinetic energy corresponding to the grid resolutions on the right side of the figure. In the  $32^3$  case (top), the CBC data (open circles) are obtained by applying a filter to the CBC energy spectra at the Nyquist limit for an  $N = 32$  grid. Similarly, for the  $64^3$  case (bottom), the CBC data are obtained from filtered spectra for an  $N = 64$  grid. (Right) Energy spectra for the  $32^3$  case (top) and the  $64^3$  case (bottom). The solid black lines are the spectral data of Comte-Bellot and Corrsin at three different points in time corresponding to downstream positions in the turbulent wind tunnel. The initial condition for the velocity field (spectra shown as black dots) in the FDS simulation is prescribed such that the energy spectrum matches the initial CBC data. The FDS energy spectra corresponding to the subsequent CBC data are shown by the red and blue dots. The vertical dashed line represents the wavenumber of the grid Nyquist limit.

#### 4.1.2 Dynamic Smagorinsky (`dsmag`)

In the previous section, all calculations were performed with a constant and uniform Smagorinsky coefficient,  $C_s = 0.2$ . For the canonical case of homogeneous decaying isotropic turbulence – *at sufficiently high Reynolds number* – this model is sufficient. However, we noticed that even for the isotropic turbulence problem when the grid Reynolds number is low (i.e., the flow is well-resolved) the constant coefficient model tends to over predict the dissipation of kinetic energy (see Fig. 4.2). This is because the eddy viscosity does not converge to zero at the proper rate; so long as strain is present in the flow (the magnitude of the strain rate tensor is nonzero), the eddy viscosity will be nonzero. This violates a guiding principle in LES development: that the method should converge to a DNS if the flow field is sufficiently resolved.

The dynamic procedure for calculating the model coefficient (set `TURBULENCE_MODEL='DYNAMIC SMAGORINSKY'` on `MISC`) alleviates this problem. The basis of the model is that the coefficient should be the same for two different filter scales within the inertial subrange. Details of the procedure are explained in the following references [56, 57, 34, 58, 48]. Here we present results for the implementation of the dynamic

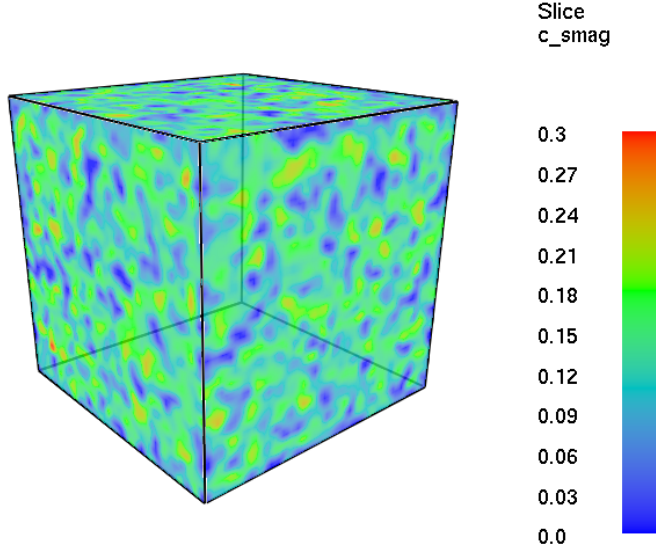


Figure 4.3: Smagorinsky coefficient for a  $64^3$  simulation of the CBC experiment.

model in FDS. In Fig. 4.3 we show contours of the Smagorinsky coefficient  $C_s(\mathbf{x}, t)$  at a time midway through a  $64^3$  simulation of the CBC experiment. Notice that the coefficient ranges from 0.00 to roughly 0.30 within the domain with the average value falling around 0.17.

Next, in Fig. 4.4, we show results for the dynamic model analogous to Fig. 4.2. For the  $32^3$  case the result is not dramatically different than the constant coefficient model. In fact, one might argue that the  $32^3$  constant coefficient results are slightly better. But there are several reasons why we should not stop here and conclude that the constant coefficient model is superior. First, as pointed out in Pope Exercise 13.34 [59],  $38^3$  is required to resolve 80 % of the total kinetic energy (for this flow) and thus put the cutoff wavenumber within the inertial subrange of turbulent length scales. Pope recommends that simulations which are under-resolved by this criterion should be termed “very large-eddy simulations”—weather forecasting is a typical example. For a  $32^3$  LES, the test filter width in the dynamic model falls at a resolution of  $16^3$ , clearly outside the inertial range. A tacit assumption underlying the original interpretation of the dynamic model is that both the grid filter scale and the test filter scale should fall within the inertial range, since this is the range in which the scales of turbulent motion (in theory) exhibit fractal-like, scale similarity (recently the procedure has been derived from other arguments [60]). With this in mind, it is perhaps not surprising that the dynamic model does not perform optimally for the low resolution case. In the higher resolution  $64^3$  case, however, the dynamic model does perform better than the constant coefficient model—and this is the desired result: we want better performance at higher resolution. As can be seen from the energy spectra (lower right), the energy near the grid Nyquist limit is more accurately retained by the dynamic model. This equates to better flow structure with fewer grid cells. Thus, for practical calculations of engineering interest the small computational overhead of computing the coefficient may be recuperated by a reduction in cell count.

#### 4.1.3 Deardorff (`deardorff`)

In this section we present the results for the FDS implantation of the Deardorff isotropic eddy viscosity model,  $\nu_t = C_V \sqrt{k_{sgs}} \Delta$ , where  $C_V = 0.1$  [59, 61]. Instead of transporting the subgrid kinetic energy, in FDS

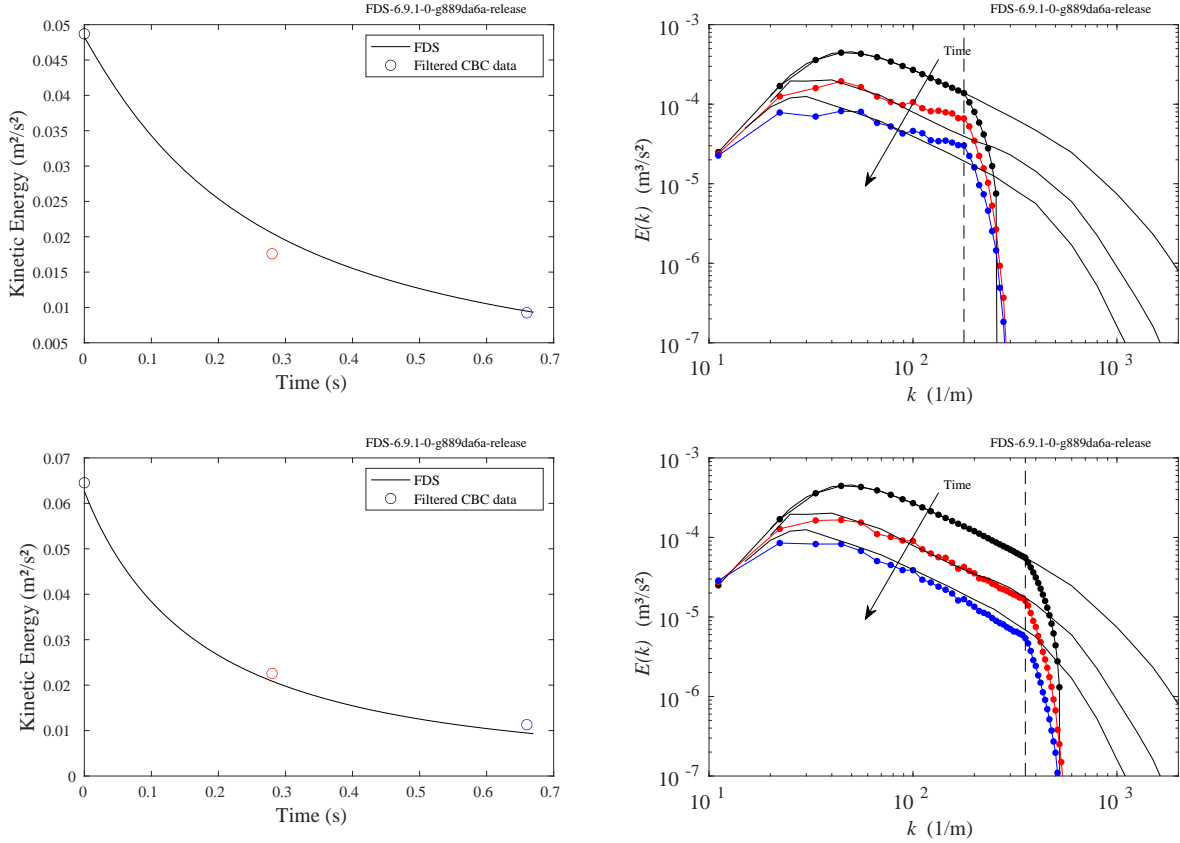


Figure 4.4: Dynamic Smagorinsky model results (analogous to Fig. 4.2) for integrated kinetic energy (left) and spectra (right).

$k_{sgs}$  is estimated with an algebraic closure based on scale similarity [62]. As may be seen in Fig. 4.5, for this case the Deardorff model is comparable to dynamic Smagorinsky. Deardorff is cheaper computationally, however, and tends to perform better for low resolution fire plume dynamics than the dynamic model. For these reasons, Deardorff is the default turbulence model in FDS.

#### 4.1.4 Vreman (vreman)

The Vreman eddy viscosity model [63] is an efficient alternative to the dynamic Smagorinsky model (DSM). In short, the spatial fields for the velocity components are expanded in Taylor series and test filtered analytically, avoiding the expensive test filtering operations required in DSM. The resulting model is superior to the constant coefficient Smagorinsky model (CSM) because, unlike CSM, with Vreman's model the subgrid dissipation automatically vanishes if the flow is fully resolved by the grid.

#### 4.1.5 WALE (wale)

The WALE (Wall Adapting Local Eddy-viscosity) model of Nicoud and Ducros [64] was developed as a near-wall eddy viscosity model with the proper scaling behavior without the need for a damping function like Van Driest damping (see [65]). Details of the model are provided in the FDS Technical Guide [48]. While WALE is designed for use a near-wall model, WALE can also perform as a bulk flow eddy viscosity

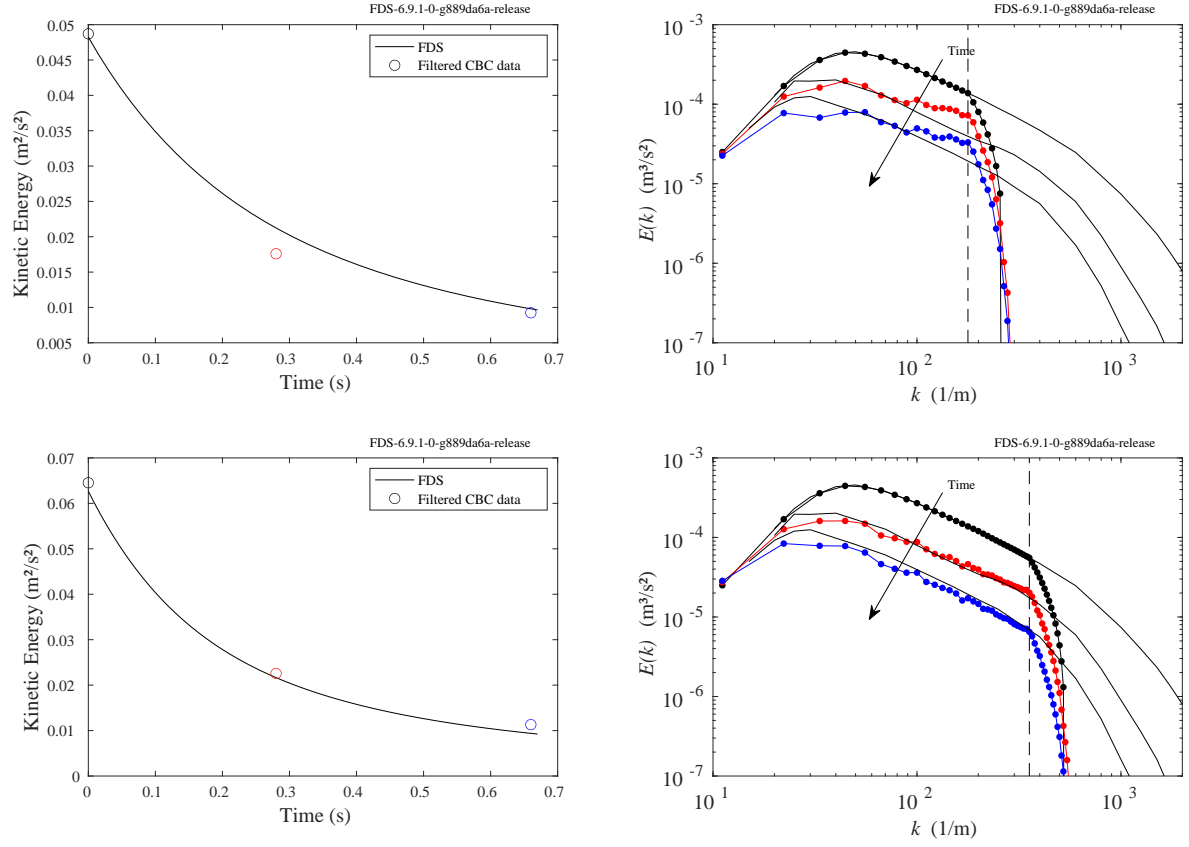


Figure 4.5: Deardorff model results (analogous to Fig. 4.2) for integrated kinetic energy (left) and spectra (right).

model. Here we confirm the appropriate choice of WALE model constant,  $C_W = 0.60$  in FDS, by performing simulation of decaying isotropic turbulence, as was also performed in [64].

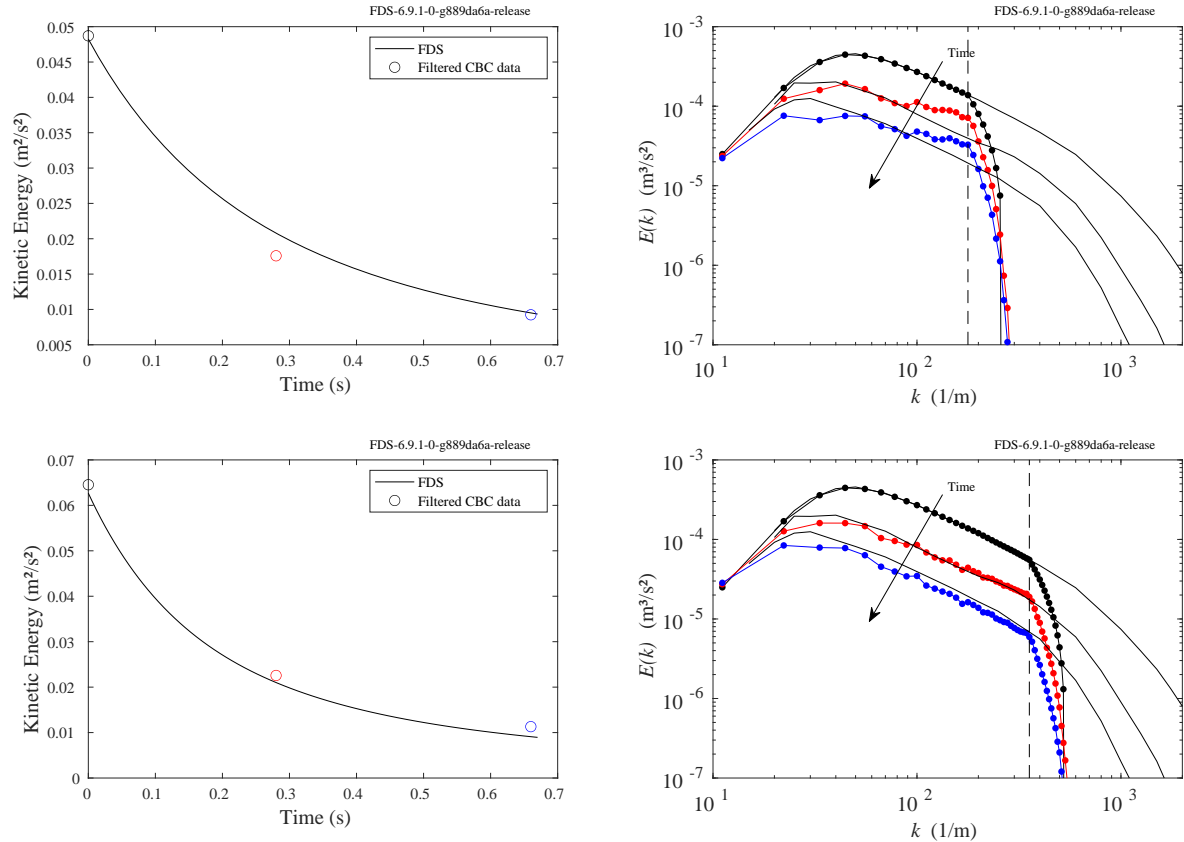


Figure 4.6: Vreman model results (analogous to Fig. 4.2) for integrated kinetic energy (left) and spectra (right).

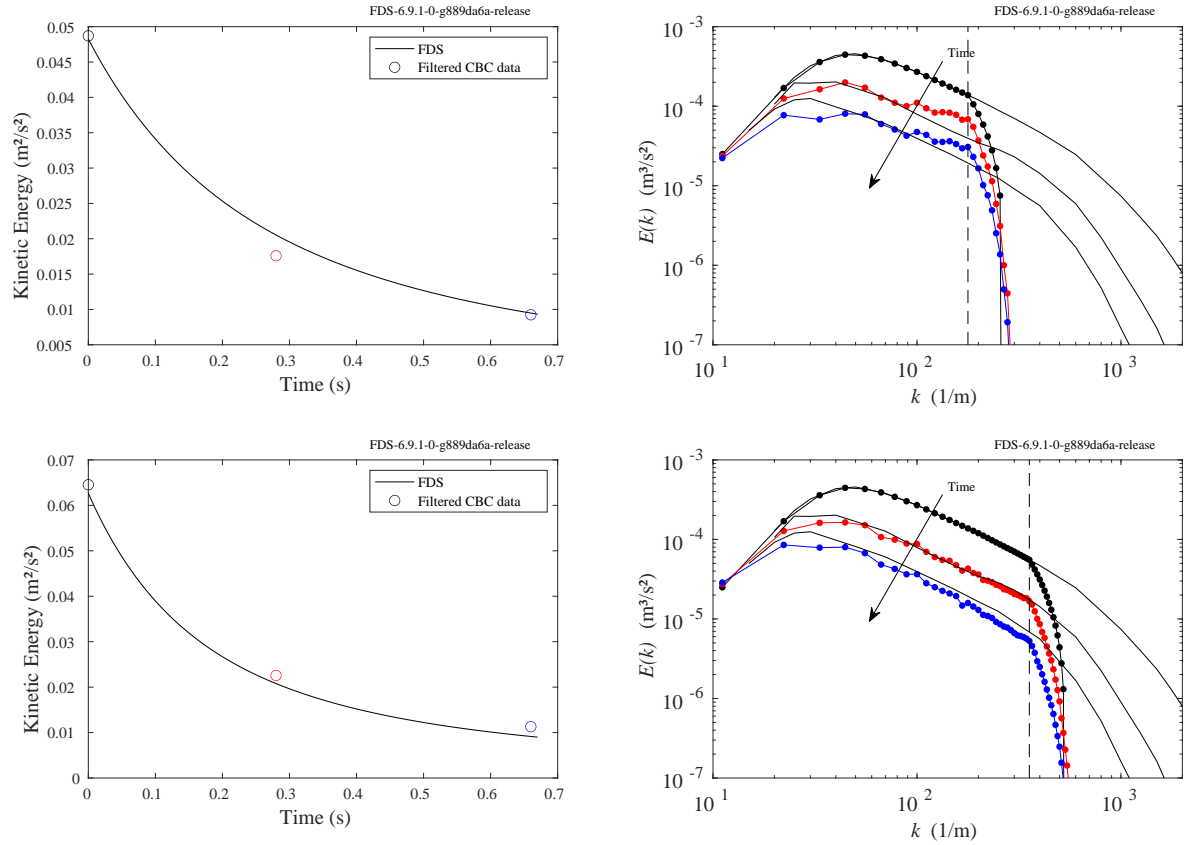


Figure 4.7: WALE model results (analogous to Fig. 4.2) for integrated kinetic energy (left) and spectra (right).

## 4.2 Jet Centerline Velocity Decay (`jet`)

Gregor Jäger, BFT Cognos GmbH, Germany

The `jet_` series in the Validation/Turbulent\_Jet directory tests the ability of subgrid stress closure (turbulence model) to correctly capture the transition from laminar to turbulent flow and subsequent momentum decay for an incompressible jet.

The FDS solution is compared with experimental observations from Kümmel [66]. In the initial region of the jet,  $x < x_0$ , the velocity  $u$  is constant near the axis and is equal to the velocity at the nozzle orifice ( $u_0$ ). For a rectangular nozzle orifice of height  $h = 0.8$  and width  $b = 0.8$ , the initial length is calculated by

$$x_0 = \frac{h}{m} \quad (4.1)$$

where the mixed number  $m$  is between 0.12 and 0.20.

In the transition region, viscous mixing spreads over the entire jet flow and the flow velocity along the axis decreases. The mean flow velocity at the jet centerline  $u_{max}(x)$  is calculated by

$$\frac{u_{max}(x)}{u_0} = \frac{x_0}{x} \sqrt{\frac{b}{h}} = \frac{1}{mx} \sqrt{bh} \quad (4.2)$$

Four turbulence models are tested: (1) Constant Smagorinsky (csmag), (2) Dynamic Smagorinsky (dsmag), (3) Deardorff (FDS default), and (4) Vreman. The results are plotted in Fig. 4.8. For each model, two grid resolutions are run, corresponding to  $h/\delta x = 8$  (colored dashed lines) and  $h/\delta x = 16$  (colored solid lines).

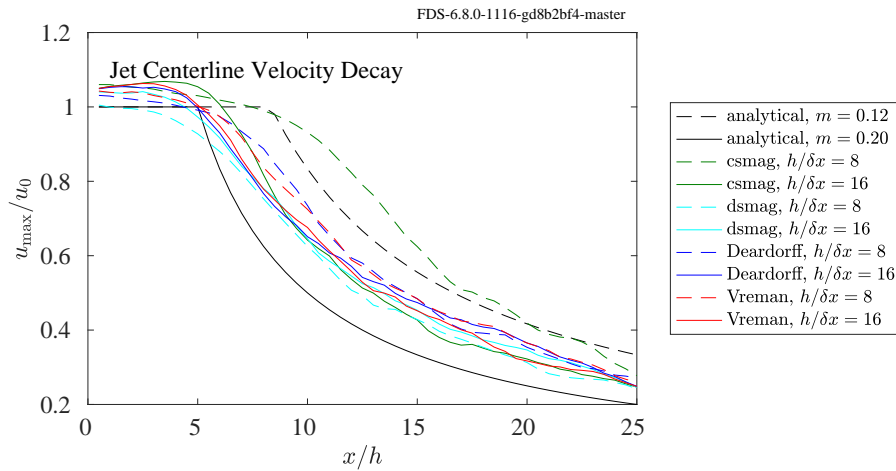


Figure 4.8: Centerline velocity decay for a high Reynolds number jet ( $\text{Re}_h = 1 \times 10^5$ ) with a square orifice of side  $h$ . FDS results (colored lines) are shown for various turbulence models at two grid resolutions. For comparison, analytical results (black lines) are shown for two values of the mixing number  $m$ .



# Chapter 5

## Boundary Effects

Wall flows have long been a challenge for large-eddy simulation (LES) [67, 68, 69, 59, 70]. In spite of their promise and sophistication, practical LES codes are resigned to *model* the wall shear stress as opposed to *resolving* the dynamically important length scales near the wall. FDS uses a log law velocity profile [59] for modeling turbulent flow near a wall.

### 5.1 The FDS Moody Chart (`poiseuille`, `moody`, `z0`)

At a minimum, a wall model should accurately reproduce the mean wall stress for flow in a straight square duct. We verify that this is true for FDS by reproducing the Moody chart, a plot of friction factor versus Reynolds number for pipe flow [71].

Details of the FDS formulation are given in the Technical Guide [48]. Here we provide only the salient components of the model necessary for treatment of constant density channel flow. The filtered continuity and momentum equations are:

$$\frac{\partial \bar{u}_i}{\partial x_i} = 0, \quad (5.1)$$

$$\frac{\partial \bar{u}_i}{\partial t} + \frac{\partial \bar{u}_i \bar{u}_j}{\partial x_j} = -\frac{1}{\rho} \left[ \frac{dp}{dx_i} + \frac{\partial \tilde{p}}{\partial x_i} + \frac{\partial \bar{\tau}_{ij}}{\partial x_j} + \frac{\partial \tau_{ij}^r}{\partial x_j} \right], \quad (5.2)$$

where  $\tau_{ij}^r$  is the deviatoric part of the residual stress tensor. In this work we specify a constant pressure drop  $dp/dx$  in the streamwise direction to drive the flow. The hydrodynamic pressure  $\tilde{p}$  is obtained from a Poisson equation which enforces (5.1). Details of the model used for the viscous stress at the wall, e.g.,  $\bar{\tau}_{xz}|_{z=0}$ , are provided in the FDS Technical Reference Guide [1].

#### 5.1.1 Laminar Results

As verification of the no-slip boundary condition and further verification of the momentum solver in FDS, we perform a simple 2-D laminar (Poiseuille) flow calculation of flow through a straight channel. The height of the channel is  $H = 1$  m and the length of the channel is  $L = 8$  m. The number of grid cells in the streamwise direction  $x$  is  $N_x = 8$ . The number of cells in the wall-normal direction  $z$  is varied  $N_z = \{8, 16, 32, 64\}$ . The fluid density is  $\rho = 1.2 \text{ kg m}^{-3}$  and the viscosity is  $0.025 \text{ kg m}^{-1} \text{ s}^{-1}$ . The mean pressure drop is prescribed to be  $dp/dx = -1 \text{ Pa m}^{-1}$  resulting in  $\text{Re}_H \approx 160$ . The (Moody) friction factor  $f$ , which satisfies

$$\Delta p = f \frac{L}{H} \frac{1}{2} \rho \bar{u}^2, \quad (5.3)$$

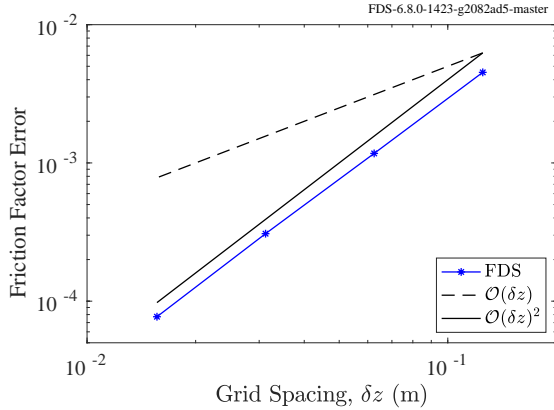


Figure 5.1: FDS exhibits second-order convergence for laminar (Poiseuille) flow in a 2-D channel.

is determined from the steady-state mean velocity  $\bar{u}$  which is output by FDS for the specified pressure drop. The exact friction factor for this flow is  $f_{exact} = 24/\text{Re}_H$ . The friction factor error  $|f - f_{exact}|$  is plotted for a range of grid spacings  $\delta z = H/N_z$  in Fig. 5.1 demonstrating second-order convergence of the laminar velocity field.

### 5.1.2 Turbulent Results

**Smooth Walls** To verify the wall model for turbulent flow we perform 3-D LES of a square duct with periodic boundaries in the streamwise direction and a constant and uniform mean pressure gradient driving the flow. The problem set up is nearly identical to the laminar cases of the previous section except here we perform 3-D calculations and maintain cubic cells as we refine the grid: we hold the ratio 8:1:1 between  $N_x : N_y : N_z$  for all cases. The cases shown below are identified by their grid resolution in the  $z$  direction. The velocity field is initially at rest and develops in time to a mean steady state driven by the specified mean pressure gradient. The presence of a steady state is the result of a balance between the streamwise pressure drop and the integrated stress from the wall model. FDS outputs the planar average velocity in the streamwise direction and once a steady state is reached this value is used to compute the Reynolds number and the friction factor. Table 5.1 provides a case matrix: nine cases for three values of specified pressure drop and three grid resolutions. The nominal Reynolds number (obtained post-run) is listed along with the friction factor from the most refined FDS case and the friction factor computed (iteratively) from the Colebrook equation,

$$\frac{1}{\sqrt{f}} = -2.0 \log_{10} \left( \frac{s/H}{3.7} + \frac{2.51}{\text{Re}_H \sqrt{f}} \right), \quad (5.4)$$

which is a fit to the turbulent range of the Moody chart (for example, see Ref. [72]). The parameter  $s/H$  is the relative roughness where  $H$  is the hydraulic diameter of the pipe or channel and  $\text{Re}_H$  is the Reynolds number based on  $H$ . To provide a qualitative picture of the flow field, Fig. 5.2 shows contours of streamwise velocity for the case  $dp/dx = -1 \text{ Pa m}^{-1}$  and  $N_z = 32$ .

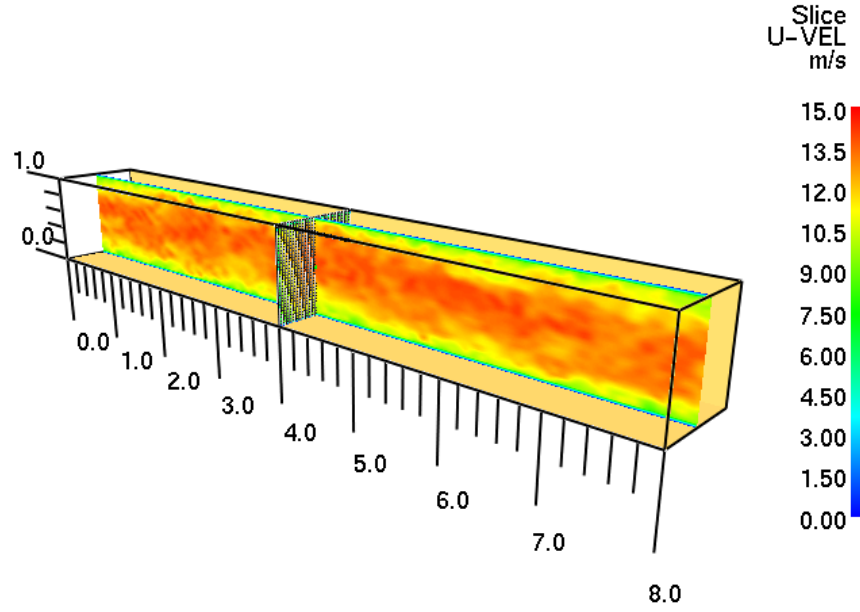


Figure 5.2: LES of square duct flow with smooth walls and periodic streamwise boundaries. For this image  $N_z = 32$  and the mean pressure drop is  $dp/dx = -1 \text{ Pa m}^{-1}$  resulting in  $\text{Re}_H = 7.5 \times 10^5$  and a friction factor of  $f = 0.0128$ .

Table 5.1: Case matrix and friction factor results for turbulent channel flow with smooth walls. The height of the first grid cell  $\delta z$  is given in viscous units  $z^+$  for each case. Additionally, the table gives the nominal Reynolds number  $\text{Re}_H$  and the FDS friction factor results compared to the Colebrook equation (5.4).

$dp/dx$ (Pa/m)	$z^+$			$\text{Re}_H$	$f$ FDS ( $N_z = 32$ )	$f$ Colebrook	Rel. error
	$N_z = 8$	$N_z = 16$	$N_z = 32$				
-0.01	190	95	47	$5.9 \times 10^4$	0.0212	0.0202	4.8
-1.	$1.9 \times 10^3$	950	470	$7.5 \times 10^5$	0.0128	0.0122	4.6
-100.	$1.9 \times 10^4$	$9.5 \times 10^3$	$4.7 \times 10^3$	$9.8 \times 10^6$	0.0077	0.0081	6.0

**Rough Walls** With the same grid set up as described above the smooth walls, a series of cases labeled as  $z_0^1$  in the repository [44] were run at various roughness heights, grid resolutions, and Reynolds numbers. The results are presented together with the smooth wall cases in Fig. 5.3. The laminar cases provide accurate results for two different Reynolds numbers. Both the smooth wall and rough wall treatments behave well over the range tested.

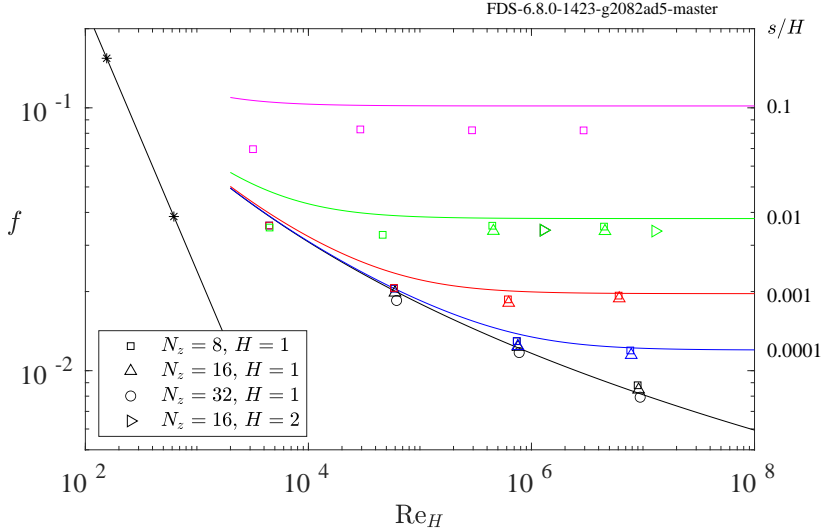


Figure 5.3: The FDS Moody chart: friction factor,  $f$ , versus Reynolds number,  $\text{Re}_H$ , based on duct height. The solid line for  $\text{Re} < 2000$  is the analytical result for 2-D Poiseuille flow,  $f = 24/\text{Re}$ . The solid lines for  $\text{Re} > 2000$  (from the Colebrook equation (5.4)) are Relative roughness  $s/H$  shown on the right axis.

## 5.2 Blasius boundary layer (`blasius`)

**Hyun-Wook Park and Jung-il Choi, Yonsei University, Seoul, South Korea**

Consider a steady flow over a semi-infinite flat plate aligned with the flow with free stream velocity,  $u_0$ . The Prandtl boundary layer equations [73] are:

$$u \frac{\partial u}{\partial x} + w \frac{\partial u}{\partial z} = v \frac{\partial^2 u}{\partial z^2}, \quad (5.5)$$

$$\frac{\partial u}{\partial x} + \frac{\partial w}{\partial z} = 0. \quad (5.6)$$

Paul Richard Heinrich Blasius found a solution to Eqs. (5.5) and (5.6) by introducing a similarity variable:

$$\eta \equiv \frac{z}{\sqrt{vx/u_0}}. \quad (5.7)$$

Substituting  $\eta$  and the stream function ( $u = \partial \psi / \partial z$ ,  $w = -\partial \psi / \partial x$ ) into Eq. (5.5) yields the following ODEs:

$$\frac{1}{2} f f'' + f''' = 0 \quad (5.8)$$

<sup>1</sup>The atmospheric community typically uses  $z_0$  to denote the roughness height. However, we also use  $s$  interchangeably with  $z_0$  to conform to the notation used in Pope [59].

$$u = u_0 f' \quad (5.9)$$

$$w = \frac{1}{2} \sqrt{\frac{\nu u_0}{x}} (\eta f' - f) \quad (5.10)$$

The solution of Eq. (5.8) is the Blasius solution [73].

The physical domain of the present verification case is a rectangle with length  $L = 0.15$  m in the streamwise direction and  $H = 0.3$  m in the wall-normal direction. The grid spacing is uniform ( $\delta x = L/N_x$ ,  $\delta z = H/N_z$ ) in each direction, and  $N_x = 1.5N_z$  with  $N_z = \{16, 32, 64\}$  for each test series. The Boundary conditions for the inlet and outlet boundaries are OPEN with the dynamic pressure set to zero at the inlet boundary. On the top boundary, the gradient of  $w$  in the  $z$  direction is zero combined with a free-slip condition that combines to yield an irrotational field. The boundary condition along the bottom of the domain is free-slip upstream of the plate ( $x < 0.5$  m) and no-slip on the plate. The initial velocity is 1 m/s and  $u_0$  is taken as the value of  $u$  at the top boundary since boundary conditions at  $z = \infty$  cannot be directly applied. The case is run with constant properties:  $\rho = 1.2$  kg/m<sup>3</sup>,  $\mu = 0.001$  kg/m.s.

Figure 5.4 (left) shows a comparison of the streamwise velocity from FDS with the Blasius solution. The FDS solution (lines) converges to Blasius (open circles) as the mesh resolution is increased. Figure 5.4 (right) shows the root mean square (RMS) error,  $\varepsilon$ , in  $u$  (streamwise component) at  $x = 0.1$  m (0.05 m from the leading edge of the plate) for the dimensional Blasius solution. The error is defined by

$$\varepsilon \equiv \sqrt{\frac{1}{N_z} \sum_{k=1}^{N_z} [u_k - u_{B,k}]^2} \quad (5.11)$$

where  $k$  is the  $z$  index. The value  $u_k$  represents the FDS result for  $u$  at the staggered grid storage location for cell  $k$ ,  $u_{B,k}$  is the dimensional Blasius solution at the corresponding location. The slight departure from second-order accuracy is likely due to numerical issues in representing the singularity in the Blasius solution at the leading edge of the plate as well as errors in the boundary conditions due to truncation of the domain.

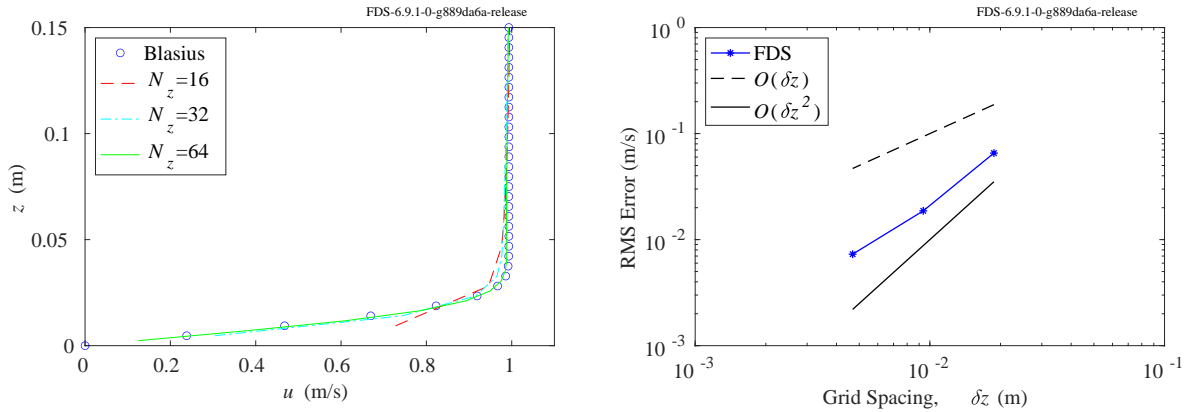


Figure 5.4: (Left) Comparison of theoretical and numerical results for the Blasius velocity profile ( $u$  component). (Right) Error between FDS and Blasius solution for  $u(z)$  plotted for each grid resolution.

### 5.3 Pohlhausen thermal boundary layer (`Pohlhausen`)

This write up follows Appendix B of [74]. The nondimensional temperature as a function of the similarity variable  $\eta$  is taken to be

$$\theta(\eta) \equiv \frac{T(\eta) - T_w}{T_\infty - T_w} \quad (5.12)$$

The energy equation may then be written as

$$\frac{d^2\theta}{d\eta^2} + \frac{1}{2}\text{Pr}f \frac{d\theta}{d\eta} = 0 \quad (5.13)$$

Given the boundary conditions  $\theta = 0$  at  $y = 0$ ,  $\eta = 0$  and  $\theta = 1$  at  $y = \infty$ ,  $\eta = \infty$ , and the function  $f(\eta)$  from the Blasius solution in Sec. 5.2, the Pohlhausen solution for the temperature profile is

$$\theta(\eta) = \frac{\int_0^\eta \exp\left(-\frac{\text{Pr}}{2} \int_0^\eta f d\eta\right) d\eta}{\int_0^\infty \exp\left(-\frac{\text{Pr}}{2} \int_0^\eta f d\eta\right) d\eta} \quad (5.14)$$

This solution is plotted in Fig. 5.5 (left) for different Prandtl numbers (Pr) and may be compared to the plot in Fig. B-2 of [74] for verification.

In this test series, the 2-D FDS domain is set 10 m in length and 1 m in height. The simulation is run as a DNS with the viscosity, conductivity, and specific heat set to provide Prandtl numbers of [0.5, 1, 2]. The grid resolution (after a convergence study) is set to  $\delta x = \delta z = 1.25$  cm. The inlet velocity is set to 1 m/s with an ambient air temperature of  $T_\infty = 20$  °C. The wall boundary is set to a fixed temperature of  $T_w = 21$  °C. The outflow is set to OPEN. The top boundary is homogeneous Neumann for velocity and Dirichlet for temperature at  $T_\infty = 20$  °C. The simulation is run to steady state. The resulting temperature profiles  $T(z)$  at  $x = 5$  m are shown in Fig. 5.5 (right).

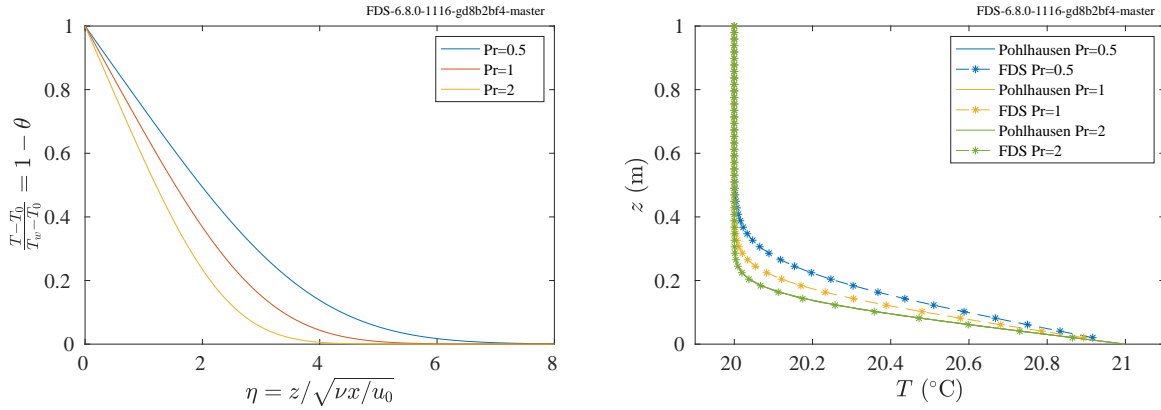


Figure 5.5: (Left) Pohlhausen similarity solution for nondimensional temperature. (Right) FDS results for vertical profile of temperature at  $x = 5$  m for different Prandtl numbers compared to the Pohlhausen solution.

## 5.4 Near-Wall Grid Resolution (`yplus`)

Abbas Jaber, NIST SURF student

The distance from the wall measured in “viscous wall units” is called  $y^+$ . In order to verify that  $y^+$  is calculated correctly within FDS, we analyze an example of Poiseuille flow in a square channel with periodic boundaries. The pressure gradient in the  $x$ -direction, the dynamic viscosity, and the dimensions of the channel are known. This allows us to easily determine the expected values of wall shear stress,

$$\tau_w = -\delta \frac{dp}{dx}, \quad (5.15)$$

where  $p$  is pressure and  $\delta$  is half the height of the channel. This, in turn, allows for determining the friction velocity,

$$u_\tau \equiv \sqrt{\frac{\tau_w}{\rho}}. \quad (5.16)$$

From here we calculate the exact value of  $y^+$  for the given flow,

$$y^+ \equiv \frac{y}{\delta} = \frac{u_\tau y}{v}. \quad (5.17)$$

In FDS,  $\tau_w$  is obtained only from the wall model. The resolution of the wall-normal streamwise velocity gradient increases with mesh resolution; the value of  $y^+$  decreases accordingly. In this verification case, a wall device is used to output  $y^+$  for different mesh resolutions in the  $y$ -direction.  $y^+$  is output for a given  $\delta y$ , height of a cell,  $\delta y = [1/8, 1/16, 1/32]$ . Then, the device values obtained are compared with the exact value of  $y^+$  for a given mesh resolution (Fig. 5.6). An FDS wall device outputs the mid-cell value of the first cell next to the wall, hence, the  $y$  value (y in Eq. (5.17)) used to determine the exact  $y^+$  varies with  $\delta y$  ( $y = \delta y/2$ ).

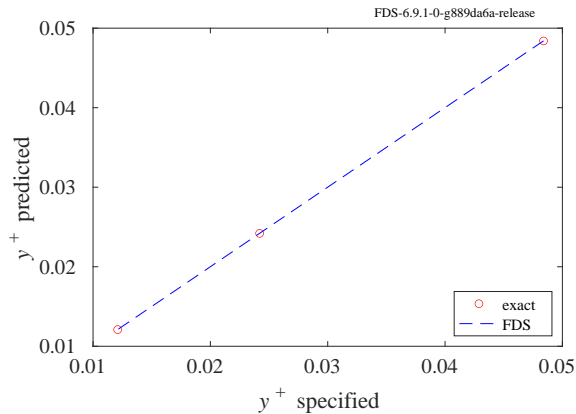


Figure 5.6: Verification of FDS  $y^+$  output for  $\delta y = [1/8, 1/16, 1/32]$ .

## 5.5 Heated Channel Flow (`heated_channel`)

The simulation of turbulent channel flow ( $Re_\tau = 180$ ) with a heat source was performed to verify the log law near-wall model for heat transfer [1]. The height of the channel is  $H = 2$  m, the width is  $W = 6$  m, and the length is  $L = 12$  m. There are 96 cells in the streamwise direction ( $\delta x = 0.125$  m) and 48 cells in the spanwise

and wall-normal directions ( $\delta y = \delta z = 0.125$  m). The midpoint of the first cell in viscous units is  $z^+ \approx 18$ , putting the first velocity unknown within the buffer layer. For this reason, the dynamic Smagorinsky SGS model is used for the residual stress. Additionally, these cases were run with (SIMULATION\_MODE='LES' on MISC), which accounts for both molecular and turbulent transport coefficients, a must for distinguishing between fluids with different molecular Prandtl or Schmidt numbers (here the Reynolds number is so low that molecular effects may dominate locally). The flow is maintained by a mean pressure gradient ( $9.0 \times 10^{-6}$  Pa/m) in the streamwise direction (follows from  $Re_\tau = 180$ ). A constant volumetric heat source ( $0.5$  W/m<sup>3</sup>) is imposed on the fluid. The boundary conditions for momentum equations are no-slip at top and bottom walls and periodic for the streamwise and spanwise directions. The boundary condition for the energy equation is constant temperature ( $T_w = 20^\circ\text{C}$ ) at the wall. To evaluate the effects of Prandtl number (Pr) and compare the DNS study [75] with FDS, the specific heat ( $c_p = 1$  kJ/(kg K)) and viscosity ( $\mu = 1.8216 \times 10^{-5}$  kg/(m s)) are fixed and the conductivity,  $k$ , of the fluid (air) is adjusted to:

Pr	$k$ (W/(m K))
0.10	$1.82 \times 10^{-1}$
0.71	$2.59 \times 10^{-2}$
1.00	$1.82 \times 10^{-2}$
2.00	$9.11 \times 10^{-3}$

In Figure 5.7, FDS results are compared to DNS data for mean streamwise velocity,  $u^+ = \langle u \rangle / u_\tau$ , and mean temperature,  $T^+ = (\langle T \rangle - T_w) / T_\tau$ . The temperature scale is given by

$$T_\tau \equiv \frac{\langle \dot{q}_w'' \rangle}{\rho c_p u_\tau}, \quad (5.18)$$

where  $\langle \dot{q}_w'' \rangle$ ,  $\rho$ , and  $c_p$  are the mean heat flux at the wall, density, and specific heat, respectively. Fully developed, statistically stationary flow is achieved after approximately 20 flow through times. Statistics are gathered between 40 and 60 flow through times.

As seen in the left side of Fig. 5.7, the velocity profile shows good agreement with the DNS result. The near-wall temperature profile for each Pr is shown on the right side of Fig. 5.7. The mean wall heat flux is correct, as indicated by the accurate result of the first off-wall grid value (in the viscous region).

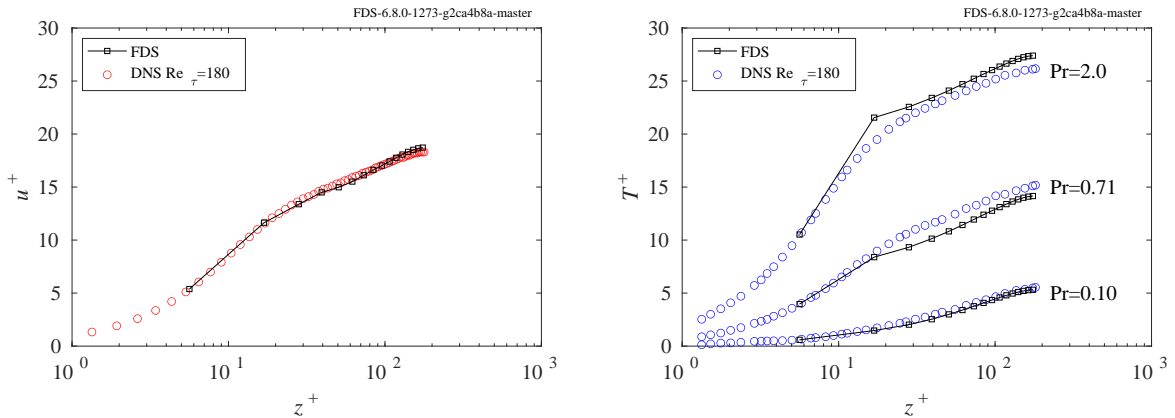


Figure 5.7: Comparison of FDS (lines with squares) with DNS (circles) for heated channel flow. (Left) Wall-normal velocity profile compared to DNS of Moser et al. [76]. (Right) Wall-normal mean profiles of temperature for molecular Prandtl numbers (Pr) = 0.10, 0.71, and 2.0, compared to DNS of Kim and Moin [75].

## 5.6 Forced Convection Flat Plate Boundary Layer (`forced_conv_flat_plate`)

In this section, we set up a series of cases to test the forced convection model in FDS. The scenario is a constant temperature turbulent flat plate boundary layer. Gravity is set to zero in order to explicitly exercise the forced convection model. The inlet flow velocity is constant and uniform at the leading edge of the plate. Three velocities are considered, [0.1, 1, 10] m/s. The free stream fluid is nitrogen ( $\rho = 1.165 \text{ kg/m}^3$ ) with constant properties: dynamic viscosity,  $\mu = 1 \times 10^{-5} \text{ kg/m/s}$ , thermal conductivity,  $k = 0.01 \text{ W/m/K}$ , and specific heat,  $c_p = 1 \text{ kJ/kg/K}$ . The free stream temperature is 20 °C and the wall temperature is a constant 30 °C. The plate is 16 m long with constant and uniform inflow velocity and an OPEN outflow boundary. The domain is 2 m in width and 2 m in height. The spanwise boundaries are PERIODIC and the top boundary is MIRROR.

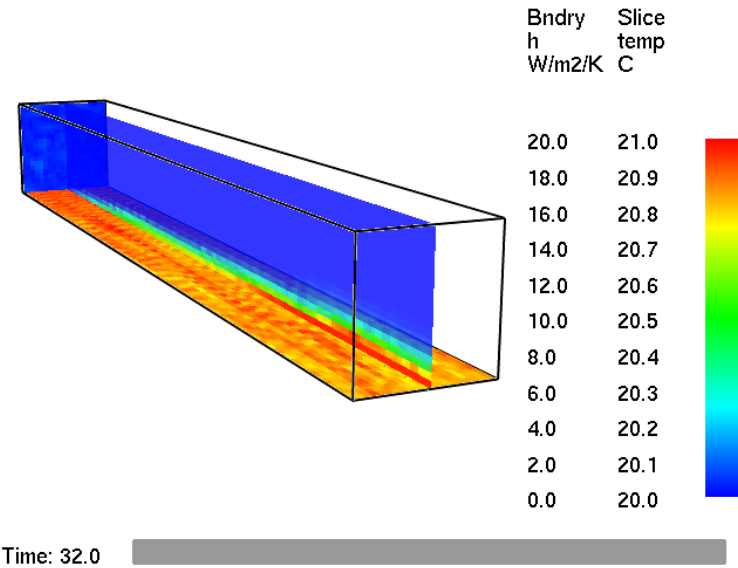


Figure 5.8: Smokeview rendering of a temperature slice through the center of the boundary layer as well as the heat transfer coefficient on the constant temperature wall boundary for the 10 m/s case at 10 cm resolution.

The boundary layer thicknesses for each of the three velocity inlet conditions are [0.5227, 0.3298, 0.2081] m, respectively, evaluated at  $x = 16$  m from the correlation  $\delta_x = 0.37x\text{Re}_x^{-1/5}$  (see [77] Table 7.7). Three grid resolutions are considered, [25, 10, 2.5] cm. The resolution of the boundary layer at the end of domain ( $\delta_{16}/\delta_x$ ) is provided below in Tab. 5.2. Note that the boundary layer is generally under-resolved ( $\delta_x/\delta_x < 10$ ). Thus, accuracy of the wall heat flux relies heavily on the model for the heat transfer coefficient. The simulation is set to run for 20 flow through times with averaging of results over the last half of the simulation. An image of the spatially developing thermal boundary layer with medium resolution and 10 m/s inflow is shown in Fig. 5.8. Also shown is the local heat transfer coefficient along the wall.

Table 5.2: Forced convection boundary layer resolution,  $\delta_{x=16 \text{ m}}/\delta_x$ .

$\delta_x$	free stream velocity		
	0.1 m/s	1 m/s	10 m/s
25 cm	2.1	1.3	0.83
10 cm	5.2	3.3	2.1
2.5 cm	21.0	13.0	8.3

The results are plotted in Fig. 5.9. We are comparing FDS output to the local turbulent forced convection correlation,

$$\text{Nu}_x = 0.0296 \text{Re}_x^{4/5} \text{Pr}^{1/3} \quad (5.19)$$

In these cases, the Prandtl number,  $\text{Pr}$ , is taken to be 0.7. The correlation is plotted as the line labeled “forced local” in the legend of the plots. The plots are comparisons of “local” Nusselt number as a function of “local” Reynolds number, as indicated by the subscript  $x$ . In these formulae, the length scale is given by the distance from the leading edge of the plate. Of course, FDS does not know this information when it is trying to determine the heat transfer coefficient on a given wall cell. Hence, it uses a constant “convective length scale”, in this case set to 1 m (the default value). Also included in each plot is a dashed line representing  $2Lx/\delta x$ . If this curve is larger than the correlation this is an indication that the “DNS” value was used for the heat transfer coefficient, that is  $h = 2k/\delta x$ . This only happens for the 0.1 m/s case at the highest grid resolution.

In order to make a comparison with the local correlation we need to scale the FDS heat transfer coefficient by the ratio of the local temperature difference to the free stream temperature difference assumed in the correlation. We add device outputs of ‘HTC’ and ‘CONVECTIVE HEAT FLUX’ along the length of the plate. From these two outputs we can discern the temperature difference at the wall,  $\Delta T_{\text{FDS}}$ . The correlation temperature difference is  $T_w - T_\infty$ . For a given heat flux the following holds,  $\dot{q}_w'' = h_{\text{FDS}} \Delta T_{\text{FDS}} = h_{\text{cor}}(T_w - T_\infty)$ . For a given location,  $x$ , along the plate the FDS results for  $\text{Nu}_x$  are taken to be,

$$\text{Nu}_x = \frac{h_{\text{cor},x} x}{k} = \left( \frac{h_{\text{FDS},x} \Delta T_{\text{FDS}}}{T_w - T_\infty} \right) \frac{x}{k} \quad (5.20)$$

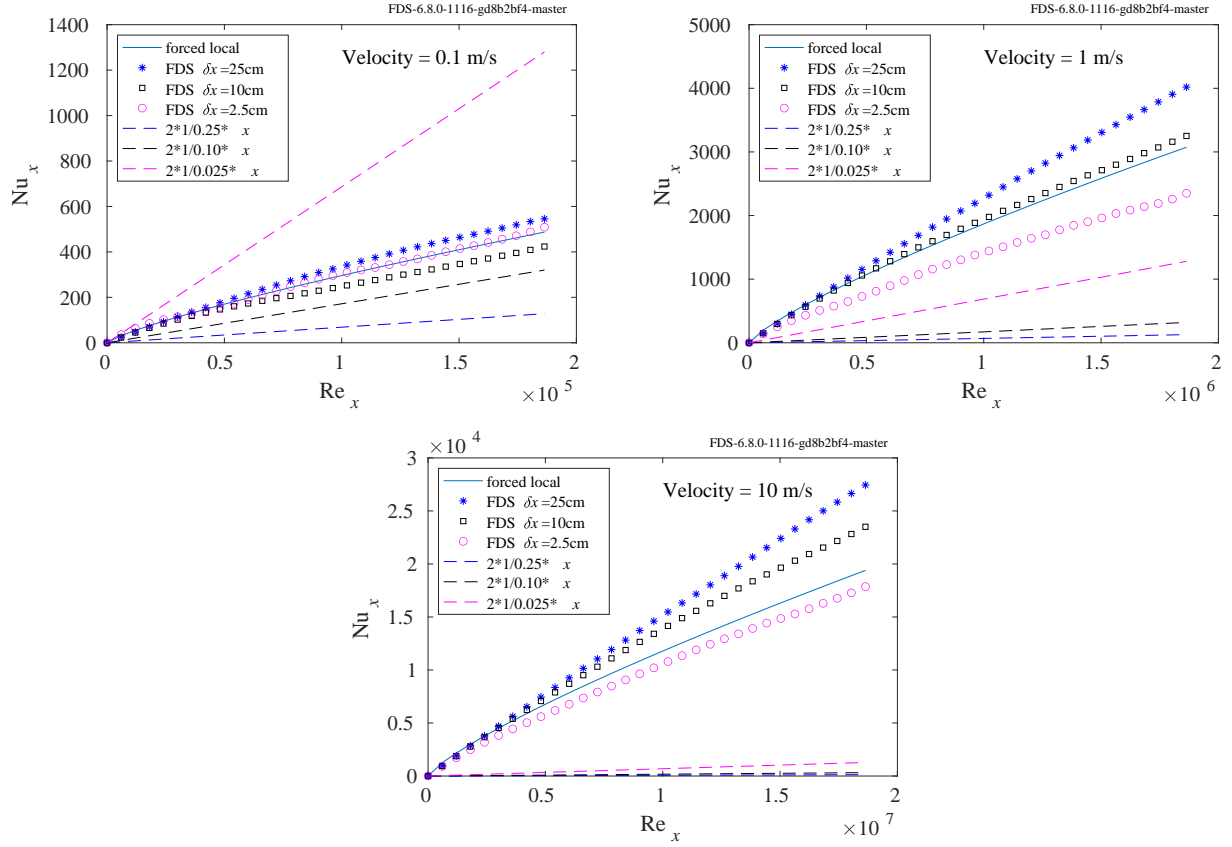


Figure 5.9: FDS results for local Nusselt number in turbulent boundary layer flow over a flat plate. Clockwise from top-left the flow velocity increases from 0.1 m/s to 10 m/s. Dashed lines indicate local Nusselt number based on  $2L/(\delta n)$ , where  $L = 1$  m is the convective length scale and  $\delta n$  is the wall-normal grid resolution.

## 5.7 Natural Convection

LES simulations in FDS use an empirical correlation to define the heat transfer coefficient for natural convection:

$$h = \frac{\text{Nu} k}{L} ; \quad \text{Nu} = C \text{Ra}^n \quad (5.21)$$

The Rayleigh number (product of Grashof and Prandtl numbers), Ra, is given by

$$\text{Ra} = \frac{g \beta |T_1 - T_2| L^3}{\nu \alpha} \quad (5.22)$$

where  $g$  is the magnitude of the gravitational acceleration,  $T_1$  and  $T_2$  are the respective free stream and surface temperatures,  $L$  is a length scale,  $\nu$  is the kinematic viscosity and  $\alpha$  is the thermal diffusivity of the fluid. The values of  $C$  and  $n$  and the definition of  $L$  vary depending on the configuration. For the test cases given below, the fluid is defined as '`LJ AIR`' with constant viscosity, specific heat, and thermal conductivity:  $\mu = 1.8216 \times 10^{-5}$  kg/m/s,  $c_p = 1$  kJ/kg/K, and  $k = 0.018216$  W/m/K, which provides a  $\text{Pr} = 1$  fluid. (Note that the correlations are valid for  $\text{Pr}$  in the range 0.5 to 2.)

### 5.7.1 Horizontal Plate (`nat_conv_hot_plate`)

Table 5.3 lists the default parameters for natural convection for a hot plate facing upwards (equivalent to a cold plate facing downwards) or a hot plate facing downwards (cold plate facing upwards). The listed ranges for the Ra number are those used within FDS. The ranges given in Ref. [77] are shown in Fig. 5.10. The length scale is defined  $L = A/P$ , where  $A$  is the area of one side of the plate and  $P$  is its perimeter. To verify these default parameters, five cases are set up for which  $10^4 < \text{Ra} < 10^{11}$ . The Ra number is varied by changing the side length,  $S$ , of the square plate and its temperature.

Table 5.3: Natural convection correlation parameters for horizontal plates,  $\text{Nu} = C \text{Ra}^n$  [77].

Configuration	Ra	$C$	$n$
Upward Facing Hot Surface	$< 1 \times 10^7$	0.54	1/4
	$> 1 \times 10^7$	0.15	1/3
Downward Facing Hot Surface	All	0.52	1/5

Three different grid resolutions are tested for the Cartesian cases:  $S/\delta x = [8, 16, 32]$ . The grid resolution is uniform with  $\delta x = \delta y = \delta z$ . All external boundaries are passive openings. The average heat flux of the plate is monitored and the simulation is run until a clear stationary state is reached. The results are presented in Fig. 5.10.

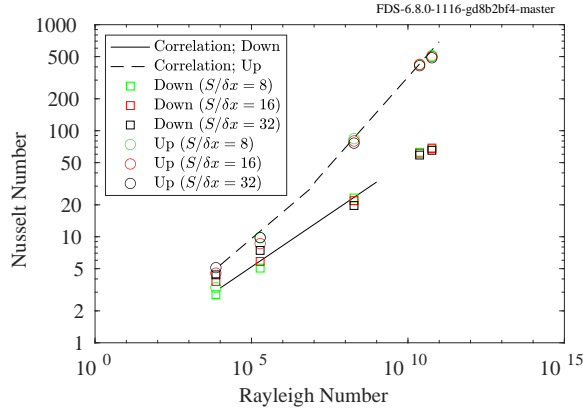


Figure 5.10: FDS results for natural convection from an upward and downward facing hot plate.

### 5.7.2 Horizontal Enclosure (`natconh`)

Consider thermal convection in an enclosure with a hot floor, cold ceiling, and adiabatic walls. Table 5.4 lists values for  $C$  and  $n$ , and the length scale,  $L$ , is taken as the height of the enclosure,  $\delta$ . There are 19 cases

Table 5.4: Natural convection correlation parameters for a horizontal enclosure,  $\text{Nu} = CRa^n$  [74].

$\text{Ra}$	$C$	$n$
< 1700	1	0
1700 – 17000	0.059	2/5
7000 – $3.2 \times 10^5$	0.212	1/4
> $3.2 \times 10^5$	0.061	1/3

for which  $1 < \text{Ra} < 10^{14}$ . The Rayleigh number is varied by changing both the enclosure height ( $\delta$  ranges from 2 mm to 20 m) and the temperature difference. The ceiling is held fixed at 20 °C and the floor is varied between 30 °C and 230 °C.

Three different grid resolutions are tested for the Cartesian cases:  $\delta/\delta z = [8, 16, 32]$ . The resolution is uniform with  $\delta x = \delta y = \delta z$ . The length and width of the computational domain are 8 times its height. The boundary conditions in the  $x$  and  $y$  directions are periodic. The average heat flux on the floor and ceiling is monitored and the simulation is run until a clear stationary state is reached. The results are presented below in Fig. 5.11 (left).

For the complex geometry cases, the grid and gravity vector are rotated by 18 degrees. A hollow cavity is formed using the `GEOM` namelist format with a hot surface below and a cold surface on top and insulated side walls. Two grid resolutions are tested:  $\delta/\delta z = [8, 16]$ . The results are shown in Fig. 5.11 (right).

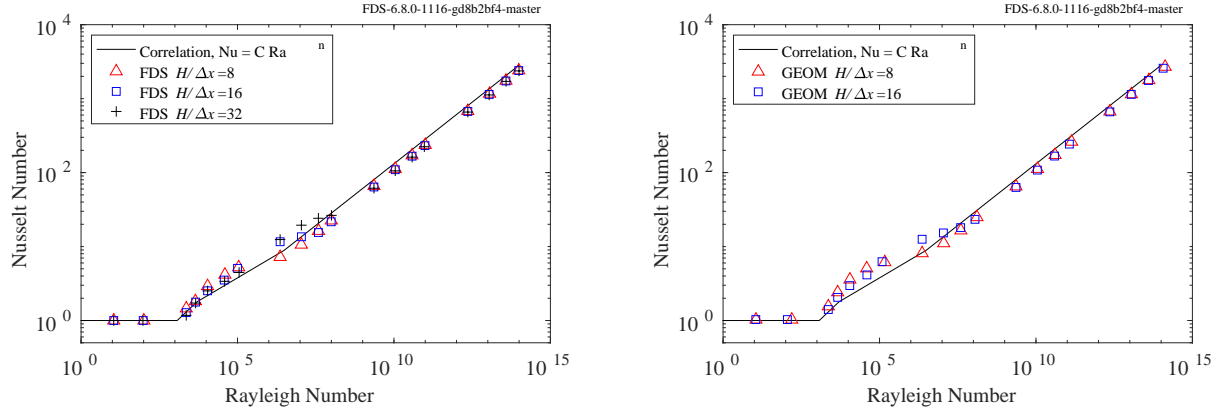


Figure 5.11: FDS results for Nusselt number in Rayleigh-Bénard convection (natural convection between horizontal plates)—(left) Cartesian geometry; (right) cutcell geometry.

### 5.7.3 Vertical Enclosure (`natconv`)

Consider now thermal convection in an enclosure with walls of fixed temperature and insulated floor and ceiling. The Nusselt number correlation requires an additional factor to account for the ratio of the height,  $H$ , to the distance between the walls  $\delta$  [74]:

$$\text{Nu} = CRa^n \left( \frac{H}{\delta} \right)^m \quad (5.23)$$

The values of  $C$ ,  $n$ , and  $m$  are given below in Tab. 5.5. The setup for this series is very similar to the

Table 5.5: Free convection correlation parameters for a vertical enclosure, valid for the ranges  $\text{Pr}=[0.5-2]$  and  $L/\delta=[11-42]$  [74].

$\text{Ra}$	$C$	$n$	$m$
$< 2000$	1	0	0
$6000 - 2 \times 10^5$	0.197	1/4	-1/9
$2 \times 10^5 - 1.1 \times 10^7$	0.073	1/3	-1/9

horizontal configuration discussed above (see Sec. 5.7.2). There are 17 cases in the range  $1 < \text{Ra} < 10^{14}$ . The distance between the walls,  $\delta$ , varies between 2 mm and 20 m. The right (cold) wall is held fixed at 20 °C and the left wall varies from 30 °C to 230 °C.

Three different grid resolutions are tested for the Cartesian cases:  $\delta/\delta x = [8, 16, 32]$ . The resolution is uniform with  $\delta x = \delta y = \delta z$ . The length (vertical dimension) and depth (spanwise dimension) of the plates are  $16\delta$  and  $4\delta$ , respectively. The boundary conditions in the  $y$  and  $z$  directions are homogeneous Neumann (MIRROR or “insulated”). The average heat flux on each wall is monitored and the simulation is run until a clear stationary state is reached. The results are presented below in Fig. 5.12 (left).

For the complex geometry cases, the grid and gravity vector are rotated by 18 degrees. A hollow cavity is formed using the GEOM namelist format with a hot surface on the left and a cold surface on the right and insulated side walls. Two grid resolutions are tested:  $\delta/\delta z = [8, 16]$ . The results are shown in Fig. 5.12 (right).

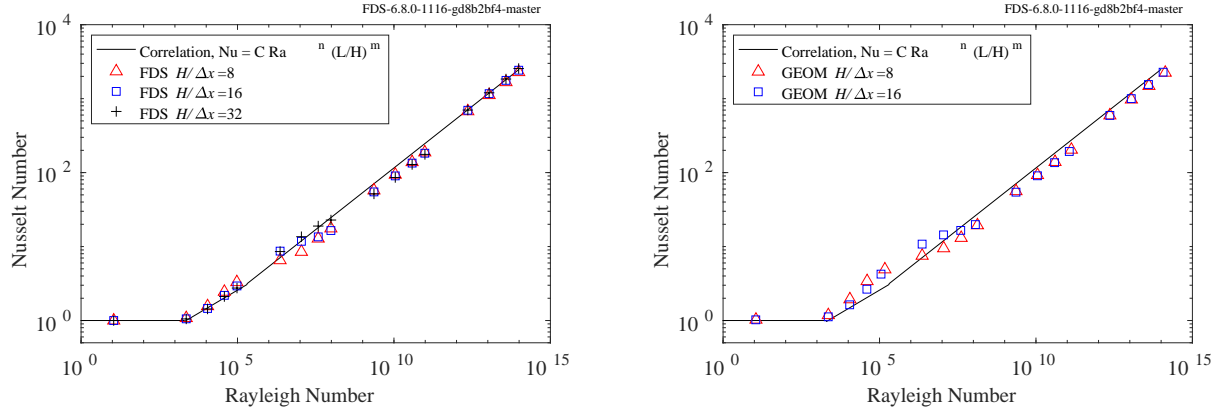


Figure 5.12: FDS results for Nusselt number in natural convection within a vertical enclosure—(left) Cartesian geometry; (right) cutcell geometry.

### 5.7.4 Sphere (`free_conv_sphere`)

Consider a heated sphere in the range  $1 < \text{Ra} < 10^9$ . Yuge [78] and Amato and Tien [79] propose the following Nusselt number correlations for natural convection from a sphere [74].

$$\text{Nu} = \begin{cases} 2 + 0.43 \text{Ra}^{1/4} & 1 < \text{Ra} < 10^5 \\ 2 + 0.50 \text{Ra}^{1/4} & 3 \times 10^5 < \text{Ra} < 8 \times 10^8 \end{cases} \quad (5.24)$$

The sphere is generated using the GEOM namelist with three levels. The surface temperature is uniform and constant at 30 °C. The Rayleigh number is changed by adjusting the diameter of the sphere from 1 mm to 1 m. Fluid properties are the same as above. The convective heat flux is integrated over the surface of the sphere. All external boundaries are OPEN and the grid resolution is uniform. Results are presented in Fig. 5.13 for two grid resolutions corresponding to  $D/\delta x = [8, 16]$ .

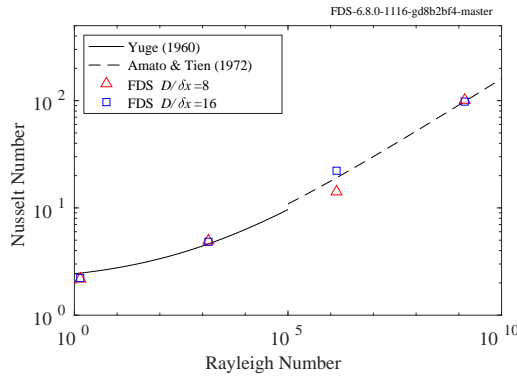


Figure 5.13: FDS results for free convection from a sphere.

## 5.8 Impinging Jet (`impinging_jet`)

Impinging jet flow poses a challenge for convective heat transfer models because the stagnation velocity goes to zero numerically near the mean stagnation point and hence the computed Reynolds number is fictitiously low leading to an under-prediction of the local heat transfer coefficient. To handle this problem, the user may specify a special impinging jet heat transfer model, as discussed in the FDS User Guide [2], which basically uses the forced convection correlation but with a velocity scale obtained from the stagnation pressure, following Huang [80, 81]. In this section, we present results from a series of cases designed to confirm the general trend that the highest heat transfer coefficient is found at the stagnation point. There is no analytical solution to this case. We take our target correlation to be that of Martin [82, 77]. The default coefficients of the impinging jet model have been tuned to match the Martin correlation for the specific case discussed below at coarse grid resolution.

The set up for the problem is a simple cubic domain 1 m on a side. The lateral boundaries are open. The top boundary is held at a fixed 20 C. A hot jet of air is injected from a 0.2 m by 0.2 m square vent at 100 C. Two Reynolds numbers are considered by changing the inlet flow velocity [10, 40] m/s. Three grid resolutions for each Reynolds number are tested,  $D/\delta x = [7, 14, 28]$ , representing *coarse*, *medium*, and *fine* resolutions. The cases are run for roughly flow through times with statistics collected over the last half of the simulation.

Figure 5.14 shows FDS results for three grid resolutions compared to the correlation in Martin [82, 77]. The plots below in Fig. 5.15 show the profile of Nu along the ceiling.

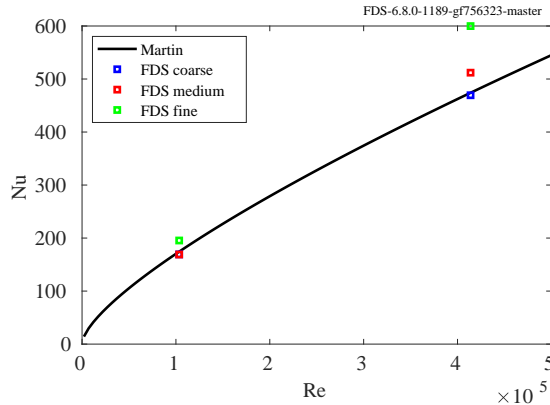


Figure 5.14: Average Nusselt number correlation for a flat plate compared to FDS results using the impinging jet heat transfer model.

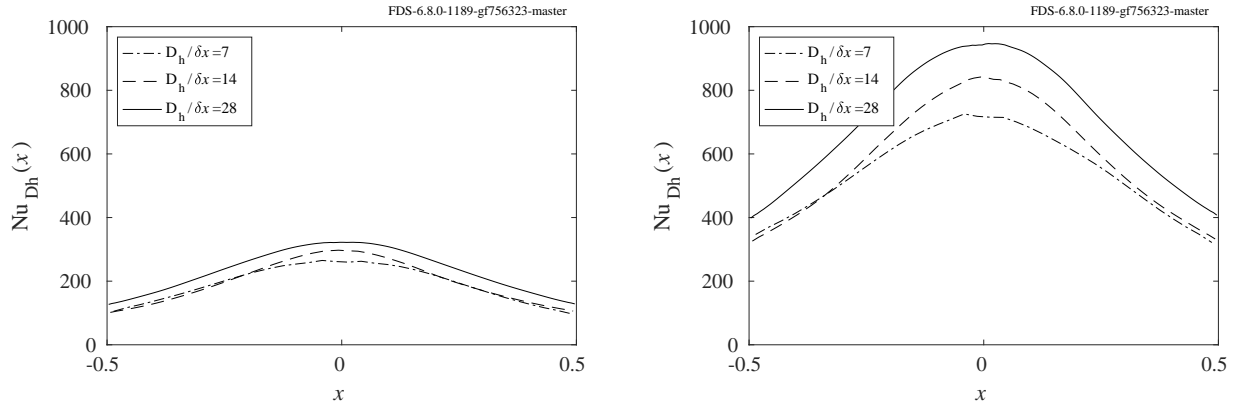


Figure 5.15: Profile of average Nusselt number (Nu) along the ceiling at Reynolds numbers (Re) based on jet diameter of  $1 \times 10^5$  (left) and  $4 \times 10^5$ .

## 5.9 Ribbed Square Duct Flow (`ribbed_channel`)

### 5.9.1 Cartesian Geometry

In this test case, we compare FDS results with particle-image velocimetry (PIV) data from Casara and Arts [83, 84] for flow in a square duct with a ribbed obstruction. This configuration was also studied numerically by [85]. The rib height is  $h = 0.03$  m and the duct height is  $D = 0.1$  m. The distance between ribs in the periodic duct (the ‘‘pitch’’) is  $10h$ . The length of our domain is therefore 0.3 m. The bulk velocity  $U_b$  is 6.2 m/s with ambient air at 20 °C (density is 1.2 kg/m<sup>3</sup> and the dynamic viscosity is  $1.86 \times 10^{-5}$  kg/m/s). The Reynolds number based on  $D$  is nominally 40,000. The streamwise mean pressure drop is adjusted to achieve the desired mean bulk flowrate (see Fig. 5.16). The FDS mesh is uniform in each direction. We test grid resolutions of  $h/\delta x = \{3, 6, 12, 24\}$ .

A side view image of mean velocity vectors in the 3-D flow is shown in Fig. 5.17 for the  $h/\delta x = 12$  case. The goals of this calculation are to predict the flow profile above the ribs and the recirculation patterns on the windward and leeward side of the ribs. To measure the FDS results, a line of devices (represented by the green dots in the figure) is placed near the floor of the duct. A change in sign of the mean  $u$  velocity component indicates a reattachment location. Results for the mean streamwise velocity near the surface are shown in the upper-left plot of Fig. 5.18. The independent axis on the plots ranges from 0 m to 0.3 m, representing the center to center distance between ribs. Note that the image is offset and ranges from -0.125 m to 0.175 m. As can be seen from the plot, the  $h/\delta x = 12$  resolution (green sideways triangles) provides sufficient accuracy of the reattachment length (note that the correspondence with the vectors in the image). Despite the fact that the coarser cases do not perfectly capture the reattachment region, it is remarkable that with  $h/\delta x = 3$  we achieve any recirculation at all. The mean streamwise velocity profile at the rib centerline is shown in the upper-right plot of Fig. 5.18. The finest resolution,  $h/\delta x = 24$ , is sufficient to accurately capture the root-mean-square velocity fluctuations on top of the rib, as can be seen in the bottom-right plot of the figure.

Note that the discrepancy between the model and experimental results for the mean streamwise profile above the rib (Fig. 5.18, upper-right) can be explained by an asymmetry in the PIV data, as can be seen in Figures 11 and 12 of [84]. These results should not be interpreted as spanwise means, they are based on PIV data along the centerline plane.

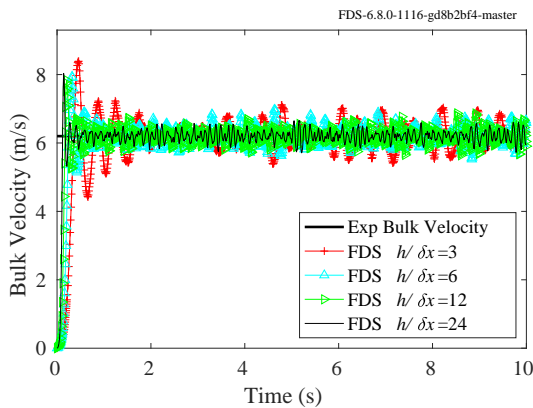


Figure 5.16: Bulk velocity for the ribbed channel cases measured in the duct section in front of the rib compared with the experimental value of 6.2 m/s (thick black line).

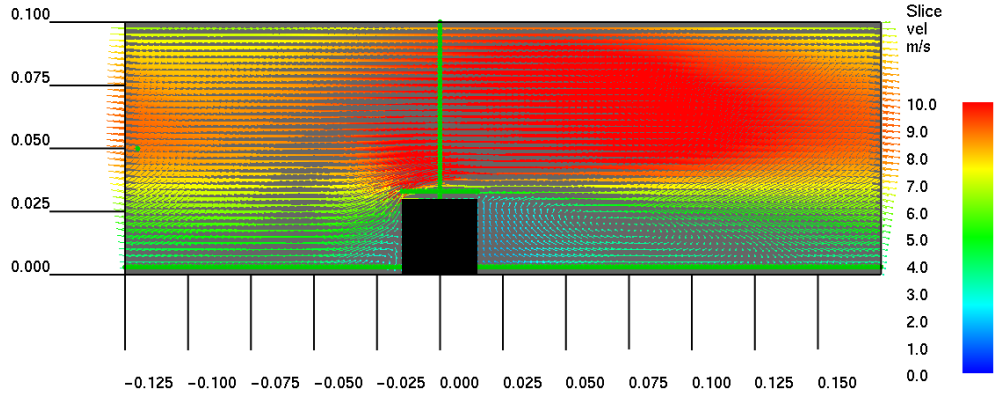


Figure 5.17: Mean velocity vectors colored by velocity magnitude for the ribbed square duct case with  $h/\delta x = 12$ .

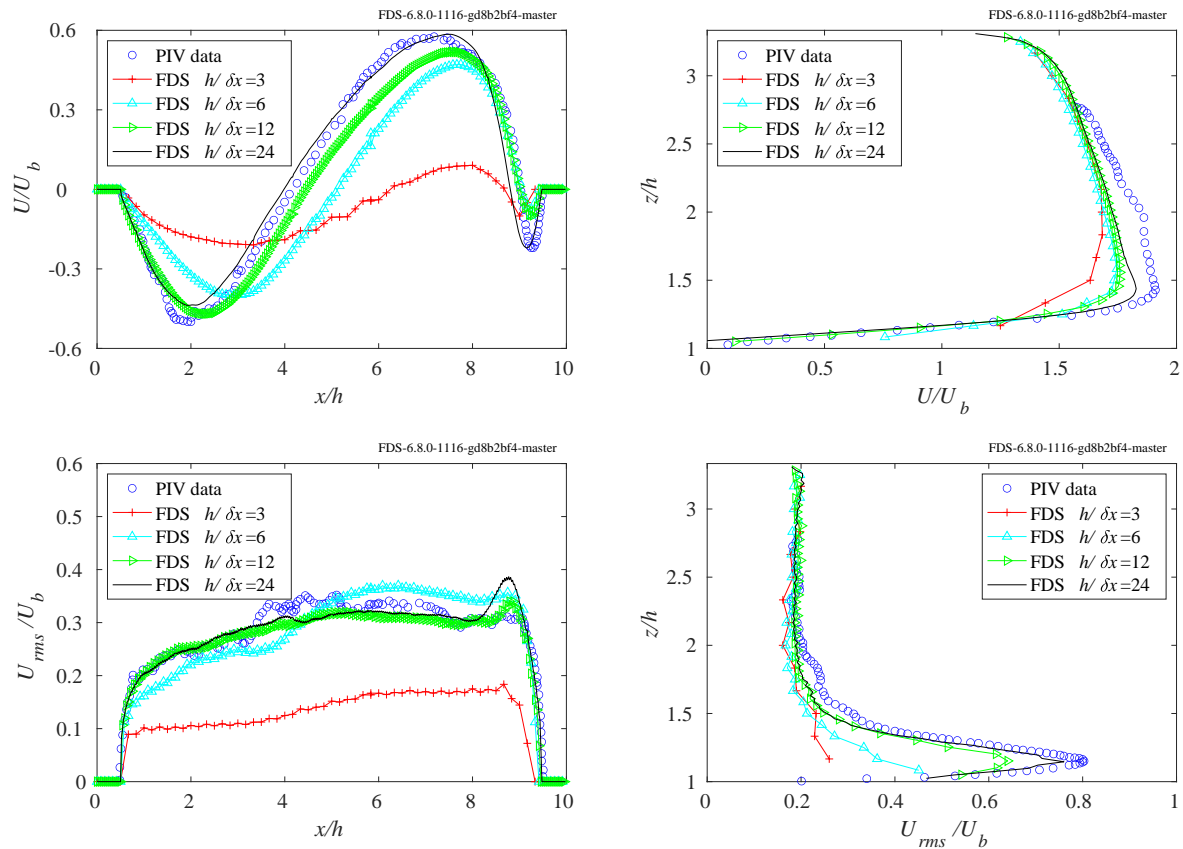


Figure 5.18: Mean and RMS velocity profiles for ribbed square duct flow. Comparison with PIV data from Casara and Arts [83, 84].

## 5.9.2 Complex Geometry

Below we plot the results for the `ribbed_channel_geom` test series. These cases are identical to the Cartesian geometry discussed above, except they use a GEOM line with a grid-aligned XB region to model the square rib. The same mean force vectors are used as in the analogous Cartesian cases.

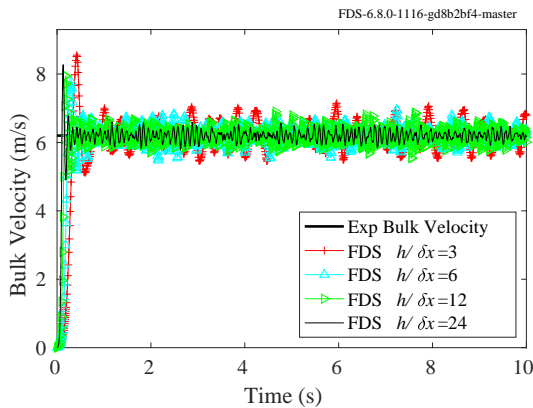


Figure 5.19: Bulk velocity for ribbed channel geom cases measured in the duct section in front of the rib compared with the experimental value of 6.2 m/s.

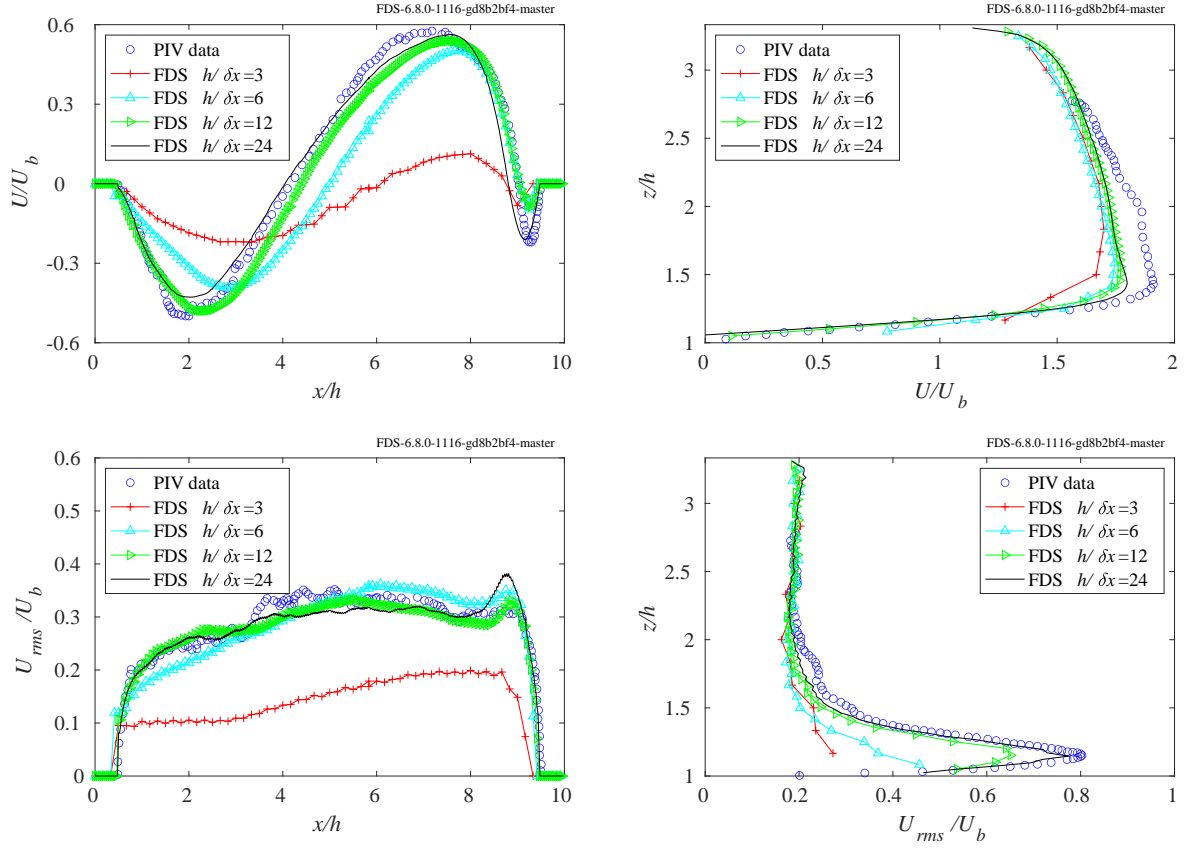


Figure 5.20: Mean and RMS velocity profiles for ribbed square duct flow with complex geometry. Comparison with PIV data from Casara and Arts [83, 84].



# Chapter 6

## Atmospheric Flows

### 6.1 Monin-Obukhov Similarity Profiles (`mo_velocity_profile`)

Atmospheric turbulence is affected by the stability of the boundary layer. A stable layer (cool, heavy air at ground level) will suppress turbulence, while an unstable layer (warm, light air at ground level) will enhance turbulent mixing as buoyant plumes rise. The theory governing these flows, Monin-Obukhov similarity theory, is discussed at some length in the FDS User Guide [2]. Here we examine velocity profiles from a stable boundary layer and an unstable boundary layer. When mean forcing is used for driving the wind field the Monin-Obukhov parameters determine the shape of the mean streamwise velocity profile. These cases use a very tight `DT_MEAN_FORCING_2` of 0.1 s in order to drive the flow field directly to the specified profile, therefore confirming the target profile is being computed correctly in FDS.

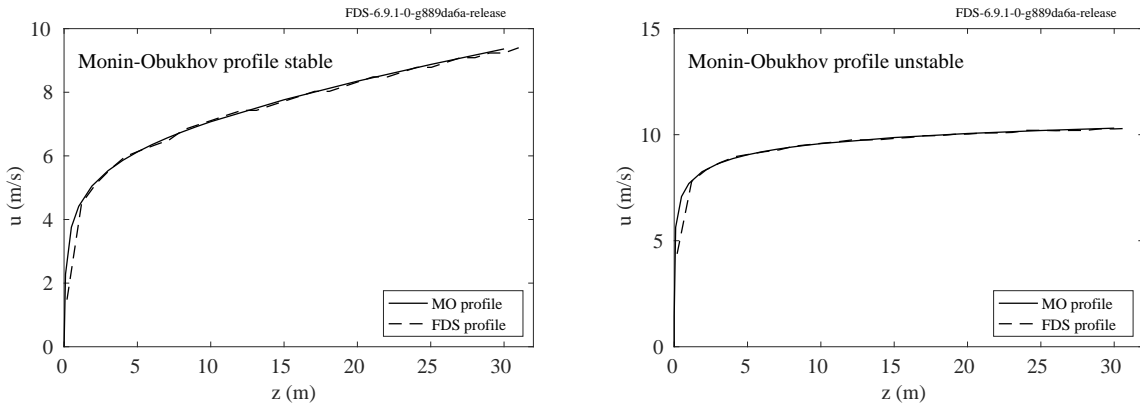


Figure 6.1: Stable (left) and unstable (right) mean streamwise velocity profiles for specified Monin-Obukhov parameters on the `WIND` line.

### 6.2 Ekman Layers (`ekman_`)

In a simple turbulent channel flow, the resulting boundary layer profile results from the balance between the streamwise pressure gradient and the turbulent stresses. In an Ekman layer, the Coriolis force is also part of the balance. With Ekman layers the Coriolis force has the effect of twisting the atmospheric boundary layer—near the surface there is a component of the wind aligned with the pressure gradient, but aloft the

winds tend to be geostrophic, meaning they run parallel to isobars (perpendicular to the pressure gradient). In FDS, input of a geostrophic wind implies a mean pressure gradient in the orthogonal direction (see FDS User Guide [2]).

In atmospheric flows, it is difficult to separate the forces for verification purposes. In this section, we will undertake an admittedly weak form of verification, namely, code-to-code comparison. We compare FDS with the results from Schoenberg [86] where OpenFOAM is modified for atmospheric flows. We use the same domain, grid resolution, and—as closely as possible—initial conditions as Schoenberg. The latitude is specified as 45° north (for specifying the Coriolis force). We use the Deardorff turbulence model with constant turbulent Prandtl number, which differs from Schoenberg, who uses a dynamic turbulent Prandtl number. The main difference in the models is that Schoenberg solves a transport equation for  $k_{sgs}$  whereas FDS uses a simple algebraic closure (see FDS Tech Guide [48]). Further, it was difficult to discern the exact initialization procedure from the Schoenberg report, so there are likely some minor differences that can account for the small discrepancies we see in the FDS results. It should also be noted that the Schoenberg simulations apply a Boussinesq assumption and thus do not account for the pressure stratification term in the energy equation. Hence, to match the Schoenberg results as closely as possible, we have set `STRATIFICATION=F` for FDS, which is counterintuitive for an atmospheric flow. In practice, this should not be done.

Three cases are run: neutral, stable, and unstable boundary layers. The domain size, grid resolution, surface flux condition, and geostrophic wind driving force are presented in Table 6.1 (adapted from [86]). Note that the density and specific heat are specified in the FDS input file such that the surface heat flux in either Km/s or W/m<sup>2</sup> are roughly the same. The boundary conditions are periodic in  $x$  and  $y$  and no flux at the top of the domain. Note that this makes achieving a steady state impossible for the stable and unstable cases. This is another reason why the code comparison is difficult—essentially we are comparing the resulting profiles after approximately 40 hours of real time evolution. Schoenberg uses a spin up process of running the neutral case for up to 30 hours before transitioning to stratification. The surface aerodynamic roughness used by Schoenberg is  $z_0 = 0.1$  m for the unstable and neutral cases and  $z_0 = 0.13$  m for the stable case. This translates to a sand grain roughness of 3.0 m and 3.9 m, respectively, in FDS. Note that the input files for the `ekman_*` series are stored with the validation suite (see `fds/Validation/Schoenberg_Ekman_Layers/`), since the cases use 16 processors and take a few hours to complete.

The differences seen in the stable case may be attributed to (i) the use of a dynamic turbulent Prandtl number by Schoenberg and (ii) FDS not making the Boussinesq approximation. It may be noted that the winds aloft in the FDS run match the specified geostrophic wind  $U_g = 7$  m/s for the stable case.

Table 6.1: Schoenberg Ekman Layer parameters.

Case	Domain Size $x \times y \times z$ (m)	$N_x \times N_y \times N_z$	Surface Heat Flux (W/m <sup>2</sup> )	$U_g$ (m/s)
Neutral	$4000 \times 2000 \times 1500$	$40 \times 40 \times 40$	0	10
Stable	$2000 \times 1000 \times 750$	$40 \times 40 \times 40$	-0.00502	7
Unstable	$4000 \times 2000 \times 1500$	$40 \times 40 \times 40$	0.02008	15

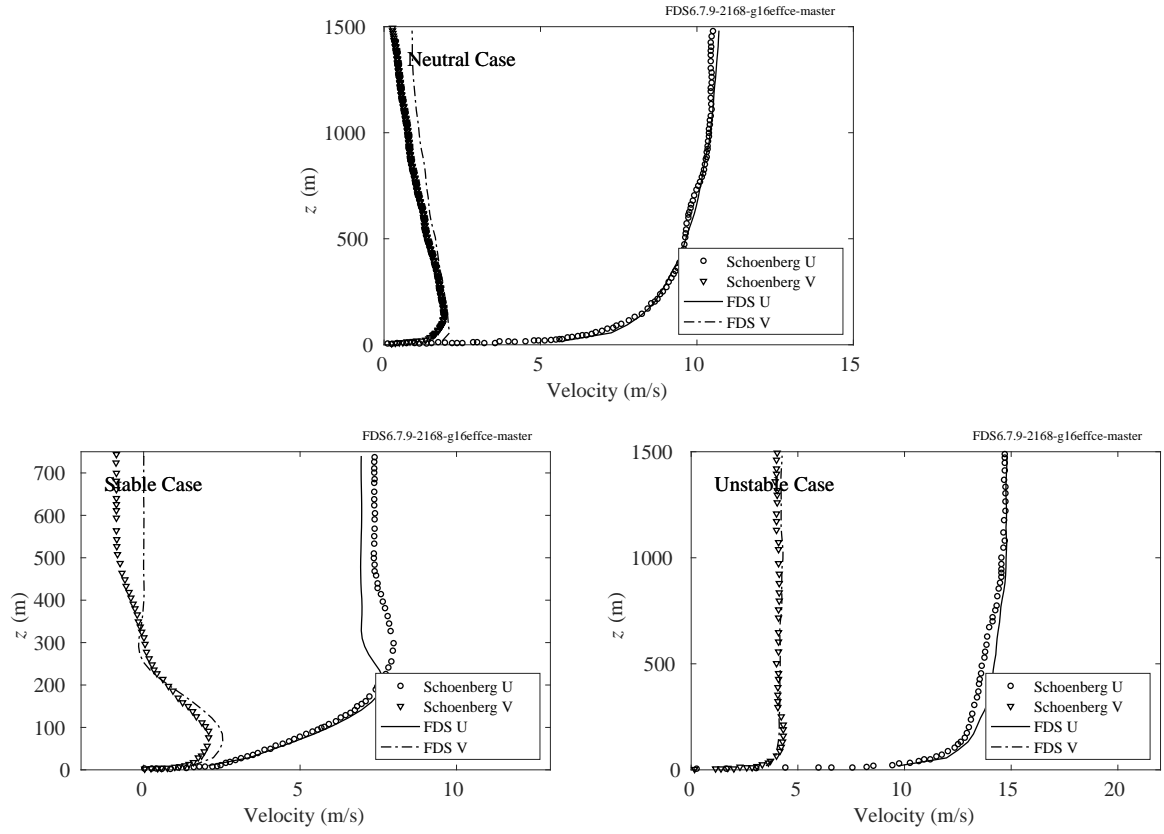


Figure 6.2: Comparison Ekman layer profiles for neutral (top), stable (bottom-left), and unstable (bottom-right) atmospheric boundary layers with the simulation results of Schoenberg [86].



# Chapter 7

## Mass and Energy Conservation

### 7.1 Mass Conservation

This section describes tests of global mass conservation.

#### 7.1.1 Flow of a Gas through a Simple Duct (`simple_duct`)

In this example, a closed chamber with a simple recirculating duct is used to demonstrate that a gas such as carbon dioxide can be transported through multiple meshes and its mass is conserved. An obstruction is created that leaks 0.5 kg of CO<sub>2</sub> over a time span of 10 s.

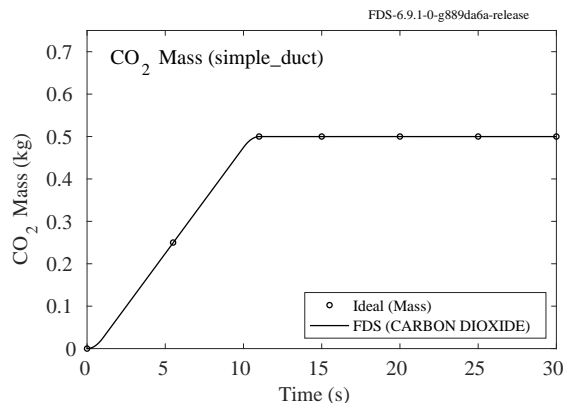


Figure 7.1: The mass of CO<sub>2</sub> contained in a simple room connected with a recirculating duct.

#### 7.1.2 Species Mass Flux (`species_conservation`)

A specified species mass flux is a commonly used boundary condition, in particular when specifying a fire. The specified heat release rate per unit area is divided by the heat of combustion, resulting in a specified fuel mass flux,  $\dot{m}_\alpha''$ , at the surface:

$$\dot{m}_\alpha'' = \rho Y_\alpha u_n - \rho D_\alpha \frac{\partial Y_\alpha}{\partial n} \quad (7.1)$$

where  $u_n$  is the face normal mass-average velocity and  $\partial/\partial n$  is the gradient normal to the face. The velocity is determined from the total mass flux and the density at the face,

$$u_n = \frac{\sum_{\alpha} \dot{m}_{\alpha}''}{\rho(\mathbf{Y}, T)} \quad (7.2)$$

The density is computed using old values of the face mass fractions and the face temperature which may be specified or computed depending on choices made by the user. The new face mass fraction is then set to satisfy (7.1). The test cases below are designed to exercise contributions from both the advective and diffusive terms in this boundary condition.

### **Case 1: Low Flux, Hot Gas Injection**

Propane is injected into a 4 m cube with 1 m<sup>2</sup> vents on all six faces. The mass flux is 0.0001 kg/(m<sup>2</sup>·s) and the surface temperature is 500 °C. The box is initially filled with air at standard conditions. The accumulation of propane in the box is shown in Fig. 7.2.

### **Case 2: Air Injection into a Pressurized Compartment**

Air is injected into one of two cubic chambers separated by a solid partition. The mass flux of air is 1 kg/(m<sup>2</sup>·s) through a vent that is 0.04 m<sup>2</sup> in area. After 25 s, the mass of air introduced should be 1 kg. The accumulation of air in the chamber is shown in Fig. 7.2.

### **Case 3: Gases Released by Solid Phase Reactions within a Solid Obstruction**

A 0.2 m solid cube undergoes a reaction that releases four different gases into a sealed unit cube. The solid has a density of 100 kg/m<sup>3</sup>. The inert gases have different yields, all summing to one, meaning that the solid cube ought to be vaporized creating a total mass of 0.8 kg. The accumulation of all the gases in the chamber is shown in Fig. 7.2. Note that in this case, when the solid cube vaporizes, its volume is filled with the background species, nitrogen. The total mass of the newly created nitrogen is 0.0093 kg.

### **Case 4: Gases Released by Solid Phase Reactions at the Boundary of the Domain**

This case is similar to Case 3. A 0.2 m by 0.2 m solid surface undergoes a reaction that releases four different gases into a sealed unit cube. The solid has a density of 100 kg/m<sup>3</sup> and thickness of 0.1 m. The inert gases have different yields, all summing to one, meaning that the solid surface ought to be vaporized creating a total mass of 0.4 kg. The accumulation of all the gases in the chamber is shown in Fig. 7.2.

#### **7.1.3 Mass Flux through Domain Boundaries (`mass_flux_wall`)**

This set of tests considers a specified mass injection of water vapor from a VENT on the floor of a compartment. The entire top of the compartment is OPEN to the ambient. The lighter water vapors are buoyant, so they rise creating a turbulent flow into and out of the domain. Therefore, the input is steady, while the outflow of water vapor is quite chaotic. To judge whether a proper mass balance is achieved by FDS we must monitor not only the inflow and outflow, but also the total mass of water vapor in the domain at a given time. Therefore, we add DEVC of quantity MASS\_FLUX\_WALL and STATISTICS='SURFACE INTEGRAL' for inflow and outflow, and we also add MASS\_FILE=.TRUE. to the DUMP line to monitor the total water vapor at any point in time in the domain. With  $\rho$  and  $Y_{H_2O}$  denoting the local mass density and mass fraction

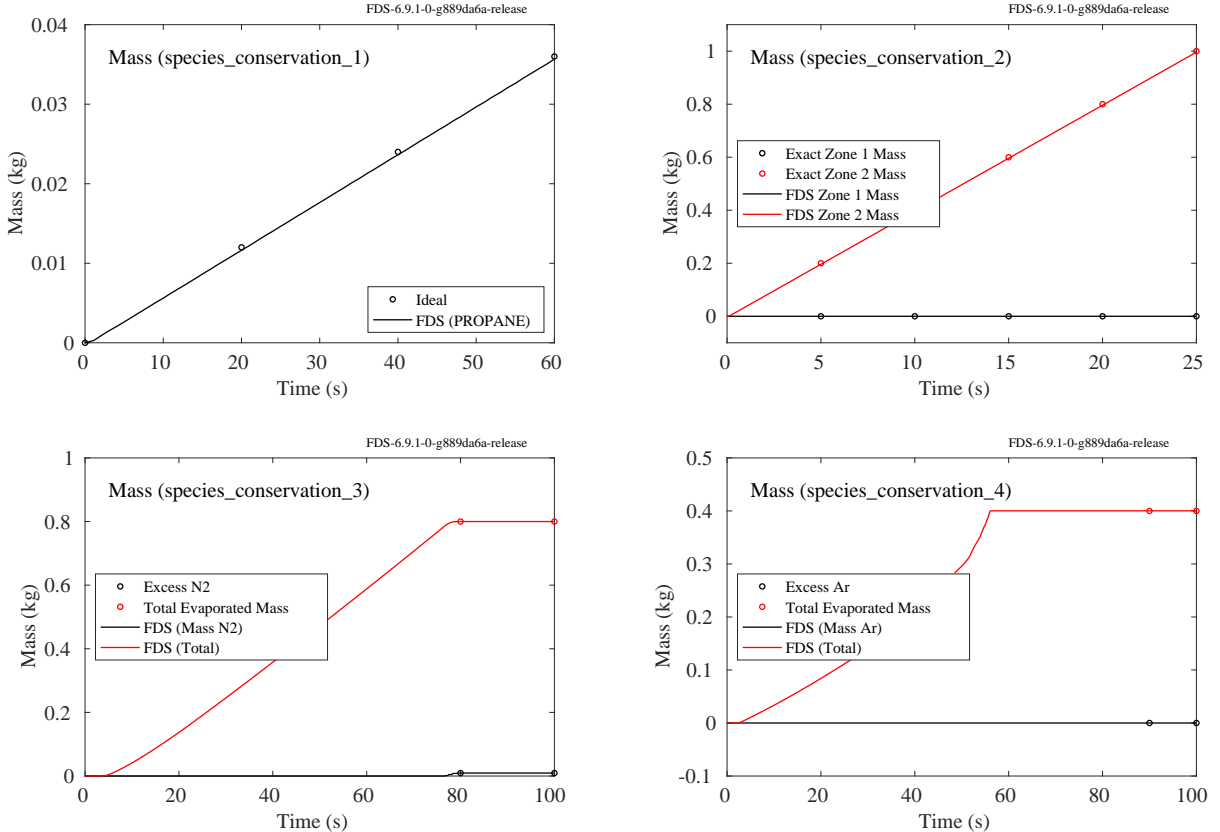


Figure 7.2: Results of the `species_conservation` test cases. Case 1: Hot gas is injected at a very low flow rate into a 4 m cube. Case 2: Air is injected into one side of a partitioned compartment. Case 3: A solid cube vaporizes yielding four gases whose total mass is 0.8 kg. A small amount of nitrogen is created to fill the void left by the vaporized solid cube. Case 4: A patch of solid surface reacts to form four gases whose total mass is 0.4 kg.

of water vapor in a cell, and with  $\dot{m}_{\text{H}_2\text{O}}''$  denoting the flux of water vapor at a cell face on the domain boundary, the mass balance may be written as,

$$\frac{d}{dt} \left( \int_V \rho Y_{\text{H}_2\text{O}} dV \right) + \int_{S_{\text{out}}} \dot{m}_{\text{H}_2\text{O}}'' dS - \int_{S_{\text{in}}} \dot{m}_{\text{H}_2\text{O}}'' dS = 0 \quad (7.3)$$

Figure 7.3 shows the results of two cases that test the mass balance of water vapor in the domain just described. The plot on the left tests lumped species balance. In this case, the background humidity is set to zero and so the only water vapor in the domain is that of the tracked species injected at the bottom boundary. In the second test case on the right we are showing the balance for the primitive species water vapor. In this test, the background humidity is the default (40 %) and so the output device must sum the water vapor contribution from the background air and the tracked species injected at the bottom. In each plot, the blue and red lines show the inflow (blue, steady) and outflow (red, turbulent) as well as the balance from Eq. 7.3 formed from the mass and devices files. The balance (yellow line) fluctuates slightly around zero because of a first-order time error in reporting the boundary fluxes. That is, within the actual simulation the mass transport equation is updated using a second-order Runge-Kutta scheme, whereas at the time the output routine is called the code does not have the machinery to perfectly reconstruct the second-order flux terms.

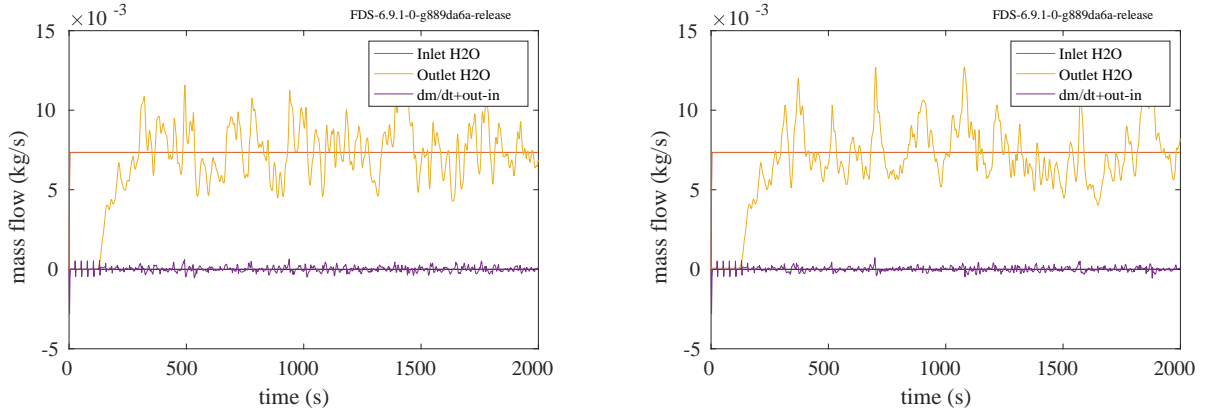


Figure 7.3: Results of the `mass_flux_wall` test cases. (Left) Lumped species balance, (Right) primitive species balance.

#### 7.1.4 Mass Balance on a Gas Control Volume (`mass_balance_gas_volume`)

Using the same computational setup as the `mass_flux_wall` series above, the `mass_balance_gas_volume` test case defines a control volume (CV) internal to the computational domain, 6 m on a side (from 2 m to 8 m in each direction). The mass of water in the CV is output using a `SPATIAL_STATISTIC= 'VOLUME INTEGRAL'` with `QUANTITY= 'DENSITY'` of the lumped species for water and the flows into and out of the CV are obtained using `QUANTITY= 'TOTAL MASS FLUX X'`, etc., with `SPATIAL_STATISTIC= 'AREA INTEGRAL'`. Figure 7.4 shows the resulting balance of accumulation ( $dm/dt$ ) and the inflow and outflow of the control volume.

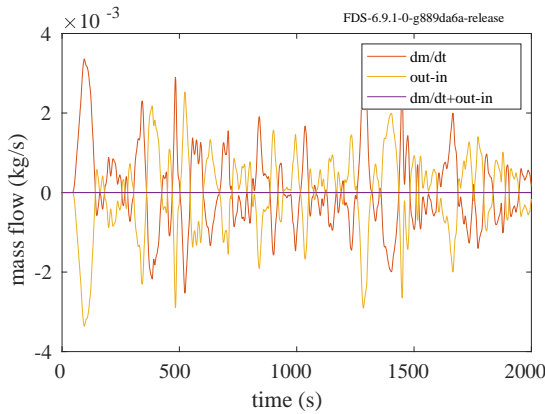


Figure 7.4: Results of the `mass_balance_gas_volume` test case showing the balance between mass accumulation ( $dm/dt$ ) and the flow in and out of the control volume.

#### 7.1.5 Mass Balance for Species in a Reacting Flow (`mass_balance_reac`)

A  $0.25 \text{ m}^2$  propane burner ramps up to 500 kW linearly in 10 s and holds this heat release rate for another 10 s. Using a mass file, appropriate wall flux devices with surface integrals, and reaction source term devices with volume integrals, we perform a detailed mass balance on all the primitive species in the reaction. The results are presented in Fig. 7.5. The mass balance can be understood through the mnemonic, “Accumula-

tion equals In minus Out plus Generation". For each species, we plot the "accumulation" term (first-order numerical differentiation of the columns in the `MASS_FILE`, which are volume integrated over the domain), the "in-out" term (surface integral of the mass fluxes over the domain boundaries), the "generation" term (volume integral of the reaction source term over the domain), and the sum of these as the "balance" (the balance should be zero).

### 7.1.6 Checking the Equation of State (`particle_offgas`)

The "particle offgas" cases include 100 randomly distributed Lagrangian particles that inject different gas species into an open domain initially filled with air. The aim of these cases is to test whether the gas temperature is maintained at ambient (20 °C) in the gas injection cases, and whether the minimum temperature remains at ambient in the cases where fuel is injected and burned.

#### Case 1: Lagrangian Particles Blowing Air

In this case, each particle injects air into the domain, and air is the background species. The temperature is not expected to rise above or drop below ambient, as shown in the upper left of Fig. 7.6.

#### Case 2: Lagrangian Particles Blowing Carbon Dioxide

In this case, each particle injects CO<sub>2</sub> into the domain, and air is the background species. The temperature is not expected to rise above or drop below ambient, as shown in the upper right of Fig. 7.6.

#### Case 3: Lagrangian Particles Blowing Propane that Combusts

In this case, each particle injects propane into the domain, and air is the background species. Combustion is expected, but the gas temperature is not expected to drop below ambient, as shown in the lower left of Fig. 7.6.

#### Case 4: A Small Solid Obstruction Blowing Propane that Combusts

In this case, the particles are replaced by a small, solid block blowing propane. Combustion is expected, but the gas temperature is not expected to drop below ambient, as shown in the lower right of Fig. 7.6.

### 7.1.7 Realizability of Species Mass Fractions (`realizable_mass_fractions`)

In order for species mass fractions to be physically realizable they must all be positive (semi-definite) and sum to unity,  $Y_\alpha \geq 0$  and  $\sum_\alpha Y_\alpha = 1$ . In this test case, a simple methane burner is used to test the realizability of mass fractions. A device is placed near the base of the center of the flame to measure the local mass fractions. In Fig. 7.7 we plot the time history of the mass fractions for Fuel, Air, and Products along with the sum (dashed line). This sum should remain perfectly one at all times.

### 7.1.8 Integral Mass Test for Complex Geometry (`geom_mass_file_test`)

A 1 m<sup>3</sup> box contains AIR at ambient conditions and has a sphere of radius 0.5 m leaving a volume of 0.4764 m<sup>3</sup>. The FDS `MASS_FILE` output is tested to ensure the correct cut cell volumes are being computed and the primitive species for AIR are correctly output. The results are shown below in Fig. 7.8.

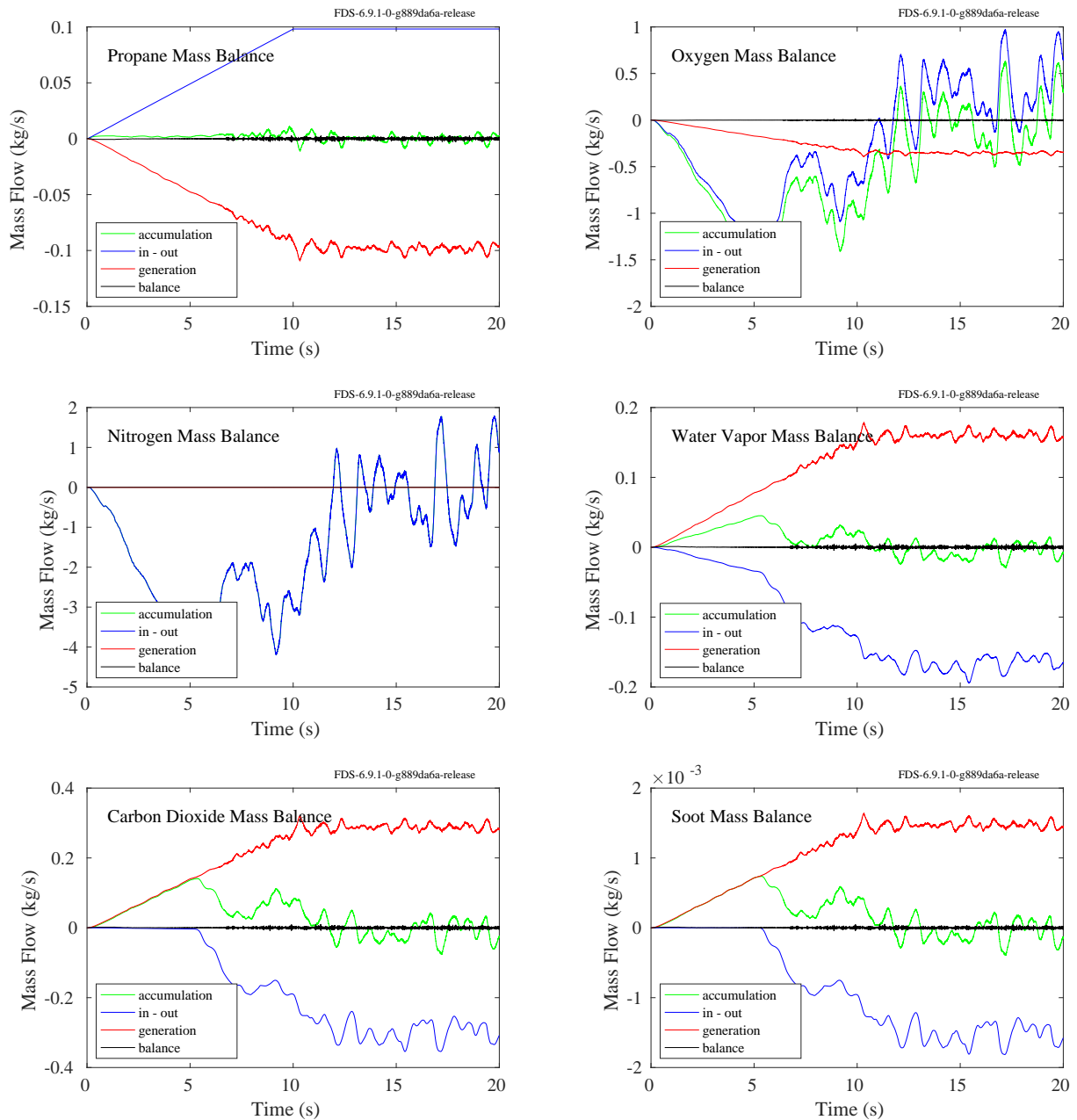


Figure 7.5: Results of the `mass_balance_reac` test case.

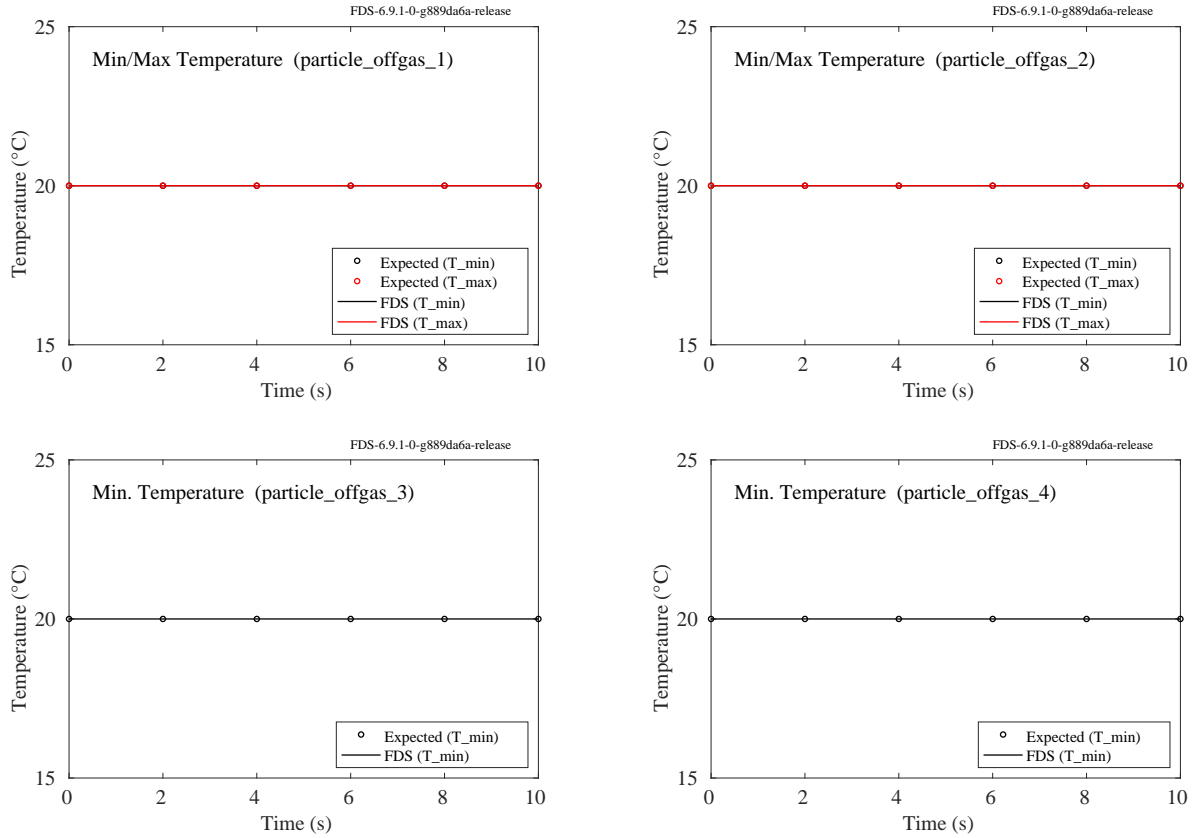


Figure 7.6: Results of the `particle_offgas` test cases. Upper left, Case 1: minimum and maximum temperature when air only is injected. Upper right, Case 2: min/max temperature when carbon dioxide is injected into air. Lower left, Case 3: minimum temperature when propane gas is injected and burned. Lower right, Case 4: minimum temperature when propane gas is injected from a solid block and burned.

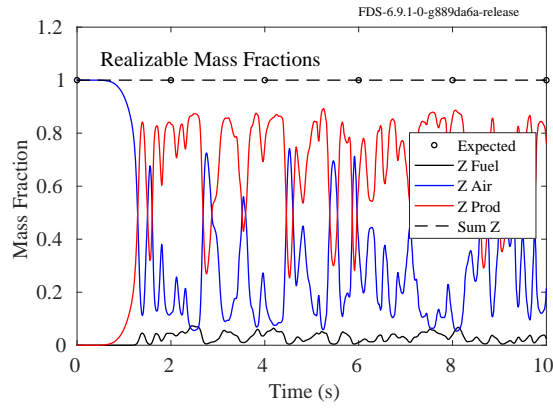


Figure 7.7: Results of the `realizable_mass_fractions` test case. The sum of the mass fractions (dashed line) should remain perfectly one at all times.

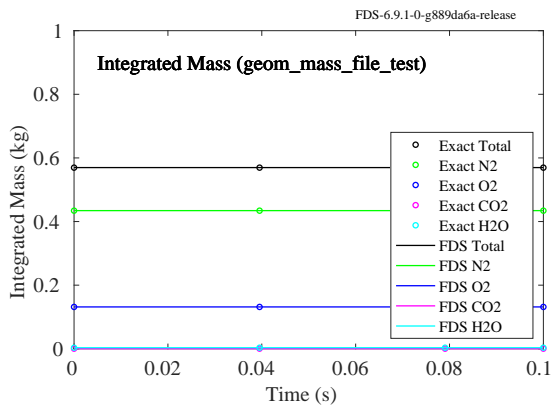


Figure 7.8: Results of the `geom_mass_file_test` test case.

## 7.2 Energy Conservation

FDS does not explicitly solve the energy conservation equation. Instead, mass transport equations are solved for the  $n$  independent gas species. The density is found from summing the individual gas species densities,  $\rho = \sum_{\alpha} \rho_{\alpha}$ . Source terms from the energy equation are incorporated in the velocity divergence,  $\nabla \cdot \mathbf{u}$ , which is factored out of the sensible enthalpy transport equation, i.e.,

$$\nabla \cdot \mathbf{u} = \frac{1}{\rho h_s} \left[ \frac{D}{Dt} (\bar{p} - \rho h_s) + \dot{q}''' + \nabla \cdot (k \nabla T) - \nabla \cdot \sum_{\alpha} h_{s,\alpha} \mathbf{J}_{\alpha} - \nabla \cdot \dot{\mathbf{q}}_r'' + \dot{q}_b''' \right]. \quad (7.4)$$

Here  $\rho$  is the mass density,  $h_s$  is the sensible enthalpy,  $\bar{p}$  is the thermodynamic pressure,  $\dot{q}'''$  is the chemical heat release,  $k$  is thermal conductivity,  $\mathbf{J}_{\alpha}$  is the diffusion flux vector,  $\dot{\mathbf{q}}_r''$  is the radiant heat flux vector, and  $\dot{q}_b'''$  is the bulk heat source due to convective heat transfer to Lagrangian particles and the heat associated with mass sources. The divergence is a fairly complicated expression, and it is important that it is computed properly to ensure global energy conservation. The examples in this section check that mass and energy are conserved for relatively simple configurations.

### 7.2.1 The Heat from a Fire (`energy_budget`)

For the purpose of verifying that the basic FDS algorithm is energy conserving, it is useful to think of a single compartment as a control volume into which energy is generated by a fire and out of which energy either flows via openings or is conducted through the walls. If the fire's heat release rate (HRR) is steady, eventually the system will reach a quasi-steady state (in an LES calculation, there is never a true "steady state"). Two simple cases, called `energy_budget_adibatic_walls` and `energy_budget_cold_walls`, illustrate that in the quasi-steady state, the energy generated by the fire is conserved. For the case with adiabatic walls, a 1200 kW fire is simulated within a compartment that is 10 m by 10 m by 5 m tall. There is a single door and a single horizontal vent in the ceiling. The walls are assumed to be adiabatic; that is, there is no net heat flux through them. Another way to look at it is that the walls are perfect insulators. To simplify the case even further, the radiation transport algorithm is turned off. It is expected that in this case 1200 kW ought to flow out of the compartment either via the door or ceiling vent. The plot in Fig. 7.9 shows both the HRR and enthalpy flow out of the compartment converging to 1200 kW. During the warm up phase, the enthalpy flow is less than the HRR because energy is consumed heating up the air within the room.

Next, the same compartment with the same fire is now assumed to have cold (20 °C) walls, and the radiation is switched back on. After a few minutes of simulation, the net enthalpy outflow is approximately 470 kW and the heat losses to the wall (both radiative and convective) are approximately 730 kW, summing to 1200 kW, the HRR of the fire. Fig. 7.10 displays the HRR, the sum of the losses (radiation, convection, conduction, species diffusion), and the net enthalpy change in the compartment. Note that energy losses are expressed as negative quantities. In steady state, the enthalpy added to the compartment by the fire is offset by losses to the walls and opening.

### 7.2.2 Gas Injection via an Isentropic Process (`isentropic`)

This example checks that if nitrogen is added to a sealed compartment with adiabatic (i.e., no heat loss) walls, that the density, pressure and temperature ought to rise according to the ideal gas law for an isentropic process:

$$\frac{p_2}{p_1} = \left( \frac{\rho_2}{\rho_1} \right)^{\gamma} = \left( \frac{T_2}{T_1} \right)^{\frac{\gamma}{\gamma-1}} \quad (7.5)$$

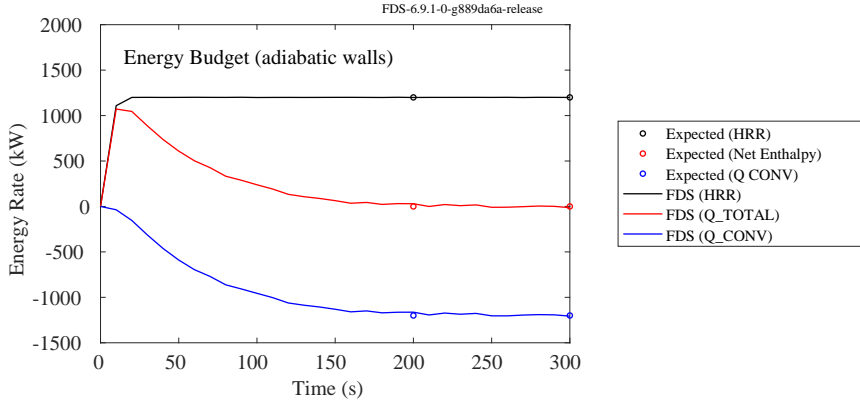


Figure 7.9: The energy budget for a simple compartment fire with adiabatic walls.

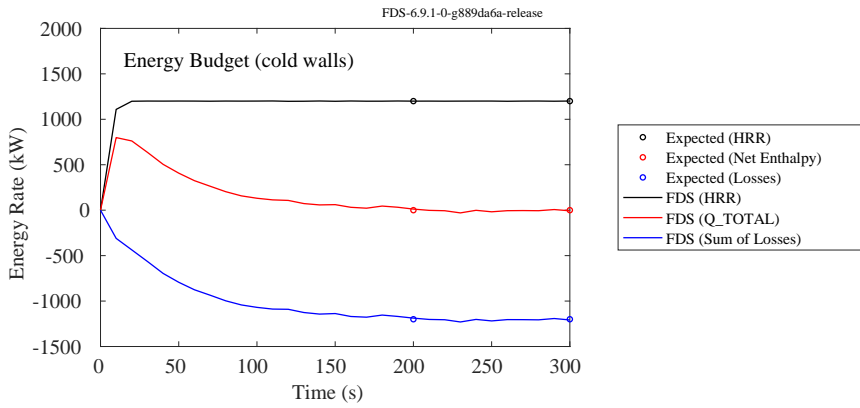


Figure 7.10: The energy budget for a simple compartment fire with cold walls.

The subscripts 2 and 1 refer to the final and initial state, respectively. Nitrogen is a diatomic gas for which  $\gamma = 1.4$ . As an additional check, the nitrogen is injected at two different rates such that in Case A the injection occurs in 10 s and in Case B the injection occurs in 50 s. The nitrogen is introduced into the domain via small spheres that do not generate or absorb heat. They do not occupy volume either. They just inject the nitrogen at a specified rate into the particular grid cell that each occupies. Results are plotted in Fig. 7.11.

### 7.2.3 Gas Injection via a Non-Isentropic Process (`isentropic2`)

This example checks that if a given mass of nitrogen is added via an external vent to a sealed compartment with adiabatic (i.e., no heat loss) walls, that the density, pressure and temperature ought to rise to the same values regardless of the duration of the injection time. The results are plotted in Fig. 7.12. In the two cases, 0.2 kg of N<sub>2</sub> are added to a compartment that is 1 m<sup>3</sup> in volume. In the first case, the injection occurs in 10 s, in the second case in 50 s. The temperature of the gas in both cases is 500 °C. It is expected that the pressure,  $p$ , should rise at the rate:

$$\frac{dp}{dt} = \frac{\gamma p u A}{V} \quad (7.6)$$

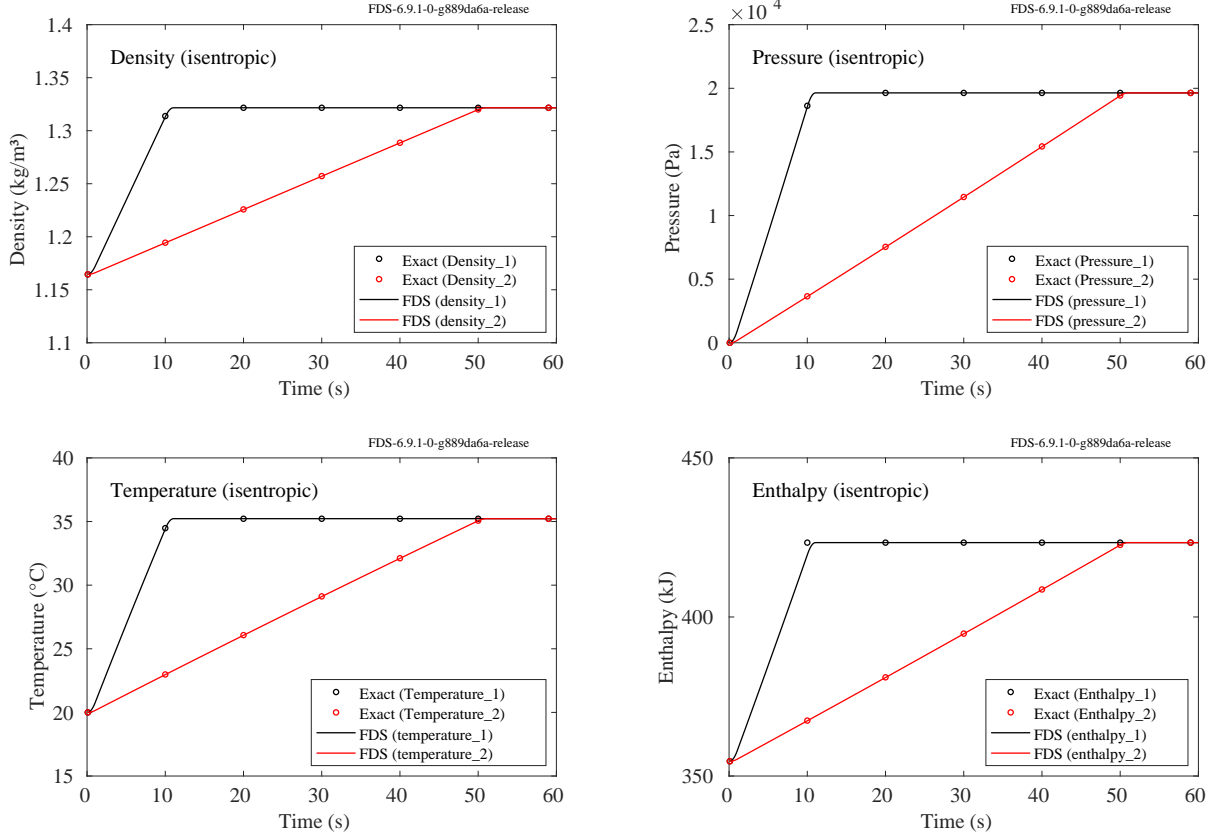


Figure 7.11: Density, pressure, temperature, and enthalpy rise due to the injection of nitrogen into a sealed compartment.

where  $u$  is the injection velocity and  $A$  is the area of the vent,  $0.04 \text{ m}^2$ . The density of the incoming  $\text{N}_2$  is found from the equation of state:

$$\rho = \frac{\bar{W} p}{R T} \quad (7.7)$$

The injection velocity is the mass flux divided by the density,  $u = \dot{m}''/\rho$ , in which case, the pressure rise can be written

$$\frac{dp}{dt} = \frac{\gamma \dot{m}'' R T A}{\bar{W} V} \quad (7.8)$$

Note that the rate of pressure rise is constant. In both the fast and slow injection cases, the pressure is expected to rise 64,253 Pa above ambient. The density and temperature rise are also linear. The density increases from  $1.165 \text{ kg/m}^3$  to  $1.365 \text{ kg/m}^3$ . The temperature increases from  $20^\circ\text{C}$  to  $35.7^\circ\text{C}$ . The change in the internal energy of the system, based on the mass and temperature of the added  $\text{N}_2$ , is:

$$\Delta E = (0.2 \text{ kg}) \times (1.039 \text{ kJ/(kg K)}) \times (773.15 \text{ K}) = 160.6 \text{ kJ} \quad (7.9)$$

Adding in the work due to the pressure yields the change in total enthalpy:

$$\Delta H = \Delta E + V \Delta P = 160.6 \text{ kJ} + (1 \text{ m}^3) \times (64.3 \text{ kJ/m}^3) = 224.9 \text{ kJ} \quad (7.10)$$

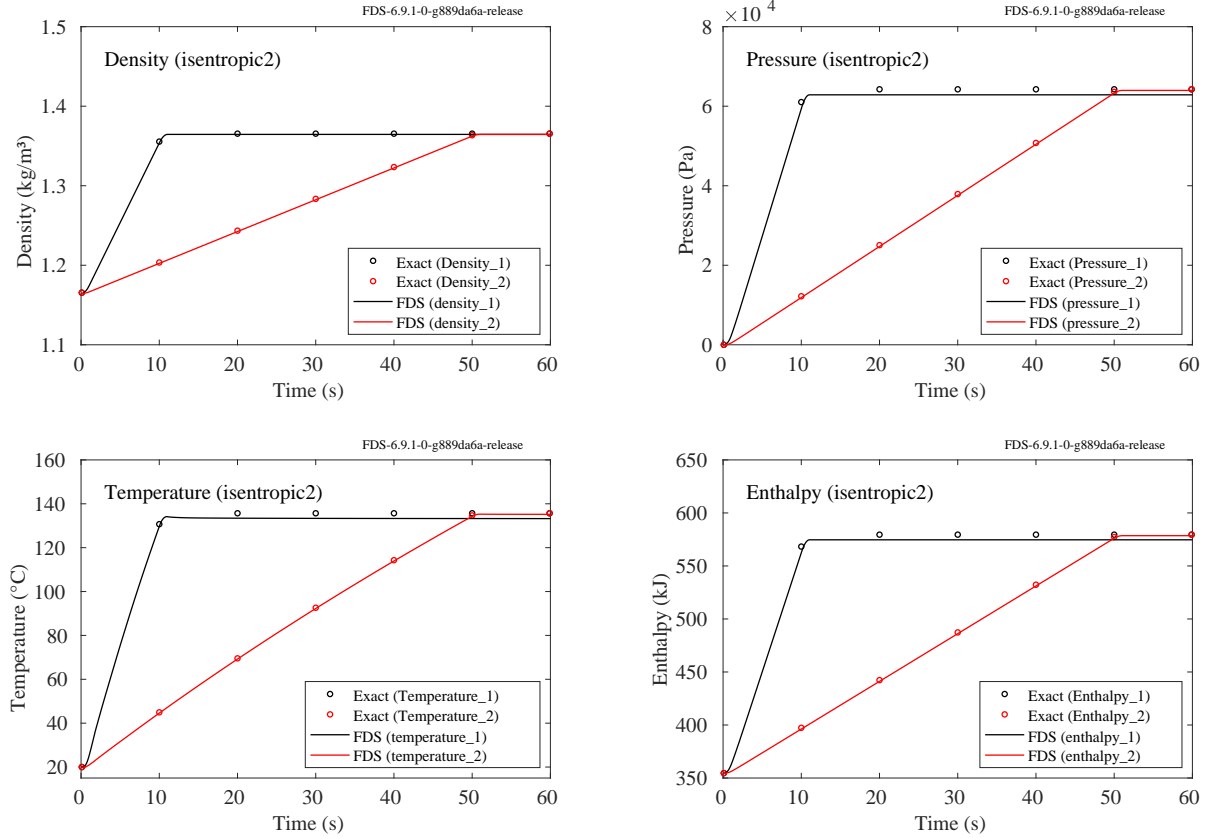


Figure 7.12: Density, pressure, temperature, and enthalpy rise due to the injection of nitrogen into a sealed compartment.

### 7.2.4 Mixing Gases (`energy_budget_dns`)

In this example, two fictitious gases are forced through tiny ducts (1 mm by 1 mm) that meet at a T-joint. The cross sectional areas of all the ducts are the same. Gas 1 has an initial temperature of  $606.3\text{ }^\circ\text{C}$  and a constant specific heat of  $1\text{ kJ/(kg K)}$ . Gas 2 has an initial temperature of  $20\text{ }^\circ\text{C}$  and a constant specific heat of  $10\text{ kJ/(kg K)}$ . Both gases have a molecular weight of 29 g/mol and a mass flow of  $1 \times 10^{-8}\text{ kg/s}$ . Typically gases of the same molecular weight have comparable, but not necessarily the same, specific heats. This is an extreme case. In steady state, it is expected that the convection and diffusion of enthalpy at the boundaries will be equal:

$$\int h_s \rho \mathbf{u} \cdot d\mathbf{S} = \sum_{\alpha} \int h_{s,\alpha} \rho D_{\alpha} \nabla Z_{\alpha} \cdot d\mathbf{S} \quad (7.11)$$

where  $Z_{\alpha}$  is the mass fraction of species  $\alpha$ . Because of the large difference in specific heats, the average velocity of the gas mixture flowing out,  $U_3$ , is not simply the sum of the velocities at the two inlets,  $U_1 + U_2$ . In fact, in order to have the proper enthalpy flow at the outlet, the volume integral of the divergence should be:

$$\int \nabla \cdot \mathbf{u} dV \equiv -A(U_1 + U_2 - U_3) = -A \frac{(U_1 - U_2)(c_{p,2} - c_{p,1})}{c_{p,1} + c_{p,2}} = -1.357 \times 10^{-8} \text{ m}^3/\text{s} \quad (7.12)$$

Figure 7.13 shows the resulting integrated divergence or net volume flow.

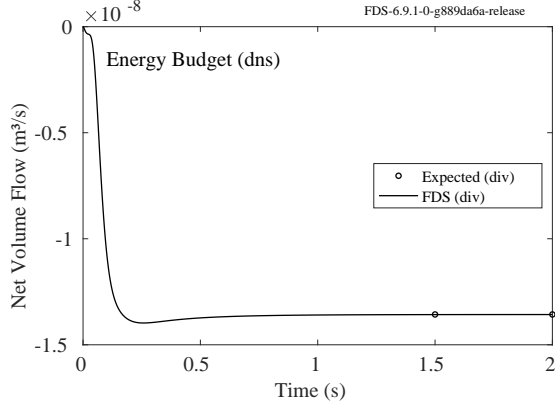


Figure 7.13: The integrated divergence or net volume flow.

### 7.2.5 Mixing with Variable Specific Heats (`energy_budget_tmix`)

This case tests the ability of FDS to properly account for temperature dependent specific heats. A coarse 2-D channel mixing case is presented where hot gas at 900 °C with a constant specific heat of  $c_p = 1 \text{ kJ}/(\text{kg K})$  enters from the bottom left vent with a flux of  $1 \text{ kg}/(\text{m}^2 \text{s})$  and cold gas at 20 °C with a constant specific heat of  $c_p = 10 \text{ kJ}/(\text{kg K})$  enters from a top left vent with the same mass flux. The gases mix in a center channel and exit the domain flowing to the right.

The enthalpy of the mixture at the outlet is  $1 \times 1 \times (900 + 273.15) + 1 \times 10 \times (20 + 273.15) = 4104.65 \text{ kJ}/(\text{m}^2 \text{s})$ . The mixture heat capacity at the outlet is  $5.5 \text{ kJ}/(\text{kg K})$  and the flux is  $2 \text{ kg}/(\text{m}^2 \text{s})$ . Therefore the outlet temperature is  $4104.65/2/5.5 - 273.15 = 100 \text{ °C}$ .

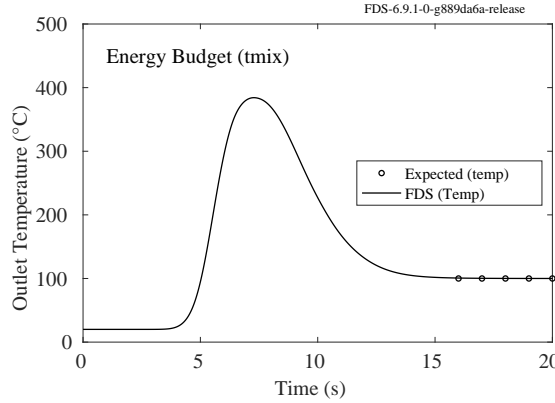


Figure 7.14: Outlet temperature for `energy_budget_tmix` case. Black circles represent the correct result of 100 °C.

### 7.2.6 Combustion Chamber (`energy_budget_combustion`)

Methanol and air are mixed and burned within an adiabatic combustion chamber 1 m on each side. Because the internal energy of the system does not change, we expect that

$$\Delta h = V \Delta p \quad (7.13)$$

where  $\Delta h$  is the increase in the enthalpy of the system (kJ),  $V$  is the volume of the chamber ( $1 \text{ m}^3$ ), and  $\Delta p$  is the increase in pressure (kPa). The enthalpy includes the heats of formation of the various gases. Figure 7.15 displays the rise in pressure and enthalpy.

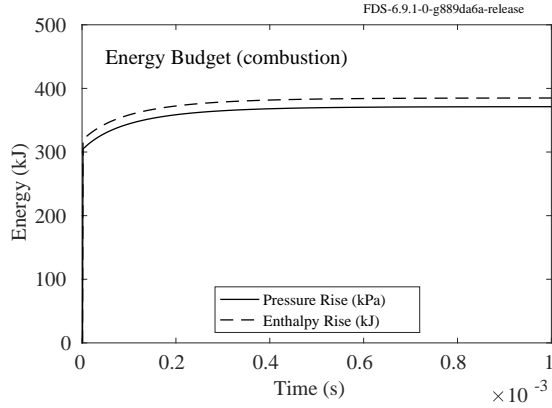


Figure 7.15: The rise in pressure and enthalpy in a sealed, adiabatic combustion chamber.

### 7.2.7 Solid phase energy conservation (energy\_budget\_solid)

This case tests the ability of FDS to properly conserve the total of the solid phase and the gas phase energy. A  $1 \text{ m}^3$  box is filled with 1 kg of a gas with a specific heat of  $1 \text{ kJ}/(\text{kg K})$ , a molecular weight of 28 g/mol, and an initial temperature of  $20^\circ\text{C}$ . All the walls, except the floor, are adiabatic. The floor is defined as a 1 mm thick layer of a material with a conductivity of  $100 \text{ W}/(\text{m K})$ , a specific heat of  $1 \text{ kJ}/(\text{kg K})$ , an initial temperature of  $150^\circ\text{C}$ , and a density of  $1,000 \text{ kg/m}^3$ . The initial enthalpy is  $1 \times 1 \times (20 + 273.15) + 1 \times 1 \times (150 + 273.15) = 716.3 \text{ kJ}$ . At the end state, the gas will have risen in temperature, the solid will have decreased in temperature, and the pressure will have risen. Since energy is conserved this occurs at a temperature of  $96.3^\circ\text{C}$ . The final enthalpy is  $1 \times 1 \times (96.3 + 273.15) + 1 \times 1 \times (96.3 + 273.15) + 22670/1000 = 716.3 \text{ kJ}$ .

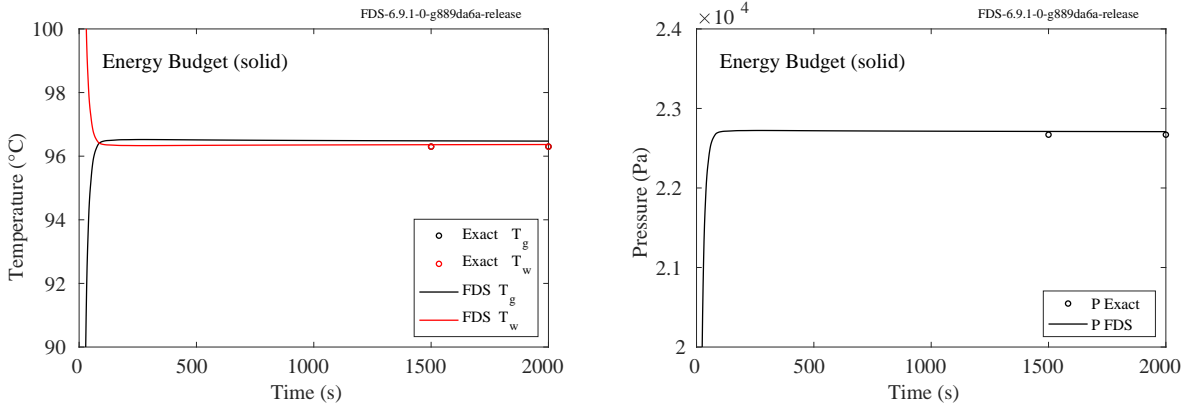


Figure 7.16: Outputs of temperature (left) and pressure (right) for the `energy_budget_solid` case. Circles represent the correct result.

## 7.2.8 Energy Conservation at Walls (`mass_heat_wall_device_test`)

To obtain tight mass and energy balances it is important to output the actual values used for boundary conditions in the transport equations in FDS. Shown in Fig. 7.17 are the results for two cases. These cases are the same except that the vents have opposite `IOR` (orientation) values. Each case has a prescribed outflow mass flux of  $1 \text{ kg}/(\text{m}^2 \text{ s})$  and exhaust vent area of  $4 \text{ m}^2$ . The inflow balances the outflow with both equal to  $4 \text{ kg/s}$ . The specific heat of the air is set to  $1 \text{ kJ}/(\text{kg K})$ . The ambient temperature is  $100^\circ\text{C}$ . The reference temperature is  $25^\circ\text{C}$ . The heat flow at the vent is, therefore,  $(4 \text{ kg/s})(1 \text{ kJ}/(\text{kg K}))(75 \text{ K}) = 300 \text{ kW}$ .

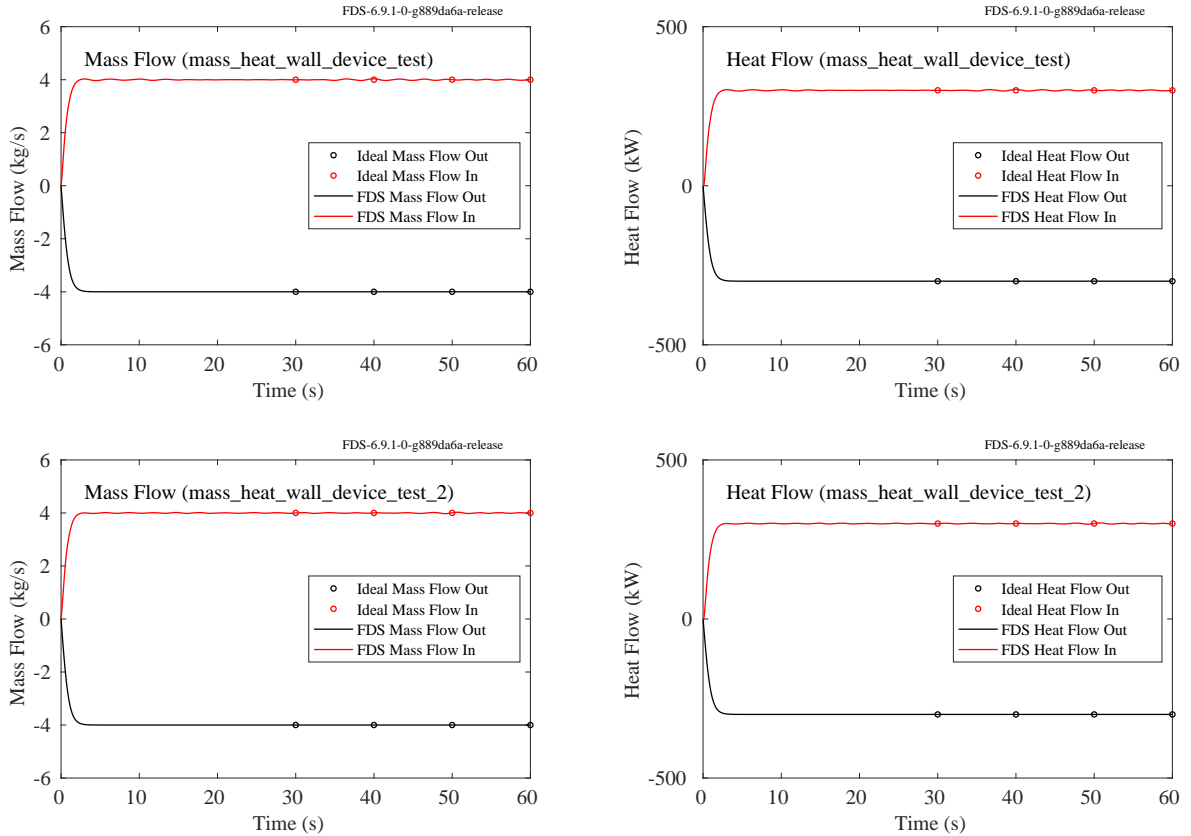


Figure 7.17: The `mass_heat_wall_device_test` flow results.

## 7.2.9 Energy Conservation for Solid Particles (`energy_budget_particles`)

A sealed, adiabatic box, 1 m on a side, is filled with 10 kg of spherically-shaped solid metallic particles, 1 cm in diameter, with a specific heat of  $1 \text{ kJ}/(\text{kg}\cdot\text{K})$ , density of  $5000 \text{ kg/m}^3$ , and conductivity of  $50 \text{ W}/(\text{m}\cdot\text{K})$ . The initial air temperature is  $100^\circ\text{C}$  and the initial particle temperature is  $20^\circ\text{C}$ . The simulation is run until thermal equilibrium is achieved. Figure 7.18 displays on the left the contributions to the sensible enthalpy of the air, most of which are negative because the air loses energy to the particles.  $Q_{\text{RADI}}$  is the net contribution of thermal radiation,  $Q_{\text{COND}}$  is the contribution of convection at the exterior wall of the box,  $Q_{\text{PRES}}$  is the contribution of pressure work on the exterior wall, and  $Q_{\text{PART}}$  is the contribution by the particles. The negative value of  $Q_{\text{PART}}$  means that the particles absorb radiative and convective energy. The plot on the right of Fig. 7.18 compares the sum of these four contributions,  $Q_{\text{TOTAL}}$ , with the computed

change in the sensible enthalpy of the air, ( $Q_{\text{ENTH}}$ ). These two quantities should be equal, as shown by the overlaying curves.

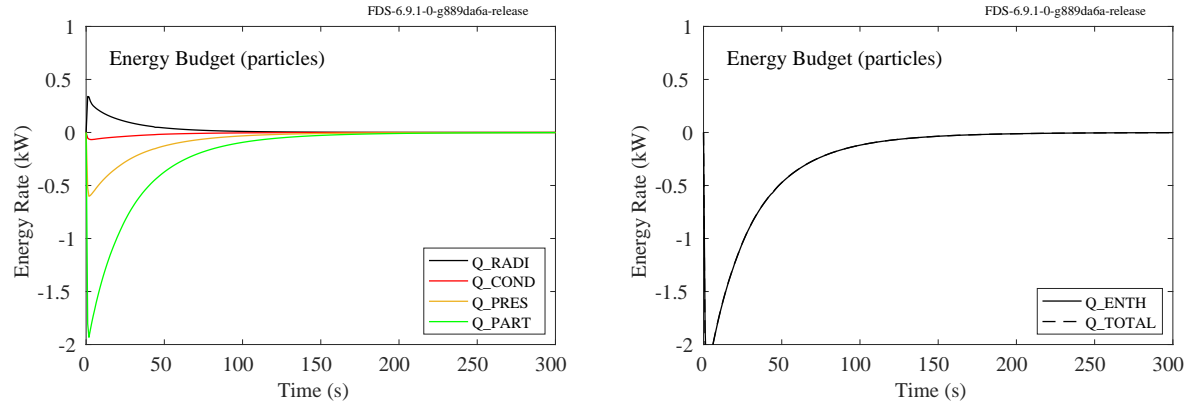


Figure 7.18: (Left) Contributions to change in sensible enthalpy. (Right) Sum of contributions versus total change in enthalpy.

# Chapter 8

## Checking for Coding Errors

This chapter presents a number of cases that are designed to check whether or not various algorithms have been programmed properly. A good way to do this is to simulate simple flows, particularly ones with symmetric features. Errors in coding are easily identified in such cases.

### 8.1 Symmetry Tests

These examples are very simple test cases that are used to determine if there are coding errors in the basic flow solver. In the absence of a small amount of “noise” that FDS uses to initialize the velocity field, a symmetric geometry ought to produce symmetric patterns of velocity, temperature, etc.

#### 8.1.1 Counter-Flowing Jets (`symmetry_test`)

A closed box, 1 m on a side, has 6 injection vents, one centered on each face. Air is pumped into the box at a steady rate. Anything that might lead to an asymmetry in the flow field is turned off, for example, gravity, atmospheric stratification, natural convection, and random noise. One case is performed on a single mesh; the other on multiple meshes. The cases are not identical. The resulting flow fields are shown at the left in Fig. 8.1. On the right are plots of the three components of velocity at equidistant corners of the enclosure. Ideally, there should be two equal and opposite time histories of the three components. Even the slightest error in coding will throw this off almost immediately.

#### 8.1.2 Fire in a Thin-Walled Pan (`symmetry_test_2`)

In this case, a steel pan is placed inside a small compartment with a small door at one end. The pan has thin walls (zero cells thick) which is particularly challenging for a symmetry test because boundary conditions must be applied on opposite sides of the thin wall. The case also involves a fire and multiple species. Radiation is not tested here. Figure 8.2 displays the temperature field in a slice plane across the pan, and at two points equidistant from the centerline.

#### 8.1.3 Axial symmetry (`cyl_test`)

FDS has an option to perform an axially-symmetric calculation, which can be useful for simulating a laminar diffusion flame, like a bunsen burner or candle. When invoking this option, the user still specifies three coordinates,  $x$ ,  $y$ , and  $z$ , but it is understood that  $x$  is the radial coordinate,  $r$ , and  $z$  is the vertical coordinate.

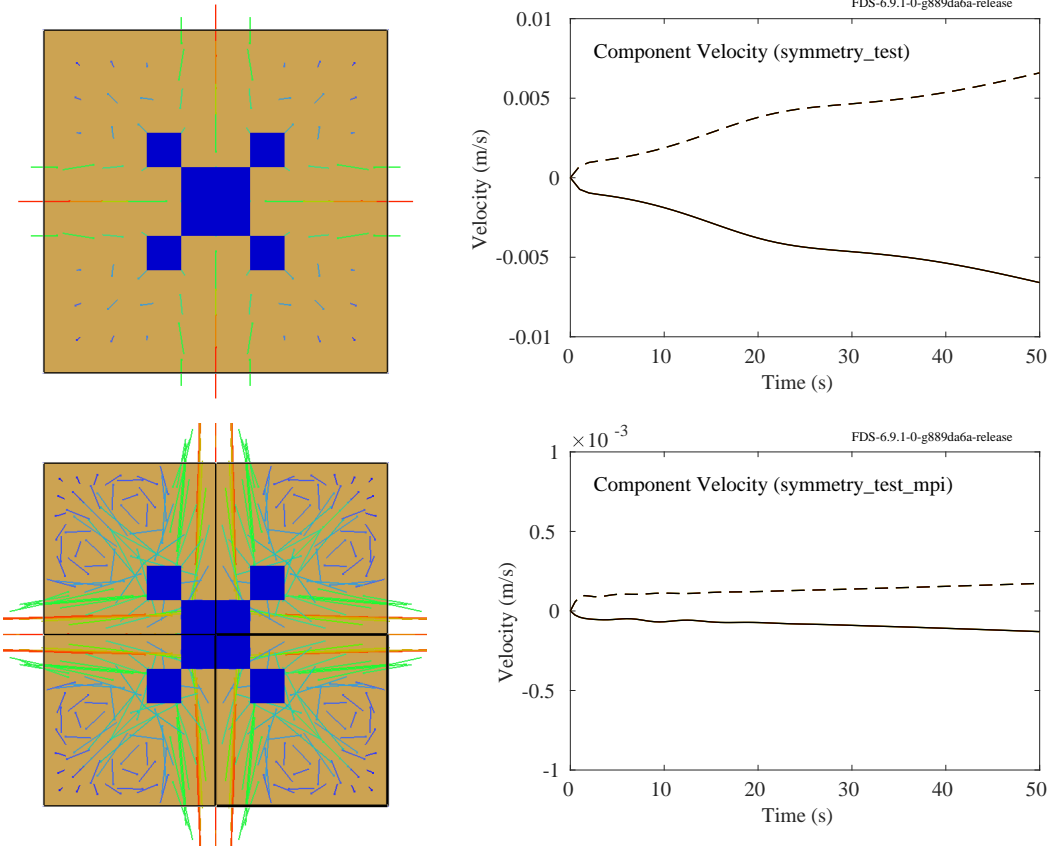


Figure 8.1: Flow field (left) and velocity component plots (right) for the `symmetry_test` cases.

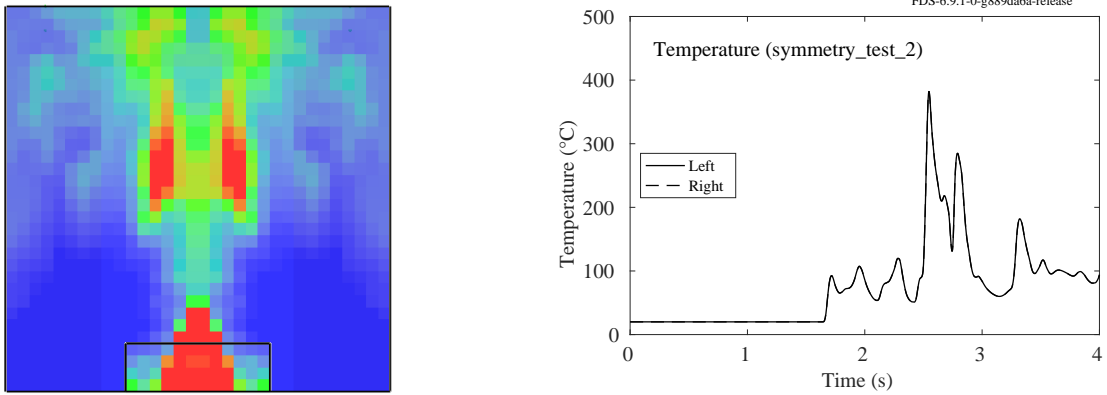


Figure 8.2: Flow field (left) and temperature plot (right) for the `symmetry_test_2` case.

The coordinate,  $y$ , is used only by Smokeview to draw the domain, and it should not influence the calculation at all. However, since FDS is primarily a three-dimensional, cartesian code, there is a possibility that a coding error might cause the specification of the  $y$  dimension to have an effect on the result. Figure 8.3 displays results of two sets of axially-symmetric simulations. On the left is an LES simulation in which the lateral size of the cells,  $\delta y$ , is 2 mm and 2 cm. The two curves ought to lie exactly upon each other, which is indicated by a single red curve. On the right is a DNS simulation of a laminar diffusion flame, with  $\delta y$

equal to 2 mm and 4 mm.

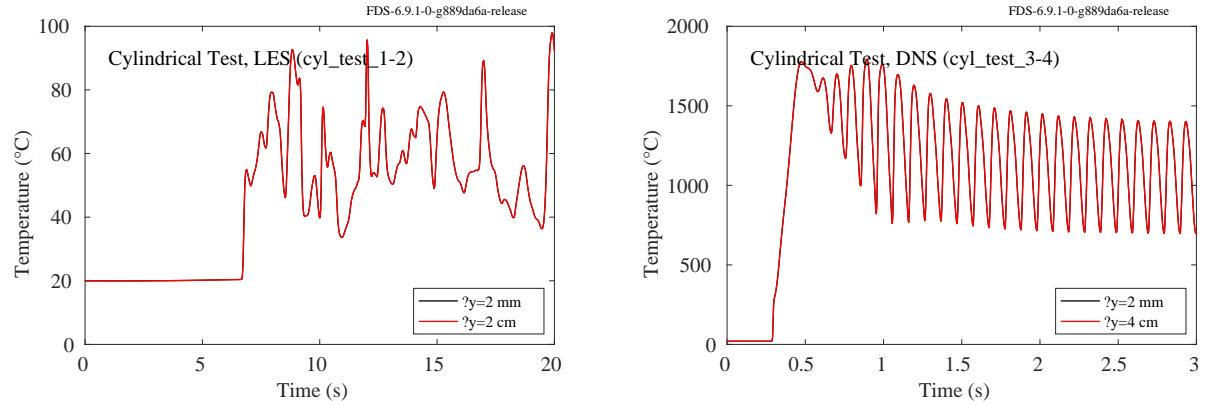


Figure 8.3: Temperature traces from axially-symmetric calculations with different values of  $\delta y$ .

## 8.2 Velocity boundary condition implementation (`velocity_bc_test`)

In this example, a simple jet is created by pushing air through a square duct. The obstructions forming the duct are built three different ways. The first way is to build the duct with thin (zero cell thick) plates. The second is to carve the duct out of a solid block. The third way is to build the duct out of one cell thick plates. The three approaches are illustrated in Fig. 8.4. Ideally, the three jets ought to be exactly the same, but subtle differences in the pressure solution and the random generation of noise lead to three unique flow patterns that are only the same in a time-averaged sense. To test this, the centerline pressure and velocity are recorded for a 2 m/s jet emanating from a 0.8 m square duct that is 5 m long. The grid resolution is fairly crude (0.2 m) because the purpose of this exercise is to show that the steady-state velocity and pressure profiles are essentially the same. Figure 8.5 displays the profiles. The curves ought to overlap each other. Errors in the implementation of the velocity boundary conditions are likely to throw the three cases out of alignment.

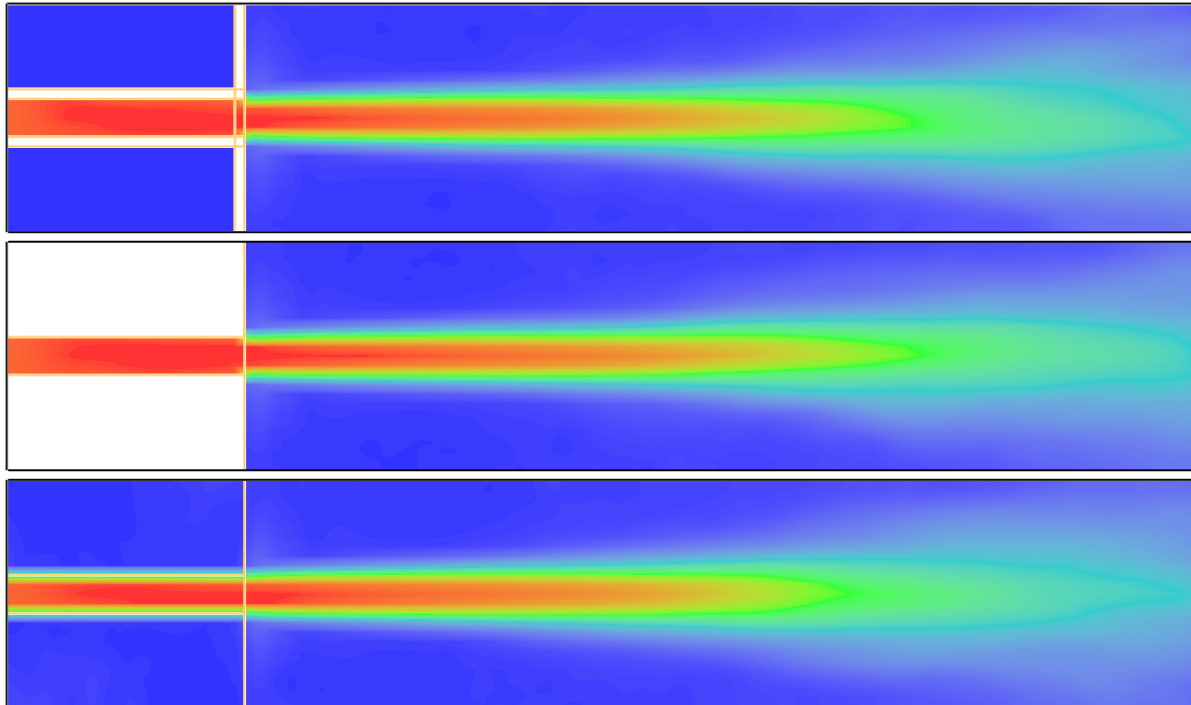


Figure 8.4: Time-averaged contours of velocity for the `velocity_bc_test` case.

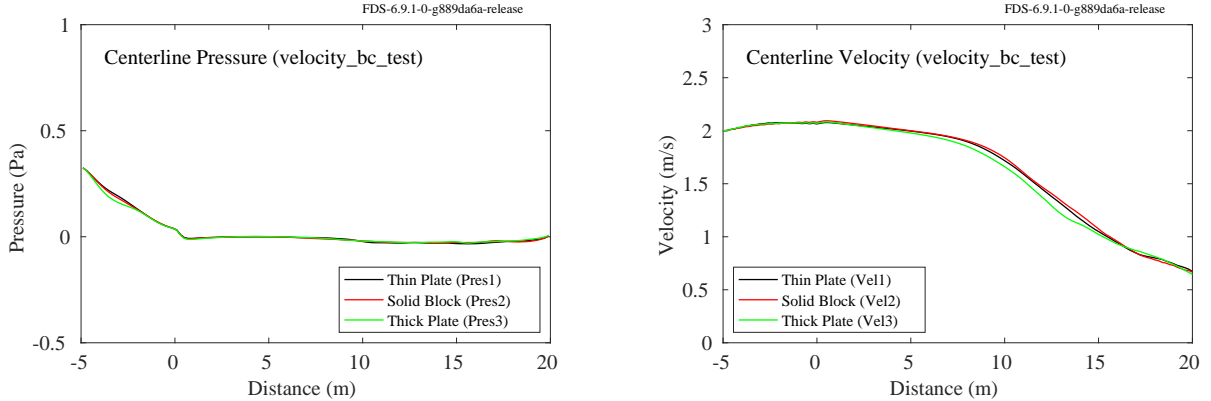


Figure 8.5: Centerline time-averaged pressure (left) and velocity (right) profiles for the `velocity_bc_test` case.

## 8.3 Checking the divergence constraint

The test cases in this section involve the divergence of the flow,  $\nabla \cdot \mathbf{u}$ , an important quantity in the low Mach number formulation of the Navier-Stokes equations.

### 8.3.1 Isothermal flow (`divergence_test_1`)

In the first example, air is pushed through a 1 m cube at a speed of 1 m/s. The air is extracted at the same rate, and there should be no pressure rise and the flow should remain divergence free. There are also a few obstructions that are created and removed during the simulation to check that this does not cause any errors. The left hand plot of Fig. 8.6 displays the minimum and maximum divergence as a function of time. These ought to remain below approximately  $1 \times 10^{-10} \text{ s}^{-1}$  in absolute value.

### 8.3.2 Sealed compartment (`divergence_test_2`)

In the second example, air is introduced into a sealed compartment at a steady rate via a single solid Lagrangian particle. In other words, the air is not introduced at the boundary, but rather within the center of the compartment. The pressure, density, and temperature increase, but the volume integral of the divergence remains zero according to the Divergence Theorem:

$$\int_{\Omega} \nabla \cdot \mathbf{u} \, dV = \int_{\partial\Omega} \mathbf{u} \cdot d\mathbf{S} = 0 \quad (8.1)$$

The right hand plot of Fig. 8.6 displays the volume integral of the divergence as a function of time. This ought to remain within machine accuracy, certainly less than  $1 \times 10^{-10} \text{ m}^3/\text{s}$  in absolute value.

### 8.3.3 Creating/Removing Obstructions (`divergence_test_3`)

In the third example, air is pushed through a two-dimensional channel where obstructions are created and removed at random times. The divergence of the flow should remain nearly zero throughout the entire domain. Figure 8.7 displays the maximum and minimum divergence as a function of time. These ought to remain less than approximately  $10^{-12} \text{ s}^{-1}$  in absolute value.

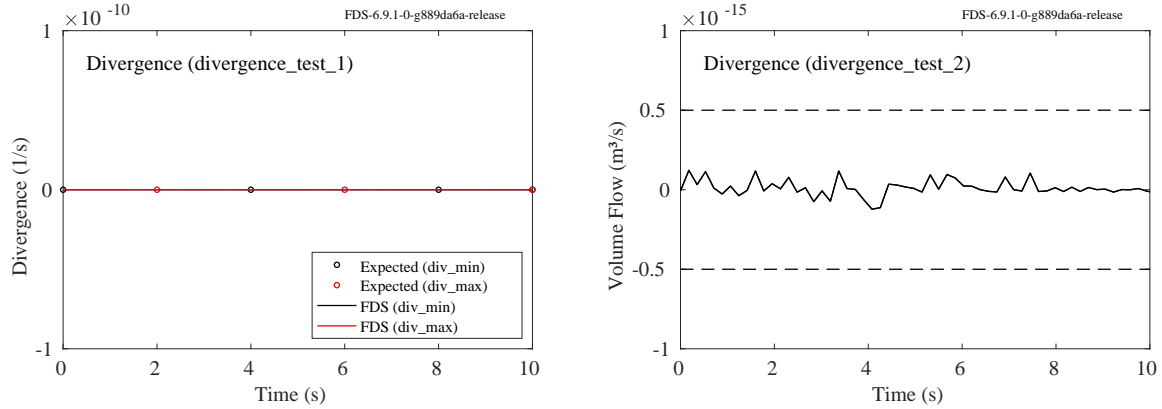


Figure 8.6: Minimum and maximum divergence for the `divergence_test` cases.

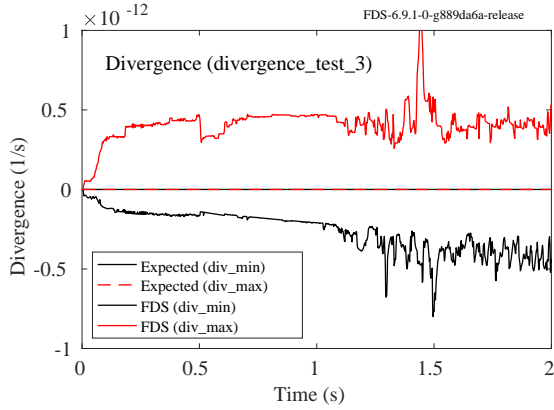


Figure 8.7: Minimum and maximum divergence for the `divergence_test_3` case.

## 8.4 Multi-mesh Pressure and Temperature Lapse (`lapse_rate`)

A  $10\text{ m} \times 10\text{ m} \times 40\text{ m}$  volume is initialized with `LAPSE_RATE=-0.01`. The volume is divided vertically into four equal meshes with each mesh having a  $10\text{ cm}$  grid resolution. There should be a smooth drop in both temperature and pressure that matches the analytic values, as shown in Fig. 8.8.

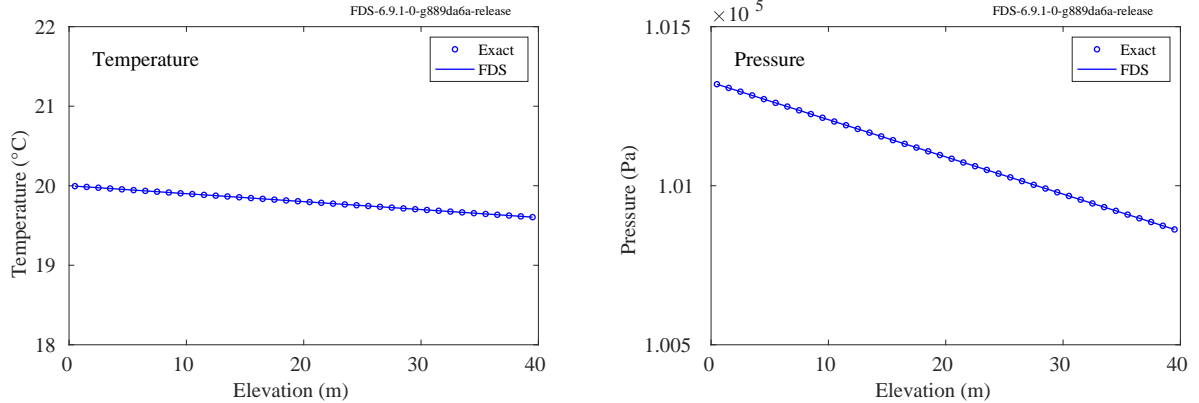


Figure 8.8: Centerline temperature (left) and pressure (right) profiles for the `lapse_rate` case.

## 8.5 Randomly Overlapping Meshes (`random_meshes`)

In most FDS simulations, multiple meshes are positioned adjacent to each other to allow two-way communication. However, in some instances, meshes need to overlap, and this case verifies the functionality of meshes that overlap in a variety of ways. It is a 2-D case that runs fast and is easy to visualize. There are five overlapping meshes shown at left in Fig. 8.9. Air is blown in at the bottom and exhausted via an open vent at the top. The volume flow rate is fixed at  $0.012 \text{ m}^3/\text{s}$ , and the plot at right in Fig. 8.9 verifies that the simulation matches to within a few percent. The case uses the default normal velocity tolerance at solid and interpolated boundaries; thus, there is some error expected in the volume flow due to the solution of the Poisson equation. As a further check that the mesh allocations are being properly handled, there is a fine mesh embedded within the coarse, and the case is run with four MPI processes rather than five.

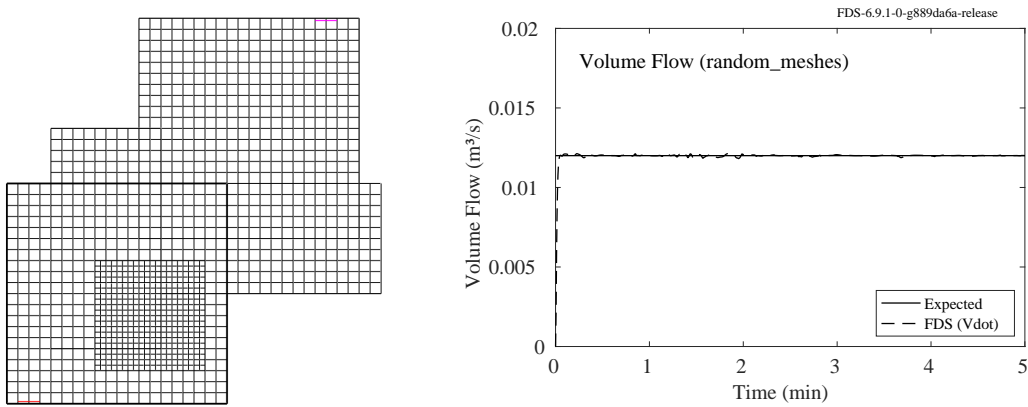


Figure 8.9: Five overlapping meshes (left) and the net volume flow through the domain (right).

## 8.6 Overlapping INIT Regions (`init_overlap`)

Typically, an FDS simulation begins at time  $t = 0$  with ambient conditions. However, ambient conditions can be changed for rectangular regions of the domain using the namelist keyword `INIT`. If two rectangular

regions defined by `INIT` overlap, it is the first of the overlapping regions that takes precedence (i.e., first come first serve) for all commonly defined inputs. That is, it is not possible to overwrite the initial conditions explicitly specified by the first `INIT` line with the initial conditions explicitly defined by the second `INIT` line. This verification case tests the overlap of `INIT` regions. Fig. 8.10 and Fig. 8.11 verify the predictions by FDS match the expected conditions.

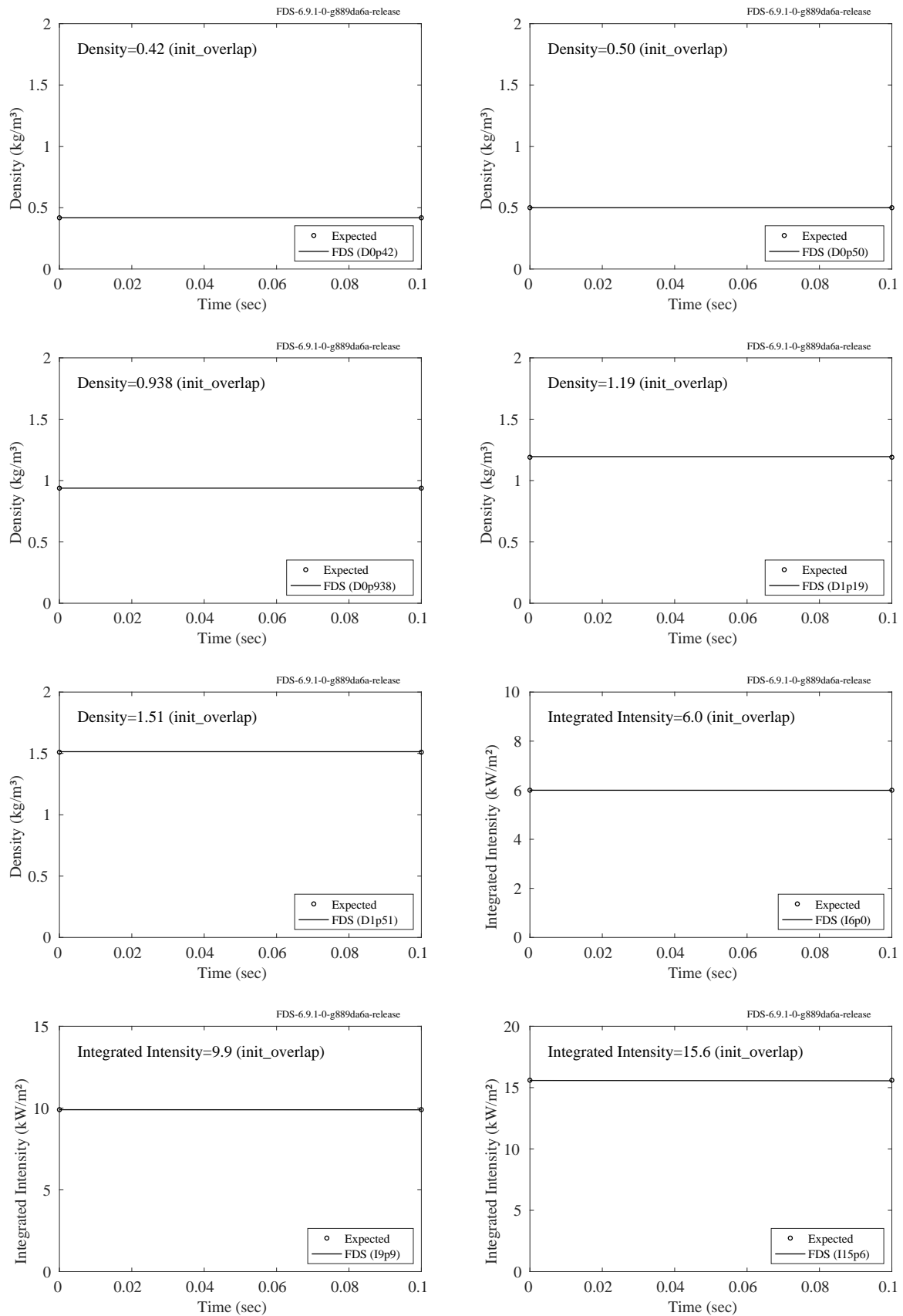


Figure 8.10: Comparison of initial conditions from FDS compared with expected initial conditions.

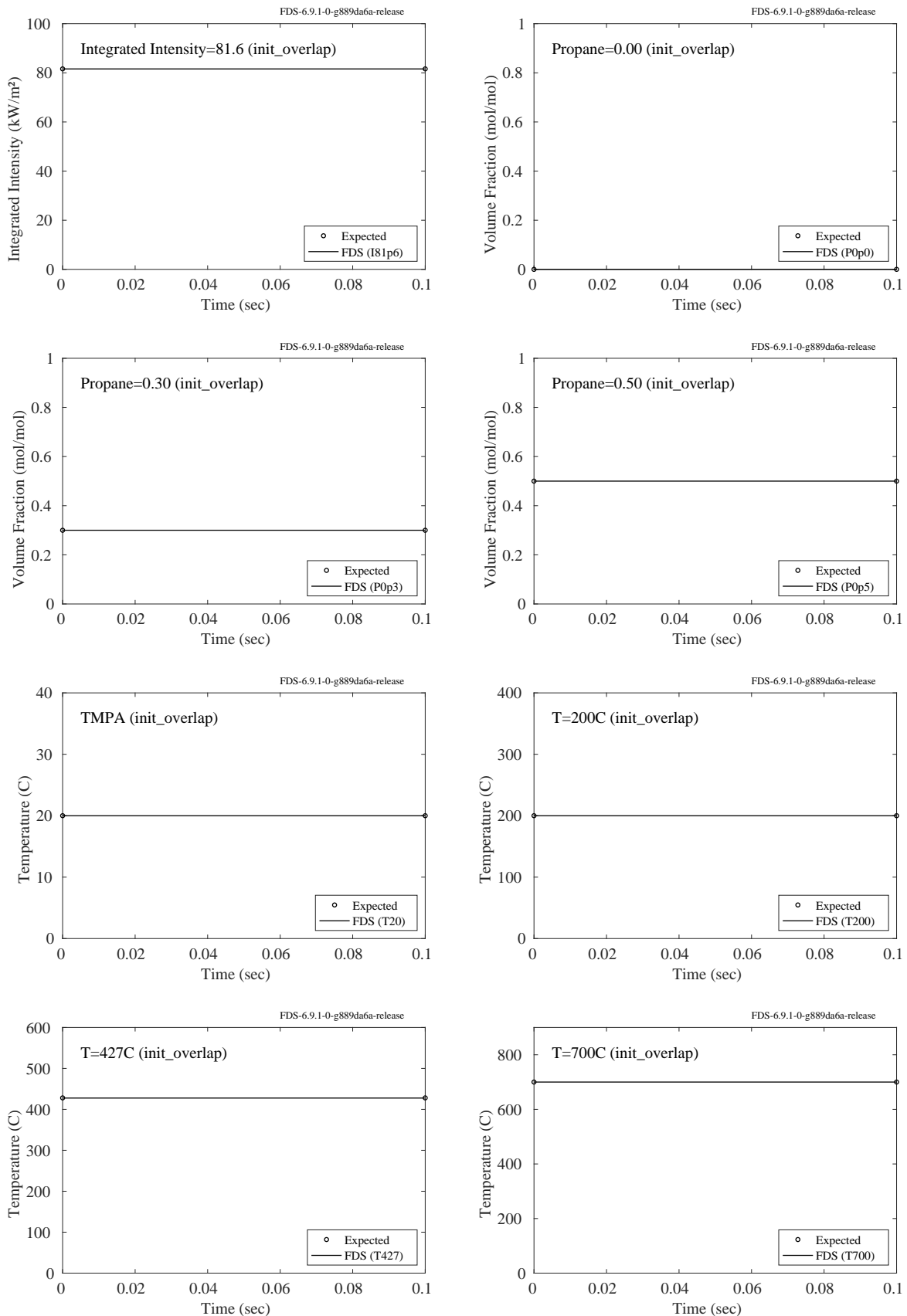


Figure 8.11: Comparison of initial conditions from FDS compared with expected initial conditions.

## 8.7 Spurious Obstruction Effects (`hole`)

It is not uncommon for subtle differences between two nearly identical input files to lead to noticeable results in the simulation output. In this particular case, a `HOLE` in an obstruction that was set to never open still led to slightly different results when compared to a case with no `HOLE`. The reason for the difference was attributed to slightly different boundary conditions at the edge of the `HOLE`. The problem has been fixed, as confirmed by Fig. 8.12.

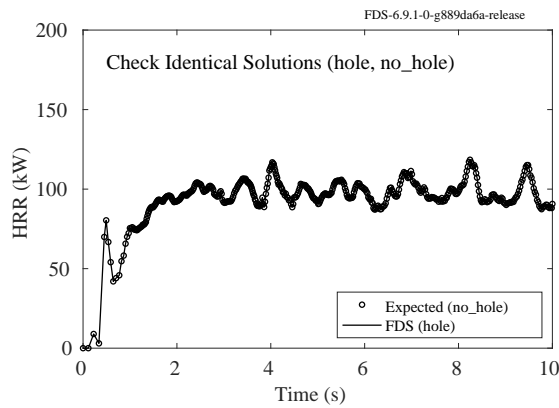


Figure 8.12: Heat release rates of two nearly identical calculations.

## 8.8 OpenMP Thread Checking (`race_test`)

OpenMP is used in FDS to sub-divide the work of the do-loops among multiple cores belonging to the same processor. Figure 8.13 displays temperature and velocity traces from two calculations, one using one OpenMP thread and one using four. The results of the two calculations ought to be identical, in which case the respective pairs of temperature and velocity traces ought to completely overlap.

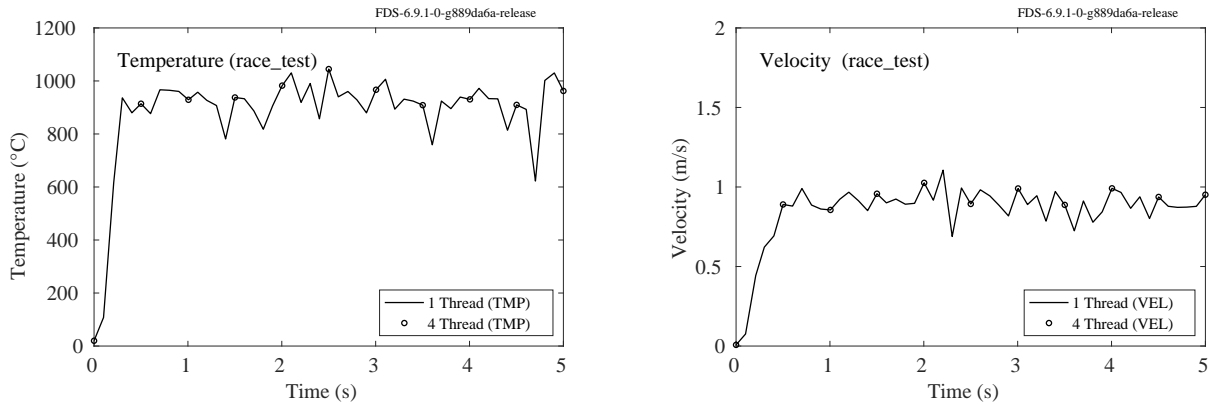


Figure 8.13: Temperature and velocity time histories of two calculations that use different numbers of OpenMP threads. The traces ought to be identical.

## 8.9 Multi-Mesh Layer Height Calculation (layer)

The test cases called `Miscellaneous/layer_1mesh.fds` and `layer_4mesh.fds` simulate a fire in a small compartment where the average smoke layer height and temperature are calculated. Figure 8.13 displays the results for both cases. Note that the 4 mesh case is run on 3 MPI processes to ensure that the layer calculation works for an arbitrary number of meshes and MPI processes.

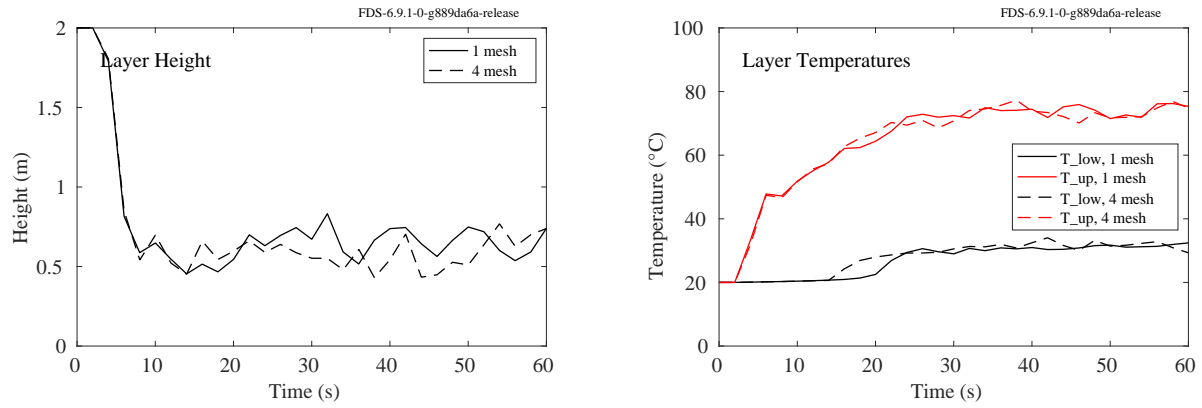


Figure 8.14: Average layer height (left) and temperatures (right) for simulations on 1 mesh and 4 meshes.

## 8.10 The Restart Feature

FDS has a feature with which users can stop and restart simulations. When a simulation is stopped, all necessary variables are packed into arrays and written out to a file. This feature can be fragile when the input file includes devices and controls that initiate actions at certain times. In the simulation named `Restart/device_restart_a.fds`, a multi-room fire simulation is stopped and then restarted at 40 s. Before the restart, at 30 s, a door is opened and high temperature gases flow from the fire room into a corridor. After the restart, the case proceeds until 60 s. Another simulation called `device_restart_base_case` runs uninterrupted. The temperature just outside of the fire room door (Fig. 8.15) should be similar in both simulations. The temperatures are not exactly the same because restarting a simulation can lead to minor changes in the algorithm at the time of the restart.

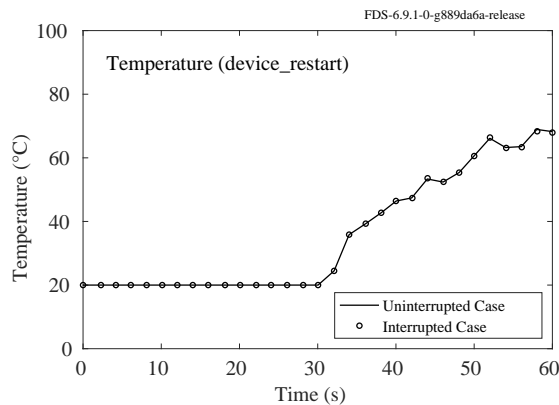


Figure 8.15: Temperature outside of a door to a fire room that is opened at 30 s.

# Chapter 9

## Thermal Radiation

There are numerous examples in the heat transfer literature of exact solutions, for simple configurations of hot and cold objects, of the radiation transport equation. This chapter presents a number of these examples, plus others aimed at assessing the influence of absorptive media.

### 9.1 Radiation View Factors

The examples in this section test the basic radiation transport solver against exact solutions derived for simple geometric shapes.

#### 9.1.1 Hot Plate (`plate_view_factor`)

These verification cases test the computation of radiative heat flux from a hot plate to a target surface 1 m away in different coordinate systems. The radiating surface is at 1000 °C and has an emissivity of 1.0. The exact values are calculated using the analytical expressions for the view factors.

Co-ordinates	Radiation source	Heat flux (kW/m <sup>2</sup> )
2D Cartesian	Infinite plate of width 2 m	105.3
3D Cartesian	Square plate of width 2 m	81.8
2D cylindrical	Circular disk of diameter 2 m	74.1

A comparison of exact values and FDS predictions at three different angular resolutions is shown in Fig. 9.1.

#### 9.1.2 Plates at a Right Angle (`geom_rad`)

In this case, two flat rectangular obstructions (0.98 m by 0.98 m,  $A = 0.9604 \text{ m}^2$ ) abut at a right angle. The view factor  $F_{12} = 0.20004$ . The vertical plate has a surface temperature of  $T_{\text{hot}} = 1273.15 \text{ K}$  and the horizontal plate has a temperature of  $T_{\text{cold}} = 293.15 \text{ K}$ . The emissivity of each surface is 1, and the convective heat transfer coefficient is assumed to be 0. Two cases are considered. The first is where the plates are input as conventional rectangular OBSTS, and the second where the plates are immersed boundary GEOMS. There should be no difference in the total energy radiated from hot to cold plates, Fig. 9.2 (left), or the incident heat flux in the center of the cold plate, Fig. 9.2 (right). The exact solution for the integrated incident (i.e. incoming) heat flux to the surface of the cold plate is  $F_{12}\sigma T_{\text{hot}}^4 A = 28.62 \text{ kW}$ . The purpose of this exercise is to ensure that both types of obstructions behave the same way.

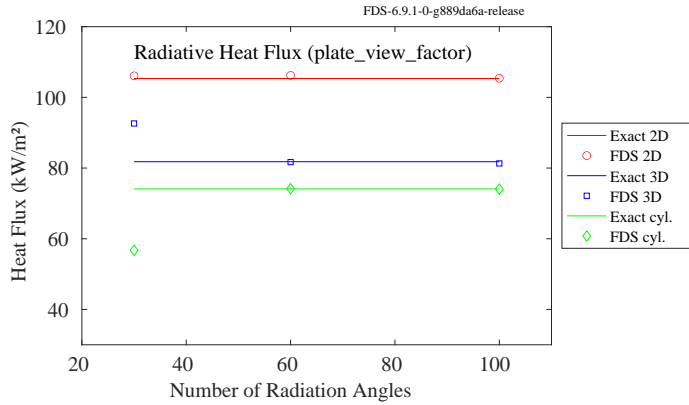


Figure 9.1: Convergence study showing increased accuracy of radiative transport equation with increasing number of angles.

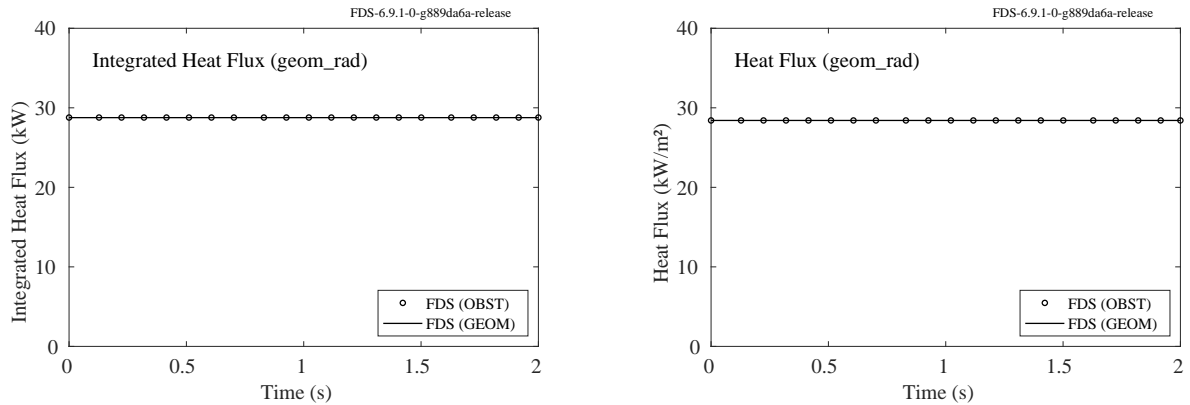


Figure 9.2: A hot wall radiates onto a cold floor. At left is the total rate of energy transfer, and at right is the heat flux to the center of the floor.

### 9.1.3 Plates at a Right Angle, Part 2 (geom\_rad\_2)

The case in the previous section is repeated, only now the two plates are not aligned with the Cartesian grid. Figure 9.3 displays the comparison of exact and computed solutions for the integrated incident heat flux to the cold plate.

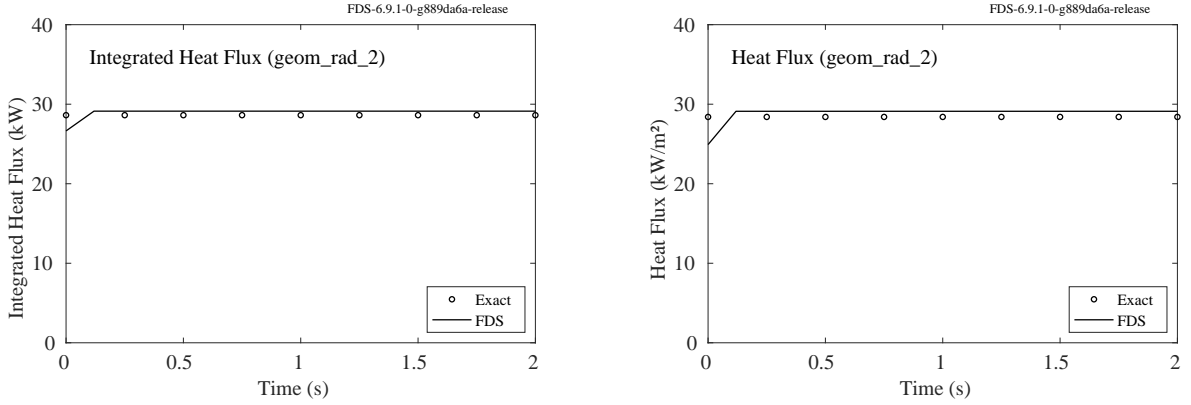


Figure 9.3: The integrated (left) and point (right) heat flux from a hot plate to a cold plate at a right angle.

## 9.2 Radiation inside a Box (`radiation_box`)

This verification case tests the computation of three-dimensional configuration factor  $\Phi$  inside a cube box with one hot wall and five cold (0 K) walls. An overview of the test geometry is shown in Fig. 9.4. The

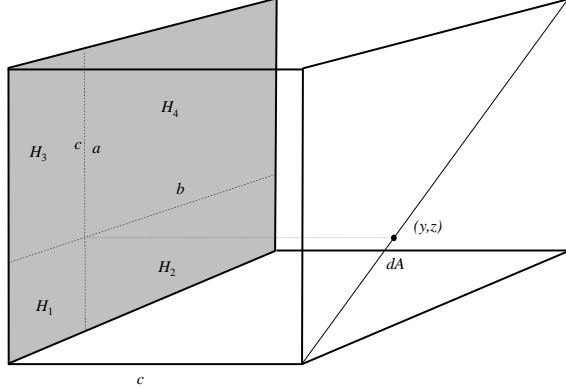


Figure 9.4: Radiation inside a box geometry.

configuration factors are calculated at the diagonal of the cold wall opposite to the hot wall. The exact values of the configuration factor from plane element  $dA$  to parallel rectangle  $H$  are calculated using the analytical solution [87]

$(y, z)$	$\Phi_{H dA}$	$(y, z)$	$\Phi_{H dA}$
0.025	0.1457	0.275	0.2135
0.075	0.1603	0.325	0.2233
0.125	0.1748	0.375	0.2311
0.175	0.1888	0.425	0.2364
0.225	0.2018	0.475	0.2391

Different variations of the case include the mesh resolution ( $20^3$  and  $100^3$  cells) and the number of radiation angles (50, 100, 300, 1000, 2000). The exact and FDS results are shown in Fig. 9.5.

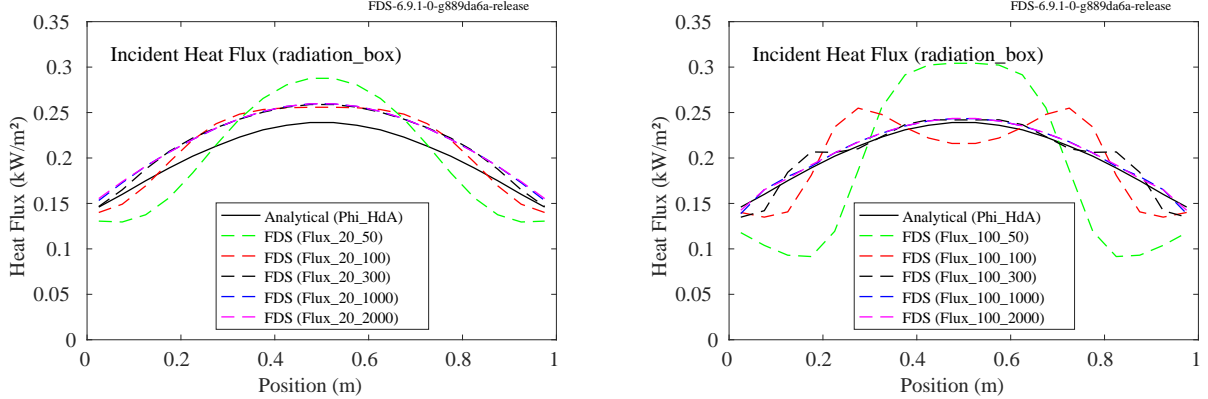


Figure 9.5: Incident heat flux.

The results provide an illustration of numerical errors due to both angular resolution and spatial resolution. With  $20^3$  cells (5-cm spatial resolution), the discrepancies between the FDS and analytical solutions decrease when increasing the number of radiation angles used in the Radiation Transfer Equation (RTE) solver: this decrease may be explained by the increasingly accurate description of the angular region occupied by the hot wall when viewed from the selected opposite wall locations. The results also show that at 5-cm spatial resolution ( $20^3$  cells), the discrepancies between the FDS and analytical solutions do not totally vanish and feature a residual error of approximately 10% even when using a large number of radiation angles: this residual error may be explained by inaccuracies in the numerical description of the configuration factors (configuration factors are defined as spatial integrals over the hot wall surface of an expression that features two cosine angles and a separation distance; the implicit evaluation of configuration factors in the RTE solver is subject to spatial integration errors). Consistent with this explanation, the results show that at 1-cm spatial resolution ( $100^3$  cells), the discrepancies between the FDS and analytical solutions decrease to very small levels and feature a residual error of less than 1%.

### 9.3 Radiation from a Polygonal Plate (`radiating_polygon`)

This example is similar to the one presented in Sec. 9.2, except now the radiating plate is a polygon with sides of even length. The incident radiation heat flux from an  $n$ -sided polygon with temperature,  $T = 1000^\circ$ , is given by the formula [87]:

$$\dot{q}_r'' = \sigma T^4 \frac{nH}{\pi \sqrt{1+H^2}} \tan^{-1} \sqrt{\frac{R^2 - H^2}{1+H^2}} \quad ; \quad H = \frac{h}{l} \quad ; \quad R = \frac{r}{l} \quad (9.1)$$

where  $h$  is the distance from the center of the polygon to the center point of any of its sides,  $r$  is the distance from the center to any vertex, and  $l$  is the distance from the center to the target surface along a perpendicular line. Figure 9.6 displays calculations performed with a range of grid and angular resolutions. Note that the number of angles used to solve the RTE is quadrupled when the number of grid cells in each coordinate direction is doubled.

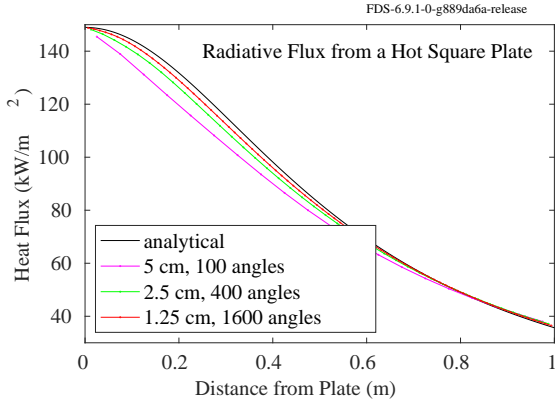


Figure 9.6: Incident heat flux from a hot square plate as a function of distance to the center of the plate.

## 9.4 Radiation from a Layer of Hot Gas (`radiation_plane_layer`)

This case tests the computation of three-dimensional radiation from a homogeneous, infinitely wide layer of hot gases. The temperature of the layer is 1273.15 K and the absorption coefficient,  $\kappa$ , is varied. The thickness of the layer is fixed at 1 m, and the optical depth is  $\tau = (1 \kappa)$ . Wall temperatures are set to 0 K. The results are compared against the exact solution  $S(\tau)$  presented in [88]

$$S(\tau) = S_b [1 - 2E_3(\tau)] \quad (9.2)$$

where  $S_b = \sigma T^4$  is the black-body heat flux from the radiating plane and  $E_3(\tau)$  is the exponential integral function (order 3) of the optical depth  $\tau$ .

The FDS results are computed at two mesh resolutions in the  $x$ -direction ( $I = 20$  and  $I = 150$ ). For  $I = 20$ , both one-band and six-band versions are included to test the correct integration of heat fluxes over multiple bands. For  $I = 20$ , 2-D versions are also computed ( $J = 1$ ). The limiting case,  $\tau = \infty$ , using a solid wall of temperature 1273.15 K, is computed to test the wall heat flux computation. The exact values and FDS predictions of the wall heat fluxes are given in the table below.

$\tau$	$S(\tau)$ (kW/m <sup>2</sup> )	FDS (I=20,J=20)		FDS (I=20,J=1)		FDS (I=150)
		1 band	6 bands	1 band	6 bands	1 band
0.01	2.8970	2.9182	2.9072	2.8351	2.8244	2.9260
0.1	24.9403	25.5518	25.4556	25.1039	25.0094	25.7062
0.5	82.9457	83.1364	82.8234	84.3764	84.0587	84.0320
1.0	116.2891	115.4127	114.9782	117.8088	117.3652	116.7828
10	148.9698	148.9717	148.4108	148.9775	148.4167	148.9793
$\infty$	148.9709	147.9145	147.3577	148.0064	147.4492	148.1923

## 9.5 Wall Internal Radiation (`wall_internal_radiation`)

In-depth absorption of thermal radiation in a solid is computed using a two-flux model. In this example, the accuracy of the two-flux model is tested in the computation of the emissive flux from a homogeneous layer of material (thickness  $L = 0.1$  m) at 1273.15 K temperature, surrounded by an ambient temperature of 1 K. The absorption coefficient  $\kappa$  is varied to cover a range [0.01, 10] of optical depth  $\tau = \kappa L$ .

The exact solutions for radiative flux are the analytical solutions of plane layer emission [88]

$$S(\tau) = S_b [1 - 2E_3(\tau)] \quad (9.3)$$

where  $S_b = \sigma T^4$  is the black-body heat flux from the radiating plane and  $E_3(\tau)$  is the exponential integral function (order 3) of optical depth,  $\tau$ . The exact solutions and FDS results are shown in the table below.

$\tau$	$S(\tau)$ (kW/m <sup>2</sup> )	FDS (kW/m <sup>2</sup> )
0.01	2.897	2.950
0.1	24.94	26.98
0.5	82.95	93.90
1.0	116.3	128.4
10.	149.0	149.0

## 9.6 Radiation Emitted by Hot Spheres (`hot_spheres`)

This case tests the calculation of the radiation heat flux from a collection of hot objects. Within two completely open volumes that are 1 m on a side, hot spheres with a diameter of 1 cm and temperature of 500 °C are situated within a smaller volume that is 0.5 m on a side. One of the open volumes contains 10 spheres, the other contains 50,000. The simulation lasts for 10 s. In the first volume, the heat loss is just the sum of the areas of the spheres multiplied by  $\sigma T^4$  (emissivity is specified as unity in this case). See the upper left plot in Fig. 9.7. In the second volume, the region is densely packed and it is expected that the collection of spheres will radiate like a solid cube that is 0.5 m on a side and whose temperature is 500 °C. This is just under 30 kW, as shown in the upper right of Fig. 9.7. The plot in the lower left of Fig. 9.7 shows the incident heat flux to a gauge positioned at the center of the densely packed volume. It is expected that this gauge would register a heat flux of  $\sigma T^4 = 20.26$  kW/m<sup>2</sup>. Finally, the plot in the lower right of Fig. 9.7 indicates the integrated intensity,  $4\sigma T^4 = 81.04$  kW/m<sup>2</sup>.

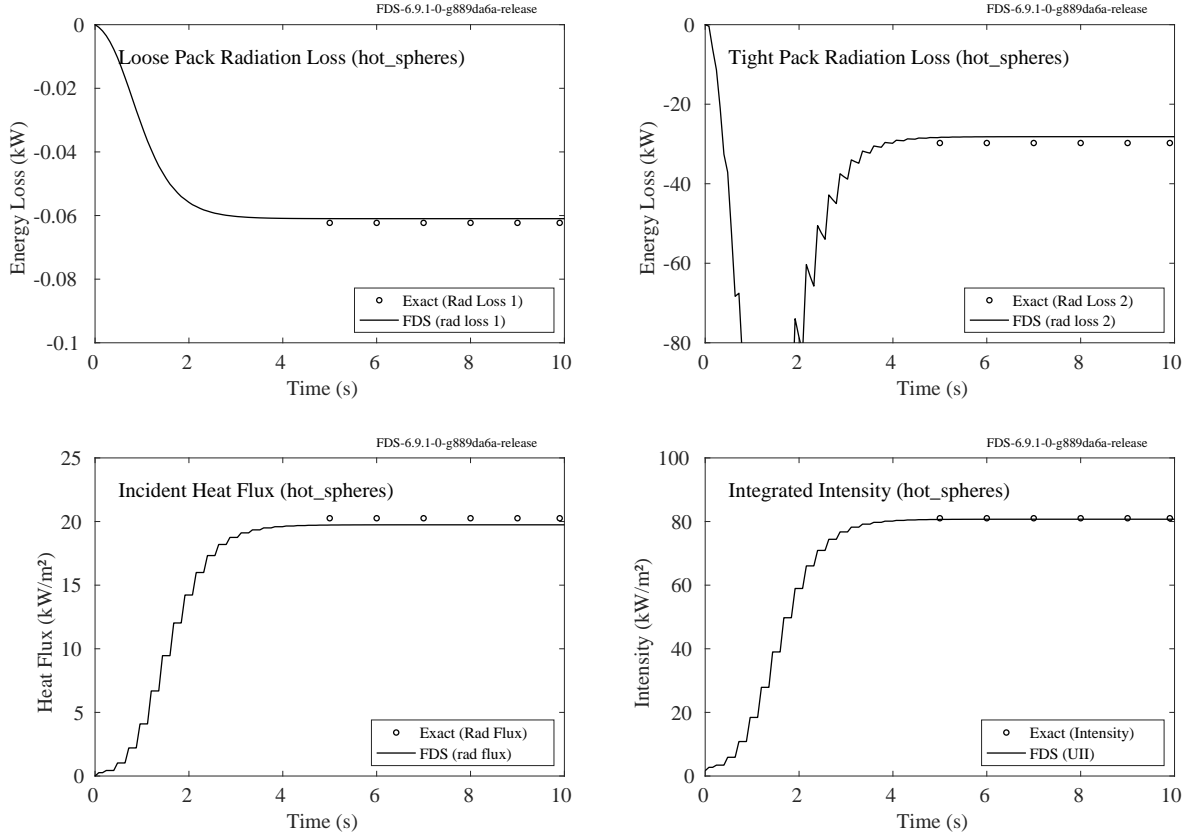


Figure 9.7: The total heat losses, radiative heat flux, and integrated intensity of a collection of loosely and densely packed radiating spheres.

## 9.7 Radiation Absorbed by Liquid Droplets (`droplet_absorption`)

These cases check that energy is conserved when radiation is absorbed by liquid droplets. We want to make sure that the absorbed thermal radiation is accurately converted into internal energy of the droplets. The rate of increase of the average droplet temperature,  $\bar{T}_p$ , is related to the rate of radiation absorption of all the droplets,  $\dot{Q}_r$ , according to the following equation:

$$m c_p \frac{d\bar{T}_p}{dt} = \dot{Q}_r \quad (9.4)$$

where  $m$  and  $c_p$  are the total mass and specific heat of the droplets, respectively. The convective heat transfer between the gas and the droplets is small because the gas phase Prandtl number has been set to an artificially high value. If the radiative intensity remains constant during the time step, the average droplet temperature over a time period,  $\Delta t$ , should be:

$$\bar{T}_p = T_0 + \frac{\Delta t \dot{Q}_r}{m c_p} \quad (9.5)$$

By setting  $T_0 = 0^\circ\text{C}$ ,  $\Delta t = 0.01$  s,  $m = 0.01$  kg, and  $c_p = 1.0$  kJ/(kg·K), the final value of  $\bar{T}_p$  should equal  $\dot{Q}_r$ . Figure 9.8 shows comparisons of the predicted average droplet temperature and the expected value in Cartesian and cylindrical coordinate systems.

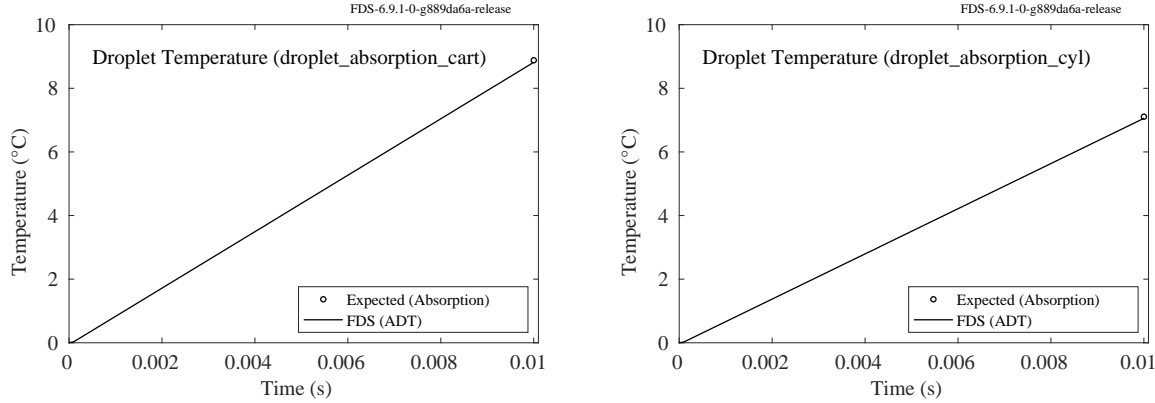


Figure 9.8: Transfer of absorbed thermal radiation energy into increased average droplet temperature.

## 9.8 Consistency of Particle Absorbed Energy and the Radiative Loss Term

Small spherical, cylindrical and planar particles with black (emissivity = 1) surfaces are placed in radiation field. Radiation is coming from black surfaces, and the gas is pure Nitrogen, i.e. non-participating. The amount of energy removed from the intensity field is measured by a device calculating spatial and temporal integrals of radiation loss term ( $Q_w$ ). The reference solution ( $E_w$ ) is the wall enthalpy increase, as observed by the one-dimensional heat conduction solver. In `particle_isotropic_radii`, the radiation field isotropic, i.e. all surfaces are black and constant temperature. In `particle_anisotropic_radii`, an anisotropic intensity field is generated by specifying one hot wall, one cold wall, and four other fields being mirrors.

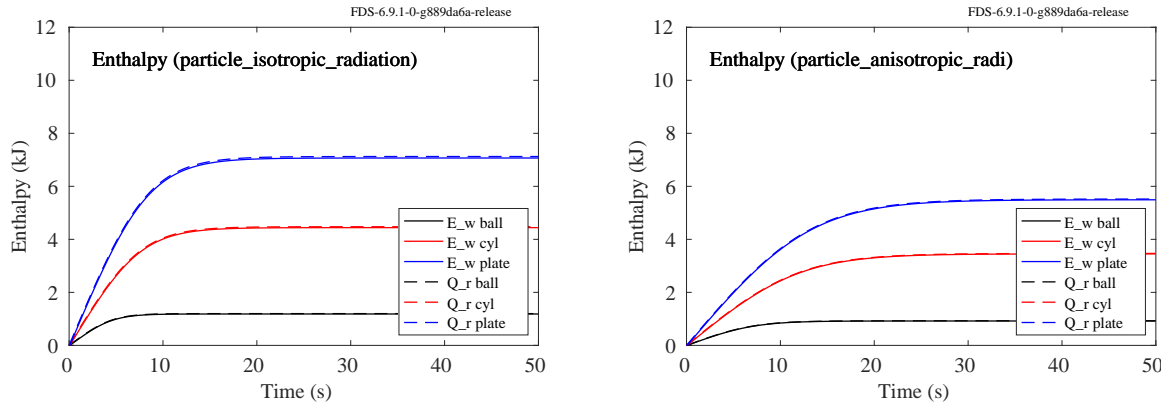


Figure 9.9: Absorbed energy of spherical, cylindrical and cartesian particles in isotropic (left) and anisotropic (right) radiation field.

## 9.9 Radiation Attenuation by Scattering Particles (`part_attenuation`)

This case is a qualitative assessment of the attenuation of thermal radiation by four different types of particles. In each case, the radiation is computed inside a one meter cube with one hot and five cold walls.

The radiative heat flux is monitored on the wall that is opposite the hot wall. In each case, 10 g of non-evaporating, monodisperse,  $100 \mu\text{m}$  particles with a density of  $1,000 \text{ kg/m}^3$  are placed inside the cube. Five different cases are computed. The reference case contains no particles. The four other cases contain transparent particles, water droplets, fuel droplets, and opaque particles. Different methods to specify the refractive index are tested. For water and fuel droplets, the FDS internal tables are used. For transparent particles, the refractive index is  $m = 1.0 + 0i$ . For opaque particles, the refractive index is  $m = 1.5 + 0.5i$ . The resulting heat fluxes are plotted in Fig. 9.10. The transparent particles do not attenuate the radiation, and the relatively opaque particles give the highest attenuation. The heat fluxes through water and fuel droplets fall between the two extremes.

This case also demonstrates the finite convergence rate of the radiation calculations with scattering media. As can be seen, the radiation field is not converged to its final value instantaneously because there are no internal iterations in the radiation solver. As a result, a slight increase of the heat flux is observed after 0.5 s, which is the third time step, i.e. the second call of the radiation solver. Further, smaller increase can be seen three steps later. In real applications with small time steps, the time lag of the radiation field is small.

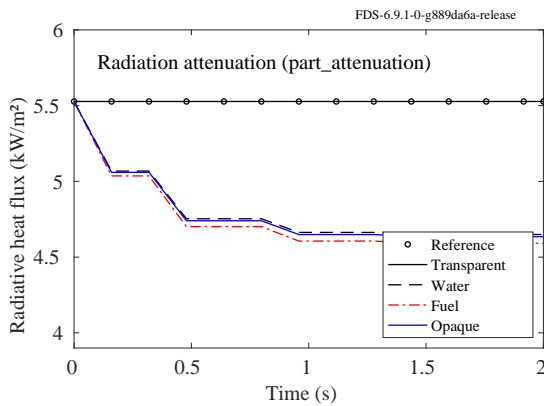


Figure 9.10: Attenuation of thermal radiation by four different classes of Lagrangian particles.

## 9.10 Radiation Attenuation by Non-Scattering Particles (radiation\_gas-veg\_consistency)

Relatively large solid particles, like idealized vegetation, act as opaque, non-scattering absorbers of thermal radiation. For a cloud of particles contained within a region  $\Omega$  with volume  $V$ , the absorption coefficient is taken to be

$$\kappa_p = \sum_{m \in \Omega} \frac{A_{s,m}}{4V} \quad (9.6)$$

where  $A_{s,m}$  is the surface area of particle  $m$ . For this test case, the space between two infinitely wide parallel plates, 1 m apart, is filled with either a gas with constant absorption coefficient,  $\kappa = 5.04 \text{ m}^{-1}$ , or a uniform distribution of monodisperse solid spheres of radius  $0.7614 \text{ mm}$  and density  $514 \text{ kg/m}^3$  such that the total mass of spheres per unit volume is  $m''' = 2.63 \text{ kg/m}^3$ . In the simulation, only one particle per grid cell is used to represent all the particles in that cell. The effective absorption coefficient can be calculated:

$$N_p = \frac{m''' V}{m_p} \quad ; \quad \kappa_p = N_p \frac{A_{s,m}}{4V} = 5.04 \text{ m}^{-1} \quad (9.7)$$

Here,  $N_p$  is the actual number of spheres represented by the single particle within a grid cell that is 10 cm on each side.

Figure 9.11 displays the radiative heat flux at various distances from the hot plate, demonstrating that the cloud of particles act the same way as a gas with constant absorption coefficient.

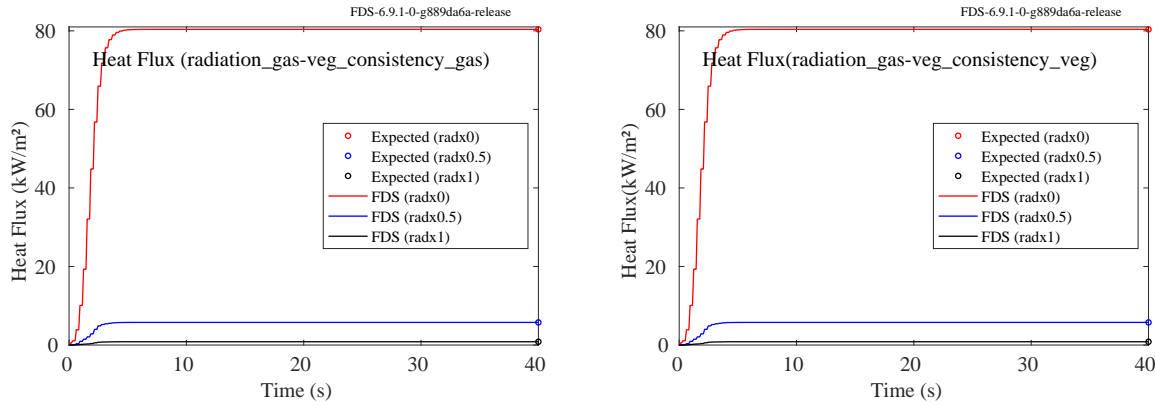


Figure 9.11: Heat flux at various distances from an infinitely wide hot plate where the radiation is attenuated by either a gas with constant absorption coefficient (left) or a cloud of monodisperse, non-scattering spheres (right).

## 9.11 Transient Thermocouple Response ( $\text{TC\_heating}$ )

A thermocouple is placed in the center of a 1 m cube with walls set to 600 °C and gas temperature set to 20 °C. The heat transfer coefficient is set to zero to eliminate convective heating. The gas temperature remains at 20 °C because there is no convective heat transfer from the walls. The thermocouple heats up according to the equation:

$$\rho_{\text{TC}} c_{\text{TC}} V_{\text{TC}} \frac{dT_{\text{TC}}}{dt} = \varepsilon_{\text{TC}} \sigma A_{\text{TC}} (T_s^4 - T_{\text{TC}}^4) \quad (9.8)$$

whose analytical solution is:

$$t = \frac{\ln(x+1) - \ln(1-x) + 2 \tan^{-1}(x)}{4 \beta T_s^3} \Big|_{T_{\text{TC}}(0)}^{T_{\text{TC}}(t)} ; \quad \beta = \frac{\varepsilon_{\text{TC}} \sigma A_{\text{TC}}}{\rho_{\text{TC}} c_{\text{TC}} V_{\text{TC}}} ; \quad x = \frac{T_{\text{TC}}}{T_s} \quad (9.9)$$

Figure 9.12 displays the thermocouple response compared to the analytical solution.

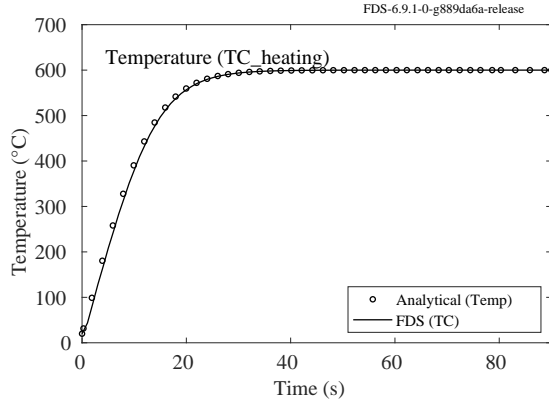


Figure 9.12: Increasing temperature of a thermocouple surrounded by walls at 600 °C.

## 9.12 Radiation and Thermocouples (`tc_view_factor`)

This case tests the radiation solver using the simple thermocouple model in FDS. Suppose that a small, thermally thin metal bead is at the center of a 1 m cube. The left half of the cube boundary surface is at 20 °C, the right half at 500 °C. Assume that there is no convective heat transfer to the bead; only radiation. Assume everything has an emissivity of 1. The bead temperature ought to rise to a steady value of

$$T_{\text{TC}} = \left( \frac{T_1^4 + T_2^4}{2} \right)^{\frac{1}{4}} - 273.15 = \left( \frac{293.15^4 + 773.15^4}{2} \right)^{\frac{1}{4}} - 273.15 = 380.3 \text{ °C} \quad (9.10)$$

The thermocouple model in FDS uses the integrated intensity divided by 4,  $U/4$ , as the average heat flux to the bead surface. In the absence of convection, the steady value of the bead temperature ought to be

$$T_{\text{TC}} = \left( \frac{U}{4\sigma} \right)^{\frac{1}{4}} - 273.15 \quad (9.11)$$

This is essentially what is plotted in Fig. 9.13, compared to the ideal value as computed in Eq. (9.10).

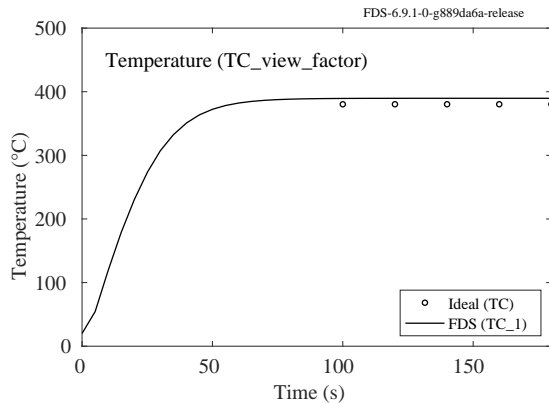


Figure 9.13: Temperature of a thermocouple equidistant from walls at temperatures of 20 °C and 500 °C.

## 9.13 Radiation Targets (`target_test`)

This case tests the functionality of particle “targets;” that is, massless Lagrangian particles that serve to record the heat flux at a given point with a given orientation. Essentially, the particle is an infinitesimally small heat flux gauge. Two unit cubes are set up, each with a top surface set to 1000 °C. In one cube, a small solid obstruction is created with a device embedded in its top facing upwards. In the other cube, a plate-shaped particle is placed at the same location and given an upward facing orientation. The radiative heat flux to both the obstruction and the particle should be the same, as shown in Fig. 9.14.

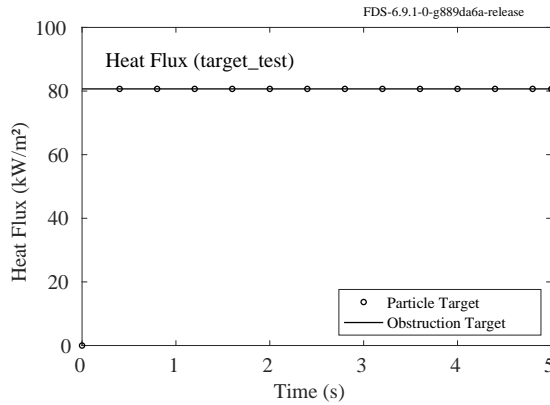


Figure 9.14: Heat flux from a hot plate to two different types of targets.

## 9.14 Radiation Shield (`radiation_shield`)

A lead radiation shield with a thickness of 0.1 mm is placed between two infinitely wide parallel plates at 500 °C and 20 °C. The computational domain has dimensions of 10 m by 0.1 m by 1 m. The sides of the domain are assumed to be symmetry planes. The emissivity,  $\varepsilon_3$ , of the lead shield is 0.48 on both sides. At 400 s, the shield is removed. Assuming that there is no convective heat transfer and that the emissivity of the hot and cold plates is 1, the steady-state heat flux to the cold plate should be [77]:

$$\dot{q}_{12}'' = \frac{\sigma(T_1^4 - T_2^4)}{\frac{1}{\varepsilon_1} + \frac{1}{\varepsilon_2} + 2\left(\frac{1-\varepsilon_3}{\varepsilon_3}\right)} = 4.76 \text{ kW/m}^2 \quad (9.12)$$

where  $T_1$  and  $T_2$  are the hot and cold plate temperatures, respectively, and  $\varepsilon_1$ ,  $\varepsilon_2$ , and  $\varepsilon_3$  are the emissivity values for the hot plate, cold plate, and lead shield, respectively. When the shield is removed at 400 s, the heat flux should increase to 19.8 kW/m<sup>2</sup>. The predicted heat flux is given in Fig. 9.15. Because the heat flux from the hot plate to the shield is equal to the heat flux from the hot plate to the cold plate, the shield temperature can be calculated using [77]:

$$\dot{q}_{12}'' = \dot{q}_{13}'' = \frac{\sigma(T_1^4 - T_3^4)}{\frac{1}{\varepsilon_1} + \frac{1}{\varepsilon_3} - 1} \quad ; \quad T_3 = 380.4 \text{ °C} \quad (9.13)$$

The predicted shield temperature is plotted in Fig. 9.15.

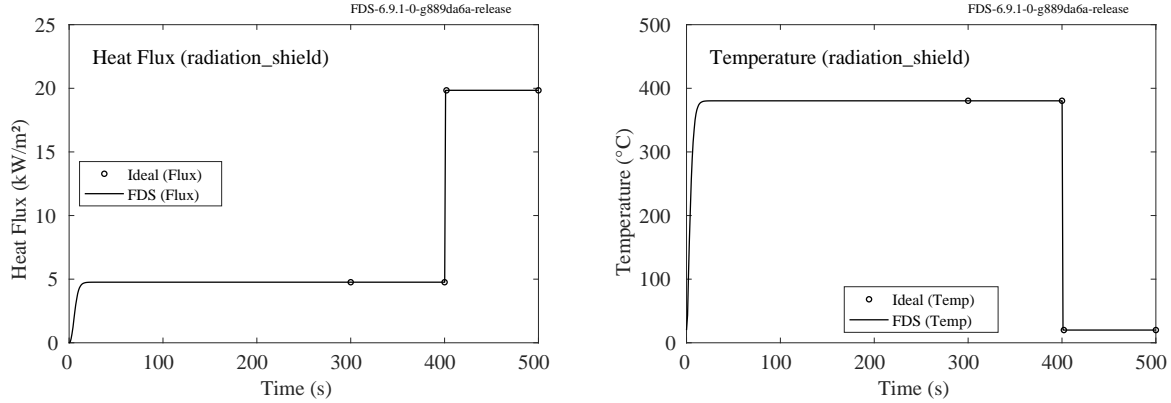


Figure 9.15: (Left) Heat flux to a cold plate separated from a hot plate by a heat shield. At 400 s, the shield is removed. (Right) Temperature of the heat shield.

## 9.15 Radiation from a gas-fired panel (`radiation_gas_panel`)

A gas-fired panel is often used as a source of thermal radiation in laboratory experiments. Here, the heat flux from an  $h = 30.48$  cm square panel is computed at distances of 10 cm, 15 cm, 25 cm, 38 cm, 46 cm, 61 cm, and 76 cm along its perpendicular center axis, and along a perpendicular line that is displaced laterally 14 cm and vertically 14 cm from the center axis, as illustrated in Fig. 9.16. We compare the results computed by FDS to those calculated using configuration factors. The temperature and emissivity of the panel are set to 1250 K and 0.7, respectively, and the ambient temperature is 273 K.

The configuration factor,  $dF_{2 \rightarrow 1}$ , describing the energy exchange between the radiant panel and a target with differential area  $dA_1$  located on a perpendicular line extending from the panel at the point  $(\bar{x}, \bar{y})$  is computed from the following:

$$dF_{2 \rightarrow 1}(R; \bar{x}, \bar{y}) = \frac{dA_1}{\pi A_2} \int_{-h/2}^{h/2} \int_{-h/2}^{h/2} \frac{R^2}{[(x - \bar{x})^2 + (y - \bar{y})^2 + R^2]^2} dx dy \quad (9.14)$$

The comparison of FDS and the exact solution is shown in Fig. 9.16.

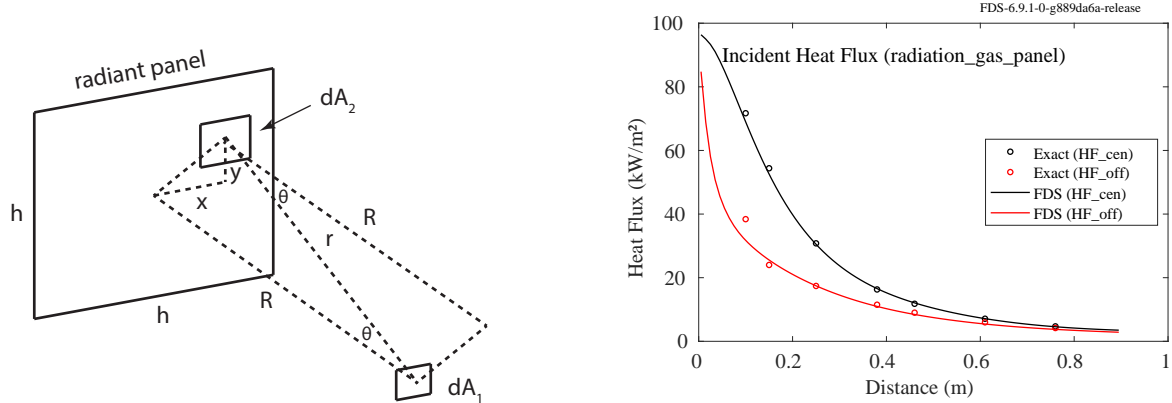


Figure 9.16: *Left:* A radiant panel and target  $dA_1$  located a distance  $R$  from the panel on its center axis. *Right:* Comparison of FDS and the exact result.

## 9.16 Radiation in Angled Geometry (net\_rad\_1000)

This verification case evaluates the radiation predicted between two angled surfaces using two approaches. The first approach uses a stair-stepping approach to represent the angled wall with rectilinear geometry. The second approach uses the cut-cell geometry for one wall.

Figure 9.17 shows the model performance with the stair-stepping approach. The two lines show the net radiation exchange on different faces of the angled geometry. Figure 9.18 shows the model performance with the cut-cell geometry approach.

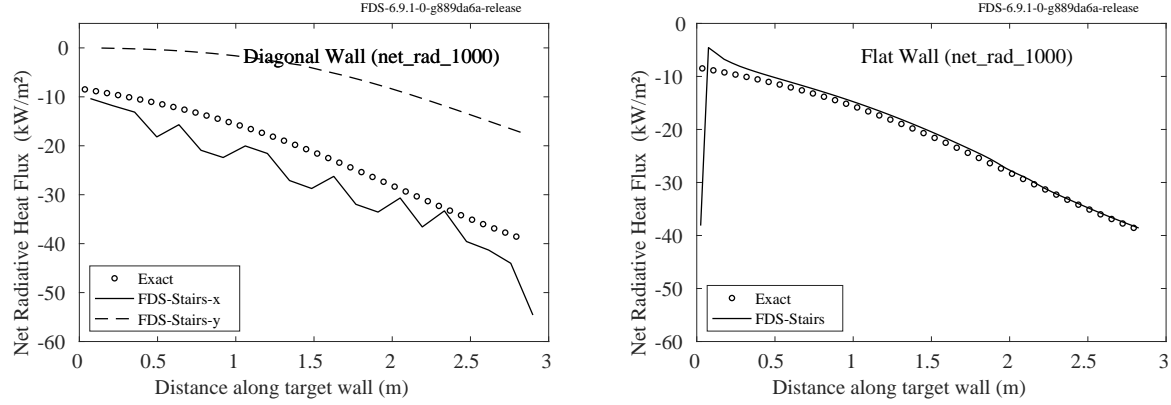


Figure 9.17: Angled geometry radiation verification, stair-stepping approach *Left*: Diagonal wall. *Right*: Flat wall.

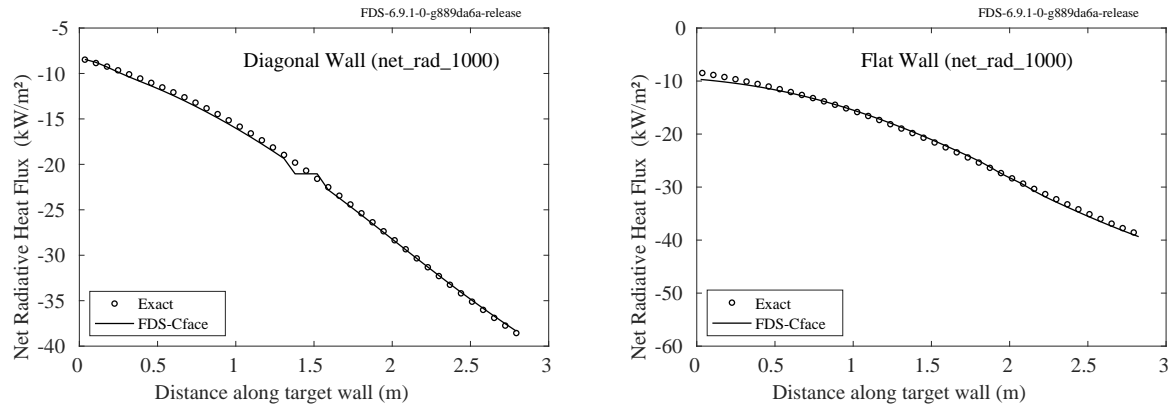


Figure 9.18: Angled geometry radiation verification, cut-cell approach *Left*: Diagonal wall. *Right*: Flat wall.

# **Chapter 10**

## **Species and Combustion**

This chapter contains examples that test the computations related to species concentrations, gas properties and combustion.

### **10.1 Gas Properties (`species_props`)**

This is a test of computing the gas properties of species mixtures. Three species are defined. The first species has a molecular weight of 10 g/m, a viscosity of 0.00001 kg/(m s), a conductivity of 0.01 W/(mK), and a specific heat of 1 kJ/(kg K). The second species multiplies the first species' inputs by two (e.g. molecular weight of 20 g/m), and the third species multiplies the first species' inputs by three. Five mixtures are tested: pure species 1; pure species 3; equal volume fractions of species 1 and species 2; equal volume fractions of all species; and volume fractions of 0.6, 0.3, and 0.1 respectively for the three species.

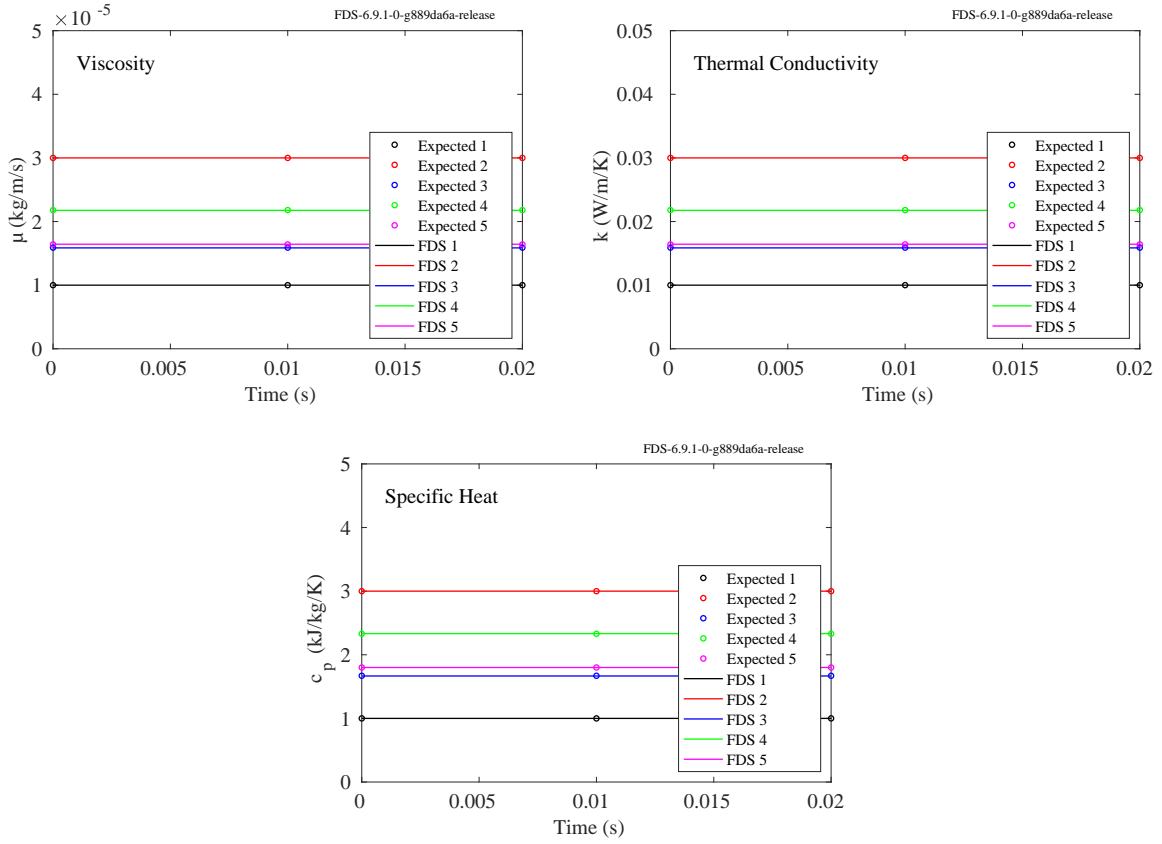


Figure 10.1: Results of the `species_props` cases.

## 10.2 Humidity (`humidity`)

This is a test of the relative humidity computation. A simple case is run with the ambient temperature set to 70 °C and the ambient humidity set to 30 %. The figure compares the FDS initial mass fraction of water vapor against a hand calculation.

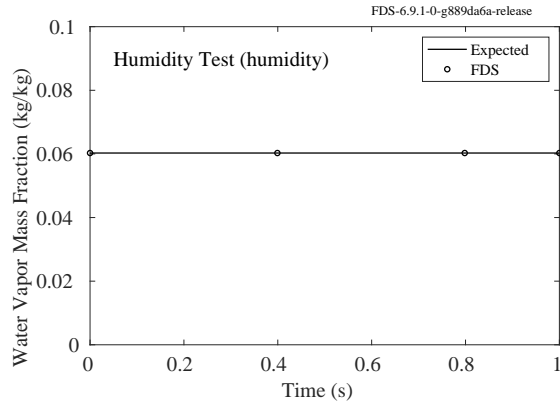


Figure 10.2: Test of 30 % relative humidity at 70 °C.

### 10.3 Product Yields (`methane_flame`)

A simple methane flame with 10 % CO yield is burned inside a closed cavity for 5 s. The total mass of CO<sub>2</sub>, H<sub>2</sub>O and CO is recorded. The simulation is performed using the three alternative ways to define the combustion reaction: *simple chemistry*, *primitive species*, and *lumped species*. The same amount of each product species should be produced in each case. The following figure compares the mass of the three combustion products. The figure compares the simple chemistry versus the primitive species versus the lumped species.

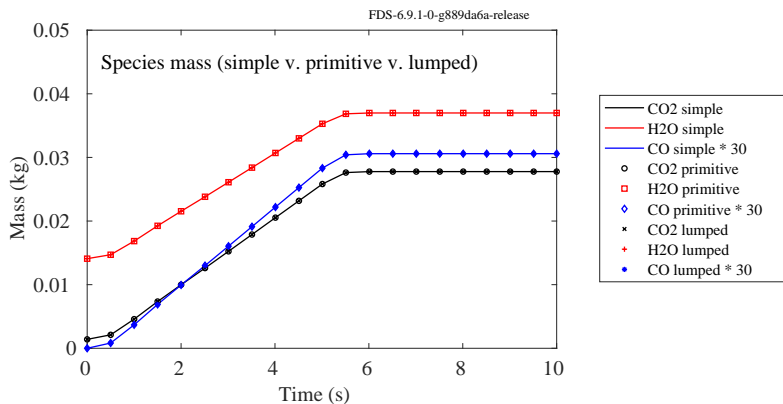


Figure 10.3: The combustion product masses using three alternative definitions of the reaction: Simple chemistry vs. primitive species vs. lumped species.

### 10.4 Reaction Rates (`reactionrate`)

This section describes a series of test cases designed to check the reaction rate mechanism using the eddy dissipation concept model for infinitely fast reactions (EDC) and finite-rate (Arrhenius) reactions. In the most basic sense, if a reaction occurs the rate of the reaction is either infinite or finite-rate. For an infinite-rate reaction, the rate is limited by the minimum reactant concentration. For  $i$  finite-rate reactions, the rate of species  $\alpha$  is dependent on factors such as local species concentration ( $Y_\alpha$ ), temperature ( $T$ ), and Arrhenius

parameters ( $E, A, a$ ):

$$\frac{dY_\alpha}{dt} = -\frac{1}{\rho} \sum_i \left( \frac{v_{\alpha,i} W_\alpha}{v_{F,i} W_F} \right) A'_i T^{n_i} e^{-E_i/RT} \prod Y_\alpha^{a_{\alpha,i}} \quad \text{where } A'_i = A_i \rho^{\sum a_\alpha} \prod W_\alpha^{-a_{\alpha,i}} \quad (10.1)$$

Detailed discussion on the combustion routines can be found in the FDS Technical Reference Guide [1].

#### 10.4.1 Mixing-Controlled Reactions (reactionrate\_EDC)

The cases presented in the section are designed to examine species evolutions for reactions of varying complexity using the EDC model with infinitely fast chemistry. The first test case is a one-step methane reaction that occurs in a constant volume, adiabatic “reactor” with a fixed mixing time of  $\tau_{\text{mix}} = 0.125$  s. Each computational cell contains a stoichiometric mixture of fuel and air. In this problem “air” is defined to be 21 % oxygen and 79 % nitrogen by volume.

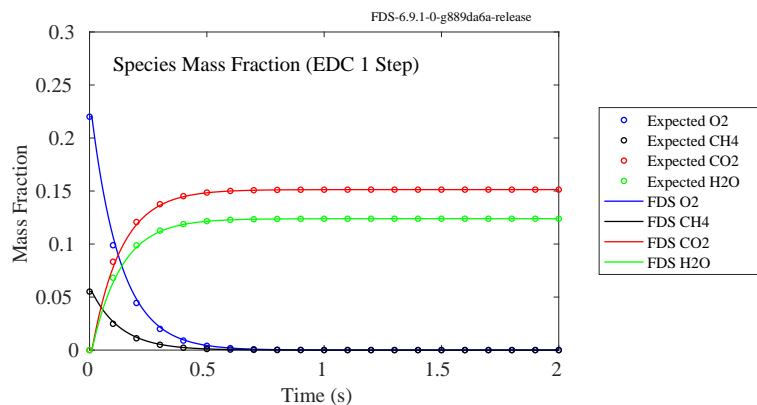


Figure 10.4: Time evolution of species mass fraction for a one-step methane EDC reaction with a fixed mixing time of  $\tau_{\text{mix}} = 0.125$  s.

In addition to species, we want to compare FDS predictions for temperature and pressure. For this reacting system, the internal energy remains constant, thus the temperature can be found from:

$$\bar{u}_{P,\alpha} - \bar{u}_{R,\alpha} = 0 \quad (10.3)$$

where P represents the products, R represents the reactants, and  $\bar{u}_\alpha = \bar{h}_\alpha - RT$ . The total enthalpy,  $\bar{h}_\alpha$ , is defined as the sum of the enthalpy of formation ( $\bar{h}_f^\circ$ ) and sensible enthalpy ( $\Delta\bar{h}$ ) for each of the  $\alpha$  species. Assuming the products behave like an ideal gas, the final pressure can be found using the equation of state for an ideal gas:

$$PV = nRT \quad (10.4)$$

Under the same conditions as the methane case, species, temperature, and pressure are compared to expected results for a one-step propane reaction:



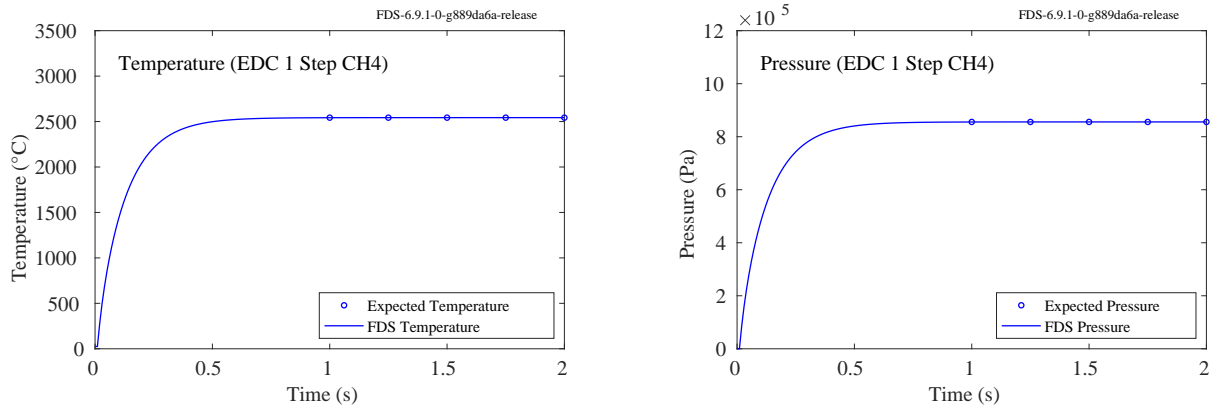


Figure 10.5: Time evolution of temperature and pressure for a one-step methane EDC reaction with a fixed mixing time of  $\tau_{mix} = 0.125$  s.

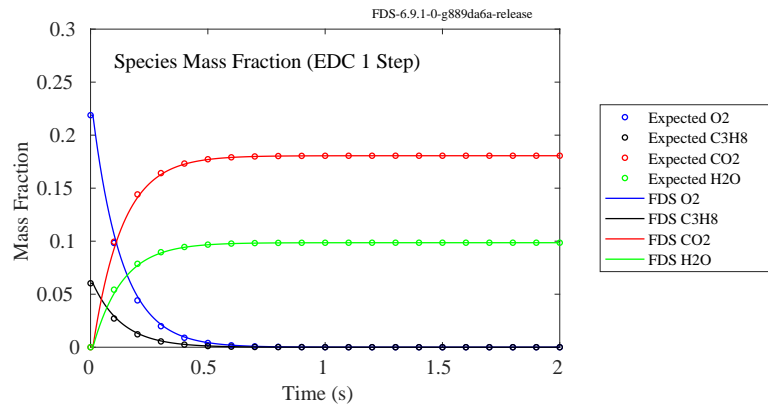


Figure 10.6: Time evolution of species mass fraction for a one-step propane EDC reaction with a fixed mixing time of  $\tau_{mix} = 0.125$  s.

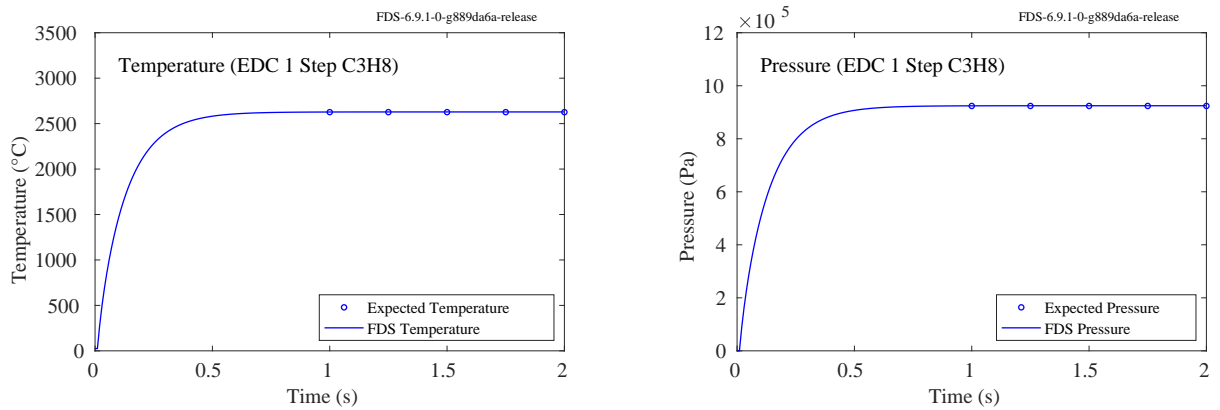


Figure 10.7: Time evolution of temperature and pressure for a one-step propane EDC reaction with a fixed mixing time of  $\tau_{mix} = 0.125$  s.

The results for the propane case are shown in Figs. 10.6 (species) and 10.7 (temperature and pressure).

In the previous two examples, each computational cell contained a stoichiometric mixture of fuel and air. For this third example, the cells are initialized to be all fuel in one part of the reactor and all air in the remaining volume. Globally, the reactor is fuel rich and follows the same one-step methane reaction as described by 10.2. Figures 10.8 and 10.9 show the species concentrations, temperature, and pressure from FDS and the expected values. In this case, the final state is not reached until approximately 35 s compared to 1 s for the cases where each cell contained a flammable composition.

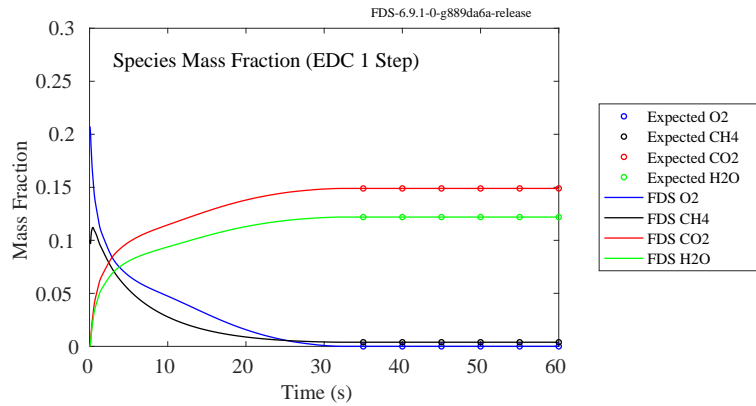


Figure 10.8: Time evolution of species mass fraction for a one-step methane EDC reaction with a fixed mixing time of  $\tau_{\text{mix}} = 0.125$  s.

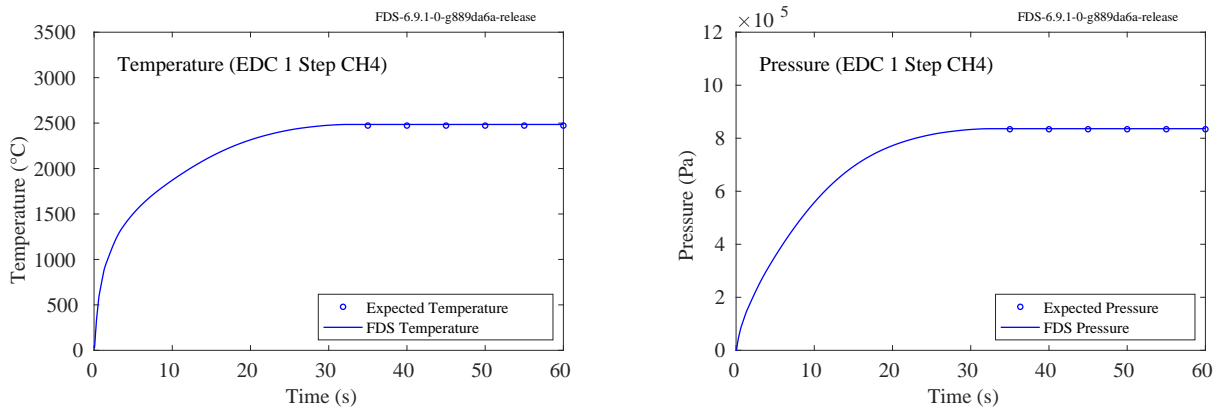


Figure 10.9: Temperature (left) and pressure (right) evolution for a one-step methane EDC reaction with a fixed mixing time of  $\tau_{\text{mix}} = 0.125$  s.

The EDC reaction implementation is also tested to check species evolution for chemical reactions of increased complexity. The first is a consecutive two-step, fuel-limited methane reaction:



Each cell in the model reaction is initialized with an oxygen rich mixture and the mixing time,  $\tau_{\text{mix}}$ , is fixed at 0.05 s (Fig. 10.10).

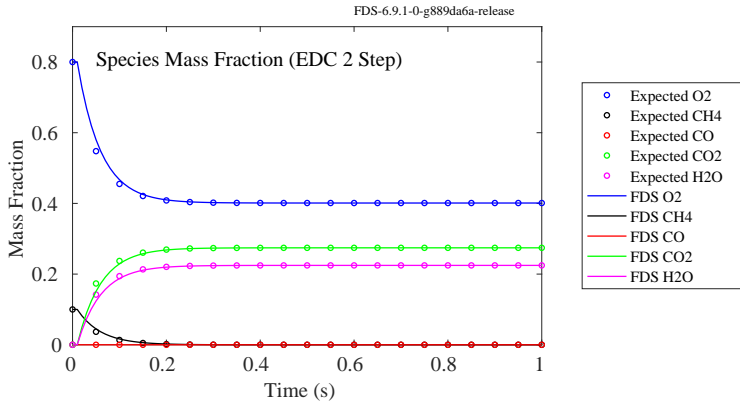
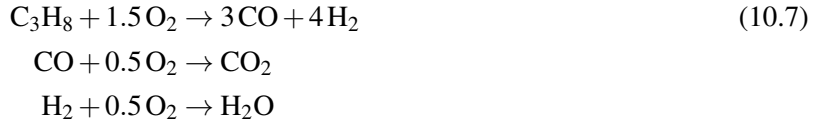


Figure 10.10: Time evolution of species mass fraction for a series, fuel-limited EDC reaction with a fixed mixing time of  $\tau_{\text{mix}} = 0.05$  s.

The second reaction test case is a consecutive three-step, fuel limited propane reaction:



The species evolutions are compared to expected values in Fig. 10.11.

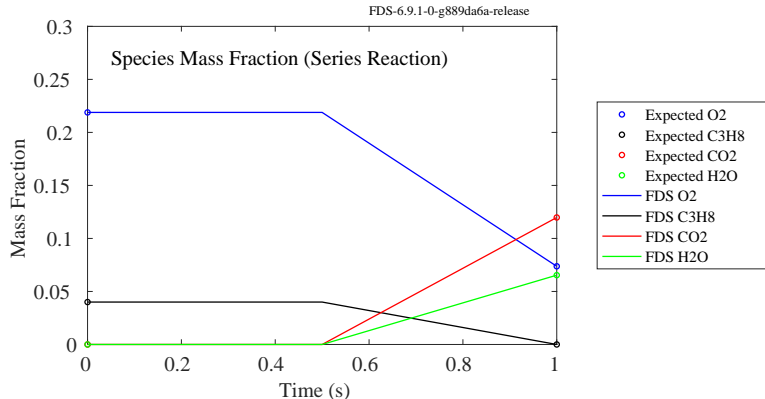


Figure 10.11: Results of the `reactionrate_series_reaction` case.

The third test case has two competing, oxygen-limited reactions; a one-step methane and one-step propane reaction.



The species evolutions are compared to expected values in Fig. 10.12.

The fourth test case has propane (fuel), competing with two identical but separately lumped air species. Each cell is initialized with stoichiometric amount of fuel and air; each air is initialized in equal quantities.



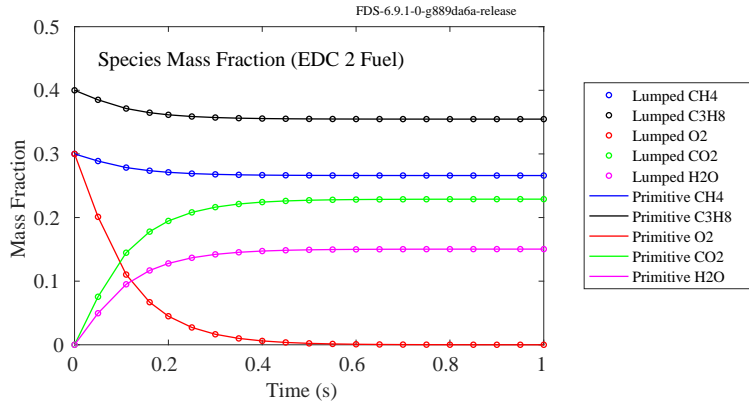
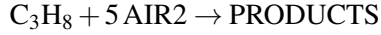


Figure 10.12: Time evolution of species mass fraction for oxygen-limited EDC two fuel reaction set with a fixed mixing time of  $\tau_{\text{mix}} = 0.1$  s.



The lumped species used in these reactions are defined by:

```
&SPEC ID = 'PROPANE' /
&SPEC ID = 'OXYGEN', LUMPED_COMPONENT_ONLY = .TRUE. /
&SPEC ID = 'NITROGEN', LUMPED_COMPONENT_ONLY = .TRUE. /
&SPEC ID = 'WATER VAPOR', LUMPED_COMPONENT_ONLY = .TRUE. /
&SPEC ID = 'CARBON DIOXIDE', LUMPED_COMPONENT_ONLY = .TRUE. /

&SPEC ID = 'AIR1', SPEC_ID = 'OXYGEN', 'NITROGEN', VOLUME_FRACTION = 1, 3.76,
BACKGROUND=.TRUE. /
&SPEC ID = 'AIR2', SPEC_ID = 'OXYGEN', 'NITROGEN', VOLUME_FRACTION = 1, 3.76 /
&SPEC ID = 'PRODUCTS', SPEC_ID = 'CARBON DIOXIDE', 'WATER VAPOR',
'NITROGEN', VOLUME_FRACTION = 3, 4, 18.8 /
```

The species evolutions are compared to expected values in Fig. 10.13.

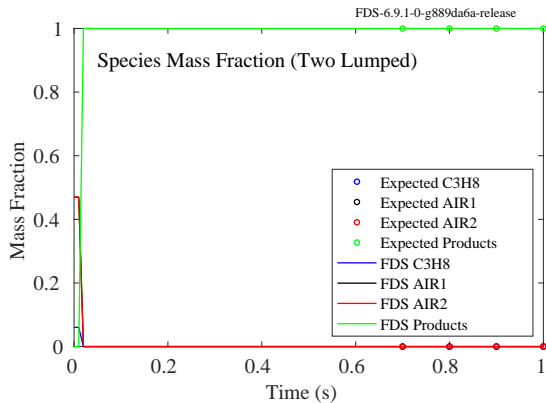


Figure 10.13: Results of the `reactionrate_lumped_two_species` case.

### 10.4.2 Finite Rate Reactions (`reactionrate_arrhenius`)

The main difference between Arrhenius rate reactions and the mixing-controlled reactions is that the reaction rate in finite rate reactions is found from local parameters such as species concentration and temperature as well as rate constants. The values of  $a_\alpha$  in Eq. (10.1) are specific to each reaction and for non-zero values,  $dY_\alpha/dt$  becomes a non-linear differential equation. We consider both linear and non-linear cases with one and two-step reaction mechanisms. First we examine two one-step cases; a zero-order and second-order reaction. Equation (10.10) shows a one-step, zero-order test case of carbon monoxide oxidation:



The reaction rate input parameters are shown in the table below.  $E$ ,  $a_\alpha$ , and  $n_\alpha$  are set to zero, and  $A$  is set such that  $k_i = 1$ . The resulting reaction rates simplify to a function of molecular weight and stoichiometric coefficients. Species evolutions results from the CO reaction in Eq. (10.10) are shown in Fig. 10.14. The

Table 10.1: Arrhenius values for a single step CO reaction;  $\alpha = [\text{CO} \text{ O}_2 \text{ CO}_2]$ .

Reaction	$v_\alpha$	$E$ (J/mol)	$A$ (cm <sup>3</sup> /mole/s)	$a_\alpha$	$n_\alpha$
10.10	[-1 -0.5 1]	0	4.244e-6	[0 0 0]	[0 0 0]

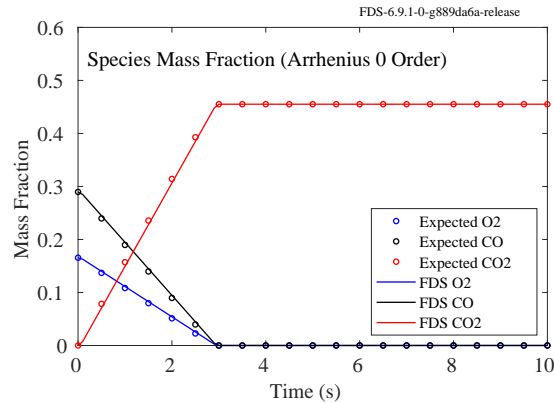


Figure 10.14: Time evolution of species mass fraction for a one-step zero-order Arrhenius finite rate reaction.

second finite rate test case is a one-step, second-order propane reaction, Eq. (10.5). The table below shows the reaction rate input parameters. In this case,  $a_\alpha = [1, 1, 0, 0]$  for propane, oxygen, carbon monoxide, and water vapor respectively. This makes the reaction second-order as  $\mathcal{O} = \sum a_\alpha$ . Species evolutions for the one-step second-order reaction are shown in Fig. 10.15. Multi-step Arrhenius finite rate reactions are also

Table 10.2: Arrhenius values for a single step C<sub>3</sub>H<sub>8</sub> reaction;  $\alpha = [\text{C}_3\text{H}_8 \text{ O}_2 \text{ CO}_2 \text{ H}_2\text{O}]$ .

Reaction	$v_\alpha$	$E$ (J/mol)	$A$ (cm <sup>3</sup> /mole/s)	$a_\alpha$	$n_\alpha$
10.5	[-1 -5 3 4]	0	4e5	[1 1 0 0]	[0 0 0 0]

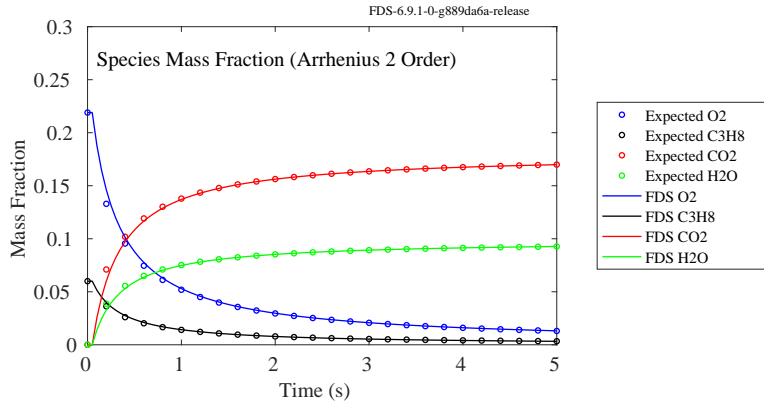


Figure 10.15: Time evolution of species mass fraction for a one-step second-order Arrhenius finite rate reaction.

examined. First, we consider a two-step forward propane reaction:

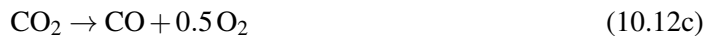


with the following reaction input parameters:

Table 10.3: Arrhenius values for a two-step C<sub>3</sub>H<sub>8</sub> reaction;  $\alpha = [\text{C}_3\text{H}_8 \text{ O}_2 \text{ CO} \text{ H}_2\text{O} \text{ CO}_2]$ .

Reaction	$v_\alpha$	E (J/mol)	A (cm <sup>3</sup> /mole/s)	$a_\alpha$	$n_\alpha$
10.11a	[-1 -3.5 3 4 0]	0	5e2	[0.1 1.65 0 0 0]	[0 0 0 0 0]
10.11b	[0 -0.5 -1 0 1]	0	8e3	[0 0.25 1 0.5 0]	[0 0 0 0 0]

The species evolutions for the two-step 1.75 order reaction mechanism are shown in Fig. 10.16. We also consider a two-step reversible propane reaction:



with the following reaction input parameters: Equations (10.12a)-(10.12c) includes the decomposition of

Table 10.4: Arrhenius values for a two-step reversible C<sub>3</sub>H<sub>8</sub> reaction;  $\alpha = [\text{C}_3\text{H}_8 \text{ O}_2 \text{ CO} \text{ H}_2\text{O} \text{ CO}_2]$ .

Reaction	$v_\alpha$	E (J/mol)	A (cm <sup>3</sup> /mole/s)	$a_\alpha$	$n_\alpha$
10.12a	[-1 -3.5 3 4 0]	0	5e2	[0.1 1.65 0 0 0]	[0 0 0 0 0]
10.12b	[0 -0.5 -1 0 1]	0	8e3	[0 0.25 1 0.5 0]	[0 0 0 0 0]
10.12c	[0 0.5 1 0 -1]	0	4e-4	[0 0 0 0 1]	[0 0 0 0 0]

CO<sub>2</sub> into CO and O<sub>2</sub> whereas the forward-only two-step mechanism, Eqs. (10.11a)-(10.11b), does not. This

reverse reaction mechanism is represented by three separate reactions on the REAC line in an FDS input file as indicated by rows a, b and c in the preceding table. Species evolutions for the 2 step reverse reaction are shown in Fig. 10.17. In the forward CO step, (row b in the two prior tables), we see that water vapor contributes to the reaction rate based on its local concentration despite not being a participant in the reaction.

Note: the values of  $E$  and  $A$  used in these examples are not necessarily representative of the chemical reactions presented. When using finite rate chemistry consult experimental data or literature for appropriate reaction parameters.

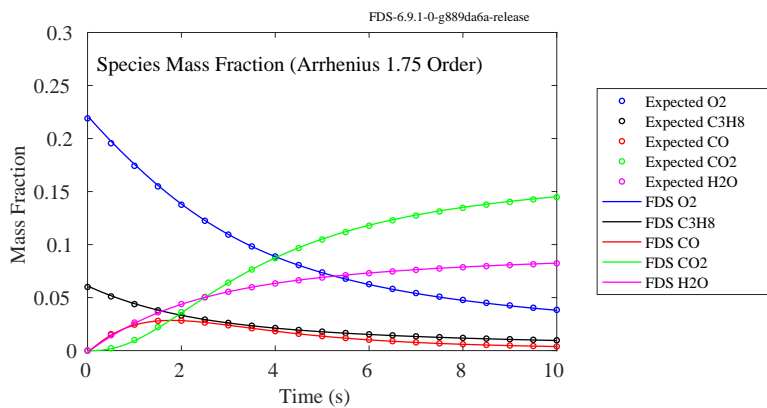


Figure 10.16: Time evolution of species mass fraction for a two-step Arrhenius finite rate propane reactions.

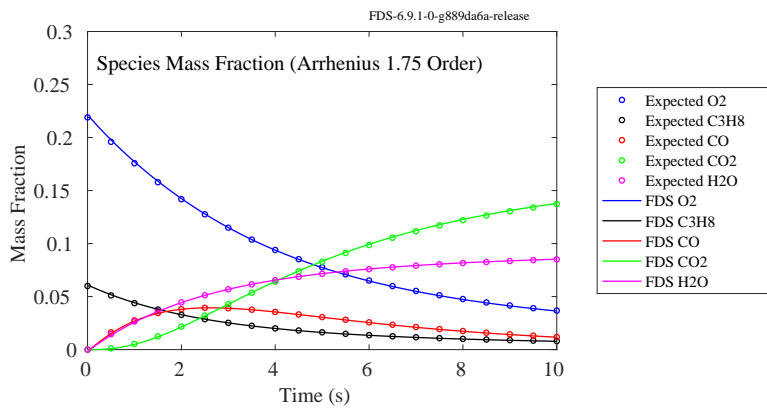


Figure 10.17: Time evolution of species mass fraction for a two-step reversible Arrhenius finite rate propane reactions.

To couple verification of species mass fraction, compartment temperature, and compartment pressure, an equilibrium example problem was setup. In this case, we examine a sealed box filled with a stoichiometric mixture of fuel, oxygen, and nitrogen. The two-step reversible reaction mechanism, Eqs. (10.12a)-(10.12c), is used to drive the FDS simulation. The initial temperature is set to 350 °C to ensure the reaction occurs in a timely manner. The reaction rate parameters in the table below are based off values in literature from Westbrook and Dryer [89]. Equilibrium values were determined using the NASA code Chemical Equilibrium with Applications (CEA) [90]. A constant volume, constant internal energy equilibrium calculation was performed where the equilibrium values were found by minimizing Helmholtz Energy. The equilibrium

Table 10.5: Arrhenius values for a two-step reversible  $\text{C}_3\text{H}_8$  reaction for equilibrium;  $\alpha = [\text{C}_3\text{H}_8 \text{ O}_2 \text{ CO H}_2\text{O CO}_2]$ .

Reaction	$v_\alpha$	E (J/mol)	A ( $\text{cm}^3/\text{mole/s}$ )	$a_\alpha$	$n_\alpha$
10.12a	[-1 -3.5 3 4 0]	125520	1.5e12	[0.1 1.65 0 0 0]	[0 0 0 0 0]
10.12b	[0 -0.5 -1 0 1]	167360	3.4e13	[0 0.25 1 0.5 0]	[0 0 0 0 0]
10.12c	[0 0.5 1 0 -1]	167360	8e8	[0 0 0 0 1]	[0 0 0 0 0]

species were limited to  $\text{C}_3\text{H}_8$ ,  $\text{O}_2$ ,  $\text{CO}$ ,  $\text{H}_2\text{O}$ , and  $\text{CO}_2$ ; the same species tracked in the FDS simulation. The results are shown in Figs. 10.18 and 10.19.

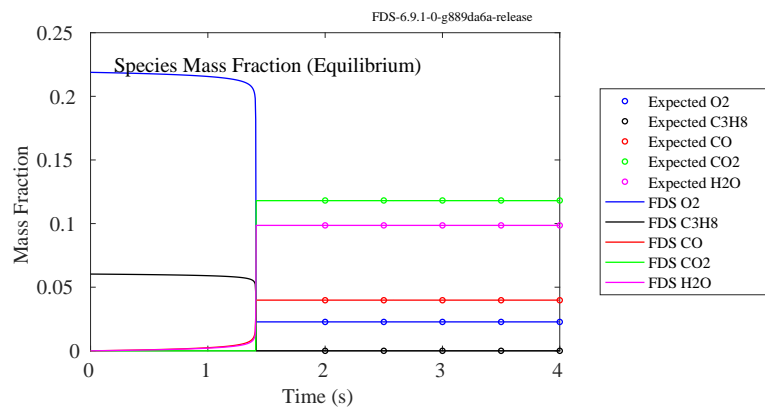


Figure 10.18: Time evolution of species mass fraction for a two-step Arrhenius finite rate reaction compared to equilibrium values.

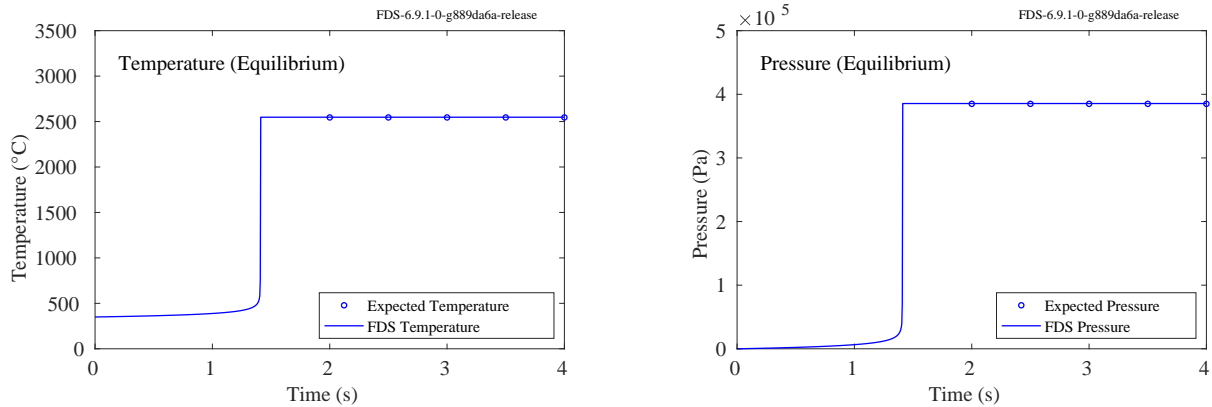


Figure 10.19: Time evolution of temperature (left) and pressure (right) for two-step Arrhenius finite rate propane reactions compared to equilibrium values.

### 10.4.3 Fast-Slow Reaction Scheme (`reactionrate_fast_slow`)

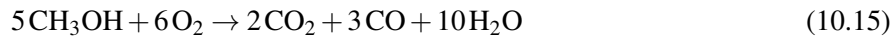
A simple two-step reaction scheme for a clean-burning fuel like methanol can be written as follows:



where the first reaction is infinitely fast and the second is not. Suppose the second reaction proceeds according to the evolution equation:

$$\frac{d[\text{CO}]}{dt} = -1 \times 10^{10} [\text{CO}] [\text{O}_2] \quad (10.14)$$

where  $[\text{CO}]$  is the concentration of CO in units of mol/cm<sup>3</sup>. To test the scheme, a sealed, adiabatic cube 1 m on a side is filled with nitrogen, fuel gas, and oxygen with initial volume fractions of 0.89, 0.05, and 0.06. Because the rates are independent of temperature, the reaction proceeds immediately assuming that the gases are thoroughly mixed via the parameter `INITIAL_UNMIXED_FRACTION=0`. Figure 10.20 shows the fuel volume fraction very quickly dropping to zero, leaving some oxygen which then reacts relatively slowly with CO to form CO<sub>2</sub>. The effective combined reaction is:



The '`EXPLICIT_EULER`' integration scheme is used with an initial gas phase time step of  $1 \times 10^{-6}$  s. The final volume fractions of CO<sub>2</sub> and CO are expected to be  $2/104 \approx 0.0192$  and  $3/104 \approx 0.0288$ , respectively.

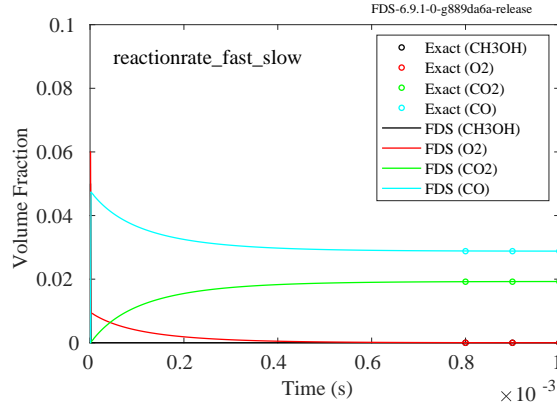


Figure 10.20: Species evolution in a fast-slow reaction scheme.

## 10.5 Heat Release Rates from Reaction Mechanisms (`hrrpuv_reac`)

One of the most important quantities computed in FDS is the heat release rate per unit volume (HRRPUV),  $\dot{q}'''$ . HRRPUV shows up in the energy equation and hence the expression for the velocity divergence (see the FDS Tech Guide [48]). The value of  $\dot{q}'''$  within a computation cell can be computed two ways, which should be equivalent. The first is to use individual species heats of formation times the respective chemical production rates:

$$\dot{q}''' = - \sum_{\alpha} \dot{m}_{\alpha}''' \Delta h_{f,\alpha}^{\circ} \quad (10.16)$$

Note that Eq. (10.16) is what is ultimately used in the FDS divergence expression.

The second is to sum the individual reaction rates times their respective heats of combustion, which are precomputed in the read routines in FDS:

$$\dot{q}''' = \sum_i r'_{F,i} \Delta H_{c,i} \quad (10.17)$$

Here F denotes the fuel for reaction  $i$ .

In this section, we show results comparing Eqs. (10.16) and (10.17) for a series of cases with different reaction mechanisms. This test series is meant to touch various pathways through the chemistry ODE solver involving mixing, fast and slow chemistry, extinction, and series and parallel reactions. The result are presented in Fig. 10.21. The measure of correctness is that the black dots (hrrpuv), taken from Eq. (10.16), exactly match with the sum of the individual reaction HRR curves denoted by the solid black line, Eq. (10.17). Below we briefly describe the key features of each case.

### Single Reaction (`hrrpuv_reac_single`)

This is a single reaction with specified lumped species without extinction.

### Series Reactions (`hrrpuv_reac_series`)

This is a set of series reactions with primitive species.

### Simple Reaction (`hrrpuv_reac_simple`)

This is FDS Simple Chemistry integrated using two Forward Euler substeps.

### **Reaction with Extinction (`hrrpuv_reac_extinction`)**

This is a single reaction with specified lumped species with extinction.

### **Parallel Reactions (`hrrpuv_reac_parallel`)**

This is a set of parallel reactions with two fuels going to one set of products.

### **Parallel Reactions (`hrrpuv_reac_parallel_2`)**

This is a set of parallel reactions with one fuel going to two products.

### **Arrhenius Reaction (`hrrpuv_reac_arrhenius`)**

This is simple Arrhenius rate law using the default ODE integrator for finite-rate chemistry, which is RK4.

### **Soot Production (`hrrpuv_reac_soot`)**

This example combines a fast reaction for the primary reaction with finite-rate chemistry for the soot oxidation reaction.

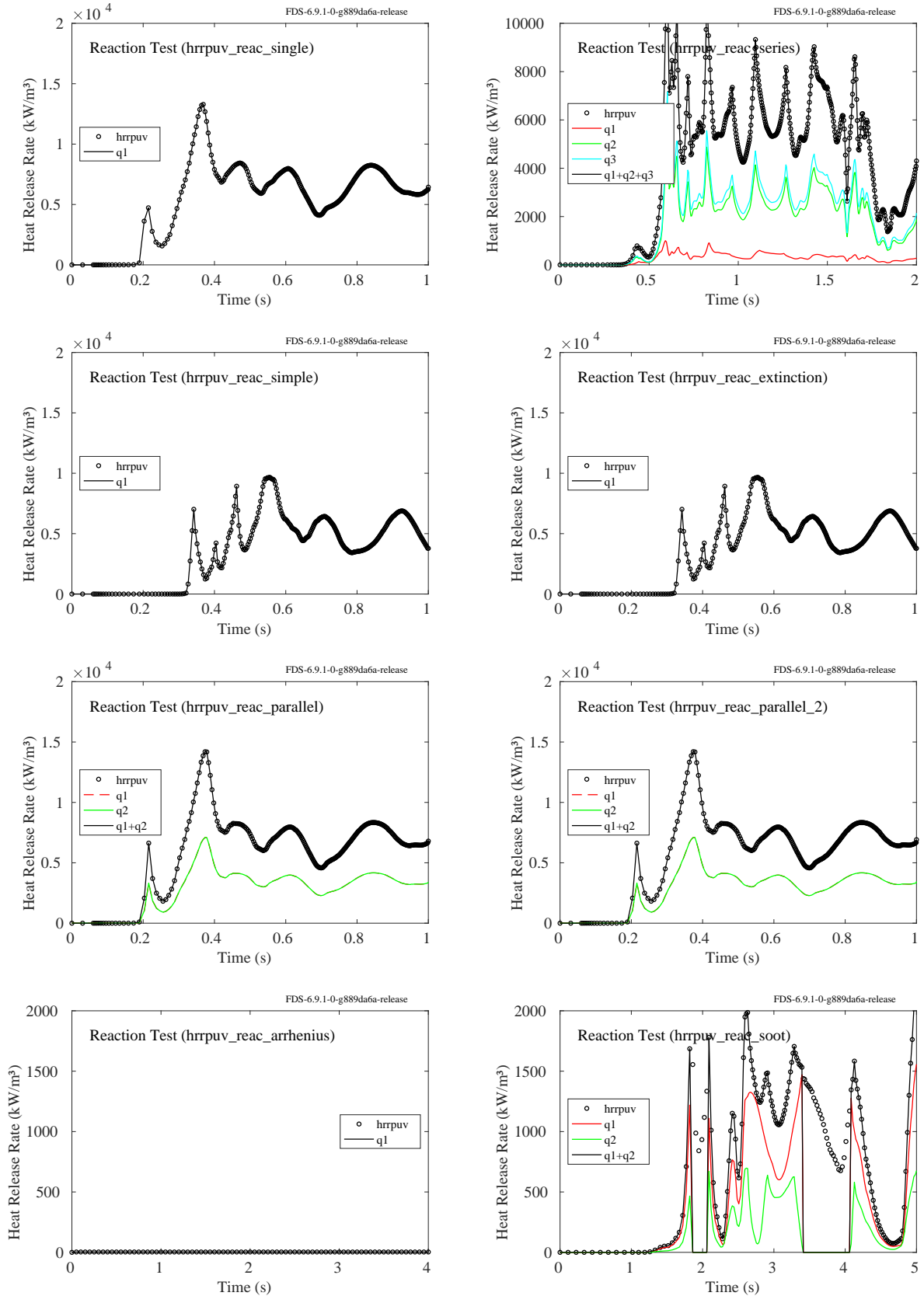
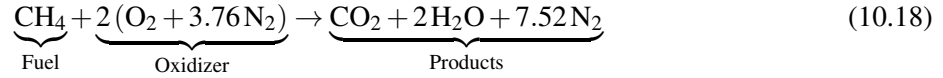


Figure 10.21: Heat release rate per unit volume for the various hrrpuv\_reac test cases.

## 10.6 Mixture Fraction (`burke_schumann`)

For simple one-step reactions of the form  $F + O \rightarrow P$ , there is an optional output quantity called the mixture fraction. To test that this output is correctly implemented we consider a set of methane-air mixtures in a test chamber that span the entire range of equivalence ratio. The complete combustion of methane is given by:



The simulation results are compared to state relationships that express temperature and species as a function of the mixture fraction,  $f$  [91]. For fuel rich mixtures ( $f_{\text{stoic}} < f \leq 1$ ), the expected species mass fractions are:

$$Y_F = \frac{f - f_{\text{stoich}}}{1 - f_{\text{stoich}}} \quad (10.19)$$

$$Y_O = 0 \quad (10.20)$$

$$Y_P = \frac{1 - f}{1 - f_{\text{stoich}}} \quad (10.21)$$

For fuel lean mixtures ( $0 \leq f < f_{\text{stoich}}$ ):

$$Y_F = 0 \quad (10.22)$$

$$Y_O = 1 - \frac{f}{f_{\text{stoich}}} \quad (10.23)$$

$$Y_P = \frac{f}{f_{\text{stoich}}} \quad (10.24)$$

Figure 10.22 demonstrates that the predicted final fuel, oxidizer, and product mass fractions obey the ideal state relations. The state relation for temperature is given by:

$$T = T_0 + (f - Y_F(f)) \frac{\Delta h_c}{c_v} \quad (10.25)$$

The specific heat,  $c_p$ , for each species is set to 1 kJ/(kg K) as in the analysis by Turns [91]. The enthalpy of formation of each of the species except for the fuel is set to zero, such that the heat of combustion of the reaction equals the heat of formation of the fuel. To obtain true adiabatic conditions in FDS, these cases were conducted inside a constant-volume reactor, so Eq. (10.25) is based on  $c_v$  rather than  $c_p$ . We use the following relationship  $c_v = c_p - R/W$  to determine  $c_v$ . The molecular weight of the species were not assumed to be uniform; thus, the average molecular weight and  $c_v$  vary with the mixture fraction. As a result, the traditional linear temperature profile is not expected. The FDS result is shown in Fig. 10.23.

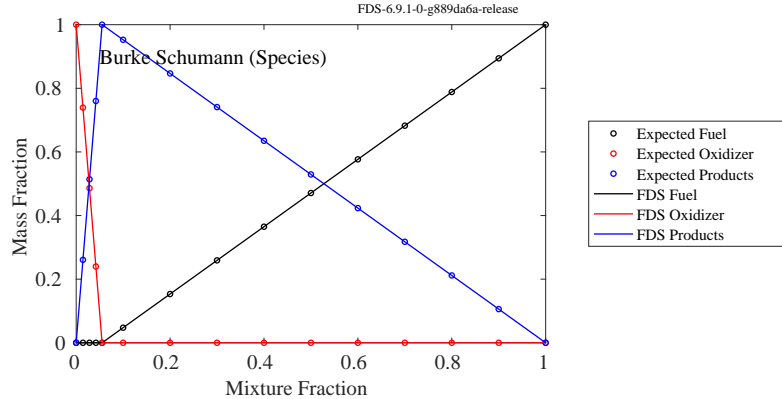


Figure 10.22: (Left) Lumped species mass fractions as a function of mixture fraction.

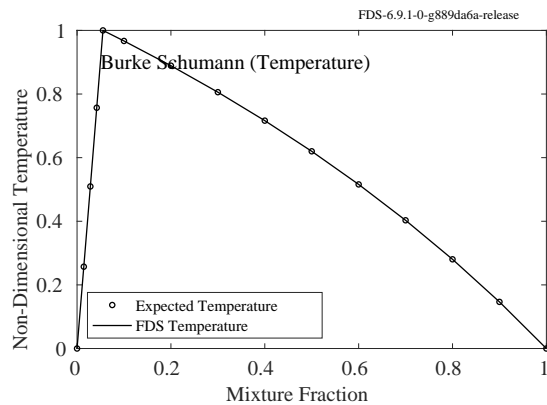


Figure 10.23: Non-dimensional temperature,  $(T - T_0)/(T_{\text{stoich}} - T_0)$ , as a function of the mixture fraction.

## 10.7 Ideal and Non-Ideal Heat of Combustion (H<sub>oc</sub>)

When using a non-predefined fuel, one may have heat of combustion data representing complete combustion but species yield data representing typical large scale conditions. When using simple chemistry, the input keyword `IDEAL=.TRUE.` on the `REAC` line will have FDS reduce the heat of combustion to account for any minor products of combustion (e.g., CO and H<sub>2</sub>O). This is done by removing energy from the heat of combustion to account for carbon that goes to CO and soot rather than CO<sub>2</sub> and for hydrogen that goes to soot rather than H<sub>2</sub>O. A custom fuel (methane) is defined with CO and soot yields of 0.1, a heat of combustion of 50000 kJ/kg, and a 40 kW fire. Two input files are created, one with the `HEAT_OF_COMBUSTION` defined with `IDEAL=.TRUE.` and the second with `IDEAL=.FALSE.`. In the `IDEAL=.FALSE.` case where the heat of combustion is not adjusted we expect a fuel mass flow rate of 0.0008 kg/(m<sup>2</sup> s). With the heat of combustion adjusted we expect a higher fuel mass flow rate of 0.000877 kg/(m<sup>2</sup> s), as shown in Fig. 10.24.

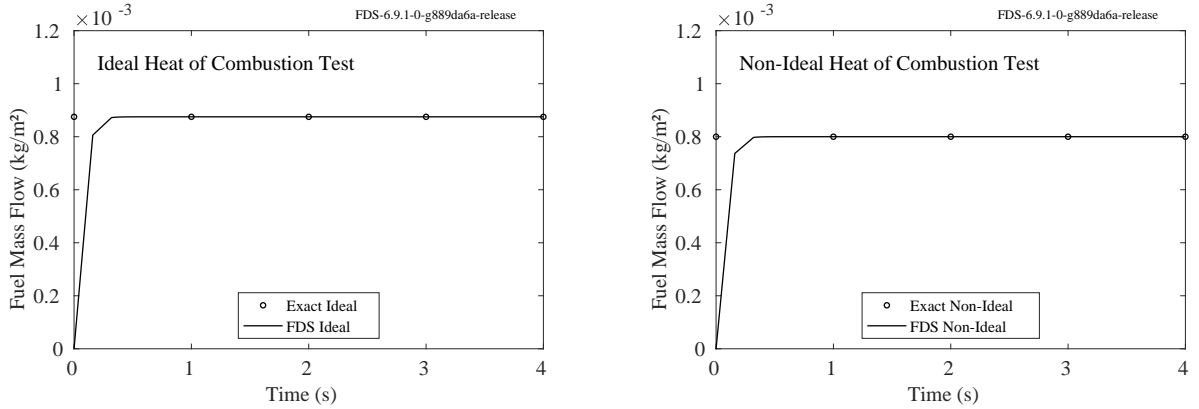


Figure 10.24: Demonstration of correct adjust to heat of combustion for minor products of combustion.

## 10.8 Single Step and Two Step Chemistry Heat of Combustion

This verification case checks that single-step and two-step simple chemistry results in the same total heat of combustion. The case consists of four  $1 \text{ m}^3$  domains with a 20 kW fire in each (one pair defined using `MLRPUA` and the other using `HRRPUA`) that burns for 8.5 s. Each burner is assigned the fuel  $\text{C}_3\text{H}_8$  (as a user defined species). In one mesh of each pair, single-step chemistry is used, and in the other mesh, two-step chemistry is used. The total heat released in all meshes should be the same as shown in Fig. 10.25.

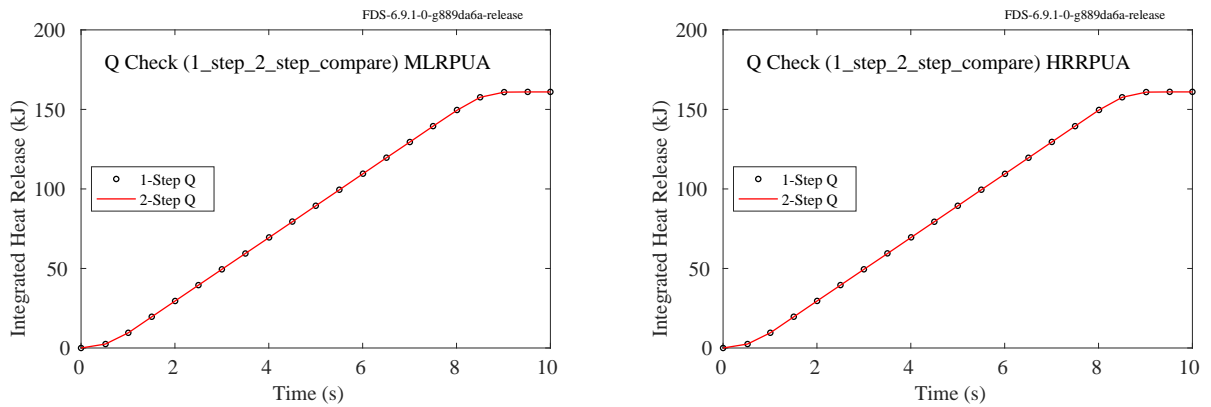


Figure 10.25: Comparison of the heat release rate for single-step and two-step simple chemistry with the `1_step_2_step_compare` test case. Left - `MLRPUA`. Right - `HRRPUA`

## 10.9 Fractional Effective Dose (FED) and Fractional Irritant Concentration (FIC) )

The Fractional Effective Dose index (FED), developed by Purser [92], is a commonly used measure of human incapacitation due to the combustion gases. The FED value is calculated as

$$\text{FED}_{\text{tot}} = (\text{FED}_{\text{CO}} + \text{FED}_{\text{CN}} + \text{FED}_{\text{NO}_x} + \text{FLD}_{\text{irr}}) \times \text{HV}_{\text{CO}_2} + \text{FED}_{\text{O}_2} \quad (10.26)$$

The fraction of an incapacitating dose of CO is calculated as

$$\text{FED}_{\text{CO}} = \int_0^t 2.764 \times 10^{-5} (C_{\text{CO}}(t))^{1.036} dt \quad (10.27)$$

where  $t$  is time (min), and  $C_{\text{CO}}$  is the CO concentration (ppm). The fraction of an incapacitating dose of CN is calculated as

$$\text{FED}_{\text{CN}} = \int_0^t \left( \frac{\exp\left(\frac{C_{\text{CN}}(t)}{43}\right)}{220} - 0.0045 \right) dt \quad (10.28)$$

where  $t$  is time (min), and  $C_{\text{CN}}$  is the concentration (ppm) of HCN corrected for the protective effect of  $\text{NO}_2$ .  $C_{\text{CN}}$  is calculated as

$$C_{\text{CN}} = C_{\text{HCN}} - C_{\text{NO}_2} \quad (10.29)$$

The fraction of an incapacitating dose of  $\text{NO}_x$  is calculated as

$$\text{FED}_{\text{NO}_x} = \int_0^t \frac{C_{\text{NO}_x}(t)}{1500} dt \quad (10.30)$$

where  $t$  is time (min), and  $C_{\text{NO}_x}$  is the sum of NO and  $\text{NO}_2$  concentrations (ppm). The Fractional Lethal Dose (FLD) of irritants is calculated as

$$\text{FLD}_{\text{irr}} = \int_0^t \left( \frac{C_{\text{HCl}}(t)}{F_{\text{FLD},\text{HCl}}} + \frac{C_{\text{HBr}}(t)}{F_{\text{FLD},\text{HBr}}} + \frac{C_{\text{HF}}(t)}{F_{\text{FLD},\text{HF}}} + \frac{C_{\text{SO}_2}(t)}{F_{\text{FLD},\text{SO}_2}} + \frac{C_{\text{NO}_2}(t)}{F_{\text{FLD},\text{NO}_2}} + \frac{C_{\text{C}_3\text{H}_4\text{O}}(t)}{F_{\text{FLD},\text{C}_3\text{H}_4\text{O}}} + \frac{C_{\text{CH}_2\text{O}}(t)}{F_{\text{FLD},\text{CH}_2\text{O}}} \right) dt \quad (10.31)$$

where  $t$  is time (min), the numerators are the instantaneous concentrations (ppm) of each irritant, and the denominators are the exposure doses of respective irritants predicted to be lethal to half the population. The lethal exposure doses [92] are given in the table below.

	HCl	HBr	HF	$\text{SO}_2$	$\text{NO}_2$	$\text{C}_3\text{H}_4\text{O}$	$\text{CH}_2\text{O}$
$F_{\text{FLD}}$ (ppm $\times$ min)	114000	114000	87000	12000	1900	4500	22500
$F_{\text{FIC}}$ (ppm)	900	900	900	120	350	20	30

The fraction of an incapacitating dose of low  $\text{O}_2$  hypoxia is calculated as

$$\text{FED}_{\text{O}_2} = \int_0^t \frac{dt}{\exp[8.13 - 0.54(20.9 - C_{\text{O}_2}(t))] \quad (10.32)}$$

where  $t$  is time (min), and  $C_{\text{O}_2}$  is the  $\text{O}_2$  concentration (volume percent). The hyperventilation factor induced by carbon dioxide is calculated as

$$\text{HV}_{\text{CO}_2} = \frac{\exp(0.1903 C_{\text{CO}_2}(t) + 2.0004)}{7.1} \quad (10.33)$$

where  $t$  is time (min), and  $C_{\text{CO}_2}$  is the  $\text{CO}_2$  concentration (volume percent).

The Fractional Irritant Concentration (FIC), also developed by Purser [92], represents the toxic effect which depends upon the immediate concentrations of irritants. The overall irritant concentration FIC is calculated as

$$\text{FIC}_{\text{irr}} = \frac{C_{\text{HCl}}(t)}{F_{\text{FIC},\text{HCl}}} + \frac{C_{\text{HBr}}(t)}{F_{\text{FIC},\text{HBr}}} + \frac{C_{\text{HF}}(t)}{F_{\text{FIC},\text{HF}}} + \frac{C_{\text{SO}_2}(t)}{F_{\text{FIC},\text{SO}_2}} + \frac{C_{\text{NO}_2}(t)}{F_{\text{FIC},\text{NO}_2}} + \frac{C_{\text{C}_3\text{H}_4\text{O}}(t)}{F_{\text{FIC},\text{C}_3\text{H}_4\text{O}}} + \frac{C_{\text{CH}_2\text{O}}(t)}{F_{\text{FIC},\text{CH}_2\text{O}}} \quad (10.34)$$

where the numerators are the instantaneous concentrations of each irritant, and the denominators are the concentrations of respective irritants expected to cause incapacitation in half the population. The incapacitating concentrations [92] are given in the table above.

### 10.9.1 FED and FIC of gas mixtures (`FED_FIC`)

The FED and FIC values were computed from specified constant gas concentrations for four cases using an external script. The gas concentrations are listed in the table below. The concentrations are in ppm.

Case ID	O <sub>2</sub> , CO <sub>2</sub> , CO	Asphyxiants	Irritants	All Gases
O <sub>2</sub>	97727	90218	209000	103055
CO <sub>2</sub>	343066	19189	0	7463
CO	3242	2456	0	1660
NO	0	134.9	0	89.34
NO <sub>2</sub>	0	0	1.139	0.569
HCN	0	265.3	0	204.0
HCl	0	0	68.33	34.17
HBr	0	0	68.33	34.17
HF	0	0	52.15	26.07
SO <sub>2</sub>	0	0	7.193	3.596
C <sub>3</sub> H <sub>4</sub> O	0	0	2.697	1.349
CH <sub>2</sub> O	0	0	13.49	6.743

Two versions of the simulations are performed. In the first simulation, the species were defined as individual tracked species. The FDS predictions and the expected FED and FIC values are compared in the figures below. In the second simulation, each species was defined as a lumped species, being part of the mixture using SMIX. Four different mixtures were defined. The results of this test are shown in Figs. 10.26 and 10.27.

### 10.9.2 FED from post-combustion yield of CO and HCN (`FED_CO_HCN`)

The calculation of FED resulting from post-combustion yields of CO<sub>2</sub>, CO and HCN, and the corresponding oxygen reduction is tested by specifying a combustion reaction of Polyisocyanurate (PIR) foam with 1 % CO yield and 0.5 % yield of HCN. The computational volume is initialized with 15 vol-% of combustion products. The species concentrations were measured by volume fraction devices, and the expected value of FED index was calculated using an external Matlab script. The results are shown in 10.28.

### 10.9.3 FED for a moving particle (`FED_moving`)

The calculation of FED for a moving particle representing an occupant is tested by specifying species concentrations at different levels throughout the domain and moving the particle through these areas. The species concentrations are initialized to known levels and the expected value of FED index was calculated using an external Matlab script. The results are shown in 10.29.

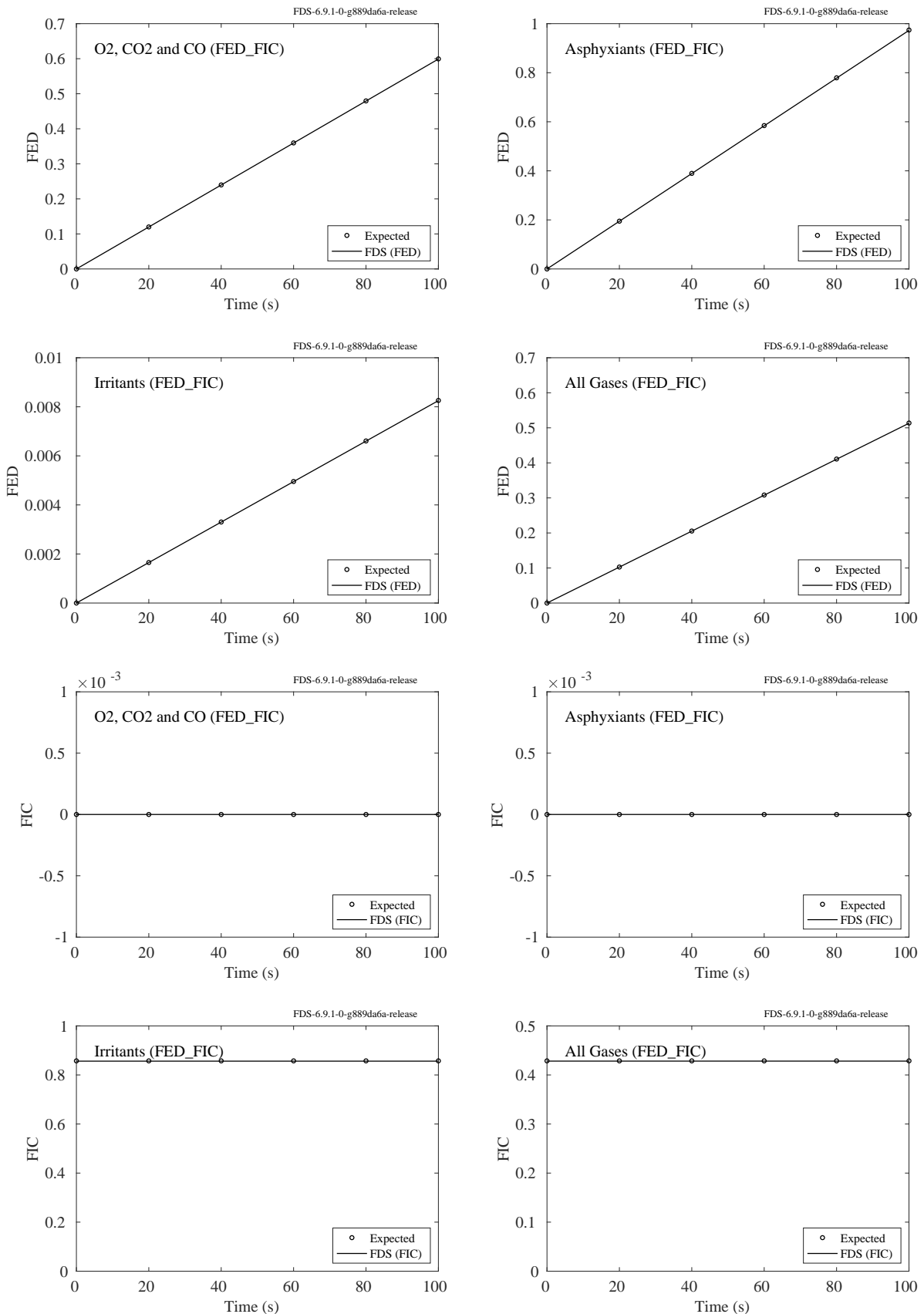


Figure 10.26: Comparison of FED and FIC predictions with expected values.

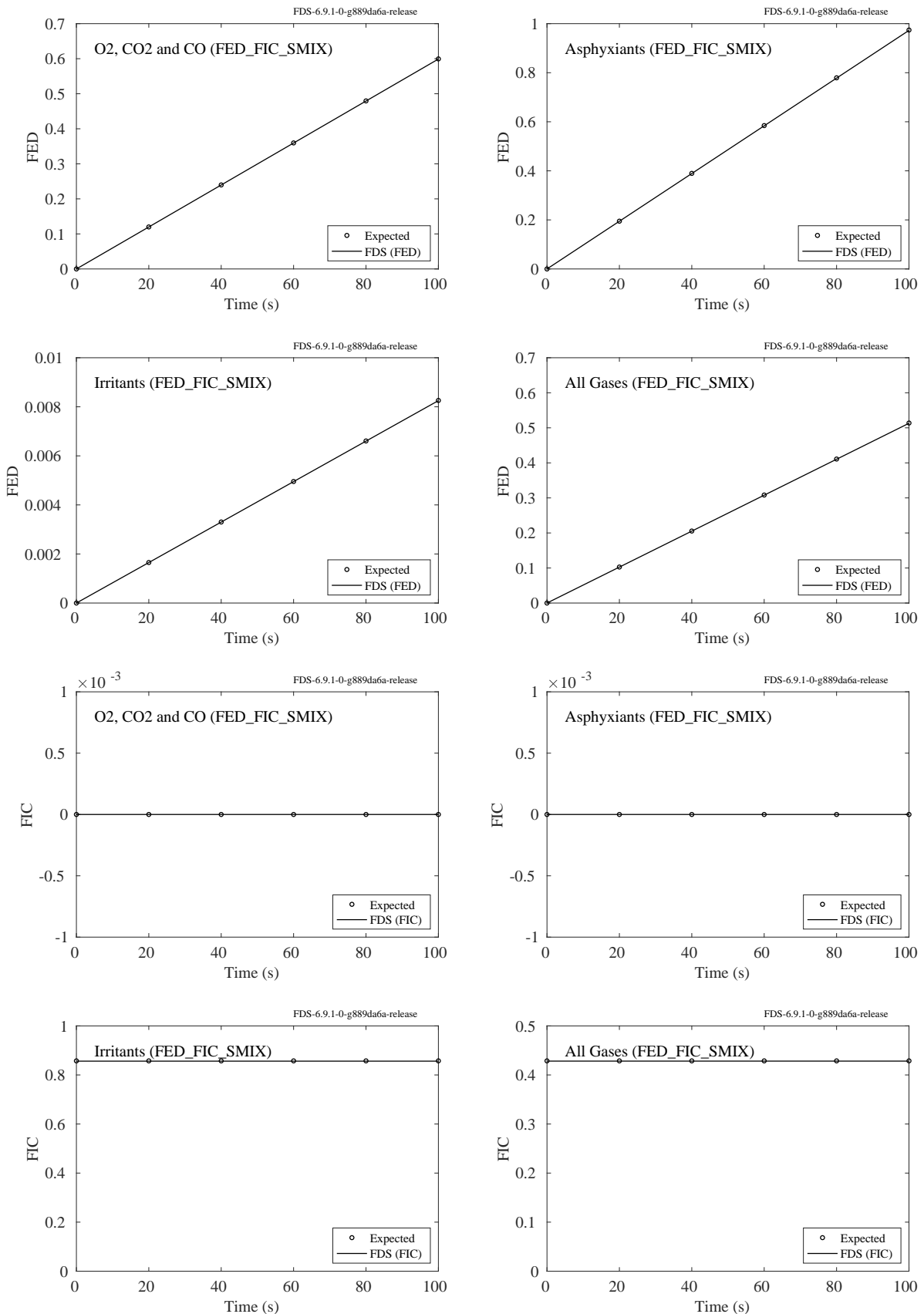


Figure 10.27: Comparison of FED and FIC predictions with expected values using SMIX.

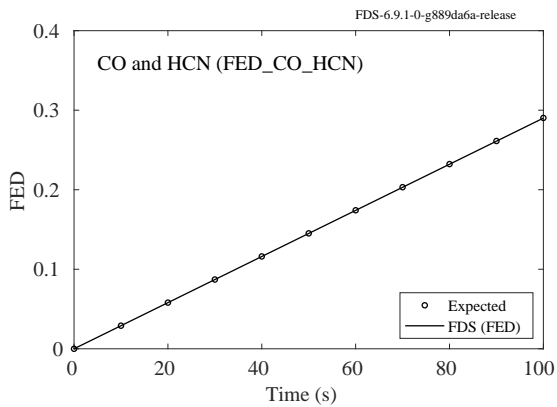


Figure 10.28: Comparison of predicted and expected FED resulting from the post-combustion yields of CO and HCN.

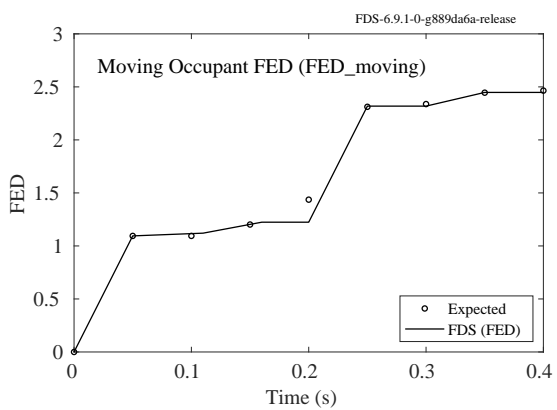


Figure 10.29: Comparison of predicted and expected FED for a moving particle.

## 10.10 Smoke Detector Model (`smoke_detector`)

The calculations described in this section check the smoke detector algorithm that computes the smoke obscuration in the sensing chamber of a detector. For this example, the initial soot mass fraction in a 1 m<sup>3</sup> box is set as 100 mg/kg via the `INIT` line. A vent on the left side injects soot at a velocity of 0.25 m/s and a mass fraction of 100 mg/kg, and the soot exhausts on the right side of the box via an open vent. By default, if a species is defined as an aerosol by setting `AEROSOL=.TRUE.` on the `SPEC` line, then all of the aerosol deposition mechanisms (gravitational, thermophoretic, and turbulent) will act upon that species. For this example, all deposition mechanisms are disabled by using the follows inputs on the `MISC` line:

```
&MISC GRAVITATIONAL_DEPOSITION = .FALSE.
    THERMOPHORETIC_DEPOSITION = .FALSE.
    TURBULENT_DEPOSITION      = .FALSE. /
```

The transient mass fraction of smoke in the sensing chamber of the detector  $Y_c$  is given as [1]

$$\frac{dY_c}{dt} = \frac{Y_e(t) - Y_c(t)}{L/\mathbf{u}} \quad (10.35)$$

where  $Y_e$  is the mass fraction of smoke in the free stream (kg/kg),  $L$  is the characteristic length of the detector geometry (m), and  $\mathbf{u}$  is the free stream velocity (m/s). For a constant mass fraction of smoke in the free stream  $Y_0$ , Eq. 10.35 has an analytical solution of the form

$$Y_c(t) = Y_0 \left[ 1 - \exp \left( -\frac{t\mathbf{u}}{L} \right) \right] \quad (10.36)$$

The resulting smoke mass fraction in the sensing chamber is converted into an obscuration by

$$O[\%/\text{m}] = \left( 1 - e^{-\kappa\rho Y_c l} \right) \times 100 \quad (10.37)$$

where  $\kappa$  is the specific extinction coefficient,  $\rho$  is the density of the external gases in the ceiling jet, and  $l$  is the preferred unit of length (1 m in this case). Fig. 10.30 shows a comparison of the analytical and simulated results for the time evolution of the smoke detector chamber obscuration.

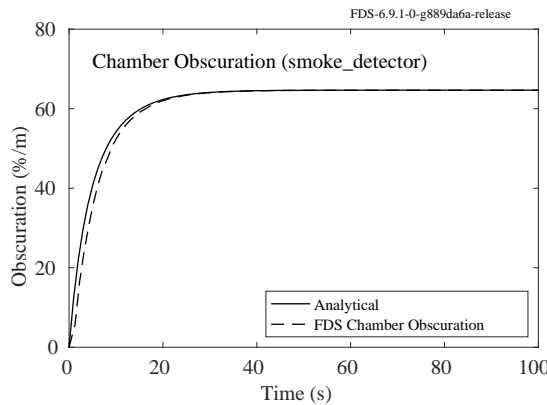


Figure 10.30: Time evolution of smoke detector chamber obscuration for `smoke_detector` case

## 10.11 Aerosol Behavior

### 10.11.1 Gravitational Settling and Deposition of Aerosols (`aerosol_gravitational_deposition`)

This verification test consists of two test cases. The second case, `aerosol_gravitational_deposition_2`, reverses the z-component of gravity. The case consists of a box 10 cm on side with adiabatic, free-slip side walls. The box is filled with two gas species each having a molecular weight of 28.8 g/mol, a viscosity of 0.00002 kg/(ms), a thermal conductivity of 0.025 W/(mK), and specific heat of 1 kJ/(kg K), and zero diffusivity. One of the gas species is defined as an aerosol with a diameter of 10  $\mu\text{m}$ , a solid phase density of 2000 kg/m<sup>3</sup>, and a solid phase conductivity of 1 W/(mK). The initial mass fraction of the aerosol is 0.00001. `STRATIFICATION`, `NOISE`, and all aerosol behaviors except for `GRAVITATIONAL_SETTLING` and `GRAVITATIONAL_DEPOSITION` are turned off. Since the box has a constant density over its height, a uniform settling rate over time is expected.

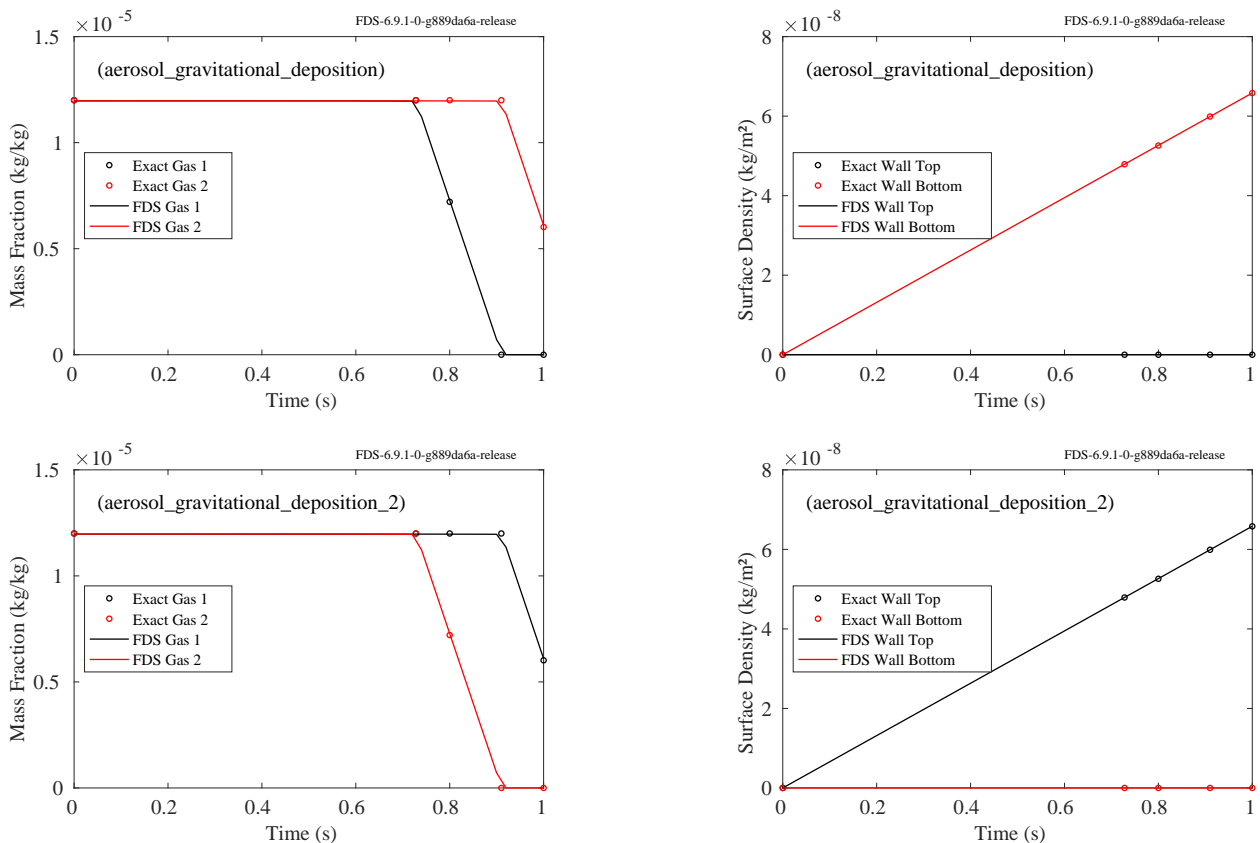


Figure 10.31: Time evolution of soot mass fraction in the gas (left) and soot surface density on the wall (right) for the `aerosol_gravitational_deposition` (Top) and `aerosol_gravitational_deposition_2` (Bottom) cases.

## 10.11.2 Thermophoretic Settling and Deposition of Aerosols (aerosol\_thermophoretic\_deposition)

This verification test consists of two test cases. The second case, `aerosol_thermophoretic_deposition_2`, reverses the temperature gradient. The case consists of a box 1 cm on side with adiabatic, free-slip side walls and a 100 K temperature gradient over the height of the box. The box is filled with two gas species each having a molecular weight of 28.8 g/mol, a viscosity of 0.00002 kg/(ms, a thermal conductivity of 0.025 W/(mK, and specific heat of 1 kJ/(kg K, and zero diffusivity. One of the gas species is defined as an aerosol with a diameter of 1  $\mu\text{m}$ , a solid phase density of 2000 kg/m<sup>3</sup>, and a solid phase conductivity of 1 W/(mK. The initial mass fraction of the aerosol is 0.00001. The gas temperature is initialized to its steady-state temperature gradient. STRATIFICATION, NOISE, and all aerosol behaviors except for THERMOPHORETIC\_SETTLING and THERMOPHORETIC\_DEPOSITION are turned off. Thermophoretic settling rates are weakly dependent on the gas density. Since there is a temperature gradient, the settling rates are not uniform over the height of the box. Unlike the gravitational settling case, this means over long enough time periods the overall settling rate is not linear in time; however, for a short time period a near linear settling rate is expected and can be determined analytically

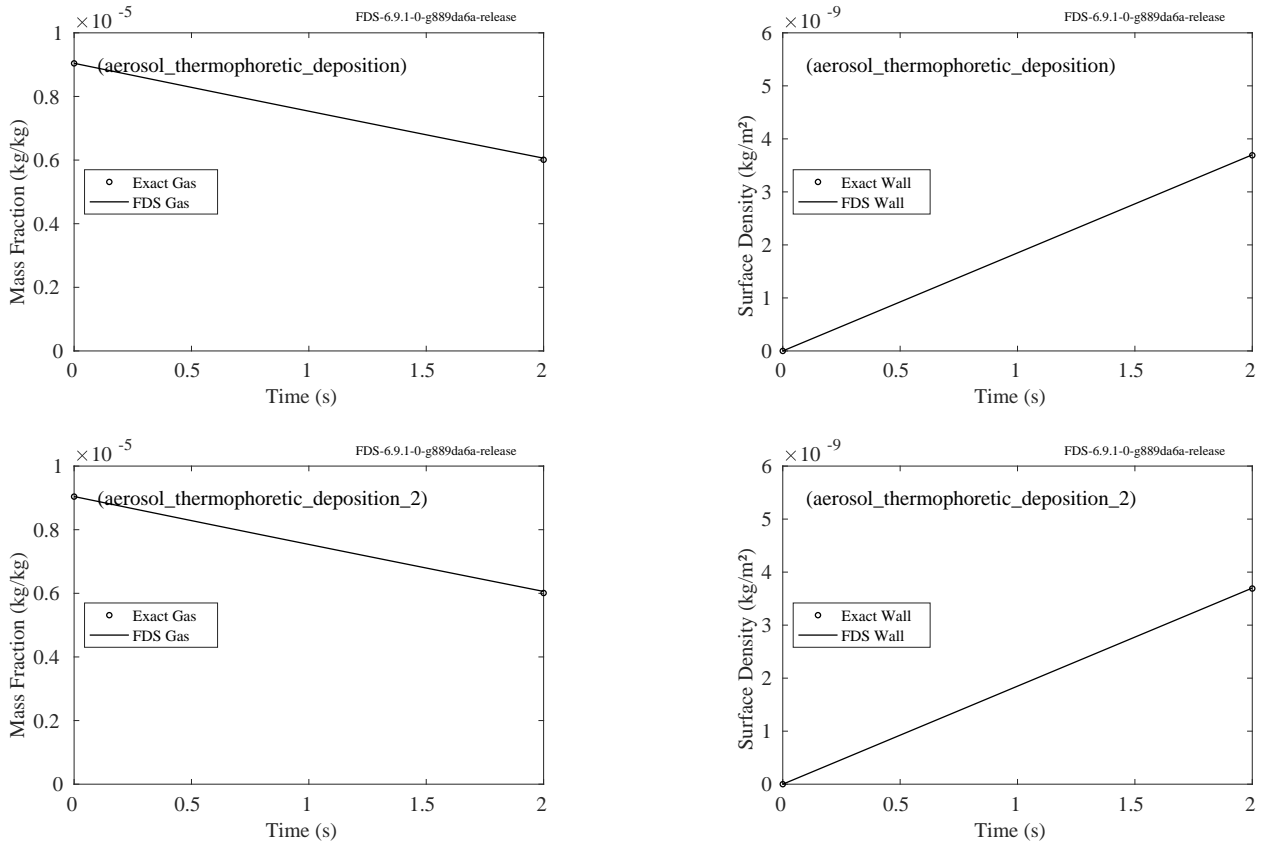


Figure 10.32: Time evolution of soot density in the gas (left) and soot surface density on the wall (right) for the `aerosol_thermophoretic_deposition` (Top) and `aerosol_thermophoretic_deposition_2` (Bottom) cases.

### 10.11.3 Turbulent Deposition of Aerosols (`aerosol_turbulent_deposition`)

This verification test consists of three tunnel like geometries 10 cm on side with adiabatic, free-slip walls. One end of the tunnel is OPEN and the other end has a constant inlet velocity of 0.001 m/s, 0.1 m/s, or 1 m/s. The tunnels are filled with two gas species each having a molecular weight of 28.8 g/mol, a viscosity of 0.00002 kg/(m s), a thermal conductivity of 0.025 W/(m K), and specific heat of 1 kJ/(kg K), and zero diffusivity. One of the gas species is defined as an aerosol with a diameter of 100  $\mu\text{m}$ , a solid phase density of 2000 kg/m<sup>3</sup>, and a solid phase conductivity of 1 W/(m K). The initial mass fraction of the aerosol is 0.00001. STRATIFICATION, NOISE, and all aerosol behaviors except for TURBULENT\_DEPOSITION are turned off. Turbulent deposition is computed using a correlation based open the wall friction velocity and the wall dimensionless stopping distance. The correlation has three parts, and the selected velocities test each part. Since the inlet condition is a constant velocity with a constant aerosol mass fraction, the first wall cell after the inlet will see a uniform settling rate over time.

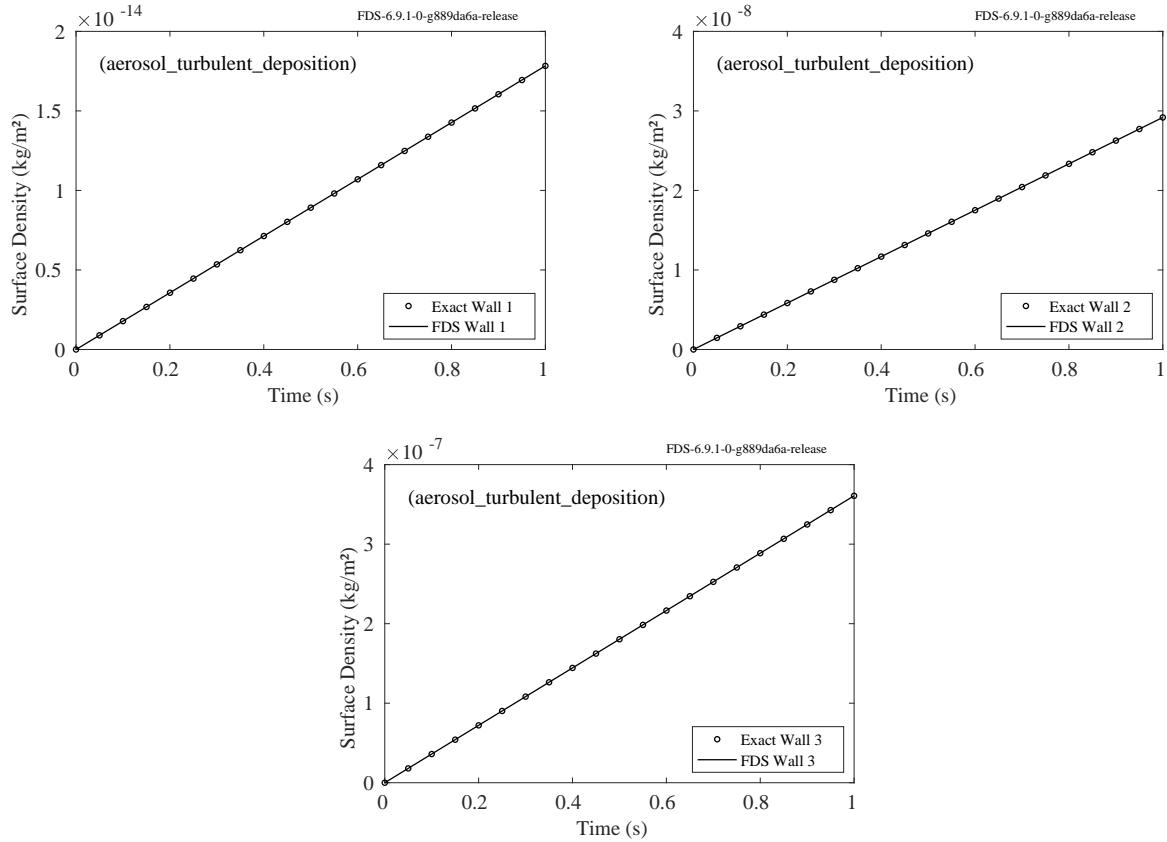


Figure 10.33: Time evolution of soot surface density on the wall for the `aerosol_turbulent_deposition`. Top left is the diffusion regime, top right is the diffusion-impaction regime, and bottom is the inertial regime.

### 10.11.4 Mass Conservation of Depositing Aerosols (`propane_flame_deposition`)

The calculations described in this section check the conservation of mass for the aerosol deposition algorithms. The example involves a reaction that invokes the aerosol deposition model in FDS (i.e., soot deposition). For this example, the fuel will be propane with a peak heat release rate of 100 kW and a 5 %

soot yield. For a 100 kW propane fire (HEAT\_OF\_COMBUSTION of 44,715 kJ/kg), the associated burning rate is 2.236 g/s. A RAMP is used to specify a burning rate from a propane burner that ramps up linearly to 2.236 g/s from 0 s to 1 s, remains steady at 2.236 g/s from 1 s to 4 s, then linearly decreases to 0 g/s from 4 s to 5 s. The total fuel mass released is 8.944 g of propane. Therefore, the resulting mass of soot should be equal to 0.447 g, or 5 % of the total amount of fuel. For a case with no aerosol deposition, we would expect the mass of soot in the gas phase to be equal to 0.447 g. For a case with aerosol deposition, we would expect some fraction of soot to exist in the gas phase and the remainder of soot to be deposited on the wall. The sum of soot in the gas phase and deposited soot should be 0.447 g.

Figure 10.34 shows the time evolution of soot in the gas phase, deposited soot, and total soot (sum of soot in the gas phase and deposited soot) for five cases. The five cases are (1) all aerosol deposition mechanisms active, (2) no aerosol deposition mechanisms active, (3) gravitational deposition only, (4) thermophoretic deposition only, and (5) turbulent deposition only.

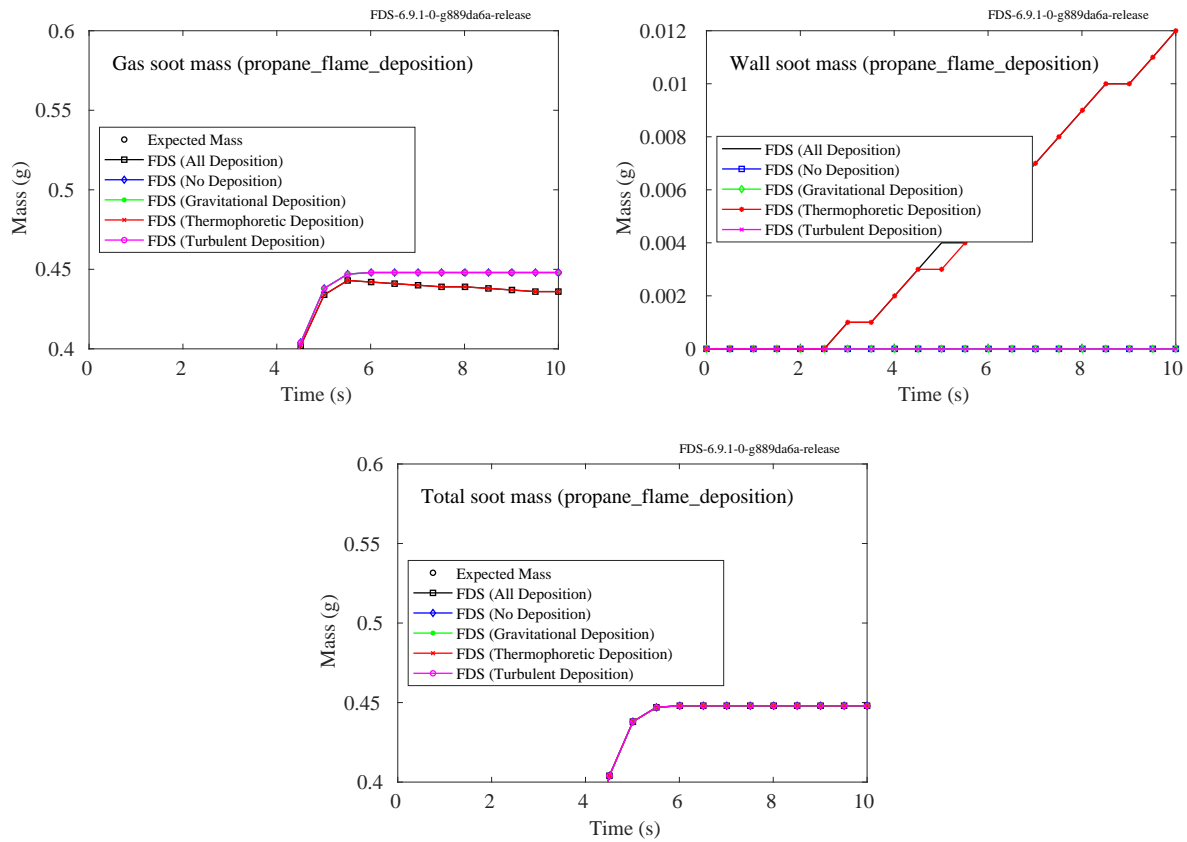


Figure 10.34: Time evolution of soot mass components for propane\_flame\_deposition cases. (Top left) Mass of soot in gas phase. (Top right) Mass of soot deposited on walls. (Bottom) Total mass of soot in gas phase and deposited on walls.

### 10.11.5 Agglomeration of Aerosols (aerosol\_agglomeration)

This verification case consists of two test cases.

The first case to be discussed consists of a box 10 cm on side with adiabatic, free-slip side walls. The box is filled with two gas species each having a molecular weight of 28.8 g/mol, a viscosity of 0.00002 kg/(m s),

a thermal conductivity of  $0.025 \text{ W}/(\text{m K})$ , and specific heat of  $1 \text{ kJ}/(\text{kg K})$ , and zero diffusivity. One of the gas species is defined as an aerosol with two particle size bins with a minimum diameter of  $1 \mu\text{m}$  and a maximum diameter of  $10 \mu\text{m}$ , a solid phase density of  $2000 \text{ kg/m}^3$ , and a solid phase conductivity of  $1 \text{ W}/(\text{m K})$ . The initial mass fraction of the first size bin of the aerosol is  $0.00001$ . STRATIFICATION, NOISE, and all aerosol behaviors except for AGGLOMERATION are turned off. In this case the only mechanisms operating are Brownian and gravitational agglomeration. The case is run for 60 s.

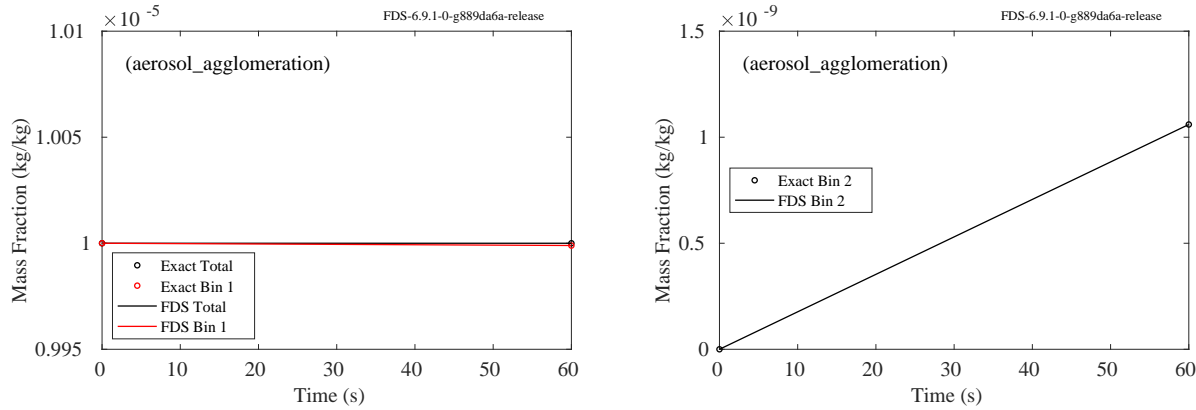


Figure 10.35: Time evolution of soot mass fraction in the gas for size bin 1 and both bins (left) and size bin 2 (right) for the `aerosol_agglomeration` case.

In the second case three pairs of small (3 mm by 3 mm) vents are placed on opposite corners of the the walls, floor, and ceiling of the box. Each pair is connected by an HVAC duct that blows air at  $1 \text{ m/s}$  at the face of the vents. The average dissipation rate in the box is  $0.0204 \text{ m}^2/\text{s}^3$ . Using the average dissipation rate, the agglomeration rate is computed and the resulting mass fractions are compared against the volume averaged mass fractions computed by FDS.

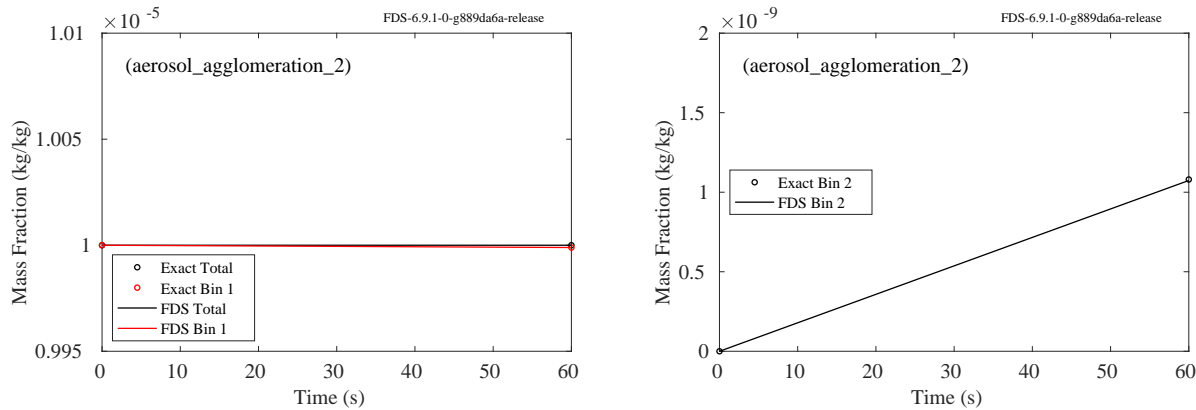


Figure 10.36: Time evolution of soot mass fraction in the gas for size bin 1 and both bins (left) and size bin 2 (right) for the `aerosol_agglomeration_2` case.

### 10.11.6 Scrubbing of Aerosols (`aerosol_scrubbing`)

This verification case tests the scrubbing of aerosols by droplet. The case consists of a box that is 0.4 m on a side with 4 cells in each direction. The box is initially filled with pure water vapor with a soot mass fraction of 0.0001. The soot has a mean diameter of 1  $\mu\text{m}$ . The calculation is initialized with a 100  $\mu\text{m}$  droplet in every cell with an initial downward velocity of 0.1 m/s. Gravity and drag is disabled so the drops do not change velocity. The drops are given an initial weight so that the total projected area is 25 % of the cell area. Since every cell always has a single drop of the same diameter and velocity, the result is a constant decay of the soot mass fraction with a decay constant of 0.0000666. After 5000 s, the case should predict a 28 % drop in soot mass fraction.

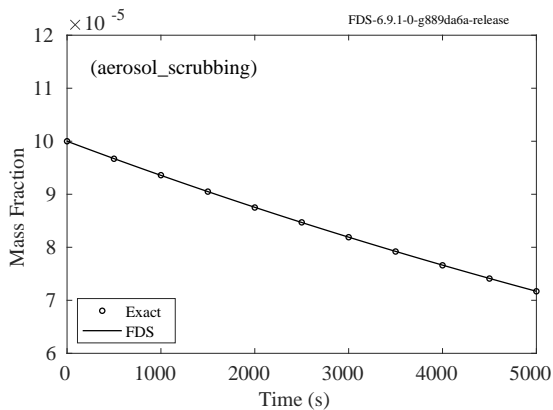


Figure 10.37: Time evolution of soot mass fraction in the gas for the `aerosol_scrubbing` case.

### 10.11.7 Oxidation of Soot on Surfaces (`soot_oxidation_wall`)

This verification case checks the routine for oxidizing soot on a surface. The calculation fills a 1  $\text{m}^3$  box with 0.1 g of soot with a mean diameter of 100 microns; the large diameter was selected so the soot would quickly settle to the floor. The case lets the soot settle for 10 s. This is followed by a one-second ramp that heats the floor from 20  $^\circ\text{C}$  to 1000  $^\circ\text{C}$ . This results in rapid oxidation of the soot. Once all the soot is oxidized, there should have been a heat release of 3.28 kJ and the production of 0.3 mg of CO<sub>2</sub> and 8.3  $\mu\text{g}$  of H<sub>2</sub>O.

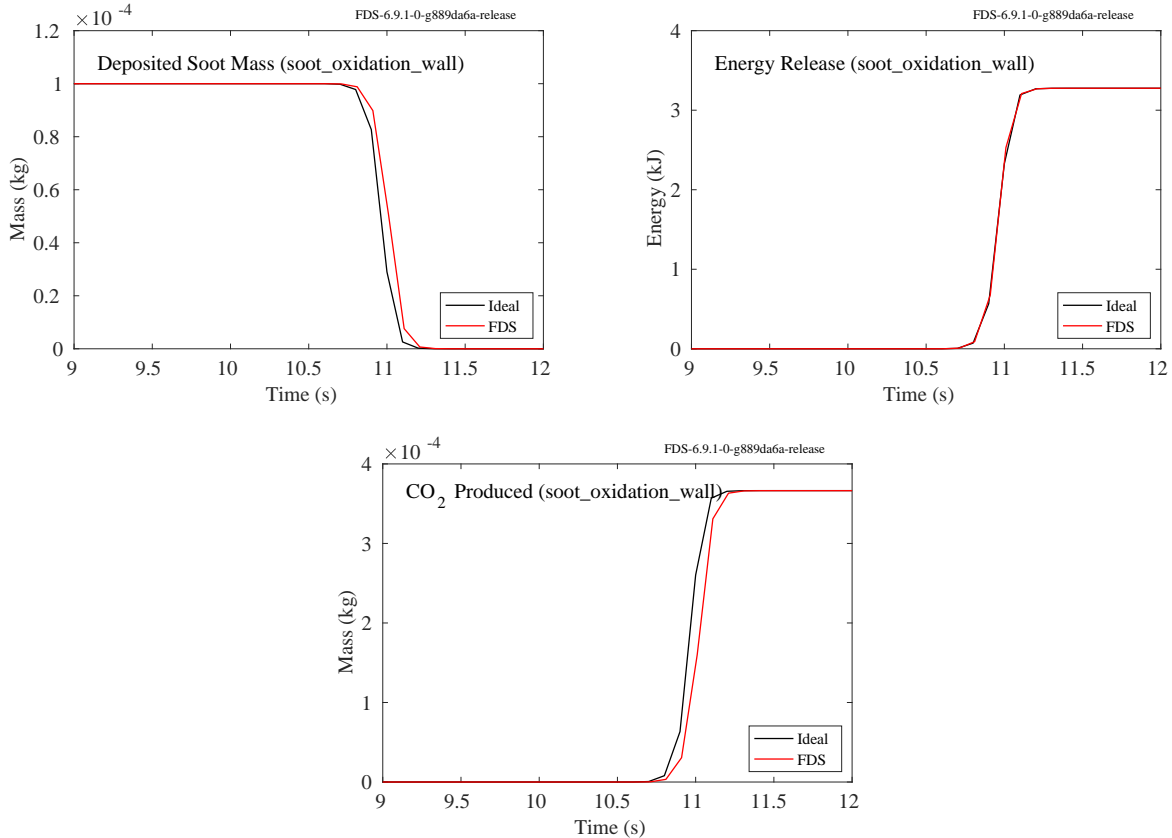


Figure 10.38: Time evolution the accumulated wall mass of soot (upper left), energy release due to soot combustion (upper right), and mass of CO<sub>2</sub> (lower left) and H<sub>2</sub>O (lower right) in the gas for the soot\_oxidation\_wall case.

## 10.12 Condensation

### 10.12.1 Condensation and Evaporation in the Gas Phase (condensation\_1 and condensation\_2)

This pair of verification cases test the condensation and evaporation of water vapor. Both cases use 1 m<sup>3</sup> box. Case `condensation_1` has an initial temperature of 200 °C and contains an initial mass fraction of condensed water vapor of 0.01 kg/kg. At equilibrium all the condensed vapor will evaporate resulting in a temperature drop of 27 °C and a pressure drop of 5800 Pa. Case `condensation_2` has an initial temperature of -100 °C and contains an initial mass fraction of water vapor of 0.01 kg/kg. At equilibrium 99.9 % of the vapor will condense resulting in a temperature rise of 36 °C and a pressure rise of 21,000 Pa.

### 10.12.2 Condensation and Evaporation in the Solid Phase (wall\_cond)

This verification cases tests the condensation and evaporation of water vapor onto and from solid surfaces. The case uses 1 m<sup>3</sup> box. The case has an initial temperature of 100 °C and contains an initial mass fraction of water vapor of 0.05 kg/kg. The walls are 1 mm thick with a density of 1000 kg/m<sup>3</sup>, a specific heat of 1 kJ/(kg K), and a conductivity of 100 W/(mK). At equilibrium the wall and gas temperature will be equal at 32 °C and the pressure drop will be -20000 Pa. Note that NUCLEATION\_SITES on MISC was set to zero

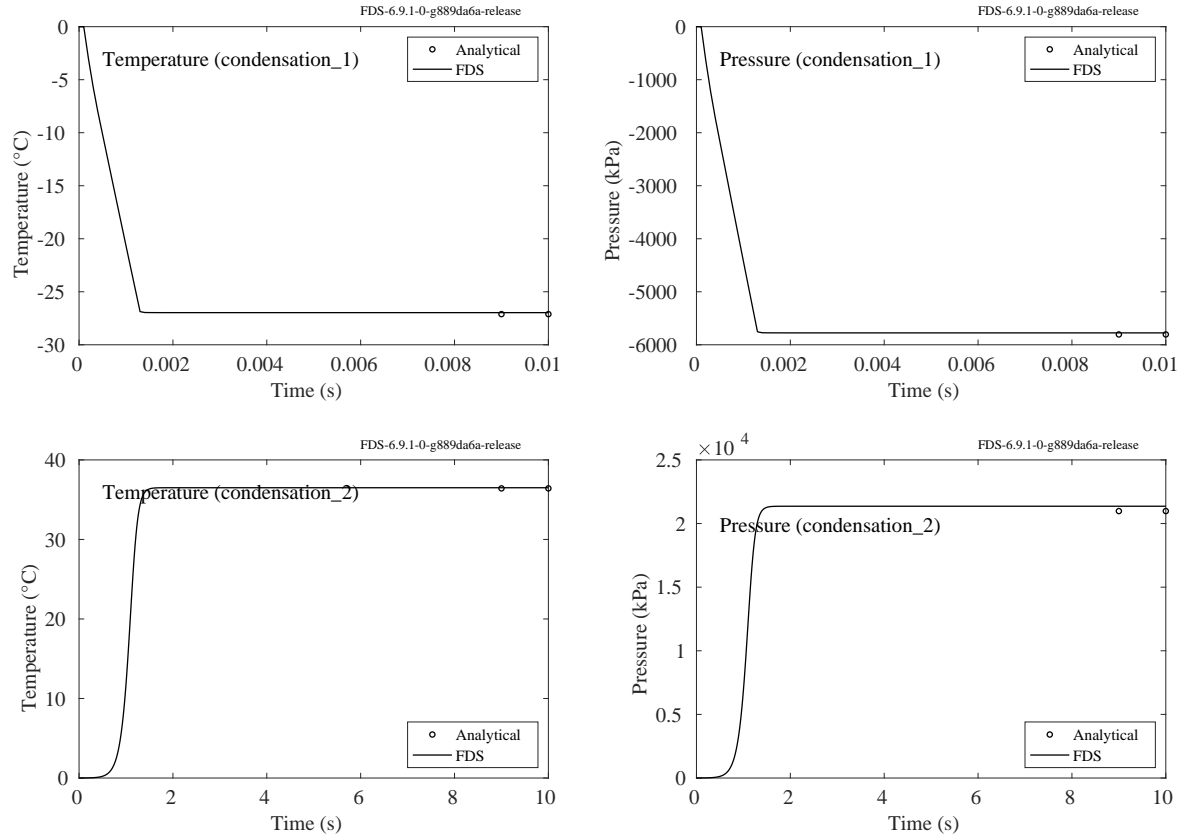


Figure 10.39: Temperature change (left) and pressure change (right) due to the evaporation (top) and condensation (bottom) of water vapor for the condensation\_1 (top) and condensation\_2 (bottom) cases.

to turn off condensation in the gas phase.

### 10.12.3 Radiation for Condensed Phase (condensation\_3)

This verification case tests that the radiation absorption of condensed vapor is equivalent to the absorption of an equivalent set of Lagrangian particles. The case contains two  $1 \text{ m}^3$  boxes filled with dry air at  $0^\circ\text{C}$ . One box is initialized with an 0.001 mass fraction of condensed water vapor with a droplet size of 1 micron. The other box is filled with one particle per cell with the same diameter and total mass of droplets. One wall of each box is set to  $1000^\circ\text{C}$ . The radiative heat flux on the opposite face should be the same in both cases.

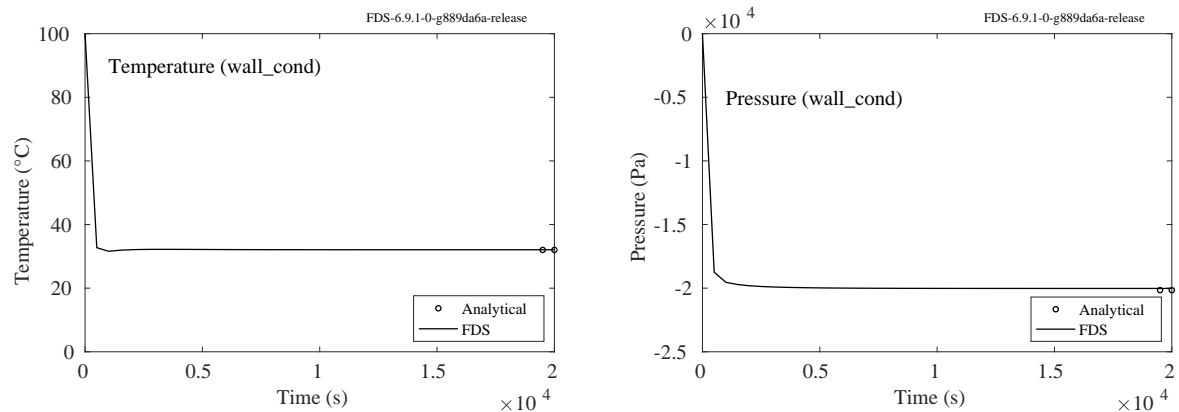


Figure 10.40: Temperature (left) and pressure change (right) for the `wall_cond` case.

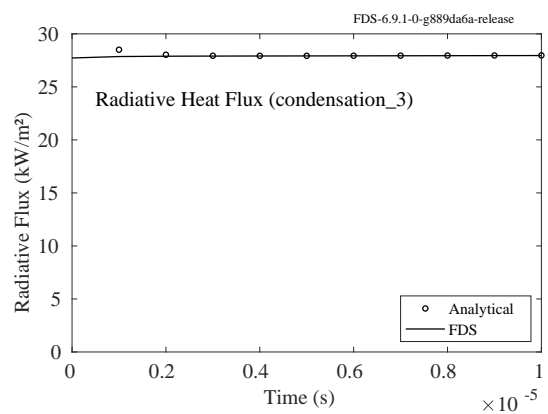


Figure 10.41: Radiative heat flux for the `condensation_3` case

# Chapter 11

## Heat Conduction

This chapter contains examples that test the one-dimensional heat conduction solver in FDS. A one-dimensional heat conduction equation for the solid phase temperature  $T_s(x,t)$  is applied in the direction  $x$  pointing into the solid (the point  $x = 0$  represents the surface)

$$\rho_s c_s \frac{\partial T_s}{\partial t} = \frac{\partial}{\partial x} k_s \frac{\partial T_s}{\partial x} + \dot{q}_s''' \quad (11.1)$$

In cylindrical and spherical coordinates, the heat conduction equation is written

$$\rho_s c_s \frac{\partial T_s}{\partial t} = \frac{1}{r} \frac{\partial}{\partial r} \left( r k_s \frac{\partial T_s}{\partial r} \right) + \dot{q}_s''' \quad ; \quad \rho_s c_s \frac{\partial T_s}{\partial t} = \frac{1}{r^2} \frac{\partial}{\partial r} \left( r^2 k_s \frac{\partial T_s}{\partial r} \right) + \dot{q}_s''' \quad (11.2)$$

FDS offers the user these options, with the assumption that the obstruction is not actually rectilinear, but rather cylindrical or spherical in shape. This option is useful in describing the behavior of small, complicated “targets” like cables or heat detection devices.

### 11.1 Heat Conduction Through a Solid Slab (`heat_conduction`)

Analytical solutions of transient, one-dimensional heat conduction through a slab can be found in Refs. [93] and [94]. Four cases are examined here. In each, a slab of thickness  $L = 0.1$  m is exposed on one face to an air temperature of  $T_g = 120$  °C. The other face is insulated (adiabatic). The convective heat transfer from the gas to the slab is  $\dot{q}_c'' = h(T_g - T_s)$ , where  $h$  is constant, and  $T_s$  is the slab face temperature. No thermal radiation is included.

Case	$k$ (W/(mK))	$\rho$ (kg/m <sup>3</sup> )	$c$ (kJ/(kgK))	$h$ (W/(m <sup>2</sup> K))	Bi $hL/k$
A	0.1	100	1	100	100
B	0.1	100	1	10	10
C	1.0	1000	1	10	1
D	10.0	10000	1	10	0.1

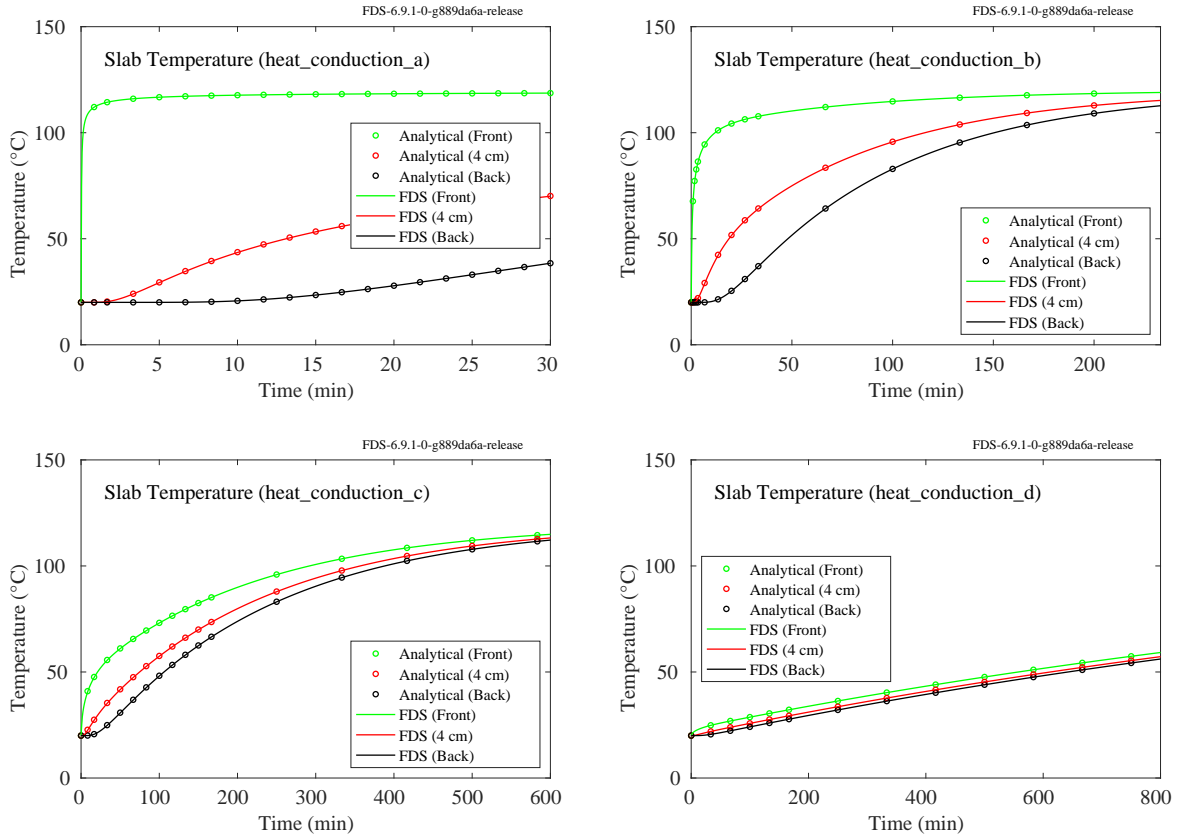


Figure 11.1: Comparison of heat conduction calculations with analytical solutions.

## 11.2 Temperature-Dependent Thermal Properties (`heat_conduction_kc`)

This example demonstrates the 1-D heat conduction in Cartesian, cylindrical, and spherical geometries with temperature-dependent thermal properties. The Cartesian solution was computed using HEATING (version 7.3), a multi-dimensional, finite-difference, general purpose heat transfer model [95]. The cylindrical and spherical solutions were computed using a commercial finite-element solver, ABAQUS.

The sample of homogeneous material is initially at 0 °C and at  $t > 0$  exposed to a gas at 700 °C. A fixed heat transfer coefficient of 10 W/(m<sup>2</sup>K) is assumed. The density of the material is 10,000 kg/m<sup>3</sup>. The conductivity and specific heat are functions of temperature with the following values:  $k(0) = 0.10 \text{ W/(mK)}$ ,  $k(200) = 0.20 \text{ W/(mK)}$ ,  $c(0) = 1.0 \text{ kJ/(kgK)}$ ,  $c(100) = 1.2 \text{ kJ/(kgK)}$ ,  $c(200) = 1.0 \text{ kJ/(kgK)}$ . The thickness (radius) of the sample is 0.01 m. In the Cartesian case, the back surface of the material is exposed to a gas at 0 °C. In the figure below, the solid lines are FDS results and the circles are the HEATING results. An example input with cylindrical geometry looks like:

```
&MATL ID='MAT_1'
  EMISSIVITY = 0.0
  CONDUCTIVITY_RAMP='K_RAMP'
  SPECIFIC_HEAT_RAMP = 'C_RAMP'
  DENSITY=10000. /

&RAMP ID = 'K_RAMP' T=0,    F= 0.10 /
&RAMP ID = 'K_RAMP' T=100, F= 0.15 /
```

```

&RAMP ID = 'K_RAMP' T=200, F= 0.20 /
&RAMP ID = 'C_RAMP' T=0, F= 1.00 /
&RAMP ID = 'C_RAMP' T=100, F= 1.20 /
&RAMP ID = 'C_RAMP' T=200, F= 1.00 /

&SURF ID='SLAB'
STRETCH_FACTOR = 1.0
GEOMETRY = 'CYLINDRICAL'
MATL_ID='MAT_1'
THICKNESS=0.01 /

```

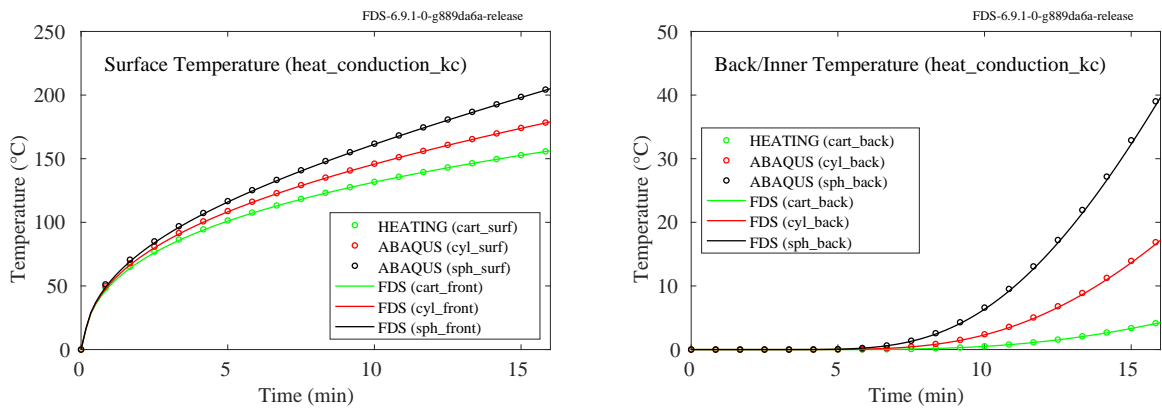


Figure 11.2: Comparison of heat conduction calculations with a finite-element model.

### 11.3 Convective Cooling (`convective_cooling`)

This example tests the convective cooling algorithm. A 1 m thick solid slab that is initially at 1000 °C is suddenly exposed to air at 0 °C. The back of the slab is insulated. Its density is 1000 kg/m<sup>3</sup>, its specific heat is 0.001 kJ/(kg·K), its conductivity is 1 W/(m·K), and its emissivity is zero, meaning there is no radiative loss from the surface. The convective heat transfer coefficient is 1 W/(m<sup>2</sup>·K). The predicted and exact temperature values at the back side of the slab are displayed in Fig. 11.3.

To test the second-order accuracy of the solid phase conduction algorithm, this case was run with increasingly finer spatial and temporal resolution. The resulting convergence study is displayed in Fig. 11.4. The plot shows the relative difference between the computed and exact solution at 1800 s as a function of grid size.

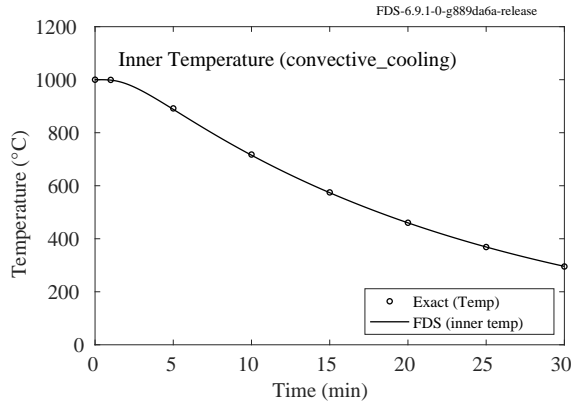


Figure 11.3: Predicted vs. exact back side temperatures of a thick slab cooled by convection alone.

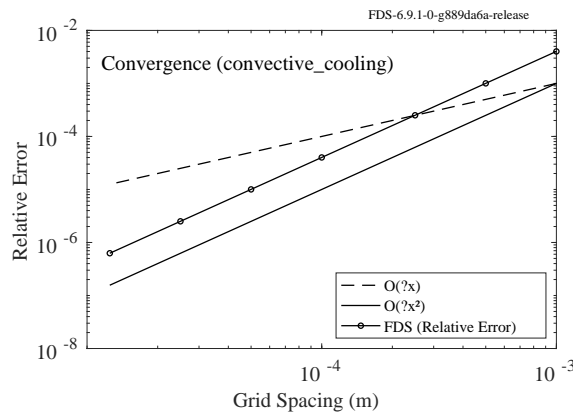


Figure 11.4: Convergence study for the `convective_cooling` test case.

## 11.4 Simple Thermocouple Model (`thermocouples`)

This example tests the simple thermocouple model in FDS. It consists of a box whose walls and gas temperatures are fixed at 500 °C. Inside the box are three thermocouples with bead diameters of 1 mm, 2 mm, and 3 mm. Also included in the box are three “targets” – small solid objects whose surfaces are assumed to be composed of small spheres of the same diameter as the thermocouples. Figure 11.5 compares the temperature rise of the objects. The thermocouple model is not compared with an analytical solutions. This is simply a comparison of the thermally thin thermocouple calculation with the thermally thick “target” calculation. Small differences in temperature are due to slightly different flow conditions in different regions of the box and numerical error due to node spacing and time step size.

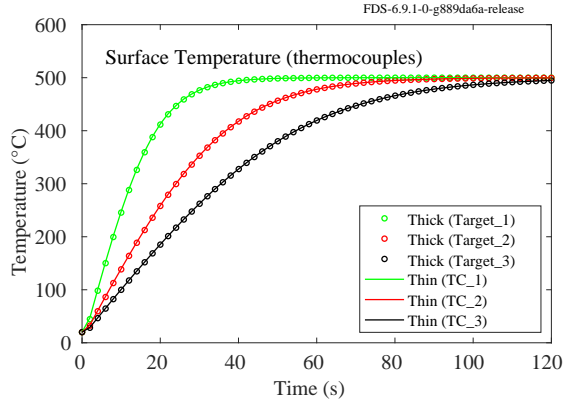


Figure 11.5: Comparison of thermally thin and thick heat conduction into a small sphere.

## 11.5 Heat Conduction through Insulated Steel (`insulated_steeel_x`)

In these examples, a 1 cm thick steel plate and pipe are coated on each side with 2 cm thick insulation material. The conductivity, specific heat, and density of the steel are 50 W/(mK), 0.5 kJ/(kgK), and 7500 kg/m<sup>3</sup>, respectively. The corresponding values for the insulation material are 0.2 W/(mK), 1 kJ/(kgK), and 200 kg/m<sup>3</sup>, respectively. The heat transfer coefficient is 10 W/(m<sup>2</sup>K). The outer surface of the composite is exposed to air at 480 °C while the inner surface is exposed to air at 20 °C. The assemblies are heated for 10 h and the steady-state temperature profiles are shown in Fig. 11.6. Neglecting thermal radiation, the heat flux through the plate is given by [77]:

$$\dot{q}'' = \frac{T_{\text{hot}} - T_{\text{cold}}}{\frac{1}{h} + \frac{L_{\text{ins}}}{k_{\text{ins}}} + \frac{L_{\text{steel}}}{k_{\text{steel}}} + \frac{L_{\text{ins}}}{k_{\text{ins}}} + \frac{1}{h}} \quad (11.3)$$

where  $h$  is the heat transfer coefficient,  $L$  is the layer thickness, and  $k$  is the thermal conductivity of the layer material. The heat flux through the inner surface of the pipe,  $r_1$ , is given by:

$$\dot{q}'' = \frac{T_{\text{hot}} - T_{\text{cold}}}{\frac{1}{h} + \frac{r_1}{k_{\text{ins}}} \ln \frac{r_2}{r_1} + \frac{r_1}{k_{\text{steel}}} \ln \frac{r_3}{r_2} + \frac{r_1}{k_{\text{ins}}} \ln \frac{r_4}{r_3} + \frac{r_1}{r_4 h}} \quad (11.4)$$

where  $r_1$  is the inner radius of the inner layer of insulation,  $r_2$  is the inner radius of the steel,  $r_3$  is the outer radius of the steel, and  $r_4$  is the outer radius of the outer layer of insulation. The heat flux through each layer is the same, and the steady-state solution can be obtained by solving for the temperature drop across each layer. The temperature gradient within each layer of the plate composite is linear. For the pipe, the temperature profile for each layer is:

$$T(r) = T_{s,i} + \frac{T_{s,i-1} - T_{s,i}}{\ln(r_{i-1}/r_i)} \ln \frac{r}{r_i} \quad i = 2, 3, 4 \quad (11.5)$$

where  $T_{s,i}$  is the surface temperature corresponding to radial coordinates 1 through 4. Note that the position of the symbols in Fig. 11.6 indicates the default finite difference nodes of the solid. Also note that the spatial coordinate refers to the distance from the outer (hot) surface of insulation.

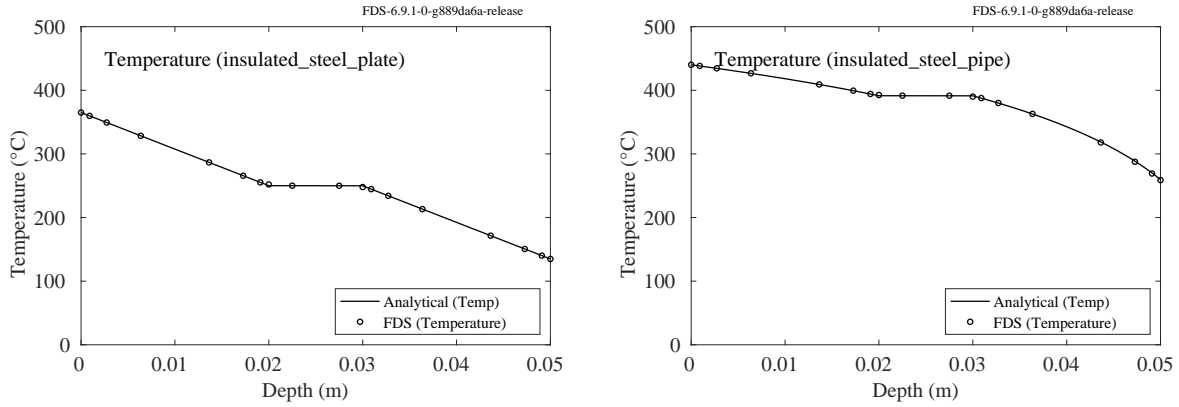


Figure 11.6: Steady-state temperature profile within an insulated steel plate and pipe.

## 11.6 Heat Conduction across Mesh Boundaries (`back_wall_test`)

In this example, a hollow cube whose walls are either zero, one, or two cells thick contains a solid cube centered inside with a fixed temperature of 500 °C. The objective of the test is to ensure that the heat conduction through the steel and across the mesh boundaries is computed properly when each wall has a specified THICKNESS of 5 cm. In the left hand plot of Fig. 11.7, the net radiative heat flux to the interior surface of the box matches the net radiative heat flux from the external surface in steady state. In the right hand plot, the external surface temperature of two sides of the box are compared. One side is a zero cell thick obstruction; the other side is a two cell thick obstruction. Since the sides all have a specified THICKNESS of 0.5 cm, the fact that the obstruction is either zero, one, or two cells thick should not matter and the temperatures should match exactly.

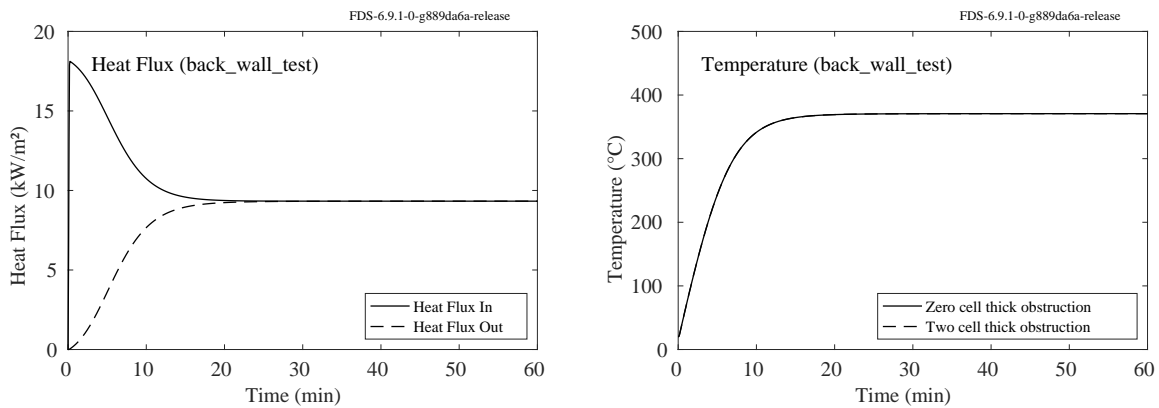


Figure 11.7: (Left) The heat flux into and out of a steel plate. (Right) The external temperature of a steel box whose sides are either zero or two cells thick.

## 11.7 Heat Conduction through Immersed Boundaries (`back_wall_test_2`)

A 0.8 m by 0.8 m plate with surface temperature 1000 °C and emissivity of 1 exposes a parallel plate separated by 0.15 m. The exposed plate is 1 cm thick, with a conductivity of 25 W/(m·K), density 1000 kg/m<sup>3</sup>, specific heat 0.1 kJ/(kg·K), emissivity 1, and a convective heat transfer coefficient of 0. Three different configurations are considered: (1) the plates are all defined as traditional FDS OBSTructions, (2) the plates are defined as immersed boundary (GEOM) obstructions, and (3) the same plates as in (2) are rotated 45°. Figure 11.8 displays the front and back surface temperatures for all three cases, compared to the exact solution where the analytically determined heat flux, Eq. (9.1), is imposed directly on the front plate surface. The error in all three cases is due mainly to the error in the radiation transport calculation on grids with 2.5 cm cells.

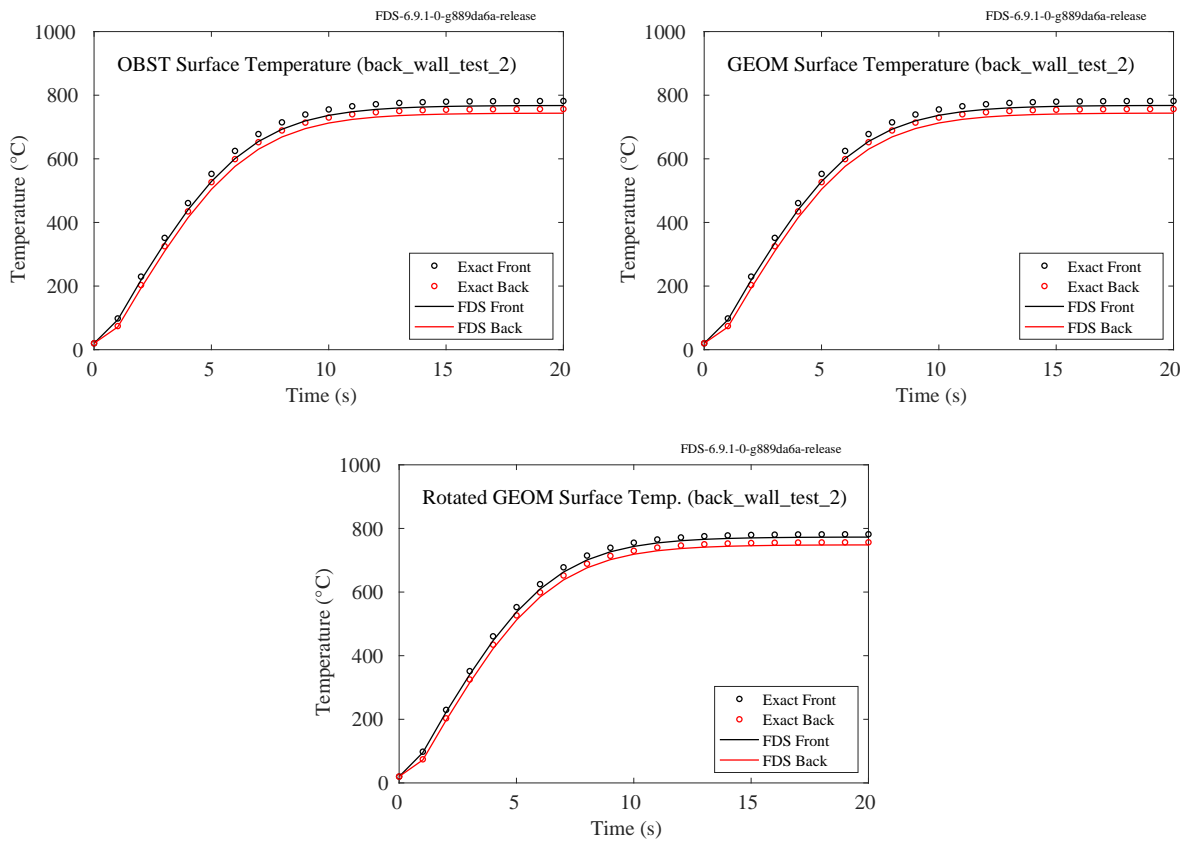


Figure 11.8: Front and back surface temperatures of a plate defined using the OBST namelist parameters (top, left); GEOM namelist parameters (top, right); GEOM parameters rotated 45°.

## 11.8 Specified Heat Flux Boundary Conditions (`adiabatic_xxx_flux`)

There are options in FDS to specify either a net (convective and radiative) or convective boundary condition at a solid surface. In these two test cases, `Heat_Transfer/adiabatic_con_flux.fds` and `Heat_Transfer/adiabatic_net_flux.fds`, a sealed cube of side length 2 m has a 0.4 m by 0.4 m area on the floor with a specified convective and net heat flux of 100 kW/m<sup>2</sup>. The case with the specified

convective heat flux boundary has the radiation turned off. The case with the net heat flux boundary has both convection and radiation enabled so that the net flux is  $100 \text{ kW/m}^2$ . The flux is applied for 30 s and then turned off. The pressure in the compartment is expected to rise according to the equation:

$$\frac{dp}{dt} = \frac{(\gamma - 1) \dot{Q}}{V} \quad (11.6)$$

where  $\dot{Q} = 16 \text{ kW}$ ,  $\gamma = 1.4$ , and  $V = 8 \text{ m}^3$ . After 30 s, the pressure rise,  $p$ , is expected to be 24 kPa (left, Fig. 11.9). The expected temperature rise,  $\Delta T$ , is found by solving the energy conservation equation:

$$\dot{Q} \Delta t = c_p \rho V \Delta T - V \Delta p \quad (11.7)$$

as shown in the right hand plots of Fig. 11.9.

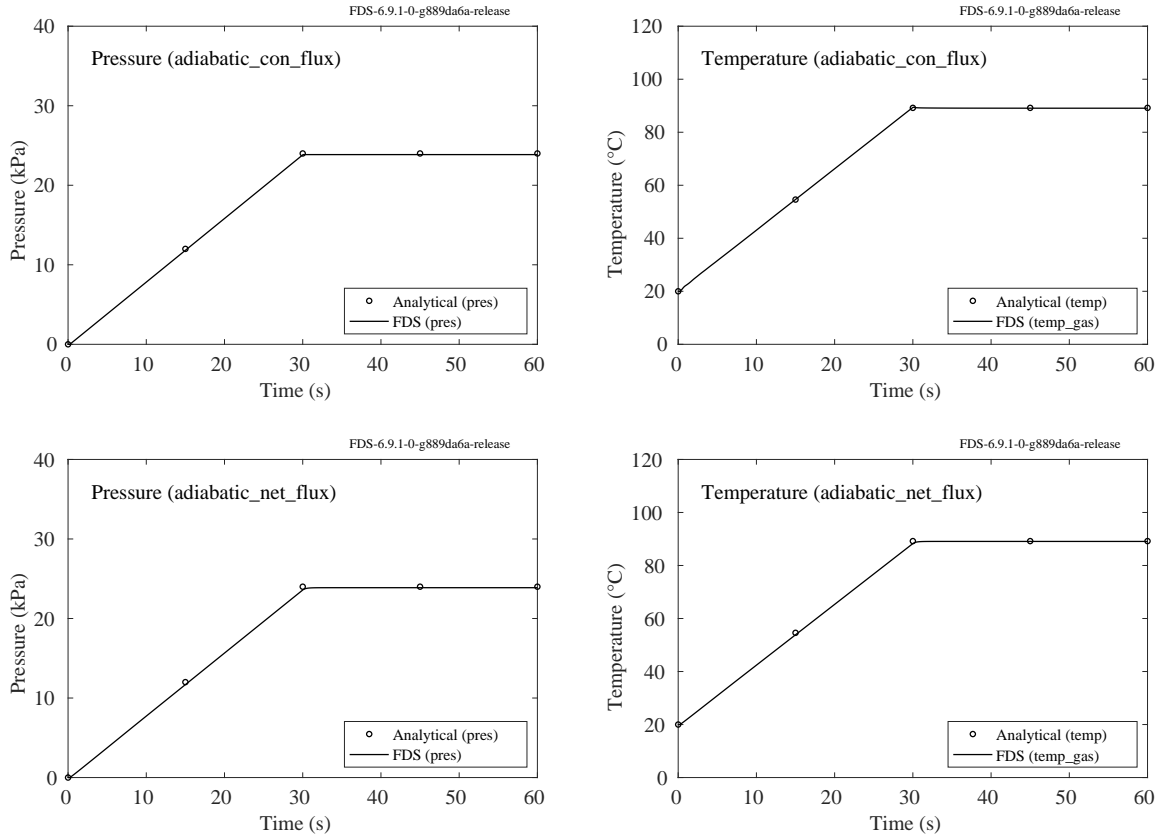


Figure 11.9: Pressure and average temperature of a small compartment with specified heat flux boundary conditions.

## 11.9 Solid Heat Transfer 3-D (Beta)

This section presents test cases for solid phase heat diffusion (conduction) in 3-D. This feature is not yet connected to the 1-D pyrolysis heat transfer code discussed in the previous sections. Currently, the purpose of the HT3D functionality is to couple FDS with structural fire calculations.

### 11.9.1 Energy Conservation in a 3-D Solid (`ht3d_energy_conservation`)

A 0.8 m by 0.8 m by 2 cm thick metal plate is exposed to a hot radiating surface for 10 s. Figure 11.10 displays the increased internal enthalpy versus the net heat flux integrated over the surface and integrated over time.

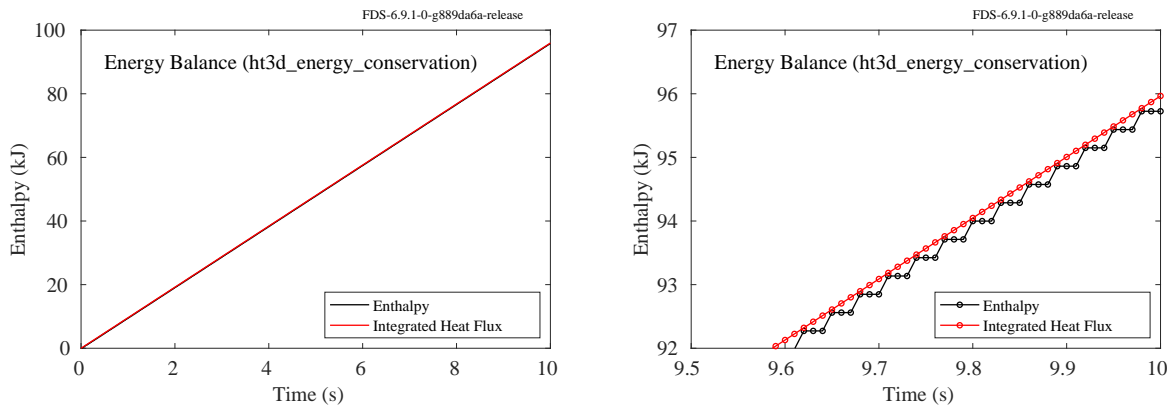


Figure 11.10: Plots of the enthalpy of a metal plate versus the surface heat flux integrated in space and time. At right is the same plot showing how the 3-D temperature field is updated over three time steps.

Figure 11.11 displays the energy balance for cases where the internal grid cell is 0.25 times the gas phase grid cell size (left plot), and where the internal grid cells stretch as they would for a 1-D heat conduction calculation (right). The grid stretching is not recommended for the 3-D solver.

Figure 11.12 compares the integrated net heat flux versus the internal enthalpy in a case where a small hot block is placed above a larger block for which 3-D heat conduction is invoked. In one case (upper left plot), the block is made of one material with a thermal conductivity of 0.1 W/m/K, typical of insulation. The internal cells cluster near all six faces of the block as would be done in a 1-D case. The calculation of the internal enthalpy can be performed in any coordinate direction, both positive and negative. In this case, the positive  $x$  direction is chosen, whereas the hot block is placed above the larger block. This ensures that the energy is properly transferred in the lateral directions. In a second case (upper right plot), the solid block consists of a thin, 1 cm thick layer of insulation over a solid block of steel. The insulation layer is specified using a one-cell thick obstruction on top of the obstruction representing the steel. In a third case (lower plot), the solid block of steel is covered by two layers of insulation of thickness 1.5 cm and 1.0 cm that are specified using the conventional SURF line with arrays of `MATL_ID` and `THICKNESS`. Each layer of insulation is composed of two different material components.

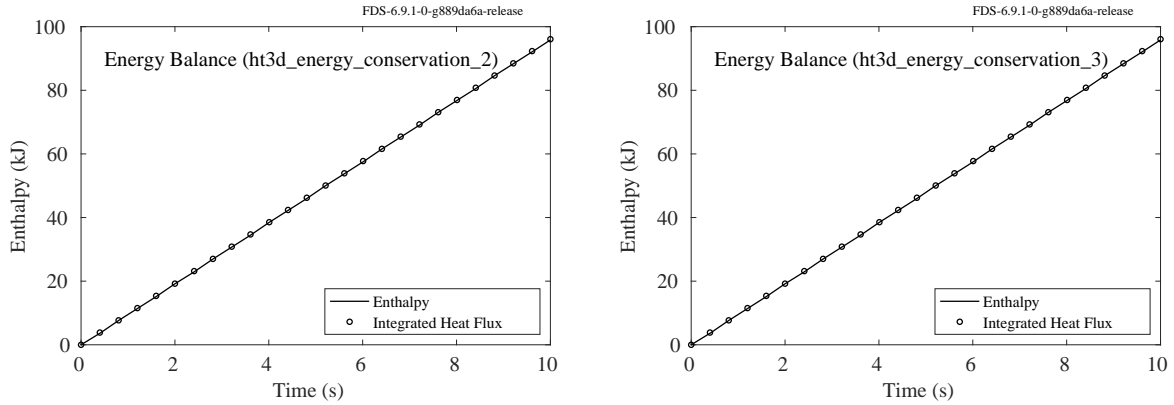


Figure 11.11: Plots of the enthalpy of a metal plate versus the surface heat flux integrated in space and time. The left plot is the case where the internal grid cells are 0.25 the size of the gas phase cells, and the right plot is the case where the internal cells stretch as is done in the 1-D solver.

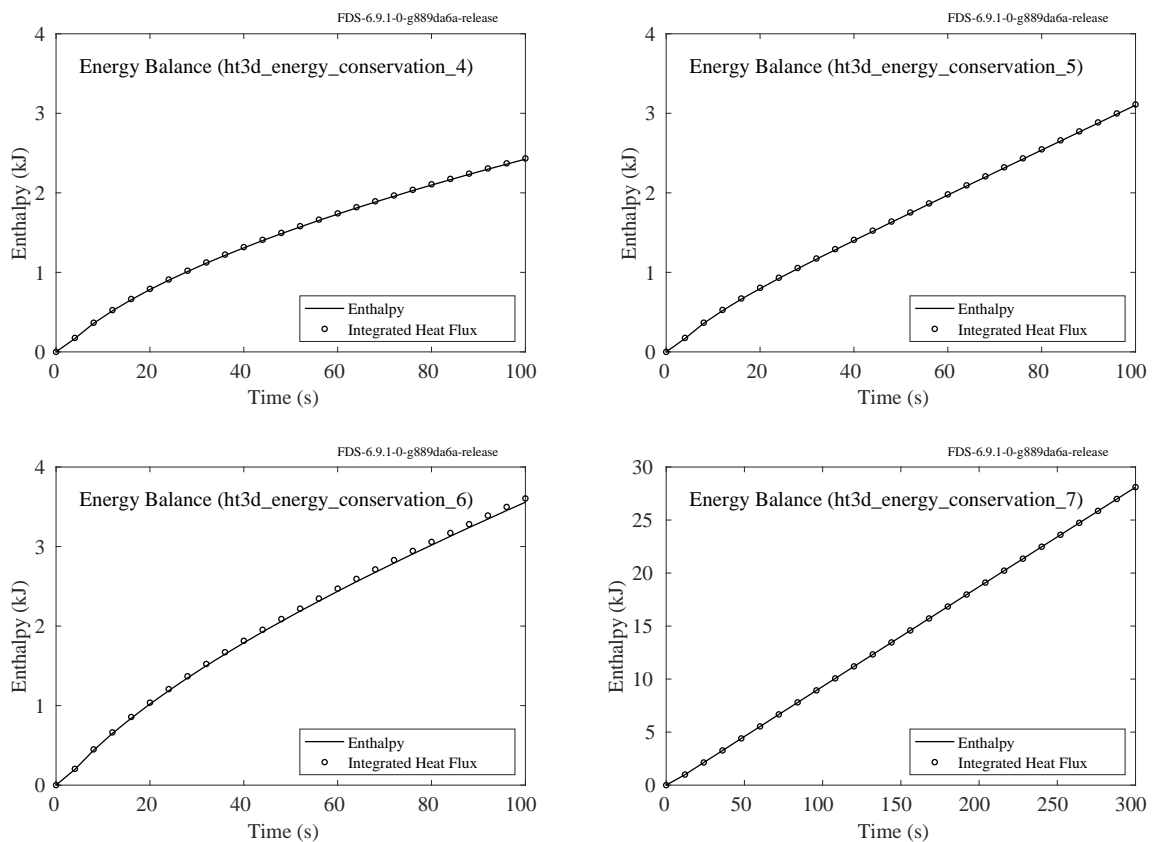


Figure 11.12: Comparison of the integrated net heat flux versus the internal enthalpy for a homogenous solid block of insulation material (upper left), a block of steel with a single layer of insulation (upper right), a block with multiple layers of multi-component insulation (bottom left), a block of steel that abuts an open boundary (bottom right).

The left plot in Fig. 11.13 compares the integrated net heat flux versus the internal enthalpy in a case where a vertical steel column is exposed to a radiant heater. The column is modeled in FDS using thin obstructions to represent a 10 mm thick web and two 18 mm thick flanges. One flange is subjected to the heat, which then passes through the web.

The right plot in Fig. 11.13 displays the heat loss from a collection of solid objects with different thermal properties. One of the objects is completely embedded within the solid and has a volume  $V = 6 \times 10^{-9} \text{ m}^3$  and generates heat at a rate of  $\dot{q}''' = 1.5 \times 10^5 \text{ kW/m}^3$ . It is expected that after a few minutes the heat flux from the surface of the collection of solids should be  $-\dot{q}''' V = -9 \times 10^{-4} \text{ kW}$ . The minus sign indicates that the solid loses heat from its surface at the same rate as the heat is generated internally.

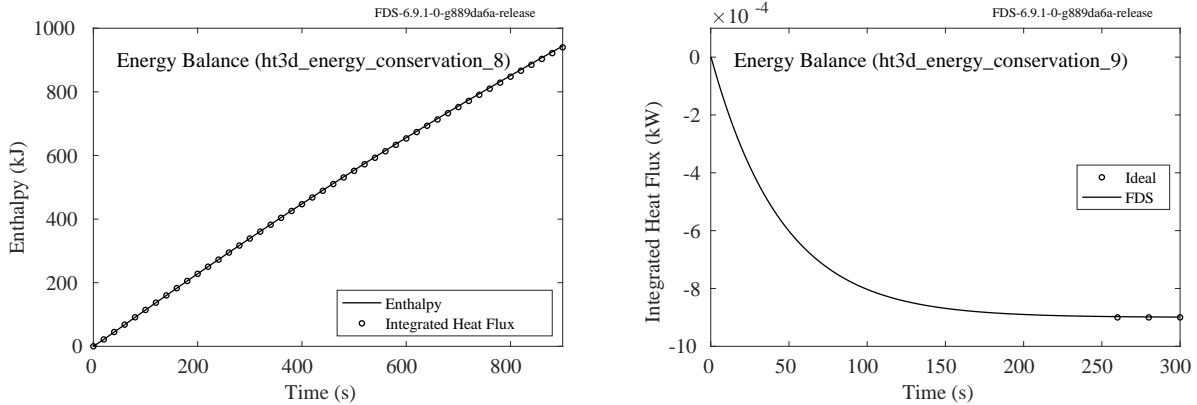


Figure 11.13: (Left) Comparison of the integrated net heat flux versus the internal enthalpy for a steel column. (Right) Integrated heat flux from a solid object with an embedded solid object that generates heat at a constant rate.

### 11.9.2 Heat Transfer to an I-Beam (`ht3d_beam_heating`)

An aluminum I-beam  $L = 1.76 \text{ m}$  long and  $d = 0.58 \text{ m}$  deep (i.e. in height), with flanges that are  $b_f = 0.22 \text{ m}$  wide and  $t_f = 0.005 \text{ m}$  thick and a web that is  $t_w = 0.006 \text{ m}$  thick, is heated within a sealed compartment with volume  $V_c = 0.8 \text{ m}^3$ , initial temperature  $T_{g,0} = 1073.15 \text{ K}$ , pressure  $p_0 = 101.325 \text{ kPa}$ , molecular weight  $W = 0.028 \text{ kg/mol}$ , specific heat  $c_g = 1 \text{ kJ/(kg}\cdot\text{K)}$ , and density  $\rho_g = p_0 W / (R T_{g,0}) \approx 0.318 \text{ kg/m}^3$ .  $R \approx 0.008314 \text{ kJ/(mol}\cdot\text{K)}$  is the universal gas constant. The aluminum has a density  $\rho_a = 2700 \text{ kg/m}^3$ , specific heat  $c_a = 0.9 \text{ kJ/(kg}\cdot\text{K)}$ , and initial temperature  $T_{a,0} = 293.15 \text{ K}$ . Initially, the gas and aluminum have internal energies given by:

$$U_g = \rho_g V_g c_g T_{g,0} - p_0 V_g \approx 189.56 \text{ kJ} \quad ; \quad U_a = \rho_a V_a c_a T_{a,0} \approx 7046.0 \text{ kJ} \quad (11.8)$$

After several minutes, the equilibrium temperature is expected to be:

$$T = \frac{U_g + U_a}{\rho_a V_a c_a + \rho_g V_g c_g - nR} \approx 298.84 \text{ K} \equiv 25.69 \text{ }^\circ\text{C} \quad (11.9)$$

where  $n = p_0 V_g / (R T_{g,0}) \approx 8.973$  is the number of moles of gas. The left hand plot in Fig. 11.14 displays the average surface temperature of the I-beam.

In a second case, the I-beam is coated with a 1 cm thick layer of thermal insulation (density  $\rho_i = 20 \text{ kg/m}^3$ , specific heat  $c_i = 1.0 \text{ kJ/(kg}\cdot\text{K)}$ ) and exposed to the same thermal environment. The expected equilibrium temperature is  $25.62 \text{ }^\circ\text{C}$ . The right hand plot in Fig. 11.14 compares the computed and exact temperatures.

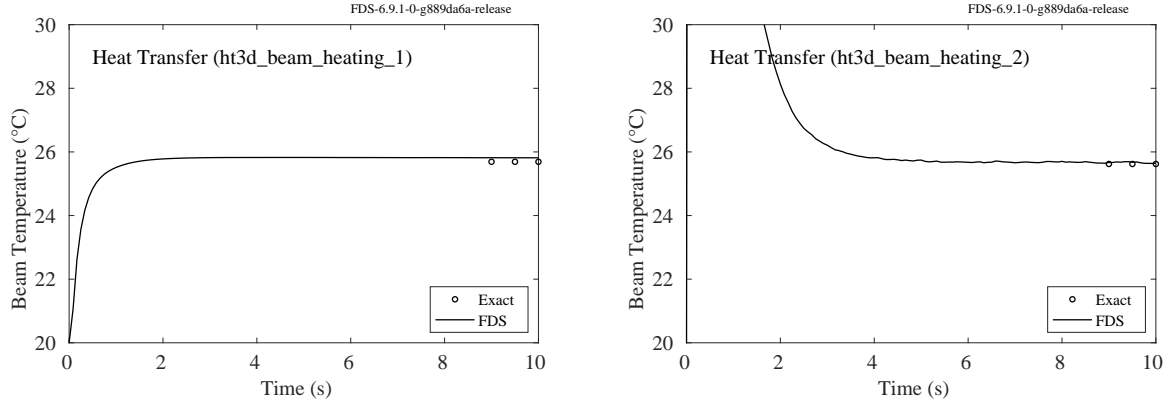


Figure 11.14: (Left) Average surface temperature of an I-beam immersed in hot gas. (Right) Average temperature of an insulated I-beam exposed to the same conditions.

### 11.9.3 Mass Conservation in a 3-D Solid (ht3d\_mass\_conservation)

Three abutting solids, one of which is thin, have a density of  $\rho_s = 400 \text{ kg/m}^3$ , moisture mass fraction  $Y_m = 0.05$ , and total volume  $V = 0.0106 \text{ m}^3$ . When exposed to hot plates of  $1000^\circ\text{C}$ , it is expected that  $\rho_s Y_m V = 0.212 \text{ kg}$  should be evaporated. The left plot of Fig. 11.15 displays the evaporated mass as a function of time.

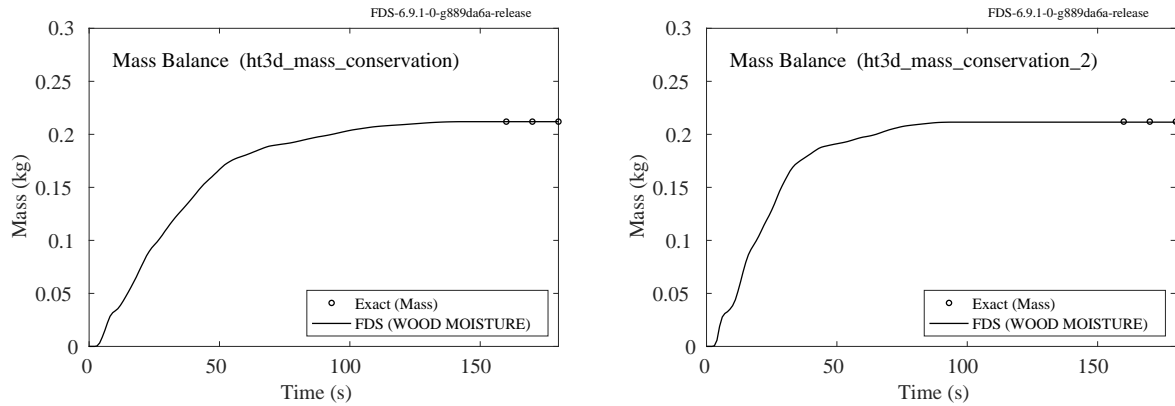


Figure 11.15: Evaporated moisture mass from a collection of solids.

In this case, the moisture is not explicitly modeled; that is, “wet wood” undergoes a single reaction becoming “dry wood” and water vapor. A variation of the case is to mix moisture and dry wood together and allow the moisture to evaporate. To mimic the conditions of the first case, the density of the dry wood is set to  $387.76 \text{ kg/m}^3$  and the moisture  $1000 \text{ kg/m}^3$ . The same mass of water vapor should be produced, as shown in the right plot of Fig. 11.15, but the time histories of the two cases are not the same because the thermal properties of the combination of two material components in the second case are different than that of the single component of the first case.

### 11.9.4 Continuous Heat Flux Boundary (ht3d\_slab)

In this test case, we utilize the non-steady state conduction solution provided in Carslaw and Jaeger [94] for a semi-infinite slab exposed to a constant ambient temperature,  $T_\infty$ , with a constant convective heat transfer coefficient,  $h$ , and no radiation (see also Drysdale [93], Eq. (2.25)). The initial temperature of the slab,  $T_0$ , is set to 1000 °C. The thermal properties of the slab,  $k = 1 \text{ W}/(\text{m K})$ ,  $\rho = 1000 \text{ kg}/\text{m}^3$ , and  $c = 0.001 \text{ kJ}/(\text{kg K})$ , are set to give a thermal diffusivity,  $\alpha$ , of 0.001 m<sup>2</sup>/s. The analytical solution for this problem for the solid temperature,  $T(x,t)$ , is given by

$$\frac{T - T_0}{T_\infty - T_0} = \operatorname{erfc}\left(\frac{x}{2\sqrt{\alpha t}}\right) - \exp\left(\frac{xh}{k} + \frac{\alpha t}{(k/h)^2}\right) \operatorname{erfc}\left(\frac{x}{2\sqrt{\alpha t}} + \frac{\sqrt{\alpha t}}{k/h}\right) \quad (11.10)$$

where  $\operatorname{erfc} = 1 - \operatorname{erf}(x)$ .

This is a 1-D problem in depth into the solid. In FDS, the problem is solved in 2-D, with the temperature varying in the  $x$  coordinate direction; there is no variation in the vertical,  $z$ , direction. While the solution is provided for a semi-infinite slab, FDS must use a finite thickness. The slab is taken to be 0.5 m in depth, with  $x = 0$  m marking the interface location between the fluid and the solid. The analytical solution for  $T(x = 0.5, t)$  is used as the “back” boundary condition of the slab. The grid resolution is chosen to be 5 cm (10 cells covering 0.5 m). The stability constraint for the time step in the heat equation is therefore,  $\delta t \leq \delta x^2/(2\alpha) = 1.25 \text{ s}$ . This is set as the initial time step in FDS, since no gas phase solution is computed.

The main purpose of this verification case is to check the accuracy of the continuous heat flux boundary condition used in the HT3D method (see the FDS Tech Guide [48] for details). Figure 11.16 shows the surface (wall) temperature,  $T_w$ , plotted as a function of time (the hot slab is cooling). Note that the exact solution for the surface temperature is taken from Eq. (11.10) with  $x = 0$  m. That is,  $T_w(t) \equiv T(0, t)$ .

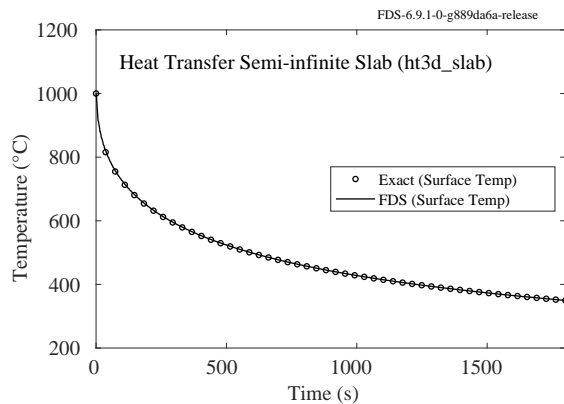


Figure 11.16: Test of continuous heat flux boundary condition for 3-D heat transfer.

### 11.9.5 3-D Heat Diffusion in a Steel I-Beam (ht3d\_ibeam)

The purpose of this test case is to compare FDS HT3D with a well-established commercial finite-element model (ANSYS) for a reasonably practical problem. We consider a steel I-beam cross-section 0.4 m on each side. The flanges are 6 cm thick and the web is 4 cm thick. The grid resolution for both FEM and FDS models is  $\Delta x = 1 \text{ cm}$ . The thermal properties of the steel are taken to be constant:  $k = 45 \text{ W}/(\text{m K})$ ,  $\rho = 7850 \text{ kg}/\text{m}^3$ , and  $c = 0.60 \text{ kJ}/(\text{kg K})$ . The boundary conditions are adiabatic except for a hot patch on the front half of the bottom flange maintained at 800 °C. The initial temperature of the steel is 20 °C and the

case is run for 3600 s. Note that the FEM model is run with a time step comparable to the explicit stability criterion ( $\Delta t \approx 1.7$  s) in order to yield time accurate results for comparison with FDS.

Figure 11.17 shows a comparison between the surface temperature contours from ANSYS (left) and FDS (right). Below that, in Fig. 11.18, we show the time history of the surface temperatures for six locations on the bottom flange (positions may be identified from the image on the left).

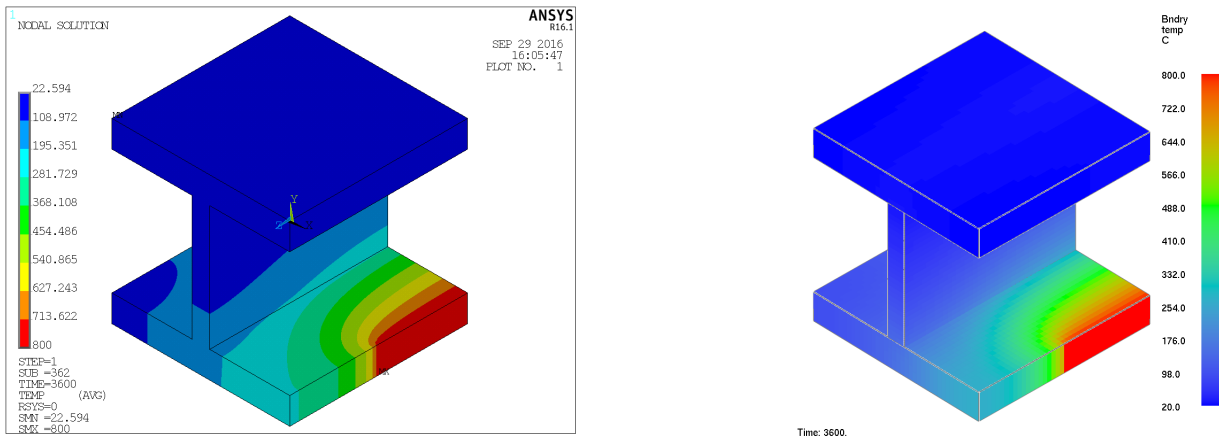


Figure 11.17: Three-dimensional heat diffusion in an I-beam, comparison between a commercial finite-element code (ANSYS, left, courtesy Chao Zhang) and FDS (right). The beam boundary conditions are adiabatic except for a hot patch maintained at 800 °C on the front right of the bottom flange. The initial temperature of the steel is 20 °C and the calculations are run for 3600 s.

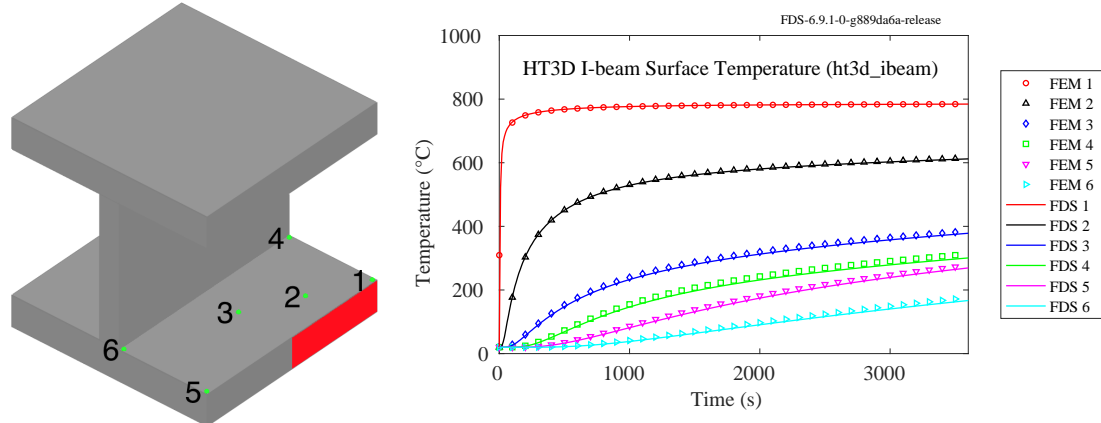


Figure 11.18: (Left) Device locations corresponding to the legend entries in the plot to the right. (Right) Time history of the surface temperature. Symbols represent the finite-element model (FEM) results and the lines represent the FDS results.

### 11.9.6 3-D Heat Diffusion in Thin Steel Plates (ht3d\_network)

This case tests the 3-D solid phase solver for a network of thin steel plates. Consider the image in Fig. 11.19 which shows a collection of connected steel plates that are 20 cm wide and 1 cm thick. Two hot panels heat

up the single plate to the left and the heat is conducted through the network of plates. Besides the left-most plate, all other plates are perfectly insulated. The plot on the right simply demonstrates that the temperature of the outer two of the four right-most extremities are the same, verifying that the distribution of heat is symmetric given a symmetric arrangement of plates.

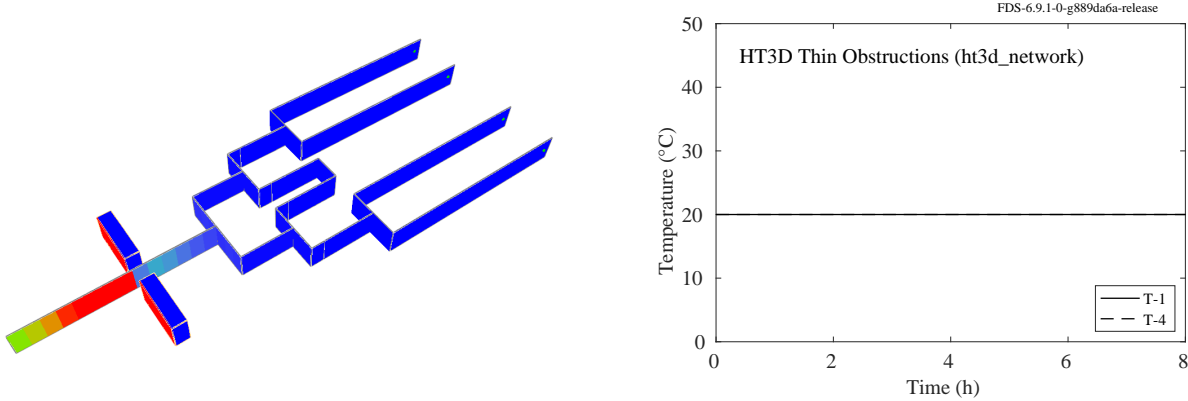


Figure 11.19: (Left) A collection of thin steel plates are heated at the left and heat is conducted laterally along the plates. (Right) The plot shows the temperature at the outer right extremities after 8 h.

### 11.9.7 3-D Heat Diffusion in a Sphere (`ht3d_sphere`)

**Salah Benkorichi, Omega Fire Engineering Ltd.**

A solid sphere of radius  $a = 0.1$  m with internal heat generated at  $\dot{q}''' = 200$  kW/m<sup>3</sup> has an initial temperature of  $T_0 = 20$  °C and its exterior surface temperature is held at this temperature. The 3-D heat conduction equation can be written as

$$\frac{\partial T}{\partial t} = \alpha \left[ \frac{1}{r^2} \frac{\partial}{\partial r^2} \left( r^2 \frac{\partial T}{\partial r} \right) + \frac{\dot{q}'''}{k} \right] ; \quad T(r, 0) = T_0 ; \quad T(a, t) = T_0 \quad (11.11)$$

where  $k$  is the thermal conductivity and  $\alpha$  is the thermal diffusivity. The exact solution to Eq. (11.11) is from [94] (Sec. 9.8, p. 243):

$$T = T_0 + \frac{\dot{q}'''}{6k} (a^2 - r^2) + 2 \frac{\dot{q}''' a^3}{k \pi^3 r} \sum_{n=1}^{\infty} \frac{(-1)^n}{n^3} \sin \left( \frac{n \pi r}{a} \right) \exp \left( -\alpha t \frac{n^2 \pi^2}{a^2} \right) \quad (11.12)$$

The simulation is run for 180 s. Shown in Fig. 11.20 is a comparison of analytical and numerical radial temperature profiles at several points in time for the high resolution case. Also shown is the  $L_\infty$  error as a function of cell size.

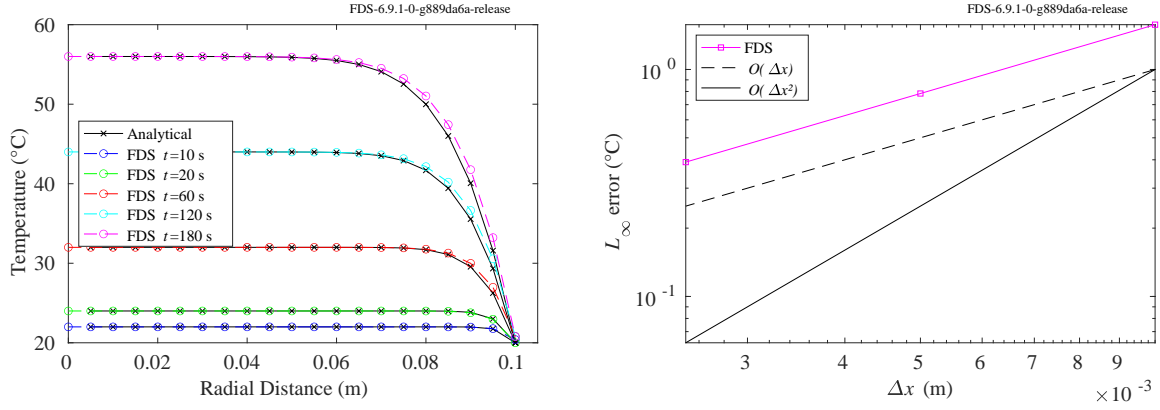


Figure 11.20: (Left) Comparison of analytical and numerical radial profiles of temperature at various times. (Right)  $L_{\infty}$  error in temperature at  $t = 180$  s for three levels of grid refinement.

### 11.9.8 3-D Heat Conduction in a Layered Solid (ht3d\_pile)

An 18 cm long solid consisting of three 6 cm long abutting rectangular obstructions, each made of a different material, has a specified surface temperature of 500 °C at one end and 20 °C at the other. After 3 h, a steady temperature profile emerges as shown in Fig. 11.21. Two simulations are performed; one in which the conduction calculation is performed using the HT1D convention, and the other with HT3D. The thermal conductivity values are 5 W/m/K, 0.2 W/m/K, and 2 W/m/K. The exact solution is found by asserting that the heat flux,  $\dot{q}'' = k \partial T / \partial x$ , is constant in each segment.

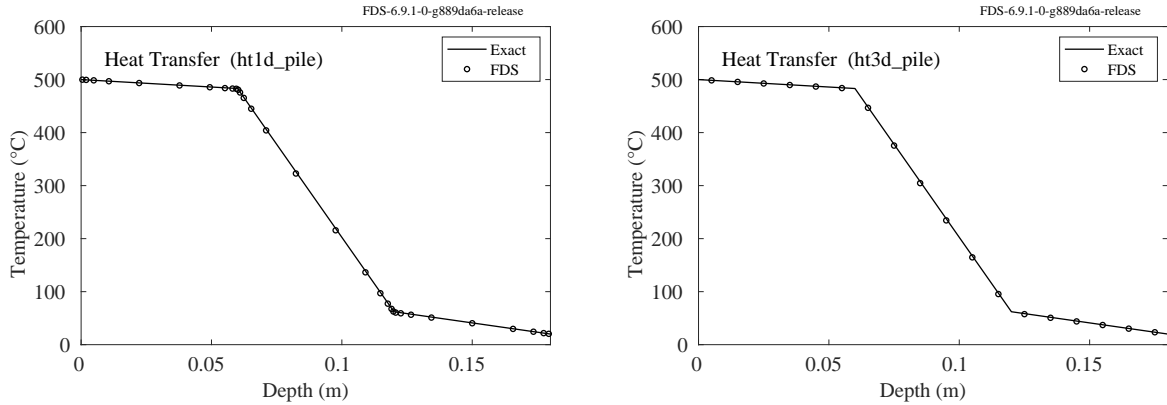


Figure 11.21: Temperature profiles through a stack of three materials with different thermal conductivities. (Left) A 1-D calculation with non-uniform internal nodes. (Right) A 3-D calculation with uniform internal nodes.

# Chapter 12

## Pyrolysis

This chapter includes tests of the routines that calculate the thermal decomposition of materials. Solid surfaces can consist of multiple layers, and each layer can consist of multiple material components. Each material component may undergo several competing reactions, and each of these reactions may produce some other solid component (residue), gaseous fuel, and/or water vapor.

### 12.1 Conservation of Pyrolyzed Mass (`surf_mass_conservation`)

The calculations described in this section check the conservation of mass produced by the pyrolysis algorithm. In the tests, four independent modeling options are varied:

1. The `SURF` line can be associated with either a solid surface as designated by a `VENT` line, or by solid particles as described by a `PART` line.
2. The `SURF` geometry can be either `CARTESIAN`, `CYLINDRICAL`, or `SPHERICAL`.
3. The `MATL` can be either charring (non-zero `NU_RESIDUE`) or non-charring.
4. The pyrolysis product can be either the fuel gas defined by the mixture fraction model, or an additional gas species, defined by a `SPEC` line.

In most cases, the wall thickness (or radius for cylindrical and spherical geometries) is 0.01 m. The material density is 360 kg/m<sup>3</sup> and the yield of gaseous products for the charring cases is 0.5, i.e., half of the original mass. For Cartesian surfaces, the mass loss per unit area is 1.8 kg/m<sup>2</sup> for charring, and 3.6 kg/m<sup>2</sup> for non-charring materials. For cylindrical surfaces, the volume per unit surface area is  $r/2$ , and thus the mass loss per unit area is  $360(1 - 0.5) \times r/2 = 0.9 \text{ kg/m}^2$  for charring, and  $1.8 \text{ kg/m}^2$  for non-charring materials. For spherical surfaces, the volume per unit surface area is  $r/3$ , and thus the mass loss per unit area is  $360(1 - 0.5) \times r/3 = 0.6 \text{ kg/m}^2$  for charring, and  $1.2 \text{ kg/m}^2$  for non-charring materials.

#### 12.1.1 Pyrolysis at a Solid Surface

The analytical mass losses are calculated by multiplying the mass per unit area by the `VENT` area, which in all cases is 1 m<sup>2</sup>. The expected and computed results for charring material are compared in Fig. 12.1. The expected and computed results for non-charring material are compared in Fig. 12.2.

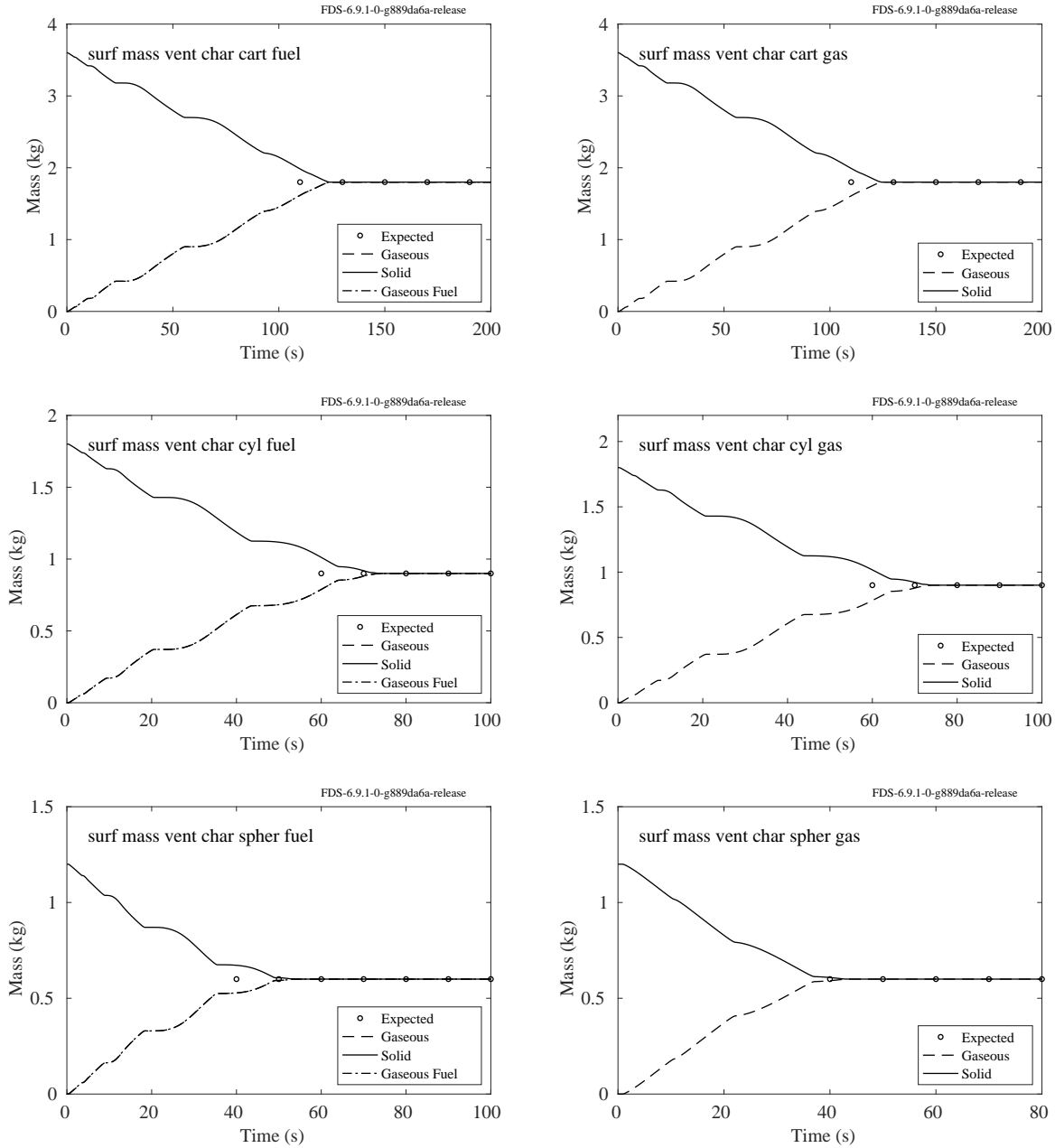


Figure 12.1: Comparison of analytical and predicted mass change for charring surfaces that are introduced as VENTS.

### 12.1.2 Pyrolysis of Discrete Particles

For Lagrangian particles, the expected values of the mass are obtained by multiplying the material density by the particle volume by the residue fraction. For Cartesian surfaces (plates), the particle area is two times the product of the parameters LENGTH and WIDTH on the SURF line, both of which are given a value of 0.05 m. As a result, the expected masses for plate particles are  $360(1 - 0.5) \times 2\delta LW = 0.009$  kg for charring, and 0.018 kg for non-charring materials. Note that the half-thickness,  $\delta = 0.01$  m, is specified on the SURF line as THICKNESS. For cylindrical particles, the LENGTH is 0.1 m, and the radius,  $r$  (specified via THICKNESS), is 0.01 m. The expected masses are thus  $360(1 - 0.5) \times \pi r^2 L = 0.00565$  kg for charring, and 0.0113 kg for

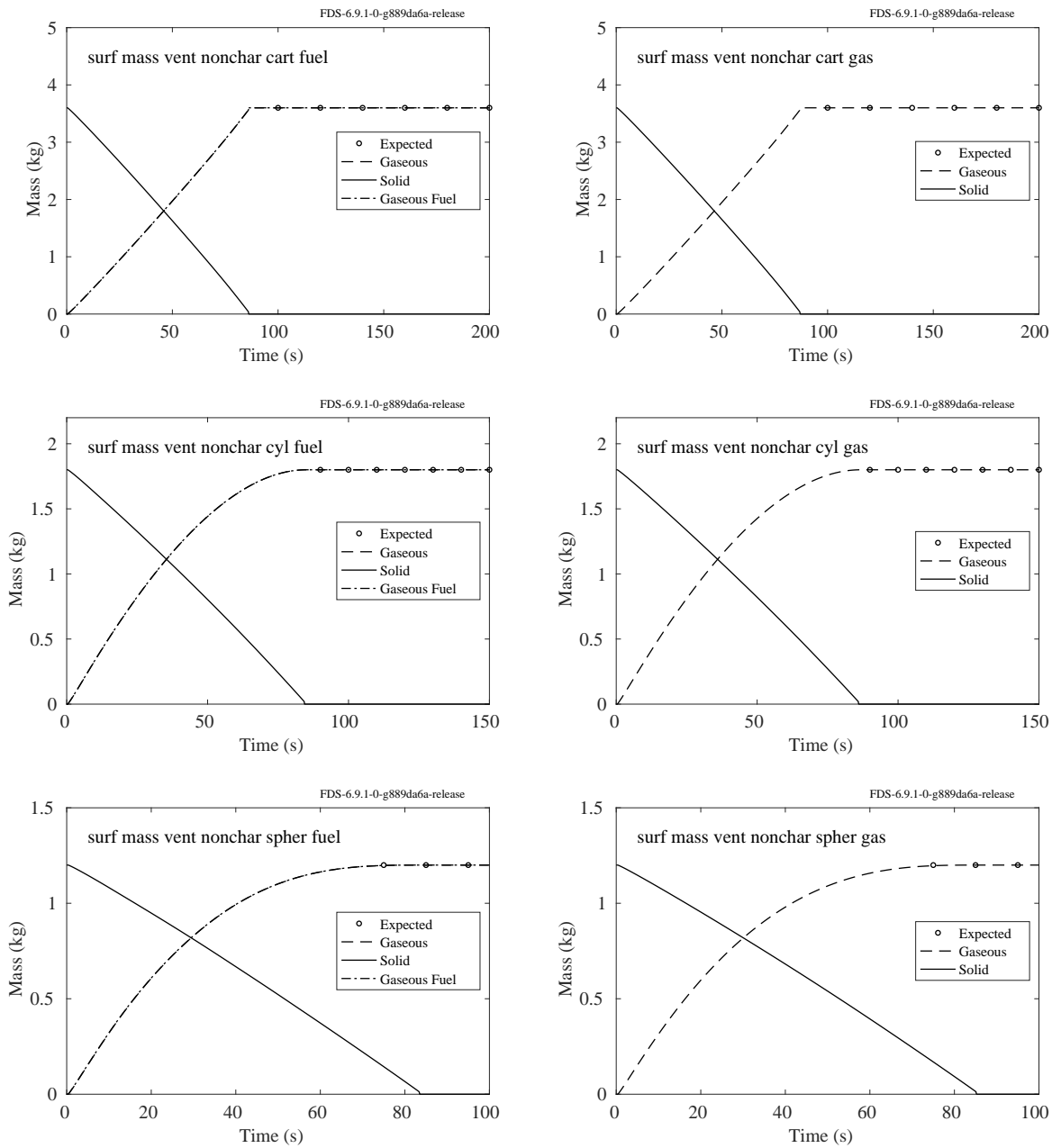


Figure 12.2: Comparison of analytical and predicted mass change for non-charring surfaces that are introduced as VENTs.

non-charring materials. For spherical particles, the expected mass is  $360(1 - 0.5) \times 4\pi r^3 / 3 = 7.54 \times 10^{-4}$  kg for charring, and  $1.51 \times 10^{-3}$  kg for non-charring materials.

## Charring Particles

The analytical and computed results for charring material are compared in Fig. 12.3. The analytical and computed results for non-charring material are compared in Fig. 12.4.

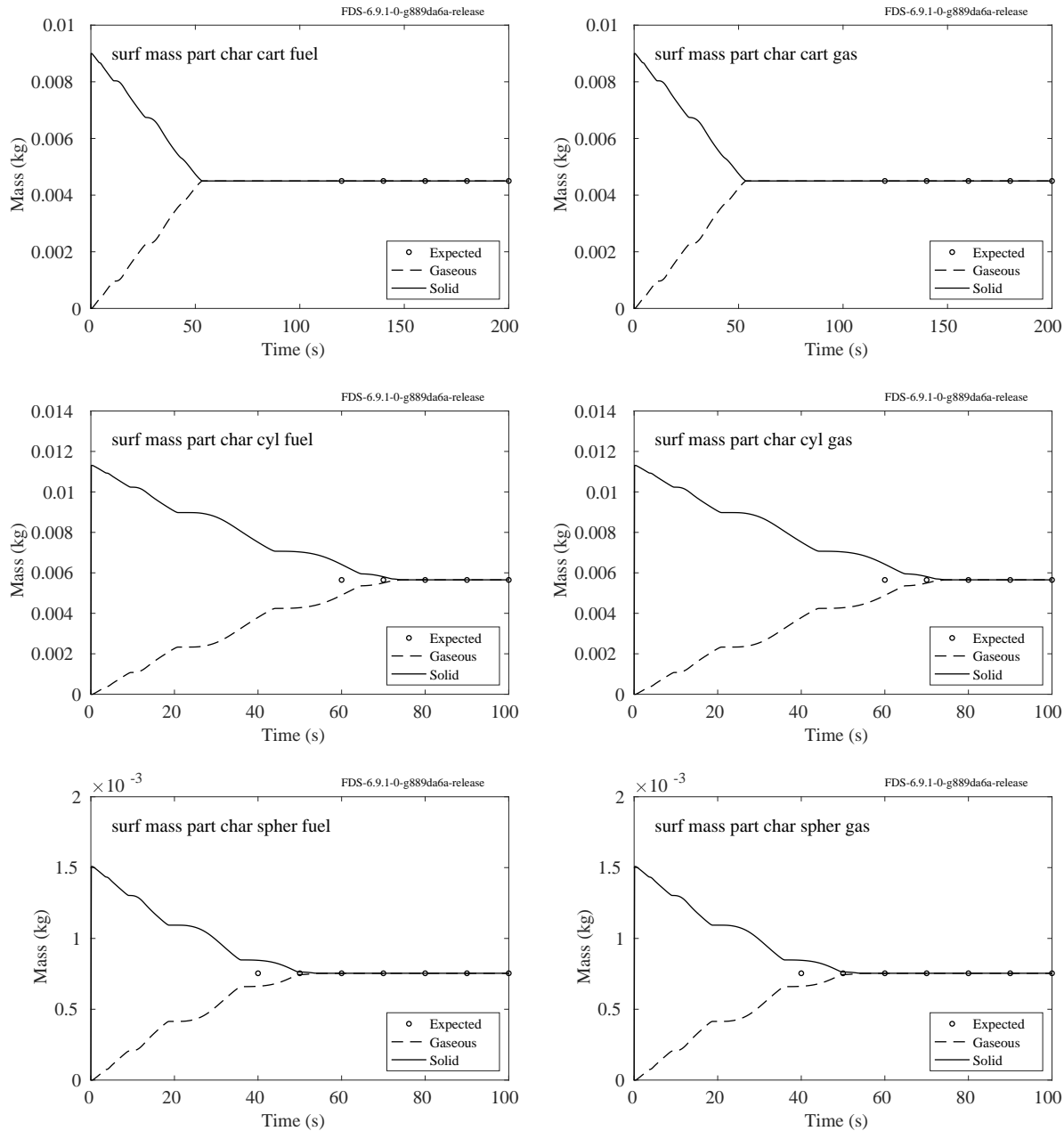


Figure 12.3: Comparison of analytical and predicted mass change for charring particle surfaces.

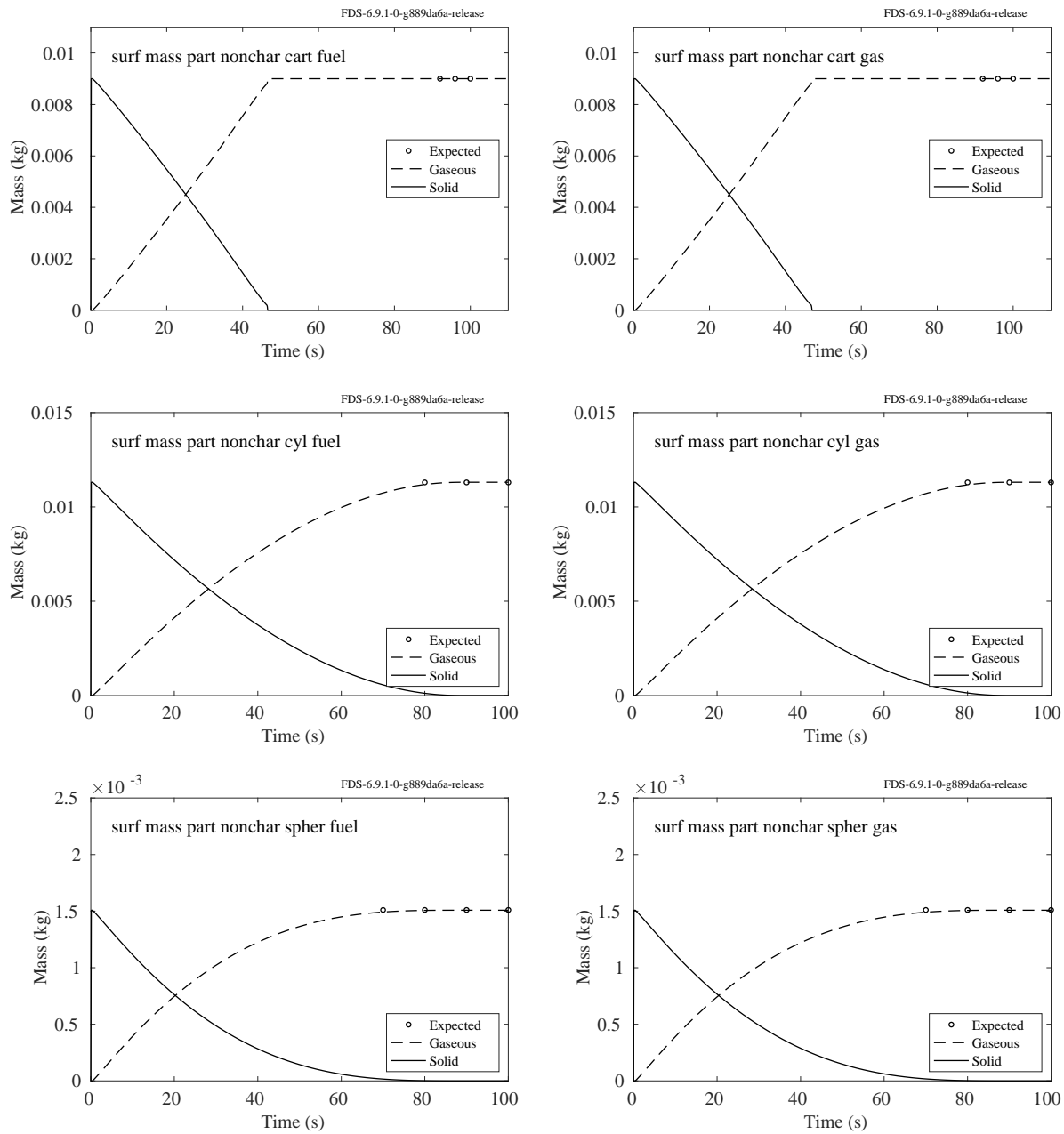


Figure 12.4: Comparison of analytical and predicted mass change for non-charring particle surfaces.

## Particles that Generate Multiple Gas Species

Figure 12.5 shows the results of three test cases involving 0.1 kg of flat, cylindrical, or spherical particles in a unit cube that simultaneously generate fuel gas and water vapor, like wood or vegetation.

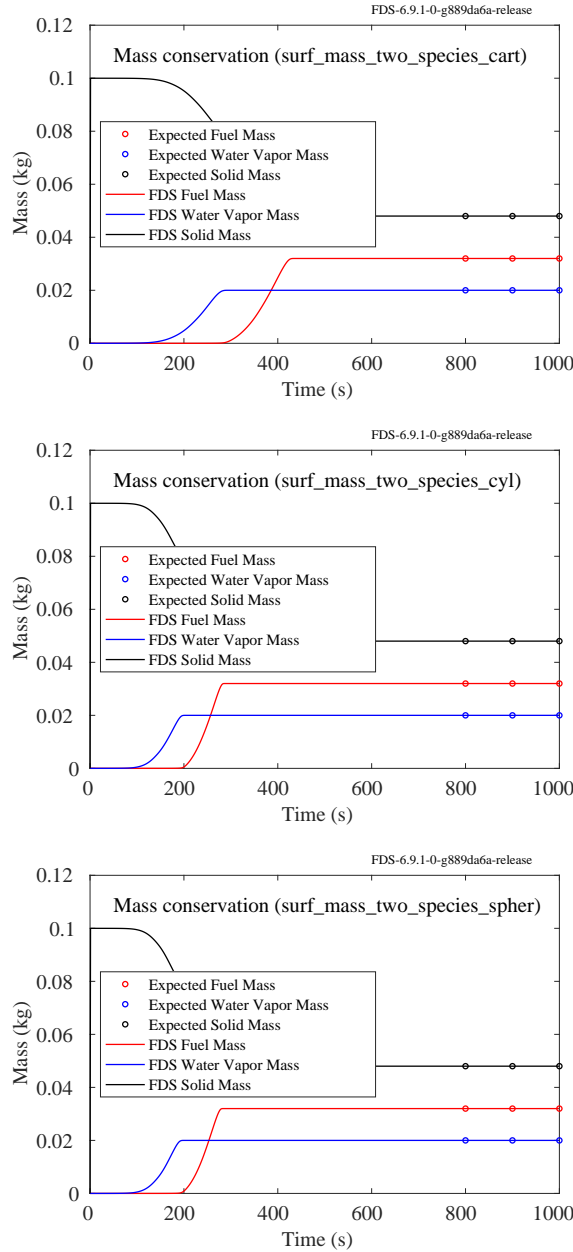


Figure 12.5: Comparison of analytical and predicted mass change for particles that generate water and fuel gas.

### 12.1.3 Rate of Solid Particle Decomposition (`part_baking_soda`)

**Paul Papas (Raytheon Technologies) and Changmin Cao (Collins Aerospace Ireland)**

In this set of cases we present a simple analytical solution for the solid phase decomposition of a spherical particle with a constant rate of reaction under isothermal conditions. Let  $m(t)$  denote the mass of a spherical particle with radius  $r(t)$ , changing with time,  $t$ . The initial mass is  $m_0 = m(t=0)$ . The extent of reaction is defined as

$$\alpha \equiv \frac{m_0 - m}{m_0} \quad (12.1)$$

#### First-order Reaction Model

The density of the material,  $\rho$ , is a constant. The volume is denoted  $V(t)$ . The rate of change of  $\alpha$  for a first-order reaction is given by [96]

$$\frac{d\alpha}{dt} = k(1 - \alpha) \quad (12.2)$$

where the rate constant of the reaction is

$$k = Ae^{-E_a/(RT)} \quad (12.3)$$

Here,  $A$  is the Arrhenius parameter (1/s) and  $E_a$  is the activation energy (J/mol);  $R$  is the gas constant (8.3145 J/mol/K) and  $T$  is temperature in K.

Integrating with constant density gives

$$\int \frac{d\alpha}{1 - \alpha} = k \int dt \Rightarrow [\ln(1 - \alpha)]_{\alpha_0}^{\alpha} = -kt \quad (12.4)$$

$$\frac{1 - \alpha}{1 - \alpha_0} = e^{-kt} ; \quad \alpha_0 = 0 ; \quad \alpha = 1 - \frac{m}{m_0} \quad (12.5)$$

$$\frac{m}{m_0} = e^{-kt} \Rightarrow \frac{\rho V}{\rho_0 V_0} = e^{-kt} \Rightarrow r^3 = r_0^3 e^{-kt} \quad (12.6)$$

#### Example

We take  $A = 3.4e11$  1/s,  $E_a = 103000$  J/mol,  $r_0 = 2.5 \mu\text{m}$ , and compare FDS with the analytical solution for  $T = [420, 450, 500]$  K. Results are presented in Fig. 12.6 below.

#### Contracting Volume Reaction Model

The rate of change of  $\alpha$  for a contracting volume is given by [96]

$$\frac{d\alpha}{dt} = k 3(1 - \alpha)^{2/3} \quad (12.7)$$

For this model, it is helpful to first convert the extent of reaction back to the particle mass,

$$\frac{dm}{dt} = -k 3 m_0^{1/3} m^{2/3} \quad (12.8)$$

Integrating gives,

$$\int m^{-2/3} dm = -k 3 m_0^{1/3} \int dt \quad (12.9)$$

$$m^{1/3} = m_0^{1/3}(1 - kt) \quad (12.10)$$

$$(\rho V)^{1/3} = (\rho_0 V_0)^{1/3}(1 - kt) \quad (12.11)$$

Physically, the density would remain constant and the volume would contract, leading to a linear decrease in the particle radius,

$$r = r_0(1 - kt) \quad (12.12)$$

However, the FDS reaction equation is not set up to mimic the contracting volume model. Instead, for the same kinetics parameters, we can achieve the correct mass decay of the particle by holding the volume constant (`ALLOW_SHRINKING=F`) and adjusting the preexponential factor to account for the initial mass. By holding the volume constant, Eq. (12.8) may be written in terms of solid density for material  $\alpha$  as follows,

$$\frac{d\rho_{s,\alpha}}{dt} = -k \underbrace{3\rho_{s,\alpha}(0)^{1/3}}_{\text{adjustment factor}} \rho_{s,\alpha}^{2/3} \quad (12.13)$$

Therefore, to match the initial decay of the contracting volume model, we must multiply  $A$  by the factor  $3\rho_{s,\alpha}(0)^{1/3}$  and change the order of the reaction to 2/3.

## Example

We consider the contracting volume model applied to a spherical baking soda ( $\text{NaHCO}_3$ ) particle. We take  $A = 3.4e11 \times 3(2200)^{1/3} = 133e11$  1/s (note: the initial density of the particle is  $2200 \text{ kg/m}^3$ ),  $E_a = 103000 \text{ J/mol}$ ,  $r_0 = 2.5 \mu\text{m}$ , and compare FDS with the analytical solution for the particle diameter with the rate constant evaluated at  $T = [420, 450, 500] \text{ K}$ . We set `ALLOW_SHRINKING=F` and we report the particle diameter as the initial diameter times the cube root of the density ratio,  $d(t) = d_0(\rho_s[t]/\rho_s[0])^{1/3}$ . The results are shown in Fig. 12.6 along with a comparison to the rate for the first-order model with the same Arrhenius parameters. It is worth noting that the contracting volume model leads to a significantly higher decay rate than the first-order reaction for the same set of parameters.

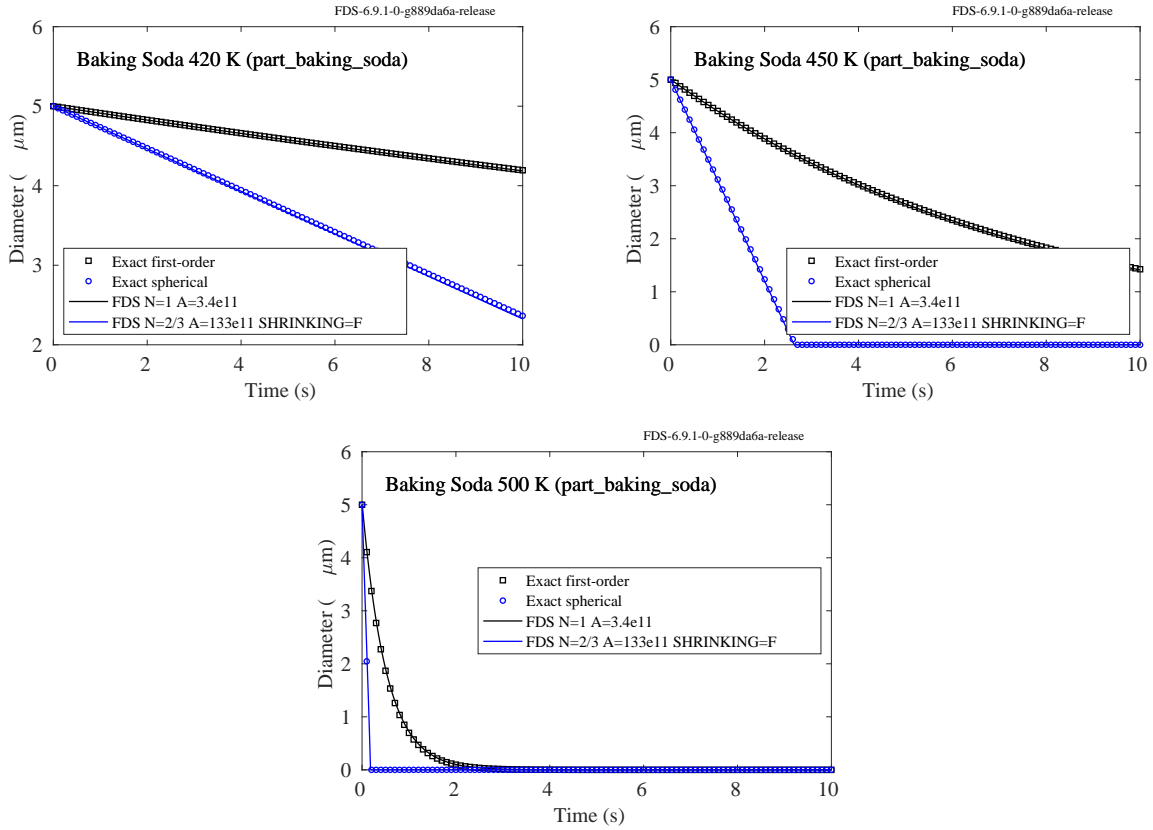


Figure 12.6: Comparison of analytical and predicted particle diameter for first-order and contracting volume solid phase reaction under isothermal conditions.

## 12.2 Conservation of Pyrolyzed Energy (`mat1_e_cons`)

Nine simple test cases are created to verify the process of ensuring the MATL reactions conserve energy. Each case is a cube 1 m on a side with 4 grid cells in each dimension. One or more materials and gas species are defined. All materials are defined with a density of 1 kg/m<sup>3</sup>. All species are defined with a molecular weight of 1000 g/mol. This is done for convenience as it means that the heat of formation in kJ/mol is the same numerical values as the enthalpy in kJ/kg. For each material that is defined, a single wall cell VENT is defined with a SURF such that the wall cell contains 1 kg of material. The WALL ENTHALPY is output for each wall cell. The cases are explained below with results shown in Figs. 12.7 and 12.8.

In case 1, there is a single species given a heat of formation of 0 kJ/mol. A single material is defined with a specific heat of 0.5 kJ/kg/K and a reaction that produces the gas species with a heat of reaction of 1000 kJ/kg at a reference temperature of 300 °C with a pyrolysis range of 40 K. This gives:

$$H_{\text{MATL1}}(300 \text{ }^{\circ}\text{C}) + H_{\text{MATL1,adj}} + 1000 \text{ kJ/kg} = H_{\text{SPEC1}}(300 \text{ }^{\circ}\text{C}) \quad (12.14)$$

$$286.575 \text{ kJ/kg} + H_{\text{MATL1,adj}} + 1000 \text{ kJ/kg} = 275 \text{ kJ/kg} \quad (12.15)$$

$$H_{\text{MATL1,adj}} = -1011.575 \text{ kJ/kg} \quad (12.16)$$

At ambient temperature this makes the expected enthalpy of the wall cell  $298.15 \text{ K} \times 0.5 \text{ kJ/kg/K} - 1011.575 \text{ kJ/kg} = -865 \text{ kJ/kg}$ .

Case 2 repeats case 1 with a species heat of formation of 1000 kJ/mol. This makes the expected ambient enthalpy -1865 kJ/kg.

Case 3 combines case 1 and case 2 into a single input. The case 1 material is changed from using a reference temperature and pyrolysis range to using the resulting A ( $7.68 \times 10^{31}$  1/s) and E (371000 J/mol) which was taken from the case 1 output file. This case tests the virtual TGA (the case 1 material will only have the same adjustment if there is the same reference temperature) and that multiple sets of reactions are correctly handled.

Case 4 takes case 1 and changes the reaction to produce equal amounts of the gas species and a second material. The second material has a specific heat of 1.5 kJ/kg/K and a reaction that produces the gas species with a heat of reaction of 500 kJ/kg at a reference temperature of 400 °C. This case has two total reactions that include two total materials. The solution can be found by hand by first finding the adjustment for the second material (following the example for case 1) and then using that adjustment to find the value for the first material.

Case 5 takes case 4 and adds a second reaction for the first material. This reaction creates a second copy of the first material with a heat of reaction of 500 kJ/kg at a reference temperature of 280 °C. This can be thought of as a phase change. The second copy also produces equal amounts of the gas species and the other material expect with a heat of reaction of 500 kJ/kg. This is now an overdetermined system as there are three materials and four reactions; however, note that the parallel paths to creating the gas species have the same total enthalpy change. The first material directly pyrolyzing has a heat of reaction of 1000 kJ/kg, and the path of the phase change also has a total enthalpy change of 1000 kJ/kg split between the phase change and the pyrolysis. Therefore, even though the system is overdetermined, an exact solution is expected. This is seen in the results where the first and second material enthalpies in case 5 match those from case 4.

Case 6 takes case 5 and increases the heat of reaction post-phase change to 1000 kJ/kg. Now an exact solution is no longer expected. It can be seen that the second material has the same enthalpy but the first material and its phase-change have different ambient enthalpies. The post-phase change material enthalpy has changed by 333 kJ/kg but the reaction enthalpy changed by 500 kJ/kg so energy is not completely conserved. As a least squares solution, it is conserved as best as it can be.

Case 7 takes case 4 and removes the reaction from the second material. This is now an underdetermined system where there are two materials and a single reaction. Following the process for case 1, one gets that

$$H_{\text{MATL1,adj}} - 0.5H_{\text{MATL2,adj}} = -719.2125 \text{ kJ/kg} \quad (12.17)$$

The minimum matrix solution is  $H_{\text{MATL1,adj}}=-575.37$  kJ/kg and  $H_{\text{MATL2,adj}}=287.68$  kJ/kg. It can be shown that this is a minimal solution by taking the norm of the solution vector. This can be expressed in terms of only  $H_{\text{MATL1,adj}}$  as

$$H_{\text{MATL1,adj}}^2 + (2(H_{\text{MATL1,adj}} + 791.2125 \text{ kJ/kg}))^2 \quad (12.18)$$

The minimum is where the derivative is zero or

$$10H_{\text{MATL1,adj}} + 8 \times 791.2125 \text{ kJ/kg} = -575.37 \text{ kJ/kg}. \quad (12.19)$$

Case 8 takes case 1 and deletes the gas production. In this case FDS will assume that a virtual material is produced with the same specific heat as the original material. This results in a least squares solution where the reaction enthalpy is split over the original material and the virgin material making the expected ambient temperature enthalpy of the wall cell  $298.15 \text{ K} \times 0.5 \text{ kJ/kg/K} - 500 \text{ kJ/kg} = -353.425 \text{ kJ/kg}$ .

Case 9 takes case 1 and produces a particle of a second material with the same specific heat as the first material. This is equivalent to case 8 and the same ambient enthalpy is expected.

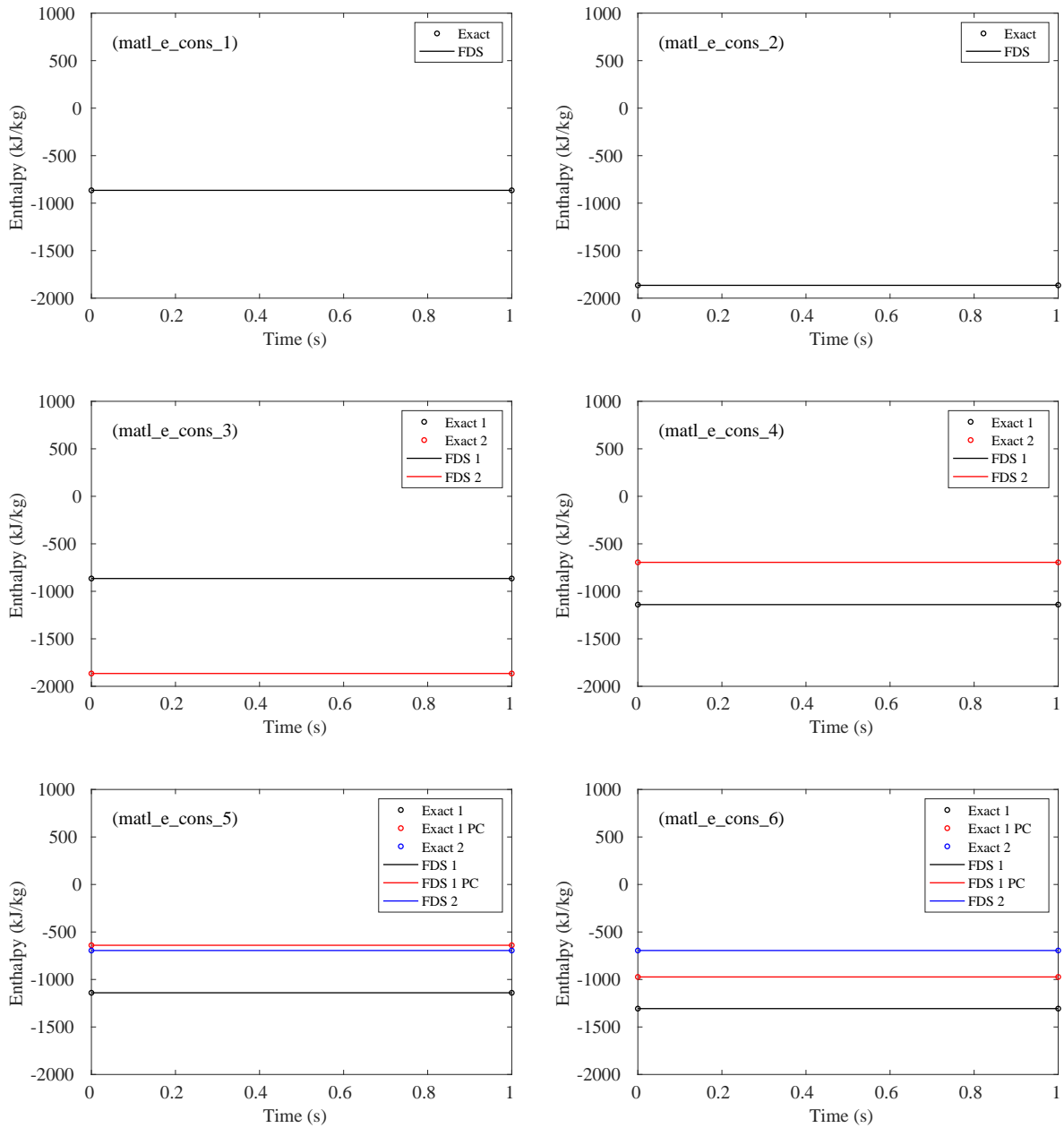


Figure 12.7: Comparison of analytical and predicted wall enthalpy for the `matl_e_cons` test cases 1-6.

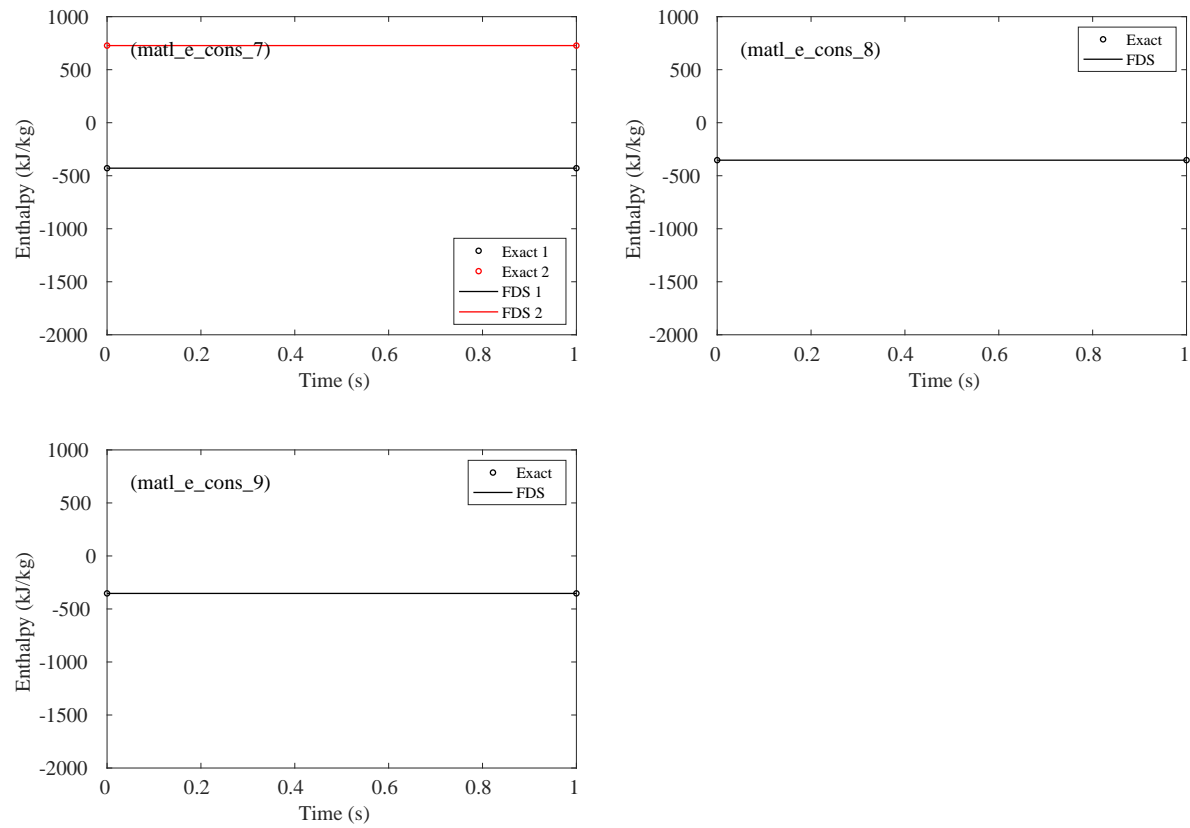


Figure 12.8: Comparison of analytical and predicted wall enthalpy for the `matl_e_cons` test cases 7-9.

## 12.3 Burning Rate of a Small Object (`cell_burn_away`)

In FDS, it is assumed that heat conduction and pyrolysis within solids are functions of depth only. This can be problematic in cases where entire solid obstructions burn away. In this example, a single grid cell, 4 cm on a side, is made up of a material with density  $\rho_s = 50 \text{ kg/m}^3$  and constant reaction rate,  $r_s = 0.05 \text{ s}^{-1}$ . The burning rate of the single grid cell,  $\dot{m}$ , is given by:

$$\dot{m} = \delta \rho_s r_s A \quad (12.20)$$

where  $\delta$  is the thickness of the surface layer and  $A$  is the area of the six faces of the single grid cell. If we set the layer thickness so that  $\delta A = V$ , where  $V$  is the volume of the cell, and note that the mass of the cell is  $m = \delta A \rho_s$ , Eq. (12.20) becomes:

$$\dot{m} = m r_s = m_0 r_s e^{-r_s t} \quad (12.21)$$

Figure 12.9 displays the computed and analytical burning rate. Note that the burning rate is proportional to the mass and the mass decays exponentially to zero in this case because we have specified the `THICKNESS` to be  $V/A$  and set the `BULK_DENSITY` to be  $50 \text{ kg/m}^3$  on the `OBST` line defining the single solid grid cell.

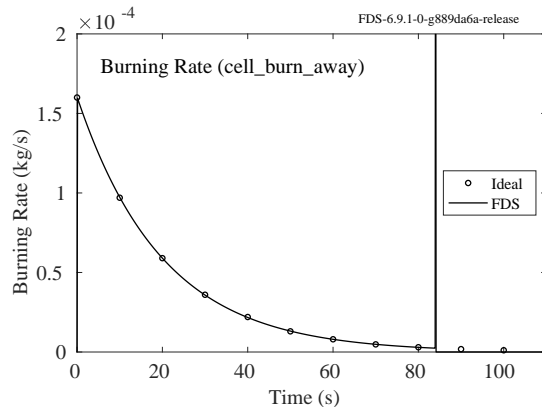


Figure 12.9: Burning rate of a single grid cell with fixed reaction rate.

## 12.4 Evaporation of a Liquid Surface

### 12.4.1 Mass Conservation (`surf_mass_vent_liquid`)

To test the liquid fuel evaporation model, a 1 cm deep pool of heptane is exposed to a  $50 \text{ kW/m}^2$  heat flux and the evolution of fuel vapor and surface density are tracked. Results are shown in Fig. 12.10. Note that in the “nonconforming” case, the specified pool dimensions do not align with the specified mesh, but the same amount of fuel vapor is expected.

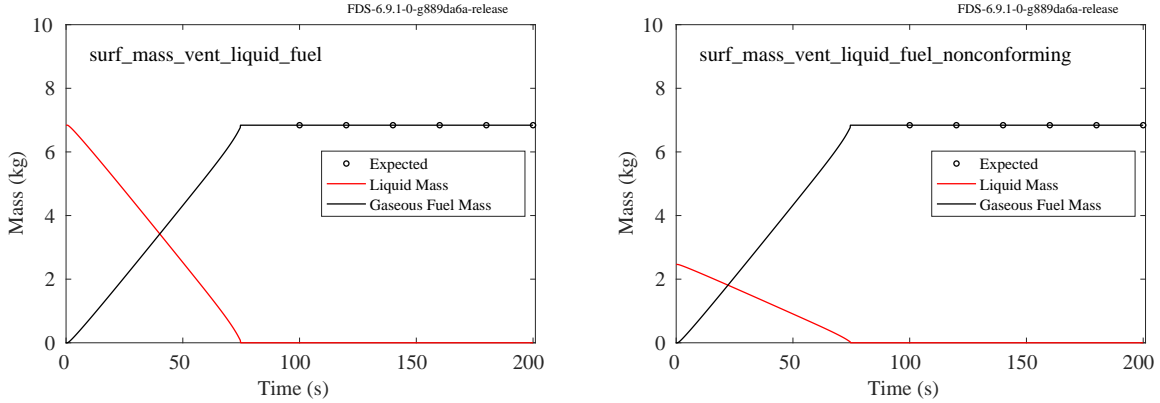


Figure 12.10: Comparison of analytical and predicted mass change for a liquid surface.

### 12.4.2 Evaporation Rate (water\_pool)

In this example, air with an RH = 25 % relative humidity and temperature  $T_a = 305$  K flows with velocity  $U = 0.15$  m/s over an  $L = 1.2$  m long,  $W = 1$  m wide pool of water with a surface temperature of  $T_s = 293$  K. The evaporation rate of water is given by the following relation:

$$\dot{m} = LW h_m \rho_{\text{film}} \ln(1 + B) \approx 1.42 \times 10^{-5} \text{ kg/s} ; \quad B = \frac{Y_{sv} - Y_g}{1 - Y_{sv}} \approx 0.00925 \quad (12.22)$$

$h_m$  is the mass transfer coefficient,  $\rho_{\text{film}}$  is the density within a thin surface layer,  $B$  is the Spalding mass transfer number,  $Y_{sv}$  is the “surface vapor” mass fraction of water vapor at the liquid surface, and  $Y_g$  is the mass fraction of water vapor in the ambient air. The composition of the surface layer is obtained from the Clausius-Clapeyron equation for the equilibrium vapor pressure. The volume and mass fraction of water vapor at the surface is:

$$X_{sv} = \exp \left[ -\frac{h_v W_{H_2O}}{R} \left( \frac{1}{T_s} - \frac{1}{T_b} \right) \right] \approx 0.0278 ; \quad Y_{sv} = \frac{X_{sv} W_{H_2O}}{X_{sv} W_{H_2O} + (1 - X_{sv}) W_{\text{air}}} \approx 0.0175 \quad (12.23)$$

The volume and mass fraction of water vapor in the ambient air is:

$$X_g = \frac{\text{RH}}{100} \exp \left[ -\frac{h_v W_{H_2O}}{R} \left( \frac{1}{T_a} - \frac{1}{T_b} \right) \right] \approx 0.0134 ; \quad Y_g = \frac{X_g W_{H_2O}}{X_g W_{H_2O} + (1 - X_g) W_{\text{air}}} \approx 0.0084 \quad (12.24)$$

Here  $h_v = 2260$  kJ/kg is the heat of vaporization of water,  $W_{H_2O} = 18$  kg/kmol is its molecular weight, and  $T_b = 373$  K is its boiling temperature.  $R = 8.3145$  kJ/kmol/K is the gas constant and  $W_{\text{air}} = 29$  kg/kmol is the molecular weight of air. The mass transfer coefficient is given by

$$h_m = \frac{\text{Sh}D}{L} \approx 1.06 \times 10^{-3} \text{ m/s} \quad (12.25)$$

Sh is the Sherwood number and  $D = 2.10 \times 10^{-5}$  m<sup>2</sup>/s is the diffusivity of water vapor into air at  $T = 293$  K. An empirical correlation for the Sherwood number is

$$\text{Sh} = 0.037 \text{ Sc}^{\frac{1}{3}} \text{ Re}^{\frac{4}{5}} \approx 60.8 ; \quad \text{Sc} = 0.71 ; \quad \text{Re} = \frac{\rho_a U L}{\mu} \approx 12062 \quad (12.26)$$

where  $\mu = 1.8 \times 10^{-5}$  kg/m/s is the viscosity of air at  $T = 293$  K. The gas density at the liquid surface is given by

$$\rho_{\text{film}} = \frac{P_0 W_{\text{air}}}{1000 R T_s} \approx 1.21 \text{ kg/m}^3 \quad (12.27)$$

where  $p_0 = 101325 \text{ Pa}$ .

Note that `ADJUST_H=F` is set in the input file to make the calculation of the analytical result easier.

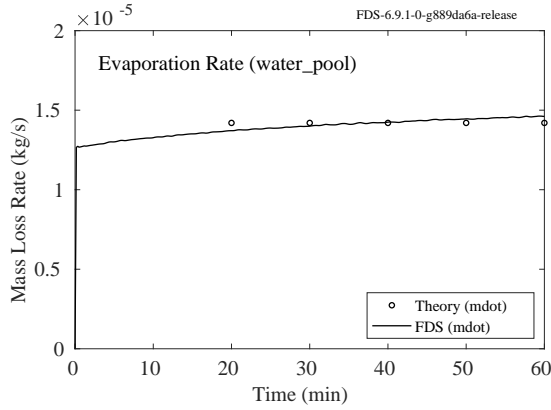


Figure 12.11: Evaporation rate of a pool of water.

Figure 12.11 compares the FDS predicted versus the theoretical evaporation rate. The prediction and theory are not exactly the same because the nominal parameters used above do not account for slight changes in surface temperature and water vapor concentration above the pool. Nevertheless, the two should be relatively close.

## 12.5 Change in Surface Emissivity (emissivity)

For thermally thick materials, the surface emissivity is computed as a mass-weighted sum of the individual values of the emissivity in the first condensed phase grid cell. In this verification test, the initial material, having emissivity of 1.0, is converted to another material, having emissivity of 0.0, at a constant rate of  $0.1 \text{ s}^{-1}$ . As a result, the surface emissivity should change linearly from 1.0 to 0.0 in 10 s (Fig. 12.12).

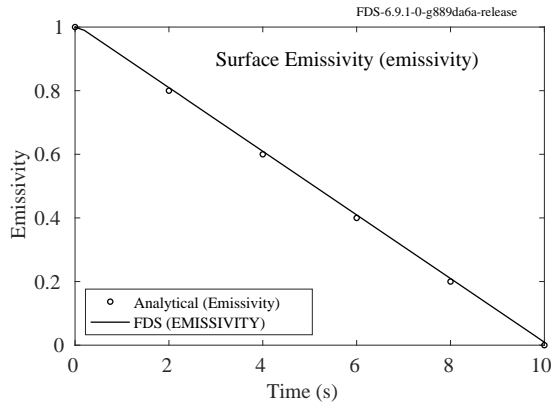


Figure 12.12: Testing the emissivity of solid materials.

## 12.6 Shrinking and swelling materials (`shrink_swell`)

A single layer of a multi-component material contains reacting material (1) and an inert matrix (2). If the product material (3) of the reaction is of higher density than the reactant ( $\rho_3 > \rho_1$ ), the layer thickness  $\Delta$  should shrink. If the product density is lower than the reactant's density ( $\rho_3 < \rho_1$ ) the layer should swell (increase) in thickness. If the inert material has a static matrix structure (`ALLOW_SHRINKING=.FALSE.` or `ALLOW_SWELLING=.FALSE.`) the layer thickness should not change. The parameters of the six test cases are shown in the following table. Figure 12.13 shows the surface densities, which obviously should not change, and the surface thicknesses over the time of the simulation.

Table 12.1: Parameters used to test the shrinking and swelling of materials.

Case	Reactant		Inert			Product	Layer			
	$\rho_1$ (kg/m <sup>3</sup> )	$Y_1$	$\rho_2$ (kg/m <sup>3</sup> )	$Y_2$	Allow shrink/swell		$\rho_3$ (kg/m <sup>3</sup> )	$\rho_s(0)$ (kg/m <sup>3</sup> )	$\rho_s(\text{end})$ (kg/m <sup>3</sup> )	$\Delta(0)$ (m)
Shrink 1	500	1	0	0	T	1000	500	1000	0.001	0.0005
Shrink 2	500	0.9	500	0.1	T	1125	500	1000	0.001	0.0005
Shrink 3	500	0.9	500	0.1	F	1125	500	500	0.001	0.001
Swell 1	1000	1	90	0	T	500	1000	500	0.001	0.002
Swell 2	1000	0.9	1000	0.1	T	450	1000	500	0.001	0.002
Swell 3	1000	0.9	1000	0.1	F	450	1000	1000	0.001	0.001

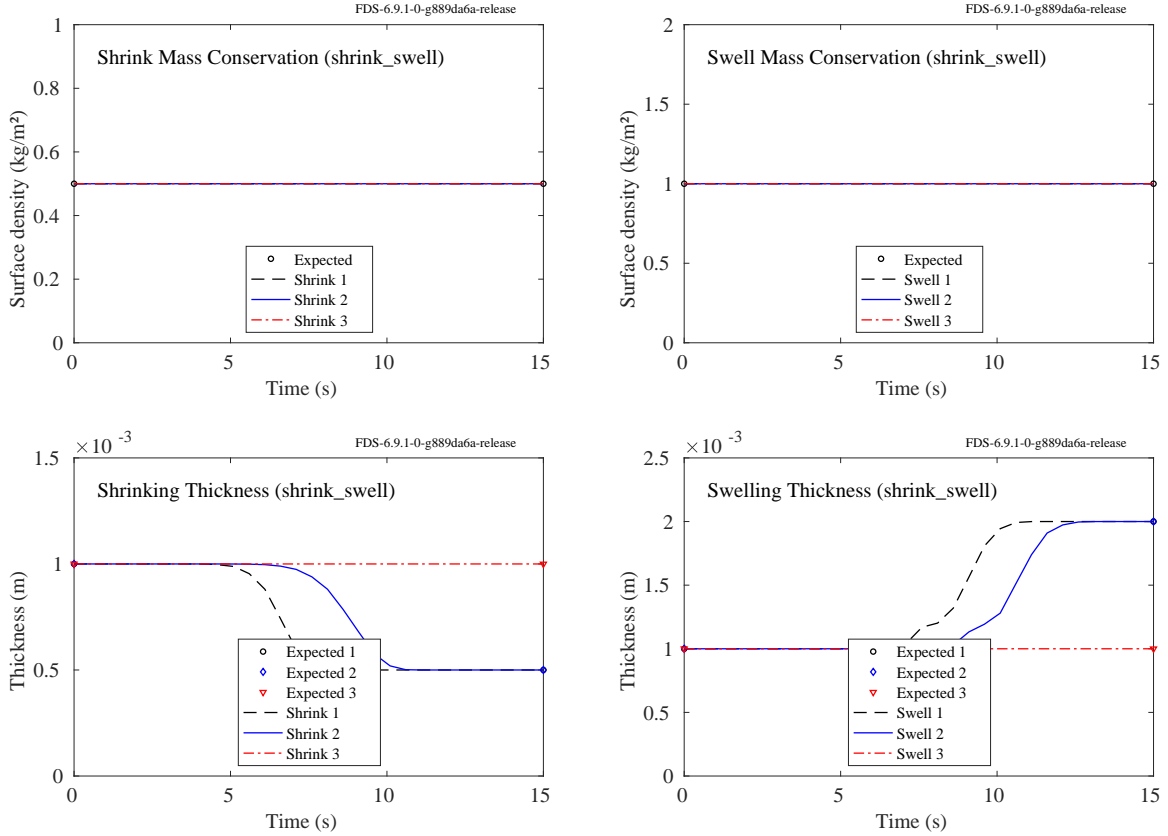


Figure 12.13: Testing the shrinking and swelling surfaces.

## 12.7 Enthalpy of Solid Materials ([enthalpy](#))

Consider a thin plate of conductive material that is exposed on one side to an elevated temperature heat source and exposed on the other to an ambient temperature void. In the thermally thin limit, the temperature of the slab is governed by the following equation

$$\frac{dT_s}{dt} = \frac{\dot{q}_{\text{front}}'' + \dot{q}_{\text{back}}''}{c_s \rho_s \delta} \quad (12.28)$$

In this example, the initial exposure to the front side of the slab is  $3 \text{ kW/m}^2$ . The original Material A undergoes a reaction to form Material B. The reaction rate is constant,  $6 \text{ kg/(m}^3\cdot\text{s)}$ , which in this case means that Material A, with an initial density of  $30 \text{ kg/m}^3$ , disappears in exactly 5 s. This is achieved by setting  $n_s$  and  $E$  to 0 and  $A$  to  $6 \text{ kg/(m}^3\cdot\text{s)}$  in the reaction rate term:

$$r = \rho_{s,A}^{n_s} A \exp\left(-\frac{E}{RT_s}\right) \quad (12.29)$$

The density and conductivity of both materials are  $30 \text{ kg/m}^3$  and  $10 \text{ W/(m K)}$ , respectively. The emissivity of the front and back is 1. The specific heat of Material A changes from  $1.0 \text{ kJ/(kg K)}$  to  $0.1 \text{ kJ/(kg K)}$  above  $80^\circ\text{C}$ , while the specific heat of material B is constant at  $1.0 \text{ kJ/(kg K)}$ . The slab is 1 mm thick. Note that the “analytical” solution is actually a simple numerical integration of the equations above with a small

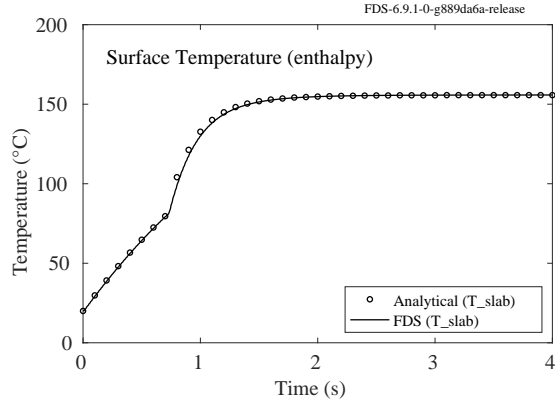


Figure 12.14: Testing the enthalpy of solid materials.

time step to ensure accuracy. This example (Fig. 12.14) tests a number of features, including the reaction rate, mass weighted specific heats, and radiation boundary conditions. Note that the convective heat transfer has been turned off, and the correct steady-state temperature is calculated by FDS.

## 12.8 A Simple Two-Step Pyrolysis Example (`two_step_solid_reaction`)

Before considering actual experimental measurements, it is necessary to check the accuracy of the ordinary differential equation solver within FDS. Consider a simplified set of ordinary differential equations describing the mass fraction of three components of a solid material undergoing thermal degradation:

$$\begin{aligned}\frac{dY_a}{dt} &= -K_{ab}Y_a \\ \frac{dY_b}{dt} &= K_{ab}Y_a - K_{bc}Y_b \\ \frac{dY_c}{dt} &= K_{bc}Y_a\end{aligned}\tag{12.30}$$

where the mass fraction of component  $a$  is 1 initially. The analytical solution is:

$$Y_a(t) = \exp(-K_{ab}t)\tag{12.31}$$

$$Y_b(t) = \frac{K_{ab}}{K_{bc} - K_{ab}} \exp(-K_{ab}t) - \exp(-K_{bc}t)\tag{12.32}$$

$$Y_c(t) = [K_{ab}(1 - \exp(-K_{bc}t)) + K_{bc} * (\exp(-K_{ab}t) - 1)] / (K_{ab} - K_{bc})\tag{12.32}$$

The analytical and numerical solution for the parameters  $K_{ab} = 0.389$  and  $K_{bc} = 0.262$  are shown in Fig. 12.15:

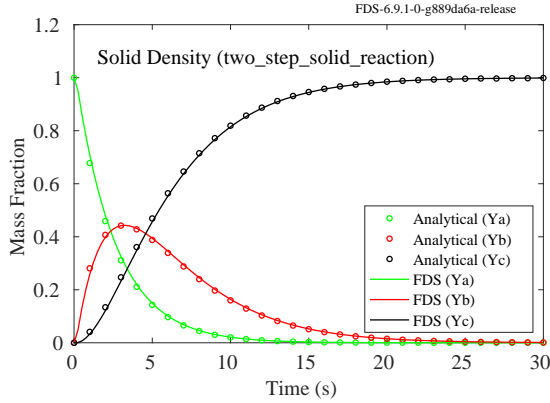


Figure 12.15: Comparison of a two-step solid pyrolysis calculation with an analytical solution.

## 12.9 Interpreting Bench-Scale Measurements

This section describes a method of deriving and applying the values of the kinetic parameters for the thermal decomposition of a solid, following the methodology described by Lyon [97]. This is the basic theory that underlies measurement methods like Thermo-Gravimetric Analysis (TGA) and Micro-Combustion Calorimetry (MCC).

### 12.9.1 General Theory

Consider a small sample of solid material that is heated at a relatively slow, constant rate. Assume that the solid consists of  $N$  material components, with each component mass fraction denoted by  $Y_\alpha(t)$ . As the solid is heated, each component undergoes a reaction to form undetermined gases or a single solid residue whose mass fraction is denoted  $Y_r(t)$  and whose yield is denoted by  $v_r$ . The governing equations for the component mass fractions are:

$$\frac{dY_\alpha}{dt} = -A_\alpha Y_\alpha \exp\left(-\frac{E_\alpha}{RT}\right) ; \quad Y_\alpha(0) = Y_{\alpha,0} ; \quad \alpha = 1, N \quad (12.33)$$

$$\frac{dY_r}{dt} = -v_r \sum_\alpha \frac{dY_\alpha}{dt} ; \quad Y_r(0) = 0 \quad (12.34)$$

In standard test apparatus, the temperature of the sample is increased linearly in time,  $dT/dt = \beta$ . Because the test results are usually expressed as a function of temperature rather than time, it is convenient to rewrite Eq. (12.33) as:

$$\frac{dY_\alpha}{dT} = -\frac{A_\alpha}{\beta} Y_\alpha \exp\left(-\frac{E_\alpha}{RT}\right) ; \quad Y(T = T_0) = Y_{\alpha,0} \quad (12.35)$$

The decomposition rate for each material component,  $-dY_\alpha/dt$ , peaks at a temperature denoted by  $T_{\alpha,p}$  with a value denoted by  $r_{\alpha,p}$ . At this temperature, the second derivative of  $Y_\alpha$  is zero:

$$\begin{aligned} \frac{d^2Y_\alpha}{dT^2} &= -\frac{A_\alpha}{\beta} \frac{dY_\alpha}{dT} \exp\left(-\frac{E_\alpha}{RT_{\alpha,p}}\right) - \frac{A_\alpha}{\beta} Y_\alpha \exp\left(-\frac{E_\alpha}{RT_{\alpha,p}}\right) \frac{E_\alpha}{RT_{\alpha,p}^2} \\ &= -\frac{dY_\alpha}{dT} \left[ \frac{A_\alpha}{\beta} \exp\left(-\frac{E_\alpha}{RT_{\alpha,p}}\right) - \frac{E_\alpha}{RT_{\alpha,p}^2} \right] = 0 \end{aligned} \quad (12.36)$$

Equation (12.35) can be integrated from  $Y_{\alpha,0}$  to  $Y_{\alpha,p}$  (the value of  $Y_{\alpha}$  at the peak), and  $T_0$  to  $T_{\alpha,p}$ :

$$\int_{Y_{\alpha,0}}^{Y_{\alpha,p}} \left( \frac{dY'_{\alpha}}{Y'_{\alpha}} \right) = -\frac{A_{\alpha}}{\beta} \int_{T_0}^{T_{\alpha,p}} \exp \left( -\frac{E_{\alpha}}{RT'} \right) dT' \approx -\frac{A_{\alpha}RT_{\alpha,p}^2}{\beta(E_{\alpha} + 2RT_{\alpha,p})} \exp \left( -\frac{E_{\alpha}}{RT_{\alpha,p}} \right) \quad (12.37)$$

Using Eq. (12.36) to eliminate  $A_{\alpha}$  yields:

$$\ln \left( \frac{Y_{\alpha,p}}{Y_{\alpha,0}} \right) = -\frac{E_{\alpha}}{E_{\alpha} + 2RT_{\alpha,p}} \approx -1 \quad (E_{\alpha} \gg 2RT_{\alpha,p}) \quad (12.38)$$

or more simply,  $Y_{\alpha,p} \approx Y_{\alpha,0}/e$ . Now, the activation energy can be evaluated using Eqs. (12.33) and (12.36):

$$E_{\alpha} = RT_{\alpha,p}^2 \frac{A_{\alpha}}{\beta} \exp \left( -\frac{E_{\alpha}}{RT_{\alpha,p}} \right) = \frac{RT_{\alpha,p}^2 r_{\alpha,p}}{\beta Y_{\alpha,p}} \approx \frac{RT_{\alpha,p}^2 e r_{\alpha,p}}{\beta Y_{\alpha,0}} \quad (12.39)$$

Then  $A_{\alpha}$  can be evaluated directly from Eq. (12.33):

$$A_{\alpha} = \frac{r_{\alpha,p}}{Y_{\alpha,p}} \exp \left( \frac{E_{\alpha}}{RT_{\alpha,p}} \right) \approx \frac{e r_{\alpha,p}}{Y_{\alpha,0}} \exp \left( \frac{E_{\alpha}}{RT_{\alpha,p}} \right) \quad (12.40)$$

Note that the formulae for  $A_{\alpha}$  and  $E_{\alpha}$  can be evaluated with parameters that are obtained directly by inspection of the plot of mass loss rate versus temperature. For each peak, the values of  $T_{\alpha,p}$  are easy to obtain by inspection. The initial mass fractions,  $Y_{\alpha,0}$ , can be estimated based on the relative area underneath each peak. The values of  $Y_{\alpha,0}$  should sum to 1.

The reaction rates,  $r_{\alpha,p}$ , require a slight interpretation. Typically, tests like TGA produce plots of the normalized sample mass,  $m/m_0$ , and its first derivative with time,  $-d(m/m_0)/dt$ . However, the reaction rate in the analysis above is interpreted as the change in the component mass fraction with time:

$$r_{\alpha} = -\frac{dY_{\alpha}}{dt} \quad (12.41)$$

The relationship between these two rates is

$$\sum_{\alpha} \frac{dY_{\alpha}}{dt} = \frac{1}{1 - v_r} \frac{d(m/m_0)}{dt} \quad (12.42)$$

Thus, the reaction rates we need for Eqs. (12.39) and (12.40),  $r_{\alpha,p}$ , are related to the normalized mass loss rate curve as follows:

$$r_{\alpha,p} = -\frac{1}{1 - v_r} \left. \frac{d(m/m_0)}{dt} \right|_{T=T_{\alpha,p}} \quad (12.43)$$

The examples in the following section describe how to interpret output from bench-scale material tests.

### 12.9.2 Interpreting TGA Data (`tga_sample`)

The solid curve of the left hand plot of Fig. 12.16 shows the measured normalized mass of a small solid sample undergoing heating at a rate of 5 °C/min in the TGA apparatus. The solid curve of the right hand plot is the mass loss rate, or minus the first derivative of the plot on the left. The goal of this example is to obtain the kinetic parameters,  $E_{\alpha}$  and  $A_{\alpha}$ , from Eqs. (12.39) and (12.40) to solve numerically the ODE, Eqs. (12.33) and (12.34). The first decision to make is the number of reactions. Usually, this corresponds to the number of peaks in the mass loss rate curve, but for realistic cases, some judgment is needed. In this example, it is assumed that there are two material components, each of which is undergoing a single

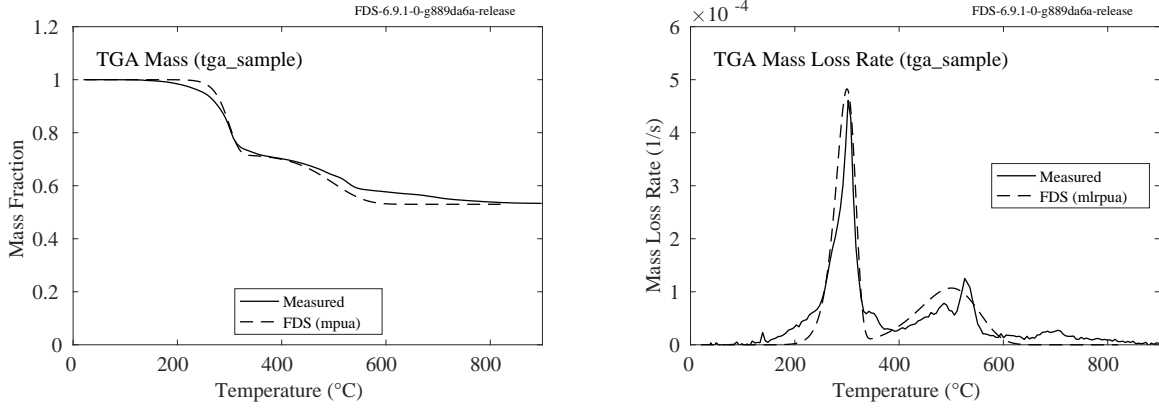


Figure 12.16: Results of a TGA analysis. At left is the normalized sample mass as a function of the temperature. At right is the corresponding mass loss rate.

reaction in the neighborhood of a certain temperature. By inspection,  $T_{1,p} = 300^\circ\text{C}$  and  $T_{2,p} = 500^\circ\text{C}$ . The next piece of information from the measurement is the residue fraction, which is obtained from the plot on the left,  $v_r = 0.53$ . From Eq. (12.43), the reaction rates are obtained by converting the peak mass loss rates from the plot on the right:  $r_{1,p} = 0.00045/0.47 \text{ s}^{-1}$  and  $r_{2,p} = 0.0001/0.47 \text{ s}^{-1}$ . Finally, the initial mass fractions of the two components are estimated from the relative areas under the peaks in the right hand plot. In this case,  $Y_{1,0} = 0.6$  and  $Y_{2,0} = 0.4$ .

In the FDS input file, `tga_sample.fds`, this information is conveyed via the following lines:

```
&SURF ID          = 'SAMPLE'
...
MATL_ID(1,1:2) = 'component 1', 'component 2'
MATL_MASS_FRACTION(1,1:2) = 0.6, 0.4 /

&MATL ID          = 'component 1'
...
N_REACTIONS      = 1
REFERENCE_TEMPERATURE = 300.
REFERENCE_RATE    = 0.0016
HEATING_RATE      = 5.
NU_SPEC           = 0.47
SPEC_ID           = 'OFF-GAS'
NU_MATL           = 0.53
MATL_ID           = 'residue' /

&MATL ID          = 'component 2'
...
N_REACTIONS      = 1
REFERENCE_TEMPERATURE = 500.
REFERENCE_RATE    = 0.0005
HEATING_RATE      = 5.
NU_SPEC           = 0.47
SPEC_ID           = 'OFF-GAS'
NU_MATL           = 0.53
MATL_ID           = 'residue' /
```

Note that `REFERENCE_RATE`, the FDS input parameter, represents the quantity,  $r_{\alpha,p}/Y_{\alpha,0}$ . Note also that both material components have the same residue yield, `NU_MATL`. Solely from TGA data, it is not possible

to determine how many unique material components there are, or what the reaction sequence is. The point of this exercise is simply to get FDS to mimic the total mass loss rate curve.

### 12.9.3 Effect of the TGA Heating Rate (`birch_tga`)

This is an example of a comparison of a candidate solid phase model with TGA data that shows the effect of the sample heating rate. The sample cases called `birch_tga_1step_2` and `birch_tga_1step_20` simulate two standard TGA experiments in which small samples of birch wood are heated up slowly at constant rates of 2 °C/min and 20 °C/min, respectively. The model of the wood consists of only one reaction that converts virgin wood to char and fuel gases. There is also a reaction in the simulation that does nothing more than evaporate the small amount of moisture in the wood. This evaporation is evident in Fig. 12.17 near the temperature of 100 °C.

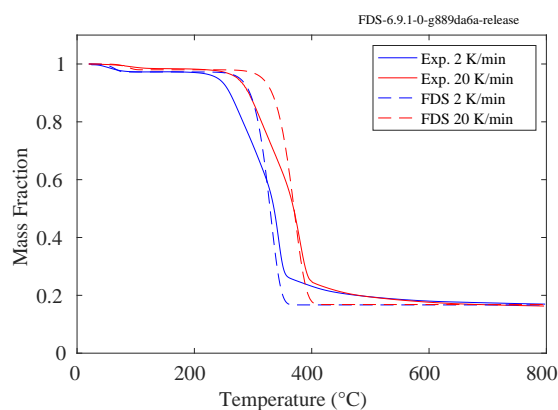


Figure 12.17: Comparison of a solid phase model of birch wood with TGA data.

### 12.9.4 TGA for a Charring Sample (`Needle_TGA`)

In this section, kinetic parameters for a longleaf pine needle are derived based on a set of TGA measurements<sup>1</sup>. Cases A and B listed in Table 12.2 have been used to derive the kinetic parameters for all eight cases. The mass and mass loss rate curves for all eight cases are shown in Figs. 12.19 through 12.22 on the following pages.

It is assumed that the pine needle consists of moisture and three solid phase components making up 0.25, 0.50, and 0.25 of the total dry mass, and reaching peak decomposition rates at 250 °C, 350 °C, and 425 °C, respectively. These estimates are obtained by inspection of the experimental data shown Fig. 12.18. It is further assumed that 0.25 of the dry mass is converted to char, and the kinetics of the oxidation reaction are estimated based on Case B.

---

<sup>1</sup>TGA data provided by the Forest Products Laboratory of the U.S. Forest Service

Table 12.2: Parameters for pine needle TGA experiments. Note that the Heating Rate refers to the linear ramp up in temperature after the sample has been dried out at approximately 100 °C.

Case	Heating Rate (K/min)	Moisture Fraction	Atmosphere
A	10	0.075	Inert
B	10	0.053	Air
C	10	1.22	Inert
D	10	1.63	Air
E	3.5	0.100	Inert
F	60	0.064	Inert
G	60	1.56	Air
H	60	1.33	Air

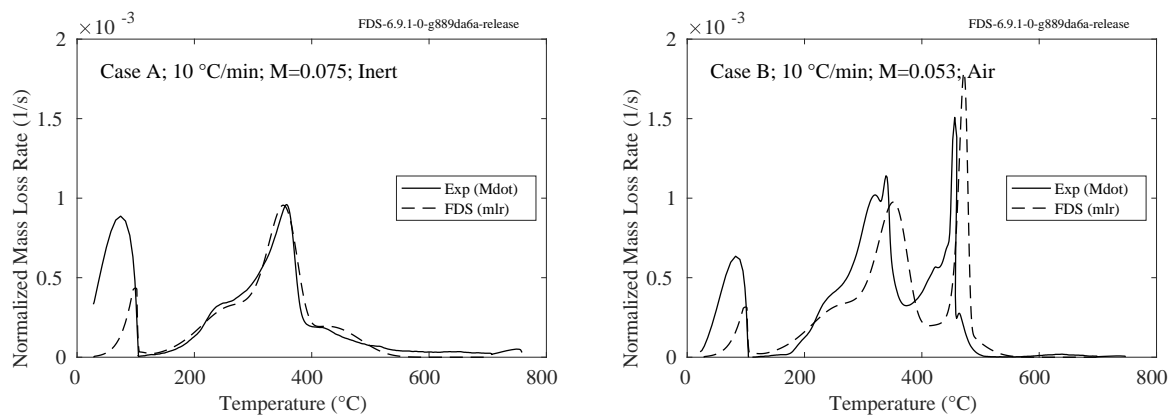


Figure 12.18: Mass loss rates for Cases A (left) and B (right). These cases are used to determine the kinetic parameters for all eight cases, A-H.

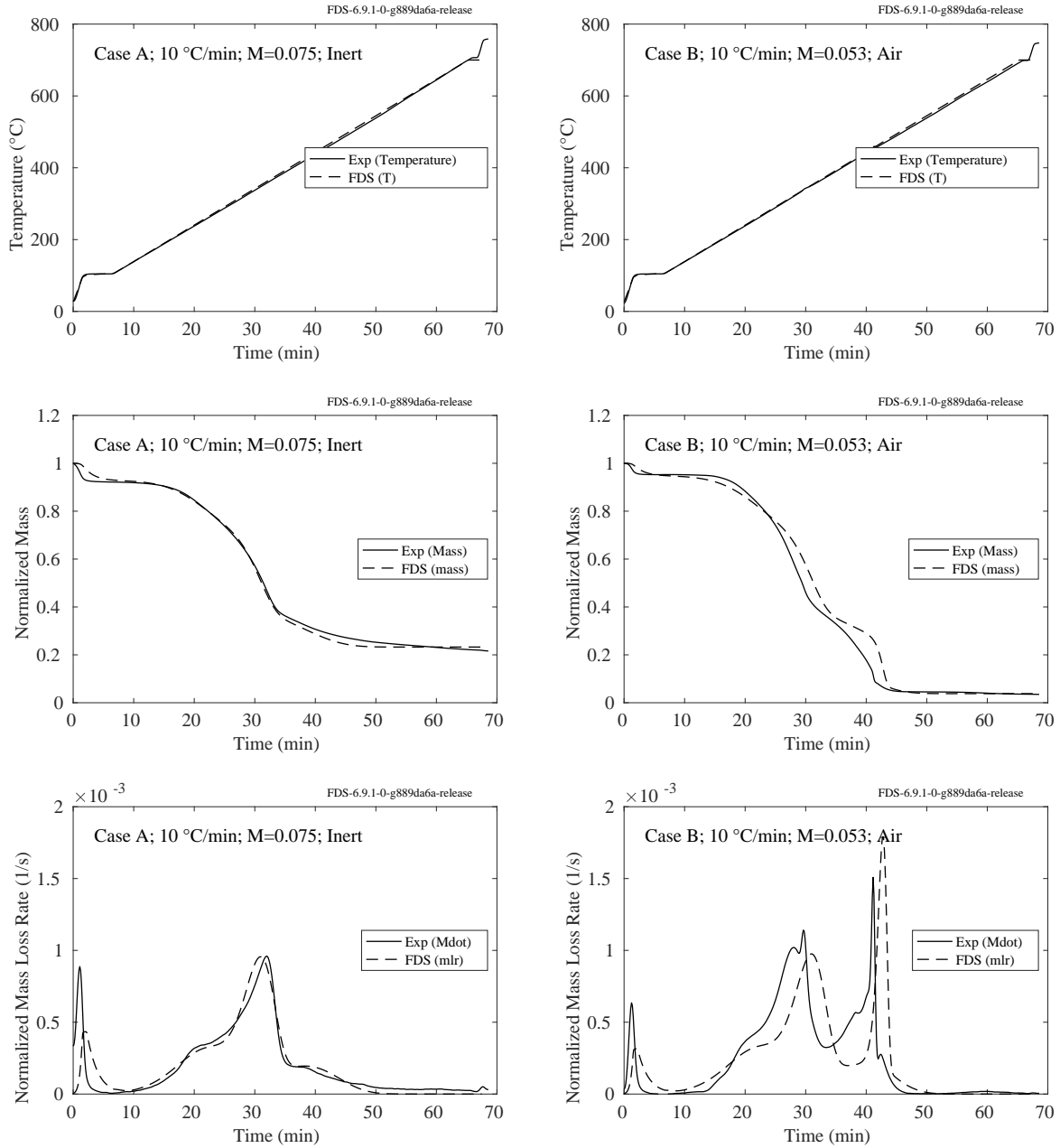


Figure 12.19: Results of TGA calibration exercise for a pine needle, Cases A (left) and B (right). (Top) Sample temperature vs time. (Middle) Sample mass fraction vs time. (Bottom) Sample mass loss rate vs time.

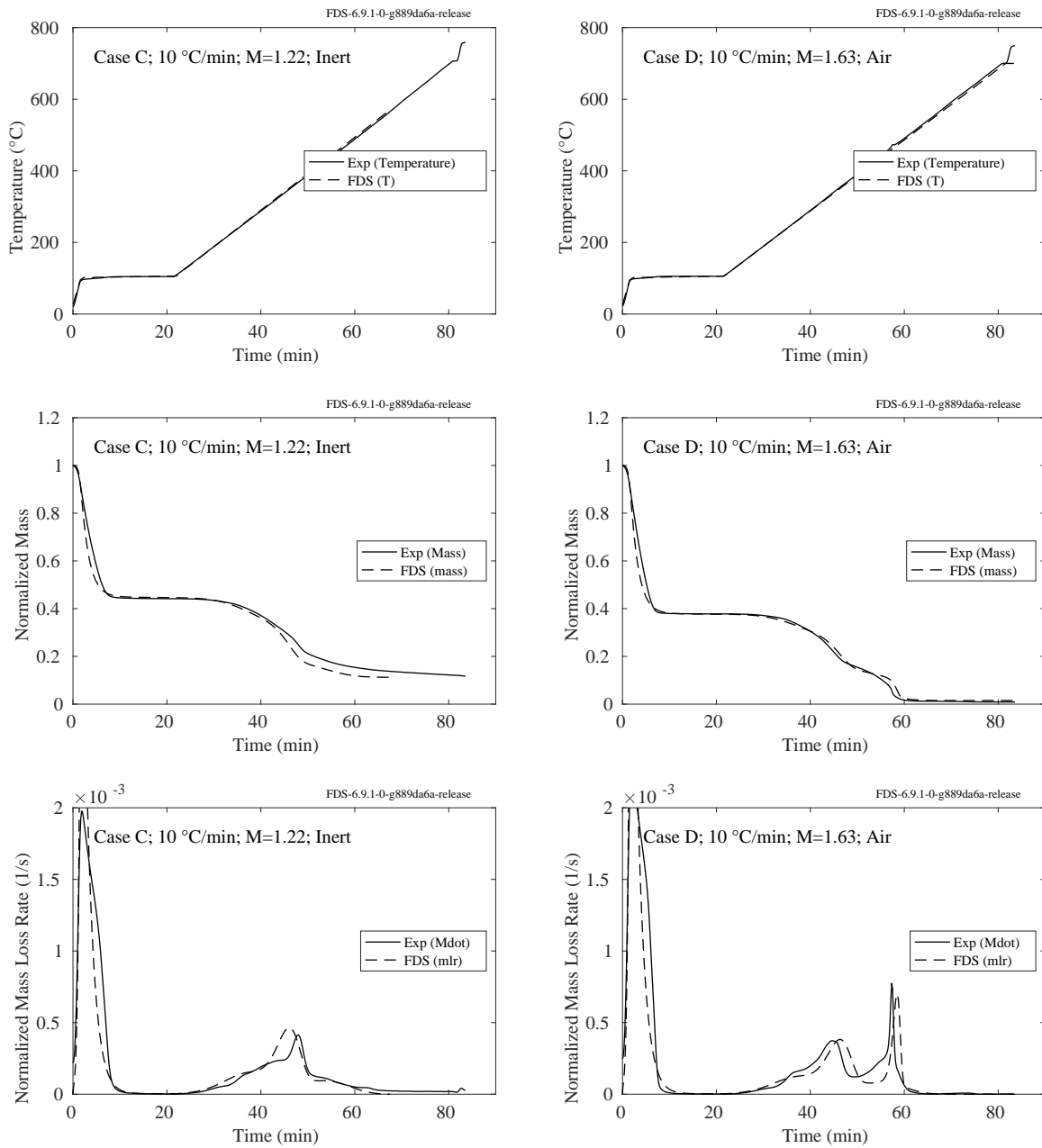


Figure 12.20: Results of TGA calibration exercise for a pine needle, Cases C (left) and D (right). (Top) Sample temperature vs time. (Middle) Sample mass fraction vs time. (Bottom) Sample mass loss rate vs time.

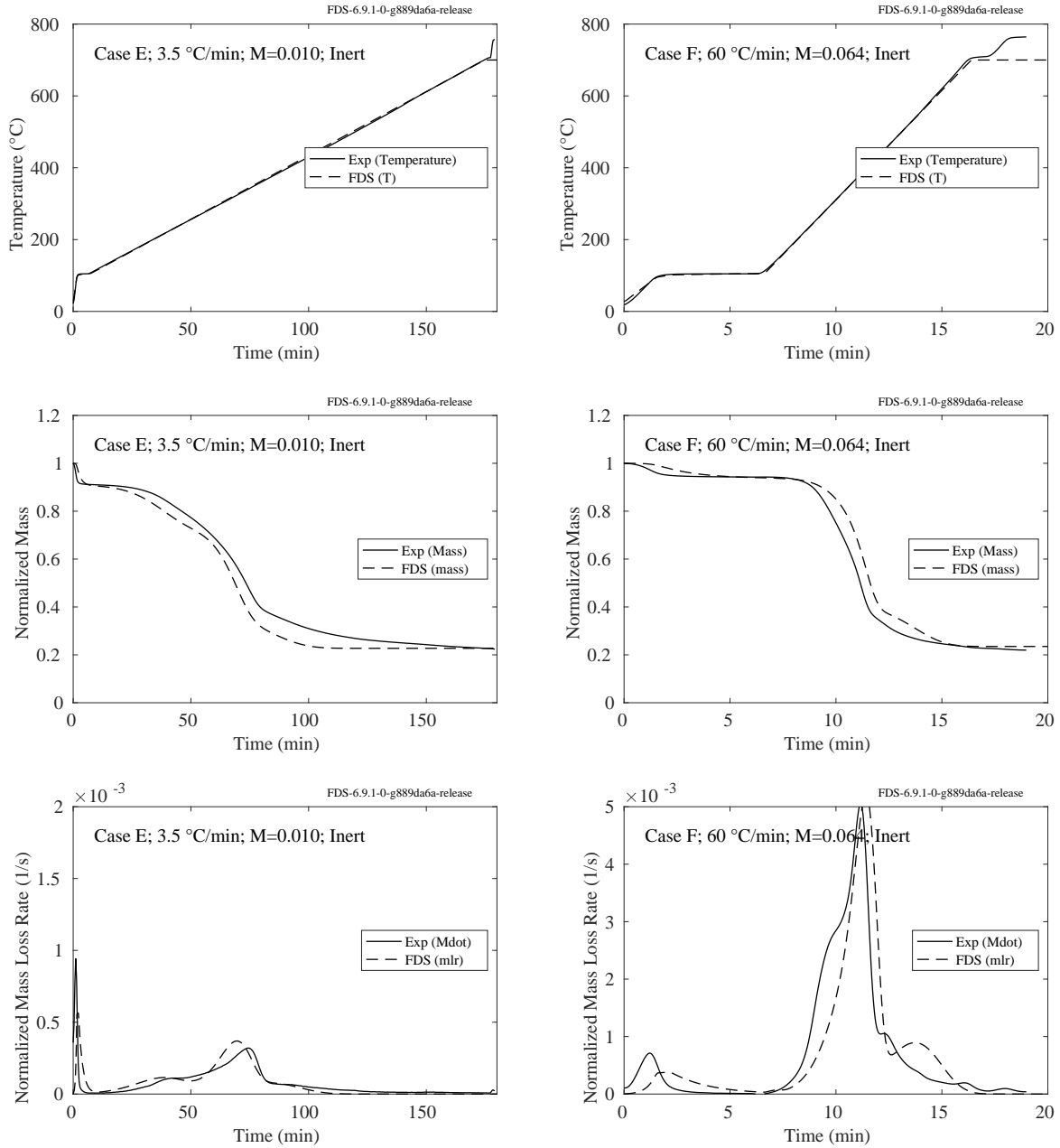


Figure 12.21: Results of TGA calibration exercise for a pine needle, Cases E (left) and F (right). (Top) Sample temperature vs time. (Middle) Sample mass fraction vs time. (Bottom) Sample mass loss rate vs time.

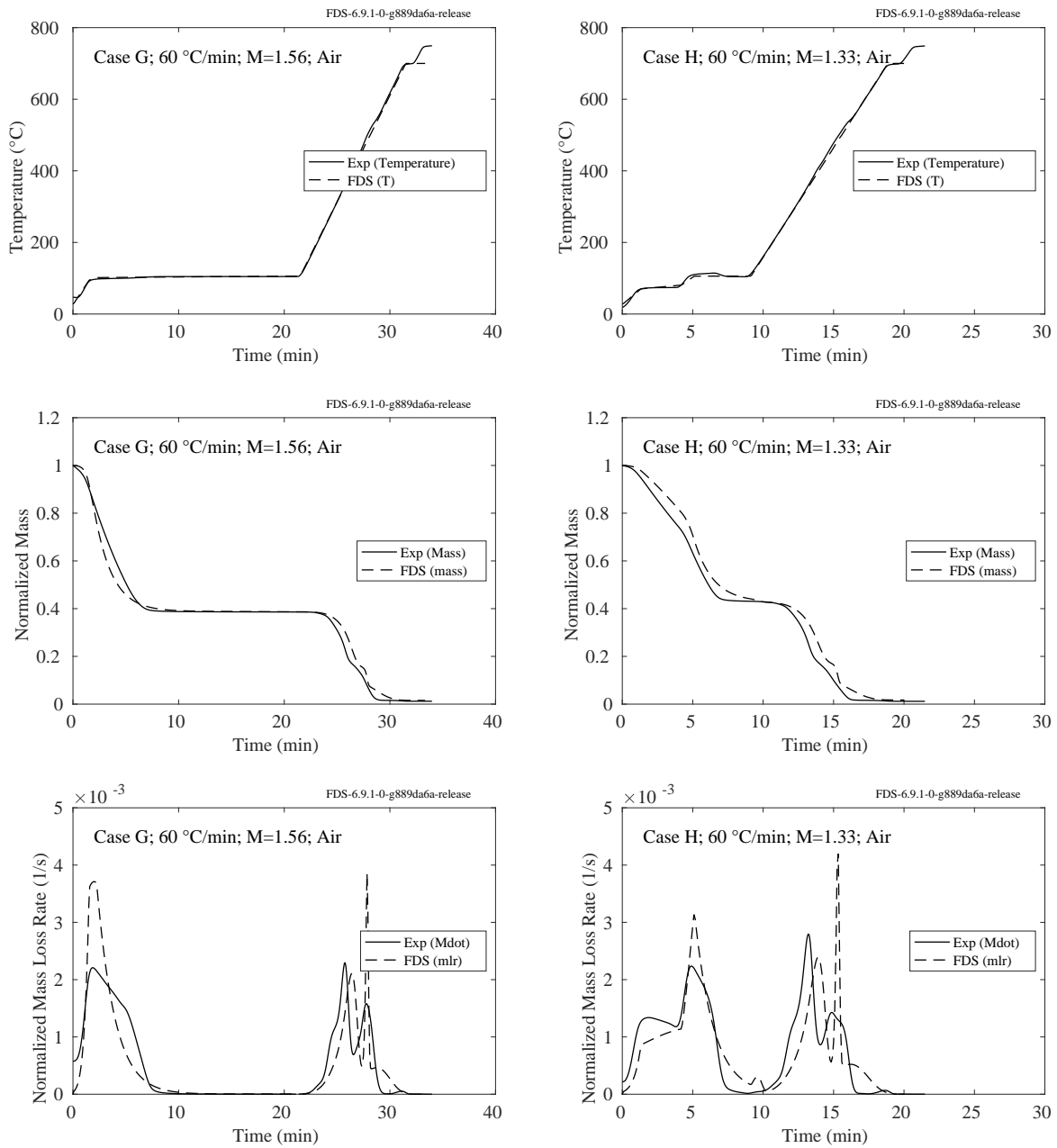


Figure 12.22: Results of TGA calibration exercise for a pine needle, Cases G (left) and H (right). (Top) Sample temperature vs time. (Middle) Sample mass fraction vs time. (Bottom) Sample mass loss rate vs time.

## 12.9.5 TGA of various Mediterranean vegetation (Morvan\_TGA)

In this section we analyze the TGA data for various Mediterranean vegetation species presented in Morvan and Dupuy, 2004 [98]. The FDS feature `TGA_ANALYSIS=T` was used with the model set up with 10 % moisture for the vegetation model. The heating rate is 1.6 °C/min, as reported in the paper. The reference temperature and pyrolysis range approach was used to tune the model to the data. The parameters can be found in the input file `Verification/WUI/Morvan_TGA.fds`. Note that an unusually high char fraction of 50 % is needed to match the TGA data. The results are shown in Fig. 12.23.

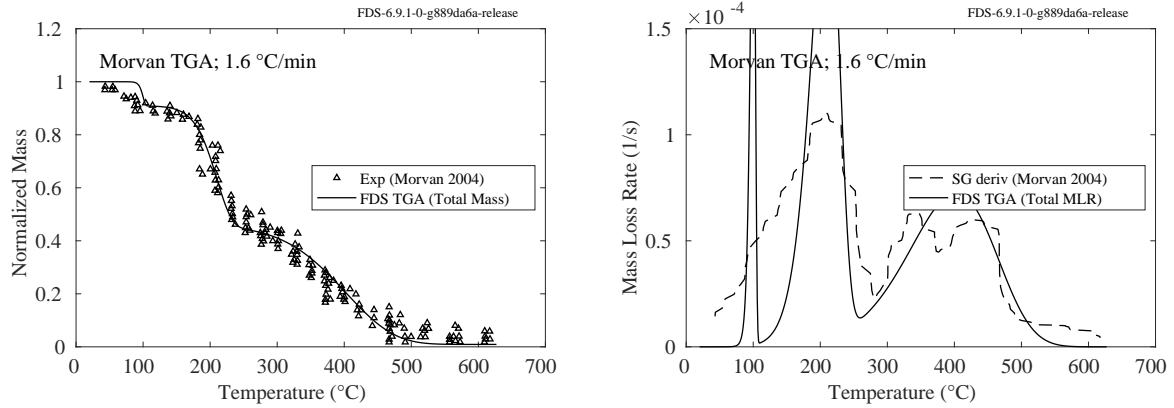


Figure 12.23: Results of performing the FDS TGA analysis on the data for various Mediterranean vegetation presented in Morvan and Dupuy, 2004 [98]. (Left) Total mass vs time. (Right) Mass loss rate vs time—the Morvan and Dupuy data were Savitsky-Golay filtered and the derivative of the resulting curve was normalized to give the dashed line.

## 12.9.6 Interpreting MCC Data (`cable_xx_mcc`)

This section describes a method for interpreting micro-combustion calorimeter (MCC) measurements. The pyrolysis combustion flow calorimeter (PCFC), developed by Lyon and Walters [99] at the U.S. Federal Aviation Administration (FAA), is a device used to measure the heat generated from the combustion of small (4 mg to 6 mg) material samples by oxygen depletion calorimetry. Samples are pyrolyzed at a specified heating rate in an anaerobic atmosphere (typically N<sub>2</sub>) and the resulting gases are mixed with excess oxygen and combusted in a separate chamber. The heat release rate from the specimen is obtained from measurements of the concentration of oxygen in the effluent exiting the combustor as a function of time. The methodology is the basis for the standard test ASTM D 7309 [100].

The results of PCFC measurements for the jacket and insulation materials of several electrical cables are shown in Fig. 12.24. These samples were pyrolyzed in the PCFC at a rate of 1 °C/s from 100 °C to 600 °C in a nitrogen atmosphere and the effluent combusted at 900 °C in a mixture consisting of 20 % O<sub>2</sub> and 80 % N<sub>2</sub>. The resulting curve shows the heat release rate of the sample as it was heated, normalized by the mass of the original sample. There are usually one, two or three noticeable peaks in the curve, corresponding to temperatures where a significant decomposition reaction occurs. Each peak can be characterized by the maximum value of the heat release rate per unit mass,  $\dot{q}_{\alpha,p}$ , the temperature,  $T_{\alpha,p}$ , and the relative fraction of the original sample mass that undergoes this particular reaction ( $Y_{\alpha,0}$ ). The area under the curve

$$\int_0^\infty \dot{q}(T) dT = \beta \Delta h' \quad (12.44)$$

is the sample heating rate,  $\beta$ , multiplied by the energy released per unit mass of the original sample,  $\Delta h'$ . This latter quantity is related to the more conventional<sup>2</sup> heat of combustion via the relation

$$\Delta h = \frac{\Delta h'}{1 - v_r} \quad (12.45)$$

where  $v_r$  is the fraction of the original mass that remains as residue. Sometimes this is referred to as the “char yield.” Note that it is assumed to be the same for all reactions.

The MCC measurement is similar to TGA in that it is possible to derive the kinetic parameters,  $A_\alpha$  and  $E_\alpha$ , for the various reactions from the heat release rate curve. As an example of how to work with MCC data, consider the two plots shown in Fig. 12.24. The solid curves in the figures display the results of micro-calorimetry measurements for the insulation and jacket material of multi-conductor control cables (the numbers have no particular meaning other than to distinguish them from other cables being studied).

Taking Cable 11 as an example, the insulation material exhibits two fairly well-defined peaks, whereas the jacket material exhibits three. Thus, the insulation material is modeled using two solid components, each undergoing a single-step reaction that produces fuel gas and a solid residue. The jacket material is modeled using three solid components. The residue yield for the insulation material is 6 %; for the jacket 49 %, obtained simply by weighing the sample before and after the measurement. It is not known which reaction produces what fraction of the residue. Rather, it is assumed that each reaction yields the same residue in the same relative amount. The dashed curves in Fig. 12.24 are the results of FDS simulations of the MCC measurements. To mimic the sample heating, a very thin sheet comprised of a mixture of the solid components with an insulated backing is heated at the rate specified in the experiment (1 °C/s or 60 °C/min, the units needed in FDS). For each reaction, the kinetic parameters are calculated using the formulae (12.39) and (12.40). The values of  $T_{\alpha,p}$  are obtained directly from the figures. The peak reaction rate for reaction  $\alpha$ ,

---

<sup>2</sup>In fire protection engineering, it is typically assumed that the heat of combustion is the energy released per unit mass of vaporized fuel.

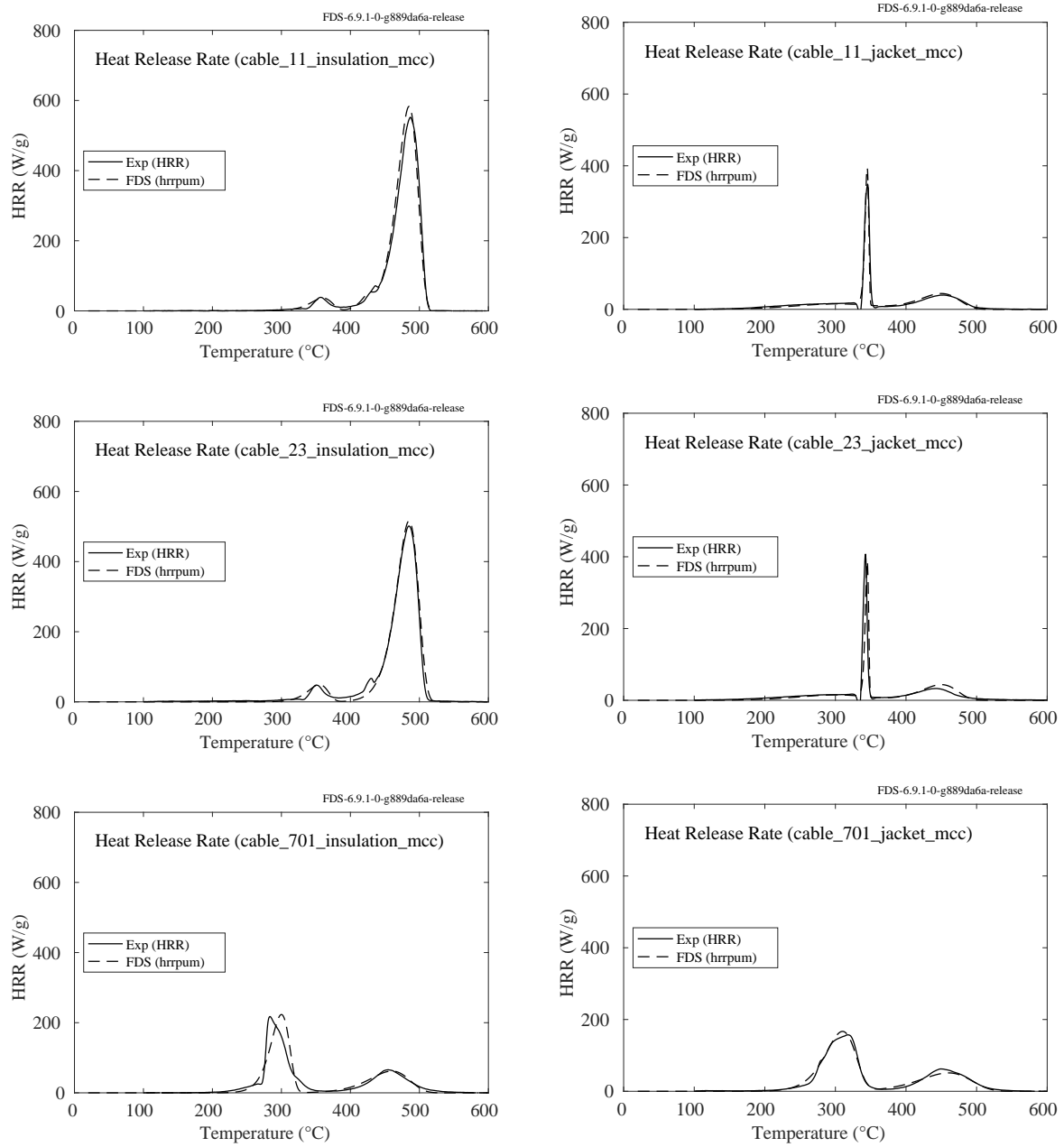


Figure 12.24: Results of a micro-calorimetry analyses of cable insulation (left) and jacket materials (right).

$r_{\alpha,p}$ , is obtained from:

$$r_{\alpha,p} = \frac{\dot{q}_{\alpha,p}}{\Delta h'} \quad ; \quad \Delta h' = \frac{1}{\beta} \int_0^{\infty} \dot{q}(T) dT \quad (12.46)$$

where  $\dot{q}_{\alpha,p}$  is the peak heat release rate corresponding to reaction  $\alpha$ . The values,  $Y_{\alpha,0}$ , can be estimated from the relative area under the curve. Their sum ought to be 1. It is important to check the units of all of these quantities because the results of these experiments are often presented in different ways depending on the particular application. A mistake in units can result in values of  $A_\alpha$  and/or  $E_\alpha$  that will invariably cause spurious results. For this reason, the direct calculation of the kinetic parameters is avoided by inputting the reaction parameters instead.

The dashed curves in Fig. 12.24 are the results of numerically integrating Eq. (12.33) within FDS for each material component. A typical input line for FDS that describes a single material component undergoing a single reaction is given by:

```
&MATL_ID          = 'Cable 11 Jacket Component A'
...
N_REACTIONS      = 1
REFERENCE_TEMPERATURE = 300.
REFERENCE_RATE    = 0.0064
HEATING_RATE      = 60.
NU_MATL           = 0.49
MATL_ID           = 'char'
NU_SPEC            = 0.51 /
```

Only the relevant parameters are shown. The other parameters are not relevant in this exercise. Note that REFERENCE\_TEMPERATURE is  $T_{\alpha,p}$  in units of °C. REFERENCE\_RATE is actually  $r_{\alpha,p}/Y_{\alpha,0}$ , in units of  $s^{-1}$ . HEATING\_RATE is  $\beta$  in units of °C/min. NU\_MATL is  $v_r$  and NU\_SPEC is  $(1 - v_r)$ . Table 12.3 lists all of the kinetic parameters for the cable insulation and jacket materials. The peak temperatures are easy to estimate, and the values of  $r_{p,i}/Y_{0,i}$  can be fine-tuned to closely match the data. Note that it is possible to compute values of  $A_i$  and  $E_i$  and input them directly into FDS, rather than inputting those listed in the table. However, the values of  $A_i$  and  $E_i$  are fairly large numbers and have little meaning in their own.

Table 12.3: Parameters used to derive the kinetic constants for Cable 11 materials. The heating rate for both is 60 °C/min.

Parameter	Insulation, $v_r = 0.06$		Jacket, $v_r = 0.49$		
	$\alpha = 1$	$\alpha = 2$	$\alpha = 1$	$\alpha = 2$	$\alpha = 3$
$T_{\alpha,p}$ (°C)	355	485	300	345	450
$r_{\alpha,p}/Y_{\alpha,0}$ ( $s^{-1}$ )	0.0384	0.2426	0.0064	0.3500	0.0156

## 12.10 Scaling Pyrolysis (SPyro) Model (`spyro_cone_demo_2` and `spyro_cone_demo_3`)

This section uses two cases to test a model for scaling heat release rate data from a cone calorimeter to heat fluxes other than the one used during the cone test. The first case tests the interpolation of a single cone curve to a heat flux different than the one the sample was tested at. A surface is assigned an `HRRPUA` and `RAMP_Q` from an inert cone test performed at  $50 \text{ kW/m}^2$ . The surface is given an `IGNITION_TEMPERATURE` of  $0^\circ\text{C}$  so it ignites immediately. The surface is exposed to a sawtooth `EXTERNAL_FLUX` that varies between  $10 \text{ kW/m}^2$  and  $110 \text{ kW/m}^2$ . The results are shown below in Fig 12.25.

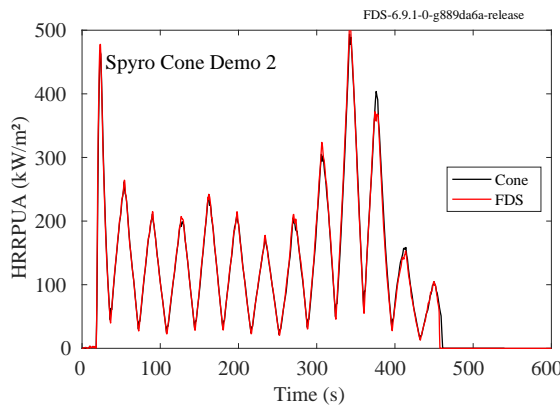


Figure 12.25: Extrapolating a single set of cone data to a time varying heat flux (the `spyro_cone_demo_2` case).

The second case tests the interpolation of multiple cone tests. In the case four cone curves (two each at two thicknesses) are defined for a surface which is then simulated at an intermediate heat flux and thickness. The results are shown below in Fig 12.26.

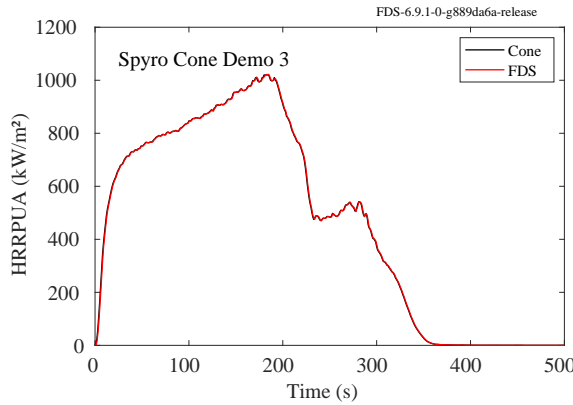


Figure 12.26: Interpolating a set of cone data to an intermediate surface thickness and exposure (the `spyro_cone_demo_3` case).

## 12.11 Melting Ice Cube (`ice_cube`)

This section tests the ability for a MATL reaction to produce particles. A 10 cm cube (1 kg) block of ice is defined with a  $10 \text{ kW/m}^2$  EXTERNAL\_FLUX. The mass of water drops produced is tracked. The results are shown below in Fig 12.27.

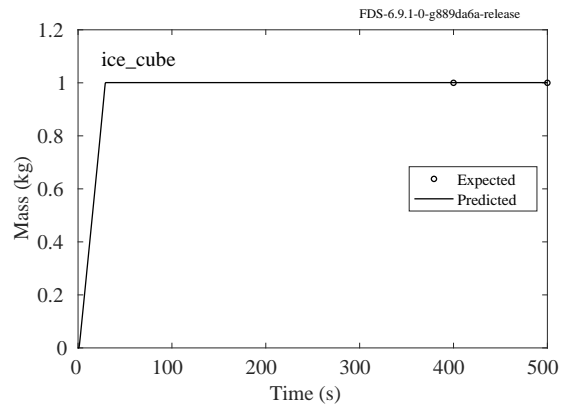


Figure 12.27: Check of the particle production by surface reaction feature.



# Chapter 13

## Lagrangian Particles

This chapter contains verification cases that test all aspects of particles, droplets, sprays, and so on. Note that in FDS, Lagrangian particles are used for a variety of purposes, not just water droplets.

### 13.1 Particle and Droplet Drag

The cases in this section test accuracy, stability, and momentum conservation for the general case of momentum transfer between solid particles or liquid droplets and air. Details of the FDS integration scheme are given in the Technical Reference Guide [1]. In short, we find an analytical solution for the case of binary fluid-particle interaction and apply this solution to the case of multiple particles by enforcing total momentum conservation within a fluid cell. The resulting scheme is guaranteed to be stable because the fluid velocity cannot overshoot the cell equilibrium velocity (total momentum of fluid and particles divided by the total mass).

#### 13.1.1 Dragless Particle (`cannon_ball`)

This simple case tests the particle transport scheme in the absence of drag. A 1 cm diameter sphere is shot from ground level with an initial velocity of  $(u_0, v_0, w_0) = (10, 10, 10)$  m/s. The ball is expected to fall back to the ground in  $t = 2w_0/g \approx 2.04$  s at which time it will have travelled a horizontal distance of  $d = t\sqrt{u_0^2 + v_0^2} \approx 28.86$  m. The grid has a resolution of 1 m, and the default time step is 0.5 s. Thus, the particle trajectory is computed via only 5 calls to particle transport routine. However, the integration is performed using sub-steps such that the particle cannot cross farther than a single grid cell in a sub-step. This ensures an accurate computation of the trajectory, as shown in Fig. 13.1.

#### 13.1.2 Particles Swept Up in a Free Stream (`fluid_part_mom`)

Consider a 1 m square duct that is 10 m long. The boundary conditions are periodic in the streamwise direction and free slip along the inside walls. The fluid velocity is initialized to be 10 m/s. A monodisperse distribution of 1000 particles is initialized with zero velocity and random positions in the first cubic meter of the duct. Gravity is set to zero. As the case proceeds momentum is exchanged between the fluid and the particles. The results for all three tests are shown in Fig. 13.2. On the top, the green symbols represent the total momentum of the system, which, as can be seen, is conserved. The fluid (blue) and the particle (red) momenta are closely following the analytical solution (solid lines) which is the basis of the scheme. The plot on the bottom shows the fluid (blue) and particle (red) velocities compared to the system equilibrium

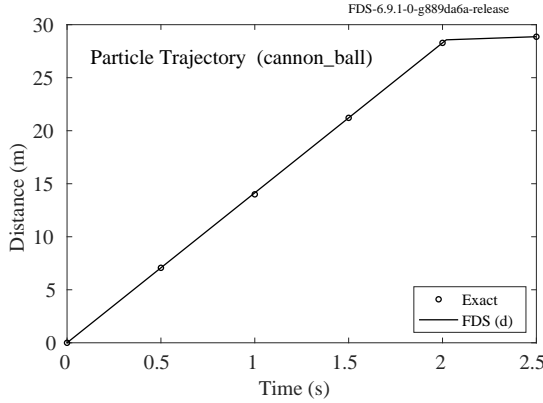


Figure 13.1: Horizontal distance travelled by a dragless sphere as a function of time.

velocity (green dashed line). By construction of the method, both the fluid and the particle velocities are approaching the equilibrium velocity at long times.

### 13.1.3 Particles Slowing Down a Gas Flow (`particle_drag`)

The particle drag test cases consider a 1 m by 1 m by 1 m channel with periodic boundary conditions on the  $x$ -faces and FREE\_SLIP walls on  $y$ - and  $z$ -faces. Static droplets are placed in the center of the channel, one particle per computational cell, so that they form a surface perpendicular to the flow direction. Gravity is set to zero. Due to the symmetry of the problem, the flow is one dimensional. Assuming that the droplets are of uniform diameter and the drag coefficient and gas density are constant, the velocity in the channel decays according to

$$u = \frac{u_0}{1 + Bu_0 t} ; \quad B = \frac{1}{2} \frac{\sum C_D \pi r_d^2}{V} \quad (13.1)$$

In the above,  $V$  is the volume of the channel,  $r_d$  is the droplet radius,  $C_D$  is the droplet drag coefficient, and  $u$  is the gas velocity in the  $x$ -direction. The summation is over all  $N$  particles. The common parameters used in all the simulations are:  $C_d = 10$ ,  $r_d = 0.005$  m. The initial velocity,  $u_0$ , for Cases A-F are 10, 50, 100, 50, 100, and 150 m/s, respectively. Comparisons of computed and analytical results are shown in Fig. 13.3.

Following the above notation, the total drag force can also be written as:

$$F_d = \rho V B \left( \frac{u_0}{1 + Bu_0 t} \right)^2 \quad (13.2)$$

Checking this quantity is useful for confirming the PARTICLE\_DRAG\_FORCE\_X/Y/Z output quantities and SPATIAL\_STATISTIC = 'SUM' for a volume of particles. The computed results for Case A are compared to the analytical solution in Fig. 13.4.

### 13.1.4 Stationary Spherical Particles in a Duct (`sphere_drag`)

Consider a 2 m long duct with a 1 m square cross section, fixed air velocity of  $u_0 = 2$  m/s, and free-slip walls. Three ducts are stacked vertically, each with its own mesh and a plane of particles spanning the duct

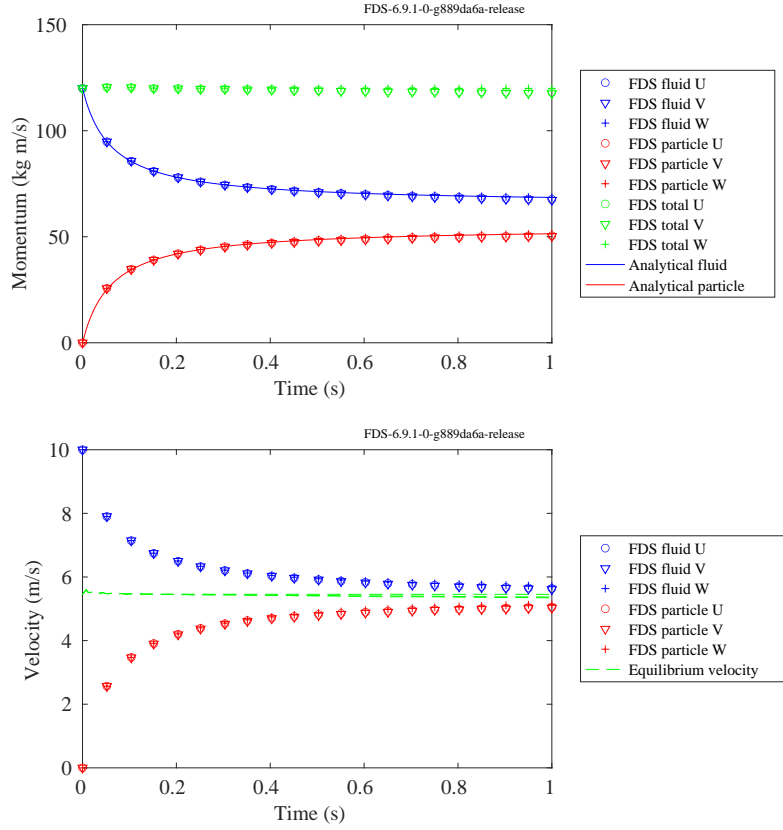


Figure 13.2: Outputs of the `fluid_part_mom` cases. (Top) The fluid momentum (blue), the particle momentum (red), and the total momentum (green) are plotted for each coordinate direction,  $x$  (circles),  $y$  (inverted triangles), and  $z$  (plus symbols). The analytical solutions for the fluid and particle equations are shown by the solid blue and red lines, respectively. The total momentum should be constant, as indicated by the green symbols. (Bottom) The fluid (blue) and particle (red) velocities are plotted for each direction. Also, the equilibrium velocity (total momentum [fluid plus particles] divided by the total mass) is shown as a dashed green line. Stability of the momentum exchange is guaranteed because, by construction, the fluid velocity cannot overshoot the equilibrium velocity; the fluid velocity relaxes toward it.

at its center point. The particles are 1 cm in diameter and 10 particles are specified in each grid cell. The expected pressure drop is given by the formula:

$$\Delta p = \frac{1}{2} \rho \frac{\sum C_d \pi r_p^2 u_0^2}{A} \quad (13.3)$$

where  $A$  is the  $1\text{ m}^2$  cross-sectional area,  $\rho = 1.2\text{ kg/m}^3$  is the density of air, and the summation is over 4000 particles. For specified drag coefficients of 5, 10, and 20 in the three ducts, the pressure drops are expected to be 3.77 Pa, 7.54 Pa, and 15.1 Pa. Comparisons of computed and analytical results are shown in the left hand plot of Fig. 13.5.

In a second test case, consider a single 10 m long, 1 m square duct. Spherical particles 2 mm in diameter with a density of  $514\text{ kg/m}^3$  are randomly distributed in the section of the duct between 4 m and 5 m from the upstream end. The particle mass per unit volume is set to  $1.66\text{ kg/m}^3$ . The number of particles included in the simulation is 10000, which means that each particle actually represents 77.1 real particles. The drag coefficient is approximately 1.6, based on the local Reynolds number, which is about 40. The free stream velocity in the duct is 0.3 m/s, but the speed varies slightly within the cloud of particles. The pressure is

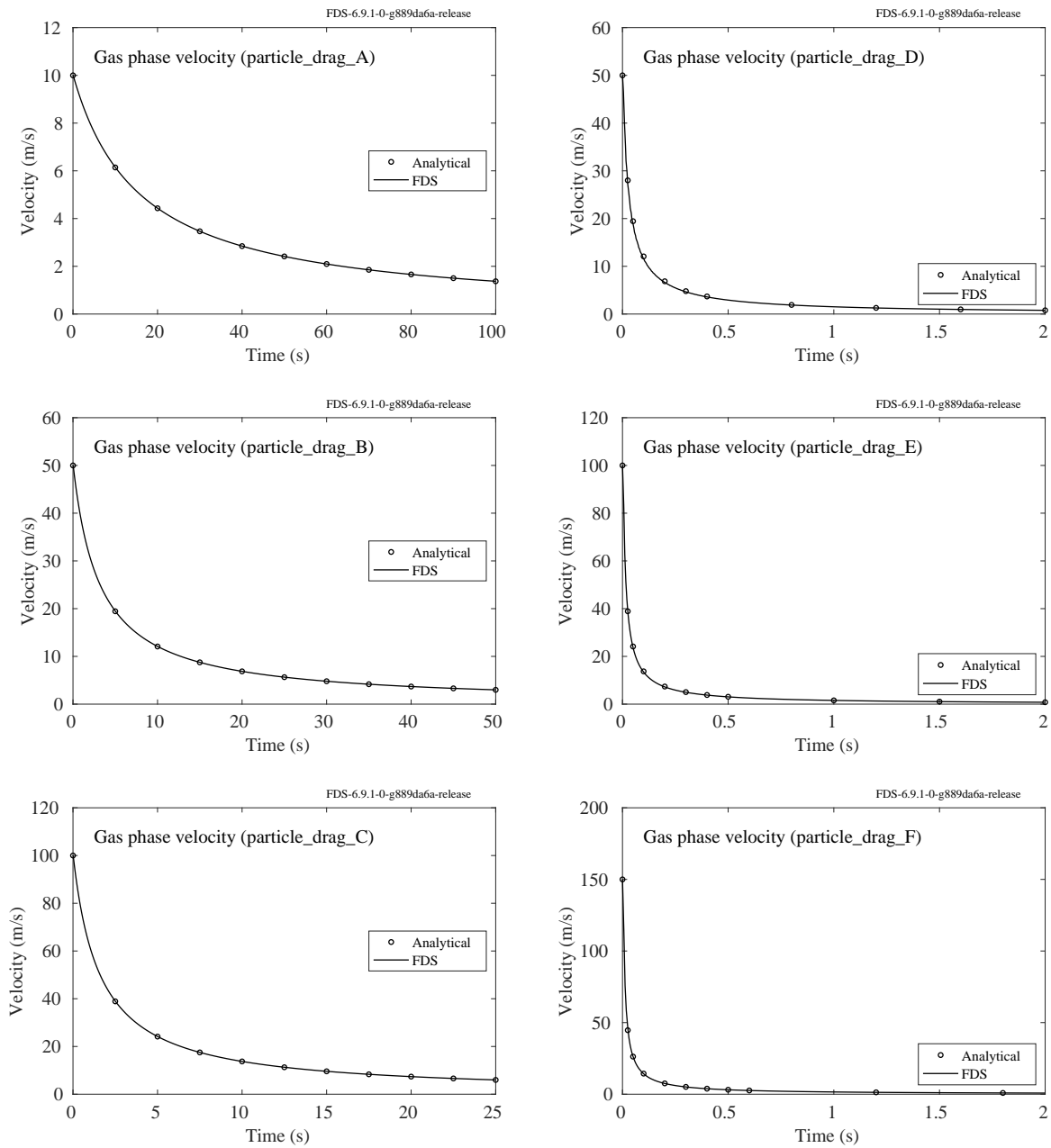


Figure 13.3: Outputs of the `particle_drag` test cases compared with analytical solutions.

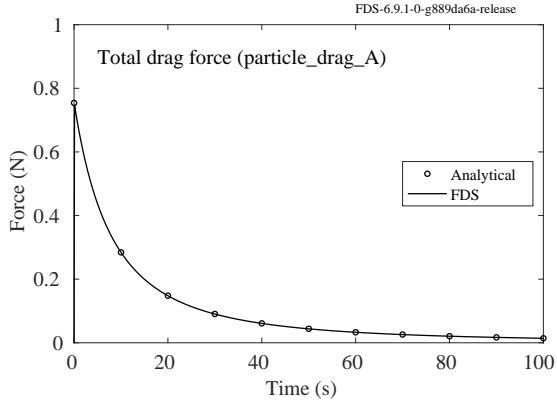


Figure 13.4: Output of total drag from the `particle_drag_U10_N16` test case compared with analytical solution.

expected to drop linearly from approximately 0.21 Pa to 0 Pa over the 1 m of duct filled by particles, as shown in the right hand plot of Fig. 13.5.

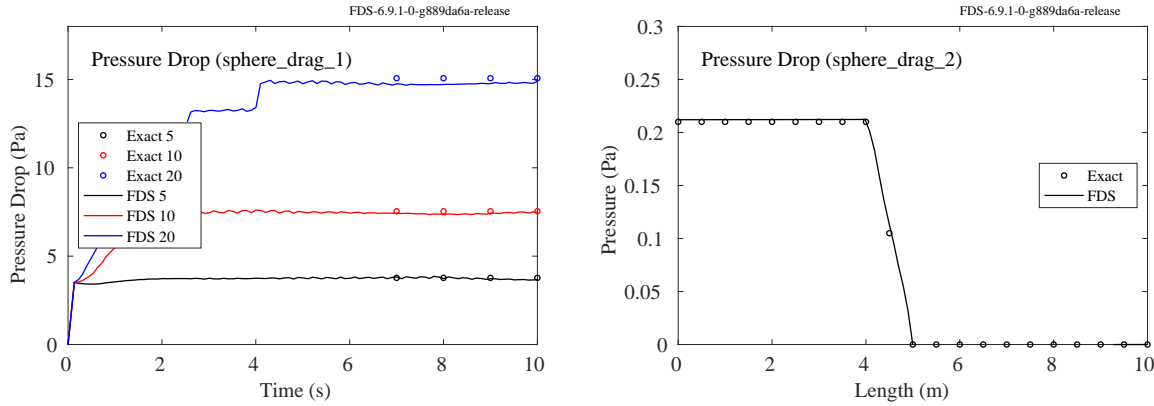


Figure 13.5: Outputs of the `sphere_drag` test cases compared with analytical solutions.

### 13.1.5 Drag Caused by Vegetation (`vegetation_drag`)

Vegetation (leaves, grasses, etc.) is sometimes modeled using Lagrangian particles with flat, cylindrical, or spherical geometries. In this test case, cylindrical particles represent pine needles. Consider a 4 m long duct with a 1 m square cross section, fixed air velocity of  $u_0 = 2$  m/s, and free-slip walls. Three ducts are stacked vertically, each with a 10 cm uniform mesh and a 1 m by 1 m by 1 m volume filled with particles spanning the duct near its center. The cylindrical particles are  $D = 1$  mm in diameter and  $L = 2$  cm long. In the lowest duct, 10000 particles are inserted randomly throughout the volume. In the middle duct, 1 particle is inserted at the center of each grid cell within the volume containing the pine needles. In the top duct, 10 particles are inserted randomly in each grid cell, for a total of 10000 particles. The drag coefficient for each cylindrical particle is given by the empirical relation:

$$C_d = 10 \frac{0.6 + 0.4 \text{Re}^{0.8}}{\text{Re}} \approx 1.55 \quad ; \quad \text{Re} = \frac{\rho u_0 D}{\mu_{\text{air}}} \approx 132.9 \quad (13.4)$$

The viscosity of air at 20 °C is  $\mu_{\text{air}} = 1.8 \times 10^{-5} \text{ kg}/(\text{m}\cdot\text{s})$ .

## Conventional Notation

The pressure drop in each duct is expected to be the same, regardless of how the particles are inserted:

$$\Delta p = -\frac{1}{2} \rho \frac{n_p C_d A_c u_0^2}{A} \approx -18.9 \text{ Pa} ; \quad n_p = \frac{m''' V}{\pi r^2 L \rho_p} \approx 254648 \quad (13.5)$$

where  $A$  is the 1 m<sup>2</sup> cross-sectional area of the duct,  $A_c = LD$  is the cross sectional area of the cylindrical particle, and  $\rho = 1.196 \text{ kg/m}^3$  is the density of air. The number of actual pine needles within the volume,  $n_p$ , is the mass per unit volume,  $m''' = 2 \text{ kg/m}^3$ , times the volume,  $V = 1 \text{ m}^3$ , divided by the mass of an individual pine needle. The density of the needle is  $\rho_p = 500 \text{ kg/m}^3$ . Comparisons of computed and analytical pressure drops are shown in the left plot of Fig. 13.6. Differences between the ideal and computed results are due to the fact that the air velocity is not exactly 2 m/s within the volume filled with the particles. In particular, the duct filled randomly with particles exhibits the greatest deviation from the ideal because the velocity does not remain uniform within the volume.

## Notation used by the Wildland Fire Community

The notation used in the previous section is inconvenient when characterizing the drag force exerted by actual vegetation that cannot be assumed to be perfect spheres or cylinders. Instead, Eq. (13.5) can be rewritten as follows:

$$\Delta p = -\frac{L}{2} \rho C_d C_s \beta \sigma u_0^2 \approx -18.9 \text{ Pa} \quad (13.6)$$

Here,  $C_s$  is the ratio of the particle's cross sectional area to surface area, which is approximately  $1/\pi$  for objects that are cylindrical in shape.  $\beta$  is the packing ratio, which is the ratio of the volume occupied by the solid particles to the overall volume of particle-laden region; 0.004 in this case.  $\sigma$  is the surface to volume ratio of an individual particle;  $2/r$  for a cylinder.

## Pressure Drop due to Mass-Generating Particles

Using this same basic configuration, another test is performed where the cylindrical particles now exert no drag force on the air flow, but instead generate additional air at a rate of 0.1 kg/(m<sup>2</sup>·s). The surface area of each of the 254648 particles is  $6.28 \times 10^{-5} \text{ m}^2$ , resulting in a total air injection rate of  $\dot{m} = 1.6 \text{ kg/s}$ . The momentum equation becomes one-dimensional and time-independent:

$$\frac{d}{dx} \left( \frac{p}{\rho} + \frac{u^2}{2} \right) = -\frac{1}{\rho} \frac{\dot{m}}{V} u \quad (13.7)$$

Using the subscript 1 to denote the upstream region of the duct, and 2 the downstream, the air velocity increases as it passes through the particles:  $u_2 = u_1 + \dot{m}/(\rho A)$ . Multiplying Eq. (13.7) by the constant density,  $\rho$ , and integrating both sides over the length of the duct containing the particles:

$$\Delta p \equiv p_2 - p_1 = -\rho \frac{u_2 + u_1}{2} (u_2 - u_1) - \frac{\dot{m}}{A} \frac{u_2 + u_1}{2} = -8.534 \text{ Pa} \quad (13.8)$$

The results are shown in the right hand plot of Fig. 13.6 for the various different methods of representing the particles in the model.

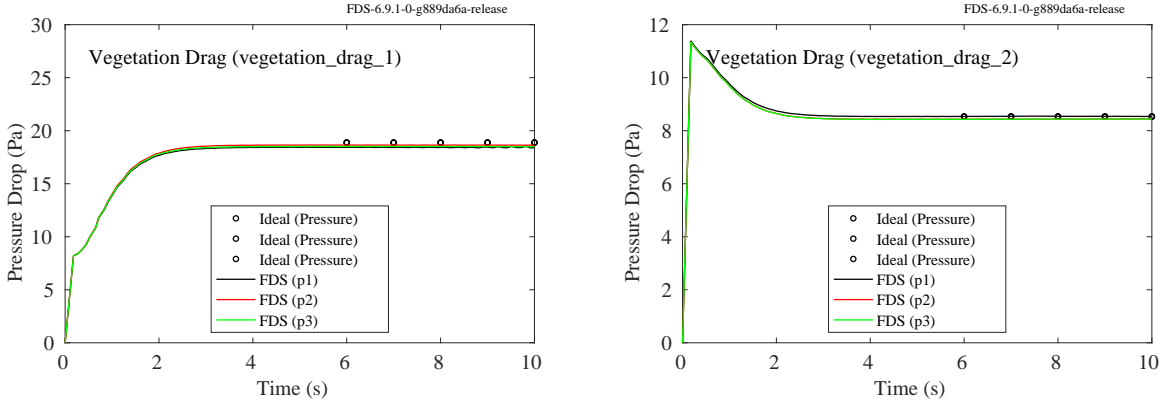


Figure 13.6: Pressure drop in duct filled with pine needles for three different particle insertion methods.

### 13.1.6 Mesh Screen in a Duct (`screen_drag`)

These two test cases consider a 1 m wide by 1 m tall by 2 m long channel with either a 2 m/s or a 20 m/s fixed velocity boundary condition fixed velocity boundary condition on one end, an `OPEN` boundary condition on the other end, and `FREE_SLIP` on the y- and z-faces. Three channels are stacked vertically (each with its own `MESH`, and a plane of particles is placed across each channel at 1 m. The plane of particles are defined as a screen with a wire diameter of 0.0003 m. A `FREE_AREA_FRACTION` of 0.1, 0.4, and 0.8 is set for the particles in the channels. According to the screen drag formula

$$\Delta p = \left( \frac{\mu}{K} u + \rho \frac{Y}{\sqrt{K}} u^2 \right) \Delta x_{\text{screen}} \quad (13.9)$$

where  $K$  and  $Y$  are empirical constants defined in the FDS User's Guide, the pressure drops for the 2 m/s inlet should be 126 Pa, 14 Pa, and 5.3 Pa, and for the 20 m/s inlet should be 1260 Pa, 168 Pa, and 124 Pa. Comparisons of computed and analytical results are shown in Fig. 13.7.

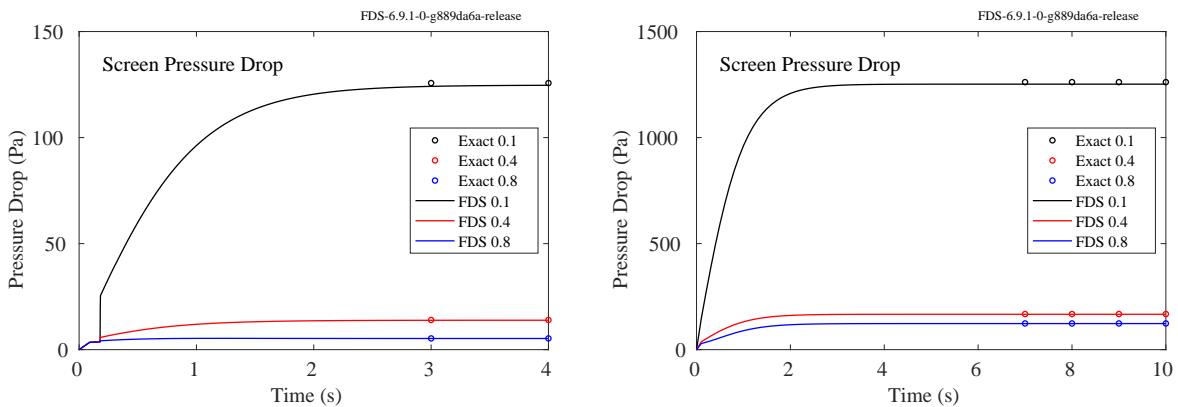


Figure 13.7: Outputs of the `screen_drag` test cases compared with analytical solutions. Left 2 m/s inlet, right 20 m/s inlet. The three cases represent different values of `FREE_AREA_FRACTION` (0.1, 0.4, and 0.8) within the channel.

### 13.1.7 Flow through Porous Media (`porous_media`)

This case involves a 2 m long duct with a 0.5 m by 0.5 m cross section and 1 m/s flow in the  $x$  direction. An 8.5 cm thick block of rigid aluminum foam is positioned in the duct. The pressure drop induced by the foam is expected to be approximately:

$$\Delta p \approx \delta \left( \frac{\mu}{K} u + \rho \frac{Y}{\sqrt{K}} u^2 \right) \quad (13.10)$$

where  $K = 1 \times 10^{-7} \text{ m}^2$  and  $Y = 0.1$  in all three coordinate directions. The block thickness  $\delta = 0.085 \text{ m}$ , the velocity  $u = 1 \text{ m/s}$ , the air density  $\rho = 1.2 \text{ kg/m}^3$ , and the air viscosity  $\mu = 1.8 \times 10^{-5} \text{ kg/m/s}$ . Comparisons of computed and analytical results for three different grid resolutions (1 corresponds to low resolution, 2 medium, 3 fine) are shown in Fig. 13.8.

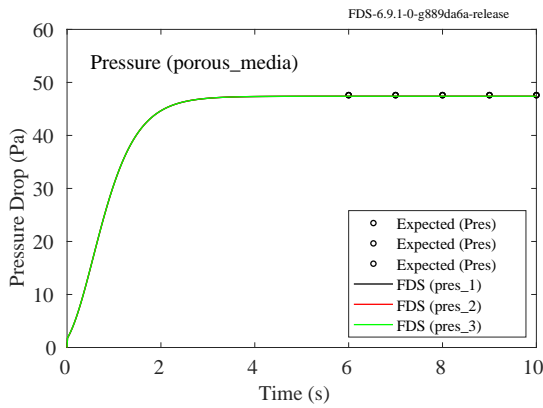


Figure 13.8: Pressure drop caused by a block of aluminum foam.

### 13.1.8 Particle Terminal Velocity (`terminal_velocity`)

If a single particle with a constant drag coefficient falls through a stationary fluid, its terminal velocity can be found analytically. The equation governing this motion is

$$\frac{du}{dt} = Ku^2 - g \quad ; \quad K \equiv \frac{\rho_a C_d A}{2m} \quad (13.11)$$

where  $\rho_a$  is the air density,  $C_d = 1$  is the drag coefficient,  $A$  is the cross-sectional area of the particle, and  $m$  is the mass. Defining  $\rho_d = 1000 \text{ kg/m}^3$  as the particle density and  $D = 0.01 \text{ m}$  as the particle diameter, the solution of the ODE is:

$$u = \frac{dx}{dt} = -\sqrt{\frac{g}{K}} \tanh\left(\sqrt{gK}t\right) \quad ; \quad x = -\frac{\ln[\cosh(\sqrt{gK}t)]}{K} \quad ; \quad K \equiv \frac{3\rho_a C_d}{4\rho_d D} \quad (13.12)$$

The  $L_\infty$  (maximum) error of the FDS computed terminal velocity and position are computed and plotted for each time step. As shown in Fig. 13.9, FDS exhibits first-order convergence for the particle position and the terminal velocity error is near machine precision.

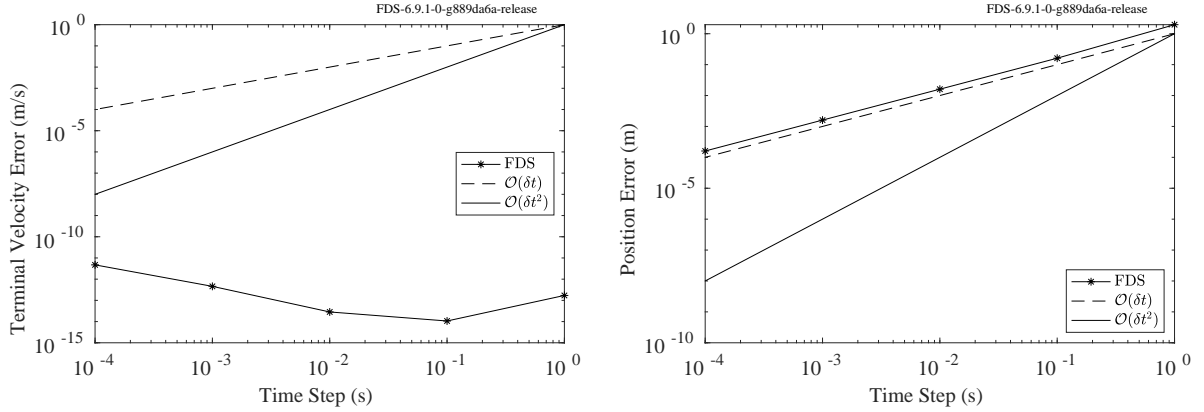


Figure 13.9: (Left) FDS convergence for the particle velocity in the `terminal_velocity` case. (Right) FDS convergence for the particle position in the `terminal_velocity` case.

### 13.1.9 Particle Trajectory (`flat_fire`)

There are no known solutions of the particle trajectory equations in multiple dimensions. However, ballisticians have developed an approximate solution useful for computing trajectories of projectiles when guns are shot within a certain range of angles. This solution makes use of the “flat fire” assumption. In short, if a particle is launched with its velocity in only the horizontal direction and its vertical velocity is relatively small compared to the horizontal velocity, then throughout the entire trajectory the horizontal velocity component,  $u_p$ , is a good approximation for the velocity magnitude,  $|\mathbf{u}_p|$ . In 2-D, this approximation decouples the horizontal ( $x$ ) equation of motion from the vertical ( $z$ ) and reduces the vertical equation of motion to a linear ODE:

$$\frac{du_p}{dt} = -K u_p^2 \quad ; \quad K \equiv \frac{3\rho_a C_d}{8\rho_p r_p} \quad (13.13)$$

$$\frac{dw_p}{dt} = -K u_p w_p - g \quad (13.14)$$

Given the initial conditions,  $x_p(0) = 0$ ,  $u_p(0) = V_0$ ,  $z_p(0) = h$ ,  $w_p(0) = 0$ , the exact solution to the ODE is:

$$x_p = \frac{\ln(V_0 K t + 1)}{K} \quad ; \quad z_p = h + \frac{g \ln(V_0 K t + 1)}{2(V_0 K)^2} - \frac{gt^2}{4} - \frac{gt}{2V_0 K} \quad (13.15)$$

$$u_p = \frac{V_0}{V_0 K t + 1} \quad ; \quad w_p = \frac{g}{2V_0 K (V_0 K t + 1)} - \frac{gt}{2} - \frac{g}{2V_0 K} \quad (13.16)$$

The following case was run in FDS and compared against the approximate solution:

Drag coefficient	$C_d$	0.2
Particle diameter	$2r_p$	5 mm
Gravitational acceleration	$g$	9.8 m/s <sup>2</sup>
Particle density	$\rho_p$	1000 kg/m <sup>3</sup>
Air density	$\rho_a$	1.2 kg/m <sup>3</sup>
Initial horizontal velocity	$V_0$	400 m/s
Initial height	$h$	8 m

Figure 13.10 compares the computed solution to the “flat fire” solution given above.

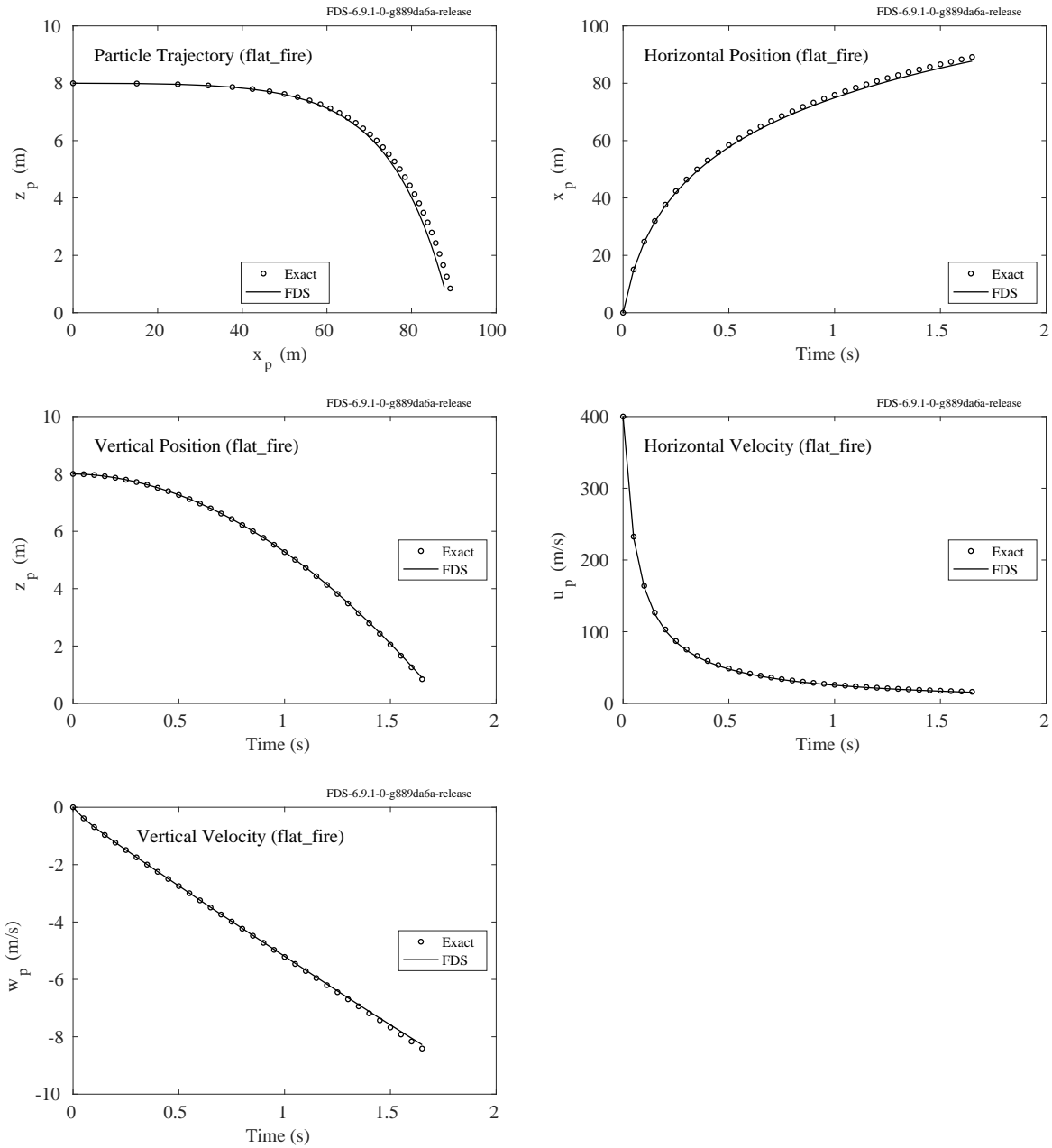


Figure 13.10: Results of the `flat_fire` test case.

## 13.2 Solid Particle Mass and Energy Transfer

### 13.2.1 Radiation Absorption by Vegetation

In this example, six channels, each measuring 4 m by 1 m by 1 m, are filled with various amounts of particles that represent vegetation. The vegetation occupies exactly one cubic meter within each channel. One end of each channel is a solid wall with temperature  $T_{\text{hot}} = 1273$  K, and the opposite end is a wall with temperature  $T_{\text{cold}} = 0$  K. Each wall has an emissivity of 1 and a heat transfer coefficient of 0. The side walls of the channels are “mirror” boundaries which essentially means that the end walls and vegetation layer are infinitely wide, rendering the configuration one-dimensional. With no particles present, the radiative intensity, or *radiance*, in the axial direction at the hot wall is  $I_0 = \sigma T_{\text{hot}}^4 / \pi \approx 47.4$  kW/(m<sup>2</sup>·sr). With particles present, the radiance is expected to attenuate according to the following:

$$I = I_0 e^{-0.25 \beta \sigma_p L} \quad (13.17)$$

$\beta = m'''/\rho_p$  is the “packing ratio,” the vegetation mass per unit volume, or “bulk density,” divided by the density of the vegetation itself,  $\rho_p = 500$  kg/m<sup>3</sup>.  $\sigma_p = 4000$  m<sup>-1</sup> is the particle surface area to volume ratio, and  $L = 1$  m is the depth of the vegetation layer. Figure 13.11 displays the comparison of the expected radiative heat flux versus that calculated by FDS.

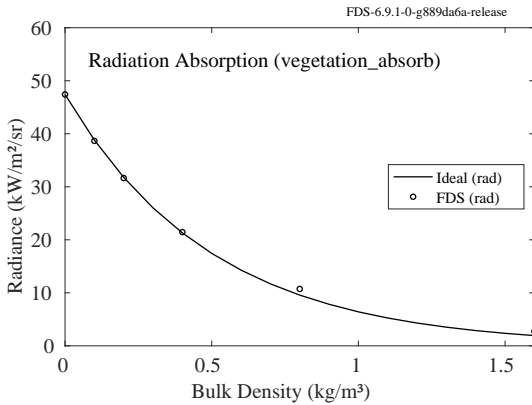


Figure 13.11: Decrease in radiance caused by layers of vegetation of various densities.

### 13.2.2 Heating a Metal Sphere via Radiation and Convection

A small metal sphere with mass,  $m_s = 0.005$  kg, is suspended in a 1 m cube filled with  $m_g = 0.318$  kg nitrogen with a specified specific heat,  $c_p = 1$  kJ/(kg·K), and initial temperature,  $T_{g,i} = 1073.15$  K. The metal has a specified specific heat,  $c_s = 1$  kJ/(kg·K), and initial temperature,  $T_{s,i} = 293.15$  K. The walls of the box are adiabatic. In the first case, `particle_heating_convection`, the sphere is heated via convection only and there is no radiation heat transfer. In the second case, `particle_heating_radiation`, the sphere is heated via radiation only. The initial heat flux in both cases is approximately 75 kW/m<sup>2</sup>, and the final temperature in both cases,  $T_f$ , is found from solving an equation that equates the internal energy gained by the solid with the internal energy lost by the gas:

$$m_s c_s (T_f - T_{s,i}) = m_g c_v (T_{g,i} - T_f) \quad ; \quad c_v = c_p - \frac{R}{W} = 1 - \frac{8.3145}{28} \approx 0.703 \text{ kJ/(kg · K)} \quad (13.18)$$

The final temperature,  $T_f = 1056.1$  K or 782.9 °C, as shown in Fig. 13.12.

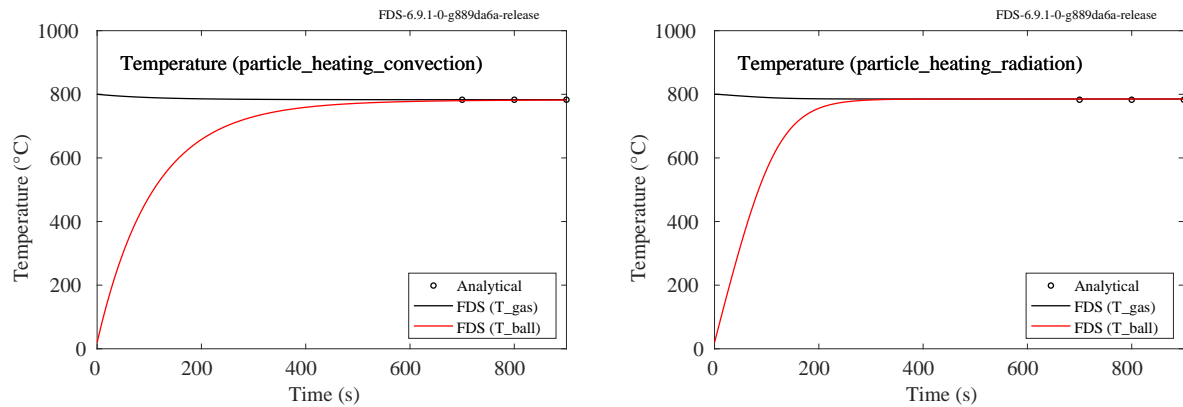


Figure 13.12: Temperature of a small cold sphere and surrounding hot gas when the sphere is heated by convection only (left) and radiation only (right).

### 13.3 Water Droplet Evaporation (`water_evaporation`)

The cases called `water_evaporation_x` test the water evaporation routine in FDS. The geometry consists either of a sealed box or a tunnel with a cross flow. The walls are assumed adiabatic, meaning that there are no leaks or heat losses. For the box cases, the air within the box is stirred to maintain uniform conditions. In each case, the numerical solutions are compared to analytical solutions.

For Cases 1-3 where the water droplets are confined to a sealed box, the change in the enthalpy of the droplets should equal the change in the enthalpy of the gas minus the work performed due to pressure. It is the internal energy of the system that is conserved. The internal energy can be expressed in terms of the enthalpy, pressure and density:

$$e = h - \frac{p}{\rho} \quad (13.19)$$

In differential form:

$$de = dh - \frac{1}{\rho} dp - p d\left(\frac{1}{\rho}\right) = dh - v dp - p dv \quad (13.20)$$

Multiplying by mass and noting that the volume,  $V$ , is constant yields:

$$dE = dH - V dp \quad (13.21)$$

The enthalpy decrease of the liquid water droplets is equal to the enthalpy gain of the gas (both expressed in kJ) minus the pressure increase times the volume in units of kPa and m<sup>3</sup>, respectively.

#### 13.3.1 Case 1

In the first case, the dimensions of the box are 1 m on a side, the initial air temperature is 200 °C, the median volumetric diameter of the droplets is 200 μm, the water temperature is 20 °C, and the total mass of water droplets is 0.01 kg. The initial mass fraction of water vapor is 0. It is expected that the droplets will all evaporate within about 10 s. Figure 13.13 displays the average enthalpy, humidity, density, temperature, pressure, and mass of water vapor within the box. The solid horizontal lines denote the expected steady-state values.

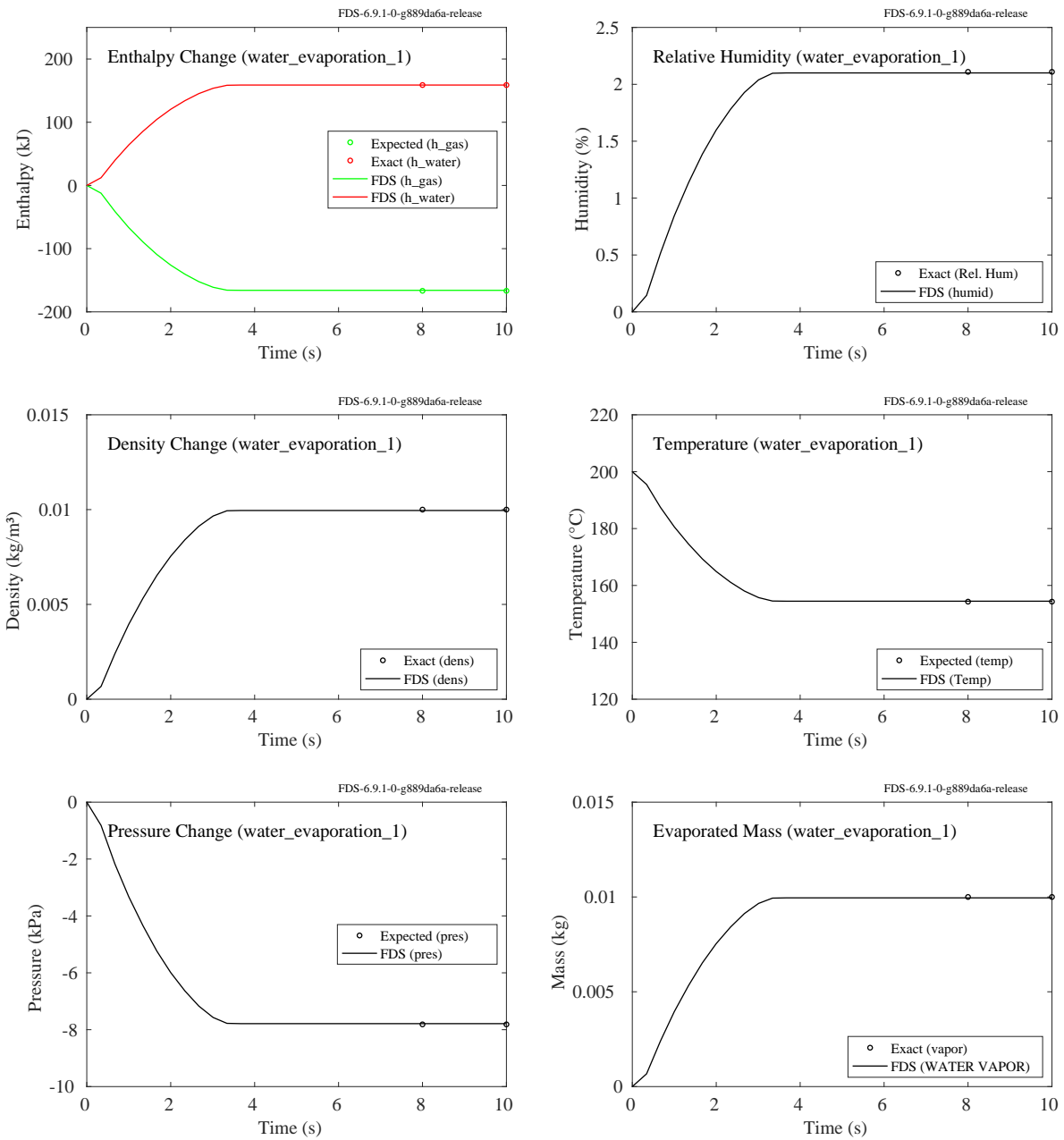


Figure 13.13: Output of the `water_evaporation_1` test case.

### 13.3.2 Case 2

In the second case, the dimensions of the box are 40 cm on a side, and the initial air temperature is 500 °C. There is only one fictitiously large water droplet in the box whose diameter is 10 cm and whose temperature is 20 °C. The initial mass fraction of water vapor is 0. It is expected that the water will evaporate until the air in the box is saturated. The analytical solution for the stationary state is derived from the first law of thermodynamics and the Clausius-Clapeyron equation by assuming that the liquid water temperature is equal to air temperature at the steady state. Results are shown in Fig. 13.14.

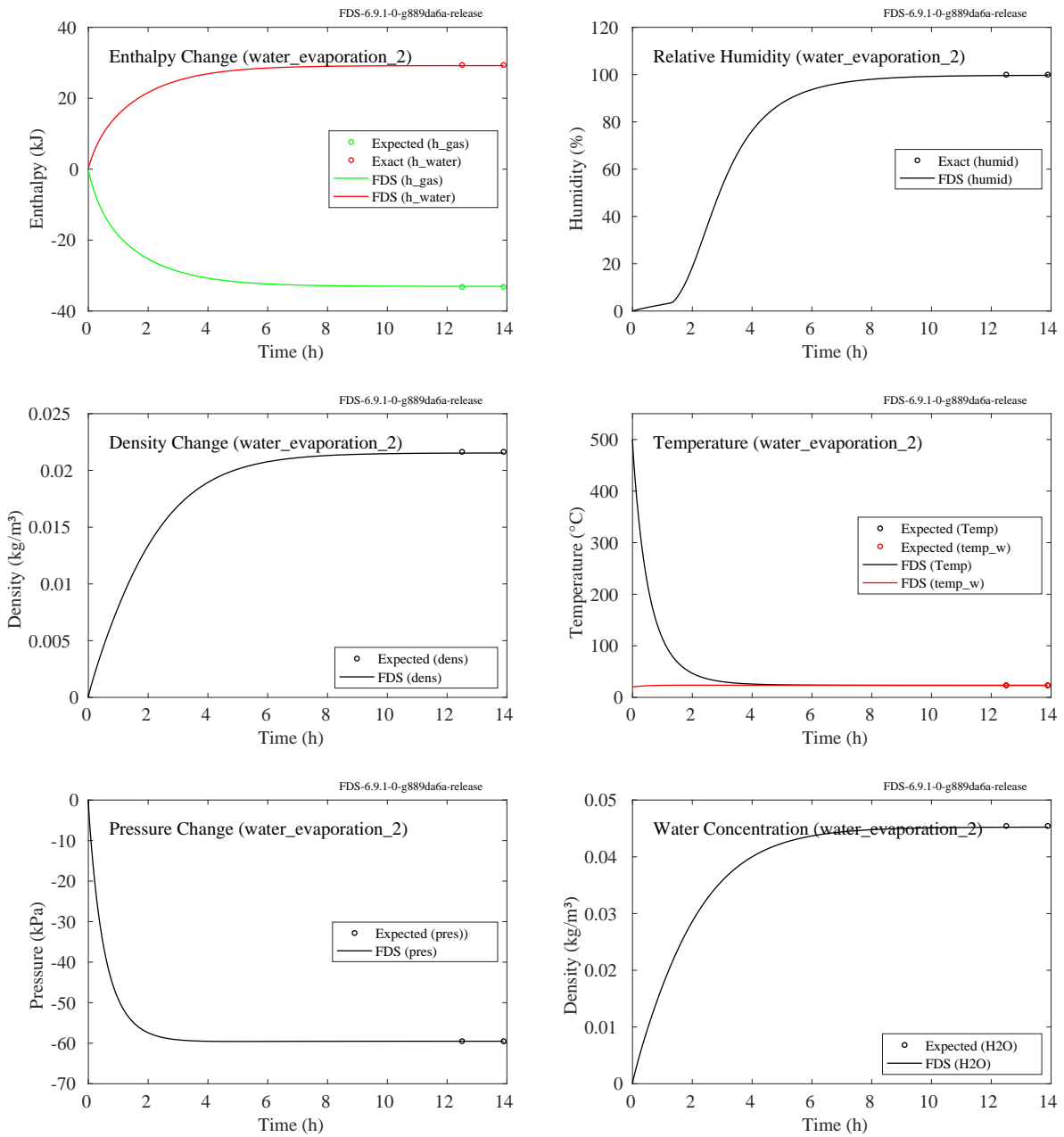


Figure 13.14: Output of the `water_evaporation_2` test case.

### 13.3.3 Case 3

In the third case, the dimensions of the box are 1 m on a side, the initial air temperature is 500 °C, the initial diameter of all the droplets is 200  $\mu\text{m}$ , the water temperature is 20 °C, and the total mass of water droplets is 0.1 kg. The initial mass fraction of water vapor is 0. It is expected to reach the saturation state. As in the second case, the analytical solution for the stationary state derives from the first principle of thermodynamics and the Clausius-Clapeyron equation by assuming that the liquid water temperature is equal to air temperature at the stationary state. Results are shown in Fig. 13.15.

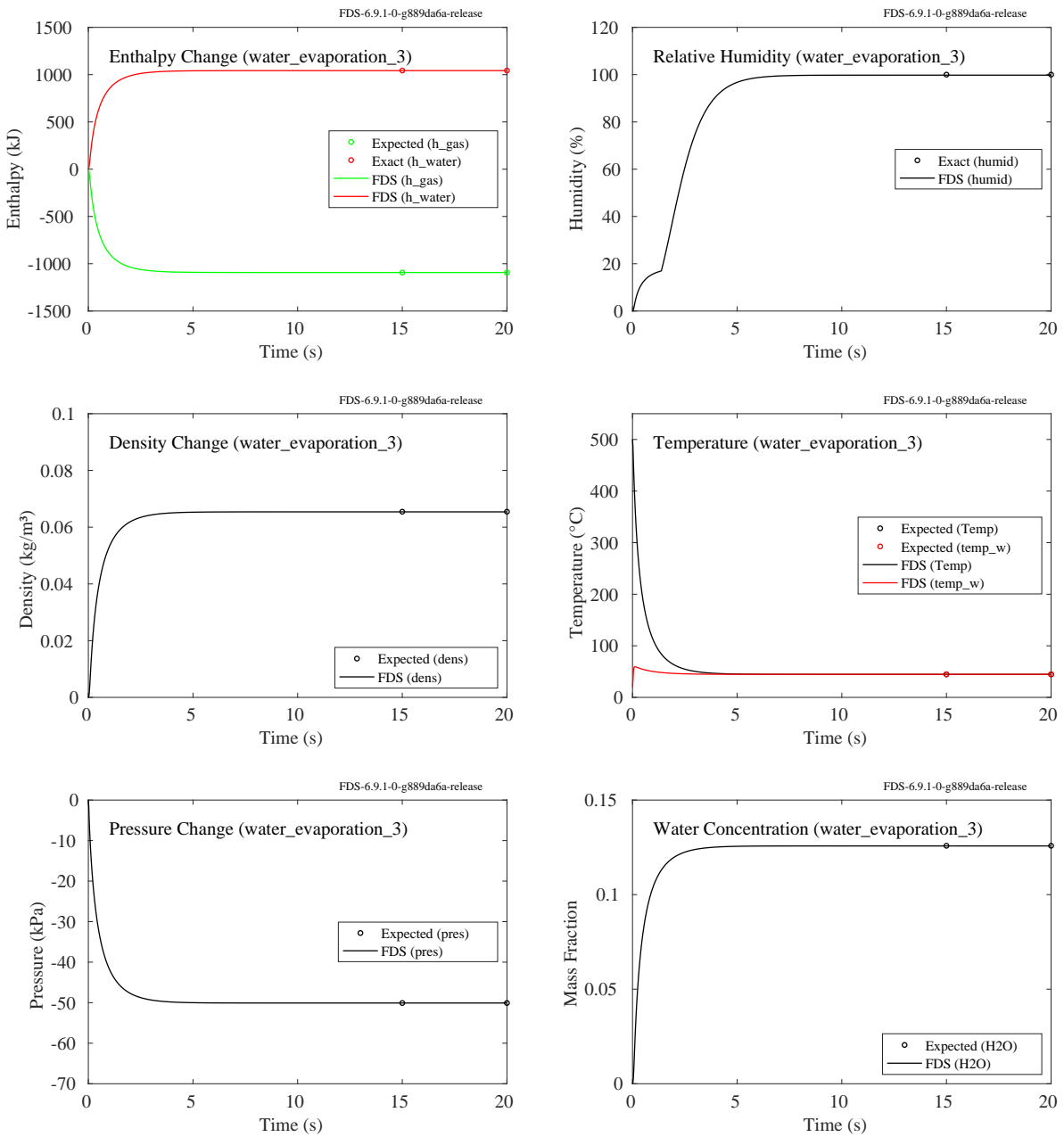


Figure 13.15: Output of the `water_evaporation_3` test case.

### 13.3.4 Case 4

In the fourth case, air at 500 °C is forced through a 3 m long, 1 m wide, 1 m tall tunnel at 1 m/s. Water droplets with a median volumetric diameter of 20  $\mu\text{m}$  are introduced in the middle of the tunnel at a rate of 0.05 kg/s, starting at 10 s. Two cases are run with different values of DT\_INSERT and N\_PARTICLES while keeping the total rate of mass injected the same. The first case uses DT\_INSERT=0.001 s and N\_PARTICLES=1000; the second case, water\_evaporation\_4\_np100, uses DT\_INSERT=0.01 s and N\_PARTICLES=100, reducing the total number of particles by a factor of 100. The water temperature is 20 °C. The mass fraction of water vapor in the hot air flowing into the tunnel is 0. The water evaporates at approximately the same rate at which it is introduced. Figure 13.16, left, displays the time history of the enthalpy flow out of the tunnel. The enthalpy flow rate of the dry hot air is 229 kW above its ambient value. The steady-state temperature is 211 °C. FDS reports heat flow as the difference in enthalpy of the flowing gas at its current temperature from that at ambient temperature. For the steady-state condition of 0.05 kg/s in the air flow at 211 °C the heat flow is expected to be 107 kW.

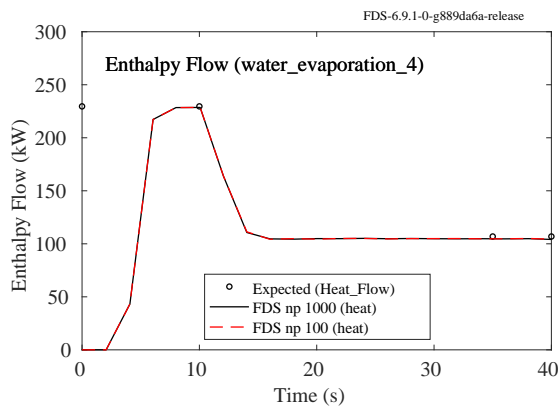


Figure 13.16: Output of water\_evaporation\_4 test case. The black line indicates the FDS results for the test case with 1000 particles injected every 0.001 s. The dashed red line shows results for FDS with 100 particles injected every 0.01 s. Note that the same total mass is injected in both cases.

### 13.3.5 Case 5

This case is based upon one of the Ranz and Marshall experiments [101] contained in the FDS Validation Guide [20] in which a single, stationary water droplet of diameter 1043  $\mu\text{m}$  in relatively dry air evaporates in approximately 15 min. The droplet is modeled using the thermally-thin liquid droplet model and the thermally-thick model usually used for solid particles. For the thermally-thick droplet, the evaporation model used for liquid pools is applied at the surface of the sphere. A temperature-dependent heat of vaporization is applied. Fig. 13.17 compares the droplet diameter of the thermally-thick and thermally-thin models compared to the experimental measurement.

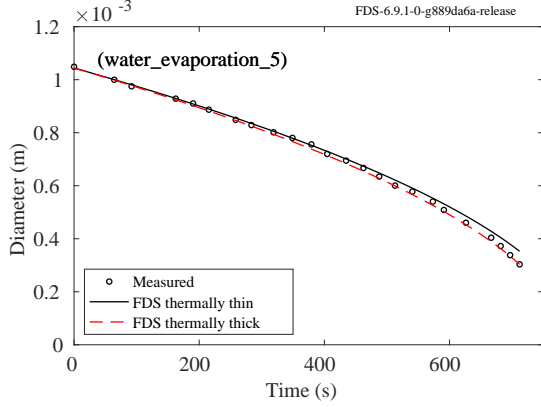


Figure 13.17: Output of water\_evaporation\_5 test case.

### 13.3.6 Case 6

This pair of cases tests the conservation of energy between droplets, surfaces, and the gas. It also demonstrates that one can specify thermophysical properties rather than rely on tabulated data. In both cases, a box with volume,  $V = 1 \text{ m}^3$ , is filled with gas with the following properties:  $m_{g,0} = 1 \text{ kg}$ ,  $c_{p,g} = 1 \text{ kJ}/(\text{kg K})$ ,  $W = 28 \text{ g/mol}$ ,  $T_{g,0} = 373.15 \text{ K}$ . The box is filled with droplets with total mass,  $m_d = 0.01 \text{ kg}$ , specific heat,  $c_l = 2 \text{ kJ}/(\text{kg K})$ , and heat of vaporization,  $h_v = 173.15 \text{ kJ/kg}$ . The droplets evaporate into the same gas as the background. The droplets have an initial temperature,  $T_{d,0} = 293.15 \text{ K}$ , and a boiling point,  $T_b = 373.15 \text{ K}$ .

In case 6, all walls of the box except the floor are adiabatic. The floor is thermally thin (e.g., high conductivity compared to its thickness), with a perfectly insulated backing. It has a total mass,  $m_w = 1 \text{ kg}$ , a specific heat,  $c_w = 1 \text{ kJ}/(\text{kg K})$ , and an initial temperature,  $T_{w,0} = 523.15 \text{ K}$ . After approximately 100 s, all the droplets evaporate, the wall and the gas temperatures converge to a single final temperature,  $T_{g,f}$ , and the pressure rises to  $p_f$  (see Fig. 13.18). The final gas temperature can be found by solving the equation,  $\Delta E = \Delta H - V\Delta p$ , where  $\Delta E$  is the energy transferred from the hot floor to the gas,  $\Delta H$  is the increased enthalpy of the gas due to the convective heating of the floor and the evaporation of the water droplets, and  $\Delta p$  is the change in gas pressure.

$$\begin{aligned}\Delta E &= m_w c_w (T_{w,0} - T_{g,f}) \\ \Delta H &= m_{g,0} c_{p,g} (T_{g,f} - T_{g,0}) + m_d (c_l (T_b - T_{d,0}) + c_{p,g} (T_{g,f} - T_b) + h_v) \\ \Delta p &= \frac{R}{WV} (m_{g,f} T_{g,f} - m_{g,0} T_{g,0}) \quad ; \quad R = 8.314 \text{ J/mol/K}\end{aligned}$$

The final temperature is calculated to be 460.0 K (186.9 °C) and the pressure increase is 27.2 kPa.

In case 6a, the floor is also set to adiabatic. For a fixed heat flux surface, FDS does not compute heat transfer between droplets and the surface as this can lead to instabilities. In this case the drops fall to the floor and begin evaporating in the hot gas without transferring heat to the walls. The internal energy of the box should change an equal and opposite amount as the enthalpy change to the droplets. The drops form a cold layer at the bottom as heat is transferred from the gas to the droplets. This temperature stratification means this case would take a very long time to reach equilibrium. For verification purposes the case is run long enough to capture the initial high rates of heat transfer until the gas around the droplets is in near equilibrium with the droplets.

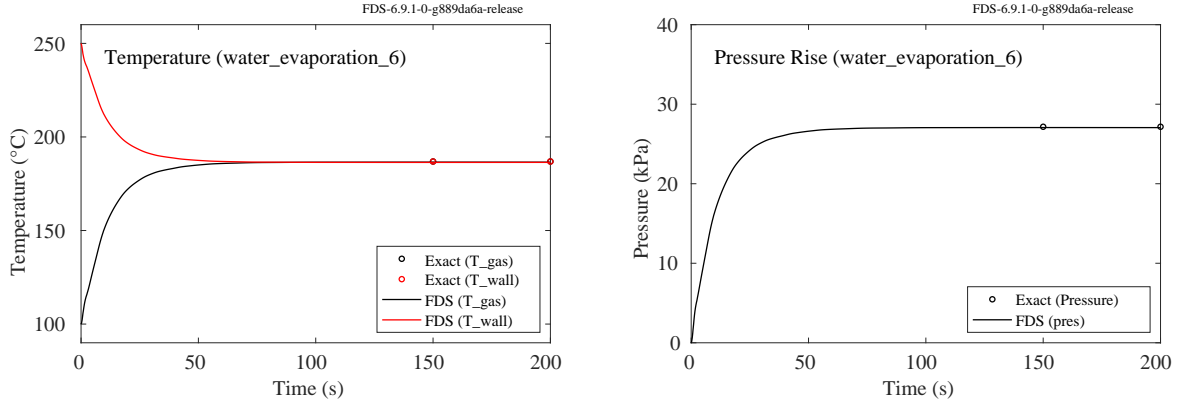


Figure 13.18: Output of water\_evaporation case 6.

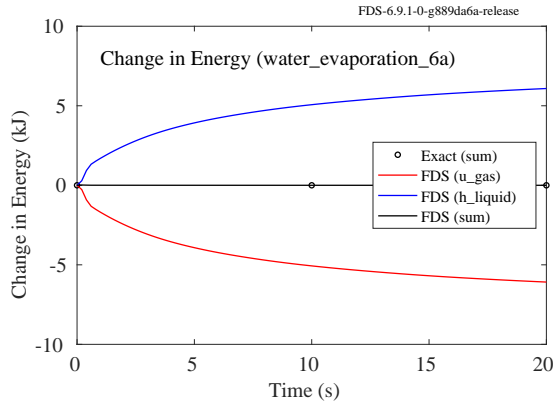


Figure 13.19: Output of water\_evaporation\_6a test case.

### 13.3.7 Case 7

A gas burner lies near the bottom of a 1 m by 1 m by 5 m high vertical channel whose walls are made of a thin sheet of insulated steel. Air at 20 °C is forced into the bottom of the channel at 1 m/s. Monodisperse water droplets with a diameter of 2000  $\mu\text{m}$  are introduced via a nozzle in the middle of the channel at a rate of 0.5 L/min, starting at 60 s. The water temperature is 20 °C, and the spray is directed at the walls with an initial velocity of 5 m/s. The water completely evaporates before it drips down to the bottom of the channel. Figure 13.20 displays the energy balance for this case. The heat release rate, HRR, of the fire is expected to be 384 kW. The rate at which the water droplets extract energy from the system,  $Q_{\text{PART}}$ , is expected to be

$$-(4.189 \text{ kJ}/(\text{kg K}) \times 80 \text{ K} + 2269 \text{ kJ/kg}) \times 0.5/60 \text{ kg/s} = -21.7 \text{ kW} \quad (13.22)$$

The sum of all the terms,  $Q_{\text{TOTAL}}$ , is expected to be zero. The three other quantities,  $Q_{\text{COND}}$ ,  $Q_{\text{RADI}}$ ,  $Q_{\text{CONV}}$ , all have plausible values, but there is no way to determine the exact values.

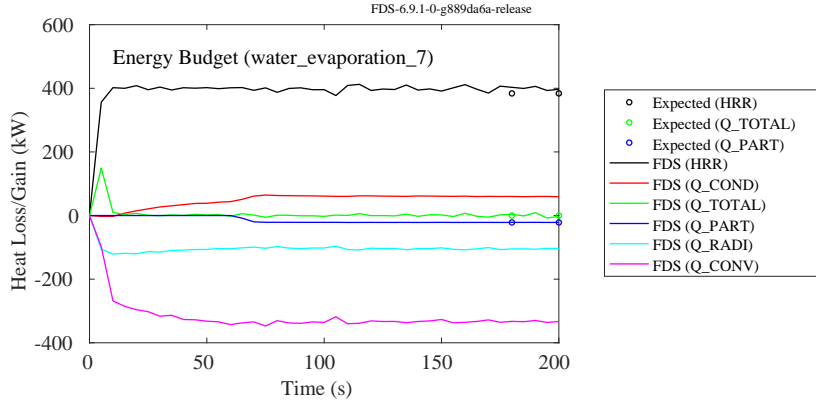


Figure 13.20: Output of water\_evaporation case 7.

### 13.3.8 Case 8

This case is similar to Case 5 except that here the droplet has a diameter of  $100 \mu\text{m}$  and it is dropped with an initial velocity of 3 m/s. The measurements are described in Li and Chow [102]. The specific case is shown in Fig. 6 of the paper. The simulation consists of an injection of a  $100 \mu\text{m}$  droplet at  $10^\circ\text{C}$  into  $60^\circ\text{C}$  air with an initial water vapor mass fraction of 10 %. The initial speed of the droplet is 3 m/s in the negative  $z$  direction (downward with gravity turned on).

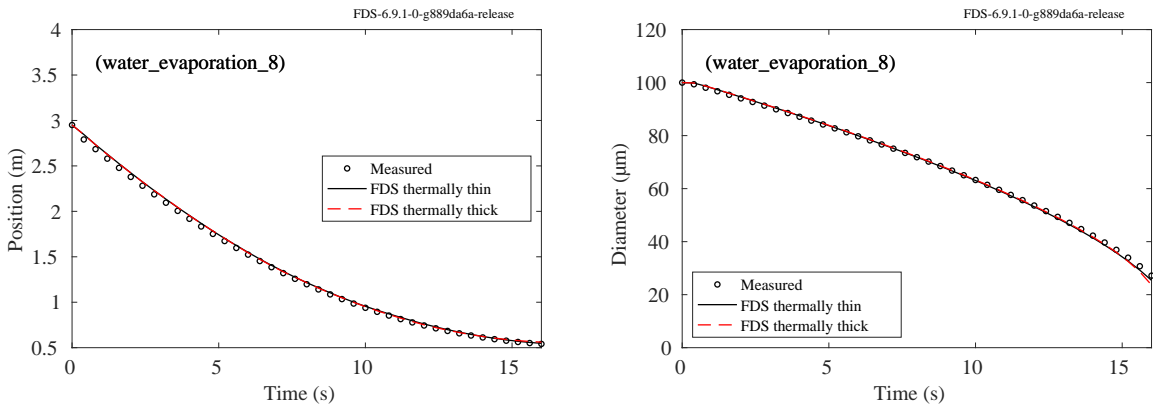


Figure 13.21: Output of water\_evaporation case 8.

## 13.4 Water Droplets on Solid Surfaces

### 13.4.1 Basic Flow and Mass Conservation (geom\_sprk\_mass)

In the test case called Sprinklers\_and\_Sprays/geom\_sprk\_mass.fds, two identical sprinklers pour water on two identical obstructions, one of which is created using the traditional OBST input parameters, the other is created using the immersed boundary GEOM parameters. The objective is simply to ensure that the droplets behave the same way in both cases. The sprinklers operate for 4 s, each discharging 10.5 L of water. The HORIZONTAL\_VELOCITY of the droplets on the solid surfaces is set to a low value of 0.05 m/s

to allow for all of the water to pool before dripping over the edge. Figure 13.22 displays the accumulated mass of water on each obstruction as a function of time, demonstrating equivalent behavior by both types of solid obstructions.

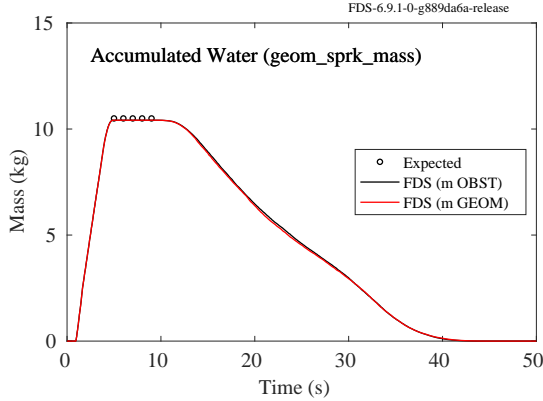


Figure 13.22: Mass of water pooled on two solid obstructions.

### 13.4.2 Obstructions of Different Orientations (geom\_particle\_cascade\_2)

In the test case called `Complex_Geometry/geom_particle_cascade_2.fds`, four identical sprinklers pour water on four obstructions, one of which is created using the traditional `OBST` input parameters, the other three are created using the immersed boundary `GEOM` parameters. The objective is simply to ensure that the droplets drip off the obstructions appropriately. The sprinklers operate for 10 s, each discharging 10 L of water. Figure 13.23 displays the accumulated mass of water on the floor as a function of time, demonstrating equivalent behavior by different types of solid obstructions.

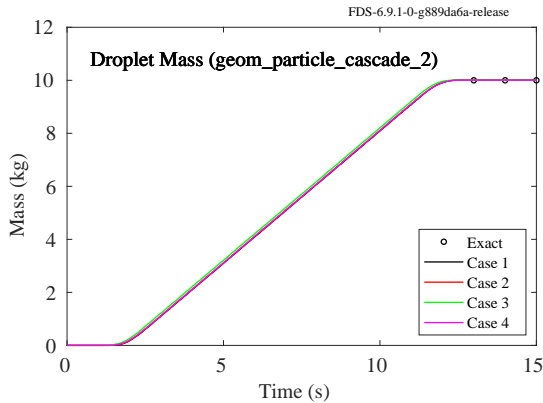


Figure 13.23: Mass of water flowing over four obstructions.

### 13.4.3 Adiabatic Surface Temperature (adiabatic\_surf\_temp\_spray)

This test case is a modified version of `Radiation/adiabatic_surface_temperature`. A thin metal plate with insulated backing is heated for 100 s. Adiabatic surface temperature (AST) is measured from the

surface of the plate. Figure 13.24 shows that after about 40 s, the plate temperature and AST match each other. At 50 s, a water spray is turned on and it starts to cool down the surface. At 100 s, the heater is turned off, and the plate cools down even more. AST and plate temperatures should match each other in the end of every 50 s period.

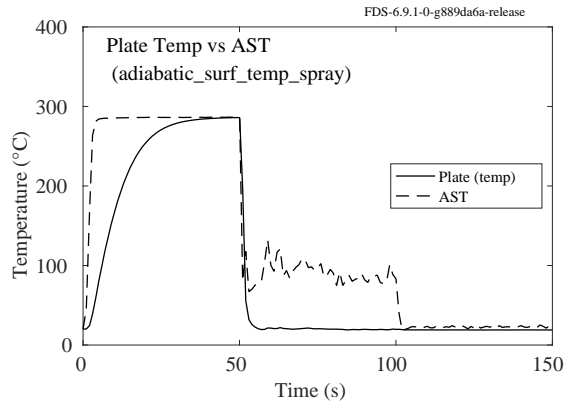


Figure 13.24: Adiabatic and true surface temperatures under radiative heating (0 - 50 s), heating and spray cooling (50-100 s) and only spray cooling (100-150 s).

#### 13.4.4 Droplet Movement on Solid Surfaces with MPI (`cascademp`)

This test case is a modified version of `cascade` (see FDS User’s Guide [2]). The single mesh is replaced with 4 meshed regions to verify that particles crossing mesh boundaries in the gas phase and along solid surfaces are handled correctly. The first meshed region uses OBST definitions for the boxes with a single mesh. The second region replaces the OBST definition with a GEOM definition. The third and fourth region use the same geometry but separate the regions into 2 meshes. The plots show the total water mass for the four meshed regions.

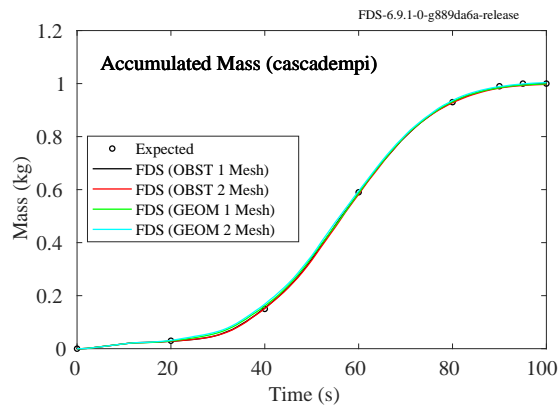


Figure 13.25: Results of the `cascademp` test case.

## 13.5 Flow Rate and Pipe Networks (`flow_rate_2`)

In this test case four sprinklers are placed in a room. The first three sprinklers are on one pipe network (`PIPE_INDEX = 1`) and the fourth sprinkler is on a second pipe network (`PIPE_INDEX = 2`). The sprinklers are defined with a pressure ramp such that all of the sprinklers within a pipe network flow at a combined rate of 10 L/min regardless of the number of open heads. The sprinklers are set to open every 15 s and to close at 60 s. After 45 s, the first three sprinklers (black line) have opened for a combined flow rate of 10 L/min and an accumulated water mass of 7.5 kg. At 60 s, the fourth sprinkler (red line) flowing at 10 L/min plus the first three sprinklers flowing at 10 L/min have produced 12.5 kg of water. The results are shown in Fig. 13.26.

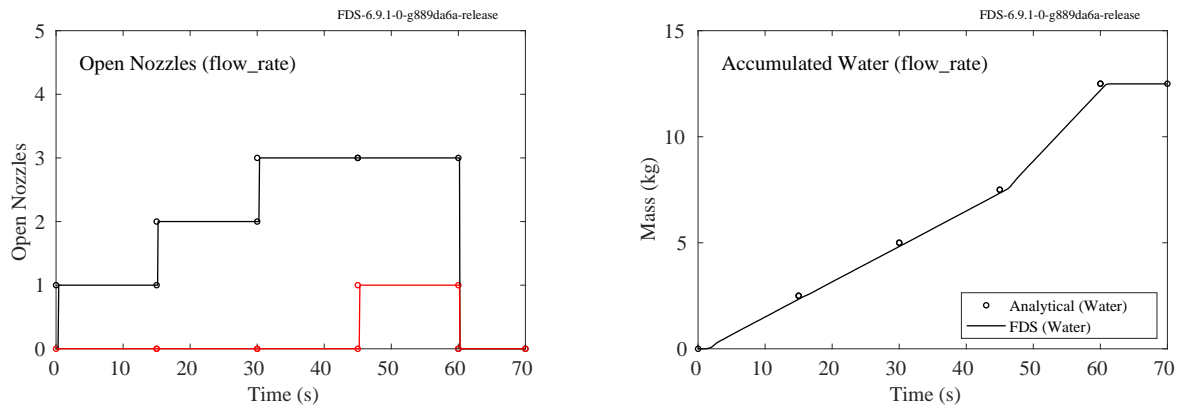


Figure 13.26: Output of the `flow_rate_2` test case.

## 13.6 Turbulent Dispersion (`random_walk`)

Two cases are set up to test the turbulent dispersion of tracer particles. Tracer particles are injected into a channel with a steady laminar flow with mean velocity 1 m/s. In the first case (`random_walk_1`), the diffusivity is set to  $D = 0.0834 \text{ m}^2/\text{s}$  (this value results from setting the dynamic viscosity to  $\mu = 0.1 \text{ kg}/(\text{m}\cdot\text{s})$  with an ambient density of  $\rho = 1.199 \text{ kg}/\text{m}^3$  and a Schmidt number of unity). In the second case (`random_walk_2`), the diffusivity is set to  $D = 0.00834 \text{ m}^2/\text{s}$ . The results are compared with Einstein's classic result for Brownian motion [103]:

$$f(z,t) = \frac{n}{4\pi D} \frac{\exp(-z^2/4Dt)}{\sqrt{t}} \quad (13.23)$$

where  $f(z,t)$  is the particle number density at lateral distance  $z$  from the source at time  $t$ ,  $n$  is the total number of particles in the system. A virtual phase doppler particle analyzer (PDPA) is set up to measure the FDS number concentration at the outlet of the channel as a function of height,  $z$ . The outlet is 15 m downstream of the point source of tracer particles. With a mean velocity of 1 m/s, the time is taken as  $t = 15$  s. The FDS results are compared with Eq. (13.23) in Fig. 13.27.

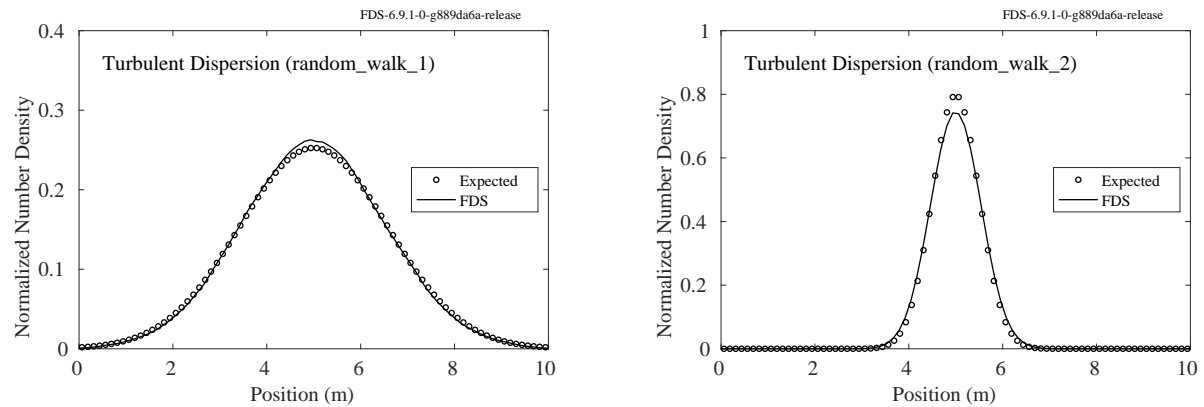


Figure 13.27: Turbulent dispersion of tracer particles `random_walk` test cases.

## Chapter 14

# Heating, Ventilating, and Air Conditioning (HVAC)

### 14.1 Duct Flow Losses (`HVAC_flow_loss`)

The pressure drop due to steady flow in a duct is given by

$$\Delta p = \frac{K\rho u^2}{2} \quad (14.1)$$

where  $K$  is the loss coefficient for the duct,  $\rho$  is the gas density, and  $u$  is the mean velocity. In this example, a duct is split at a tee joint into two ducts. All ducts have the same cross sectional area. The primary duct is assigned a constant flow rate of  $0.3 \text{ m}^3/\text{s}$ . The other two ducts are assigned loss coefficients of 4 and 16 and outlets at the same elevation. From Eq. (14.1), it can be shown that since the two branch ducts have the same pressure at their outlets, the steady-state velocities in the three ducts should be 3 m/s, 2 m/s, and 1 m/s. FDS results are shown in Fig. 14.1.

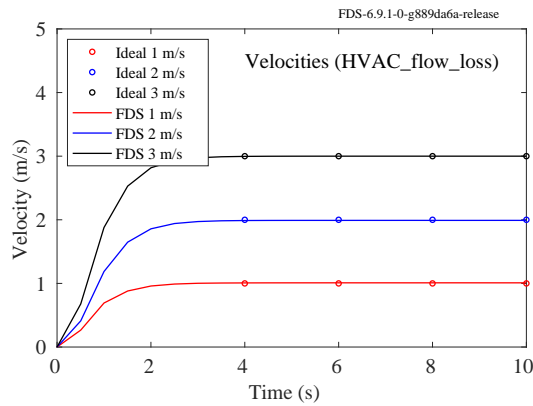


Figure 14.1: Duct velocities in three ducts with different loss coefficients.

### 14.2 Node Flow Losses (`HVAC_tee_loss_1`, `HVAC_tee_loss_2`)

These two cases use the same geometry as in Sec. 14.1. However, instead of losses assigned to the ducts, the losses are assigned to the duct nodes. In the first case, `HVAC_tee_loss_1`, the flow goes into the primary

leg of the tee. The secondary branches are assigned loss coefficients of 15 and 3 and the discharge nodes are assigned losses of 1. This gives total losses of 16 and 4. In the second case, `HVAC_tee_loss_2`, the flow goes out the primary leg of the tee. Duct directions are reversed so the sign on velocity remains the same as in the first case. The same flow losses are assigned. In the first case, the two exhaust ducts are expected to have the same losses as in Sec. 14.1 and the duct velocities should be the same (3 m/s, 2 m/s, and 1 m/s). In the second case, the exhaust ducts now function as supply ducts, and the supply duct now functions as an exhaust duct. This means that only the duct with the specified sees the pressure drop imposed by the tee as the other two ducts are now upstream of the tee. Since those ducts do not have any losses other than the node losses of 1, both ducts have the same total loss and see the same pressure drop. In this case the expected flows are 3 m/s, 1.5 m/s, and 1.5 m/s. FDS results are shown in Fig. 14.2.

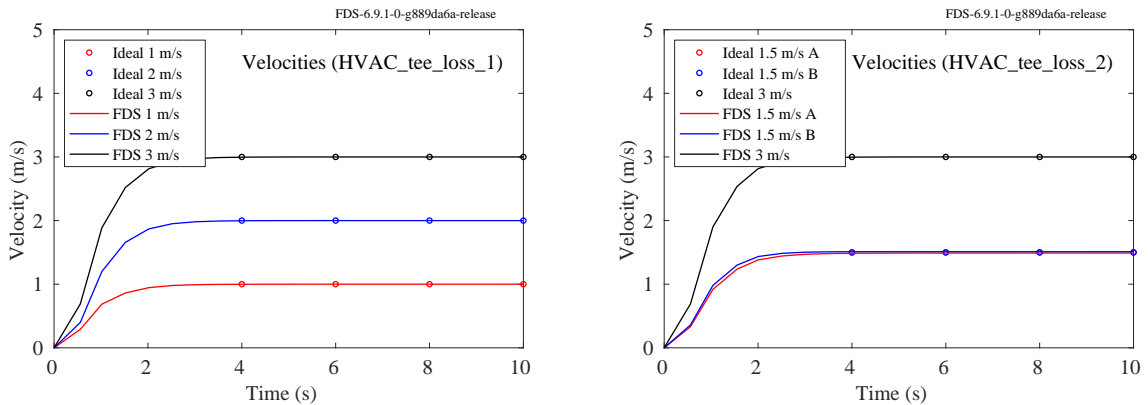


Figure 14.2: Duct velocities with varied node loss. `HVAC_tee_loss_1` (left) and `HVAC_tee_loss_2` (right).

### 14.3 HVAC Mass Conservation (`HVAC_mass_conservation`)

A 1 m by 1 m by 1 m compartment is initialized with the lower half of the compartment being filled with a species called `SPEC1` having the same molecular weight as air, see Fig. 14.3. An HVAC system of two ducts is created with one duct taking suction from the lower half (red vent) and discharging into the upper half (blue vent), and the second duct taking suction from the upper half (green vent) and discharging into the lower half (yellow vent). The two ducts are assigned the same volume flow rate. It is expected that the total mass in the compartment will be conserved, that the mass of the second species will be conserved (at 50 % of the total mass), and that at the start of the computation a slice file of species will show pure ambient being discharged in the lower half and pure `SPEC1` being discharged in the upper half.

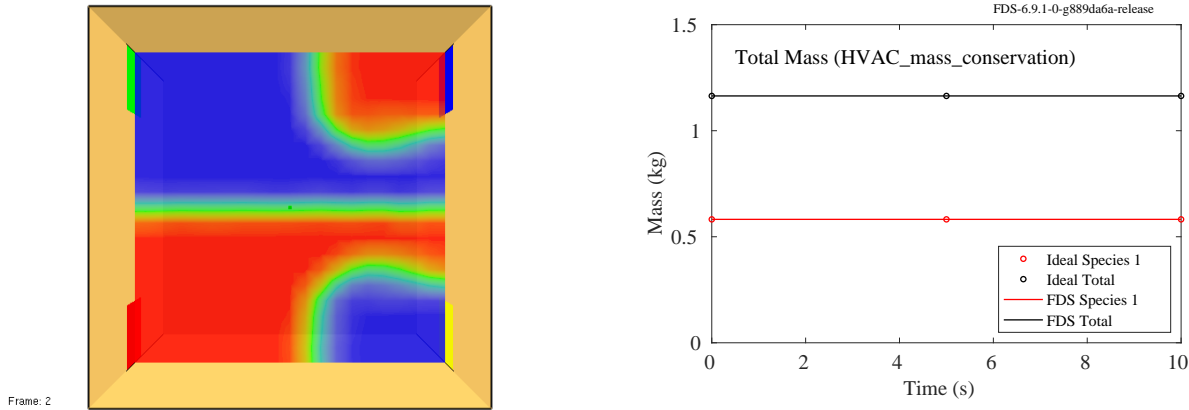


Figure 14.3: SPEC1 mass fraction at 1 s (left) and SPEC1 and total mass (right).

## 14.4 HVAC Energy Conservation and Pressure (`HVAC_energy_pressure`)

A 1 m by 1 m by 1 m box is divided into two equal compartments by a vertical wall, see Fig. 14.4. The ambient species is defined with a molecular weight of 28 g/mol, a specific heat of 1 kJ/(kg K) and a specific enthalpy of 293.15 kJ/kg at the reference temperature of 293.15 K. The left side of the compartment is initialized to twice the ambient temperature. A simple HVAC system of ducts is created. The first duct takes suction from the lower left half and discharges into the lower right half and is given an area of  $0.1 \text{ m}^2$  and fixed volume flow rate  $0.1 \text{ m}^3/\text{s}$ . The second duct is placed in the upper half of the compartment and is assigned a flow loss of 1 and an area of  $0.01 \text{ m}^2$ . It is expected that the top and bottom duct velocities will be 10 m/s and 1 m/s respectively, the total energy will be conserved, that at the start of the computation hot gas will be seen entering the lower right and cold gas entering the upper left, and that at the end of the computation the pressure difference between the two sides will be 56.3 Pa based on Eq. (14.1)

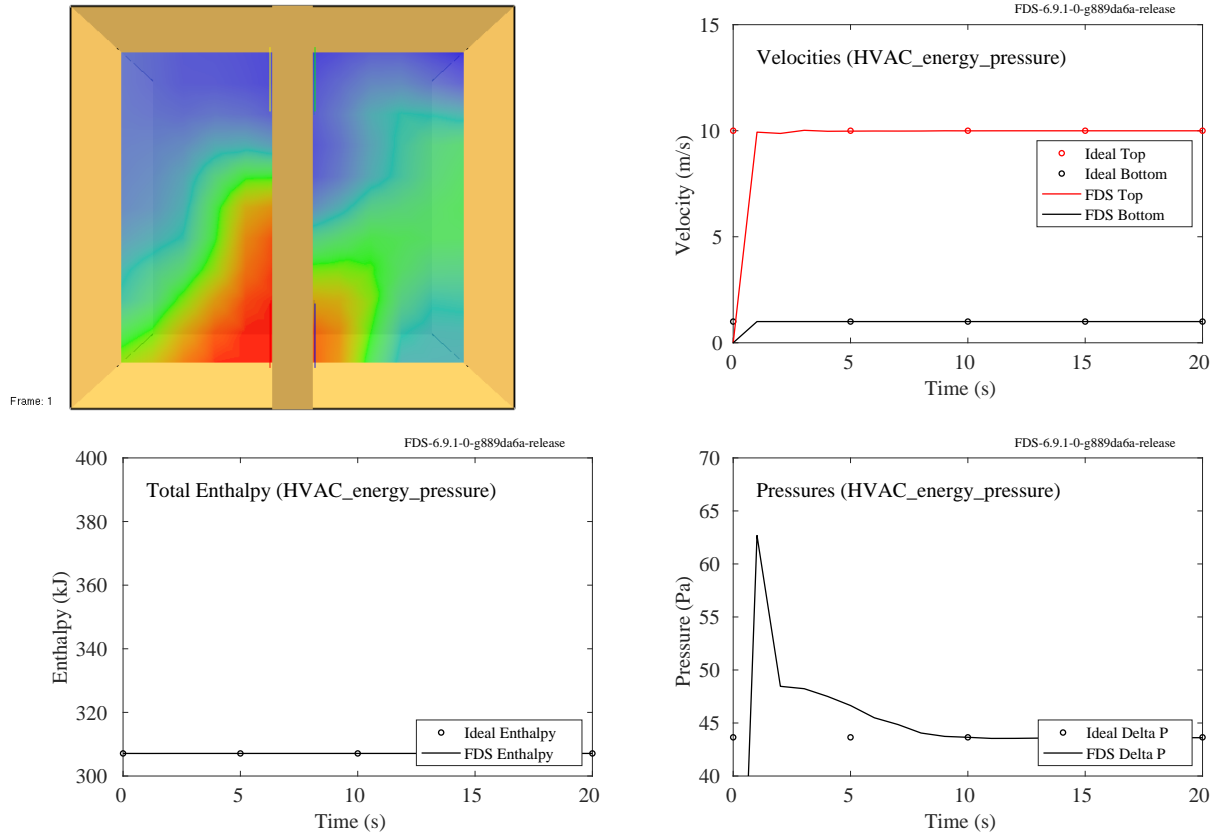


Figure 14.4: Clockwise from top left: Temperature at 1 s, duct velocities, total enthalpy in the domain, and duct node pressures for the top duct.

## 14.5 HVAC Dampers (`HVAC_damper`)

The `HVAC_damper` example case is a simple duct network of three ducts connected by a tee. A damper is present in one of the ducts and linked to a `DEVC` that will change state at 10 s. With the damper open, the respective duct flow speeds should be 3 m/s, 1 m/s, and 2 m/s. When the damper closes, the respective duct flow speeds should be 3 m/s, 3 m/s, and 0 m/s. Results of this are shown in Fig. 14.5.

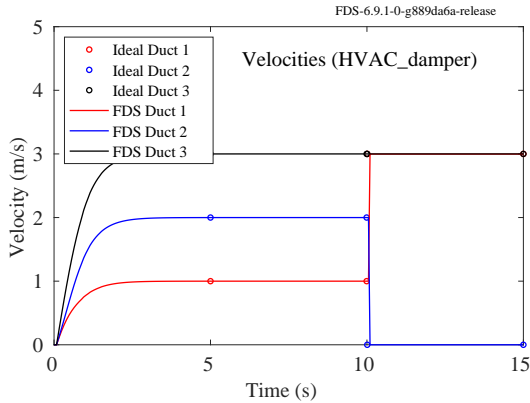


Figure 14.5: Simple duct network with a damper, case HVAC\_damper.

## 14.6 HVAC Filters (hvac\_filter)

The sample case `HVAC_filter` demonstrates the use of the filter input. A  $1 \text{ m}^3$  compartment is initialized with a particulate species with a mass fraction of 0.001. A 100 % efficient filter with a clean loss of 1 and a loading loss of  $7732.446 \text{ kg}^{-1}$  (gives a total loss of 10 when all the soot in the compartment is filtered). A quadratic fan in a  $0.01 \text{ m}^2$  duct with a maximum pressure of 20 Pa and a maximum flow of  $0.2 \text{ m}^3/\text{s}$  takes suction from one side of the compartment and discharges into the other. Over time, the filter removes the particulate from the compartment. However, since the filter loss increases with the mass of particulate filtered, the rate of removal will decrease over time. Applying the conservation of energy to the compartment and the steady state duct momentum equation to the duct, we can solve for the compartment temperature and pressure and the duct velocity. These results along with the loading of the filter and the mass of particulate in the compartment are shown in Fig. 14.6.

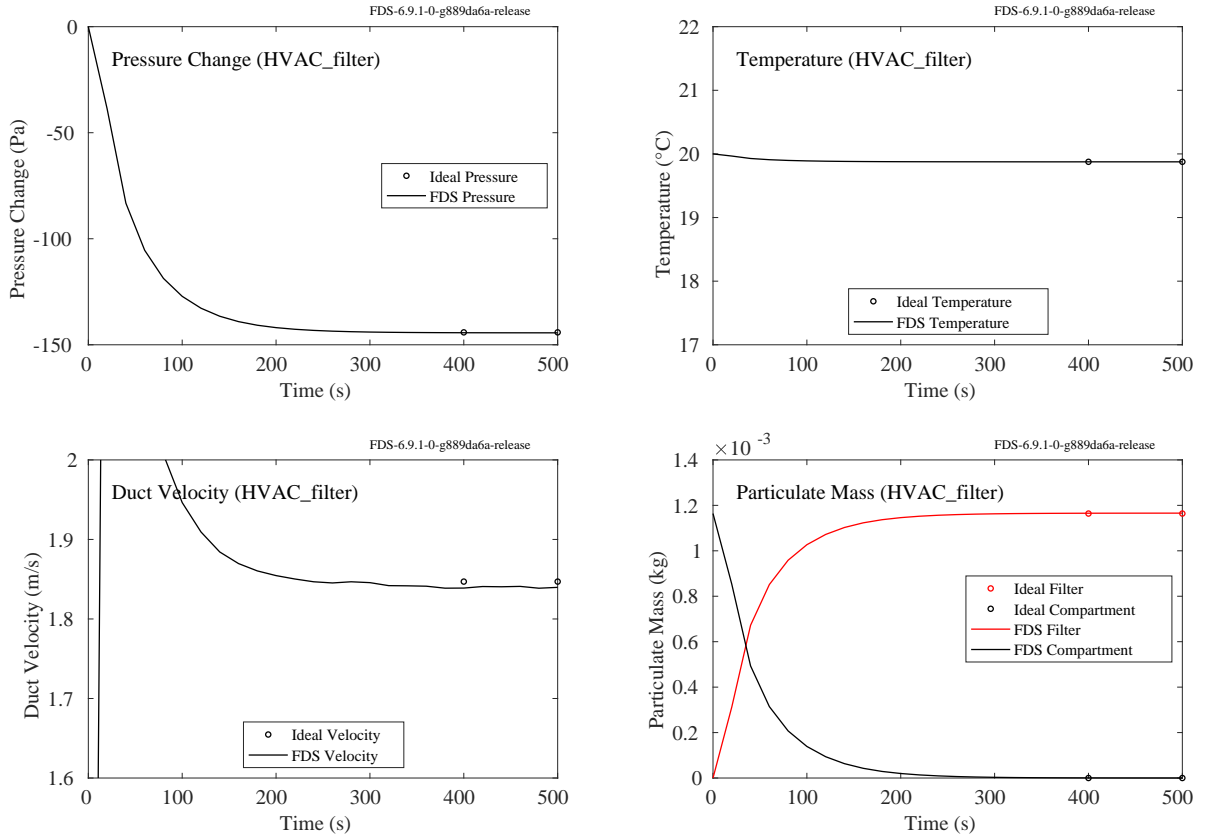


Figure 14.6: Compartment pressure (upper left), compartment temperature (upper right), duct velocity (lower left), and particulate mass in the compartment and on the filter (lower right).

## 14.7 HVAC Fans (`fan_test`)

This case tests a quadratic fan using the default approach to finding the fan operation point. Two compartments share a common wall. Both compartments are considered as separate “pressure zones.” Two,  $0.04 \text{ m}^2$  HVAC ducts are defined. One duct has a quadratic fan with a maximum volumetric flow of  $0.16 \text{ m}^3/\text{s}$  and a stall pressure of  $10 \text{ Pa}$ . The second is an open duct with a flow loss of  $10$ . The volume flow through the fans is obtained from the equation below:

$$\dot{V}_{\text{fan}} = \dot{V}_{\max} \operatorname{sign}(\Delta p_{\max} - \Delta p) \sqrt{\frac{|\Delta p - \Delta p_{\max}|}{\Delta p_{\max}}} \quad (14.2)$$

$\dot{V}_{\max} = 0.16 \text{ m}^3/\text{s}$  is the maximum output of the fan from Zone 1 to Zone 2 and  $0.2 \text{ m/s}$  is the flow speed from Zone 2 to Zone 1.  $\Delta p_{\max} = 10 \text{ Pa}$  is the maximum pressure difference at which the fan can operate. In steady state, the volume flow from compartment to compartment should be equal and opposite in sign. This occurs when the positive pressure added by the fan equals the pressure drop due to the flow loss,  $K$ , through the return duct. The volume flow through the duct for a given pressure drop can be found from the duct momentum equation ignoring all terms but the flow loss:

$$\dot{V}_{\text{fan}} = A_{\text{duct}} \sqrt{\frac{2\Delta p}{\rho K}} \quad (14.3)$$

Setting the above equation equal to Eq. (14.2), the pressure drop can be determined:

$$\sqrt{\frac{2|p_2 - p_1|}{(1.2 \text{ kg/m}^3)10}}(0.04 \text{ m}^2) = (0.16 \text{ m}^3/\text{s}) \sqrt{\frac{|p_1 - p_2 - 10 \text{ Pa}|}{10 \text{ Pa}}} \quad (14.4)$$

The solution is  $p_2 = 4.5 \text{ Pa}$  and  $p_1 = -4.5 \text{ Pa}$  (see Fig. 14.7). Note that the sign of the volume flow in the duct indicates whether the flow is moving from the first node to the second (positive) or the second node to the first (negative). This convention can make these types of calculations a bit tricky.

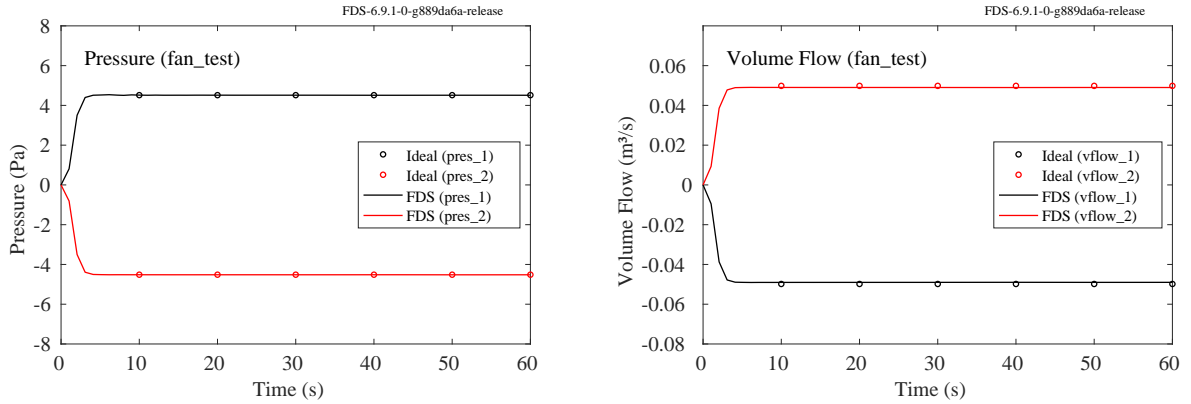


Figure 14.7: Compartment pressure and volume flow for the `fan_test` case.

## 14.8 HVAC Operation Point Single Fan (`qfan_test`)

This case tests a quadratic fan using the system curve approach to finding the fan operation point. Two compartments share a common wall. Both compartments are considered as separate “pressure zones.” Two,  $0.04 \text{ m}^2$  HVAC ducts are defined. One duct has a quadratic fan with a maximum volumetric flow of  $0.16 \text{ m}^3/\text{s}$  and a stall pressure of  $10 \text{ Pa}$ . Both ducts have a flow loss of 5. At each time step system curve is generated by fitting a quadratic to two points. The first point is using the current compartment pressure difference and solving for the system flow with the fan off ( $\dot{V}_{\text{system } 0}$ ).

$$\dot{V}_{\text{system } 0} = A_{\text{duct}} \text{sign}(\Delta p) \sqrt{\frac{2|\Delta p|}{\rho K}} \quad (14.5)$$

The second point applies the maximum fan pressure and determines the volume flow with the fan applying its full force on the flow ( $\dot{V}_{\text{system max}}$ ).

$$\dot{V}_{\text{system max}} = A_{\text{duct}} \text{sign}(\Delta p - \Delta p_{\text{max}}) \sqrt{\frac{2|\Delta p - \Delta p_{\text{max}}|}{\rho K}} \quad (14.6)$$

The operation point for the fan at each timestep will be where the fan curve intersects a quadratic between the two points just defined. At steady-state the operation point flow rate through the duct with the fan must match the flow rate through the duct without the fan. If it doesn’t, then pressures in the compartments will change and the condition won’t be steady-state. This sets up two functions. One function

is the operation point as a function of the pressure difference between the two compartments. The second function is the flow through the duct without a fan as a function the pressure difference between the two compartments. These two functions will equal each other at a pressure difference of 4.52 Pa split equally between the compartments and a flow rate of  $0.0491 \text{ m}^3/\text{s}$ .

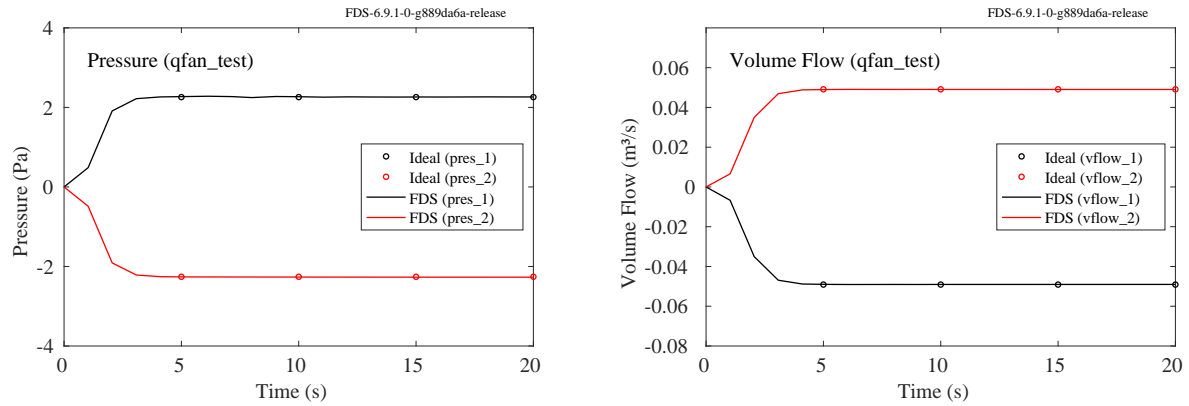


Figure 14.8: Compartment pressure and volume flow for the `qfan_test` case.

## 14.9 HVAC Operation Point Multiple Fans (`qfan_multi`)

This case tests the system curve approach for the cases a multiple fans in a duct run. Two duct runs are defined. In one case two fans take parallel suction and discharge through a combined exhaust. In the second case there are two fans in series. All ducts are defined with an area of  $0.04 \text{ m}^2$  and a loss of 5. In each case two different quadratic fans are used. The first fan has a maximum volumetric flow of  $0.2 \text{ m}^3/\text{s}$  and a stall pressure of 10 Pa. The first fan has a maximum volumetric flow of  $0.6 \text{ m}^3/\text{s}$  and a stall pressure of 30 Pa. Since the domain is open, for all fans the zero fan pressure flow will be  $0.0 \text{ m}^3/\text{s}$ . With two fans in each duct run, two full fan pressure points are created, one for each fan. When the first fan is being solved for, the pressure of the second fan is set to zero and vice versa. This means in the parallel case that the system solution will mean some air exhausting through the duct branch with the fan that is off.

In the parallel case the two full fan system points are (10 Pa,  $0.0653 \text{ m}^3/\text{s}$ ) and (30.0 Pa,  $0.113 \text{ m}^3/\text{s}$ ). In the series case the values are (10 Pa,  $0.0517 \text{ m}^3/\text{s}$ ) and (30 Pa,  $0.0895 \text{ m}^3/\text{s}$ ). The parallel case is higher since the effective exhaust duct area is  $0.2 \text{ m}^2$  rather than  $0.1 \text{ m}^2$ .

The fan pressures that intersect the system curves are 9.03 Pa and 29.0 Pa for the parallel case and 9.37 Pa and 29.4 Pa for the serial case. For the serial case this results in a system flow of  $0.102 \text{ m}^3/\text{s}$ . In the case of the parallel fans, the larger fan actually pushes flow out the smaller fans inlet. The predicted flows are  $-0.0258 \text{ m}^3/\text{s}$  for the small fan,  $0.0999 \text{ m}^3/\text{s}$  for the large fan, and  $0.0741 \text{ m}^3/\text{s}$  out the exhaust duct.

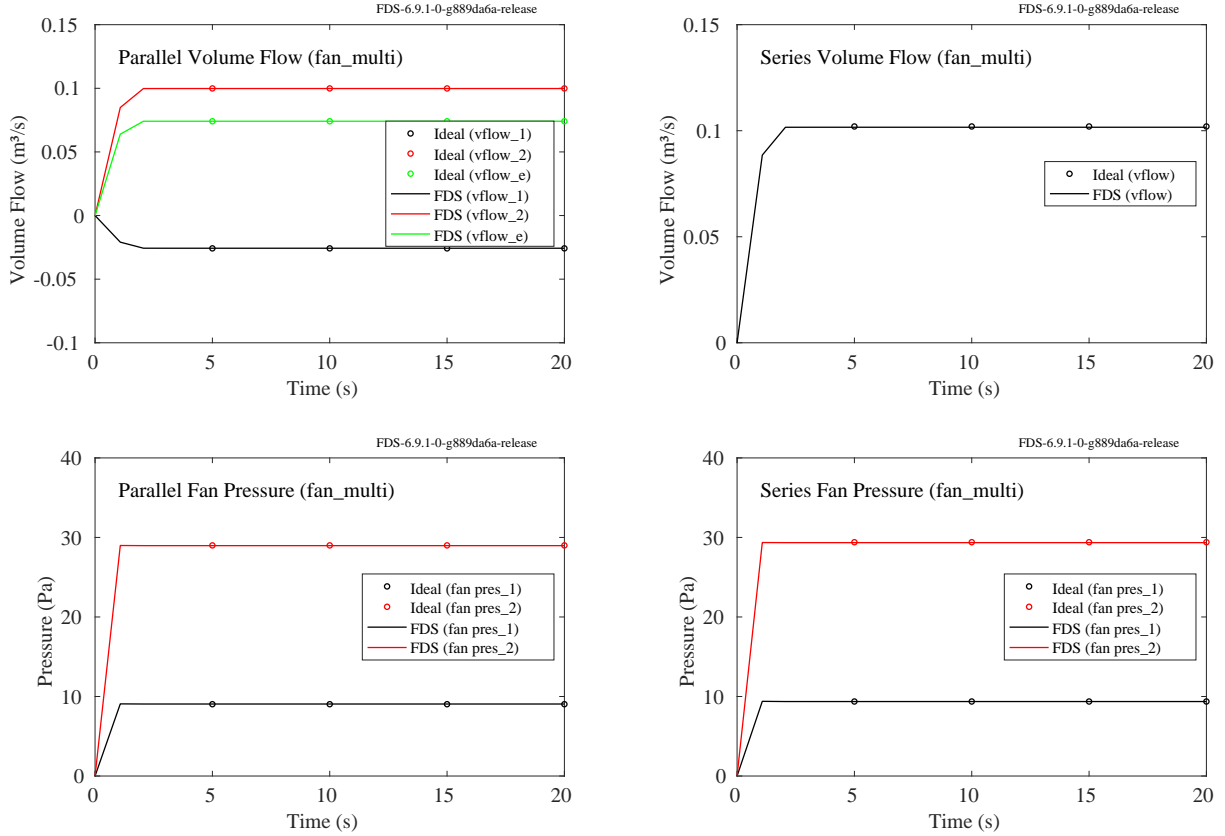


Figure 14.9: Volume flow and fan pressure for the `qfan_multi`. Left is two fans in parallel, and right is two fans in series. Top is volume flow, and bottom is fan pressure.

## 14.10 Leakage

In the following examples, both leaks and fans are demonstrated.

### 14.10.1 Single Zone Leakage (`leak_test`)

Two compartments (each 0.9 m by 1 m by 1 m) are connected by a small fan and a leak at the floor. The volume flow rate of the fan is given by the “fan curve”:

$$\dot{V}_{\text{fan}} = A_{\text{duct}} U_{\max} \operatorname{sign}(\Delta p_{\max} - \Delta p) \sqrt{\frac{|\Delta p - \Delta p_{\max}|}{\Delta p_{\max}}} \quad (14.7)$$

where  $\Delta p$  is the difference in pressure and  $A_{\text{duct}} = 0.1 \text{ m}^2$ ,  $U_{\max} = 0.6 \text{ m/s}$ , and  $\Delta p_{\max} = 300 \text{ Pa}$ . The volume flow due to the leak is given by:

$$\dot{V}_{\text{leak}} = A_{\text{leak}} \sqrt{\frac{2\Delta p}{\rho}} \quad (14.8)$$

where  $A_{\text{leak}} = 0.002 \text{ m}^2$  and  $\rho$  is the density at the discharge side. Equating the fan and leak volume flow rates, we can solve for  $\Delta p$ . The results are shown in Fig. 14.10.

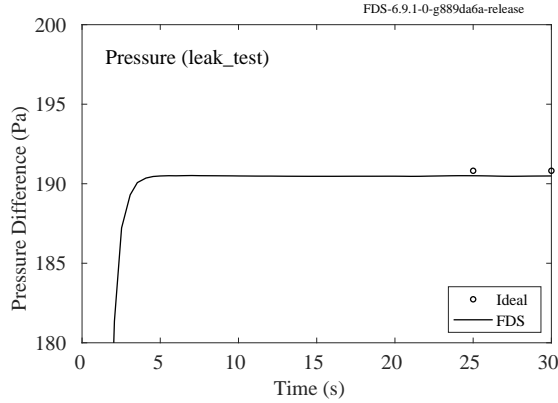


Figure 14.10: Pressure difference between two compartments with leakage connected by a fan.

#### 14.10.2 Multiple Zone Leakage (`leak_test_2`)

This case starts with the same input as `leak_test`. A second leakage vent is added to the floor of the discharge side of the fan. This vent leaks to the ambient. When the simulation starts the fan pushes air from one compartment to the other. As the pressure rises, the leakage increases until the leakage flow rate is equal to the fan flow rate. Since some air from the interior compartment is being discharged to the ambient, the average pressure of the two compartments decreases until the pressure of the interior compartment is equal to that of the ambient. At this point in time, there is no more leakage to the outside and the fan flow rate equals the leakage flow rate between the two compartments. Given the leakage area and the fan curve, this occurs when the pressure difference between the two compartments is the same as the pressure difference from `leak_test`, only now the discharge side should be at 0 Pa.

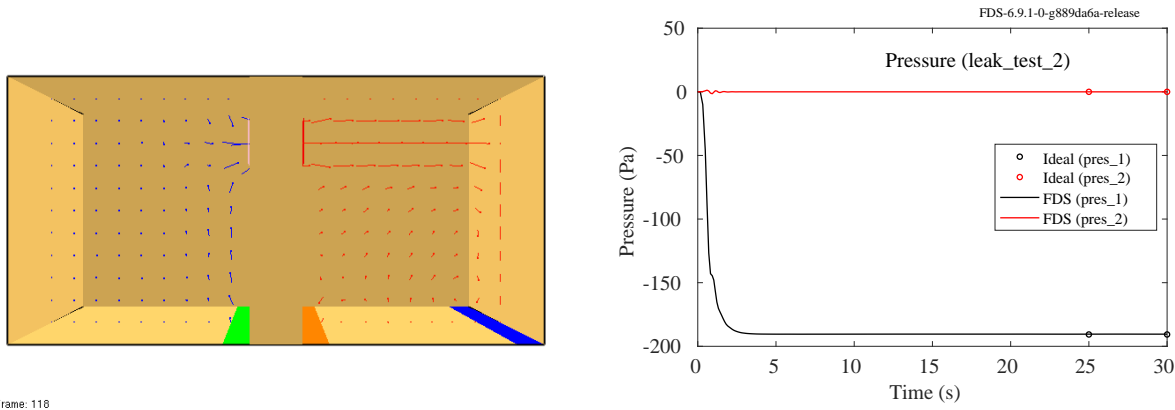


Figure 14.11: Vector plot of pressure at 10 s with geometry clipped to show compartment interiors (left) and a plot of zone pressures (right).

#### 14.10.3 Leakage through Immersed Boundary Wall (`leak_test_3`)

This case is intended to ensure that an immersed boundary obstruction (`GEOM`) handles leakage in the same way as a simple grid-conforming obstruction (`OBST`). Two rooms are separated by a wall specified via either an `OBST` line or a `GEOM` line. Air is pumped into the room on one side of the wall at a rate of  $\dot{V} = 0.02 \text{ m}^3/\text{s}$ ,

and the wall is assigned a leakage area  $A_L = 0.001 \text{ m}^2$ . The room on the other side of the wall leaks to the outside through a hole of equal area. The pressure rise in rooms 1 and 2,  $\Delta p_1$  and  $\Delta p_2$ , are found by solving:

$$\dot{V} = A_L \sqrt{\frac{2|\Delta p_1 - \Delta p_2|}{\rho_0}} \quad ; \quad \dot{V} = A_L \sqrt{\frac{2|\Delta p_2|}{\rho_0}} \quad (14.9)$$

The solution is that  $\Delta p_1 = 480 \text{ Pa}$  and  $\Delta p_2 = 240 \text{ Pa}$ , as shown in Fig. 14.12.

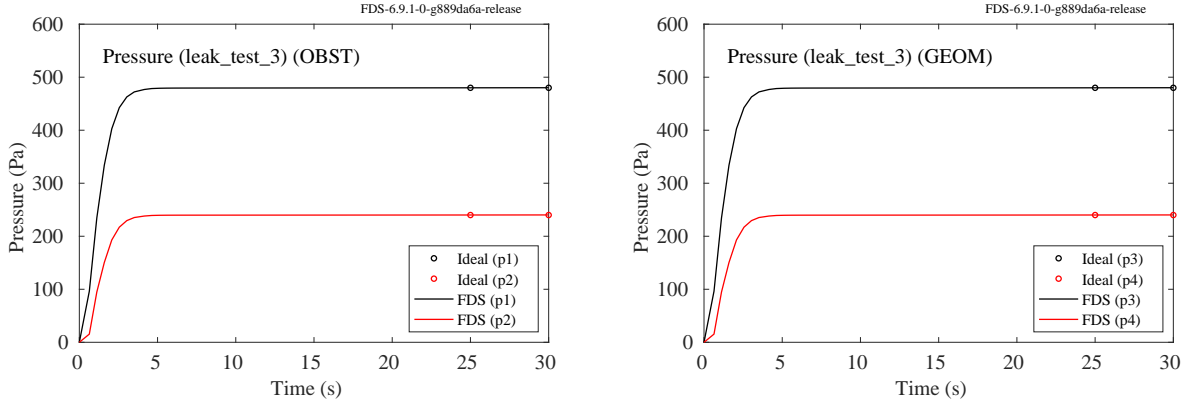


Figure 14.12: Pressure rise in adjacent compartments separated by an OBST (left) and GEOM (right) wall.

#### 14.10.4 Leakage through Immersed Boundary Compartment (`leak_test_4`)

This case is intended to ensure that a simple compartment constructed of immersed boundary obstructions (GEOM) handles leakage in the same way as a simple grid-conforming compartment. Air is pumped into the compartment via a small rotated cube inside at a rate of  $\dot{V} = 0.024 \text{ m}^3/\text{s}$ , and the walls are assigned a total leakage area  $A_L = 0.001 \text{ m}^2$ . The pressure rise,  $\Delta p$  is found by solving:

$$\dot{V} = A_L \sqrt{\frac{2|\Delta p|}{\rho_0}} \quad ; \quad \rho_0 = 1.195 \text{ kg/m}^3 \quad (14.10)$$

The solution is that  $\Delta p = 344.16 \text{ Pa}$ , as shown in Fig. 14.13.

#### 14.10.5 Localized Leakage (`leak_enthalpy`)

A domain that is 2 m by 1 m by 1 m with 10 cm grid resolution is divided into two halves by a 20 cm thick wall. In the left side is given a  $100 \text{ kW/m}^3$  heat source in its entire volume that lasts for 4 s. A localized leakage path that is  $0.001 \text{ m}^2$  is defined for one grid cell at the center on either side of the dividing wall. The parameter `LEAK_PATH` is set to true. All the boundaries are defined as adiabatic. The heat source creates pressure on the left side which force heated air into the right side. The localized leakage should conserve mass, and the energy source should add 360 kJ to the domain. Results are shown in Fig. 14.14

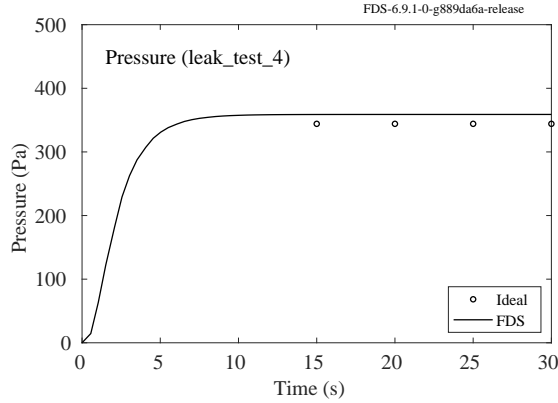


Figure 14.13: Pressure rise in a compartment constructed of immersed boundary obstructions.

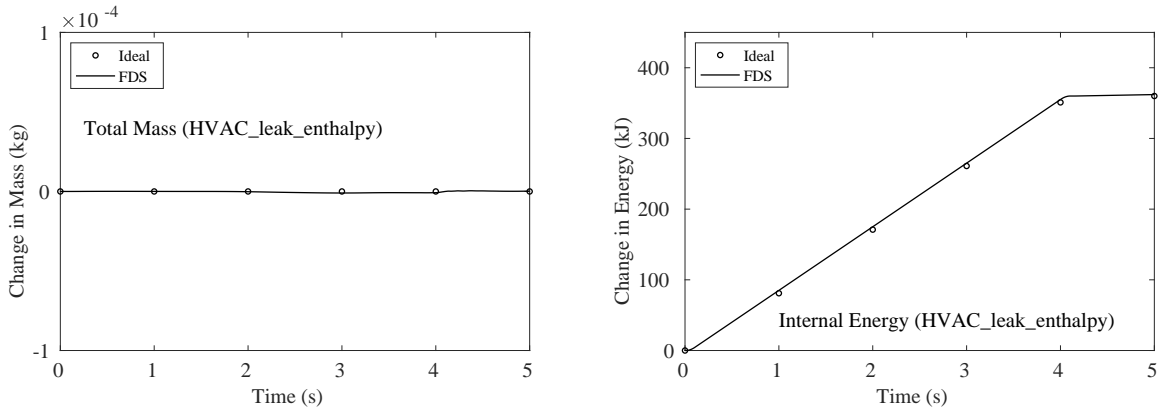


Figure 14.14: Change in mass (left) and energy (right) in the domain.

#### 14.10.6 Multiple Zone, Multiple Mesh Leakage (`zone_shape_2`)

A duct with a square 1 m cross section winds its way through a 2 by 2 by 2 array of meshes that span a sealed 6.2 m cubic domain. A fan forces air into one end of the duct at a rate of  $\dot{V} = 0.1 \text{ m}^3/\text{s}$ . The other end of the duct has a leak with effective area  $A_L = 0.007746 \text{ m}^2$ . The expected pressure difference between the interior and exterior of the duct is

$$\Delta p = \frac{\rho}{2} \left( \frac{\dot{V}}{A_L} \right)^2 \approx 100 \text{ Pa} \quad (14.11)$$

The overall mass in the domain should not change. Figure 14.15 displays the pressure difference and overall mass.

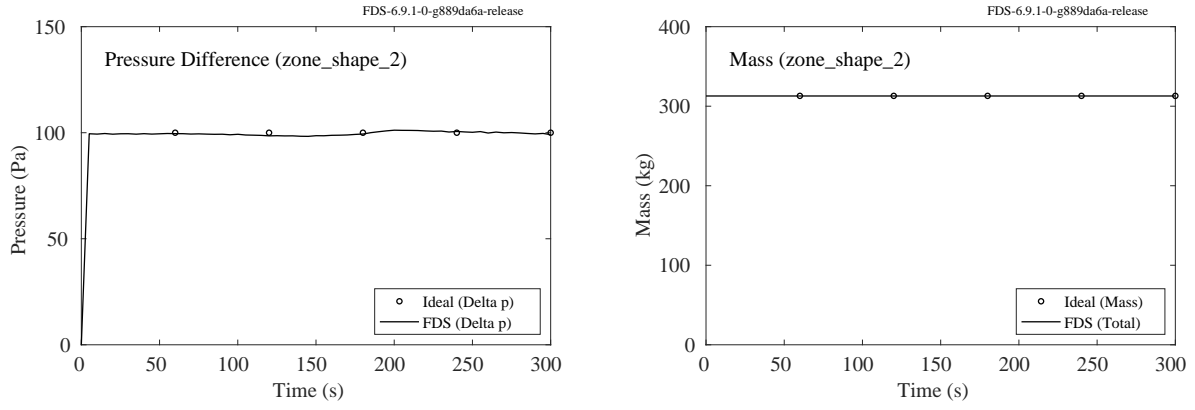


Figure 14.15: (Left) Pressure difference between interior and exterior of the duct. (Right) Overall mass.

#### 14.10.7 Leak Pressure Exponent (`HVAC_leak_exponent`)

As the interior pressure rises in a typical building, the leakage area will grow as small gaps, cracks, and other leakage paths open up. Leakage tests performed according to test standards such as ASTM E779 provide two additional data points to quantify this behavior. These are the `LEAK_PRESSURE_EXPONENT` and the `LEAK_REFERENCE_PRESSURE`. The use of these additional inputs are shown in the equation below as  $n$  and  $\Delta p_{\text{ref}}$  respectively where  $A_{L,\text{ref}}$  is given by `LEAK_AREA`. Additionally, a discharge coefficient,  $C_d$ , is often applied in practice.

$$\dot{V}_L = C_d A_{L,\text{ref}} \left( \frac{|\Delta p|}{\Delta p_{\text{ref}}} \right)^{n-0.5} \sqrt{\frac{2|\Delta p|}{\rho_0}} \quad (14.12)$$

By default,  $C_d = 1$ ,  $n = 0.5$  and  $\Delta p_{\text{ref}} = 4 \text{ Pa}$ , meaning that the leak area will not change with pressure unless you specify an exponent other than 0.5.

The first verification case involves three  $1000 \text{ m}^3$  compartments that have  $0.01 \text{ m}^2$  of leakage to the ambient. Each compartment is supplied with  $0.16 \text{ m}^3/\text{s}$  of inlet flow. The first compartment has the default values for the exponent and reference pressure, the second changes the exponent to 0.6, and the third changes exponent and the reference pressure respectively to 0.6 and 10 Pa. The expected leakage velocities for these conditions are 160 m/s, 11.8 m/s, and 12.8 m/s. Note in the left plot of Fig. 14.16 that the velocities are negative because the FDS output for the leakage velocity is from the lower numbered pressure zone (in this case ambient) to the higher number (inside the compartment). Negative velocity indicates flow from inside to outside as expected.

The second case involves a steel enclosure with four localized leaks, two near the bottom and two near the top. The air flow into the compartment is ramped up slowly, and the right hand plot of Fig. 14.16 shows the ideal and predicted relationship between the volume flow and compartment pressure. In this case,  $C_d = 0.61$ ,  $n = 0.6$ ,  $\Delta p_{\text{ref}} = 1 \text{ Pa}$ , and  $A_{L,\text{ref}} = 0.18$  at each of the four “cracks.”

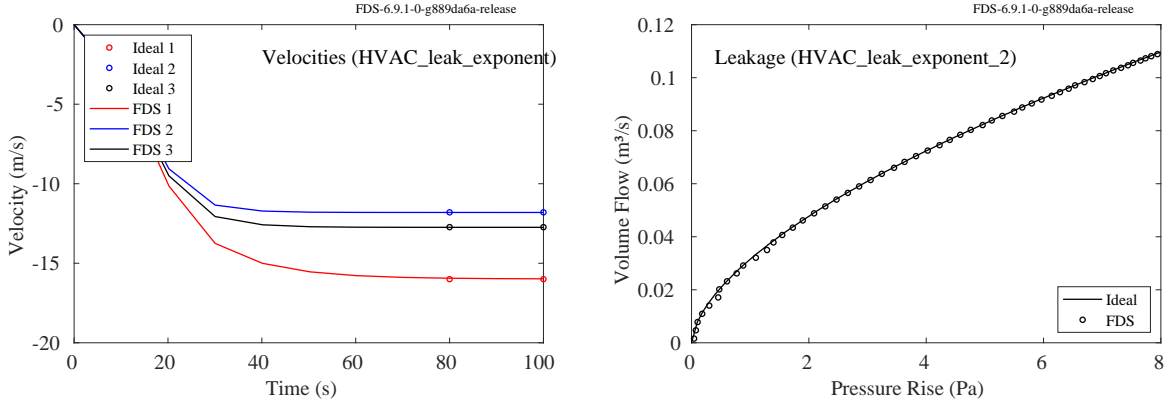
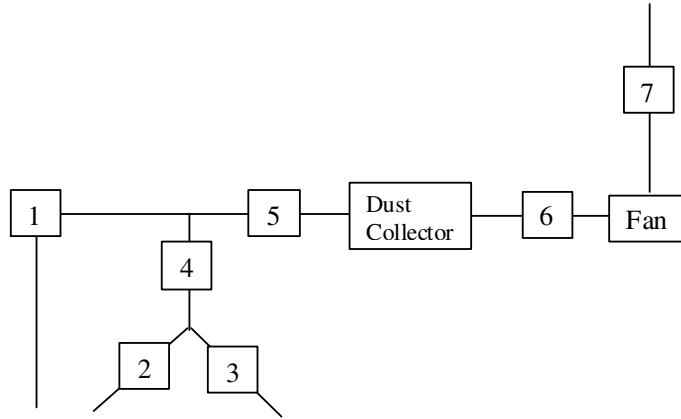


Figure 14.16: (Left) Leakage velocities resulting from varying LEAK\_PRESSURE\_EXPONENT and LEAK\_REFERENCE\_PRESSURE. (Right) Volume flow versus pressure for a leaking steel enclosure.

## 14.11 ASHRAE Sample Problem 7

([ashrae\\_7\\_fixed\\_flow](#), [ashrae\\_7\\_quadratic](#), [ashrae\\_7\\_table](#))

ASHRAE Sample Problem 7 [104] is a simple HVAC system that represents a metal working exhaust system for a machine shop where particulates from three pieces of equipment are removed by a dust collector. The network, shown in Fig. 14.17, consists of three inlets, two tees, the dust collector, and a fan. The lengths, diameters, and friction losses for all the components are specified, as well as the fan flow rate. The pressure drops and flow rates can be computed by hand. Also listed in Fig. 14.17 are the predicted pressure drops for a fan with a fixed flow rate, a fan with a quadratic fan curve (MAX\_FLOW=2.4094, MAX\_PRESSURE=3000.) that includes the fixed flow state (i.e., the flow rate of 1.45 m<sup>3</sup>/s and pressure drop of 1913.5 Pa from the fixed flow simulation sits on the quadratic curve), and a fan with a RAMP to define the same quadratic fan curve at 500 Pa intervals. The hand calculations assume a constant density, whereas the FDS computation will have a slightly non-uniform density in the network due to pressure drops. It is expected that there will be small differences that will be more noticeable at higher pressure changes. Additionally since specifying a fan curve via a table results in a piecewise linear approximation, it is expected that the user-defined fan curve results will vary slightly from the quadratic and fixed flow results.



Duct Number	1	2	3	4	5	56	6	7
Experiment	716.200	441.200	441.200	275.000	121.300	731.100	32.200	313.200
Fixed Flow	714.326	440.088	440.088	274.255	120.952	728.779	32.111	312.023
Quadratic	715.572	440.854	440.854	274.734	121.164	730.060	32.167	312.564
Table	713.734	439.723	439.724	274.027	120.851	728.170	32.084	311.765

Figure 14.17: Schematic of ASHRAE Sample Problem 7, and tabulated pressure drops (Pa) for a fixed flow fan curve, quadratic fan curve, and a table defined fan curve.

## 14.12 HVAC transient mass transport

This section documents verification of the mass transport subroutine of the HVAC module. Unless otherwise stated, the general test case has a  $1\text{ m}^3$  domain split into two equally sized compartments (being their own pressure zones) connected in some manner by an HVAC network. The left and right compartments are initialized with species 1 and species 2 respectively. Both species have an initial density of  $1.0\text{ kg/m}^3$ . The ducts have a cross sectional area of  $0.01\text{ m}^2$  and a flow rate of  $0.01\text{ m}^3/\text{s}$  (velocity of  $1\text{ m/s}$ ).

### 14.12.1 Convergence study for HVAC mass transport (`hvac_convergence_study_x`)

The time-dependent mass transport subroutine is an explicit Euler method solver which uses a Godunov upwinding scheme. This method is formally first-order accurate in space and should exhibit L1 and L2 norm error decay rates of  $O(\Delta x)$  for a continuous solution.

We undertake a convergence study to demonstrate that the adopted numerical method exhibits the expected spatial error decay. The two compartments are connected with a single  $1\text{ m}$  long duct which is initialized using linear interpolation between the upstream and downstream duct node. In this manner the mass fraction of species 1 linearly decreases from 1 to  $0\text{ kg/kg}$ . If we examine the species 1 mass fraction at the downstream node we expect to see its value increase linearly from 0 to  $1\text{ kg/kg}$  between  $0\text{ s}$  to  $1\text{ s}$  and then to remain at  $1\text{ kg/kg}$  until the end of the simulation. The mass fraction of species 1 at the downstream duct node is examined and compared to the analytical result for a range of duct cell numbers (20, 40, 80, 160 and 320). The time step is fixed to satisfy the CFL of the case cell size ( $\text{CFL} = \Delta x/2u$ ); this ensures

that the  $\Delta x/\Delta t$  ratio is fixed for each case. Fig. 14.18 shows the mass fraction at the downstream duct node for all cases and the analytical solution. Fig. 14.19 gives the L1 and L2 norm errors.

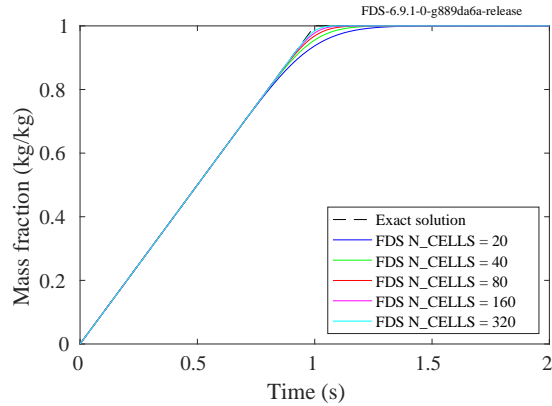


Figure 14.18: Species 1 mass fraction in the downstream duct node for the cell size convergence study. The mass fraction starts at zero and then linearly increases due to the initial conditions in the duct. At 1 s the mass fraction reaches its maximum and remains at this value until the end of the simulation. The figure illustrates that at lower cell counts (blue line) there is increased numerical diffusivity and that, for higher cell counts (cyan line), the numerical solution converges towards the analytical solution (black dashed line).

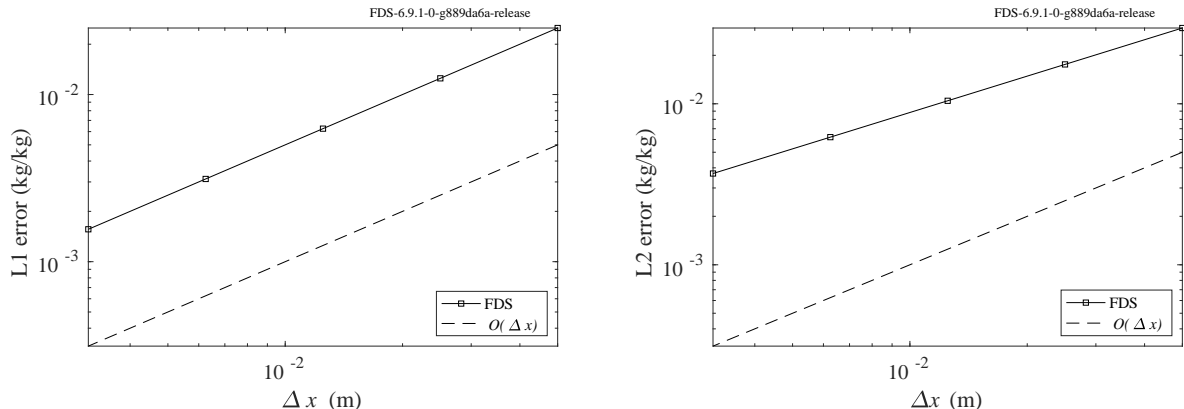


Figure 14.19: L1 (left) and L2 (right) norm errors in mass fraction for the convergence study using various cell numbers (320, 160, 80, 40, 20 from left to right). The plot demonstrates errors decreasing for increasing cell numbers (i.e., decreasing cell size).

### 14.12.2 Transport time (HVAC\_mass\_transport)

A single 10 m long duct connects the two compartments. The duct is initialized using data from the right duct node (i.e. species 2). As HVAC does not account for diffusion in the duct (only advection) we expect to see species 1 mass fraction at the downstream duct node start and remain at 0 kg/kg until 10 s and then instantaneously increase to 1 kg/kg. Ideal result and FDS output is presented in Fig. 14.20.

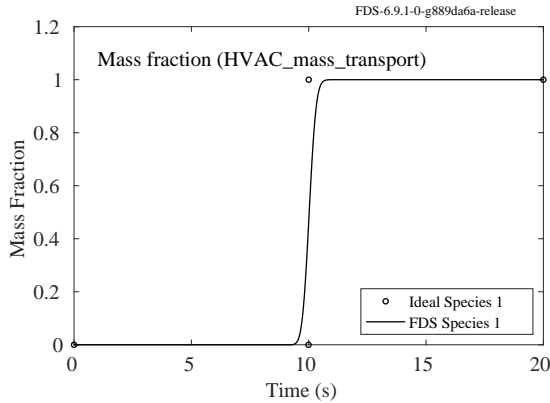


Figure 14.20: Species 1 mass fraction in the downstream duct node.

#### 14.12.3 Duct definition sensitivity analysis (`HVAC_mass_transport_x`)

A sensitivity analysis is carried out to verify that results are not sensitive to differing methods of defining the same duct network. The general arrangement is identical to that of Sec. 14.12.2. Test cases 1 to 4 incorporate the use of increasing numbers of `DUCTS` (one, two, four and five respectively) and affiliated `DUCTNODES` but the number of cells in the discretized duct (`N_CELLS`), and hence the cell size, remains identical. We look at species 1 mass fraction at the downstream `DUCTNODE` and expect to see no variation in the results for the differing number of `DUCTS`. Ideal result and FDS output is presented in Fig. 14.21.

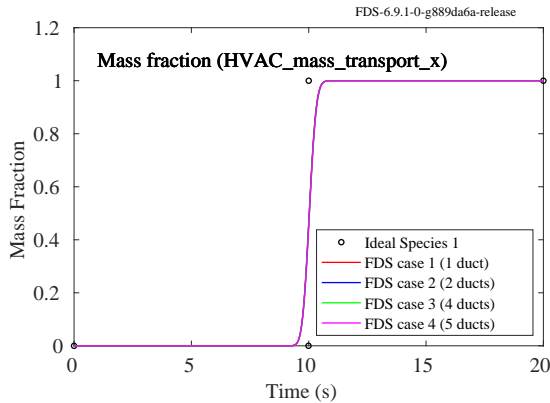


Figure 14.21: Species 1 mass fraction in the downstream duct node for different duct definitions. Although different numbers of ducts are used, the number of cells is identical for all cases. Therefore the output for all cases should also be identical.

#### 14.12.4 Mass conservation 1 (`HVAC_mass_transport_conservation_1`)

The two compartments are connected by two ducts, A and B, each being 10 m long with areas of  $0.01 \text{ m}^2$ . The ducts are initialized with species 1 with Duct A having flow from left to right and duct B having flow from right to left. The total mass in the FDS domain and in both compartments is expected to remain the same. The mass of species 1 in the left compartment is expected to decrease from 0.5 kg to 0.292 kg and in the right compartment it is expected to increase from 0 kg to 0.292 kg. The spatially mirrored behavior is

expected of species 2 with ending values of 0.208 kg. Fig. 14.22 shows mass in the left compartment, right compartment and in the whole FDS domain. Fig. 14.23 presents the species 1 and 2 masses in the left and right compartments.

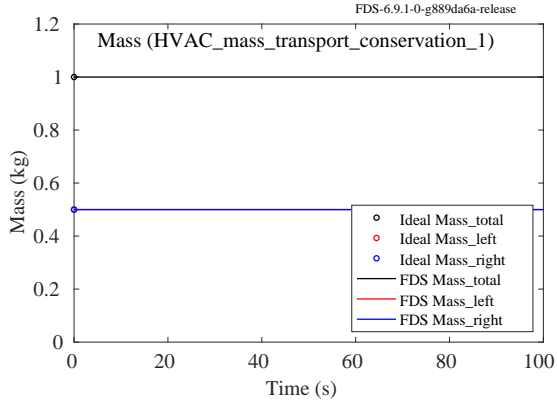


Figure 14.22: Total mass in the FDS domain and total mass in the left and right compartments.

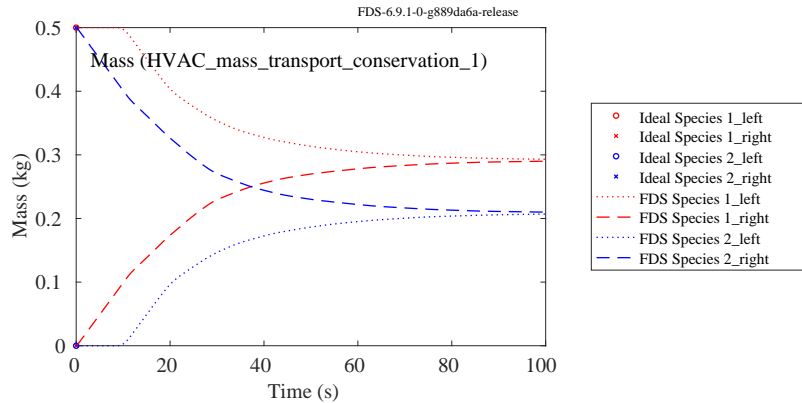


Figure 14.23: Species 1 and 2 masses in the left and right compartments.

#### 14.12.5 Mass conservation 2 (HVAC\_mass\_transport\_conservation\_2)

The case setup is identical to that of Sec. 14.12.4 with the exception of the length of duct A is reduced to 5 m and the length of duct B is increased to 20 m. This gives a total FDS and HVAC domain species 1 : species 2 mass ratio of 0.6 : 0.4. We expect that the species 1 and 2 masses within the FDS domain will come to equilibrium at this ratio. Fig. 14.24 shows the total masses of species 1 and 2.

#### 14.12.6 Mass conservation 3 (HVAC\_mass\_transport\_conservation\_3)

The case setup is identical to that of Sec. 14.12.4 except that both ducts A and B have a length of 12.5 m and are initialized with species 2. This gives a total domain (FDS and HVAC) species 1 : species 2 mass ratio of

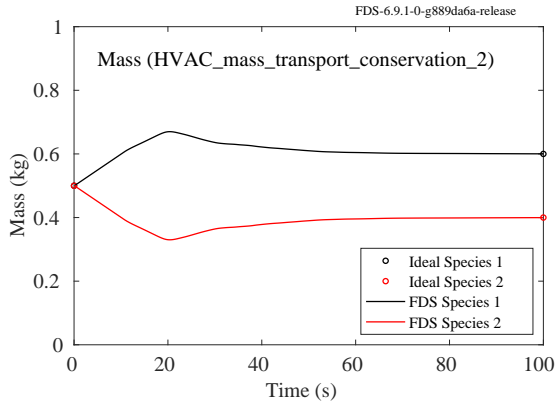


Figure 14.24: Total species 1 and 2 masses in the FDS domain. The initial equilibrium is prior to species 1 entering duct B and species 2 entering duct A.

0.4: 0.6. We expect that the species 1 and 2 masses within the FDS domain will come to equilibrium at this ratio. Fig. 14.25 presents the ideal and FDS total masses of species 1 and 2.

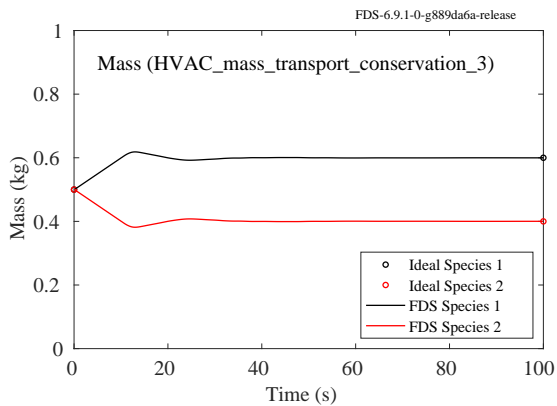


Figure 14.25: Total species 1 and 2 masses in the FDS domain. Due to the initial contents of the two ducts (species 2) the mass ratio of species 1 and 2 is 0.4: 0.6; therefore at equilibrium this ratio should be observed throughout the domain.

#### 14.12.7 Transient transport branching ducts (`HVAC_mass_transport_branch`)

The two compartments are connected by an HVAC network comprising a single 5 m feed duct which branches into two ducts (ducts A and B) at a tee with both ducts discharging to the right compartment. Ducts A and B each have a cross-sectional area of  $0.005 \text{ m}^2$ , half that of the feed duct, and will therefore both have a velocity of 1 m/s. Duct A has a length of 5 m and duct B has a length of 10 m. The duct network is initialized using data from the right compartment. Based on the duct lengths and a constant velocity we expect to see the species 1 mass fraction at outlet A and B increase from 0 to 1 kg/kg at 10 s and 15 s respectively. Ideal result and FDS output is presented in Fig. 14.26.

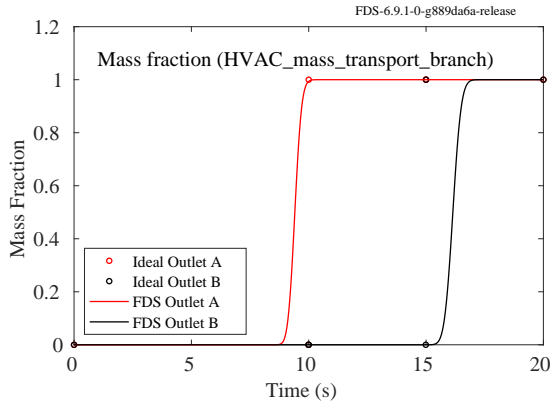


Figure 14.26: Species 1 mass fraction in the downstream duct nodes. The distance from the inlet to outlet A and from the inlet to outlet B is 10 m and 15 m respectively. Given a constant velocity of 1 m/s through the network, the transport time from inlet to outlets A and B should be 10 s and 15 s respectively.

#### 14.12.8 Transient transport combining ducts (`HVAC_mass_transport_combine`)

The left compartment is separated into two sub-compartments, A and B. These sub-compartments are initialized with species 1 and 2 respectively. An inlet vent is located in each sub-compartment and these vents are connected to separate ducts, of lengths 1 m and 2 m respectively, which combine at an internal tee. A single duct, with a length of 1 m, connects this tee to the right compartment where it discharges to a single outlet into the right compartment. The right compartment and the duct network is initialized with species 3. If we examine species mass fractions at the downstream outlet duct node we expect to see a species 3 mass fraction of 1 kg/kg for 2 s, a species 1 and 3 mass fraction of 0.5 kg/kg each from 2 s to 3 s and a species 1 and 2 mass fraction of 0.5 kg/kg each from 3 s until the end of the simulation. Ideal result and FDS output is presented in Fig. 14.27.

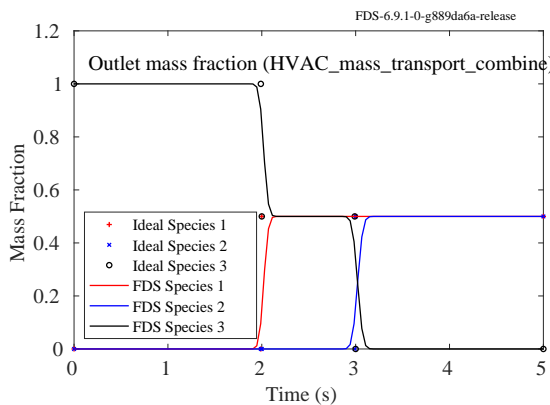


Figure 14.27: Species mass fractions at the outlet duct node. Species 3 starts and remains at 1 kg/kg for 2 s as the initial contents of the duct flows out of the outlet. At 2 s the species from the sub-compartment connected via the shorter duct and the remaining initial species from the longer duct flows out of the outlet. At 3 s the species from the sub-compartment connected by the longer duct reaches the outlet and the mass fraction is split between the species from the two upstream sub-compartments - no initial species remains in the ducts.

### 14.12.9 Energy conservation and pressure (HVAC\_mass\_transport\_energy)

The left compartment is initialized with a temperature of 100 °C, the right compartment remains at ambient (20 °C). Both compartments and the duct network are initialized with a single species. The species has a specific heat of 1 kJ/(kgK). The compartments are connected by two separate ducts, duct A and duct B, both with a length of 1 m. Duct A has a specified flow from left to right with a velocity of 1 m/s, duct B has no defined flow and a minor losses coefficient of 2. Duct A and B are initialized using gas data from the left and right compartment duct nodes respectively. Based on Eq. 14.13 enthalpy in the FDS domain should be 293.15 kJ and should remain constant. Based upon Eq. 14.1 the pressure difference between the upstream and downstream duct node of duct B should be 0.8928 Pa. Duct node pressure difference and total enthalpy are presented in Fig. 14.28.

$$h_{\text{CFD}} = c_p \frac{V(T_{\text{left}})}{2} \rho_{\text{left}} + T_{\text{right}} \rho_{\text{right}} \quad (14.13)$$

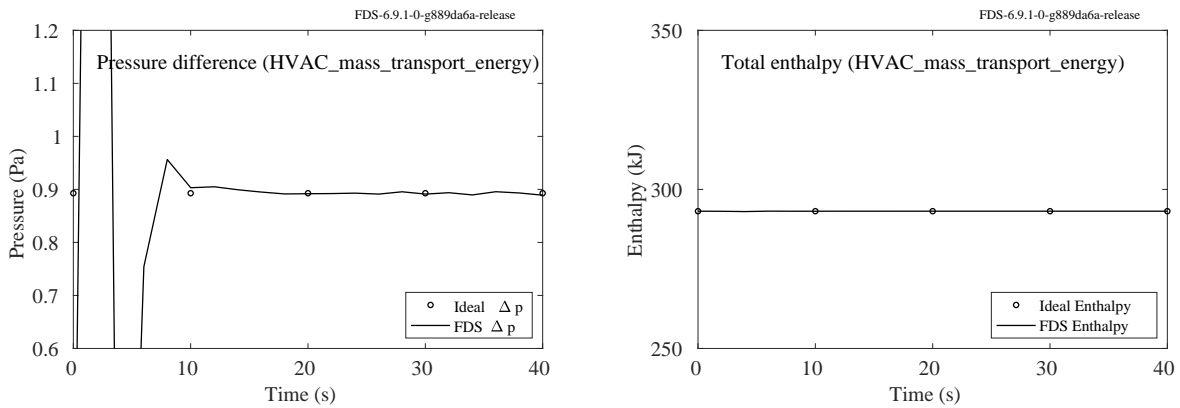


Figure 14.28: Pressure difference between the inlet and outlet of duct B (left). Total enthalpy in the CFD domain (right).



# Chapter 15

## Wildland Fire Spread

This chapter deals with verification cases which are specific to solving problems related to wildland and Wildland-Urban Interface (WUI) fires. Currently, some relevant verification tests can also be found in other sections (light blue links refer to the User's Guide):

- Convective heating in vegetation: Figure 17.4.4;
- Radiation attenuation by vegetation: Figures 9.11 and 17.4.3;
- Mass and energy conservation in burning vegetation: Figures 17.3 and 17.4.

### 15.1 Level Set Model

The level set model refers to an approach for solving parameterized fire spread over a surface using a Eulerian approach to front tracking [105]. FDS allows for several levels of complexity in level set simulations, and the sections here deal with verification of relevant aspects.

#### 15.1.1 Elliptical Fire Spread

One possible approach for advancing the fire front, and the default for level set in FDS, is to assume that point ignitions grow in an elliptical shape. Thus, the spread rate at any point along the front can be determined by assuming elliptical growth from this point (Huygens' principle) [106, 107]. The shape of the ellipse is determined by the Rothermel fire spread equation [108] and empirical assumptions regarding the length-to-breadth ratio [109] and the head-to-backing fire spread ratio [107]. The orientation of the ellipse at a given point along the fireline is determined by the angle between the normal vector to the fireline and the vector summation of the wind and slope direction (with slope treated as an effective wind). Further details of the relevant equations and the solution technique employed in FDS can be found in Bova et al. [110].

In the simplest configuration of a static uniform wind field (`LEVEL_SET_MODE = 1`), a uniform slope, and a uniform fuel it is possible to solve the equations for elliptical spread directly and to calculate the spread in all directions from a point ignition. This allows verification of the algorithm in FDS. Four cases are configured to test the influence of wind and slope:

- `LS_ellipse_0ms_00deg.fds`: no wind and no slope;
- `LS_ellipse_5ms_00deg.fds`: a 5 m/s wind from the west and no slope;
- `LS_ellipse_0ms_30deg.fds`: no wind and a 30° slope oriented to the northeast;

- LS\_ellipse\_5ms\_30deg.fds: a 5 m/s wind from the west and a 30° slope oriented to the northeast.

The cases involve a point ignition at  $(x,y) = (0,0)$  and a fuel with an arbitrary zero-wind zero-slope spread rate (VEG\_LSET\_ROS\_00) of 0.05 m/s. The fuel layer has the default packing ratio (VEG\_LSET\_BETA) of 0.01 and surface-to-volume ratio (VEG\_LSET\_SIGMA) of  $5000 \text{ m}^{-1}$ , which are used to calculate the effect of wind and slope on fire spread [108]. The default fuel height (VEG\_LSET\_HT) of 1 m is also applied, which is used to calculate the midflame wind speed from the value of the wind aloft [111].

The shapes of the fire fronts are shown in Figure 15.1. The relative errors between the FDS cases and the empirical model are shown in Figure 15.2.

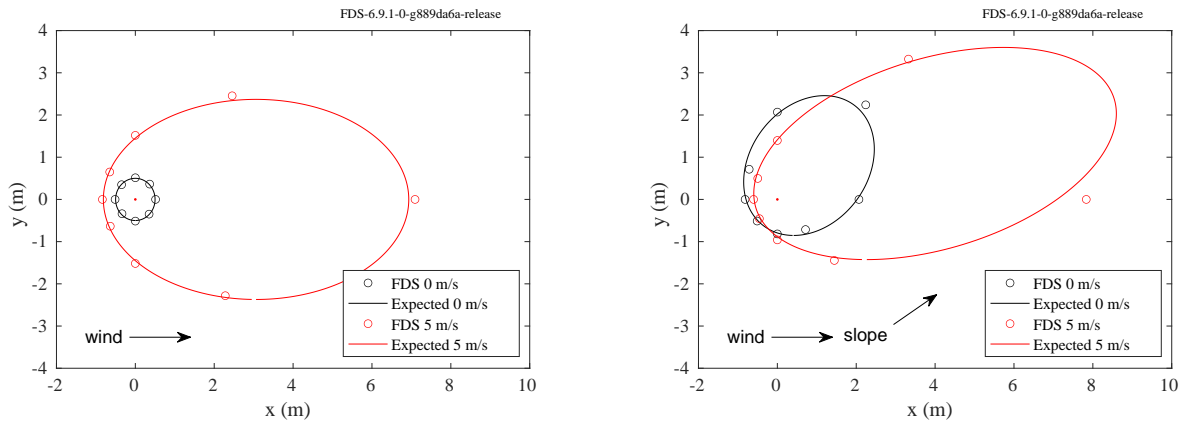


Figure 15.1: Expected versus predicted shape of fire front after a period of 10 s. The cases on the left are for zero slope, and those on the right have 30° slope oriented to the northeast.

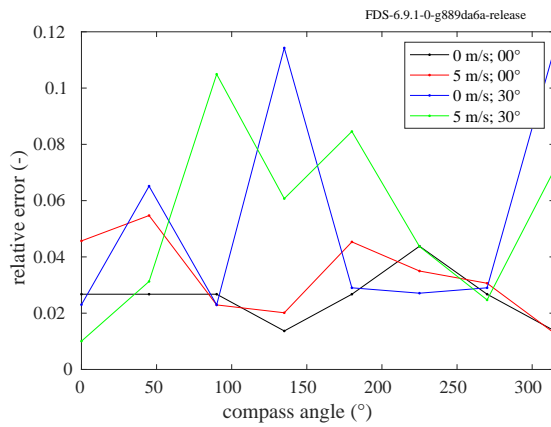


Figure 15.2: Relative error between FDS and empirical model. FDS spread rates are obtained from arrival times at devices placed 4 m from the ignition point at compass angle increments of 45°.

### 15.1.2 Ember Generation (`LS4_ember_yield`)

This case tests the application of an ember yield to a `LEVEL_SET_MODE = 4` calculation. A hypothetical fuel layer with a no-wind, no-slope spread rate of 0.15 m/s is specified, using the default values for fuel properties. These defaults include a fuel load of 0.3 kg/m<sup>2</sup> and a char yield of 0.2. We set `EMBER_YIELD` to 0.05 kg/kg and verify this value by integrating the total mass of embers produced and total mass of fuel burned over the duration of the simulation. The inputs are as follows:

```
&SURF_ID          = 'fuel'
VEG_LSET_ROS_00   = 0.15
VEL_PART          = 0.
EMBER_GENERATION_HEIGHT = 0.0, 0.5
EMBER_YIELD        = 0.05
EMBER_TRACKING_RATIO = 100
PART_ID            = 'brands' /
```

where the `PART_ID` corresponds to a `PART` line that defines the properties of a single ember. The cumulative yield is shown in Figure 15.3. We also verify the use of `EMBER_TRACKING_RATIO` by checking the average weighting factor for all Lagrangian particles (the number of embers each represents).

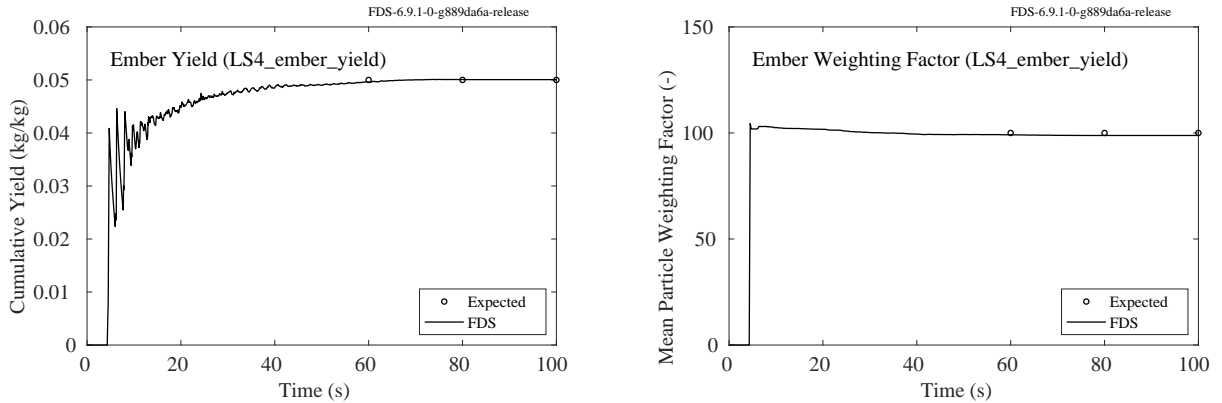


Figure 15.3: Expected versus predicted (left) yield of embers and (right) average weighting factor for each Lagrangian particle.

### 15.1.3 Ember ignition (`LS4_ember_ignition`)

This case tests the ember ignition model intended for use with `LEVEL_SET_MODE = 4`. As with the previous example, a hypothetical fuel layer with a no-wind, no-slope spread rate of 0.15 m/s is specified, using the default fuel load of 0.3 kg/m<sup>2</sup> and char yield of 0.2. `EMBER_IGNITION_POWER_MEAN` is set to 0.005 kW and `EMBER_IGNITION_POWER_SIGMA` is left at the default value of 0.001 kW. Two meshes are configured each with a single ember dropped on the fuel bed. The power of the embers is determined by:

$$\dot{q}_{\text{ember}} = A_s [h_c (T_{\text{ember}} - T_{\infty}) + \sigma \varepsilon (T_{\text{ember}}^4 - T_{\infty}^4)] \quad (15.1)$$

Both embers have a surface area of  $A_s = 5 \times 10^{-5}$  m<sup>2</sup>, an emissivity of  $\varepsilon = 1$ , and a convective heat transfer coefficient of  $h_c = 20$  W/m<sup>2</sup>/K. The ember in mesh 1 has a surface temperature of  $T_{\text{ember}} = 500$  °C resulting in a power of 0.0018 kW. The ember in mesh 2 has a surface temperature of  $T_{\text{ember}} = 1000$  °C resulting in

a power of 0.0087 kW. Based on the ember ignition probability distribution, we expect a 0 % probability of ignition for the lower temperature particle and a 100 % probability for the higher temperature. This is confirmed by checking the final amount of fuel consumed, where each mesh has 6 kg of fuel available to burn.

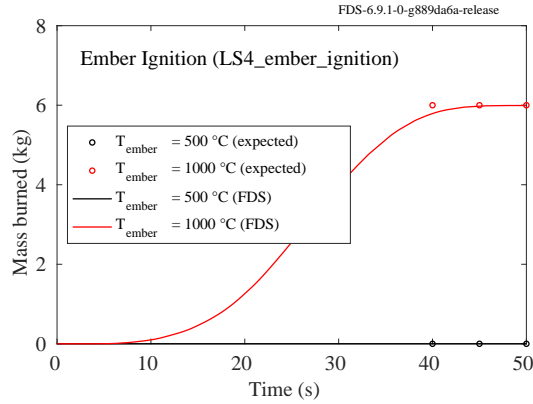


Figure 15.4: Test of level set fire spread when initiated from spot fire based on EMBER\_IGNITION\_POWER\_MEAN.

# Chapter 16

## Unstructured Geometry (Beta)

This section describes some of the test cases used to verify that FDS and Smokeview are computing and visualizing unstructured geometric objects correctly. Also here, the behavior of the different algorithms used to include unstructured geometries within FDS is tested. Several test cases that showcase and test the use of the `GEO` line are presented, followed by accuracy and conservation tests.

### 16.1 Verification of setup checks on broken geometries

This subsection describes some of the test cases used to verify that FDS correctly enforces on geometries the quality rules.

The following verification cases contain specific broken geometries in an otherwise correctly formatted FDS input file:

- `geom_bad_inconsistent_normals.fds`: a cube with only one face normal inverted;
- `geom_bad_inverted_normals.fds`: a cube with all face normals inverted;
- `geom_bad_non_manifold_edge.fds`: a cube and a box sharing the same non manifold edge;
- `geom_bad_open_surface.fds`: a cube missing one face, that is an open surface;

To allow Firebot to consider the test successful if it catches the error condition, each of the above input files contain the following parameter in the `MISC` line:

```
&MISC POSITIVE_ERROR_TEST = T
```

The effect of this parameter is replacing the `ERROR` label of the message with a `SUCCESS` label.

After Firebot is run, the `geom_positive_errors.m` Matlab script checks the existence of the planned error condition in the `CHID.err` file, reporting in cases where the condition is not met.

## 16.2 Simple geometry and properties definitions

### 16.2.1 Simple Geometry

Figure 16.1 was created using the following input. The VERTS keyword is used to specify 3 vertices and the FACES keyword is used to specify the indices of the triangular face and the SURF\_ID the face has.

```
&GEOM ID='geom1', VERTS=0.0,0.0,0.0, 1.0,0.5,0.0, 1.0,1.0,1.0,  
      FACES=1,2,3,1 SURF_ID='surf1' /
```

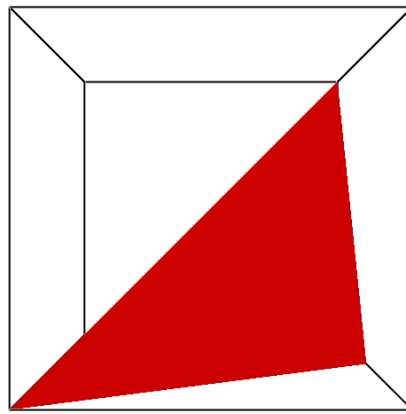


Figure 16.1: A triangle created using 3 vertices and 1 face. Case: geom\_simple.fds

### 16.2.2 Cuboid Obstacle

Figure 16.2 was created using the following MOVE and GEOM features. The XB keyword is used the same way to specify a block as on a OBST or VENT line.

```
&MOVE ID='RotOBST', AXIS=0.,0.5,-0.866, ROTATION_ANGLE=90 /  
&GEOM ID='obst',SURF_ID='surf1', XB=-0.6,0.6,-0.6,0.6,-0.2,0.2, MOVE_ID='RotOBST' /
```

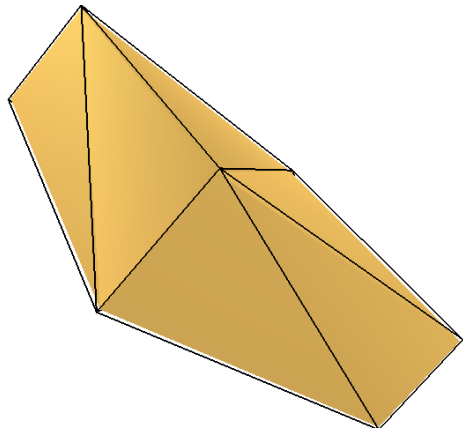


Figure 16.2: A block generated using the XB keyword. The block is refined automatically to be consistent with the underlying grid resolution. Case: `geom_obst.fds`

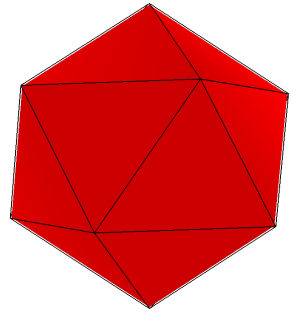
### 16.2.3 Self-generated Sphere Geometry

Figure 16.3 was created using `LEVEL=n` in the following GEOM namelist where `n` ranges from 0 to 5.

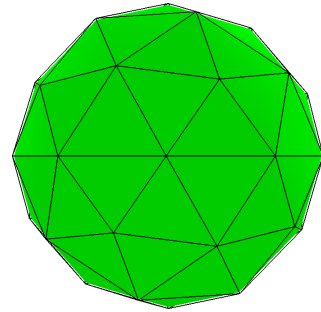
```
&GEOM ID='sphere',SURF_ID='surf1',SPHERE_RADIUS=0.5,
      N_LEVELS=n,SPHERE_ORIGIN=0.0,0.0,0.0 /
```

The `N_LEVELS` keyword is used to specify the resolution of the sphere, larger `N_LEVELS` values result in a more highly resolved sphere. `LEVEL=0` produces a 20 sided sphere approximation, an icosahedron. `LEVEL=n` produces a sphere approximation with four times as many triangles as the sphere produced with `LEVEL=n-1`. The `SPHERE_RADIUS` and `SPHERE_ORIGIN` keywords are used to specify the size and location of the sphere. This discretization technique should result in equilateral triangles at each recursion level.

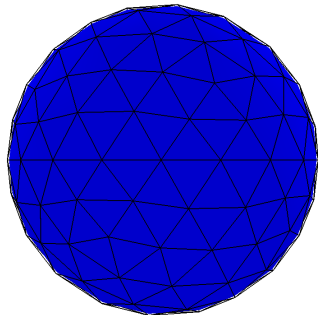
Figure 16.4 was created by using `N_LAT` and `N_LONG` keywords in a GEOM namelist to split a sphere in latitudinal (north/south) and longitudinal (east/west) directions respectively. The minimum values of `N_LAT` and `N_LONG` permitted are 3 and 6. This discretization technique results in triangles with high aspect ratios near the poles at higher discretization levels.



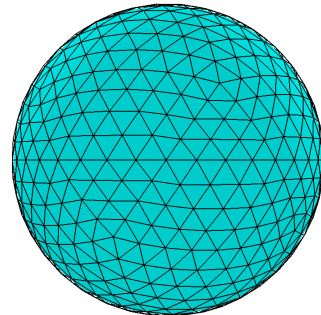
LEVEL=0



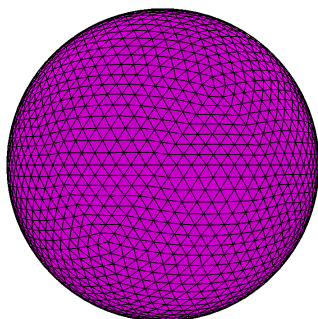
LEVEL=1



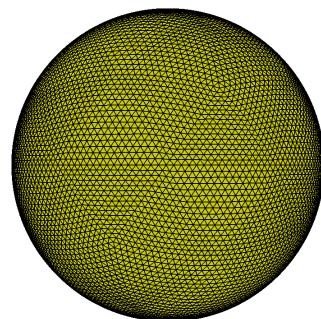
LEVEL=2



LEVEL=3



LEVEL=4



LEVEL=5

Figure 16.3: Recursive sphere discretization. A sphere at a given level is obtained by splitting each triangle from the previous level into four parts and renormalizing added vertices. Cases: geom\_sphere1a.fds,...,geom\_sphere1f.fds

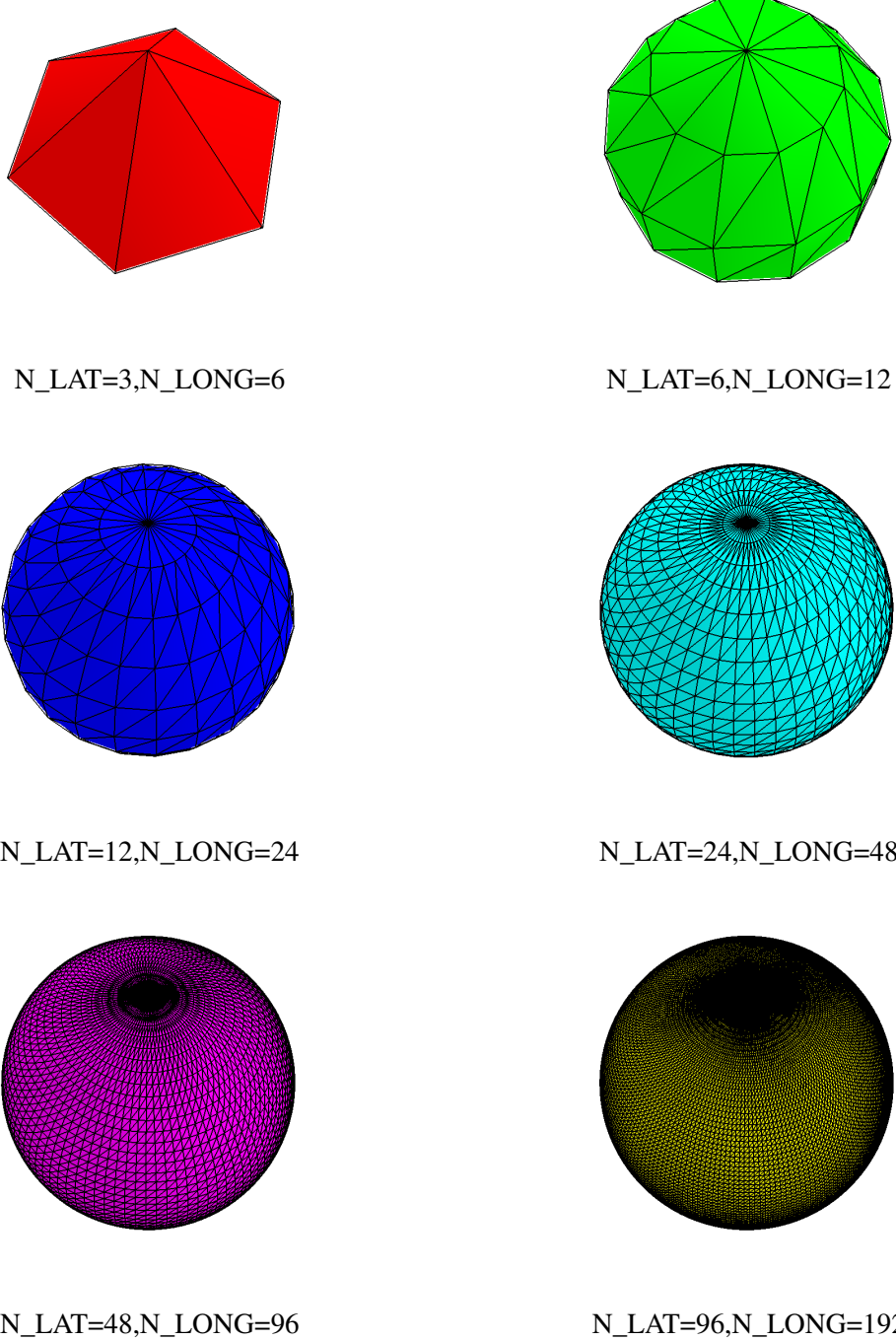


Figure 16.4: Latitude/longitude sphere discretization. Spheres are split in longitudinal (east-west) and latitudinal (north/south) directions using the `N_LAT` and `N_LONG` keywords. Cases: `geom_sphere3a.fds`, ..., `geom_sphere3f.fds`

#### 16.2.4 Terrain from Digital Elevation Map

The terrain of Fig. 16.5 was created using the ZVALS keyword for &GEOM.

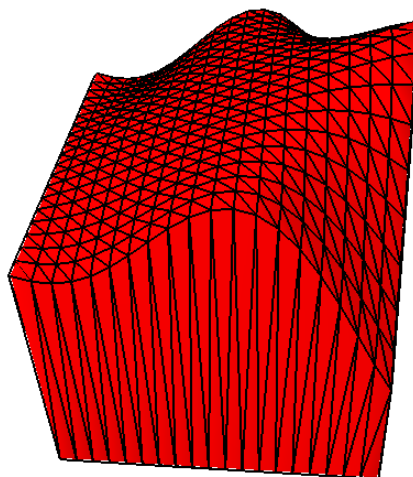


Figure 16.5: Elevations are defined on a rectangular array of grid points using the ZVALS keyword. Case: gridgeom\_terrain.fds

#### 16.2.5 Adding Texture Map

Figure 16.6 was created using the following SURF and GEOM namelists. The TEXTURE\_MAP keyword on the SURF is used to specify the name of the image file used to texture map the geometric object.

```
&SURF ID='surf1',TEXTURE_MAP='nistleft.jpg',TEXTURE_WIDTH=0.6,  
       TEXTURE_HEIGHT=0.2,COLOR='BLUE' /  
  
&GEOM ID='texture',  
VERTS=0.0,0.0,0.0, 1.0,0.0,0.0, 1.0,1.0,0.0,  
FACES=1,2,3,1, SURF_ID='surf1'/
```

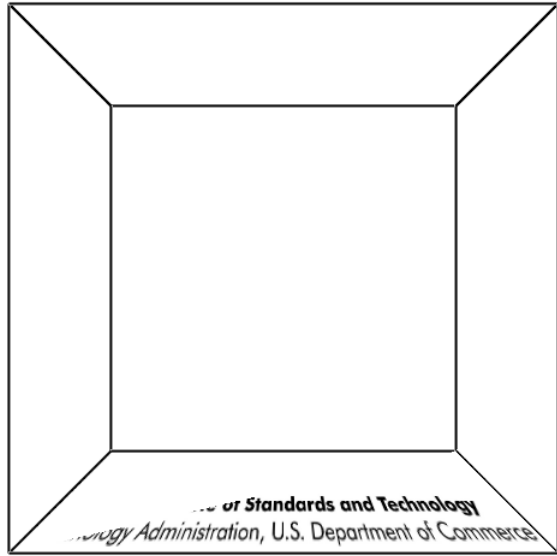


Figure 16.6: A texture is applied to a triangle. Case: geom\_texture.fds

### 16.2.6 Adding Multiple Texture Maps

Figure 16.7 was created using the following SURF and GEOM namelists. The TEXTURE\_MAP keyword on the SURF is used to specify the name of the image file used to texture map the geometric object. This example has two textures.

```
&SURF ID='surf1' TEXTURE_MAP='nistleft.jpg',
       TEXTURE_WIDTH=0.6,TEXTURE_HEIGHT=0.2,COLOR='BLUE' /
&SURF ID='surf2',TEXTURE_MAP='grass.jpg',
       TEXTURE_WIDTH=0.6,TEXTURE_HEIGHT=0.2,COLOR='GREEN' /

&GEOM ID='texture',
       VERTS=0.0,0.0,0.0, 1.0,0.0,0.0, 1.0,1.0,0.0,
       FACES=1,2,3,1 SURF_ID='surf1'

&GEOM ID='texture2',
       VERTS=0.0,0.0,0.0, 1.0,1.0,0.0, 0.0,1.0,0.0,
       FACES=1,2,3,1 SURF_ID='surf2'
```

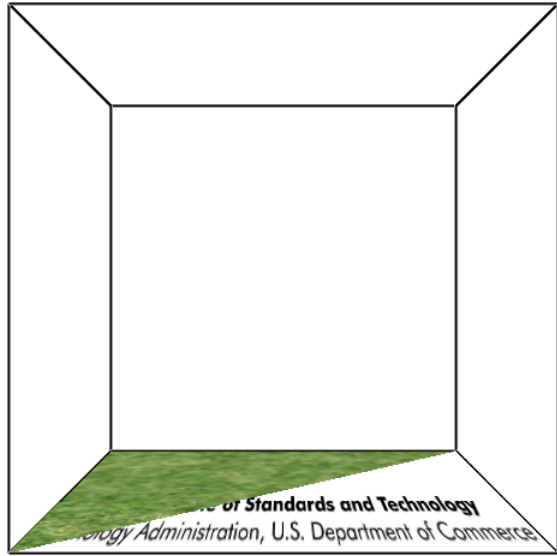


Figure 16.7: Two texture maps are applied to two separate triangles. Case: geom\_texture2.fds

### 16.2.7 Adding Texture Maps with Different Methods

The spheres in Figure 16.8 were created using SURF and GEOM namelists similar to the following.

```
&SURF ID='surf1',TEXTURE_MAP='sphere_cover_03.png'COLOR='BLUE',
       TEXTURE_WIDTH=1.0,TEXTURE_HEIGHT=1.0

&GEOM ID='sphere1',SURF_ID='surf1',
       N_LAT=50,N_LONG=50,SPHERE_RADIUS=0.25,SPHERE_ORIGIN=0.25,0.5,0.5,
       TEXTURE_ORIGIN=0.25,0.5,0.5,TEXTURE_MAPPING='SPHERICAL' /

&GEOM ID='sphere2',SURF_ID='surf3',
       N_LEVELS=3,SPHERE_RADIUS=0.25,SPHERE_ORIGIN=0.75,0.5,0.5,
       TEXTURE_ORIGIN=0.75,0.5,0.5,TEXTURE_MAPPING='SPHERICAL' /
```

The TEXTURE\_MAP keyword is used to specify the name of the image file applied to the geometric object. The SPHERICAL setting indicates that the texture map image is applied to the object using spherical coordinates.

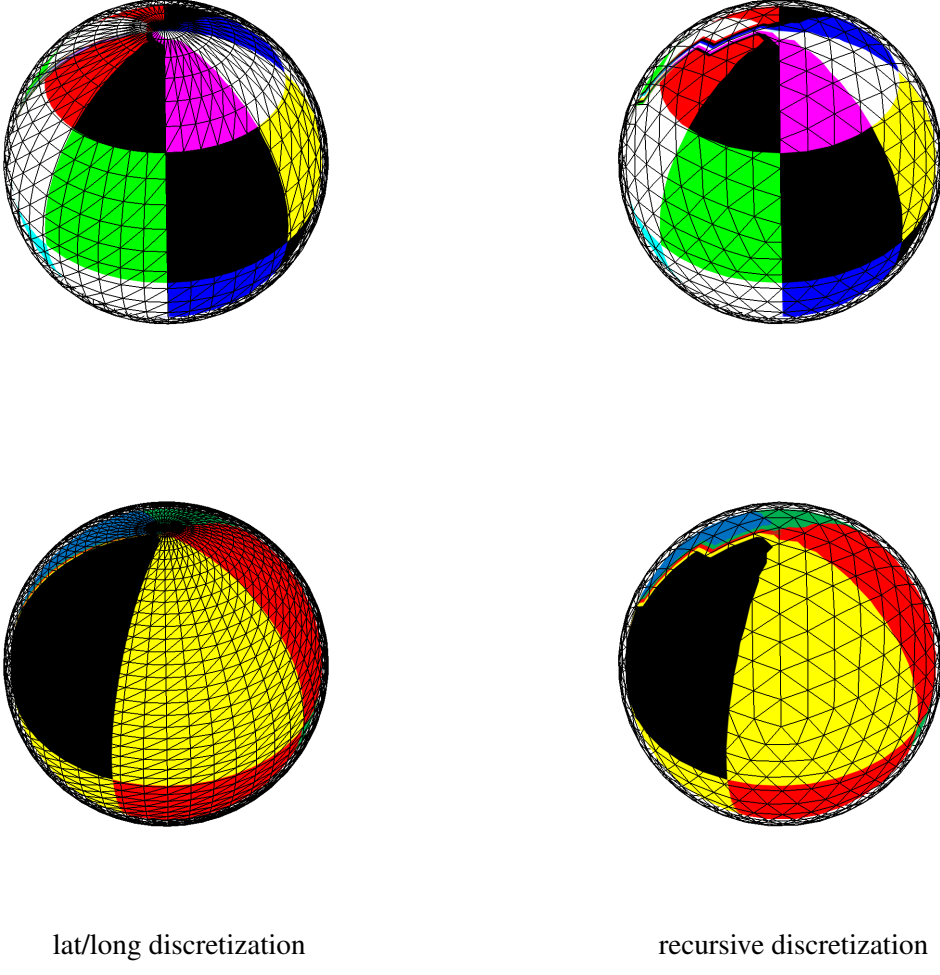


Figure 16.8: Texture maps applied to spheres discretized using two different methods. The two spheres on the left are discretized by splitting the sphere along longitudinal (east/west) and latitudinal (north/south) directions. The two spheres on the right are discretized recursively starting with an icosahedron (20 sided polyhedron). Texture maps applied to the top two sphere have 8 segments. Texture map applied to the bottom two spheres have 5 segments. Cases: `geom_texture3a.fds`, `geom_texture3b.fds`, `geom_texture4a.fds`, `geom_texture4b.fds`

## 16.3 Computational Geometry

### 16.3.1 Cut-cell Definition Around Immersed Cone: Split Cells, Piercing and Alignment

We test the computational geometry algorithm on its treatment of degenerate cases [112], namely, split cells within a cartesian cell, cartesian cell piercing, and body surface-grid alignment. A cone of base diameter  $D_B$  and height  $H = 4D_B$  is placed centered in a Cartesian domain of size  $x = [-1.5D_B : 1.5D_B]$ ,  $y = [-1.5D_B : 1.5D_B]$ ,  $z = [-2D_B : 6D_B]$ , as shown in figure 16.9a. The cone is composed of 316 vertices and 628 triangles. A single Cartesian mesh is used with  $n_x = 5$ ,  $n_y = 5$  and  $n_z = 12$  cells in each corresponding direction.

A center column of cartesian cells and corresponding cut-cells is shown in Fig. 16.9b. FDS correctly defines cut-faces and polyhedrons in three situations, namely: Solid piercing a cartesian cell, split cut-cells,

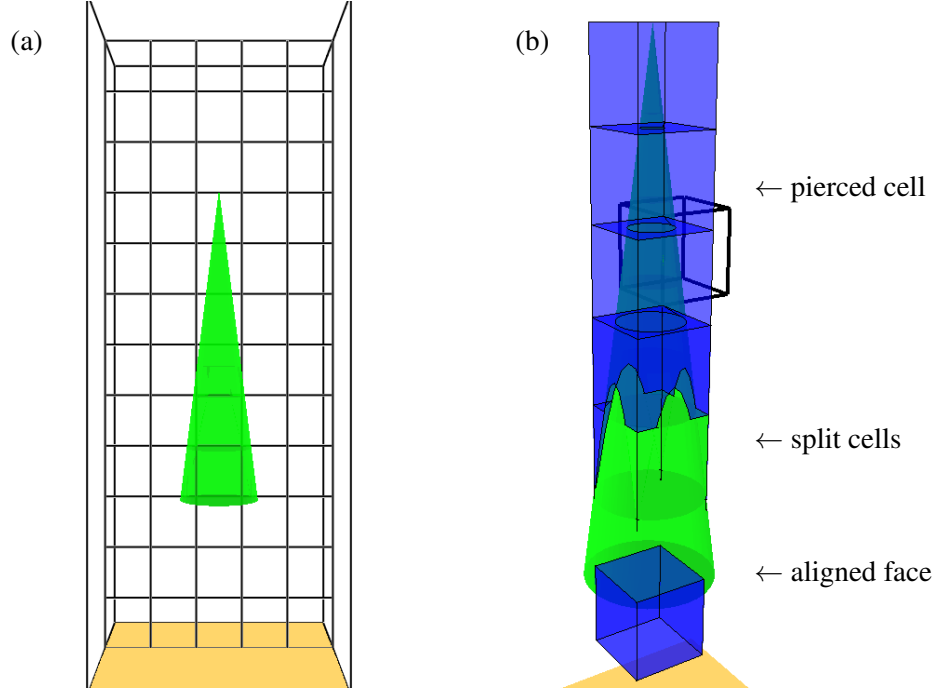


Figure 16.9: Polyhedra computation around immersed cone: (a) problem setup and grid on a  $y$  plane. (b) Cut-cells on mid cell column along  $z$  direction: (*pierced cell*) cut-cell formed by cartesian cell pierced by object; (*split cells*) cartesian cell complement of body defines 4 split cells of which one is kept in numerical simulations, other are blocked; and (*aligned face*) cut-cell of same size of regular cell contains boundary cut-faces aligned with  $z = 0$  grid plane.

and cells defined from the cone base aligned with grid plane  $z = 0$ .

Three integral conservation tests are defined for a completely immersed geometry problem. These are namely, relative difference of areas computed from the surface triangulation or from the computed boundary cut-faces  $|A_{B,\tau} - A_{B,CF}|/A_{B,\tau}$ ; relative difference of  $G$  region volumes computed from the body triangulation and from the cut-cells and  $G$  region regular cells  $|V_{GB} - V_{GRC}|/V_{GB}$ ; and finally, difference on the  $G$  region centroid computed from body centroid or cut-cells and  $G$  cells centroids  $|\mathbf{x}_{GB} - \mathbf{x}_{GRC}|_\infty$ . See Appendix C for a formal definition of these tests.

The results of the three tests on this cone problem can be seen on table 16.1. We note that cone area and  $G$  region volume computed either through the solid triangulation or through the polyhedra produced by the method match up to relative values of  $10^{-15}$ , commensurate with the floating point tolerance  $\varepsilon = 10^{-12}L_z$  used. The centroid of the  $G$  region computed through the two different avenues matches up to  $10^{-16}D_B$ , and is an excellent integral test of the proposed method to compute both cut-face and cut-cell centroids. Note that centroids along  $x$  and  $y$  direction are not zero, due to the asymmetry of the geometry triangulation employed. Given that the numerical scheme for momentum and scalars integration is defined for one cut-cell per cartesian cell, the cut-cell with largest volume is kept and others are blocked as solid.

$A_{B,\tau}$	$A_{B,CF}$	$\frac{ A_{B,\tau} - A_{B,CF} }{A_{B,\tau}}$
0.7104E+01	0.7104E+01	0.6252E-15
$V_{GB}$	$V_{GRC}$	$\frac{ V_{GB} - V_{GRC} }{V_{GB}}$
0.7096E+02	0.7096E+02	0.2212E-14
$\mathbf{x}_{GB}$	$\mathbf{x}_{GRC}$	$ \mathbf{x}_{GB} - \mathbf{x}_{GRC} _\infty$
(-0.306E-6, 0.586E-6, 0.202E+1)	(-0.306E-6, 0.586E-6, 0.202E+1)	0.1856E-15

Table 16.1: Results for conservation tests on polyhedra defined on immersed cone problem.

## 16.4 Cut-cell Method for Scalar Transport - Stress Method

### 16.4.1 Temporal Error Analysis for Variable Density Projection

This case is a variation of problem 3.4 for a domain that includes an imposed cut-cell region, where the cut-cells have same geometry as regular cells. The problem allows us to verify the temporal accuracy of our scalar transport implementation for cut-cells. The problem is defined by the advection of a non-reacting mixture of two fluids with different densities (10:1 ratio) in one cartesian direction. Zero diffusivity is prescribed. For the problem definition and temporal error computation details, we refer the reader to problem 3.4. The domain is defined by a mesh containing  $N_x = 512$  cells in the  $x$  direction, where the domain  $x = [-1, 1]$ . Note that the problem defined is one-dimensional in  $x$ . On this domain, cut-cells with same shape and size of regular cells are defined in the space  $x = [-0.5, 0.5]$ . The test verifies that the implementation details of this cut-cell region does not affect the temporal order of accuracy seen on the default verification case of Sec. 3.4.

Three cases are defined corresponding to default FDS DNS mode in cells not covered by cut-cells, and in the cut-cell region, for CFL numbers 0.25, 0.125, 0.0625. These cases are defined in `/Complex_Geometry/saad_CC_explicit_*.fds`.

Same procedure as explained in Sec. 3.4 is used to define the temporal order of accuracy  $p$ . As noted there, this procedure filters out the spatial error from the computed temporal convergence. Initial and final fields for temperature and mixture fraction for the smallest integration time step are shown in the top figures of Fig. 16.10. Fields advect to the right with unitary velocity. The bottom figure shows the order  $p$  computed point wise in the  $x$  direction for explicit time integration on the cut-cell region. Deviations from  $p \approx 2$  are dependent on the formula used to compute  $p$ , as explained in Sec. 3.4. The  $l_2$  norm of  $p$  computed pointwise for explicit integration in cut-cells is 2.0053.

### 16.4.2 Variable-Density Manufactured Solution

We test the manufactured solution test case 3.5 for scalar transport, including an internal region of the two dimensional domain where cut-cells with same shape and size as regular Cartesian cells are artificially defined. This problem allows us to check the overall accuracy (spatial+temporal) of the cut-cell implementation for scalar transport on the cut-cell region. The parameters of the test follow the ones defined by Shunn et al. [43] and described in Sec. 3.5.

The treatment of sources for scalar transport and momentum equations due to the manufactured solution is essentially the same as defined in Sec. 3.5. Therefore, source terms from manufactured solution are treated following the time integration method defined in FDS. The domain is defined on a square of length ( $L = 2$  m), with periodicity prescribed in its boundaries. A smaller square of length ( $L = 1$  m) centered on the previous is filled with cut-cells of regular cell geometry.

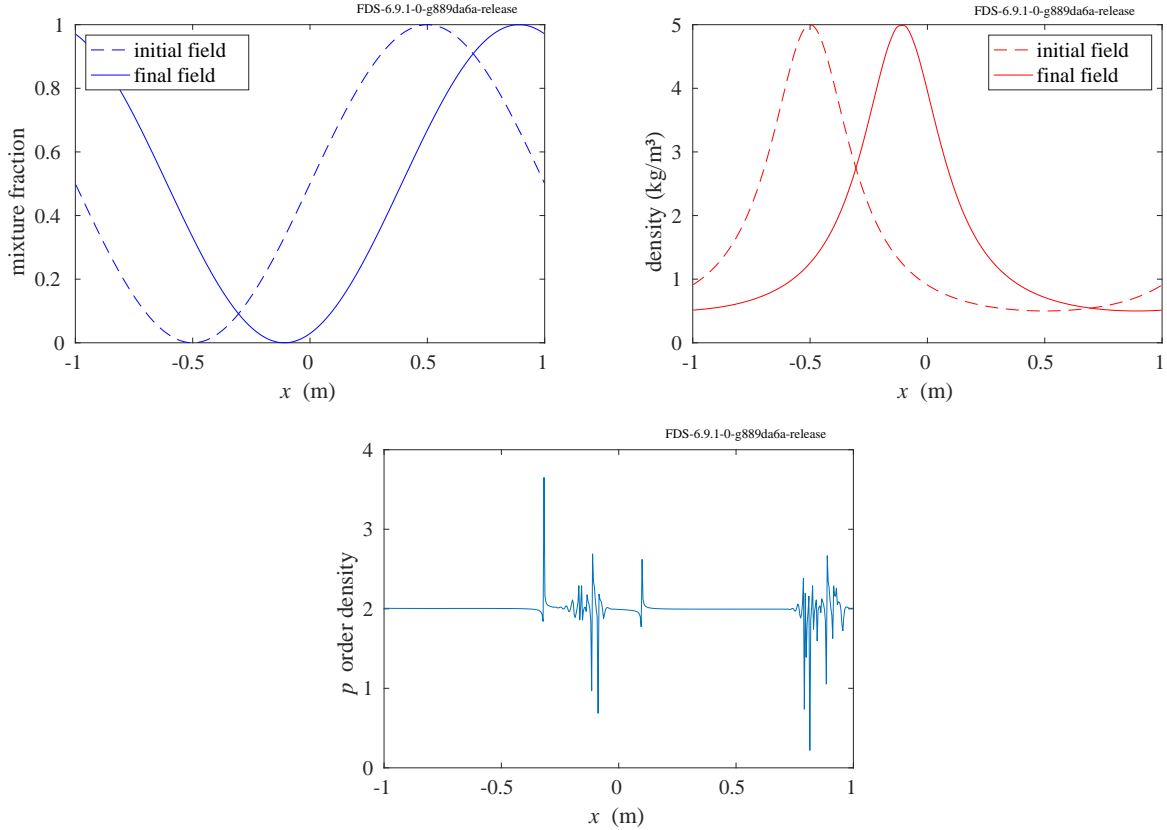


Figure 16.10: Temporal order for a variable-density projection on domain including cut-cell region. (Upper-left) Initial and final field for mixture fraction, explicit time integration on cut-cells. (Upper-right) Initial and final field for density, explicit time integration on cut-cells. (Bottom)  $p$  computed pointwise for density at final time, explicit integration on cut-cells. Fluctuations are due to degenerate points in the formula for  $p$ .

Simulations were performed for  $N = \{32, 64, 128, 256, 320\}$ , where  $N$  is the number of cells in each direction, using an adaptive time step satisfying a CFL number of 0.25. The scalar transport equations for both species defined on Sec. 3.5, are solved using the GODUNOV flux limiter and the DNS default CHARM limiter. Figure 16.11, presents the  $L_2$  error norm defined on the whole domain (regular+cut-cells) at time  $t = 0.9$  as a function of grid spacing,  $\Delta x = L/N$ . Time integration in the cut-cell region produces second-order accurate solutions for density, mixture fraction, and velocity, when CHARM interpolation is used to define the advective mass flux. As expected, these variables exhibit asymptotic first order accuracy when the GODUNOV flux limiter is used. Note that central differences are used on the diffusive terms of these equations, rendering a second order accurate approximation of diffusion on these regular shaped cells. The pressure  $H$  is, in same fashion as seen on Sec. 3.5, first order accurate. This is consistent with the projection scheme used for time integration of velocities used by FDS.

### 16.4.3 Stress Method on Manufactured Solution Around Rotated Cube

Consider the solution of the following constant density, incompressible flow, momentum and scalar transport equations:

$$\frac{\partial \rho \mathbf{u}(\mathbf{x}, t)}{\partial t} = -[\mathbf{F}_v(\mathbf{u}, \mathbf{x}, t) + \nabla p(\mathbf{x}, t) + \mathbf{f}_{e_v}(\mathbf{u}, p)] \quad (16.1)$$

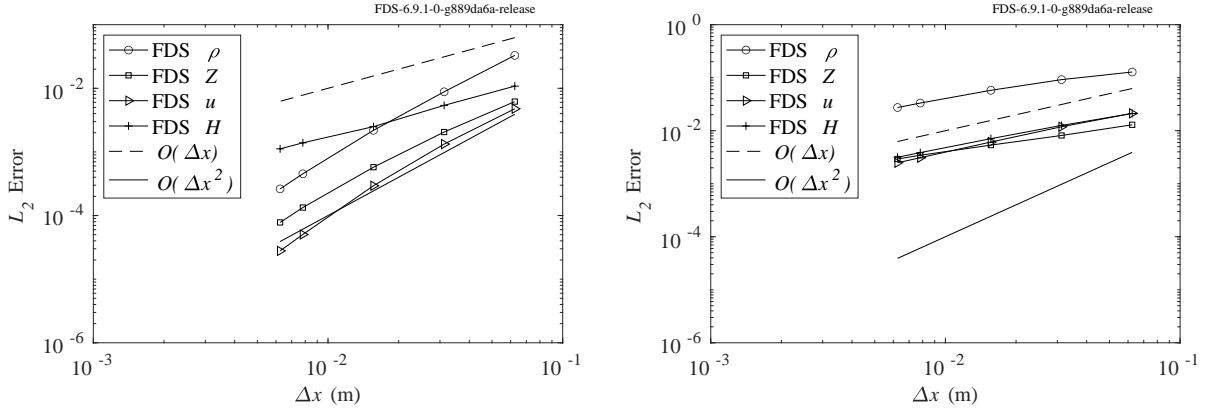


Figure 16.11: Overall accuracy for manufactured solution variable-density projection on domain including cut-cell region. The  $L_2$  error defined on the whole domain at time  $t = 0.9$  s is plotted as a function of grid spacing for  $N = \{32, 64, 128, 256, 320\}$  points in each direction. Two flux limiting options for scalar advection are used: CHARM and GODUNOV. (Left) Convergence for explicit scalar time integration and CHARM flux limiter for advection. (Right) Convergence for explicit scalar time integration and GODUNOV flux limiter.

$$\frac{\partial \rho Z}{\partial t} = -[F_z(\mathbf{u}, \mathbf{x}, t) + fe_Z(\mathbf{u}, Z)] \quad (16.2)$$

which are extended by the manufactured solution (MMS) sources  $\mathbf{f}_{\mathbf{v}}(\mathbf{u}, p)$  and  $fe_Z(\mathbf{u}, Z)$  respectively. The vectors  $\mathbf{F}_v = -\mu \nabla^2(\mathbf{u}) + \nabla \cdot (\rho \mathbf{u} \otimes \mathbf{u})$  and  $F_z = \nabla \cdot (\rho Z \mathbf{u} - \rho D_z \nabla Z)$  contain the corresponding advection and diffusion operators.

Now, consider in Fig. 16.12, a local set of fixed axes  $x', y'$  and a manufactured solution defined on the fluid region  $\Omega - \Omega_1$  of the form:

$$u'(\mathbf{x}'_{Bp}, t) = -\sin(t) \sin(kx')^2 \sin(2ky') \quad (16.3)$$

$$v'(\mathbf{x}'_{Bp}, t) = \sin(t) \sin(2kx') \sin(ky')^2 \quad (16.4)$$

$$p(\mathbf{x}'_{Bp}, t) = \frac{\sin(t)}{4} (2 + \cos(2kx')) (2 + \cos(2ky')) - \sin(t) \quad (16.5)$$

$$Z(\mathbf{x}'_{Bp}, t) = \frac{A_Z \sin(t)}{3} \left[ \left( 1 - \cos(2k(x' - \frac{\pi}{2})) \right) \left( 1 - \cos(2k(y' - \frac{\pi}{2})) \right) - 1 \right] + Z_{mean} \quad (16.6)$$

which is similar on velocities and pressure to the functions given in Ref. [113]. These functions imply zero initial conditions, a divergence free velocity field and the following

$$u'(\mathbf{x}', t) = v'(\mathbf{x}', t) = 0, \quad \frac{\partial p}{\partial n} = \frac{\partial Z}{\partial n} = 0, \quad \text{for } kx' = ky' = m\pi; m \in \mathbb{N} \quad (16.7)$$

which can be used as *no-slip wall* conditions in square boundaries defined by the integer  $m$ . The MMS sources  $\mathbf{f}_{\mathbf{v}}'$  and  $fe'_Z$  are computed analytically as functions of  $(\mathbf{x}', t)$  replacing definitions (16.3)-(16.6) in the governing equations (16.1)-(16.2) and computing symbolically the corresponding terms. See the Matlab script `Utilities/Matlab/scripts/source_mms_rotcube.m` in the FDS repository for said sources derivations.

We take values  $m = 0, 1$  and wavenumber  $k = 1$ , and consider the external flow to the resulting square immersed body, as seen in figure 16.12. The velocity field function inside the immersed object  $\Omega_1$  (i.e. solid region) is assumed zero at all times, consistent with the fixed rigid body hypothesis. An angular parameter  $\alpha$  defines the orientation of the local axes  $x', y'$  respect to the Eulerian frame coordinates  $x, y$ . The center of

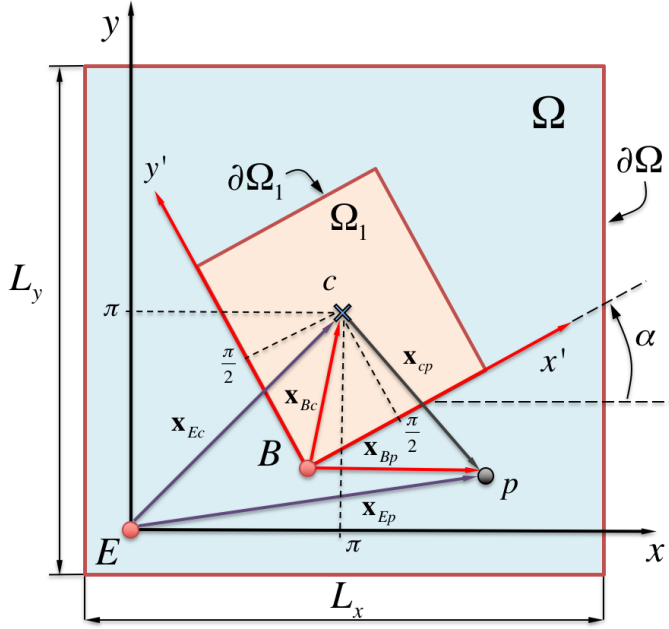


Figure 16.12: Reference frames for Eulerian ( $E$ ) and immersed body local system ( $B$ ), and vectors relating a generic point  $p$  on the fluid region  $\Omega - \Omega_1$ .

$\Omega_1$  in the Eulerian frame is situated in position  $\mathbf{x}_{Ec} = (\pi, \pi)$ . The rotation matrix from Eulerian  $E$  to local frame  $B$  coordinates is

$$[\mathbf{T}_{BE}] = \begin{bmatrix} \cos(\alpha) & \sin(\alpha) \\ -\sin(\alpha) & \cos(\alpha) \end{bmatrix} \quad (16.8)$$

In the local system, the center of the square in local coordinates is given by  $\mathbf{x}'_{Bc} = (\pi/2, \pi/2)$ . Then, the location of a general point  $p$  in the local system is:

$$\mathbf{x}'_{Bp} = \mathbf{x}'_{Bc} + \mathbf{x}'_{cp} \quad (16.9)$$

The same point  $p$  location can be defined in terms of the  $E$  frame as  $\mathbf{x}_{Ep} = \mathbf{x}_{Ec} + \mathbf{x}_{cp}$  (Eulerian coordinates). Then

$$\mathbf{x}'_{cp} = [\mathbf{T}_{BE}]\mathbf{x}_{cp} = [\mathbf{T}_{BE}](\mathbf{x}_{Ep} - \mathbf{x}_{Ec}) \quad (16.10)$$

and finally

$$\mathbf{x}'_{Bp} = \mathbf{x}'_{Bc} + [\mathbf{T}_{BE}](\mathbf{x}_{Ep} - \mathbf{x}_{Ec}) \quad (16.11)$$

This last equation is employed to translate a given point  $\mathbf{x}_{Ep}$  in the Eulerian frame (with Eulerian frame coordinates  $x, y$ ) to the local frame coordinates where equations (16.3)-(16.6) are defined. This transformation is used to define the initial conditions in the local frame, for points collocated in the Eulerian frame aligned fluid grid. It is also used to compute the source terms  $\mathbf{f}_{\mathbf{e}_v}'$  and  $f_{e_Z}'$  in local coordinates at different time levels. To transform  $\mathbf{f}_{\mathbf{e}_v}'$  and  $f_{e_Z}'$  to their Eulerian counterparts used in the numerical integration we use:

$$\mathbf{f}_{\mathbf{e}_v} = [\mathbf{T}_{BE}]^T \mathbf{f}_{\mathbf{e}_v}' \quad (16.12)$$

$$f_{e_Z} = f_{e_Z}' \quad (16.13)$$

Similarly, the manufactured variables can be defined at the final time to define error norms. The velocity components of interest are the ones defined in the Eulerian frame, and can be readily computed as

$$\left\{ \begin{array}{c} u \\ v \end{array} \right\}_p = [\mathbf{T}_{BE}]^T \left\{ \begin{array}{c} u' \\ v' \end{array} \right\}_p \quad (16.14)$$

We assume periodic boundary conditions on  $\partial\Omega$ . Then, the size of the domain  $\Omega$  depends on the periodicity lengths for a rotated flow field. When  $\alpha = 0$ , a domain  $\Omega$  of size  $L_x = L_y = 2\pi$  centered in  $\mathbf{x}_{E_c}$  is sufficient for application of periodic boundary conditions. Then, for  $\alpha = \arctan(1/r)$ ,  $r = 1, 2, 3, \dots$  the periodicity lengths on the Eulerian reference frame are  $L_x = L_y = 2\pi\sqrt{1+r^2}$ . That is, if  $\alpha = \arctan(1)$ , the periodicity length increases to  $L_x = L_y = \sqrt{8}\pi$ . If  $\alpha = \arctan(1/2)$ ,  $L_x = L_y = \sqrt{20}\pi$ .

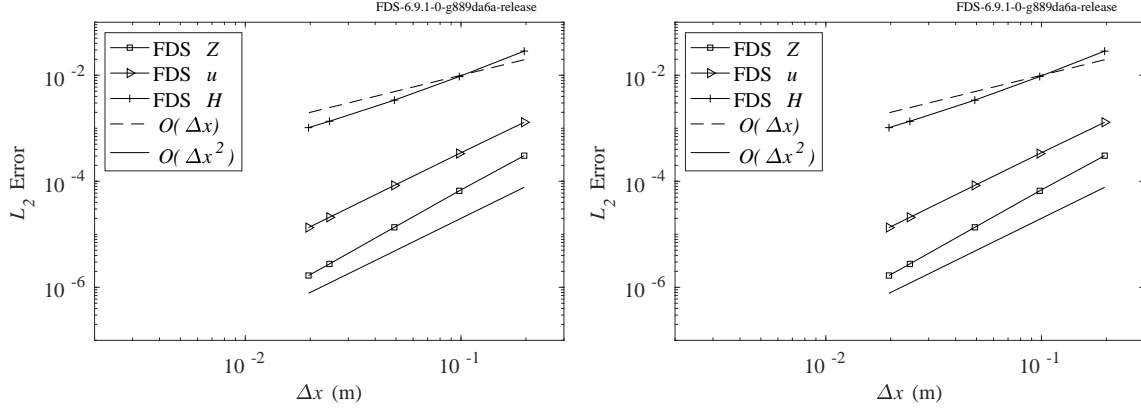


Figure 16.13: Zero degree rotation. The  $L_2$  error defined on the whole domain at time  $t = 0.95$  s is plotted as a function of grid spacing for  $N = \{32, 64, 128, 256, 320\}$  points in each direction. (Left) Stress method, (Right) square defined by &OBST.

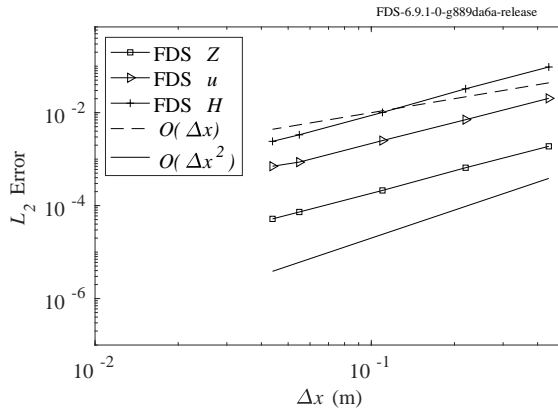


Figure 16.14: 27 degree rotation. The  $L_2$  error defined on the whole domain at time  $t = 0.95$  s is plotted as a function of grid spacing for  $N = \{32, 64, 128, 256, 320\}$  points in each direction. Stress method.

Although the different orientation angles correspond to different periodicity lengths and domain sizes all cases were run with  $N = \{32, 64, 128, 256, 320\}$  points in each direction for accuracy testing. The different inclination angles and grids were run with the stress method for shear stress imposition. The cases with zero inclination were also run with the &OBST functionality for comparison. Calculations were run at constant  $CFL = 0.1$  and errors were computed on the solution at the first time level after  $t = 0.95$ . The cases input files are found on /Complex\_Geometry/rotated\_cube\_\*deg\_\*\_.fds.

Overall the error norm behaves as  $\mathcal{O}(\Delta x)$  for the scalar transport equation in cases where the cube is inclined. This is expected as the diffusive flux differences used are of this spatial accuracy. Note that for

the non inclined cases of figure 16.13 the scalar  $Z$  presents better accuracy, simply because the two point centroid to centroid difference coincides with a central difference. The  $\mathcal{O}(\Delta x^2)$  accuracy in  $Z$  is also seen for OBST in the right figure of 16.13, which use central differences for diffusive fluxes. For OBST and grid aligned stress method where the momentum equations are solved on velocity points next to the surface, velocities behave as  $\mathcal{O}(\Delta x^2)$ , in accordance to the discretization schemes used (right figure 16.13). For the stress method and inclined cases the spatial accuracy is higher than  $\mathcal{O}(\Delta x)$ . Note that pressure spatial accuracy is  $\mathcal{O}(\Delta x)$  across all tests, consistent with the fractional step projection method used by FDS.

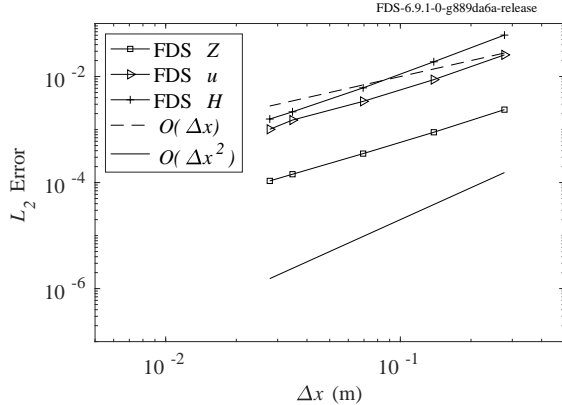


Figure 16.15: 45 degree rotation. The  $L_2$  error defined on the whole domain at time  $t = 0.95$  s is plotted as a function of grid spacing for  $N = \{32, 64, 128, 256, 320\}$  points in each direction. Stress method.

#### 16.4.4 Poiseuille Flow in Channel Created by Two GEOMs

Consider a gas with density  $\rho = 1.165 \text{ kg/m}^3$ , and molecular viscosity  $\mu = 0.025 \text{ kg/m/s}$ , being advected through a 2-D channel of height  $H = 1 \text{ m}$  and length  $L = 10 \text{ m}$ , by means of a constant force field along the channel direction  $F_x = 1 \text{ N/m}^3$ . This force field is equivalent to a pressure drop  $dp/dx = -1 \text{ Pa/m}$ . The analytical solution for the friction factor in this laminar flow is:

$$f_{an} = 24/Re_H \quad (16.15)$$

where in our case  $Re_H = \rho \bar{u} H / \mu \simeq 155$ , being the analytical value for the bulk velocity  $\bar{u} = 3.3 \text{ m/s}$ . The (Moody) friction factor formula for pressure losses is:

$$\Delta p/L = f \frac{L}{H} \frac{1}{2} \rho \bar{u}^2 \quad (16.16)$$

which can be used to compute the simulation error in  $f$ , as a function of the mean velocity evaluated on the numerical mesh. To evaluate the solution quality of the cut-cell scheme we consider three sets of test cases. See figure 16.16. We define as  $h$  the distance from the lower geometry wall to the closest grid line within it. The we consider discretizations with 10, 20, 40, 80 cells along the  $z$  direction and cases: grid aligned  $h = 0$ , grid dependent  $h = \Delta z/3$ , and fixed  $h = \Delta z_{10}/11$ , where  $\Delta z_{10}$  is the wall normal cell size in the coarsest discretization used.

For stress method for cross velocities (STM) and unlinked cut-cells, the friction factor error  $|f - f_{an}|$  convergence can be seen in Figs. 16.17a,b.

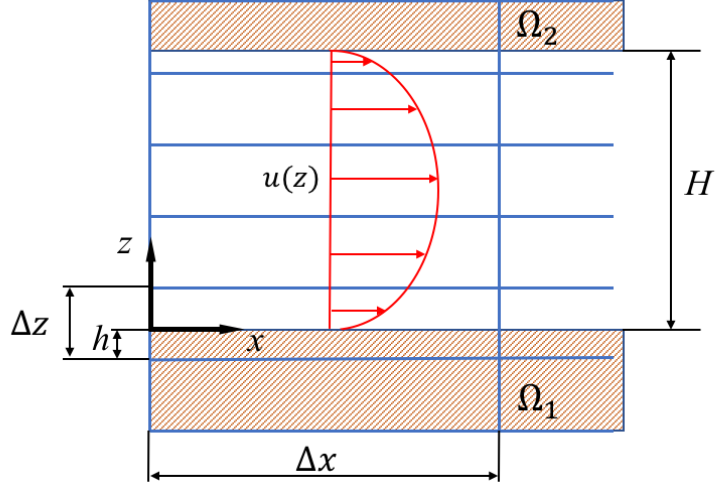


Figure 16.16: Poiseuille flow created by two geometries  $\Omega_1, \Omega_2$ : Location of channel walls respect to Cartesian grid lines (in blue).

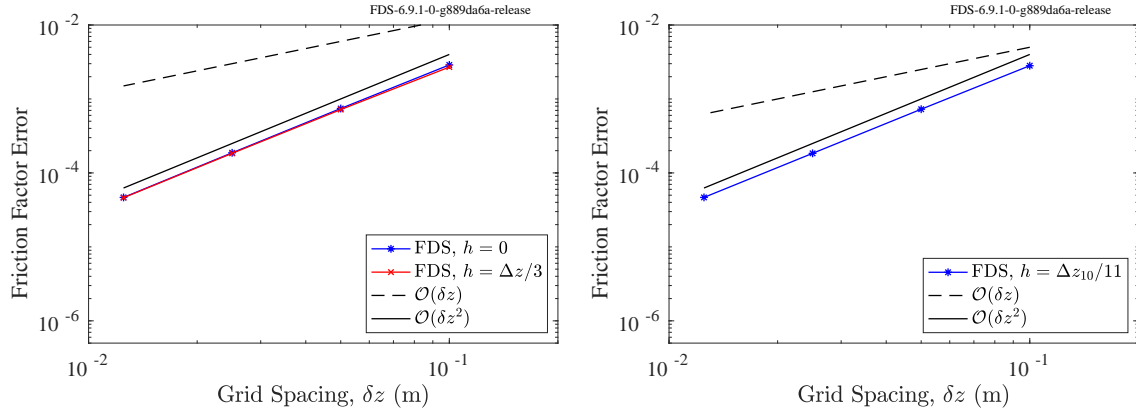


Figure 16.17: Poiseuille flow created by two geometries, STM for cross velocities: Convergence trends on friction factor (Moody) for  $h = 0$ , grid dependent  $h = \Delta z/3$  and fixed  $h = \Delta z_{10}/11$ .

## 16.5 Geometry Tests Involving Heat and Mass Transfer

### 16.5.1 Radiating Sphere

A sphere with a radius of 1 m and a surface temperature of  $T = 773.15$  K is centered in a box that is 4 m on a side with a surface temperature of 0 K. The emissivity of all surfaces is 1, and there is no convective heat transfer to or from any surface. The heat flux from the hot sphere to the nearest cold wall surface 1 m away is expected to be  $\sigma T^4/4 = 5.065$  kW/m<sup>2</sup>. The results are shown in Fig. 16.18.

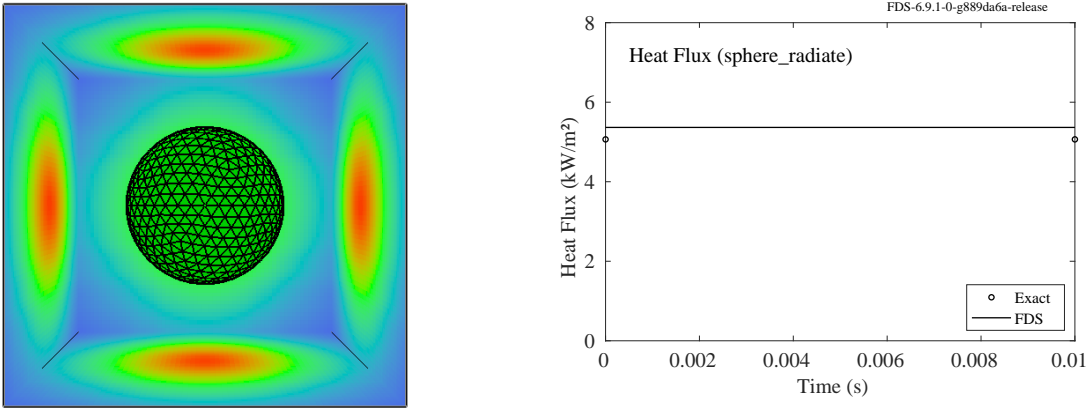


Figure 16.18: Left: a radiating hot sphere. Right: heat flux to the nearest wall surface.

### 16.5.2 Leaking Sphere

A hollow sphere with an inner radius of 1 m has a small cube within it that is blowing air into the sphere at a rate of  $\dot{V} = 0.008 \text{ m}^3/\text{s}$ . The sphere is assigned a leakage area of  $A = 0.0001 \text{ m}^2$ . It is expected that the pressure rise within the sphere shall be

$$\Delta p = \frac{\rho_\infty}{2} \left( \frac{\dot{V}}{A} \right)^2 \approx 3840 \text{ Pa} \quad (16.17)$$

as shown in Fig. 16.19.

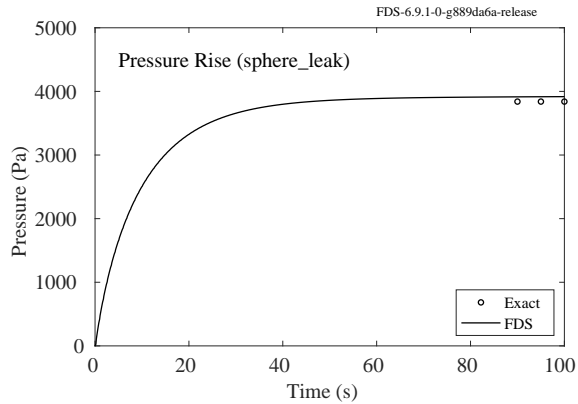


Figure 16.19: Pressure rise in a leaking sphere.

## 16.6 Restart Function

In this test, a GEOM cube is heated from below by a surface at a fixed temperature. The internal temperature inside the geometry is monitored. The full calculation runs for 1,200 s. At 700 s, a RESTART is performed and compared with the base case. The results are shown in Fig. 16.20.

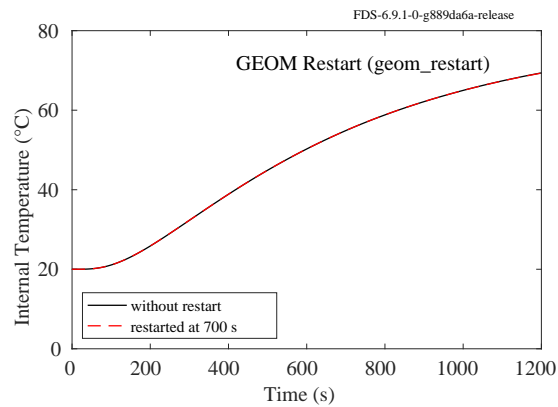


Figure 16.20: Test of restart functionality for complex geometry.



# Chapter 17

## Outputs

### 17.1 Statistical Quantities

#### 17.1.1 RMS, Co-Variance, and Cross-Correlation (`rms_cov_corr`)

FDS can output the root mean square (RMS), co-variance, and cross-correlation for both point and line DEVC outputs. To test these outputs a 1 m<sup>3</sup> box with open sides and a 10 cm grid size is defined with two inlet vents centered on adjacent faces. This results in two orthogonal flow streams that collide at the center of the box and exit diagonally. Within the diagonal portion of the flow, are placed point measurements for the FDS outputs of the u-velocity RMS, the u-velocity/w-velocity co-variance, and the u-velocity/w-velocity cross-correlation.

Computation of the these quantities by their typical statistical definition would require having the entire time history for the velocities. This is obviously not possible during run-time. Instead FDS computes the values using logarithmic averaging and a user-defined averaging window. One would expect, once steady-state conditions are reached, that the FDS predicted values should approach the analytic values. Results are shown in Fig. 17.1. In each figure the red line represents the value computed using the entire time history after steady-state is reached. As seen, the FDS predicted values approach the analytic values.

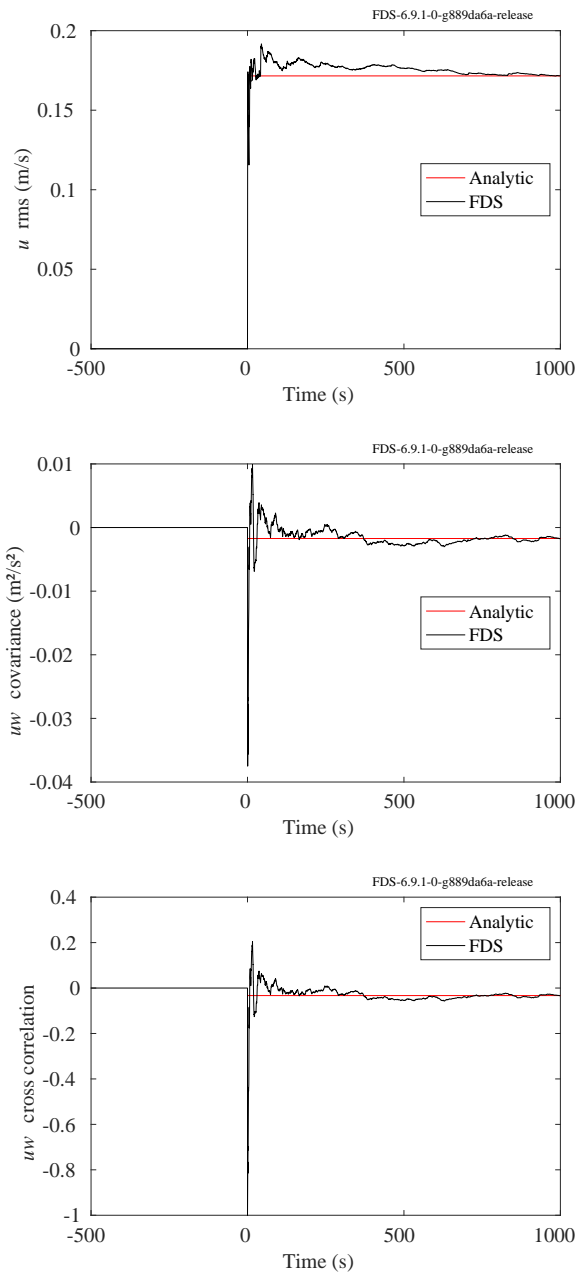


Figure 17.1: Output of the `rms_cov_corr` test case. By construction, the statistic matches the analytical result at time  $t = T_{\text{END}}$ .

### 17.1.2 RMS as a Running Average (`rms_example`)

In this example, we want to compute the mean and rms of a hypothetical velocity time series

$$u(t) = \tanh(t) + \mathcal{U}(-0.5, 0.5) \quad (17.1)$$

where  $\mathcal{U}(-0.5, 0.5)$  is a uniformly distributed random variable. The expected RMS of the time series beyond its initial transient is equal to the standard deviation of the uniform distribution over the unit interval,  $\sigma = \sqrt{1/12} \approx 0.2887$ . The expected mean is 1. This exercise is as much a check of the intrinsic random number generator in Fortran as it is the computation within FDS. Figure 17.2 displays the result. Note that

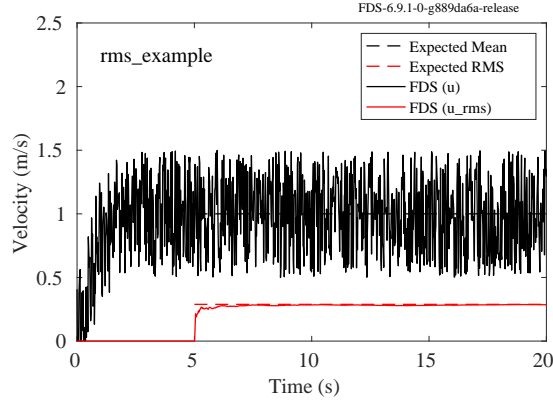


Figure 17.2: Output of the `rms_example` test case in which the mean and RMS of the time series is compared to expected values.

this example is also a useful demonstration of how to use the math functions within FDS. Although there is not a `tanh` function included, it can be constructed from the expression:

$$\tanh(t) = \frac{e^t - e^{-t}}{e^t + e^{-t}} \quad (17.2)$$

using the base functions as shown below.

```
&DEVC ID='rn', QUANTITY='RANDOM NUMBER', XYZ=0,0,0 /
&DEVC ID='t', QUANTITY='TIME', XYZ=0,0,0 /
&DEVC ID='u', QUANTITY='CONTROL VALUE', CTRL_ID='sum', XYZ=0,0,1, UNITS='m/s' /
&DEVC ID='u_rms', QUANTITY='CONTROL VALUE', CTRL_ID='sum', XYZ=0,0,1, UNITS='m/s',
    STATISTICS='RMS', STATISTICS_START=5. /

&CTRL ID='exp(t)', FUNCTION_TYPE='EXP', INPUT_ID='t' /
&CTRL ID='-t', FUNCTION_TYPE='MULTIPLY', INPUT_ID='t', 'CONSTANT', CONSTANT=-1. /
&CTRL ID='exp(-t)', FUNCTION_TYPE='EXP', INPUT_ID='-t' /
&CTRL ID='num', FUNCTION_TYPE='SUBTRACT', INPUT_ID='exp(t)', 'exp(-t)' /
&CTRL ID='den', FUNCTION_TYPE='SUM', INPUT_ID='exp(t)', 'exp(-t)' /
&CTRL ID='tanh', FUNCTION_TYPE='DIVIDE', INPUT_ID='num', 'den' /
&CTRL ID='rn2', FUNCTION_TYPE='SUBTRACT', INPUT_ID='rn', 'CONSTANT', CONSTANT=0.5 /
&CTRL ID='sum', FUNCTION_TYPE='SUM', INPUT_ID='tanh', 'rn2' /
```

### 17.1.3 Favre Average (`shunn3_Favrez`)

The Shunn manufactured solution (see Sec. 3.5) provides a 2-D analytical solution for both the density and mixture fraction. In this section, to test the statistical output `TEMPORAL_STATISTIC='FAVRE AVERAGE'`

we compare FDS results at two grid resolutions,  $\delta x = [L/32, L/64]$ , with  $L = 2$ . The case is run to  $t = 10$  s. Both the running average and Favre average are output at  $(x = 0, y = 0)$ , the center of the domain. Note that this imparts an  $\mathcal{O}(\delta x)$  error to the output. The higher grid resolution is therefore more accurate.

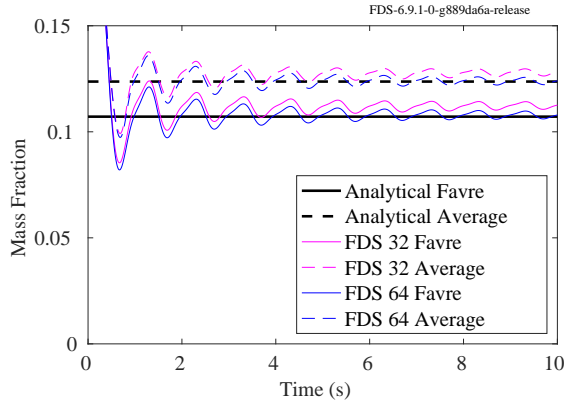


Figure 17.3: Output of the `shunn3_FavreZ` test cases in which the Favre average (continuous line) and running average (dashed line) at  $(x = 0, y = 0)$  are compared against expected values from the Shunn manufactured solution (see Sec. 3.5).

## 17.2 Interpolation

For line devices (`POINTS=...`) used together with `SPATIAL_STATISTIC='INTERPOLATION'` the near wall values are usually truncated to the cell value. However, with temperature and velocity components the wall value is used to provide an interpolation between the first cell value and the wall value. In the test cases below, a linear field of velocity and temperature are generated with 100 points along the device and only 5 cells across the domain. Three linear point arrays are created, one at each end along the periodic mesh boundary, and one in the center of the domain, which is also a cell center.

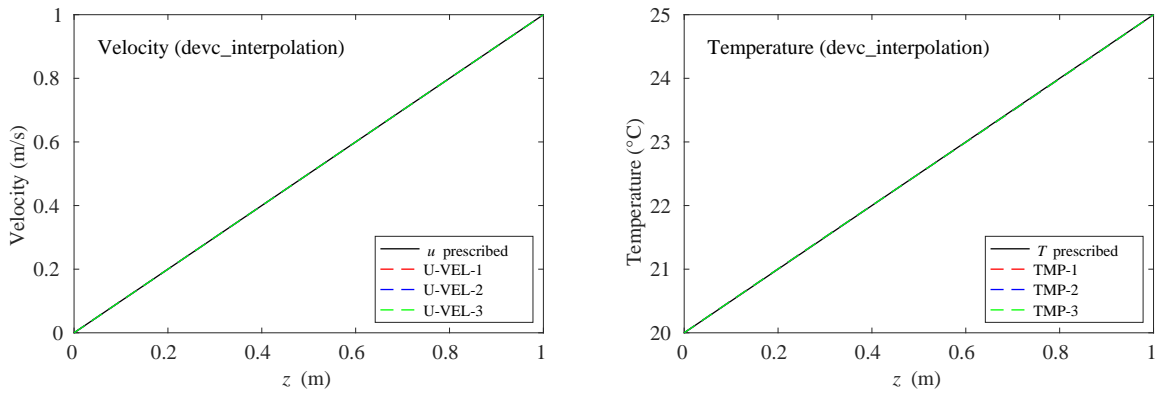


Figure 17.4: Output of the `devc_interpolation` test cases.

# Bibliography

- [1] K. McGrattan, S. Hostikka, R. McDermott, J. Floyd, C. Weinschenk, and K. Overholt. *Fire Dynamics Simulator, Technical Reference Guide*. National Institute of Standards and Technology, Gaithersburg, Maryland, USA, and VTT Technical Research Centre of Finland, Espoo, Finland, sixth edition, September 2013. Vol. 1: Mathematical Model; Vol. 2: Verification Guide; Vol. 3: Validation Guide; Vol. 4: Software Quality Assurance. [v](#), [55](#), [61](#), [128](#), [149](#), [209](#)
- [2] K. McGrattan, S. Hostikka, R. McDermott, J. Floyd, C. Weinschenk, and K. Overholt. *Fire Dynamics Simulator, User's Guide*. National Institute of Standards and Technology, Gaithersburg, Maryland, USA, and VTT Technical Research Centre of Finland, Espoo, Finland, sixth edition, September 2013. [v](#), [70](#), [77](#), [78](#), [232](#)
- [3] American Society for Testing and Materials, West Conshohocken, Pennsylvania. *ASTM E1355-12, Standard Guide for Evaluating the Predictive Capabilities of Deterministic Fire Models*, 2012. [v](#), [1](#), [9](#)
- [4] W. Mell, K.B. McGrattan, and H. Baum. Numerical Simulation of Combustion in Fire Plumes. In *Twenty-Sixth Symposium (International) on Combustion*, pages 1523–1530. Combustion Institute, Pittsburgh, Pennsylvania, 1996. [3](#)
- [5] K.B. McGrattan, H.R. Baum, and R.G. Rehm. Large Eddy Simulations of Smoke Movement. *Fire Safety Journal*, 30:161–178, 1998. [3](#)
- [6] H.R. Baum, R.G. Rehm, P.D. Barnett, and D.M. Corley. Finite Difference Calculations of Buoyant Convection in an Enclosure, Part I: The Basic Algorithm. *SIAM Journal of Scientific and Statistical Computing*, 4(1):117–135, March 1983. [3](#)
- [7] H.R. Baum and R.G. Rehm. Finite Difference Solutions for Internal Waves in Enclosures. *SIAM Journal of Scientific and Statistical Computing*, 5(4):958–977, December 1984. [3](#)
- [8] H.R. Baum and R.G. Rehm. Calculations of Three Dimensional Buoyant Plumes in Enclosures. *Combustion Science and Technology*, 40:55–77, 1984. [3](#)
- [9] R.G. Rehm, P.D. Barnett, H.R. Baum, and D.M. Corley. Finite Difference Calculations of Buoyant Convection in an Enclosure: Verification of the Nonlinear Algorithm. *Applied Numerical Mathematics*, 1:515–529, 1985. [3](#)
- [10] K.B. McGrattan, T. Kashiwagi, H.R. Baum, and S.L. Olson. Effects of Ignition and Wind on the Transition to Flame Spread in a Microgravity Environment. *Combustion and Flame*, 106:377–391, 1996. [4](#)

- [11] T. Kashiwagi, K.B. McGrattan, S.L. Olson, O. Fujita, M. Kikuchi, and K. Ito. Effects of Slow Wind on Localized Radiative Ignition and Transition to Flame Spread in Microgravity. In *Twenty-Sixth Symposium (International) on Combustion*, pages 1345–1352. Combustion Institute, Pittsburgh, Pennsylvania, 1996. [4](#)
- [12] W. Mell and T. Kashiwagi. Dimensional Effects on the Transition from Ignition to Flame Spread in Microgravity. In *Twenty-Seventh Symposium (International) on Combustion*, pages 2635–2641. Combustion Institute, Pittsburgh, Pennsylvania, 1998. [4](#)
- [13] W. Mell, S.L. Olson, and T. Kashiwagi. Flame Spread Along Free Edges of Thermally-Thin Samples in Microgravity. In *Twenty-Eighth Symposium (International) on Combustion*, pages 2843–2849. Combustion Institute, Pittsburgh, Pennsylvania, 2000. [4](#)
- [14] K. Prasad, Y. Nakamura, S.L. Olson, O. Fujita, K. Nishizawa, K. Ito, and T. Kashiwagi. Effect of Wind Velocity on Flame Spread in Microgravity. In *Twenty-Ninth Symposium (International) on Combustion*, pages 2553–2560. Combustion Institute, Pittsburgh, Pennsylvania, 2002. [4](#)
- [15] Y. Nakamura, T. Kashiwagi, K.B. McGrattan, and H.R. Baum. Enclosure Effects on Flame Spread over Solid Fuels in Microgravity. *Combustion and Flame*, 130:307–321, 2002. [4](#)
- [16] W.E. Mell, K.B. McGrattan, and H.R. Baum. g-Jitter Effects on Spherical Diffusion Flames. *Microgravity Science and Technology*, 15(4):12–30, 2004. [4](#)
- [17] A. Mukhopadhyay and I.K. Puri. An Assessment of Stretch Effects on Flame Tip Using the Thin Flame and Thick Formulations. *Combustion and Flame*, 133:499–502, 2003. [4](#)
- [18] A. Hamins, M. Bundy, I.K. Puri, K.B. McGrattan, and W.C. Park. Suppression of Low Strain Rate Non-Premixed Flames by an Agent. In *Proceedings of the 6th International Microgravity Combustion Workshop, NASA/CP-2001-210826*, pages 101–104. National Aeronautics and Space Administration, Lewis Research Center, Cleveland, Ohio, May 2001. [4](#)
- [19] K.B. McGrattan, R.G. Rehm, and H.R. Baum. Fire-Driven Flows in Enclosures. *Journal of Computational Physics*, 110(2):285–291, 1994. [4](#)
- [20] K. McGrattan, S. Hostikka, R. McDermott, J. Floyd, C. Weinschenk, and K. Overholt. *Fire Dynamics Simulator, Technical Reference Guide, Volume 3: Validation*. National Institute of Standards and Technology, Gaithersburg, Maryland, USA, and VTT Technical Research Centre of Finland, Espoo, Finland, sixth edition, September 2013. [5](#), [9](#), [227](#)
- [21] P. Friday and F. W. Mowrer. Comparison of FDS Model Predictions with FM/SNL Fire Test Data. NIST GCR 01-810, National Institute of Standards and Technology, Gaithersburg, Maryland, April 2001. [6](#)
- [22] A. Bounogui, N. Benichou, C. McCartney, and A. Kashef. Optimizing the Grid Size Used in CFD Simulations to Evaluate Fire Safety in Houses. In *3rd NRC Symposium on Computational Fluid Dynamics, High Performance Computing and Virtual Reality*, pages 1–8, Ottawa, Ontario, Canada, December 2003. National Research Council, Canada. [6](#)
- [23] R.L. Alpert. *SFPE Handbook of Fire Protection Engineering*, chapter Ceiling Jet Flows. Springer, New York, 5th edition, 2016. [6](#)

- [24] A. Bounagui, A. Kashef, and N. Benichou. Simulation of the Dynamics of the Fire for a Section of the L.H.-La Fontaine Tunnel. IRC-RR- 140, National Research Council Canada, Ottawa, Canada, K1A0R, September 2003. [6](#)
- [25] Y. Xin. Assessment of Fire Dynamics Simulation for Engineering Applications: Grid and Domain Size Effects. In *Proceedings of the Fire Suppression and Detection Research Application Symposium, Orlando, Florida*. National Fire Protection Association, Quincy, Massachusetts, 2004. [6](#)
- [26] J.A. Ierardi and J.R. Barnett. A Quantitative Method for Calibrating CFD Model Calculations. In *Proceedings of the CIB-CTBUH International Conference on Tall Buildings*, pages 507–514. International Council for Research and Innovation in Building and Construction (CIB), 2003. [6](#)
- [27] G. Heskstad. *SFPE Handbook of Fire Protection Engineering*, chapter Fire Plumes, Flame Height and Air Entrainment. Springer, New York, 5th edition, 2016. [6](#)
- [28] N.M. Petterson. Assessing the Feasibility of Reducing the Grid Resolution in FDS Field Modeling. Fire Engineering Research Report 2002/6, University of Canterbury, Christchurch, New Zealand, March 2002. [6](#)
- [29] A. Musser, K. B. McGrattan, and J. Palmer. Evaluation of a Fast, Simplified Computational Fluid Dynamics Model for Solving Room Airflow Problems. NISTIR 6760, National Institute of Standards and Technology, Gaithersburg, Maryland, June 2001. [7](#)
- [30] W. Zhang, A. Hamer, M. Klassen, D. Carpenter, and R. Roby. Turbulence Statistics in a Fire Room Model by Large Eddy Simulation. *Fire Safety Journal*, 37:721–752, 2002. [7](#)
- [31] J. Smagorinsky. General Circulation Experiments with the Primitive Equations. I. The Basic Experiment. *Monthly Weather Review*, 91(3):99–164, March 1963. [7](#)
- [32] M. Germano, U. Piomelli, P. Moin, and W.H. Cabot. A Dynamic Subgrid-Scale Eddy Viscosity Model. *Physics of Fluids A*, 3(7):1760–1765, 1991. [7](#)
- [33] D.K. Lilly. A Proposed Modification of the Germano Subgrid-Scale Closure Method. *Physics of Fluids A*, 4(3):633–635, 1992. [7](#)
- [34] P. Moin, K. Squires, W. Cabot, and S. Lee. A dynamic subgrid-scale model for compressible turbulence and scalar transport. *Phys. Fluids A*, 3(11):2746–2757, 1991. [7, 47](#)
- [35] S. Hostikka. Development of fire simulation models for radiative heat transfer and probabilistic risk assessment. VTT Publications 683, VTT Technical Research Centre of Finland, Espoo, Finland, 2008. [8](#)
- [36] J. Hietaniemi, S. Hostikka, and J. Vaari. FDS Simulation of Fire Spread – Comparison of Model Results with Experimental Data. VTT Working Papers 4, VTT Building and Transport, Espoo, Finland, 2004. [8](#)
- [37] C. Lautenberger, G. Rein, and C. Fernandez-Pello. The Application of a Genetic Algorithm to Estimate the Material Properties for Fire Modeling from Bench-Scale Fire Test Data. *Fire Safety Journal*, 41:204–214, 2006. [9](#)
- [38] J.C. Adams, W.S. Brainerd, J.T. Martin, B.T. Smith, and J.L. Wagener. *Fortran 95 Handbook: Complete ISO/ANSI Reference*. MIT Press, Cambridge, Massachusetts, 1997. [9](#)

- [39] R. McDermott. A nontrivial analytical solution to the 2-d incompressible Navier-Stokes equations. [https://sites.google.com/site/randymcdermott/NS\\_exact\\_soln.pdf](https://sites.google.com/site/randymcdermott/NS_exact_soln.pdf), 2003. 11
- [40] R. J. Leveque. *Finite Volume Methods for Hyperbolic Problems*. Cambridge University Press, New York, 2002. 20
- [41] A. Biglari, T. Saad, and J. Sutherland. An efficient and explicit pressure projection method for reacting flow simulations. In *8th US National Combustion Meeting*, 2013. 23
- [42] P. Moin. *Fundamentals of Engineering Numerical Analysis*. Cambridge University Press, 2001. 23
- [43] L. Shunn, F. Ham, and P. Moin. Verification of variable-density flow solvers using manufactured solutions. *Journal of Computational Physics*, 231:3801–3827, 2012. 24, 25, 26, 27, 271
- [44] <https://github.com/firemodels/fds>. 25, 39, 58
- [45] S. Armfield and R. Street. An analysis and comparison of the time accuracy of fractional-step methods for Navier-Stokes equations on staggered grids. *Int. J. Num. Meth. Fluids*, 38:255–282, 2001. 26, 28
- [46] J.-C. Jouhaud. Benchmark on the vortex preservation. <http://elearning.cerfacs.fr/pdfs/numerical/TestCaseVortex2D.pdf>, 2010. 30
- [47] D.K. Kahaner, W.F. Lawkins, and S. Thompson. On the use of rootfinding ODE software for the solution of a common problem in nonlinear dynamical systems. *Journal of Computational and Applied Mathematics*, 28:219–230, 1989. 33
- [48] K. McGrattan, S. Hostikka, R. McDermott, J. Floyd, C. Weinschenk, and K. Overholt. *Fire Dynamics Simulator, Technical Reference Guide, Volume 1: Mathematical Model*. National Institute of Standards and Technology, Gaithersburg, Maryland, USA, and VTT Technical Research Centre of Finland, Espoo, Finland, sixth edition, September 2013. 33, 34, 37, 47, 49, 55, 78, 138, 171
- [49] R.L. Curl. Disperse phase mixing: I. theory and effects in simple reactors. *AIChE Journal*, 9:175, 1963. 34
- [50] G. Comte-Bellot and S. Corrsin. Simple Eulerian time correlation of full- and narrow-band velocity signals in grid-generated, ‘isotropic’ turbulence. *J. Fluid Mech.*, 48:273–337, 1971. 45
- [51] Stephen M. de Bruyn Kops. *Numerical simulation of non-premixed turbulent combustion*. PhD thesis, The University of Washington, 1999. 45
- [52] R. McDermott, A. Kerstein, R. Schmidt, and P. Smith. Characteristics of 1D spectra in finite-volume large-eddy simulations with one-dimensional turbulence subgrid closure. In *58th Annual Meeting of the American Physical Society, Division of Fluid Dynamics*, Chicago, Illinois, November 2005. 45, 46
- [53] Y. Morinishi, T. S. Lund, O. V. Vasilyev, and P. Moin. Fully conservative high order finite difference schemes for incompressible flow. *Journal of Computational Physics*, 143:90–124, 1998. 46
- [54] F. E. Ham, F. S. Lien, and A. B. Strong. A fully conservative second-order finite difference scheme for incompressible flow on non-uniform grids. *Journal of Computational Physics*, 177:117–133, 2002. 46

- [55] R. McDermott. Discrete kinetic energy conservation for variable-density flows on staggered grids. In *60th Annual Meeting of the American Physical Society, Division of Fluid Dynamics*, Salt Lake City, Utah, November 2007. [46](#)
- [56] M. Germano, U. Piomelli, P. Moin, and W. Cabot. A dynamic subgrid-scale eddy viscosity model. *Physics of Fluids A*, 3(7):1760–1765, 1991. [47](#)
- [57] M. Pino Martin, U. Piomelli, and G. Candler. Subgrid-scale models for compressible large-eddy simulation. *Theoret. Comput. Fluid Dynamics*, 13:361–376, 2000. [47](#)
- [58] T. S. Lund. On the use of discrete filters for large eddy simulation. Center for Turbulence Research Annual Research Briefs, 1997. [47](#)
- [59] Stephen B. Pope. *Turbulent Flows*. Cambridge University Press, 2000. [48](#), [55](#), [58](#)
- [60] S.B. Pope. Ten questions concerning the large-eddy simulation of turbulent flows. *New Journal of Physics*, 6:1–24, 2004. [48](#)
- [61] J.W. Deardorff. Stratocumulus-capped mixed layers derived from a three-dimensional model. *Boundary-Layer Meteorol.*, 18:495–527, 1980. [48](#)
- [62] J. Bardina, J. H. Ferziger, and W. C. Reynolds. Improved Subgrid Scale Models for Large Eddy Simulation. In *AIAA 13th Fluid & Plasma Dynamics Conference*, AIAA-80-1357, Snowmass, Colorado, July 1980. American Institute of Aeronautics and Astronautics. [49](#)
- [63] B. Vreman. An eddy-viscosity subgrid-scale model for turbulent shear flow: Algebraic theory and applications. *Physics of Fluids*, 16(10):3670–3681, 2004. [49](#)
- [64] F. Nicoud and F. Ducros. Subgrid-Scale Stress Modelling Based on the Square of the Velocity Gradient Tensor. *Flow, Turbulence, and Combustion*, 62:183–200, 1999. [49](#), [50](#)
- [65] D.C. Wilcox. *Turbulence Modeling for CFD*. DCW Industries, Inc., 2nd edition, 1998. [49](#)
- [66] W. Kümmel. Technische strömungsmechanik. Technical report, B.G. Teubner, 3. Auflage, 2007. [53](#)
- [67] J. S. Baggett. Some modeling requirements for wall models in large eddy simulation. *Stanford Center for Turbulence Research Annual Research Briefs*, 1997. [55](#)
- [68] J. S. Baggett. On the feasibility of merging LES with RANS for the near-wall region of attached turbulent flows. *Stanford Center for Turbulence Research Annual Research Briefs*, 1998. [55](#)
- [69] W. Cabot. Large-eddy simulations with wall models. *Stanford Center for Turbulence Research Annual Research Briefs*, 1995. [55](#)
- [70] Pierre Sagaut. *Large Eddy Simulation for Incompressible Flows*. Springer, 2001. [55](#)
- [71] L. F. Moody. Friction factors for pipe flow. *Transactions of the ASME*, 66, 1944. [55](#)
- [72] Bruce R. Munson, Donald F. Young, and Theodore H. Okiishi. *Fundamentals of Fluid Mechanics*. John Wiley and Sons, 1990. [56](#)
- [73] R.L. Panton. *Incompressible Flow*. Wiley, New Jersey, 2005. [58](#), [59](#)
- [74] J.P. Holman. *Heat Transfer*. McGraw-Hill, New York, 7th edition, 1990. [60](#), [67](#), [68](#), [69](#)

- [75] J. Kim and P. Moin. Transport of Passive Scalars in Turbulent Channel Flow. Technical Memorandum 89463, National Aeronautics and Space Administration, Moffet Field, California, September 1987. [62](#)
- [76] R. Moser, J. Kim, and N. Mansour. Direct numerical simulation of turbulent channel flow up to  $Re_\tau = 590$ . *Phys. Fluids*, 11:943–945, 1999. [62](#)
- [77] T.L. Bergman, A.S. Lavine, F.P. Incropera, and D.P. DeWitt. *Fundamentals of Heat and Mass Transfer*. John Wiley and Sons, New York, 7th edition, 2011. [63](#), [66](#), [70](#), [122](#), [163](#)
- [78] T. Yuge. Experiments on Heat Transfer from Spheres Including Combined Natural and Forced Convection. *Journal of Heat Transfer*, 82:214, 1960. [69](#)
- [79] W.S. Amato and C.L. Tien. Free Convection Heat Transfer from Isothermal Spheres in Water. *Int. J. Heat Mass Transfer*, 15:327, 1972. [69](#)
- [80] G.C. Huang. Investigations of Heat-Transfer Coefficients for Air Flow Through. *J. Heat Transfer*, 85(3):237–245, 1963. [70](#)
- [81] J.N.B. Livingood and P. Hrycak. Impingement Heat Transfer from Turbulent Air Jets to Flat Plates - A Literature Survey. NASA Technical Memorandum 1973, National Aeronautics and Space Administration, Washington, D.C., May 1973. [70](#)
- [82] H. Martin. *Advances in Heat Transfer*, volume 13, chapter Heat and Mass Transfer Between Impinging Gas Jets and Solid Surfaces. Academic Press, New York, 1977. [70](#)
- [83] L. Casara and T. Arts. Aerodynamic Performance of a Rib Roughened Cooling Channel Flow with High Blockage Ratio. In *Eleventh International Symposium on Application of Laser Techniques to Fluid Mechanics*, Lisbon, Portugal, 2002. [72](#), [73](#), [75](#)
- [84] L. Casara and T. Arts. Experimental Investigation of the Aero-thermal Performance of a High Blockage Rib-Roughened Cooling Channel. *Journal of Turbomachinery*, 127:580–588, 2005. [72](#), [73](#), [75](#)
- [85] M. Lohász, P. Rambaud, and C. Benocci. LES Simulation of Ribbed Square Duct Flow with Fluent and Comparison with PIV Data. In *The 12th International Conference on Fluid Flow Technologies*, Budapest, Hungary, 2003. [72](#)
- [86] P. von Schoenberg. Development of a Large-Eddy Simulation code for the atmospheric boundary layer. FOI-R-1533-SE, Swedish Defense Research Agency, 2004. [78](#), [79](#)
- [87] R. Siegel and J. R. Howell. *Thermal Radiation Heat Transfer*. Taylor & Francis, New York, 4th edition, 2002. [113](#), [114](#)
- [88] Y.B. Zel'dovich and Y.P. Raizer. *Physics of shock waves and high-temperature hydrodynamic phenomena*. Dover Publications, New York, 2002. Translated from the Russian and then edited by W.D.Hayes and R.F. Probstein. [115](#)
- [89] C.K. Westbrook and F.L. Dryer. Simplified Reaction Mechanisms for the Oxidation of Hydrocarbon Fuels in Flames. *Combustion Science and Technology*, 27:31–43, 1981. [135](#)
- [90] S. Gordon and B.J. McBride. Computer program for calculation of complex chemical equilibrium compositions and applications. NASA Reference Publication 1311, National Aeronautics and Space Administration, Office of Management, Scientific and Technical Information Program, Cleveland, Ohio, 1994. [135](#)

- [91] S.R. Turns. *An Introduction to Combustion*. McGraw-Hill, New York, 2nd edition, 1996. 141
- [92] D.A. Purser. *SFPE Handbook of Fire Protection Engineering*, chapter Combustion Toxicity. Springer, New York, 5th edition, 2016. 143, 144
- [93] D. Drysdale. *An Introduction to Fire Dynamics*. John Wiley and Sons, New York, 2nd edition, 2002. 159, 171
- [94] H.S. Carslaw and J.C. Jaeger. *Conduction of Heat in Solids*. Oxford University Press, 2nd edition, 1959. 159, 171, 173
- [95] K.W. Childs. HEATING 7: Multidimensional, Finite-Difference Heat Conduction Analysis Code System. Technical Report PSR-199, Oak Ridge National Laboratory, Oak Ridge, TN, 1998. 160
- [96] A. Khawam and D. R. Flanagan. Solid-State Kinetic Models: Basics and Mathematical Fundamentals. *J. Phys. Chem. B*, 110:17315–17328, 2006. 181
- [97] R.E. Lyon. Heat Release Kinetics. *Fire and Materials*, 24:179–186, 2000. 193
- [98] D. Morvan and J.L. Dupuy. Modeling the propagation of a wildfire through a Mediterranean shrub using a multiphase formulation. *Combustion and Flame*, 138(3):199–210, 2004. 202
- [99] R.E. Lyon and R.N. Walters. Pyrolysis Combustion Flow Calorimetry. *Journal of Analytical and Applied Pyrolysis*, 71(1):27–46, March 2004. 203
- [100] American Society for Testing and Materials, West Conshohocken, Pennsylvania. *ASTM D 7309-11, Standard Test Method for Determining Flammability Characteristics of Plastics and Other Solid Materials Using Microscale Combustion Calorimetry*, 2011. 203
- [101] W. E. Ranz and W. R. Marshall. Evaporation from drops - Part II. *Chemical Engineering Progress*, 48:173–180, March 1952. 227
- [102] Y.F. Li. and W.K. Chow. Study of water droplet behavior in hot air layer in fire extinguishment. *Fire Technology*, 44:351–381, 2008. 230
- [103] C.W. Gardiner. *Handbook of Stochastic Methods for Physics, Chemistry and the Natural Sciences*. Springer-Verlag, Berlin, 3rd edition, 2004. 233
- [104] M.S. Owen. *2009 ASHRAE Handbook: Fundamentals*. American Society of Heating, Refrigerating, and Air-Conditioning Engineers, Inc., Atlanta, GA, 2009. 248
- [105] R.G. Rehm and R. McDermott. Fire-Front Propagation Using the Level Set Method. NISTTN 1611, National Institute of Standards and Technology, Gaithersburg, Maryland, April 2009. 257
- [106] G.D. Richards. An elliptical growth model of forest fire fronts and its numerical solution. *International Journal for Numerical Methods in Engineering*, 30:1163–1179, 1990. 257
- [107] M.A. Finney. Fire Area Simulator – Model, Development and Evaluation. Research Paper RMRS-RP-4 Revised, United States Forest Service, Rocky Mountain Research Station, Missoula, Montana, February 2004. <http://www.fs.fed.us/rm/pubs/rmrp004.pdf>. 257
- [108] R.C. Rothermel. A Mathematical Model for Predicting Fire Spread in Wildland Fuels. Research Paper INT-115, Intermountain Forest and Range Experiment Station, USDA Forest Service, Ogden, Utah, January 1972. <http://www.treesearch.fs.fed.us/pubs/32533>. 257, 258

- [109] H.E. Anderson. Predicting wind-driven wild land fire size and shape. Research Paper INT-305, Intermountain Forest and Range Experiment Station, USDA Forest Service, Ogden, Utah, 1983. [257](#)
- [110] A.S. Bova, W.E. Mell, and C.M. Hoffman. A comparison of level set and marker methods for the simulation of wildland fire front propagation. *International Journal of Wildland Fire*, 25(2):229–241, 2015. <http://dx.doi.org/10.1071/WF13178>. [257](#)
- [111] P.L. Andrews. Modeling wind adjustment factor and midflame wind speed for Rothermel’s surface fire spread model. General Technical Report RMRS-GTR-266, Rocky Mountain Research Station, USDA Forest Service, Fort Collins, Colorado, 2012. [258](#)
- [112] M. Berger. Chapter 1 - cut cells: Meshes and solvers. In Rémi Abgrall and Chi-Wang Shu, editors, *Handbook of Numerical Methods for Hyperbolic Problems*, volume 18 of *Handbook of Numerical Analysis*, pages 1–22. Elsevier, 2017. [269](#)
- [113] Weinan E and Jian-Guo Liu. Gauge Method for Viscous Incompressible Flows. *Communications in Mathematical Sciences*, 1(2):317–332, 2003. [273](#)
- [114] G.E. Danielson and R.H. Lagdon. Safety Software Guide for Use with 10 CFR 830 Subpart A, Quality Assurance Requirements, and DOE O 414.1C, Quality Assurance. DOE G 414.1-4, U.S. Department of Energy, Washington, DC, June 2005. [313](#)
- [115] F. Odar. Software Quality Assurance Procedures for NRC Thermal Hydraulic Codes. NUREG-1737, U.S. Nuclear Regulatory Commission, Washington, DC, December 2000. [313](#)

## Appendix A

# Summary of Verification Results

This appendix summarizes the accuracy of cases in the FDS verification suite. These cases are an integral part of the continuous integration process for FDS in which daily source code changes are checked each night against this growing list of cases to verify the overall accuracy of FDS and to quickly identify errors introduced into the source code.

The verification cases that are listed in Table A.1 are described either in the FDS Verification Guide or the FDS User's Guide. Those cases that are in the User's Guide help to explain various input parameters. Dark blue links refer to sections in the Verification Guide; light blue links refer to the User's Guide. For each case, there are one or more point to point comparisons between an FDS predicted value and an exact or expected value. If the relative or absolute difference between the predicted and exact/expected values is within the specified tolerance, the case passes.

Table A.1: Summary of verification cases.

Case Name	Section	Expected Quantity	Expected Value	Predicted Quantity	Predicted Value	Type of Error	Error Tolerance	Within Tol.
1_step_2_step_M	10.8	Q1S	1.61e+02	Q2S	1.61e+02	Relative	1.53e-04	5.00e-03
1_step_2_step_H	10.8	Q3S	1.61e+02	Q4S	1.61e+02	Relative	2.50e-04	5.00e-03
activate_vents	18.5.11	controller 1	1.00e+00	controller 1	1.00e+00	Relative	0.00e+00	0.00e+00
activate_vents	18.5.11	controller 3	1.00e+00	controller 3	1.00e+00	Relative	0.00e+00	0.00e+00
adibatic_con_flux	18.5.11	controller 4	1.00e+00	controller 4	1.00e+00	Relative	0.00e+00	0.00e+00
adibatic_con_flux	11.8	pres	2.40e+04	pres	2.39e+04	Relative	6.01e-03	1.00e-02
adibatic_net_flux	11.8	temp	6.92e+01	temp_gas	6.91e+01	Relative	1.97e-03	1.00e-02
adibatic_net_flux	11.8	pres	2.40e+04	pres	2.39e+04	Relative	5.27e-03	1.00e-02
adiabatic_surface_temperature	22.10.13	temp	6.92e+01	temp_gas	6.91e+01	Relative	1.84e-03	1.00e-02
adiabatic_surface_temperature	22.10.13	AST	3.36e+02	AST	3.36e+02	Relative	3.12e-04	1.00e-02
aerosol_agglomeration	10.11.5	Exact Total	1.00e-05	FDS Total	1.00e-05	Relative	0.00e+00	1.00e-04
aerosol_agglomeration	10.11.5	Exact Bin 1	1.00e-05	FDS Bin 1	1.00e-05	Relative	4.00e-06	2.00e-02
aerosol_agglomeration	10.11.5	Exact Bin 2	1.06e-09	FDS Bin 2	1.06e-09	Relative	2.17e-06	2.00e-02
aerosol_agglomeration	10.11.5	Exact Total	1.00e-05	FDS Total	1.00e-05	Relative	0.00e+00	2.00e-02
aerosol_agglomeration	10.11.5	Exact Bin 1	1.00e-05	FDS Bin 1	1.00e-05	Relative	2.63e-06	2.00e-02
aerosol_agglomeration	10.11.5	Exact Bin 2	1.08e-09	FDS Bin 2	1.07e-09	Relative	5.79e-03	2.00e-02
aerosol_gravitational_deposition	10.11.1	Exact Gas 1	7.21e-06	FDS Gas 1	7.28e-06	Relative	9.73e-03	2.50e-02
aerosol_gravitational_deposition	10.11.1	Exact Gas 2	1.20e-05	FDS Gas 2	1.20e-05	Relative	2.67e-03	2.50e-02
aerosol_gravitational_deposition	10.11.1	Exact Wall Top	1.00e-12	FDS Wall Top	1.00e-12	Relative	0.00e+00	2.00e-02
aerosol_gravitational_deposition	10.11.1	Exact Wall Bottom	5.26e-08	FDS Wall Bottom	5.27e-08	Relative	1.03e-03	2.00e-02
aerosol_gravitational_deposition	10.11.1	Exact Gas 1	1.20e-05	FDS Gas 1	1.20e-05	Relative	2.67e-03	2.50e-02
aerosol_gravitational_deposition	10.11.1	Exact Gas 2	7.21e-06	FDS Gas 2	7.28e-06	Relative	9.73e-03	2.50e-02
aerosol_gravitational_deposition	10.11.1	Exact Wall Top	5.26e-08	FDS Wall Top	5.27e-08	Relative	1.03e-03	2.00e-02
aerosol_gravitational_deposition	10.11.1	Exact Wall Bottom	1.00e-12	FDS Wall Bottom	1.00e-12	Relative	0.00e+00	2.00e-02
aerosol_gravitational_deposition	10.11.2	Exact Gas 1	6.01e-06	FDS Gas	6.00e-06	Relative	8.28e-03	2.00e-02
aerosol_gravitational_deposition	10.11.2	Exact Wall	3.69e-09	FDS Wall	3.70e-09	Relative	2.54e-03	2.00e-02
aerosol_gravitational_deposition	10.11.2	Exact Gas	6.01e-06	FDS Gas	6.00e-06	Relative	8.28e-03	2.00e-02
aerosol_gravitational_deposition	10.11.2	Exact Wall	3.69e-09	FDS Wall	3.70e-09	Relative	2.54e-03	2.00e-02
aerosol_gravitational_deposition	10.11.3	Exact Wall 1	1.78e-14	FDS Wall 1	1.78e-14	Relative	9.86e-05	2.00e-02
aerosol_gravitational_deposition	10.11.3	Exact Wall 2	2.92e-08	FDS Wall 2	2.92e-08	Relative	1.00e-04	2.00e-02
aerosol_gravitational_deposition	10.11.3	Exact Wall 3	3.61e-07	FDS Wall 3	3.61e-07	Relative	1.00e-04	2.00e-02
aerosol_turbulent_deposition	10.11.6	MF	1.00e-04	MF	1.00e-04	Relative	0.00e+00	2.00e-02
aerosol_scrubbing	14.11	Duct 1	7.16e+02	Duct 1	7.14e+02	Relative	2.62e-03	1.00e-02
ashrae7_fixed_flow	14.11	Duct 2	4.41e+02	Duct 2	4.40e+02	Relative	2.52e-03	1.00e-02
ashrae7_fixed_flow	14.11	Duct 3	4.41e+02	Duct 3	4.40e+02	Relative	2.52e-03	1.00e-02
ashrae7_fixed_flow	14.11	Duct 4	2.75e+02	Duct 4	2.74e+02	Relative	2.71e-03	1.00e-02
ashrae7_fixed_flow	14.11	Duct 5	1.21e+02	Duct 5	1.21e+02	Relative	2.87e-03	1.00e-02
ashrae7_fixed_flow	14.11	Duct 56	7.31e+02	Duct 56	7.29e+02	Relative	3.17e-03	1.00e-02
ashrae7_fixed_flow	14.11	Duct 6	3.22e+01	Duct 6	3.21e+01	Relative	2.78e-03	1.00e-02
ashrae7_fixed_flow	14.11	Duct 7	3.13e+02	Duct 7	3.12e+02	Relative	3.76e-03	1.00e-02
ashrae7_quadratic	14.11	Duct 1	7.16e+02	Duct 1	7.16e+02	Relative	8.77e-04	1.00e-02

Case Name	Section	Expected Quantity	Expected Value	Predicted Quantity	Predicted Value	Type of Error	Error	Error Tolerance	Within Tol.
ashrae7_quadratic		Duct 2	4.41e+02	Duct 2	4.41e+02	Relative	7.85e-04	1.00e-02	Yes
ashrae7_quadratic		Duct 3	4.41e+02	Duct 3	4.41e+02	Relative	7.84e-04	1.00e-02	Yes
ashrae7_quadratic		Duct 4	2.75e+02	Duct 4	2.75e+02	Relative	9.67e-04	1.00e-02	Yes
ashrae7_quadratic		Duct 5	1.21e+02	Duct 5	1.21e+02	Relative	1.12e-03	1.00e-02	Yes
ashrae7_quadratic		Duct 56	7.31e+02	Duct 56	7.30e+02	Relative	1.42e-03	1.00e-02	Yes
ashrae7_quadratic		Duct 6	3.22e+01	Duct 6	3.22e+01	Relative	1.01e-03	1.00e-02	Yes
ashrae7_quadratic		Duct 7	3.13e+02	Duct 7	3.13e+02	Relative	2.03e-03	1.00e-02	Yes
ashrae7_table		Duct 1	7.16e+02	Duct 1	7.14e+02	Relative	3.44e-03	1.00e-02	Yes
ashrae7_table		Duct 2	4.41e+02	Duct 2	4.40e+02	Relative	3.35e-03	1.00e-02	Yes
ashrae7_table		Duct 3	4.41e+02	Duct 3	4.40e+02	Relative	3.35e-03	1.00e-02	Yes
ashrae7_table		Duct 4	2.75e+02	Duct 4	2.74e+02	Relative	3.54e-03	1.00e-02	Yes
ashrae7_table		Duct 5	1.21e+02	Duct 5	1.21e+02	Relative	3.70e-03	1.00e-02	Yes
ashrae7_table		Duct 56	7.31e+02	Duct 56	7.28e+02	Relative	4.01e-03	1.00e-02	Yes
ashrae7_table		Duct 6	3.22e+01	Duct 6	3.21e+01	Relative	3.62e-03	1.00e-02	Yes
ashrae7_table		Duct 7	3.13e+02	Duct 7	3.12e+02	Relative	4.58e-03	1.00e-02	Yes
ideal			4.57e+01	asp1	4.62e+01	Relative	1.17e-02	2.00e-02	Yes
Flux_in			9.33e+00	Flux_out	9.33e+00	Relative	3.61e-06	5.00e-03	Yes
Temp_thinner			3.71e+02	T_F1	3.71e+02	Relative	0.00e+00	5.00e-03	Yes
Temp_thinner			7.82e+02	T_F2	7.68e+02	Relative	1.83e-02	2.00e-02	Yes
T_F_Target			7.56e+02	T_B1	7.43e+02	Relative	1.72e-02	2.00e-02	Yes
T_B_Target			7.82e+02	T_F2	7.68e+02	Relative	1.81e-02	2.00e-02	Yes
T_F_Target			7.82e+02	T_B2	7.44e+02	Relative	1.70e-02	2.00e-02	Yes
T_B_Target			7.56e+02	T_F3	7.73e+02	Relative	1.15e-02	2.00e-02	Yes
T_F_Target			7.82e+02	T_B3	7.48e+02	Relative	1.09e-02	2.00e-02	Yes
T_B_Target			7.56e+02	beam_1	9.56e+01	Relative	8.61e-06	1.00e-02	Yes
Obs			9.56e+01	beam_1	9.56e+01	Relative	1.03e-05	1.00e-02	Yes
beam_2			9.56e+01	beam_3	9.56e+01	Relative	5.27e-06	1.00e-02	Yes
beam_detector			1.00e-01	XF1	1.00e-01	Absolute	0.00e+00	1.00e-03	Yes
bound_test_1			1.00e-12	XAI	1.19e-17	Absolute	1.00e-12	1.00e-03	Yes
bound_test_1			1.00e-12	XP1	4.00e-01	Absolute	0.00e+00	1.00e-03	Yes
bound_test_1			1.00e-12	XF2	1.00e-12	Absolute	0.00e+00	1.00e-03	Yes
bound_test_1			3.00e-01	XAI	3.00e-01	Absolute	0.00e+00	1.00e-03	Yes
bound_test_1			2.00e-01	XP2	2.00e-01	Absolute	0.00e+00	1.00e-03	Yes
bound_test_1			1.00e+00	SUM	1.00e+00	Absolute	0.00e+00	1.00e-03	Yes
bound_test_1			1.00e-12	XF1	1.00e-12	Absolute	0.00e+00	1.00e-03	Yes
bound_test_2			2.40e-01	XF2	2.40e-01	Absolute	0.00e+00	1.00e-03	Yes
bound_test_2			2.40e-01	XAI	2.40e-01	Absolute	0.00e+00	1.00e-03	Yes
bound_test_2			1.00e-12	XA2	2.98e-17	Absolute	1.00e-12	1.00e-03	Yes
bound_test_2			1.00e-12	XP1	1.20e-01	Absolute	0.00e+00	1.00e-03	Yes
bound_test_2			1.20e-01	P2	3.20e-01	Absolute	0.00e+00	1.00e-03	Yes
bound_test_2			3.20e-01	P3	8.00e-02	Absolute	0.00e+00	1.00e-03	Yes
bound_test_2			8.00e-02	SUM	1.00e+00	Absolute	0.00e+00	1.00e-03	Yes
box_burn_away1			1.00e+00	Mass fuel	1.28e+00	Relative	8.52e-04	2.00e-02	Yes
box_burn_away1			1.00e+00	Mass GAS	1.28e+00	Relative	4.77e-06	2.00e-02	Yes
box_burn_away2			1.28e+00	Mass fuel	1.29e+00	Relative	4.89e-03	2.00e-02	Yes
box_burn_away3			9.60e-01	Mass fuel	9.62e-01	Relative	2.35e-03	2.00e-02	Yes
box_burn_away4			1.28e+00	Mass fuel	1.28e+00	Relative	5.31e-06	2.00e-02	Yes
box_burn_away5			1.28e+00						

Case Name	Section	Expected Quantity	Expected Value	Predicted Quantity	Predicted Value	Type of Error	Error	Error Tolerance	Within Tol.
box_burn_away6	9.2.8	Mass_residue (kg)	6.40e-01	Mass fuel 1	6.40e-01	Relative	1.20e-04	2.00e-02	Yes
box_burn_away6	9.2.8	Mass (kg)	1.28e+00	Mass fuel 2	1.28e+00	Relative	1.20e-04	2.00e-02	Yes
box_burn_away7	9.2.8	Mass (kg)	3.20e-02	Mass fuel	3.20e-02	Relative	5.00e-04	2.00e-02	Yes
box_burn_away_2D	9.2.8	Mass (kg)	1.28e+00	Mass fuel	1.28e+00	Relative	1.42e-04	2.00e-02	Yes
box_burn_away_2D	9.2.8	Mass_end (kg)	1.00e-12	Mass solid	1.00e-12	Relative	0.00e+00	2.00e-02	Yes
box_burn_away8	9.2.8	Mass4 (kg)	9.60e-01	Mass fuel	9.62e-01	Relative	2.35e-03	2.00e-02	Yes
box_burn_away9	9.2.8	Mass	6.59e-01	Mass fuel	6.59e-01	Relative	3.33e-04	1.00e-02	Yes
box_burn_away10	9.2.8	Mass (kg)	1.35e+00	Mass fuel	1.35e+00	Relative	5.13e-04	2.00e-02	Yes
box_burn_away11	9.2.8	Mass (kg)	4.80e-01	Mass fuel	4.78e-01	Relative	3.64e-03	1.00e-02	Yes
box_burn_away_2D_residue	9.2.8	Mass_residue (kg)	6.40e-01	Mass fuel	6.40e-01	Relative	1.84e-04	2.00e-02	Yes
box_burn_away_2D_residue	9.2.8	Mass_end (kg)	1.00e-12	Mass solid	1.00e-12	Relative	0.00e+00	2.00e-02	Yes
bucket_test_1	22.9.1	Mass (kg)	9.00e+01	Mass	8.87e+01	Relative	1.46e-02	2.00e-02	Yes
bucket_test_2	18.3.1	Mass (kg)	5.00e+00	Mass	4.93e+00	Relative	1.42e-02	3.00e-02	Yes
bucket_test_3	15.5.3	Mass (kg)	8.00e-03	Mass	7.98e-03	Relative	2.84e-03	2.00e-02	Yes
bucket_test_4	22.9.3	Mass (kg)	2.75e-02	total	2.75e-02	Relative	0.00e+00	2.00e-02	Yes
bucket_test_4	22.9.3	Mass Flux (kg/s)	5.00e-04	flux	5.01e-04	Relative	2.31e-03	5.00e-02	Yes
bulk_density_file	17.2.2	dry canopy mass	3.50e+02	dry canopy mass	3.50e+02	Absolute	3.00e-05	1.00e-03	Yes
burke_schumann_spec	10.6	Fuel	1.00e+00	FDS_Fuel	1.00e+00	Absolute	0.00e+00	1.00e-03	Yes
burke_schumann_spec	10.6	Ox	1.00e-12	FDS_Ox	1.00e-12	Absolute	0.00e+00	1.00e-03	Yes
burke_schumann_spec	10.6	Prod	1.00e-12	FDS_Prod	1.00e-12	Absolute	0.00e+00	1.00e-03	Yes
burke_schumann_temp	10.6	Temperature	1.00e-12	FDS_Temperature	1.00e-12	Absolute	0.00e+00	1.00e-03	Yes
cable_11_insulation	12.9.6	HRR (W/g)	2.44e-04	hrrpm	2.51e+04	Relative	2.88e-02	3.00e-02	Yes
cable_23_insulation	12.9.6	HRR (W/g)	2.34e-04	hrrpm	2.35e+04	Relative	4.61e-03	1.00e-02	Yes
cable_701_insulation	12.9.6	HRR (W/g)	1.27e+04	hrrpm	1.20e+04	Relative	5.64e-03	1.00e-02	Yes
cable_11_jacket	12.9.6	HRR (W/g)	8.10e+03	hrrpm	7.89e+03	Relative	2.54e-02	5.00e-02	Yes
cable_23_jacket	12.9.6	HRR (W/g)	7.34e+03	hrrpm	7.14e+03	Relative	2.76e-02	5.00e-02	Yes
cable_701_jacket	12.9.6	HRR (W/g)	1.41e+04	hrrpm	1.41e+04	Relative	4.49e-03	1.00e-02	Yes
cannon_ball	13.1.1	Distance	2.89e+01	d	2.89e+01	Relative	1.94e-04	1.00e-02	Yes
cascade	15.7.1	Mass	1.00e+00	water mass	9.99e-01	Relative	1.41e-03	2.00e-02	Yes
cascadempi	13.4.4	Mass	4.43e+01	OBST-S-water mass	4.39e+01	Relative	7.68e-03	2.00e-02	Yes
cascadempi	13.4.4	Mass	4.43e+01	OBST-M-water mass	4.38e+01	Relative	1.17e-02	2.00e-02	Yes
cascadempi	13.4.4	Mass	4.43e+01	GEOM-S-water mass	4.42e+01	Relative	2.26e-03	2.00e-02	Yes
clocks_restart	8.10	HRR	1.26e+03	GEOM-M-water mass	4.46e+01	Relative	8.29e-03	2.00e-02	Yes
cell_burn_away	12.3	m_dot	3.25e-03	HR	1.20e+03	Relative	2.11e-05	1.00e-02	Yes
char_oxidation_1	17.1.3	HR	1.01e+03	MLR_PROPANE	3.20e-03	Relative	1.61e-02	4.00e-02	Yes
char_oxidation_1	17.1.3	mass	5.31e-04	HR	9.90e+02	Relative	2.22e-02	3.00e-02	Yes
char_oxidation_1	17.1.3	Delta e_part	-2.41e-01	mass foliage	5.31e-04	Relative	3.77e-04	1.00e-02	Yes
char_oxidation_2	17.1.3	Delta e_gas	2.41e-01	Delta e_part dry needle	-2.41e-01	Relative	1.19e-04	1.00e-01	Yes
char_oxidation_2	17.1.3	mass	2.95e-05	Delta e_gas dry needle	2.41e-01	Relative	1.56e-04	1.00e-01	Yes
char_oxidation_2	17.1.3	mass CO2	2.58e-05	mass fuel gas dry needle	2.95e-05	Relative	1.93e-05	1.00e-02	Yes
char_oxidation_2	17.1.3	mass foliage	1.96e-07	mass CO2 dry needle	2.95e-05	Relative	1.36e-06	1.00e-02	Yes
char_oxidation_2	17.1.3	mass O2	-1.62e-05	dry needle mass	1.96e-07	Relative	1.78e-03	1.00e-02	Yes
char_oxidation_2	17.1.3	H1	1.94e+02	mass O2 dry needle	-1.62e-05	Relative	7.18e-05	1.00e-02	Yes
checkerboard	8.4.4	Mdot	1.57e-02	Q_net	1.94e+02	Relative	8.64e-04	1.00e-02	Yes
circular_burner	74.2	temp	-2.71e+01	MLR_PROPANE	1.57e-02	Relative	7.13e-05	1.00e-02	Yes
condensation_evaporation	10.12.1	pres	-5.80e+03	Temp	-2.70e+01	Relative	5.20e-03	2.00e-02	Yes
condensation_evaporation	10.12.1		-5.78e+03	pres	-5.78e+03	Relative	5.09e-03	2.00e-02	Yes

Case Name	Section	Expected Quantity	Expected Value	Predicted Quantity	Predicted Value	Type of Error	Error	Error Tolerance	Within Tol.
condensation_evaporation	10.12.1	temp	3.64e+01	Temp	3.65e+01	Relative	2.22e-03	2.00e-02	Yes
condensation_evaporation	10.12.1	temp	2.10e+04	temp	2.14e+04	Relative	1.82e-02	2.00e-02	Yes
condensation_radiation	10.12.3	PART	2.80e+01	COND	2.80e+01	Relative	5.52e-04	1.00e-02	Yes
condensation_evaporation	10.12.1	Tgas	3.20e+01	Temp	3.21e+01	Relative	1.90e-03	5.00e-02	Yes
control_test_2	10.12.1	dP	-2.02e+04	pres	-2.00e+04	Relative	6.70e-03	5.00e-02	Yes
control_test_2	18.5.9	Add	3.00e+01	CF Add	3.00e+01	Relative	6.13e-06	1.00e-02	Yes
control_test_2	18.5.9	Multiply	1.00e+01	CF Multiply	1.00e+01	Relative	5.70e-06	1.00e-02	Yes
control_test_2	18.5.9	Subtract	-1.00e+01	CF Subtract	-1.00e+01	Relative	4.10e-05	1.00e-02	Yes
control_test_2	18.5.9	Divide	2.00e+00	CF Divide	2.00e+00	Relative	3.54e-05	1.00e-02	Yes
control_test_2	18.5.9	Power	3.16e+00	CF Power	3.16e+00	Relative	7.06e-04	1.00e-02	Yes
control_test_2	18.5.9	PID	-1.50e+00	CF PID	-1.50e+00	Relative	3.33e-04	1.00e-02	Yes
control_test_2	11.3	Temp	2.95e+02	inner temp	2.96e+02	Relative	1.82e-03	1.00e-02	Yes
couch	9.22	HRR	4.20e+03	HRR	4.82e+03	Relative	1.47e-01	2.00e-01	Yes
cyl_test	8.1.3	temp1	9.24e+01	temp2	9.24e+01	Relative	0.00e+00	1.00e-02	Yes
cyl_test	8.1.3	temp1	7.15e+02	temp1	7.15e+02	Relative	0.00e+00	1.00e-02	Yes
dancing_eddies	21.1.3	press	-9.16e-02	Absolute	-9.17e-02	Absolute	9.03e-05	3.00e-01	Yes
dancing_eddies	21.1.3	press	-9.16e-02	press	-9.18e-02	Absolute	1.74e-04	1.00e-02	Yes
dancing_eddies	21.1.3	pres	-9.16e-02	pres	-9.17e-02	Absolute	9.63e-05	1.00e-02	Yes
device_restart	8.1.0	temp	6.82e+01	temp	6.79e+01	Absolute	3.08e-01	5.00e+00	Yes
devc_interpolation	17.2	u	1.00e+00	U-VEL-3	1.00e+00	Absolute	0.00e+00	1.00e-02	Yes
devc_interpolation	17.2	T	2.50e+01	TMP-3	2.50e+01	Absolute	1.00e+00	1.00e-02	Yes
div_min	8.3.1	div_min	1.00e-12	div_min	4.22e-14	Absolute	1.04e-12	1.00e-10	Yes
div_max	8.3.1	div_max	1.00e-12	div_max	2.30e-14	Absolute	9.77e-13	1.00e-10	Yes
div_min	8.3.2	div_min	-5.00e-16	div_min	-1.30e-17	Absolute	4.87e-16	1.00e-10	Yes
div_max	8.3.2	div_max	5.00e-16	div_max	-1.30e-17	Absolute	5.13e-16	1.00e-10	Yes
div_min	8.3.3	div_min	1.00e-12	div_min	-4.60e-13	Absolute	1.46e-12	1.00e-10	Yes
div_max	8.3.3	div_max	1.00e-12	div_max	5.37e-13	Absolute	4.63e-13	1.00e-10	Yes
divergence_test_1	10.3.2	divergence	9.94e+02	Pressure	9.90e+02	Relative	4.22e-03	2.00e-02	Yes
divergence_test_1	10.3.2	divergence	-5.00e-16	Vdot	1.52e+02	Relative	4.71e-02	8.00e-02	Yes
divergence_test_2	10.3.2	divergence	5.00e-16	Vdot	-1.30e-17	Absolute	9.46e-03	5.00e-02	Yes
divergence_test_3	10.3.2	divergence	1.00e-12	div_min	4.60e-13	Absolute	4.74e-03	1.00e-10	Yes
divergence_test_3	17.2.3	div_max	1.00e-12	div_max	8.82e+00	Relative	6.80e-03	1.00e-02	Yes
door_crack	9.7	Absorption	7.11e+00	ADT	7.06e+00	Relative	6.97e-03	1.00e-02	Yes
door_crack	9.7	Absorption	5.78e-02	LN_M	5.86e-02	Relative	1.32e-02	2.00e-02	Yes
dragon_5a	15.3.3	Mass	5.78e-02	RR-LN_M	5.84e-02	Relative	9.46e-03	2.00e-02	Yes
dragon_5a	15.3.3	Mass	5.78e-02	RR_M	5.78e-02	Relative	5.40e-04	2.00e-02	Yes
droplet_absorption_cart	15.3.3	Mass	5.78e-02	USER_M	5.78e-02	Relative	1.34e-03	2.00e-02	Yes
droplet_absorption_cyl	15.3.3	Flow	1.00e+00	flow_out	9.66e-01	Relative	3.41e-02	5.00e-02	Yes
droplet_distributions	21.1.2	Flow	1.00e+00	flow_out	1.00e+00	Relative	0.00e+00	5.00e-02	Yes
droplet_distributions	21.1.2	HRR	1.00e+00	HRR_1	1.13e+01	Absolute	1.25e+00	3.00e+00	Yes
duct_flow	15.7.2	HRR	1.00e+01	HRR_2	1.12e+01	Absolute	1.21e+00	3.00e+00	Yes
e_coefficient	15.7.2	HRR	1.00e+01	EMISSIVITY	9.00e-03	Absolute	9.00e-03	1.00e-01	Yes
e_coefficient	12.12	Emissivity	1.00e-12	HRR	1.20e+03	Absolute	2.73e-02	1.20e+01	Yes
energy_budget_adiabatic_walls	7.2.1	Net Enthalpy Change	1.00e-12	Q_TOTAL	4.61e+00	Absolute	4.61e+00	1.20e+01	Yes
energy_budget_adiabatic_walls	7.2.1	Q_CONV	1.20e+03	Q_CONV	1.20e+03	Absolute	1.35e+00	1.20e+01	Yes
energy_budget_adiabatic_wo_fuels	13.2.4	HRR	1.20e+03	HRR	1.20e+03	Absolute	7.52e-01	1.20e+01	Yes
energy_budget_cold_walls	7.2.1	HRR	1.20e+03	HRR	1.20e+03	Absolute	1.20e-02	2.00e+01	Yes
energy_budget_cold_walls	7.2.1	Net Enthalpy Change	1.00e-12	Q_TOTAL	5.57e+00	Absolute	5.57e+00	2.00e+01	Yes

Case Name	Section	Expected Quantity	Expected Value	Predicted Quantity	Predicted Value	Type of Error	Error	Error Tolerance	Within Tol.
energy_budget_cold_walls	7.2.1	Losses	1.20e+03	Q_RADD+Q_COND+Q_DIFF	1.21e+03	Absolute	5.56e+00	2.00e+01	Yes
energy_budget_combustion	7.2.6	dp	3.71e+02	3.85e+02	3.68e+02	Relative	5.00e-02	5.00e-02	Yes
energy_budget_dns_100	7.2.4	div	-1.36e-08	-1.36e-08	1.00e-02	Relative	2.97e-04	1.00e-02	Yes
energy_budget_particles	7.2.9	Q_ENTH	-7.50e+01	-7.50e+01	1.00e+02	Relative	1.37e-04	1.00e-02	Yes
energy_budget_mix	7.2.5	Temp	1.00e+02	1.00e+02	1.00e+02	Relative	2.35e-04	1.00e-02	Yes
energy_budget_solid	7.2.7	T_g FDS	9.63e+01	9.65e+01	Relative	1.80e-03	1.00e-02	Yes	
energy_budget_solid	7.2.7	T_w FDS	9.63e+01	9.64e+01	Relative	6.87e-04	1.00e-02	Yes	
energy_budget_solid	7.2.7	P FDS	2.27e+04	2.27e+04	Relative	1.69e-03	1.00e-02	Yes	
enthalpy	12.7	T_slab	1.56e+02	1.56e+02	Relative	7.81e-04	1.00e-02	Yes	
external_control	18.8	T	1.00e+03	1.00e+03	Absolute	0.00e+00	1.00e-03	Yes	
external_control	18.8	V	1.00e-12	3.47e-06	Relative	3.47e-06	1.00e-04	Yes	
fan_test	14.7	pres_1	4.52e+00	4.51e+00	Relative	1.20e-03	4.00e-02	Yes	
fan_test	14.7	pres_2	-4.52e+00	-4.52e+00	Relative	1.12e-03	4.00e-02	Yes	
fan_test	14.7	vflow1	-4.98e-02	-4.90e-02	Relative	1.66e-02	2.00e-02	Yes	
fan_test	14.7	vflow2	4.98e-02	4.90e-02	Relative	1.67e-02	2.00e-02	Yes	
qfan_test	14.8	pres_1	2.26e+00	2.26e+00	Relative	1.99e-03	4.00e-02	Yes	
qfan_test	14.8	pres_2	-2.26e+00	-2.27e+00	Relative	4.27e-03	4.00e-02	Yes	
qfan_test	14.8	vflow1	-4.91e-02	-4.90e-02	Relative	1.69e-03	2.00e-02	Yes	
qfan_test	14.8	vflow2	4.91e-02	4.90e-02	Relative	1.73e-03	2.00e-02	Yes	
qfan_multi	14.9	fpp1	9.03e+00	9.05e+00	Relative	7.75e-03	5.00e-02	Yes	
qfan_multi	14.9	fpp2	2.90e+01	2.90e+01	Relative	1.09e-03	5.00e-02	Yes	
qfan_multi	14.9	vflow1	-2.58e-02	-2.57e-02	Relative	4.17e-03	2.00e-02	Yes	
qfan_multi	14.9	vflow2	2.58e-02	2.57e-02	Relative	4.18e-03	2.00e-02	Yes	
qfan_multi	14.9	vflowpe	7.41e-02	7.41e-02	Relative	8.38e-05	2.00e-02	Yes	
qfan_multi	14.9	fsp1	9.37e+00	9.36e+00	Relative	5.70e-04	2.00e-02	Yes	
qfan_multi	14.9	fsp2	2.94e+01	2.93e+01	Relative	1.84e-03	2.00e-02	Yes	
qfan_multi	14.9	vflows	1.02e-01	1.02e-01	Relative	3.59e-03	2.00e-02	Yes	
FED_FIC	10.9.1	FED (O2 CO2 CO)	5.99e-01	5.99e-01	Relative	6.73e-04	1.00e-02	Yes	
FED_FIC	10.9.1	FED (Asphyxiants)	9.74e-01	9.73e-01	Relative	1.51e-03	1.00e-02	Yes	
FED_FIC	10.9.1	FED (Irritants)	8.26e-03	8.25e-03	Relative	8.75e-04	1.00e-02	Yes	
FED_FIC	10.9.1	FED (All)	5.14e-01	5.13e-01	Relative	1.38e-03	1.00e-02	Yes	
FED_FIC	10.9.1	FIC (O2 CO2 CO)	1.00e-12	1.00e-12	Absolute	0.00e+00	1.00e-02	Yes	
FED_FIC	10.9.1	FIC (Asphyxiants)	1.00e-12	1.00e-12	Absolute	0.00e+00	1.00e-02	Yes	
FED_FIC	10.9.1	FIC (Irritants)	8.57e-01	8.56e-01	Relative	1.26e-03	1.00e-02	Yes	
FED_FIC	10.9.1	FIC (All)	4.29e-01	4.28e-01	Relative	1.06e-03	1.00e-02	Yes	
FED_FIC	10.9.1	FED (O2 CO2 CO)	5.99e-01	5.99e-01	Relative	6.73e-04	1.00e-02	Yes	
FED_FIC	10.9.1	FED (Asphyxiants)	9.74e-01	9.73e-01	Relative	1.51e-03	1.00e-02	Yes	
FED_FIC	10.9.1	FED (Irritants)	8.26e-03	8.25e-03	Relative	8.75e-04	1.00e-02	Yes	
FED_FIC	10.9.1	FED (All)	5.14e-01	5.13e-01	Relative	1.38e-03	1.00e-02	Yes	
FED_FIC_SMX	10.9.1	FIC (O2 CO2 CO)	1.00e-12	1.00e-12	Absolute	0.00e+00	1.00e-02	Yes	
FED_FIC_SMX	10.9.1	FIC (Asphyxiants)	1.00e-12	1.00e-12	Absolute	0.00e+00	1.00e-02	Yes	
FED_FIC_SMX	10.9.1	FIC (Irritants)	8.57e-01	8.56e-01	Relative	1.26e-03	1.00e-02	Yes	
FED_FIC_SMX	10.9.1	FIC (All)	4.29e-01	4.28e-01	Relative	1.06e-03	1.00e-02	Yes	
FED_FIC_SMX	10.9.1	FED (O2 CO2 CO)	1.00e-12	1.00e-12	Absolute	0.00e+00	1.00e-02	Yes	
FED_FIC_SMX	10.9.1	FIC (Asphyxiants)	1.00e-12	1.00e-12	Absolute	0.00e+00	1.00e-02	Yes	
FED_FIC_SMX	10.9.1	FIC (Irritants)	8.57e-01	8.56e-01	Relative	1.26e-03	1.00e-02	Yes	
FED_FIC_SMX	10.9.1	FIC (All)	4.29e-01	4.28e-01	Relative	1.06e-03	1.00e-02	Yes	
FED_FIC_SMX	10.9.1	FED (O2 CO2 CO)	1.00e-05	1.00e-05	Absolute	0.00e+00	1.00e-02	Yes	
FED_FIC_SMX	10.9.1	FIC (Asphyxiants)	1.00e-05	1.00e-05	Absolute	0.00e+00	1.00e-02	Yes	
FED_FIC_SMX	10.9.1	FIC (Irritants)	3.00e-05	3.00e-05	Relative	8.16e-04	1.00e-02	Yes	
FED_CO_HCN	10.9.2	MU_0	1.00e-05	1.00e-05	Absolute	0.00e+00	1.00e-02	Yes	
species_props	10.1	MU_1	3.00e-05	3.00e-05	Absolute	0.00e+00	1.00e-02	Yes	
species_props	10.1	MU_2	1.59e-05	1.59e-05	Absolute	4.21e-08	1.00e-02	Yes	

Case Name	Section	Expected Quantity	Expected Value	Predicted Quantity	Predicted Value	Type of Error	Error	Error Tolerance	Within Tol.
species_props	10.1	MU_3	2.18e-05	MU_3	2.18e-05	Absolute	4.29e-08	1.00e-02	Yes
species_props	10.1	MU_4	1.64e-05	MU_4	1.64e-05	Absolute	3.59e-08	1.00e-02	Yes
species_props	10.1	K_0	1.00e-02	K_0	1.00e-02	Relative	0.00e+00	1.00e-02	Yes
species_props	10.1	K_1	3.00e-02	K_1	3.00e-02	Relative	0.00e+00	1.00e-02	Yes
species_props	10.1	K_2	1.59e-02	K_2	1.59e-02	Relative	2.65e-03	1.00e-02	Yes
species_props	10.1	K_3	2.18e-02	K_3	2.18e-02	Relative	1.97e-03	1.00e-02	Yes
species_props	10.1	K_4	1.64e-02	K_4	1.64e-02	Relative	2.19e-03	1.00e-02	Yes
species_props	10.1	CP_0	1.00e+00	CP_0	1.00e+00	Relative	0.00e+00	1.00e-02	Yes
species_props	10.1	CP_1	3.00e+00	CP_1	3.00e+00	Relative	0.00e+00	1.00e-02	Yes
species_props	10.1	CP_2	1.67e+00	CP_2	1.67e+00	Relative	2.00e-03	1.00e-02	Yes
species_props	10.1	CP_3	2.33e+00	CP_3	2.33e+00	Relative	1.14e-03	1.00e-02	Yes
species_props	10.1	CP_4	1.80e+00	CP_4	1.80e+00	Relative	0.00e+00	1.00e-02	Yes
dp_exact	3.9.2	dH_FDS	2.81e+04	dH_FDS	2.81e+04	Relative	5.14e-02	1.00e-02	Yes
dp_exact	3.9.2	dp_FDS	6.28e+04	dp_FDS	6.28e+04	Relative	6.20e-06	1.00e-05	Yes
flat_fire	13.1.9	x	8.91e+01	x1	8.77e+01	Relative	1.60e-02	2.00e-02	Yes
flat_fire	13.1.9	z	-7.10e+00	z1	-7.11e+00	Relative	6.51e-03	1.00e-02	Yes
flat_fire	13.1.9	u	-3.84e+02	u1	-3.85e+02	Relative	1.77e-03	1.00e-02	Yes
flat_fire	13.1.9	w	-8.41e+00	w1	-8.28e+00	Relative	1.59e-02	2.00e-02	Yes
flat_fire	13.1.9	z	-7.10e+00	z1	-7.11e+00	Relative	6.51e-03	1.00e-02	Yes
flow_rate	18.3.2	Water	1.00e+01	Water mass	9.99e+00	Relative	1.47e-03	1.00e-02	Yes
Nozzles	18.3.2	Nozzles	4.00e+00	Nozzles	4.00e+00	Relative	0.00e+00	0.00e+00	Yes
Water	13.5	Water	1.25e+01	Water mass	1.25e+01	Relative	6.64e-04	1.00e-02	Yes
Nozzles 1	13.5	Nozzles 1	3.00e+00	Nozzles 1	3.00e+00	Relative	0.00e+00	0.00e+00	Yes
Nozzles 2	13.5	Nozzles 2	1.00e+00	Nozzles 2	1.00e+00	Relative	0.00e+00	0.00e+00	Yes
PDF	15.4.4	PDF	5.00e-04	PDF rods	5.00e-04	Relative	2.17e-16	1.00e-02	Yes
Mass	15.4.4	Mass	7.00e-01	Mass 2	7.02e-01	Relative	2.99e-03	1.00e-02	Yes
HYDROGEN	12.1.1	Mass	3.00e+00	HYDROGEN	3.00e+00	Relative	3.87e-05	1.00e-02	Yes
Q	7.2.9	Q	8.75e+01	HRR	8.75e+01	Relative	0.00e+00	1.00e-03	Yes
HRR	16.6	HRR	8.33e+05	Nozzles 1	8.33e+05	Relative	3.73e-03	1.00e-02	Yes
Total	7.1.8	Total	5.69e-01	Total	5.70e-01	Relative	3.81e-04	1.00e-03	Yes
NITROGEN	7.1.8	NITROGEN	4.34e-01	NITROGEN	4.34e-01	Relative	3.78e-04	1.00e-03	Yes
OXYGEN	7.1.8	OXYGEN	1.32e-01	OXYGEN	1.32e-01	Relative	3.81e-04	1.00e-03	Yes
CARBON DIOXIDE	7.1.8	CARBON DIOXIDE	3.37e-04	CARBON DIOXIDE	3.37e-04	Relative	3.79e-04	1.00e-03	Yes
WATER VAPOR	7.1.8	WATER VAPOR	3.38e-03	WATER VAPOR	3.38e-03	Relative	4.18e-04	1.00e-03	Yes
Mass	13.4.2	Mass	1.00e+01	Mass	1.00e+01	Relative	5.41e-04	1.00e-02	Yes
m1	13.4.2	m1	1.00e+01	m2	1.00e+01	Relative	5.41e-04	1.00e-02	Yes
Mass	13.4.2	Mass	1.00e+01	m3	1.00e+01	Relative	5.41e-04	1.00e-02	Yes
Mass	13.4.2	Mass	1.00e+01	m4	1.00e+01	Relative	5.41e-04	1.00e-02	Yes
E_OB	9.1.2	E_OB	2.88e+01	E GE	2.88e+01	Relative	4.94e-04	1.00e-03	Yes
HF_OB	9.1.2	HF_OB	2.84e+01	HF GE	2.84e+01	Relative	1.11e-05	1.00e-03	Yes
Energy Flow	9.1.3	Energy Flow	2.86e+01	E	2.91e+01	Relative	1.77e-02	3.00e-02	Yes
Heat Flux	9.1.3	Heat Flux	2.84e+01	HF	2.91e+01	Relative	2.50e-02	3.00e-02	Yes
q_net	9.16	q_net	2.16e+01	DIAG WALL	2.17e+01	Relative	8.26e-03	2.00e-02	Yes
q_net	9.16	q_net	2.16e+01	DIAG-1	2.77e+01	Relative	1.59e-02	2.00e-02	Yes
q_net	9.16	q_net	2.16e+01	DIAG-2	5.94e+00	Relative	7.24e-01	1.00e+00	Yes
q_net	9.16	q_net	2.16e+01	WALL	2.14e+01	Relative	9.79e-03	8.00e-01	Yes

Case Name	Section	Expected Quantity	Expected Value	Predicted Quantity	Predicted Value	Type of Error	Error	Error Tolerance	Within Tol.
geom_restart	16.6	S_15	6.94e+01	S_15	6.92e+01	Relative	6.54e-04	1.00e-03	Yes
geom_sprk_mass	13.4.1	Mass	1.05e+01	m OBST	1.04e+01	Relative	8.08e-03	2.00e-02	Yes
geom_sprk_mass	13.4.1	Mass	1.05e+01	m GEOM	1.04e+01	Relative	8.07e-03	2.00e-02	Yes
geom_stretched_grid	6.2	psolver mesh 1	3.00e+00	psolver mesh 1	3.00e+00	Relative	0.00e+00	1.00e-03	Yes
geom_stretched_grid	6.2	psolver mesh 2	1.00e-12	psolver mesh 2	1.00e-12	Relative	0.00e+00	1.00e-03	Yes
ground_vegetation_conv	17.4.4	T_A	2.71e+02	temp 1A	2.62e+02	Relative	3.31e-02	5.00e-02	Yes
ground_vegetation_conv	17.4.4	T_A	2.71e+02	temp 2A	2.66e+02	Relative	1.94e-02	5.00e-02	Yes
ground_vegetation_conv	17.4.4	T_B	2.43e+02	temp 1B	2.32e+02	Relative	4.54e-02	5.00e-02	Yes
ground_vegetation_conv	17.4.4	T_B	2.43e+02	temp 2B	2.38e+02	Relative	2.23e-02	5.00e-02	Yes
ground_vegetation_drag	17.4.2	pres 1	6.25e-01	pres 2	5.99e-01	Relative	4.15e-02	5.00e-02	Yes
ground_vegetation_load	17.4.1	Mass 1	3.28e-01	Mass 1	3.28e-01	Relative	1.75e-04	1.50e-01	Yes
ground_vegetation_load	17.4.1	Mass 2	3.28e-01	Mass 2	3.29e-01	Relative	4.57e-04	1.50e-01	Yes
ground_vegetation_radi	17.4.3	HF	1.17e+01	hf 1	1.27e+01	Relative	8.70e-01	2.00e-01	Yes
hallways	22.10.1	Q_ENTH	3.65e-01	Q_TOTAL	2.17e-01	Absolute	1.47e-01	3.00e+00	Yes
heat_conduction_a	11.1	Front	1.19e+02	Front	1.19e+02	Relative	3.18e-05	1.00e-02	Yes
heat_conduction_a	11.1	4 cm	7.28e+01	4 cm	7.27e+01	Relative	1.57e-03	1.00e-02	Yes
heat_conduction_a	11.1	Back	4.21e+01	Back	4.20e+01	Relative	3.05e-04	1.00e-02	Yes
heat_conduction_b	11.1	Front	1.19e+02	Front	1.19e+02	Relative	4.61e-05	1.00e-02	Yes
heat_conduction_b	11.1	4 cm	1.15e+02	4 cm	1.15e+02	Relative	1.09e-04	1.00e-02	Yes
heat_conduction_b	11.1	Back	1.13e+02	Back	1.13e+02	Relative	8.65e-05	1.00e-02	Yes
heat_conduction_c	11.1	Front	1.18e+02	Front	1.18e+02	Relative	5.37e-05	1.00e-02	Yes
heat_conduction_c	11.1	4 cm	1.18e+02	4 cm	1.18e+02	Relative	8.49e-05	1.00e-02	Yes
heat_conduction_c	11.1	Back	1.17e+02	Back	1.17e+02	Relative	8.26e-05	1.00e-02	Yes
heat_conduction_d	11.1	Front	6.04e+01	Front	6.04e+01	Relative	2.68e-04	1.00e-02	Yes
heat_conduction_d	11.1	4 cm	5.85e+01	4 cm	5.84e+01	Relative	3.16e-04	1.00e-02	Yes
heat_conduction_d	11.1	Back	5.74e+01	Back	5.73e+01	Relative	2.23e-04	1.00e-02	Yes
heat_surf	11.2	cart_front	1.59e+02	cart_front	1.59e+02	Relative	5.92e-04	1.00e-02	Yes
heat_surf	11.2	cyl_front	1.82e+02	cyl_front	1.82e+02	Relative	1.17e-03	1.00e-02	Yes
heat_surf	11.2	sph_front	1.10e+02	sph_front	1.10e+02	Relative	1.80e-03	1.00e-02	Yes
heat_surf	11.2	cart_back	4.99e+00	cart_back	4.94e+00	Relative	1.08e-02	2.00e-02	Yes
heat_surf	11.2	cyl_back	2.00e+01	cyl_back	1.97e+01	Relative	1.40e-02	2.00e-02	Yes
heat_surf	11.2	sph_back	4.54e+01	sph_back	4.48e+01	Relative	1.23e-02	2.00e-02	Yes
Temp	3.8.2	Temp	2.50e+01	maxT	2.50e+01	Absolute	0.00e+00	1.00e-06	Yes
Temp	3.8.2	Temp	2.50e+01	mint	2.50e+01	Absolute	0.00e+00	1.00e-06	Yes
H_S	3.8.2	H_S	1.00e-12	maxHS	7.57e-13	Absolute	2.43e-13	1.00e-06	Yes
helium_id_isothermal	3.8.2	H_S	1.00e-12	minHS	1.72e-14	Absolute	9.83e-13	1.00e-06	Yes
helium_id_isothermal	3.8.2	W	1.00e+00	maxW	1.00e+00	Absolute	0.00e+00	1.00e-06	Yes
helium_id_isothermal	3.8.2	W	1.00e+00	minW	1.00e+00	Absolute	1.00e-08	1.00e-06	Yes
helium_id_isothermal	3.9.1	Temp	2.50e+01	maxT	2.50e+01	Absolute	0.00e+00	1.00e-06	Yes
helium_id_isothermal	3.9.1	Temp	2.50e+01	mint	2.50e+01	Absolute	3.55e+02	1.00e-06	Yes
helium_id_isothermal	3.9.1	H_S	3.55e+02	maxHS	3.55e+02	Absolute	0.00e+00	1.00e-06	Yes
helium_id_isothermal	3.9.1	H_S	3.55e+02	minHS	3.55e+02	Absolute	0.00e+00	1.00e-06	Yes
helium_id_isothermal	3.9.1	W	1.00e+00	maxW	1.00e+00	Absolute	0.00e+00	1.00e-06	Yes
helium_id_isothermal	3.9.1	W	1.00e+00	minW	1.00e+00	Absolute	1.00e-08	1.00e-06	Yes
helium_id_isothermal	3.8.2	Isothermal	2.00e+01	maxT	2.00e+01	Absolute	1.20e-04	1.00e-02	Yes
helium_id_isothermal	3.8.2	Isothermal	-2.00e+01	mint	-2.00e+01	Absolute	1.90e-03	1.00e-02	Yes
helium_id_isothermal	3.8.3	Isothermal	2.00e+01	maxT	2.00e+01	Absolute	2.55e-02	5.00e-02	Yes

Case Name	Section	Expected Quantity	Expected Value	Predicted Quantity	Predicted Value	Type of Error	Error	Error Tolerance	Within Tol.
helium_air_jet_floor	3.8.3	Isothermal	-2.00e+01	minIT	-2.00e+01	Absolute	1.00e-06	5.00e-02	Yes
HoC_Ideal	10.7	Ideal	8.75e-04	MLR_METHANE	8.75e-04	Relative	3.74e-06	1.00e-04	Yes
HoC_Nonideal	10.7	Non-ideal	8.00e-04	MLR_METHANE	8.00e-04	Relative	0.00e+00	1.00e-04	Yes
hole	8.7	HRR	9.07e+01	HR	9.07e+01	Absolute	0.00e+00	1.00e-04	Yes
hot_spheres	9.6	Rad Loss 1	-6.23e-02	rad loss 1	-6.10e-02	Relative	2.11e-02	3.00e-02	Yes
hot_spheres	9.6	Rad Loss 2	-2.98e+01	rad loss 2	-2.82e+01	Relative	5.34e-02	6.00e-02	Yes
hot_spheres	9.6	Rad Flux	2.03e+01	rad flux	1.97e+01	Relative	2.56e-02	4.00e-02	Yes
hot_spheres	9.6	Intensity	8.10e+01	UII	8.07e+01	Relative	3.84e-03	1.00e-02	Yes
hrppuv_reac_arrhenius	10.5	hrppuv	2.98e+00	q1	2.98e+00	Relative	0.00e+00	1.00e-03	Yes
hrppuv_reac_extinction	10.5	hrppuv	3.78e+03	q1	3.78e+03	Relative	1.32e-07	1.00e-05	Yes
hrppuv_reac_parallel	10.5	hrppuv	6.80e+03	q1+q2	6.80e+03	Relative	1.32e-07	1.00e-05	Yes
hrppuv_reac_parallel_2	10.5	hrppuv	6.92e+03	q1+q2	6.92e+03	Relative	1.45e-07	1.00e-05	Yes
hrppuv_reac_series	10.5	hrppuv	4.30e+03	q1+q2+q3	4.30e+03	Relative	9.30e-09	1.00e-05	Yes
hrppuv_reac_simple	10.5	hrppuv	3.78e+03	q1	3.78e+03	Relative	0.00e+00	1.00e-05	Yes
hrppuv_reac_single	10.5	hrppuv	6.44e+03	q1	6.44e+03	Relative	1.40e-07	1.00e-05	Yes
hrppuv_reac_soot	10.5	hrppuv	2.23e+03	q1+q2	2.23e+03	Relative	4.48e-09	1.00e-05	Yes
ht1d_pile	11.9.8	Temperature	-7.02e+03	Left	-7.03e+03	Relative	1.41e-03	1.00e-02	Yes
ht3d_beam_heating	11.9.8	Temperature	-7.02e+03	Left	-7.03e+03	Relative	1.38e-03	1.00e-02	Yes
ht3d_beam_heating	11.9.2	T	5.69e+00	wall temp	5.69e+00	Relative	2.20e-02	4.00e-02	Yes
ht3d_demo	11.9.2	T	5.62e+00	wall temp	5.64e+00	Relative	2.91e-03	4.00e-02	Yes
ht3d_energy_conservation	11.9.1	E3D	8.55e+00	Q_net	8.56e+00	Relative	6.92e-04	1.00e-02	Yes
ht3d_energy_conservation	11.9.1	E3D	9.57e+01	Q_net	9.60e+01	Relative	5.82e-03	1.00e-02	Yes
ht3d_energy_conservation	11.9.1	E3D	9.58e+01	Q_net	9.61e+01	Relative	6.91e-03	1.00e-02	Yes
ht3d_energy_conservation	11.9.1	E3D	9.58e+01	Q_net	9.61e+01	Relative	2.51e-03	1.00e-02	Yes
ht3d_energy_conservation	11.9.1	H1	2.42e+00	Q_net	2.43e+00	Relative	3.86e-03	1.00e-02	Yes
ht3d_energy_conservation	11.9.1	H1	3.10e+00	Q_net	3.11e+00	Relative	3.11e-03	1.00e-02	Yes
ht3d_energy_conservation	11.9.1	H1	3.56e+00	Q_net	3.60e+00	Relative	2.51e-03	1.00e-02	Yes
ht3d_energy_conservation	11.9.1	H1	2.81e+01	Q_net	2.84e+01	Relative	4.97e-04	1.00e-02	Yes
ht3d_energy_conservation	11.9.1	H1	9.44e+02	Q_net	9.40e+02	Relative	2.46e-03	1.00e-02	Yes
ht3d_ibeam	11.9.1	Q_net	-9.00e-04	Q_net	-8.99e-04	Relative	2.94e-03	1.00e-02	Yes
ht3d_ibeam	11.9.5	Ts_x195_40	7.64e-02	Relative	7.64e+02	Relative	9.75e-05	8.00e-02	Yes
ht3d_ibeam	11.9.5	Ts_x145_30	5.93e+02	Relative	5.92e+02	Relative	1.45e-03	8.00e-02	Yes
ht3d_ibeam	11.9.5	Ts_x095_20	3.62e+02	Relative	3.58e+02	Relative	9.70e-03	8.00e-02	Yes
ht3d_ibeam	11.9.5	Ts_x025_40	2.89e+02	Relative	2.81e+02	Relative	3.00e-02	8.00e-02	Yes
ht3d_ibeam	11.9.5	Ts_x195_1	2.53e+02	Relative	2.49e+02	Relative	1.47e-02	8.00e-02	Yes
ht3d_ibeam	11.9.5	Ts_x025_1	1.52e+02	Relative	1.47e+02	Relative	3.16e-02	8.00e-02	Yes
ht3d_ibeam	11.9.5	Mass	2.12e-01	Relative	2.12e-01	Relative	2.19e-04	1.00e-02	Yes
ht3d_ibeam	11.9.5	Mass	2.12e-01	Relative	2.12e-01	Relative	2.35e-03	1.00e-02	Yes
ht3d_ibeam	11.9.6	T-1	2.00e+01	Relative	2.00e+01	Relative	1.00e-03	1.00e-03	Yes
ht3d_ibeam	11.9.6	Ts	3.50e+02	Relative	3.50e+02	Relative	2.62e-04	1.00e-03	Yes
Ideal_Q	10.2.6	Ideal Q	4.52e+01	FDS Q	4.52e+01	Relative	0.00e+00	1.00e-02	Yes
Ideal_T	10.2.6	Ideal T	5.89e+01	FDS T	5.89e+01	Relative	3.40e-08	1.00e-02	Yes
Ideal Duct 1	14.5	3.00e+00	FDS Duct 1	3.00e+00	Relative	9.13e-04	5.00e-03	Yes	
Ideal Duct 2	14.5	1.00e-12	FDS Duct 2	1.00e-12	Relative	0.00e+00	5.00e-03	Yes	
Ideal Duct 3	14.5	3.00e+00	FDS Duct 3	3.00e+00	Relative	0.00e+00	5.00e-03	Yes	
Ideal Top	14.4	1.00e+01	FDS Top	1.00e+01	Relative	4.34e-04	1.00e-02	Yes	

Case Name	Section	Expected Quantity	Expected Value	Predicted Quantity	Predicted Value	Type of Error	Error	Error Tolerance	Within Tol.
HVAC_energy_pressure	14.4	Ideal Bottom	1.00e+00	FDS Bottom	1.00e+00	Relative	0.00e+00	1.00e-02	Yes
HVAC_energy_pressure	14.4	Ideal Delta P	4.36e+01	FDS Delta P	4.36e+01	Relative	8.05e-04	1.00e-02	Yes
HVAC_energy_pressure	14.4	Ideal Enthalpy	3.07e+02	FDS Energy	3.07e+02	Relative	1.92e-06	1.00e-02	Yes
HVAC_filter	14.6	Ideal Filter	1.16e-03	FDS Filter	1.17e-03	Absolute	1.83e-08	1.00e-05	Yes
HVAC_filter	14.6	Ideal Compartment	1.00e-12	FDS Compartment	7.03e-08	Absolute	7.03e-08	1.00e-05	Yes
HVAC_filter	14.6	Ideal Velocity	1.85e+00	FDS Velocity	1.86e+00	Relative	9.06e-03	7.00e-02	Yes
HVAC_filter	14.6	Ideal Temperature	1.99e+01	FDS Temperature	1.99e+01	Relative	2.09e-05	1.00e-02	Yes
HVAC_filter	14.6	Ideal Pressure	-1.44e+02	FDS Pressure	-1.44e+02	Relative	1.57e-03	1.00e-02	Yes
HVAC_flow_loss	14.1	Ideal 1 m/s	1.00e+00	FDS 1 m/s duct	1.01e+00	Relative	9.14e-03	2.00e-02	Yes
HVAC_flow_loss	14.1	Ideal 2 m/s	2.00e+00	FDS 2 m/s duct	1.99e+00	Relative	4.69e-03	2.00e-02	Yes
HVAC_flow_loss	14.1	Ideal 3 m/s	3.00e+00	FDS 3 m/s duct	3.00e+00	Relative	0.00e+00	2.00e-02	Yes
HVAC_leak_exponent	14.10.7	Ideal 1	-1.60e+01	L1	-1.60e+01	Relative	1.33e-03	1.00e-02	Yes
HVAC_leak_exponent	14.10.7	Ideal 2	-1.18e+01	L2	-1.18e+01	Relative	7.31e-04	1.00e-02	Yes
HVAC_leak_exponent	14.10.7	Ideal 3	-1.27e+01	L3	-1.27e+01	Relative	1.09e-03	1.00e-02	Yes
HVAC_leak_exponent	14.10.7	Vdot (m3/s)	1.09e-01	Vdot	1.09e-01	Relative	4.37e-04	1.00e-02	Yes
HVAC_leak_exponent_2	14.10.5	Mass	1.00e-12	TM	2.43e-07	Absolute	2.43e-07	1.00e-05	Yes
leak_enthalpy	14.10.5	Energy	3.60e+02	TE	3.62e+02	Relative	5.71e-03	1.00e-02	Yes
HVAC_mass_conservation	14.3	Ideal Species 1	5.82e-01	FDS Species 1	5.82e-01	Relative	1.74e-05	1.00e-02	Yes
HVAC_mass_conservation	14.3	Ideal Total	1.16e+00	FDS Total	1.16e+00	Relative	0.00e+00	1.00e-02	Yes
HVAC_mass_transport	14.12.2	Ideal Species 1	1.00e+00	FDS Species 1	1.00e+00	Relative	2.62e-05	1.00e-02	Yes
HVAC_mass_transport_1	14.12.3	Ideal Species 1	1.00e+00	FDS Species 1	1.00e+00	Relative	2.62e-05	1.00e-02	Yes
HVAC_mass_transport_1	14.12.3	Ideal Species 1	1.00e+00	FDS Species 1	1.00e+00	Relative	2.62e-05	1.00e-02	Yes
HVAC_mass_transport_2	14.12.3	Ideal Species 1	1.00e+00	FDS Species 1	1.00e+00	Relative	2.61e-05	1.00e-02	Yes
HVAC_mass_transport_3	14.12.3	Ideal Species 1	1.00e+00	FDS Species 1	1.00e+00	Relative	2.58e-05	1.00e-02	Yes
HVAC_mass_transport_4	14.12.3	Ideal Species 1	1.00e+00	FDS Species 1	1.00e+00	Relative	2.57e-05	1.00e-02	Yes
HVAC_mass_transport_branch	14.12.7	Ideal Outlet A	1.00e+00	FDS Outlet A	1.00e+00	Relative	4.31e-05	1.00e-02	Yes
HVAC_mass_transport_branch	14.12.7	Ideal Outlet B	1.00e+00	FDS Outlet B	1.00e+00	Relative	0.00e+00	1.00e-02	Yes
HVAC_mass_transport_branch	14.12.4	Ideal Mass_total	1.00e+00	FDS Mass_total	1.00e+00	Relative	0.00e+00	1.00e-02	Yes
HVAC_mass_transport_branch	14.12.4	Ideal Mass_left	5.00e-01	FDS Mass_left	5.00e-01	Relative	0.00e+00	1.00e-02	Yes
HVAC_mass_transport_branch	14.12.4	Ideal Mass_right	5.00e-01	FDS Mass_right	5.00e-01	Relative	0.00e+00	1.00e-02	Yes
HVAC_mass_transport_branch	14.12.4	Ideal Species 1_left	2.92e-01	FDS Species 1_left	2.92e-01	Relative	3.59e-04	1.00e-02	Yes
HVAC_mass_transport_branch	14.12.4	Ideal Species 1_right	2.92e-01	FDS Species 1_right	2.92e-01	Relative	4.14e-04	1.00e-02	Yes
HVAC_mass_transport_branch	14.12.4	Ideal Species 2_left	2.08e-01	FDS Species 2_left	2.08e-01	Relative	5.03e-04	1.00e-02	Yes
HVAC_mass_transport_branch	14.12.4	Ideal Species 2_right	2.08e-01	FDS Species 2_right	2.08e-01	Relative	5.80e-04	1.00e-02	Yes
HVAC_mass_transport_branch	14.12.5	Ideal Species 1	6.00e-01	FDS Species 1	6.00e-01	Relative	4.64e-04	1.00e-02	Yes
HVAC_mass_transport_branch	14.12.5	Ideal Species 2	4.00e-01	FDS Species 2	4.00e-01	Relative	6.96e-04	1.00e-02	Yes
HVAC_mass_transport_branch	14.12.6	Ideal Species 1	6.00e-01	FDS Species 1	6.00e-01	Relative	4.01e-04	1.00e-02	Yes
HVAC_mass_transport_branch	14.12.6	Ideal Species 2	4.00e-01	FDS Species 2	4.00e-01	Relative	6.01e-04	1.00e-02	Yes
HVAC_mass_transport_branch	14.12.8	Ideal Species 1	5.00e-01	FDS Species 1	5.00e-01	Absolute	0.00e+00	1.00e-02	Yes
HVAC_mass_transport_branch	14.12.8	Ideal Species 2	5.00e-01	FDS Species 2	5.00e-01	Absolute	0.00e+00	1.00e-02	Yes
HVAC_mass_transport_branch	14.12.8	Ideal Species 3	1.00e-12	FDS Species 3	2.34e-15	Absolute	9.98e-13	1.00e-02	Yes
HVAC_mass_transport_branch	14.12.9	Ideal Enthalpy	2.93e+02	FDS Enthalpy	2.93e+02	Relative	1.01e-06	1.00e-02	Yes
HVAC_mass_transport_branch	14.12.9	Ideal Delta P	8.93e-01	FDS Delta P	8.92e-01	Relative	4.88e-04	1.00e-02	Yes
HVAC_mass_transport_combine	14.2	Ideal 1 m/s	1.00e+00	FDS 1 m/s duct	1.00e+00	Relative	7.73e-05	1.00e-02	Yes
HVAC_mass_transport_combine	14.2	Ideal 2 m/s	2.00e+00	FDS 2 m/s duct	2.00e+00	Relative	2.02e-04	1.00e-02	Yes
HVAC_tee_loss_1	14.2	Ideal 3 m/s	3.00e+00	FDS 3 m/s duct	3.00e+00	Relative	0.00e+00	1.00e-02	Yes
HVAC_tee_loss_2	14.2	Ideal 1.5 m/s A	1.50e+00	E 1	1.49e+00	Relative	7.16e-03	1.00e-02	Yes
HVAC_tee_loss_2	14.2	Ideal 1.5 m/s B	1.50e+00	E 2	1.51e+00	Relative	7.23e-03	1.00e-02	Yes

Case Name	Section	Expected Quantity	Expected Value	Predicted Quantity	Predicted Value	Type of Error	Error	Error Tolerance	Within Tol.	
HVAC_tee_loss_2	14.2	Ideal 3 m/s	3.00e+00	S 1	3.00e+00	Relative	0.00e+00	1.00e-02	Yes	
insulated_steele_pipe	11.5	Temp	2.60e+02	Temperature	2.59e+02	Relative	3.37e-03	1.00e-02	Yes	
isentropic	7.2.2	Density_1	1.35e+02	density_1	1.35e+02	Relative	1.80e-04	1.00e-02	Yes	
isentropic	7.2.2	Density_2	1.32e+00	density_2	1.32e+00	Relative	8.32e-07	1.00e-02	Yes	
isentropic	7.2.2	Pressure_1	1.32e+00	pressure_1	1.32e+00	Relative	8.32e-07	1.00e-02	Yes	
isentropic	7.2.2	Pressure_2	1.96e+04	pressure_2	1.96e+04	Relative	1.18e-04	1.00e-02	Yes	
isentropic	7.2.2	Temperature_1	1.96e+04	temperature_1	1.96e+04	Relative	2.21e-05	1.00e-02	Yes	
isentropic	7.2.2	Temperature_2	3.52e+01	temperature_2	3.52e+01	Relative	1.65e-04	1.00e-02	Yes	
isentropic	7.2.2	Enthalpy_1	3.52e+01	enthalpy_1	3.52e+01	Relative	2.79e-05	1.00e-02	Yes	
isentropic	7.2.2	Enthalpy_2	4.23e+02	enthalpy_2	4.23e+02	Relative	1.91e-05	1.00e-02	Yes	
isentropic	7.2.2	Density_1	4.23e+02	density_1	4.23e+02	Relative	3.50e-06	1.00e-02	Yes	
isentropic2	7.2.3	Density_1	1.37e+00	density_1	1.36e+00	Relative	6.90e-04	1.00e-02	Yes	
isentropic2	7.2.3	Density_2	1.37e+00	density_2	1.36e+00	Relative	6.89e-04	1.00e-02	Yes	
isentropic2	7.2.3	Pressure_1	6.43e+04	pressure_1	6.29e+04	Relative	2.16e-02	3.00e-02	Yes	
isentropic2	7.2.3	Pressure_2	6.43e+04	pressure_2	6.40e+04	Relative	4.33e-03	3.00e-02	Yes	
isentropic2	7.2.3	Temperature_1	1.36e+02	temperature_1	1.35e+02	Relative	1.79e-05	3.00e-02	Yes	
isentropic2	7.2.3	Temperature_2	1.36e+02	temperature_2	1.35e+02	Relative	3.50e-03	3.00e-02	Yes	
isentropic2	7.2.3	Enthalpy_1	5.80e+02	enthalpy_1	5.75e+02	Relative	8.40e-03	1.00e-02	Yes	
isentropic2	7.2.3	Enthalpy_2	5.80e+02	enthalpy_2	5.79e+02	Relative	1.68e-03	1.00e-02	Yes	
lapse_rate	8.4	T	1.96e+01	T	1.96e+01	Relative	1.49e-05	1.00e-03	Yes	
lapse_rate	8.4	P	1.01e+05	P	1.01e+05	Relative	5.82e-07	1.00e-03	Yes	
layer	8.9	z_int	6.61e-01	z_int	5.87e-01	Relative	1.12e-01	2.00e-01	Yes	
layer	8.9	T_low	3.02e+01	T_low	3.10e+01	Relative	2.56e-02	1.00e-01	Yes	
layer	8.9	T_up	7.29e+01	T_up	7.26e+01	Relative	4.86e-03	1.00e-01	Yes	
layer	8.9	pres_diff	1.91e+02	pres_diff	1.90e+02	Absolute	2.48e-02	1.90e+00	Yes	
leak_test	14.10.1	pres_1	-1.91e+02	pres_1	-1.17e-02	Absolute	1.17e-02	1.90e+00	Yes	
leak_test	14.10.2	pres_2	1.00e-12	pres_2	4.80e+02	Relative	3.26e-04	1.00e-02	Yes	
leak_test	14.10.3	p1	4.80e+02	p1	2.40e+02	Relative	8.80e-04	1.00e-02	Yes	
leak_test	14.10.3	p2	2.40e+02	p2	4.80e+02	Relative	3.33e-04	1.00e-02	Yes	
leak_test	14.10.3	p1	4.80e+02	p1	2.40e+02	Relative	9.03e-04	1.00e-02	Yes	
leak_test	14.10.3	p2	2.40e+02	p2	4.80e+02	Relative	4.29e-02	5.00e-02	Yes	
leak_test	14.10.4	p	3.44e+02	p	5.01e-02	Relative	6.27e+04	1.00e-02	Yes	
leak_test	14.10.4	mass	6.29e+04	mass	N-HEXANE	Relative	2.54e-04	1.00e-02	Yes	
leak_test	17.5.1	Fuel Mass	1.27e+00	Fuel Mass	2.05e-01	Relative	7.44e-04	1.00e-02	Yes	
leak_test	9.2.6	Water Mass	2.05e-01	Water Mass	1.00e-12	Relative	0.00e+00	1.00e-02	Yes	
leak_test	9.2.6	m_T_low	1.00e-12	m_T_low	5.99e+00	Relative	1.30e-03	1.00e-02	Yes	
leak_test	15.1.3	m_T_high	6.00e+00	m_T_high	Yield	5.01e-02	Relative	1.26e-03	1.00e-02	Yes
leak_test	15.1.3	Yield	5.00e-02	Yield	5.01e-02	Relative	9.88e+01	1.18e-02	Yes	
leak_test	15.1.2	pwt	1.00e+02	pwt	1.60e-03	Relative	3.13e-04	1.00e-02	Yes	
LS4 Ember Yield	22.10.10	mdot	1.60e-03	mdot	1.60e-03	Relative	3.82e-04	1.00e-02	Yes	
mass flux comparison	22.10.10	MF vent	1.60e-03	MF vent	-4.00e+00	Relative	0.00e+00	1.00e-02	Yes	
mass heat wall device test	7.2.8	MF open	4.00e+00	MF open	4.00e+00	Relative	5.28e-04	1.00e-02	Yes	
mass heat wall device test	7.2.8	HF vent	-3.00e+02	HF vent	3.00e+02	Relative	1.71e-04	1.00e-02	Yes	
mass heat wall device test	7.2.8	HF open	3.00e+02	HF open	1.98e-04	Relative	0.00e+00	1.00e-02	Yes	
mass heat wall device test	7.2.8	MF vent	-4.00e+00	MF vent	4.00e+00	Relative	2.10e-03	1.00e-02	Yes	
mass heat wall device test	7.2.8	MF open	4.00e+00	MF open	3.99e+00	Relative	0.00e+00	1.00e-02	Yes	

Case Name	Section	Expected Quantity	Expected Value	Predicted Quantity	Predicted Value	Type of Error	Error	Error Tolerance	Within Tol.
mass_heat_wall_device_test_2	7.2.8	HF vent	-3.00e+02	HF vent	-3.00e+02	Relative	1.00e-05	1.00e-02	Yes
mass_heat_wall_device_test_2	7.2.8	HF open	3.00e+02	HF open	2.99e+02	Relative	2.22e-03	1.00e-02	Yes
methane_flame	10.3	CO2	2.78e-02	pCO2	2.78e-02	Relative	1.04e-01	1.00e-02	Yes
methane_flame	10.3	pCO2	1.24e-01	HC02	1.24e-01	Relative	7.92e-04	1.00e-02	Yes
methane_flame	10.3	CO2	2.78e-02	CO2	2.78e-02	Relative	4.09e-04	1.00e-02	Yes
methane_flame	10.3	CO2	2.78e-02	H2O	3.70e-02	Relative	2.66e-04	1.00e-02	Yes
methane_flame	10.3	H2O	3.70e-02	CO	3.06e-02	Relative	4.31e-04	1.00e-02	Yes
multiple_reac_hrpua	9.1	CO	3.06e-02	CH4	2.00e-04	Relative	6.59e-04	1.00e-02	Yes
multiple_reac_hrpua	9.1	CH4	2.00e-04	C2H6	1.94e-04	Relative	8.34e-04	1.00e-02	Yes
multiple_reac_hrpua	9.1	C2H6	1.94e-04	C3H8	4.85e-05	Relative	8.34e-04	1.00e-02	Yes
multiple_reac_hrpua	9.1	C3H8	4.85e-05	CHO	9.23e-04	Relative	1.12e-04	1.00e-02	Yes
multiple_reac_hrpua	9.1	CHO	9.23e-04	H2+C7H8	1.24e-04	Relative	2.32e-03	1.00e-02	Yes
multiple_reac_hrpua	9.1	H2+C7H8	1.24e-04	CH4_CO	4.46e-03	Relative	4.32e-03	1.00e-02	Yes
multiple_reac_n_simple	13.1.3	CH4_CO	4.46e-03	CH4_H2	6.41e-04	Relative	6.59e-04	1.00e-02	Yes
multiple_reac_n_simple	13.1.3	CH4_H2	6.41e-04	C3H8_CO	1.98e-03	Relative	1.51e-04	1.00e-02	Yes
multiple_reac_n_simple	13.1.3	C3H8_CO	1.98e-03	C3H8_H2O	1.76e-02	Relative	2.44e-05	1.00e-02	Yes
multiple_reac_n_simple	13.1.3	C3H8_H2O	1.76e-02	C2H6_CO	2.92e-02	Relative	1.56e-05	1.00e-02	Yes
multiple_reac_n_simple	13.1.3	C2H6_CO	2.92e-02	C2H6_H2	3.15e-03	Relative	8.82e-06	1.00e-02	Yes
multiple_reac_n_simple	13.1.3	C2H6_H2	3.15e-03	mdot	1.60e-02	Relative	8.76e-03	1.50e-02	Yes
multiple_reac_n_simple	13.1.3	mdot	1.60e-02	Tb	6.47e-02	Relative	3.83e-03	1.50e-02	Yes
multiple_reac_n_simple	13.1.3	Tb	6.47e-02	Tsurf	u	Relative	3.29e-02	5.00e-02	Yes
multiple_reac_n_simple	13.1.3	u	2.24e+02	u	2.96e+02	Relative	2.77e-02	5.00e-02	Yes
multiple_reac_n_simple	13.1.3	u	2.88e+02	maxT	2.00e+01	Absolute	0.00e+00	1.00e-06	Yes
methanol_evaporation	9.2.6	Isothermal	2.00e+01	mint	-2.00e+01	Absolute	0.00e+00	1.00e-06	Yes
methanol_evaporation	9.2.6	Isothermal	-2.00e+01	UVEL	1.10e+00	Relative	1.70e-04	1.00e-02	Yes
methanol_evaporation	9.2.6	u-vel	1.09e+00	DP	-1.47e+00	Absolute	1.47e+00	2.00e+00	Yes
methanol_evaporation	9.2.6	DP	1.00e-12	DP	9.43e-11	Absolute	9.33e-11	1.00e-10	Yes
MO_velocity_profile_stable	6.1	3.8.4	2.00e+01	per-r-max	2.15e+03	Relative	1.12e-04	1.00e-02	Yes
MO_velocity_profile_stable	6.1	3.8.4	-2.00e+01	pres	1.37e+00	Absolute	2.06e-04	1.00e-02	Yes
mwest_cfl	3.1	3.1	1.09e+00	U-VEL	5.99e+00	Absolute	1.80e-03	1.00e-02	Yes
mwest_cfl	3.1	10.3.1	1.00e-12	U-VEL	3.90e+00	Absolute	3.98e-03	1.00e-02	Yes
ns2d_64_nuptl	10.3.1	10.3.1	1.00e-12	U-VEL	3.92e-01	Absolute	2.73e-03	1.00e-02	Yes
obst_coarse_fine_interface	10.3.1	10.3.1	1.00e-12	U-VEL	3.15e-01	Absolute	1.93e-03	1.00e-02	Yes
opening_uhat	10.5	10.5	1.00e-12	U-VEL	2.65e-01	Absolute	1.48e-04	1.00e-02	Yes
parabolic_profile	13.1.3	13.1.3	1.00e-12	drag force	-1.42e-02	Relative	3.75e-03	1.00e-02	Yes
particle_drag_U10_N16	13.1.3	13.1.3	1.00e-12	mass	6.40e-01	Relative	6.41e-01	1.00e-03	Yes
particle_drag_U50_N16	13.1.3	13.1.3	1.00e-12	T_gas	7.83e+02	Relative	7.87e-05	1.00e-02	Yes
particle_drag_U100_N16	13.1.3	13.1.3	1.00e-12	T_ball	7.82e+02	Relative	1.19e-03	1.00e-02	Yes
particle_drag_U50_N1600	13.1.3	13.1.3	1.00e-12	T_gas	7.85e+02	Relative	2.95e-03	1.00e-02	Yes
particle_drag_U100_N1600	13.1.3	13.1.3	1.00e-12	T_ball	7.85e+02	Relative	2.95e-03	1.00e-02	Yes
particle_drag_U150_N1600	13.1.3	13.1.3	1.00e-12	Q_rad ball	1.20e+00	Relative	1.18e-02	1.50e-02	Yes
particle_drag_U10_N16	13.1.3	13.1.3	1.00e-12	Q_rad cyl	4.48e+00	Relative	7.92e-03	1.50e-02	Yes
particle_heating_radiation	13.2.2	13.2.2	1.00e-12	Q_rad plate	7.12e+00	Relative	7.93e-03	1.50e-02	Yes
particle_heating_radiation	13.2.2	13.2.2	1.00e-12	Q_rad ball	9.27e-01	Relative	7.65e-03	1.00e-02	Yes
particle_isotropic_radii	9.8	9.8	1.00e-12	Q_rad cyl	3.47e+00	Relative	5.11e-03	1.00e-02	Yes
particle_isotropic_radii	9.8	9.8	1.00e-12	Q_rad plate	5.52e+00	Relative	5.11e-03	1.00e-02	Yes
particle_anisotropic_radii	9.8	9.8	1.00e-12	T_min	1.00e-12	Absolute	0.00e+00	1.00e-03	Yes
particle_offsetgas_1	7.1.6	7.1.6	1.00e-12						

Case Name	Section	Expected Quantity	Expected Value	Predicted Quantity	Predicted Value	Type of Error	Error	Error Tolerance	Within Tol.
particle_ofgas_1	7.1.6	T_max	1.00e-12	T_max	1.00e-12	Absolute	0.00e+00	1.00e-03	Yes
particle_ofgas_2	7.1.6	T_min	1.00e-12	T_min	1.00e-12	Absolute	0.00e+00	1.00e-03	Yes
particle_ofgas_2	7.1.6	T_max	1.00e-12	T_max	1.00e-12	Absolute	0.00e+00	1.00e-03	Yes
particle_ofgas_3	7.1.6	T_min	1.00e-12	T_min	1.00e-12	Absolute	0.00e+00	1.00e-03	Yes
particle_ofgas_4	7.1.6	T_min	1.00e-12	T_min	1.00e-12	Absolute	0.00e+00	1.00e-03	Yes
part_orientation_ramp	15.5.4	HF	1.00e+01	HF	9.99e+00	Relative	5.75e-04	1.00e-02	Yes
part_path_ramp_jog	15.5.3	Z	8.00e-01	Z	8.00e-01	Relative	0.00e+00	1.00e-03	Yes
part_baking_soda	12.1.3	Dia (mu-m)	First-order 420 K	diam first-order	4.59e+01	Relative	8.11e-04	1.00e-02	Yes
part_baking_soda	12.1.3	Dia (mu-m)	Spherical 420 K	SPHERE DIA	3.68e+01	Relative	5.43e-03	1.00e-02	Yes
part_baking_soda	12.1.3	Dia (mu-m)	First-order 450 K	diam first-order	2.84e+01	Relative	3.57e-03	5.00e-02	Yes
part_baking_soda	12.1.3	Dia (mu-m)	Spherical 450 K	SPHERE DIA	6.58e+00	Relative	9.50e-03	5.00e-02	Yes
part_baking_soda	12.1.3	Dia (mu-m)	First-order 500 K	diam first-order	2.59e+00	Relative	1.82e-02	1.00e-01	Yes
part_baking_soda	12.1.3	Dia (mu-m)	Spherical 500 K	SPHERE DIA	4.57e+01	Relative	4.79e-03	1.00e-01	Yes
pine_needles	17.2	Fuel Gas	6.40e-01	fuel gas mass	6.40e-01	Relative	0.00e+00	1.00e-02	Yes
pine_needles	17.2	Water Vapor	2.00e-01	water vapor mass	2.00e-01	Relative	0.00e+00	1.00e-02	Yes
porous_media	13.1.7	Char	1.60e-01	solid mass	1.60e-01	Relative	0.00e+00	1.00e-02	Yes
porous_media	13.1.7	Pres	4.76e+01	pres_1	4.74e+01	Relative	4.50e-03	1.00e-02	Yes
porous_media	13.1.7	Pres	4.76e+01	pres_2	4.74e+01	Relative	4.46e-03	1.00e-02	Yes
pressure_rise	10.3.1	Pres	5.00e+04	pres_3	4.74e+01	Relative	4.48e-03	1.00e-02	Yes
pressure_rise	10.3.1	Temp	5.50e+01	Temp_3	4.98e+04	Relative	3.02e-03	1.00e-02	Yes
pressure_rise	10.3.1	Dens	1.60e+00	Temp_3	5.46e+01	Relative	7.80e-03	2.00e-02	Yes
pressure_rise	10.3.1	HRR	4.49e+01	Dens_3	1.60e+00	Relative	3.02e-03	1.00e-02	Yes
propane_flame_2rec	13.1.3	Q_RADI	-9.28e+00	HRR	4.49e+01	Relative	4.48e-03	1.00e-02	Yes
propane_flame_2rec	13.1.3	Mass	4.48e-04	Q_RADI	-9.28e+00	Relative	2.48e-07	1.00e-02	Yes
propane_flame_deposition	10.11.4	Mass	4.48e-04	depo_none	4.48e-04	Relative	2.23e-04	1.00e-02	Yes
propane_flame_deposition	10.11.4	Mass	4.48e-04	depo_all	4.48e-04	Relative	2.23e-04	1.00e-02	Yes
pvc_combustion	13.2.2	CO2	1.55e-01	CO2	1.55e-01	Absolute	3.96e-04	1.00e-03	Yes
pvc_combustion	13.2.2	CO	1.44e-02	CO	1.44e-02	Absolute	3.25e-05	1.00e-03	Yes
pvc_combustion	13.2.2	H2O	6.59e-02	H2O	6.60e-02	Absolute	1.28e-04	1.00e-03	Yes
pvc_combustion	13.2.2	S	3.93e-02	S	3.96e-02	Absolute	2.94e-04	1.00e-03	Yes
pvc_combustion	13.2.2	HCL	1.33e-01	HCL	1.34e-01	Absolute	2.60e-04	1.00e-03	Yes
pvc_combustion	13.2.2	TMP	9.62e+02	TMP	9.62e+02	Absolute	0.00e+00	1.00e-02	Yes
race_test	8.8	VEL	9.51e-01	VEL	9.51e-01	Absolute	0.00e+00	1.00e-02	Yes
race_test	8.8	Phi_HdA	2.01e-01	Phi_HdA	2.05e-01	Relative	1.66e-02	2.00e-02	Yes
radiation_box	9.2	HF_cen	3.08e+01	HF_cen	3.05e+01	Relative	9.65e-03	2.00e-02	Yes
radiation_gas_panel	9.1.5	HF_off	1.74e+01	HF_off	1.75e+01	Relative	3.05e-03	2.00e-02	Yes
radiation_gas_panel	9.1.5	radx0	8.04e+01	radx0	8.04e+01	Relative	5.85e-07	1.00e-02	Yes
radiation_gas_veg_consistency_gas	9.1.0	radx0.5	5.76e+00	radx0.5	5.70e+00	Relative	1.61e-05	1.00e-02	Yes
radiation_gas_veg_consistency_gas	9.1.0	radx1	8.35e-01	radx1	8.35e-01	Relative	3.49e-05	1.00e-02	Yes
radiation_gas_veg_consistency_veg	9.1.0	radx1	8.04e+01	radx0	8.04e+01	Relative	1.02e-04	1.00e-02	Yes
radiation_gas_veg_consistency_veg	9.1.0	radx0.5	5.76e+00	radx0.5	5.70e+00	Relative	3.98e-04	1.00e-02	Yes
radiation_gas_veg_consistency_veg	9.1.0	radx1	8.35e-01	radx1	8.35e-01	Relative	5.40e-04	1.00e-02	Yes
radiation_shield	9.14	Flux	4.76e+00	Flux	4.70e+00	Relative	4.19e-04	1.00e-02	Yes
radiation_shield	9.14	Temp	3.80e+02	Temp	3.80e+02	Relative	2.21e-04	1.00e-02	Yes
ramp_chi_r	14.5	CHI_R	1.40e-01	chi_r_max	1.40e-01	Absolute	0.00e+00	1.00e-03	Yes
random_meshes	8.5	Vdot	1.20e-02	Vdot	1.20e-02	Relative	2.30e-04	2.00e-02	Yes
random_obstructions_fit	21.1.4	Error	1.00e-12	vel_max	1.25e-02	Absolute	1.25e-02	1.25e-02	Yes

Case Name	Section	Expected Quantity	Expected Value	Predicted Quantity	Predicted Value	Type of Error	Error	Error Tolerance	Within Tol.
random_obstructions_fit	21.1.4	Iterations	1.00e-12	iterations	8.90e+01	Absolute	8.90e+01	1.00e+02	Yes
random_walk	13.6	f_1	2.52e-01	npw	2.63e-01	Relative	4.11e-02	5.00e-02	Yes
random_walk	13.6	f_2	7.91e-01	npw	7.41e-01	Relative	6.31e-02	1.00e-01	Yes
reactionrate_arhenius_Order_1step	10.4.2	O2	6.57e-05	O2	6.57e-05	Absolute	4.47e-08	1.00e-03	Yes
reactionrate_arhenius_Order_1step	10.4.2	CO	5.40e-11	CO	7.27e-11	Absolute	1.87e-11	1.00e-03	Yes
reactionrate_arhenius_Order_1step	10.4.2	CO2	4.55e-01	CO2	4.55e-01	Absolute	3.74e-06	1.00e-03	Yes
reactionrate_arhenius_Order_1step	10.4.2	O2	1.30e-02	O2	1.32e-02	Absolute	1.26e-04	1.00e-03	Yes
reactionrate_arhenius_Order_1step	10.4.2	C3H8	3.36e-03	C3H8	3.27e-03	Absolute	9.00e-05	1.00e-03	Yes
reactionrate_arhenius_Order_1step	10.4.2	CO2	1.70e-01	CO2	1.70e-01	Absolute	6.30e-05	1.00e-03	Yes
reactionrate_arhenius_Order_1step	10.4.2	H2O	9.27e-02	H2O	9.27e-02	Absolute	2.60e-05	1.00e-03	Yes
reactionrate_arhenius_Order_1step	10.4.2	O2	3.84e-02	O2	3.80e-02	Absolute	3.64e-04	1.00e-03	Yes
reactionrate_arhenius_Order_1step	10.4.2	C3H8	9.72e-03	C3H8	9.52e-03	Absolute	2.00e-04	1.00e-03	Yes
reactionrate_arhenius_Order_1step	10.4.2	CO	3.90e-03	CO	3.83e-03	Absolute	6.85e-05	1.00e-03	Yes
reactionrate_arhenius_Order_1step	10.4.2	CO2	1.45e-01	CO2	1.45e-01	Absolute	4.10e-04	1.00e-03	Yes
reactionrate_arhenius_Order_1step	10.4.2	H2O	8.23e-02	H2O	8.25e-02	Absolute	2.19e-04	1.00e-03	Yes
reactionrate_arhenius_Order_1step	10.4.2	O2	3.68e-02	O2	3.64e-02	Absolute	3.76e-04	1.00e-03	Yes
reactionrate_arhenius_Order_1step	10.4.2	C3H8	8.01e-03	C3H8	7.83e-03	Absolute	1.81e-04	1.00e-03	Yes
reactionrate_arhenius_Order_1step	10.4.2	CO	1.19e-02	CO	1.17e-02	Absolute	2.31e-04	1.00e-03	Yes
reactionrate_arhenius_Order_1step	10.4.2	CO2	1.37e-01	CO2	1.38e-01	Absolute	6.05e-04	1.00e-03	Yes
reactionrate_arhenius_Order_1step	10.4.2	H2O	8.51e-02	H2O	8.53e-02	Absolute	1.84e-04	1.00e-03	Yes
reactionrate_arhenius_Order_1step	10.4.2	O2	2.27e-02	O2	2.27e-02	Absolute	4.09e-05	1.00e-03	Yes
reactionrate_arhenius_Order_1step	10.4.2	C3H8	1.00e-12	C3H8	7.25e-14	Absolute	9.28e-13	1.00e-03	Yes
reactionrate_arhenius_Order_1step	10.4.2	CO	3.98e-02	CO	3.98e-02	Absolute	8.74e-05	1.00e-03	Yes
reactionrate_arhenius_Order_1step	10.4.2	CO2	1.18e-01	CO2	1.18e-01	Absolute	1.43e-04	1.00e-03	Yes
reactionrate_arhenius_Order_1step	10.4.2	H2O	9.86e-02	H2O	9.86e-02	Absolute	3.34e-06	1.00e-03	Yes
reactionrate_arhenius_Order_1step	10.4.2	TEMP	2.55e+03	TEMP	2.55e+03	Relative	1.04e-03	1.00e-02	Yes
reactionrate_arhenius_Order_1step	10.4.2	PRES	3.85e+05	PRES	3.86e+05	Relative	1.37e-03	1.00e-02	Yes
reactionrate_arhenius_Order_1step	10.4.1	O2	3.40e-05	O2	7.48e-06	Absolute	2.65e-05	1.00e-03	Yes
reactionrate_arhenius_Order_1step	10.4.1	CH4	3.75e-01	CH4	3.75e-01	Absolute	6.41e-06	1.00e-03	Yes
reactionrate_arhenius_Order_1step	10.4.1	CO2	6.87e-02	CO2	6.88e-02	Absolute	1.83e-05	1.00e-03	Yes
reactionrate_arhenius_Order_1step	10.4.1	H2O	5.63e-02	H2O	5.63e-02	Absolute	1.47e-05	1.00e-03	Yes
reactionrate_arhenius_Order_1step	10.4.1	CH4	2.66e-01	CH4	2.66e-01	Absolute	0.00e+00	1.00e-03	Yes
reactionrate_arhenius_Order_1step	10.4.1	C3H8	3.55e-01	C3H8	3.55e-01	Absolute	0.00e+00	1.00e-03	Yes
reactionrate_arhenius_Order_1step	10.4.1	O2	1.51e-05	O2	1.51e-05	Absolute	9.00e-12	1.00e-03	Yes
reactionrate_arhenius_Order_1step	10.4.1	CO2	2.29e-01	CO2	2.29e-01	Absolute	0.00e+00	1.00e-03	Yes
reactionrate_arhenius_Order_1step	10.4.1	H2O	1.50e-01	H2O	1.50e-01	Absolute	0.00e+00	1.00e-03	Yes
reactionrate_arhenius_Order_1step	10.4.1	CH4	1.00e-06	CH4	1.50e-06	Absolute	4.98e-07	1.00e-03	Yes
reactionrate_arhenius_Order_1step	10.4.1	O2	1.00e-12	O2	6.72e-09	Absolute	6.72e-09	1.00e-03	Yes
reactionrate_arhenius_Order_1step	10.4.1	CO2	1.51e-01	CO2	1.51e-01	Absolute	3.10e-07	1.00e-03	Yes
reactionrate_arhenius_Order_1step	10.4.1	H2O	1.24e-01	H2O	1.24e-01	Absolute	1.00e-08	1.00e-03	Yes
reactionrate_arhenius_Order_1step	10.4.1	TEMP	2.54e+03	TEMP	2.54e+03	Relative	8.58e-05	1.00e-02	Yes
reactionrate_arhenius_Order_1step	10.4.1	PRES	8.56e+05	PRES	8.56e+05	Relative	8.32e-05	1.00e-02	Yes
reactionrate_arhenius_Order_1step	10.4.1	C3H8	1.00e-12	C3H8	2.67e-08	Absolute	2.67e-08	1.00e-03	Yes
reactionrate_arhenius_Order_1step	10.4.1	O2	4.00e-06	O2	3.93e-06	Absolute	7.04e-08	1.00e-03	Yes
reactionrate_arhenius_Order_1step	10.4.1	C02	1.81e-01	C02	1.81e-01	Absolute	1.90e-07	1.00e-03	Yes
reactionrate_arhenius_Order_1step	10.4.1	H2O	9.86e-02	H2O	9.86e-02	Absolute	2.35e-07	1.00e-03	Yes
reactionrate_arhenius_Order_1step	10.4.1	TEMP	2.63e+03	TEMP	2.63e+03	Relative	8.85e-04	1.00e-02	Yes

Case Name	Section	Expected Quantity	Expected Value	Predicted Quantity	Predicted Value	Type of Error	Error	Error Tolerance	Within Tol.
reactionrate_EDC_film_1step_C3H8	10.4.1	PRES	9.24e+05	PRES	9.25e+05	Relative	8.86e-04	1.00e-02	Yes
reactionrate_EDC_film_2step	10.4.1	O2	4.01e-01	O2	4.01e-01	Absolute	3.50e-07	1.00e-03	Yes
reactionrate_EDC_film_2step	10.4.1	CH4	1.00e-12	CH4	2.52e-10	Absolute	2.51e-10	1.00e-03	Yes
reactionrate_EDC_film_2step	10.4.1	CO	1.00e-12	CO	2.86e-26	Absolute	1.00e-12	1.00e-03	Yes
reactionrate_EDC_film_2step	10.4.1	CO2	2.74e-01	CO2	2.74e-01	Absolute	3.70e-07	1.00e-03	Yes
reactionrate_EDC_film_2step	10.4.1	H2O	2.25e-01	H2O	2.25e-01	Absolute	2.00e-08	1.00e-03	Yes
reactionrate_EDC_1step_CH4_nomix	10.4.1	O2	1.00e-12	O2	9.67e-11	Absolute	9.57e-11	1.00e-03	Yes
reactionrate_EDC_1step_CH4_nomix	10.4.1	CH4	3.90e-03	CH4	3.91e-03	Absolute	6.89e-06	1.00e-03	Yes
reactionrate_EDC_1step_CH4_nomix	10.4.1	CO2	1.49e-01	CO2	1.49e-01	Absolute	8.35e-06	1.00e-03	Yes
reactionrate_EDC_1step_CH4_nomix	10.4.1	H2O	1.22e-01	H2O	1.22e-01	Absolute	7.14e-06	1.00e-03	Yes
reactionrate_EDC_1step_CH4_nomix	10.4.1	TEMP	2.47e+03	TEMP	2.49e+03	Relative	5.02e-03	1.00e-02	Yes
reactionrate_EDC_1step_CH4_nomix	10.4.1	PRES	8.34e+05	PRES	8.36e+05	Relative	2.40e-03	1.00e-02	Yes
reactionrate_EDC_1step_CH4_nomix	10.4.1	CH3OH	1.00e-12	CH3OH	5.73e-18	Absolute	1.00e-12	1.00e-03	Yes
reactionrate_fast_slow	10.4.3	O2	1.00e-12	O2	1.13e-05	Absolute	1.13e-05	1.00e-03	Yes
reactionrate_fast_slow	10.4.3	CO2	1.92e-02	CO2	1.93e-02	Absolute	6.00e-05	1.00e-03	Yes
reactionrate_fast_slow	10.4.3	CO	2.88e-02	CO	2.88e-02	Absolute	1.37e-05	1.00e-03	Yes
reactionrate_jumped_two_air	10.4.1	C3H8	1.00e-12	C3H8	3.83e-05	Absolute	3.83e-05	1.00e-03	Yes
reactionrate_jumped_two_air	10.4.1	AIR1	1.00e-12	AIR1	1.88e-11	Absolute	1.78e-11	1.00e-03	Yes
reactionrate_jumped_two_air	10.4.1	AIR2	1.00e-12	AIR2	1.88e-11	Absolute	1.78e-11	1.00e-03	Yes
reactionrate_jumped_two_air	10.4.1	P1	1.00e+00	P1	1.00e+00	Absolute	3.83e-05	1.00e-03	Yes
reactionrate_jumped_two_air	10.4.1	O2	7.37e-02	O2	7.37e-02	Absolute	6.39e-06	1.00e-03	Yes
reactionrate_jumped_two_air	10.4.1	C3H8	2.00e-06	C3H8	1.88e-08	Absolute	1.98e-06	1.00e-03	Yes
reactionrate_jumped_two_air	10.4.1	CO2	1.20e-01	CO2	1.20e-01	Absolute	5.40e-06	1.00e-03	Yes
reactionrate_jumped_two_air	10.4.1	H2O	6.54e-02	H2O	6.54e-02	Absolute	2.92e-06	1.00e-03	Yes
reactionrate_series_reaction	10.4.1	Sum	1.00e+00	Sum	1.00e+00	Absolute	0.00e+00	1.00e-06	Yes
reactionrate_series_reaction	17.1.7	mean	1.00e+00	mean	9.96e-01	Relative	4.44e-03	4.00e-02	Yes
realizable_mass_fractions	17.1.2	sd	2.89e-01	sd	2.80e-01	Relative	3.17e-02	4.00e-02	Yes
rms_example	13.1.6	Exact 0.1	1.26e+02	FDS 0.1	1.25e+02	Relative	8.35e-03	3.00e-02	Yes
screen_drag_1	13.1.6	Exact 0.4	1.40e+01	FDS 0.4	1.39e+01	Relative	7.99e-03	3.00e-02	Yes
screen_drag_1	13.1.6	Exact 0.8	5.29e+00	FDS 0.8	5.26e+00	Relative	6.98e-03	3.00e-02	Yes
screen_drag_1	13.1.6	Exact 0.1	1.26e+03	FDS 0.1	1.25e+03	Relative	7.60e-03	8.00e-02	Yes
screen_drag_2	13.1.6	Exact 0.4	1.68e+02	FDS 0.4	1.67e+02	Relative	6.92e-03	8.00e-02	Yes
screen_drag_2	13.1.6	Exact 0.8	1.24e+02	FDS 0.8	1.23e+02	Relative	5.11e-03	8.00e-02	Yes
shrink_swell	12.6	M_1 (kg/m2)	5.00e-01	M_1	5.00e-01	Relative	0.00e+00	1.00e-02	Yes
shrink_swell	12.6	M_4 (kg/m2)	1.00e+00	M_4	1.00e+00	Relative	0.00e+00	1.00e-02	Yes
shrink_swell	12.6	L_1 (m)	5.00e-04	L_1	5.00e-04	Relative	0.00e+00	1.00e-02	Yes
shrink_swell	12.6	L_4 (m)	2.00e-03	L_4	2.00e-03	Relative	0.00e+00	1.00e-02	Yes
simple_duct	7.1.1	Mass	5.00e-01	Mass	5.00e-01	Relative	3.01e-04	1.00e-02	Yes
smoke_detector	10.10	Obscuration	6.47e+01	SD	6.46e+01	Relative	2.68e-04	1.00e-02	Yes
soot_oxidation_wall	10.11.7	Mass	9.18e-16	SOOT W	8.98e-11	Absolute	8.98e-11	1.00e-06	Yes
soot_oxidation_wall	10.11.7	Energy	3.28e+00	E	3.28e+00	Relative	3.93e-05	1.00e-03	Yes
soot_oxidation_wall	10.11.7	CO2	3.66e-04	CO2 G	3.66e-04	Relative	3.90e-05	1.00e-03	Yes
special_time_ramps	18.6.2	Exact	1.00e-12	sin function	6.82e-08	Absolute	6.82e-08	1.00e-02	Yes
species_conservation_1	7.1.2	Mass	3.60e-02	PROPANE	3.57e-02	Relative	9.08e-03	1.00e-02	Yes
species_conservation_2	7.1.2	M1	1.00e-12	M1	1.00e-12	Absolute	0.00e+00	1.00e-02	Yes
species_conservation_2	7.1.2	M2	1.00e+00	M2	9.96e-01	Absolute	3.78e-03	1.00e-02	Yes
species_conservation_3	7.1.2	Mass N2	9.31e-03	Mass N2	9.31e-03	Relative	3.97e-04	1.00e-01	Yes

Case Name	Section	Expected Quantity	Expected Value	Predicted Quantity	Predicted Value	Type of Error	Error	Tolerance	Within Tol.
species_conservation_3	7.1.2	Total Mass Ar	8.00e-01	Total Mass Ar	8.00e-01	Relative	9.31e-06	1.00e-01	Yes
species_conservation_4	7.1.2	1.00e-12	1.74e-08	Absolute	1.74e-08	5.00e-03	5.00e-03	5.00e-03	Yes
sphere_drag_1	7.1.2	4.00e-01	4.00e-01	Total	4.00e-01	2.44e-04	5.00e-03	5.00e-03	Yes
sphere_drag_1	13.1.4	3.77e+00	3.74e+00	FDS 5	3.77e+00	7.85e-03	5.00e-02	5.00e-02	Yes
sphere_drag_1	13.1.4	7.54e+00	7.41e+00	FDS 10	7.54e+00	1.68e-02	5.00e-02	5.00e-02	Yes
sphere_drag_2	13.1.4	1.51e+01	1.48e+01	FDS 20	1.51e+01	2.10e-02	5.00e-02	5.00e-02	Yes
spray_burner	13.1.4	2.10e-01	2.12e-01	pres	2.10e-01	1.17e-02	2.00e-02	2.00e-02	Yes
stack_effect	15.3.1	8.00e+04	7.96e+04	HRR	8.00e+04	4.90e-03	5.00e-02	5.00e-02	Yes
stack_effect	16.5.1	4.15e+00	4.10e+00	FDS Upper	4.15e+00	1.20e-02	5.00e-02	5.00e-02	Yes
stack_effect	16.5.1	3.95e+00	3.94e+00	FDS Lower	3.95e+00	2.27e-03	5.00e-02	5.00e-02	Yes
stack_effect	16.5.1	1.23e+00	1.23e+00	FDS Upper Exterior	1.23e+00	1.69e-03	1.00e-02	1.00e-02	Yes
stack_effect	16.5.1	1.24e+00	1.24e+00	FDS Lower Exterior	1.24e+00	1.64e-03	1.00e-02	1.00e-02	Yes
stack_effect	16.5.1	1.19e+00	1.18e+00	FDS Upper Interior	1.19e+00	2.08e-03	1.00e-02	1.00e-02	Yes
stack_effect	16.5.1	1.20e+00	1.20e+00	FDS Lower Interior	1.20e+00	1.66e-03	1.00e-02	1.00e-02	Yes
stairwell	21.4	5.00e-01	5.07e-01	Vdot	5.00e-01	1.37e-02	5.00e-02	5.00e-02	Yes
spyro_cone_demo_2	12.10	1.68e+02	1.69e+02	RRRPUA	1.68e+02	6.29e-03	1.00e-02	1.00e-02	Yes
spyro_cone_demo_3	12.10	4.58e+02	4.58e+02	RRRPUA	4.58e+02	1.12e-05	1.00e-02	1.00e-02	Yes
surf_mass_vent_nonchar_cart_fuel	12.1.1	3.60e+00	3.60e+00	density	3.60e+00	1.50e-06	1.00e-02	1.00e-02	Yes
surf_mass_vent_char_cart_fuel	12.1.1	1.80e+00	1.80e+00	density	1.80e+00	2.28e-06	1.00e-02	1.00e-02	Yes
surf_mass_vent_nonchar_cyl_fuel	12.1.1	1.80e+00	1.80e+00	density	1.80e+00	6.67e-07	1.00e-02	1.00e-02	Yes
surf_mass_vent_char_cyl_fuel	12.1.1	9.00e-01	9.00e-01	density	9.00e-01	1.39e-06	1.00e-02	1.00e-02	Yes
surf_mass_vent_nonchar_spher_fuel	12.1.1	1.20e+00	1.20e+00	density	1.20e+00	2.50e-07	1.00e-02	1.00e-02	Yes
surf_mass_vent_char_spher_fuel	12.1.1	6.00e-01	6.00e-01	density	6.00e-01	1.50e-07	1.00e-02	1.00e-02	Yes
surf_mass_part_nonchar_cart_fuel	12.1.2	9.00e-03	9.00e-03	density	9.00e-03	0.00e+00	1.00e-02	1.00e-02	Yes
surf_mass_part_char_cart_fuel	12.1.2	4.50e-03	4.50e-03	density	4.50e-03	0.00e+00	1.00e-02	1.00e-02	Yes
surf_mass_part_nonchar_cyl_fuel	12.1.2	1.13e-02	1.13e-02	density	1.13e-02	8.61e-04	1.00e-02	1.00e-02	Yes
surf_mass_part_char_cyl_fuel	12.1.2	5.65e-03	5.63e-03	density	5.65e-03	8.61e-04	1.00e-02	1.00e-02	Yes
surf_mass_part_nonchar_spher_fuel	12.1.2	1.51e-03	1.51e-03	density	1.51e-03	1.35e-03	1.00e-02	1.00e-02	Yes
surf_mass_part_char_spher_fuel	12.1.2	7.54e-04	7.54e-04	density	7.54e-04	2.36e-05	1.00e-02	1.00e-02	Yes
surf_mass_vent_nonchar_cart_gas	12.1.1	3.60e+00	3.60e+00	density	3.60e+00	8.33e-08	1.00e-02	1.00e-02	Yes
surf_mass_vent_char_cart_gas	12.1.1	1.80e+00	1.80e+00	density	1.80e+00	3.33e-07	1.00e-02	1.00e-02	Yes
surf_mass_vent_nonchar_cyl_gas	12.1.1	1.80e+00	1.80e+00	density	1.80e+00	5.56e-08	1.00e-02	1.00e-02	Yes
surf_mass_vent_char_cyl_gas	12.1.1	9.00e-01	9.00e-01	density	9.00e-01	4.33e-07	1.00e-02	1.00e-02	Yes
surf_mass_vent_nonchar_spher_gas	12.1.1	1.20e+00	1.20e+00	density	1.20e+00	2.50e-05	1.00e-02	1.00e-02	Yes
surf_mass_vent_char_spher_gas	12.1.1	6.00e-01	6.00e-01	density	6.00e-01	5.00e-07	1.00e-02	1.00e-02	Yes
surf_mass_part_nonchar_cart_gas	12.1.2	9.00e-03	9.00e-03	density	9.00e-03	0.00e+00	1.00e-02	1.00e-02	Yes
surf_mass_part_char_cart_gas	12.1.2	4.50e-03	4.50e-03	density	4.50e-03	0.00e+00	1.00e-02	1.00e-02	Yes
surf_mass_part_nonchar_cyl_gas	12.1.2	1.13e-02	1.13e-02	density	1.13e-02	8.61e-04	1.00e-02	1.00e-02	Yes
surf_mass_part_char_cyl_gas	12.1.2	5.65e-03	5.65e-03	density	5.65e-03	8.61e-04	1.00e-02	1.00e-02	Yes
surf_mass_part_nonchar_spher_gas	12.1.2	1.51e-03	1.51e-03	density	1.51e-03	1.35e-03	1.00e-02	1.00e-02	Yes
surf_mass_part_char_spher_gas	12.1.2	7.54e-04	7.54e-04	density	7.54e-04	2.36e-05	1.00e-02	1.00e-02	Yes
surf_mass_part_specified	15.4.7	5.00e-03	4.99e-03	Ar mass	5.00e-03	4.99e-03	1.00e-02	1.00e-02	Yes
surf_mass_part_specified	15.4.7	6.28e-03	6.27e-03	SO2 mass	6.28e-03	2.72e-03	1.00e-02	1.00e-02	Yes
surf_mass_part_specified	15.4.7	2.51e-03	2.51e-03	He mass	2.51e-03	2.64e-03	1.00e-02	1.00e-02	Yes
surf_mass_two_species_cart	12.1.2	3.20e-02	3.20e-02	fuel gas mass	3.20e-02	2.69e-02	1.00e-02	1.00e-02	Yes
surf_mass_two_species_cart	12.1.2	2.00e-02	2.00e-02	water vapor mass	2.00e-02	2.75e-06	2.00e-02	2.00e-02	Yes
surf_mass_two_species_cart	12.1.2	4.80e-02	4.80e-02	solid mass	4.80e-02	4.00e+00	2.00e-02	2.00e-02	Yes

Case Name	Section	Expected Quantity	Expected Value	Predicted Quantity	Predicted Value	Type of Error	Error	Error Tolerance	Within Tol.
surf_mass_two_species_cyl	12.1.2	Mass (fuel)	3.20e-02	fuel gas mass	3.20e-02	Relative	5.78e-05	4.00e-02	Yes
surf_mass_two_species_cyl	12.1.2	Mass (H <sub>2</sub> O)	2.00e-02	water vapor mass	2.00e-02	Relative	1.12e-05	4.00e-02	Yes
surf_mass_two_species_cyl	12.1.2	Mass (total)	4.80e-02	solid mass	4.80e-02	Relative	0.00e+00	4.00e-02	Yes
surf_mass_two_species_spher	12.1.2	Mass (fuel)	3.20e-02	fuel gas mass	3.20e-02	Relative	7.81e-05	4.00e-02	Yes
surf_mass_two_species_spher	12.1.2	Mass (H <sub>2</sub> O)	2.00e-02	water vapor mass	2.00e-02	Relative	1.65e-05	4.00e-02	Yes
surf_mass_two_species_spher	12.1.2	Mass (total)	4.80e-02	solid mass	4.80e-02	Relative	0.00e+00	4.00e-02	Yes
surf_mass_vent_liquid_fuel	12.4.1	Mass (kg)	6.84e+00	Burning rate	6.84e+00	Relative	0.00e+00	1.00e-02	Yes
surf_mass_vent_liquid_fuel_nonconforming	12.4.1	Mass (kg)	6.84e+00	Burning rate	6.84e+00	Relative	0.00e+00	1.00e-02	Yes
ice_cube	12.11	Mass (kg)	1.00e+00	AMPUA	1.00e+00	Relative	8.14e-04	1.00e-02	Yes
symmetry_test	8.1.1	u_1	3.85e-03	u_2	3.85e-03	Absolute	0.00e+00	1.00e-02	Yes
symmetry_test	8.1.1	v_1	3.85e-03	v_2	3.85e-03	Absolute	0.00e+00	1.00e-02	Yes
symmetry_test	8.1.1	w_1	3.85e-03	w_2	3.85e-03	Absolute	0.00e+00	1.00e-02	Yes
symmetry_test_mpi	8.1.1	u_1	5.66e-04	u_2	5.80e-04	Absolute	1.41e-05	1.00e-02	Yes
symmetry_test_mpi	8.1.1	v_1	5.66e-04	v_2	5.80e-04	Absolute	1.41e-05	1.00e-02	Yes
symmetry_test_mpi	8.1.1	w_1	5.66e-04	w_2	5.80e-04	Absolute	1.41e-05	1.00e-02	Yes
symmetry_test_2	8.1.2	T_left	9.40e+01	T_right	9.40e+01	Relative	2.21e-05	1.00e-03	Yes
tangential_velocity	10.1.4	u	2.00e+00	u	2.00e+00	Relative	8.12e-04	4.00e-02	Yes
tangential_velocity	10.1.4	v	3.00e+00	v	2.92e+00	Relative	2.79e-02	4.00e-02	Yes
target_test	9.1.3	flux_1	8.07e+01	flux_2	8.07e+01	Relative	2.90e-06	1.00e-02	Yes
TC_heating	9.11	Temp	6.00e+02	TC	6.00e+02	Relative	0.00e+00	1.00e-02	Yes
TC_view_factor	9.12	TC	3.80e+02	TC_1	3.90e+02	Relative	2.47e-02	3.00e-02	Yes
tga_sample	12.9.2	Mass	5.33e-01	mpa	5.30e-01	Relative	6.19e-03	1.00e-02	Yes
thermocouples	11.4	MLR	4.61e-04	mlrpa	4.83e-04	Relative	4.68e-02	5.00e-02	Yes
thermocouples	11.4	Target_1	5.00e+02	TC_J	5.00e+02	Relative	0.00e+00	1.00e-02	Yes
thermocouples	11.4	Target_2	5.00e+02	TC_J_2	5.00e+02	Relative	0.00e+00	1.00e-02	Yes
thermocouple_time_constant	11.4	Target_3	4.95e+02	TC_3	4.95e+02	Relative	4.04e-05	1.00e-02	Yes
thermocouple_time_constant	11.4	T_0.5	2.63e+01	T_0.5	2.64e+01	Relative	2.01e-03	1.00e-02	Yes
thermocouple_time_constant	22.10.8	T_3.0	2.63e+01	T_3.0	2.63e+01	Relative	1.98e-03	1.00e-02	Yes
thermocouple_time_constant	22.10.8	T_8.0	2.63e+01	T_8.0	2.63e+01	Relative	8.58e-03	1.00e-02	Yes
test_hrr_2d_cyl	22.10.1	HRR	1.56e+02	HR	1.55e+02	Relative	3.99e-03	1.00e-02	Yes
tmp_lower_limit	3.8.5	T	2.00e+01	mint	2.00e+01	Absolute	1.99e-02	2.00e-01	Yes
tmp_lower_limit	3.8.5	T	2.00e+01	minT	2.00e+01	Absolute	1.10e-03	1.00e-02	Yes
tmp_lower_limit	3.8.5	T	2.00e+01	minT	2.00e+01	Absolute	1.51e-03	1.00e-02	Yes
tunnel_const_gamma	3.10.1	p	7.78e-01	7.78e-01	Relative	3.66e-04	1.00e-02	Yes	
tunnel_const_gamma	3.10.1	u	1.71e+00	1.71e+00	Relative	4.89e-05	1.00e-02	Yes	
tunnel_const_gamma	3.10.1	rho	7.02e-01	7.02e-01	Relative	4.34e-04	1.00e-02	Yes	
tunnel_const_gamma	3.10.1	T	2.27e+02	T	2.28e+02	Relative	1.35e-03	1.00e-02	Yes
tunnel_linear_cp	3.10.2	p	7.72e-01	7.72e-01	Relative	8.55e-05	1.00e-02	Yes	
tunnel_linear_cp	3.10.2	u	1.70e+00	1.70e+00	Relative	5.08e-05	1.00e-02	Yes	
tunnel_linear_cp	3.10.2	rho	7.05e-01	7.05e-01	Relative	4.92e-05	1.00e-02	Yes	
tunnel_linear_cp	3.10.2	T	2.26e+02	T	2.26e+02	Relative	5.18e-05	1.00e-02	Yes
tunnel_demo	21.3	v_target	-1.00e-01	v_target	-9.18e-05	Absolute	9.99e-02	1.00e-02	Yes
tunnel_demo	21.3	p_target	-5.00e+02	p_target	-2.00e-06	Absolute	5.00e+02	1.00e+05	Yes
tunnel_demo_gmat	21.3	v_target	-1.00e-01	v_target	-8.67e-19	Absolute	1.00e-01	1.00e+05	Yes
two_step_solid_reaction	12.8	rho	3.60e-09	Absolute	5.00e+02	Pressure Error	2.85e-11	1.00e-02	Yes
two_step_solid_reaction	12.8	Y_a	3.57e-09	Absolute	6.34e-06	Velocity Error	2.85e-11	1.00e-02	Yes
two_step_solid_reaction	12.8	Y_b	6.25e-06	Absolute	8.64e-08	Velocity Error	6.25e-06	1.00e-02	Yes

Case Name	Section	Expected Quantity	Expected Value	Predicted Quantity	Predicted Value	Type of Error	Error	Error Tolerance	Within Tol.
two_step_solid_reaction	12.8	Yc	1.00e+00	Yc	1.00e+00	Absolute	6.34e-06	1.00e-02	Yes
vegetation_absorb	13.2.1	rad	2.13e+01	rad	2.14e+01	Relative	7.04e-03	3.00e-02	Yes
vegetation_drag_1	13.1.5	Pressure	1.89e+01	p1	1.84e+01	Relative	2.55e-02	3.00e-02	Yes
vegetation_drag_1	13.1.5	Pressure	1.89e+01	p2	1.86e+01	Relative	1.28e-02	3.00e-02	Yes
vegetation_drag_1	13.1.5	Pressure	1.89e+01	p3	1.85e+01	Relative	1.99e-02	3.00e-02	Yes
vegetation_drag_2	13.1.5	Pressure	8.53e+00	p1	8.54e+00	Relative	1.34e-04	2.00e-02	Yes
vegetation_drag_2	13.1.5	Pressure	8.53e+00	p2	8.45e+00	Relative	1.03e-02	2.00e-02	Yes
vegetation_drag_2	13.1.5	Pressure	8.53e+00	p3	8.44e+00	Relative	1.10e-02	2.00e-02	Yes
velocity_bc_test	8.2	Vell	1.64e+00	Vell2	1.62e+00	Relative	1.34e-02	3.00e-02	Yes
velocity_bc_test	8.2	Pres1	2.13e-02	Pres2	2.02e-02	Absolute	1.13e-03	5.00e-02	Yes
volume_flow_1	10.1.1	vflow	1.00e-02	vflow	9.99e-03	Relative	8.65e-04	1.00e-02	Yes
volume_flow_2	10.1.1	vflow	1.00e-02	vflow	1.00e-02	Relative	9.84e-05	1.00e-02	Yes
water_evap_1_const_gamma	3.9.3	Rel_Hum	2.11e+00	humid	2.10e+00	Relative	4.55e-03	1.00e-02	Yes
water_evap_1_const_gamma	3.9.3	h_gas	-2.77e+01	h_gas	-2.76e+01	Relative	3.27e-03	1.00e-02	Yes
water_evap_1_const_gamma	3.9.3	h_water	1.98e+01	h_water	1.98e+01	Relative	0.00e+00	1.00e-02	Yes
water_evap_1_const_gamma	3.9.3	dens	1.00e-02	dens	9.95e-03	Relative	4.65e-03	1.00e-02	Yes
water_evap_1_const_gamma	3.9.3	temp	1.54e+02	Temp	1.54e+02	Relative	1.04e-03	1.00e-02	Yes
water_evap_1_const_gamma	3.9.3	pres	-7.90e+03	pres	-7.88e+03	Relative	3.27e-03	1.00e-02	Yes
water_evap_1_const_gamma	3.9.3	vapor	1.00e-02	WATER VAPOR	9.95e-03	Relative	4.65e-03	1.00e-02	Yes
water_evap_1_const_gamma	13.3.1	Rel_Hum	2.11e+00	humid	2.10e+00	Relative	4.55e-03	1.00e-02	Yes
water_evaporation_1	13.3.1	h_gas	-1.67e+02	h_gas	-1.66e+02	Relative	4.42e-03	1.00e-02	Yes
water_evaporation_1	13.3.1	h_water	1.59e+02	h_water	1.59e+02	Relative	1.58e-03	1.00e-02	Yes
water_evaporation_1	13.3.1	dens	1.00e-02	dens	9.95e-03	Relative	4.65e-03	1.00e-02	Yes
water_evaporation_1	13.3.1	temp	1.54e+02	Temp	1.54e+02	Relative	1.04e-03	1.00e-02	Yes
water_evaporation_1	13.3.1	pres	-7.81e+03	pres	-7.79e+03	Relative	3.30e-03	1.00e-02	Yes
water_evaporation_1	13.3.1	vapor	1.00e-02	WATER VAPOR	9.95e-03	Relative	4.65e-03	1.00e-02	Yes
water_evaporation_1	13.3.2	humid	1.00e+02	humid	9.97e+01	Relative	3.07e-03	1.00e-02	Yes
water_evaporation_1	13.3.2	h_gas	-3.32e+01	h_gas	-3.30e+01	Relative	4.66e-03	1.00e-02	Yes
water_evaporation_1	13.3.2	h_water	2.94e+01	h_water	2.92e+01	Relative	5.77e-03	1.00e-02	Yes
water_evaporation_1	13.3.2	dens	2.16e-02	dens	2.15e-02	Relative	4.92e-03	1.00e-02	Yes
water_evaporation_1	13.3.2	Temp	2.34e+01	Temp	2.34e+01	Relative	8.53e-04	1.00e-02	Yes
water_evaporation_2	13.3.2	temp_w	2.34e+01	temp_w	2.34e+01	Relative	9.63e-04	1.00e-02	Yes
water_evaporation_2	13.3.2	pres	-5.95e+04	H2O	-5.95e+04	Relative	2.95e-04	1.00e-02	Yes
water_evaporation_2	13.3.2	H2O	4.54e-02	Temp	4.52e-02	Relative	4.70e-03	1.00e-02	Yes
water_evaporation_2	13.3.2	humid	1.00e+02	humid	9.98e+01	Relative	2.16e-03	1.00e-02	Yes
water_evaporation_2	13.3.2	h_gas	-1.09e+03	h_gas	-1.09e+03	Relative	1.09e+03	1.00e-02	Yes
water_evaporation_2	13.3.2	dens	6.55e-02	dens	6.54e-02	Relative	8.42e-04	2.00e-02	Yes
water_evaporation_2	13.3.2	Temp	4.46e+01	Temp	4.47e+01	Relative	7.63e-04	1.00e-02	Yes
water_evaporation_3	13.3.3	temp_w	4.46e+01	temp_w	4.47e+01	Relative	7.63e-04	1.00e-02	Yes
water_evaporation_3	13.3.3	pres	-5.01e+04	H2O	-5.01e+04	Relative	5.67e-05	1.00e-02	Yes
water_evaporation_3	13.3.3	H2O	1.26e-01	H2O	1.26e-01	Relative	7.36e-04	2.00e-02	Yes
water_evaporation_3	13.3.3	Heat_Flow	1.07e+02	heat	1.04e+02	Relative	2.60e-02	6.00e-02	Yes
water_evaporation_3	13.3.3	Heat_Flow	1.07e+02	heat	1.04e+02	Relative	2.34e-02	6.00e-02	Yes
water_evaporation_3	13.3.3	D_thin	3.04e-04	D_thin	3.53e-04	Absolute	4.92e-05	1.00e-04	Yes
water_evaporation_3	13.3.3	D_thick	3.04e-04	T_gas	3.03e-04	Absolute	4.60e-07	1.00e-04	Yes
water_evaporation_3	13.3.3	T_gas	1.87e+02	T_gas	1.87e+02	Relative	1.93e-03	1.00e-02	Yes
water_evaporation_3	13.3.3	T_wall	1.87e+02	T_wall	1.86e+02	Relative	2.55e-03	1.00e-02	Yes

Case Name	Section	Expected Quantity	Expected Value	Predicted Quantity	Predicted Value	Type of Error	Error	Within Tol.
water_evaporation_6	13.3.6	Pressure sum	2.72e+04	pres	2.71e+04	Relative	3.93e-03	1.50e-02
water_evaporation_6	13.3.6	HRR	1.00e-12	u_gas	1.33e-03	Absolute	1.33e-03	1.00e-02
water_evaporation_7	13.3.7	z	2.17e+01	HRR	2.16e+01	Relative	5.52e-03	1.00e-02
water_evaporation_8	13.3.8	z	5.41e-01	z_thin	5.48e-01	Absolute	6.87e-03	5.00e-02
water_evaporation_8	13.3.8	z	5.41e-01	z_thick	5.61e-01	Absolute	1.99e-02	5.00e-02
water_evaporation_8	13.3.8	d	2.72e+01	D_thin	2.54e+01	Absolute	1.77e+00	5.00e+00
water_evaporation_8	13.3.8	d	2.72e+01	D_thick	2.37e+01	Absolute	3.52e+00	5.00e+00
water_pool	12.4.2	mdot	1.42e-05	mdot	1.46e-05	Relative	2.89e-02	6.00e-02
wind_example_5	16.1	u_ideal	1.00e-12	u_mean	2.15e-02	Absolute	2.15e-02	1.00e+00
wind_example_5	16.1	v_ideal	5.00e+00	v_mean	4.97e+00	Absolute	3.00e-02	1.00e+00
wind_example_10	16.1	u_ideal	1.00e-12	u_mean	1.16e-02	Absolute	1.16e-02	1.00e+00
wind_example_10	16.2.2	v_ideal	5.00e+00	v_mean	4.97e+00	Absolute	2.64e-02	1.00e+00
wind_example_32	16.2.2	u_ideal	7.64e+00	u	7.74e+00	Absolute	9.88e-02	1.00e+00
wind_example_32	16.2.2	T_ideal	1.85e+01	T	1.85e+01	Absolute	2.55e-02	1.00e+00
zone_break_slow	10.3.1	Pres1	1.97e+03	pres_1	1.97e+03	Relative	1.38e-03	2.00e-02
zone_break_slow	10.3.1	Pres2	1.00e+03	pres_2	1.02e+03	Relative	1.31e-02	2.00e-02
zone_break_slow	10.3.1	Pres3	1.00e+03	pres_3	1.01e+03	Relative	6.29e-03	2.00e-02
zone_break_fast	10.3.1	Pres1	1.97e+03	pres_1	1.97e+03	Relative	1.38e-03	2.00e-02
zone_break_fast	10.3.1	Pres2	1.00e+03	pres_2	1.01e+03	Relative	1.18e-02	2.00e-02
zone_break_fast	10.3.1	Pres3	1.00e+03	pres_3	1.01e+03	Relative	1.18e-02	2.00e-02
zone_break_slow_umat	10.3.1	Pres1	1.97e+03	pres_1	1.97e+03	Relative	1.38e-03	2.00e-02
zone_break_slow_umat	10.3.1	Pres2	1.00e+03	pres_2	1.02e+03	Relative	1.31e-02	2.00e-02
zone_break_slow_umat	10.3.1	Pres3	1.00e+03	pres_3	1.01e+03	Relative	6.30e-03	2.00e-02
zone_break_fast_umat	10.3.1	Pres1	1.97e+03	pres_1	1.97e+03	Relative	1.38e-03	2.00e-02
zone_break_fast_umat	10.3.1	Pres2	1.00e+03	pres_2	1.01e+03	Relative	1.18e-02	2.00e-02
zone_break_fast_umat	10.3.1	Pres3	1.00e+03	pres_3	1.01e+03	Relative	1.18e-02	2.00e-02
zone_break_fast_umat	10.3.1	Pres1	1.97e+03	pres_1	1.97e+03	Relative	1.38e-03	2.00e-02
zone_break_fast_umat	10.3.1	Pres2	1.00e+03	pres_2	1.02e+03	Relative	1.31e-02	2.00e-02
zone_shape_2	14.10.6	Delta p	1.00e+02	pres_1	1.97e+03	Relative	8.99e-03	1.50e-02
zone_shape_2	14.10.6	Mass	3.13e+02	pres_2	1.01e+03	Relative	9.09e-03	1.00e-02
humidity	10.2	H2Ov	6.03e-02	pres_3	1.01e+03	Relative	1.18e-02	2.00e-02
matl_e_cons	M1	-8.65e+02	H_M1	-8.63e+02	Relative	1.39e-07	5.00e-03	
matl_e_cons	M1	-1.86e+03	H_M1	-1.87e+03	Relative	2.68e-07	5.00e-03	
matl_e_cons	M1	-8.65e+02	H_M1	-8.65e+02	Relative	1.98e-04	5.00e-03	
matl_e_cons	M2	-1.86e+03	H_M2	-1.87e+03	Relative	2.68e-07	5.00e-03	
matl_e_cons	M1	-1.14e+03	H_M1	-1.14e+03	Relative	8.77e-08	5.00e-03	
matl_e_cons	M2	-6.95e+02	H_M2	-6.95e+02	Relative	1.15e-07	5.00e-03	
matl_e_cons	M1	-1.14e+03	H_M1	-1.14e+03	Relative	8.77e-08	5.00e-03	
M1 PC	M2	-6.40e+02	H_M1a	-6.40e+02	Relative	1.50e-07	5.00e-03	
M1 PC	M2	-6.95e+02	H_M2	-6.95e+02	Relative	1.15e-07	5.00e-03	
M1 PC	M1	-1.31e+03	H_M1	-1.31e+03	Relative	2.45e-06	5.00e-03	
M1 PC	M2	-9.73e+02	H_M1a	-9.73e+02	Relative	3.52e-06	5.00e-03	
M1 PC	M2	-6.95e+02	H_M2	-6.95e+02	Relative	1.15e-07	5.00e-03	
M1 PC	M1	-4.29e+02	H_M1	-4.29e+02	Relative	1.17e-07	5.00e-03	
M1 PC	M2	-7.27e+02	H_M2	-7.27e+02	Relative	2.75e-08	5.00e-03	
M1 PC	M1	-1.22e+03	H_M1	-3.53e+02	Relative	1.20e-03	5.00e-03	
M1 PC	M2	-3.53e+02	H_M1	-3.53e+02	Relative	1.20e-03	5.00e-03	

sphere_radiate	16.5.1	HF	5.07e+00	5.37e+00	Relative	5.94e-02	7.00e-02	Yes
----------------	--------	----	----------	----------	----------	----------	----------	-----

## Appendix B

# Installation Testing

The use of computer software for safety purposes is sometimes regulated under a software quality assurance (SQA) program by the Authority Having Jurisdiction. For example, in the United States, both the Department of Energy (DOE) via DOE G 414.1-4 [114] and the Nuclear Regulatory Commission (NRC) via NUREG-1737 [115] impose specific requirements on software used for certain safety purposes. In addition to imposing general requirements on configuration management and verification and validation, SQA programs often impose an acceptance testing requirement. For simulation software, this involves a test program in which the software is used to execute a number of sample cases and the results are compared to accepted values. The purpose of this testing process is to ensure that the software installation was successful and that no corruption of the software executable or libraries has occurred. The acceptance test procedure is as follows:

1. Obtain and install the version of FDS you will be running. Note that this procedure will need to be repeated for each version of the FDS executable being used.
2. Find the files shown in Table B.1 in the Examples folder of the FDS-SMV installation package. The Folder listed in the table is a subfolder of the Examples folder.
3. Run each of the FDS input files listed in Table B.1.
4. Compare the results of each FDS Output File listed in Table B.1 with the exact/expected results in the corresponding Expected Results File. The Expected Results Files can be found at  
<https://github.com/firemodels/fds/tree/master/Verification>  
This is a link to the FDS repository hosted by GitHub.
5. Verify that the expected results match the results from Step 3 using the criteria shown in Appendix A.

Table B.1: FDS Installation Test Suite. Details of each case may be found in the listed section or reference. Note that the light blue colored links refer to the FDS User's Guide.

Folder	Reference	Input File	FDS Output File	Expected Results File
Controls	<a href="#">18.5.1.1</a>	activate_vents.fds	activate_vents_cirl.csv	activate_vents.csv
Pressure_Effects	7.2.3	isenropic2.fds	isenotropic2_devc.csv	isenotropic2.csv
Energy_Budget	7.2.5	energy_budget_tmix.fds	energy_budget_tmix_devc.csv	energy_budget_tmix.csv
Energy_Budget	7.2.1	energy_budget_cold_walls.fds	energy_budget_cold_walls_hrr.csv	energy_budget_cold_walls.csv
Fires	<a href="#">15.3.1</a>	spray_burner.fds	spray_burner_hrr.csv	spray_burner.csv
Heat_Transfer	11.2	heat_conduction_kc.fds	heat_conduction_kc_devc.csv	heat_conduction_kc.csv
HVAC	14.11	ashrae7_table.fds	ashrae7_table_devc.csv	ashrae7_exp.csv
Pressure_Solver	<a href="#">21.1.2</a>	duct_flow.fds	duct_flow_devc.csv	duct_flow.csv
Pressure_Solver	<a href="#">21.1.2</a>	duct_flow_ugimat.fds	duct_flow_ugimat_devc.csv	duct_flow.csv
Pyrolysis	12.7	enthalpy.fds	enthalpy_devc.csv	enthalpy.csv
Pyrolysis	12.6	shrink_swell.fds	shrink_swell_devc.csv	shrink_swell.csv
Radiation	9.14	radiation_shield.fds	radiation_shield_devc.csv	radiation_shield.csv
Species	<a href="#">10.4.1</a>	reactionrate_EDC_1step_CH4_nomix.fds	reactionrate_EDC_1step_CH4_nomix_devc.csv	reactionrate_EDC_nomix_spec.csv
Species	10.4.2	reactionrate_arhenius_2order_1step.fds	reactionrate_arhenius_2order_1step_devc.csv	reactionrate_arhenius_2order_1step_soln.csv
Sprinklers_and_Sprays	<a href="#">13.3.1</a>	water_evaporation_1.fds	water_evaporation_1_devc.csv	water_evaporation_1.csv
Sprinklers_and_Sprays	13.1.3	particle_drag_U50_N16.fds	particle_drag_U50_N16_devc.csv	particle_drag_U50_N16.csv

## Appendix C

# Unstructured Geometry Integral Conservation Tests

Consider an immersed body  $B$ , with surface defined by  $N_\tau$  triangles, completely immersed in a domain  $\Omega$  divided in  $M$  cartesian mesh blocks. Three geometry conservation tests can be defined for the polyhedra definition around this body:

1. Surface area: The total body  $B$  surface area can be computed from the triangulation  $A_{B,\tau} = \sum_{i_\tau=1}^{N_\tau} A_{i_\tau}$ , where  $N_\tau$  is the number of triangles in the surface and  $A_{i_\tau}$  their areas. It can also be calculated from the boundary cut-face areas computed by the cut-cell definition algorithm,  $A_{B,CF} = \sum_{icf=1}^{N_{bcf}} A_{icf}$ , where  $N_{bcf}$  is the number of cut-faces that have been computed on the body surface. These two areas should match.
2. Gas ( $G$ ) region volume: This is the volume of region  $\Omega - \Omega_B$ . It can be computed from the solid volume  $V_B$  and the domain volume  $V_\Omega$  as  $V_{GB} = V_\Omega - V_B$ . Here:

$$V_\Omega = \sum_{nm=1}^M V_{nm}; V_{nm} = L_{x,nm} L_{y,nm} L_{z,nm} \quad (\text{C.1})$$

where  $L_{x,nm}$ ,  $L_{y,nm}$  and  $L_{z,nm}$  are the  $nm$  mesh sizes in each cartesian direction ( $M = 1$ ,  $L_{x,1} = 3D_B$ ,  $L_{y,1} = 3D_B$  and  $L_{z,1} = 8D_B$  in the cone problem of Sec. 16.3.1). The discrete volume of the solid can be computed from the triangulation applying the divergence theorem to a field  $\mathbf{F}_v = x\hat{\mathbf{i}}$ , such that  $\nabla \cdot \hat{\mathbf{F}}_v = 1$ , to the surface triangles:

$$V_B = \int_{\Omega_B} \nabla \cdot \mathbf{F}_v dV = \int_{\partial\Omega_B} \mathbf{F}_v \cdot \hat{\mathbf{n}} dA = \sum_{i=1}^{N_\tau} (\hat{\mathbf{i}} \cdot \hat{\mathbf{n}}_i) x_{ci} A_i \quad (\text{C.2})$$

where  $x_{ci}$  is the  $i$ th triangle centroid position in the  $x$  direction, and  $A_i$  its area. The  $G$  region volume can also be computed from the sum of cut-cells and regular  $G$  cells volumes over all  $M$  cartesian meshes:

$$V_{GRC} = \sum_{icc=1}^{N_{cc}} V_{icc} + N_{rg} \Delta x \Delta y \Delta z \quad (\text{C.3})$$

where  $N_{rg}$  the number of regular cells in the  $G$  region, and  $\Delta x, \Delta y, \Delta z$  the uniform grid cell sizes. The  $N_{cc}$  cut-cell volumes  $V_{icc}$  are computed in similar manner to equation (C.2):

$$V_{icc} = \int_{\partial\Omega_{icc}} \mathbf{F}_v \cdot \hat{\mathbf{n}} dA = \sum_{icf=1}^{ncf} (\hat{\mathbf{i}} \cdot \hat{\mathbf{n}}_{icf}) \int_{\Omega_{icf}} x dA \quad (\text{C.4})$$

where  $ncf$  is the number of faces (cut-face or regular) which are boundary of cut-cell  $icc$ .

In this test  $V_{GB}$  and  $V_{GRC}$  should agree.

3.  $G$  region centroid location: The centroid of the  $G$  region can be computed from cut-cells and regular  $G$  cells as:

$$\mathbf{x}_{GRC} = \frac{1}{V_{GRC}} \left[ \sum_{icc=1}^{N_{cc}} \mathbf{x}_{c(icc)} V_{icc} + \sum_{irg=1}^{N_{rg}} \mathbf{x}_{c(irg)} \Delta x \Delta y \Delta z \right] \quad (\text{C.5})$$

Where  $\mathbf{x}_{c(irg)}$  is the cell center location for regular cell  $irg$ , and the scalar components in each coordinate direction  $\{\hat{\mathbf{i}}, \hat{\mathbf{j}}, \hat{\mathbf{k}}\}$  of cut-cell centroids  $\mathbf{x}_{c(icc)}$  are obtained from:

$$x_{ci(icc)} = \frac{1}{V_{icc}} \int_{\Omega_{icc}} \nabla \cdot \mathbf{F}_{c(i)} dV = \frac{1}{V_{icc}} \int_{\partial\Omega_{icc}} \mathbf{F}_{c(i)} \cdot \hat{\mathbf{n}} dA = \frac{1}{2V_{icc}} \sum_{icf=1}^{ncf} (\hat{\mathbf{e}}_i \cdot \hat{\mathbf{n}}_{icf}) \int_{\Omega_{icf}} x_i^2 dA \quad (\text{C.6})$$

where  $\mathbf{F}_{c(i)} = 1/2x_i^2 \hat{\mathbf{e}}_i$ . Here,  $x_i = \{x, y, z\}$  and  $\hat{\mathbf{e}}_i = \{\hat{\mathbf{i}}, \hat{\mathbf{j}}, \hat{\mathbf{k}}\}$ .

The centroid of the domain  $\Omega$  is:

$$\mathbf{x}_\Omega = \frac{1}{V_\Omega} \sum_{nm=1}^M \mathbf{x}_{nm} V_{nm} \quad (\text{C.7})$$

where  $\mathbf{x}_{nm} = \mathbf{x}_{low,nm} + \frac{1}{2}(L_{x,nm}, L_{y,nm}, L_{z,nm})$ , where  $\mathbf{x}_{low,nm}$  is the vector of low boundary coordinates for mesh  $nm$ . In the single mesh cone problem (Sec. 16.3.1)  $\mathbf{x}_{low,1} = (-1.5D_B, -1.5D_B, -2D_B)$ .

Also, the centroid  $\mathbf{x}_B$  of the discretized solid can be computed applying equation (C.6) to the surface triangulation  $\tau$ , in same manner to what was done for cut-faces. From domain and solid the centroid of the  $G$  region can be obtained as:

$$\mathbf{x}_{GB} = \frac{1}{V_{GB}} [\mathbf{x}_\Omega V_\Omega - \mathbf{x}_B V_B] \quad (\text{C.8})$$

Consistency of the computed centroids requires that  $\mathbf{x}_{GRC}$  and  $\mathbf{x}_{GB}$  should correspond.